An International Forum For The AE Science and Technology

JOURNAL OF ACOUSTIC EMISSION

Vol.19/January-December 2001

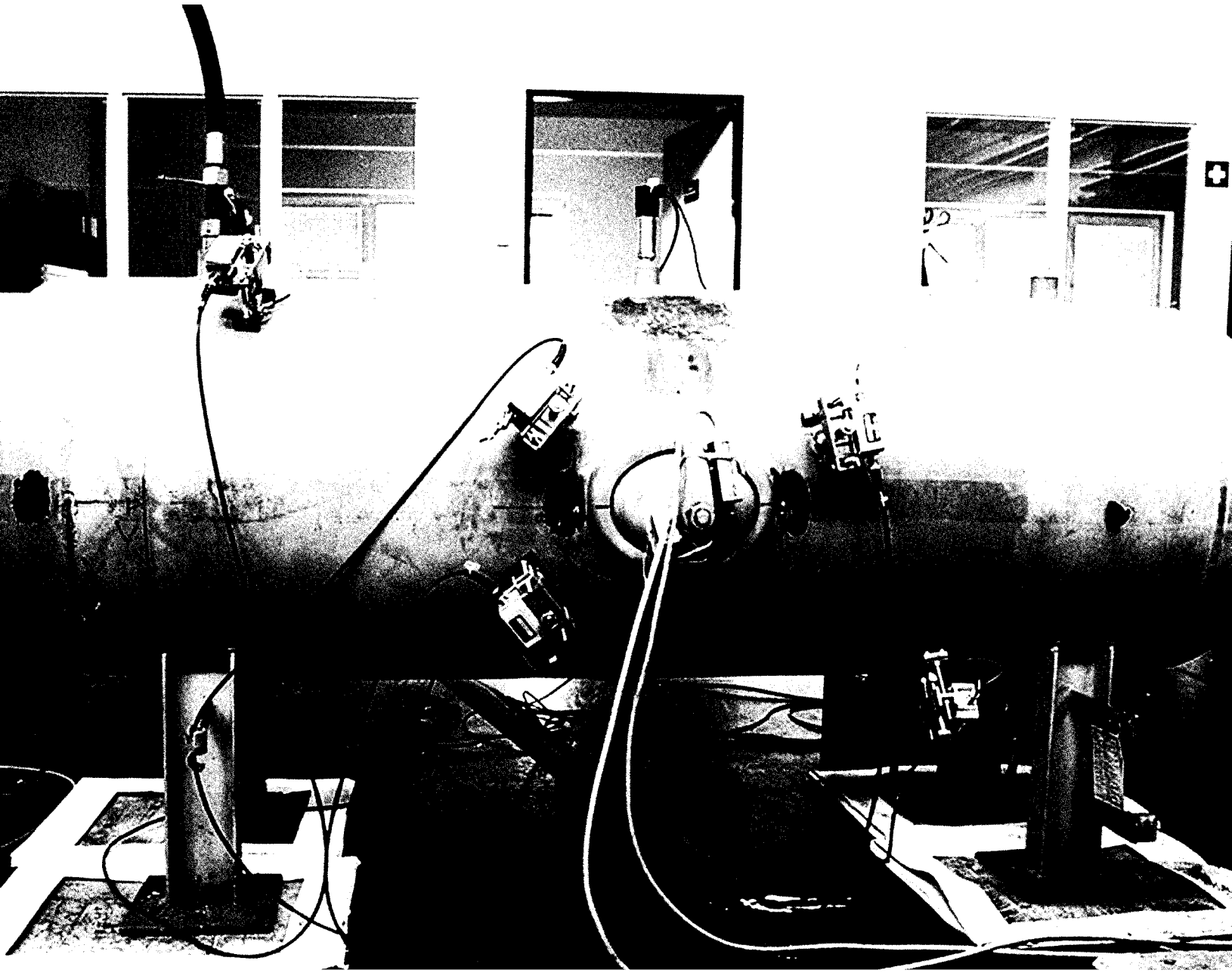

Pressure Vessel Test at Vienna University of Technology

Endorsed by AEWG and EWGAE

Published by
Acoustic Emission Group
Encino, CA USA

An International Forum For The AE Science and Technology

JOURNAL OF ACOUSTIC EMISSION

Vol.19/January-December 2001

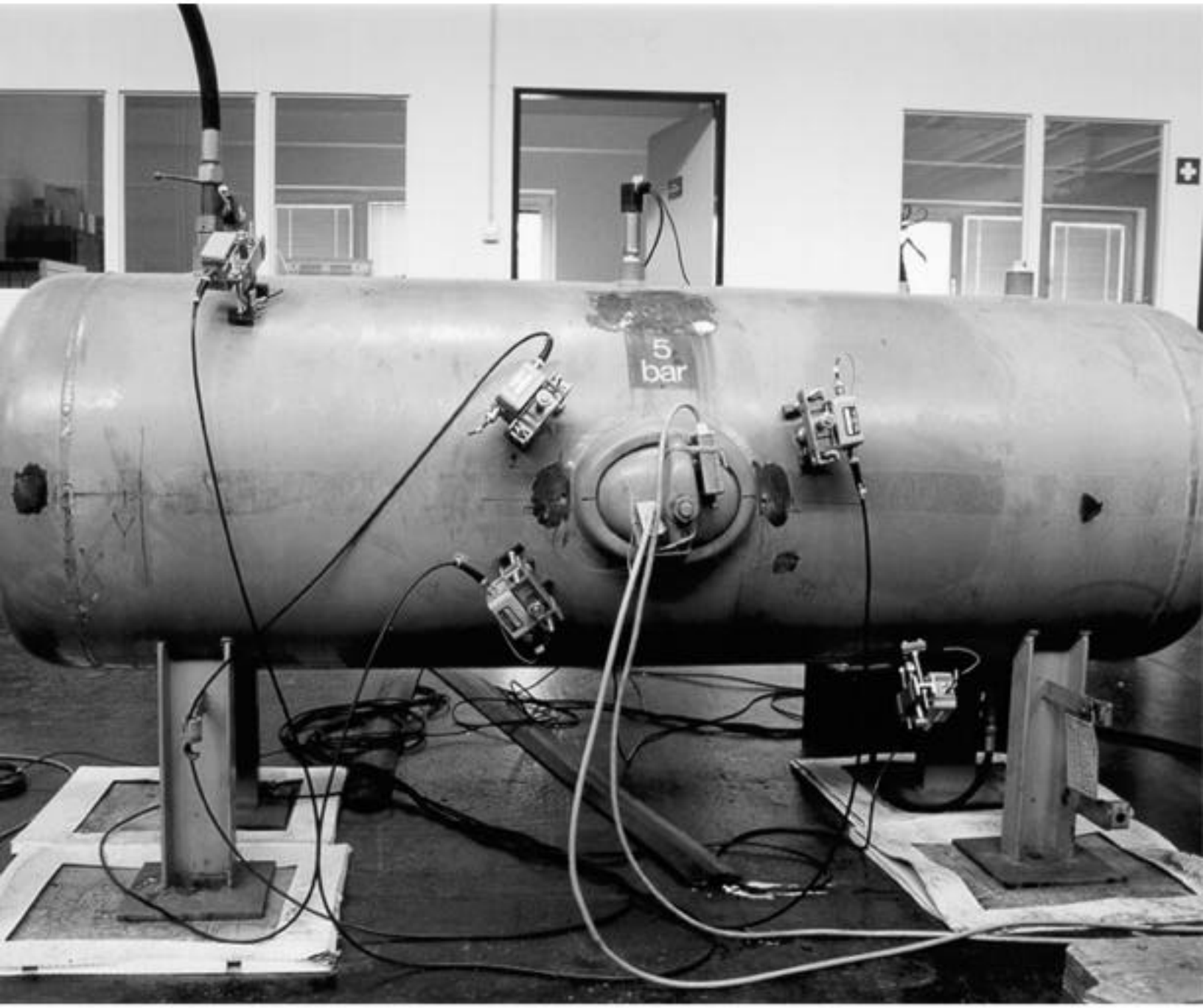

Pressure Vessel Test at Vienna University of Technology

Endorsed by
AEWG
and
EWGAE

Published by
Acoustic Emission Group
Encino, CA USA

JOURNAL OF ACOUSTIC EMISSION
VOLUME 19, 2001

You need a software that can read a pdf-file. Two folders are provided for Windows 95/98/ME/2000 and for Macintosh. Each contains Adobe Acrobat Reader® Installer (ACRD5ENU.EXE or Reader Installer). Install one first before going further.

Adobe Acrobat®, which can be purchased from Adobe: www.adobe.com, or from other suppliers, will enable you to utilize "Search" function using an INDEX file provided (in the Index folder). This allows you to perform full-text search (Launch Acrobat and choose Search button in the toolbar. See Acrobat Search.pdf for detail. Go also to "Using the Search command" in the Acrobat online help.)

Contents are listed below and in **19Conts.pdf.** Authors Index, selected authors' e-mail, AE Literature, and meeting calendar are also available in the 19Conts file. Individual papers have file names of **19-xxx.pdf**, with xxx as their first page number.

Online Text: The pdf files of Volume 19 will become available online (but with security code) soon. Look for them at www.e-jae.com.

ISSN 0730-0050 Coden JACEDO

VIEWING AN ARTICLE

A. Use Adobe Acrobat Reader® (or Acrobat®) and open an individual file, 19-xxx.pdf.
B. Open READ-ME.pdf file, go to CONTENTS and browse the titles and authors, use a HAND tool of Acrobat and click on the file you want to open.

CONTENTS

AE LITERATURE (CARP, Texas DOT, Wavelet, Indices, Meetings)

EWGAE 2002 (Prague, Czech Rep.) IAES-16 (Tokushima, Japan)

JAE Cumulative Index for vol. 1-10, 1982-1992

JAE Cumulative Index for vol. 11-18, 1993-2000

2002 SUBSCRIPTION RATE

Base rate (CD-ROM) for one year		$ 96.00
Add Postage of	U.S. - Priority rate	$ 8.00
	All others - Air mail rate	$ 8.00
CD-ROM + printed copy, surface mail: add		$ 40.00
New for 2002 Print copy only	surface	$134.00

VISA and Mastercard orders accepted. Payment must be in U.S. dollars drawn on a U.S. bank. Bank transfer accepted. (Account No. 080-03416470) at
California Bank and Trust, San Fernando Valley Office
16140 Ventura Blvd,
Encino, CA 91436 USA

One volume of four issues per year through vol. 17. Index included in the last issue. Back issues available at $50 per volume for Vols. 1-3, $90 per volume for Vols. 4-8, $96 per volume for Vols. 9-18. (CD-ROM for Vol. 18). US surface postage $8 per volume. For Canada and overseas surface delivery, add $11 and for air mail, add $30 per volume (shipping charges will be adjusted for multi-volume order).

All orders should be sent to (or Fax 1-818-990-1686): Note our new address.
Acoustic Emission Group
PMB 409, 4924 Balboa Blvd.,
Encino, CA 91316 USA

For inquiry through Internet, use the following address: ono@ucla.edu
Editor-Publisher Kanji Ono Tel. (310) 825-5233
Publication Date of This Issue (Volume 19): 30 November 2001.

An International Forum For The AE Science and Technology

JOURNAL OF ACOUSTIC EMISSION

Vol.19/January-December 2001

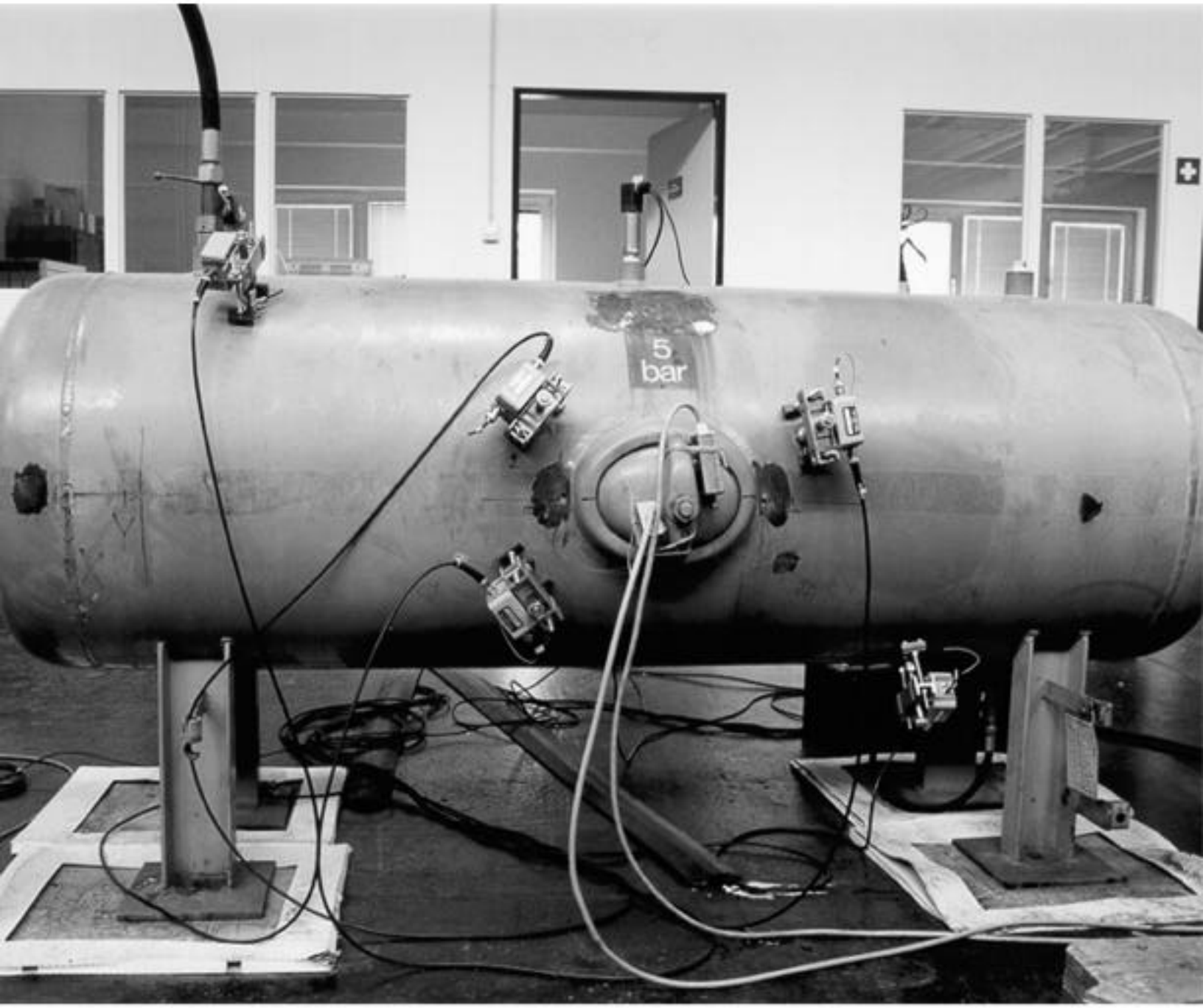

Pressure Vessel Test at Vienna University of Technology

Endorsed by
AEWG
and
EWGAE

Published by
Acoustic Emission Group
Encino, CA USA

JOURNAL OF ACOUSTIC EMISSION

1. Aims and Scope of the Journal

Journal of Acoustic Emission is an international journal designed to be of broad interest and use to both researcher and practitioner of acoustic emission. It will publish original contributions of all aspects of research and significant engineering advances in the sciences and applications of acoustic emission. The journal will also publish reviews, the abstracts of papers presented at meetings, technical notes, communications and summaries of reports. Current news of interest to the acoustic emission communities, announcements of future conferences and working group meetings and new products will also be included.

Journal of Acoustic Emission includes the following classes of subject matters;

A. Research Articles: Manuscripts should represent completed original work embodying the results of extensive investigation. These will be judged for scientific and technical merit.

B. Applications: Articles must present significant advances in the engineering applications of acoustic emission. Material will be subject to reviews for adequate description of procedures, substantial database and objective interpretation.

C. Technical Notes and Communications: These allow publications of short items of current interest, new or improved experimental techniques and procedures, discussion of published articles and relevant applications.

D. AE Literature section will collect the titles and abstracts of papers published elsewhere and those presented at meetings and conferences. Reports and programs of conferences and symposia will also be presented.

E. AE Program and Data Files: Original program files and data files that can be read by others and analyzed will be distributed in CD-ROM.

Reviews, Tutorial Articles and Special Contributions will address the subjects of general interest. Nontechnical part will cover book reviews, significant personal and technical accomplishments, current news and new products.

2. Endorsement

Acoustic Emission Working Group (AEWG), European Working Group on Acoustic Emission (EWGAE), Committee on Acoustic Emission from Reinforced Composites (CARP), and Acoustic Emission Working Group of India have endorsed the publication of Journal of Acoustic Emission.

3. Governing Body

The Editor and Associate Editors will implement the editorial policies described above. The Editorial Board will advise the editors on any major change. The Editor, Professor Kanji Ono, has the general responsibility for all the matters. Associate Editors assist the review processes as lead reviewers. Mr. T.F. Drouillard is responsible for the AE Literature section. The members of the Editorial Board are selected for their knowledge and experience on AE and will advise and assist the editors on the publication policies and other aspects. The Board presently includes the following members:

4. Publication

Journal of Acoustic Emission is published annually in CD-ROM by Acoustic Emission Group, PMB 409, 4924 Balboa Blvd, Encino, CA 91316. It may also be reached at 6531 Boelter Hall, University of California, Los Angeles, California 90095-1595 (USA). tel. 310-825-5233. FAX 818-990-1686. e-mail: ono@ucla.edu

5. Subscription

Subscription should be sent to Acoustic Emission Group. Annual rate for 2001 and 2002 is US $104.00 including CD-ROM delivery, by priority mail in the U.S. and by air for Canada and elsewhere. For additional print copy, add $32. Overseas orders must be paid in US currencies with a check drawn on a US bank. VISA/MC accepted. Inquire for individual (with institutional order) and bookseller discounts.

6. Advertisement

No advertisement will be accepted, but announcements for books, training courses and future meetings on AE will be included without charge.

ISSN 0730-0050

- CODEN: JACEDO

JOURNAL OF ACOUSTIC EMISSION, VOLUME 19, 2001

CONTENTS

AUTHORS INDEX, Volume 19

e-MAIL ADDRESSES OF SELECTED AUTHORS

Mulu Bayray <mbayray@iaa1.iaa.tuwien.ac.at>

Juergen Bohse <Juergen.Bohse@bam.de>

Phil Cole <philcoleuk@aol.com>

Leszek Golaski <bmtlg@tu.kielce.pl>

Marvin Hamstad <hamstad@boulder.nist.gov>, <mhamstad@du.edu>

Yakichi Higo <yhigo@pi.titech.ac.jp>

Ken-ichi Itakura <itakura@epsilon2.csse.muroran-it.ac.jp>

T. Kamada <kamada@cc.gifu-u.ac.jp>

Chiaki Kato <multi@popsvr.tokai.jaeri.go.jp>

Atsushi Korenaga <korenaga@mel.go.jp>

Dan Lindahl <dan.lindahl@csm.se>

M. Maeda <maeda@hihakaikensa.co.jp>

Gerd Manthei <gmugmrh@t-online.de>

David Mba <D.Mba@cranfield.ac.uk>

Isamu Ohsawa<ohsawa@ygg.naoe.t.u-tokyo.ac.jp>

Masayasu Ohtsu <ohtsu@gpo.kumamoto-u.ac.jp>

Kanji Ono <ono@ucla.edu>

Alan Proust <epa.mkg@wanadoo.fr>

Gary Qi <gangqi@memphis.edu>

Tomoki, Shiotani <shiotani@mx1.alpha-web.ne.jp>, <t.shiotani@citg.tudelft.nl>

Thomas Spies <thomas.spies@bgr.de>

Mikio Takemoto <takemoto@me.aoyama.ac.jp>

Sotirios J. Vahaviolos <sotirios@pacndt.com>

Kenichi Yoshida <yoshida@me.tokushima-u.ac.jp>

Shigenori Yuyama <aeyuyama@sh0.po.iijnet.or.jp>

AE LITERATURE

TWO SECURE PDF FILES: CARP and TEXAS DOT

The following two documents were provided by the courtesy of Professor Tim Fowler, University of Texas. Both documents are working papers at this time and should be treated as "to be copyrighted" materials. That is, these are not in the public domain. Since the CARP is dormant at present, the CARP document publication is not imminent, while Texas DOT is expected to complete its work soon. However, both will be valuable to AE workers and are included here with security code. If interested, please send request for the security codes to the Editor at ono@ucla.edu and the best possible accommodation will be attempted.

CARP, RECOMMENDED PRACTICE FOR ACOUSTIC EMISSION EVALUATION OF FIBER REINFORCED PLASTIC (FRP) TANKS AND PRESSURE VESSELS, Draft I, October 1999. (CARP.PDF)

TEXAS DEPARTMENT OF TRANSPORTATION, PROCEDURE FOR ACOUSTIC EMISSION MONITORING OF PRESTRESSED CONCRETE GIRDERS, Draft B, May 2001. (TEXAS.PDF)

AGU-VALLEN WAVELET

A free software, *AGU-Vallen Wavelet* is online and can be downloaded as Zip-file. A password is required to unpack the file, which can be requested from the same site.

http://www.vallen.de/wavelet

Text file of the site follows:

AGU-Vallen Wavelet

AGU-Vallen Wavelet is a tool which allows to calculate and display the wavelet transform on individual waveforms. AGU-Vallen wavelet is free!! See below how to request it.

AGU-Vallen Wavelet has been developed in collaboration between Vallen-Systeme GmbH and Aoyama Gakuin University (AGU), Tokyo, Japan. The AGU group has pioneered in the research of wavelet analysis in the field of Acoustic Emission and Vallen has actively generated software tools.

About Wavelet Transformation

A wavelet transform (WT) of an AE signal provides information which wave modes carry significant energy and where in a mode the energy as a function of frequency and time is to be found. Thereby a WT can communicate very useful information. In the following diagram you see an example for a waveform (top) and the corresponding wavelet transform (below). The superposed curves show the result of a dispersion curve calculation (by Vallen Dispersion). The wave modes are identified by arrows. [See figures at Vallen site. Ed.]

Contributors

AGU-Vallen Wavelet has been developed in collaboration between Vallen-Systeme GmbH and with Aoyama Gakuin University (AGU), Tokyo, Japan. The AGU group has pioneered in the research of wavelet analysis in the field of Acoustic Emission and Vallen has actively generated software tools. The following is a list of persons, who have significantly contributed to the AGU-Vallen Wavelet program:

Prof. Mikio Takemoto, Aoyama Gakuin University (AGU), Tokyo, Japan

Head of Materials Science Laboratory, Aoyama Gakuin University (AGU). Prof. Takemoto has guided the development of the AGU-wavelet from the first stage. Together with Prof. Ono (UCLA), Prof. Takemoto ignited the initial spark to start the development of AGU-Vallen Wavelet project.

Prof. Kanji Ono, University of California (UCLA), Los Angeles, USA

Prof. Ono has participated in wavelet research at AGU and facilitated a contact between AGU and Vallen. Prof. Ono is author of many AE and wavelet papers published or presented at international conferences. See also the literature references at the end of this page.

Prof. Yasuhisa Hayashi*, Shizuoka University, Shizuoka, Japan

Dr. Hideo Cho*, Tohoku University, Sendai, Japan

Dr. Hiroaki Suzuki*, Chiyoda Co., Kawasaki, Japan

Tetsuo Kinjo**, Ishikawajima-Harima Heavy Industries Co. Ltd.

* Former assistants of Materials Science Laboratory in AGU.

** Graduate of Graduate School, AGU.

Prof. Hayashi, Dr. Suzuki and Mr. Kinjo created the initial AGU-wavelet software for Acoustic Emission analysis. Prof. Hayashi and Dr. Cho demonstrated the usage of wavelet transform for determining the group velocity of elastic waves.

Dr. Yoshihiro Mizutani, Aoyama Gakuin University (AGU), Tokyo, Japan

Assistant, Experimental Solid Mechanics Laboratory, AGU. Graduate of Materials Science Laboratory in AGU.Dr. Mizutani completely upgraded the original AGU wavelet algorithm for arbitrary frequency analysis. His algorithm is implemented in the AGU-Vallen Wavelet program with kind permission of Dr. Mizutani and Prof. Takemoto.

Prof. Marvin A. Hamstad, National Institute of Standards and Technology (NIST), Boulder, Co USA and University of Denver, Co. USA

Prof. Hamstad is the very first scientific user of AGU-Vallen Wavelet. He accompanied the development of the program and contributed data samples created by finite element modelling (FEM) and an overview presentation about the use and value of wavelet transformation. This presentation together with FEM samples is included in the distribution of AGU-Vallen Wavelet with the kind permission of Prof. Hamstad and can be downloaded below.

Presentation of Professor Hamstad

An Illustrated Overview of the Use and Value of a Wavelet Transformation to Acoustic Emission Technology (hamstad.pdf: ca. 661 KB)

References

Takemoto M., Nishino H., Ono K., "Wavelet Transform - Applications to AE Signal Analysis", Acoustic Emission - Beyond the Millennium, Elsevier (2000), pp. 35-56.

Suzuki H., Kinjo T., Hayashi Y., Takemoto M., Ono K., Appendix by Hayashi Y., "Wavelet Transform of Acoustic Emission Signals", Journal of Acoustic Emission, Vol. 14, No. 2 (1996, April-June), pp. 69-84.

Hayashi Y., Ogawa S., Cho H., Takemoto M., "Non-contact estimation of thickness and elastic properties of metallic foils by wavelet transform of laser-generated waves", NDT and E International, Vol. 32, No. 1 (1999, January) pp. 21-27 (1999).

Yamada H., Mizutani Y., Nishino H., Takemoto M. Ono K., "Lamb Wave Source Location of Impact on Anisotropic Plates", Journal of Acoustic Emission, Vol. 18, (2000, December), pp. 51-60.

INDICES OF J. OF ACOUSTIC EMISSION, 1982-2000

Two pdf files are included with this CD-ROM. These are

JAE1-10.pdf (for 1982-1992) and JAE11-18.pdf (for 1993-2000)

and list the contents of Journal of Acoustic Emission from the beginning. These are indexed together with Volume 19 so that subject and author search can be made.

MEETING CALENDAR

EWGAE 2002: 25-th European Conference on Acoustic Emission Testing

September 11 - 13, 2002, Prague, Czech Republic

EWGAE 2002 will be organised by European Working Group on Acoustic Emission, Czech Society for Non-destructive Testing (Acoustic Emission Working Group), Czech Technical University in Prague, Brno University of Technology.

October 31, 2001	• submitting paper abstract (200-300 words)
November 2001	• notification of acceptance, second call for papers
May 31, 2002	• full papers, preliminary payment
August 2002	• announcement of the final programme

Further information on web site: http://www.cndt.cz: E-mail: cndt@cndt.cz
See also EWGAE.pdf.

The 16-th International Acoustic Emission Symposium (IAES-16)

November 12 – 15, 2002: The University of Tokushima, Tokushima, JAPAN

Prospective authors are requested to submit title, author's names, affiliation and address by fax or e-mail with an abstract of 100-200 words with key words. The official language of the symposium and the proceedings will be English. IAES-16 will be organized by the Japan Soc. For Non-Destructive Inspection, T. Kishi and Y. Higo, co-chairs. Please note dates changed from an earlier announcement.

April 30, 2002	Deadline for arrival of abstract.
June 30, 2002	Notification of acceptance and instruction for authors.
August 31, 2002	Deadline for full papers. Registration and remittance of fee.
September 30, 2002	Second announcement and program.

Symposium secretary and e-Mail Address:
Prof. Kenichi YOSHIDA
E-mail: yoshida@me.tokushima-u.ac.jp: See also IAES-16.pdf.

The 45-th Meeting of AEWG

Details to be announced. To be held in 2002 at Northwestern University, Evanston, IL.
Send inquiry to David Prine (dprine@northwestern.edu).

JOURNAL OF ACOUSTIC EMISSION, VOLUME 19

Two folders are provided for Windows 95/98/ME/2000 and for Macintosh. Each contains Adobe Acrobat Reader® Installer (ACRD4ENU.EXE or Reader Installer). If you don't have a software that can read a pdf-file, install one first. Adobe Acrobat®, which can be purchased from Adobe: www.adobe.com, will enable you to utilize "Search" function using an INDEX file provided (in the Index folder). This allows you to perform full-text search (Launch Acrobat and choose Edit > Search > Quary.)

Contents are listed in 19Conts.pdf. Authors Index, selected authors' e-mail, AE Literature, and meeting calendar are also available in the 19Conts file.

Online Text: The pdf files of Volume 19 will become available online (but with security code) soon. Look for them at www.e-jae.com.

ISSN 0730-0050 Coden JACEDO

2002 SUBSCRIPTION RATE

Base rate (CD-ROM) for one year			$ 96.00
Add Postage of	U.S. - Priority rate		$ 8.00
	All others - Air mail rate		$ 8.00
CD-ROM + printed copy, surface mail: add			$ 40.00
New for 2002	Print copy only	surface	$134.00

VISA and Mastercard orders accepted. Payment must be in U.S. dollars drawn on a U.S. bank.
Bank transfer accepted. (Account No. 080-03416470) at

California Bank and Trust
San Fernando Valley Office
16140 Ventura Blvd,
Encino, CA 91436 USA

One volume of four issues per year through vol. 17. Index included in the last issue. Back issues available at $50 per volume for Vols. 1-3, $90 per volume for Vols. 4-8, $96 per volume for Vols. 9-18. (CD-ROM for Vol. 18). US surface postage $8 per volume. For Canada and overseas surface delivery, add $11 and for air mail, add $30 per volume (shipping charges will be adjusted for multi-volume order).

All orders should be sent to (or Fax 1-818-990-1686): Note our new address.

Acoustic Emission Group
PMB 409, 4924 Balboa Blvd.
Encino, CA 91316 USA

For inquiry through Internet, use the following address: ono@ucla.edu
Editor-Publisher Kanji Ono Tel. (310) 825-5233
Publication Date of This Issue (Volume 19): 30 November 2001.

Notes for Contributors

1. General

The Journal will publish contributions from all parts of the world and manuscripts for publication should be submitted to the Editor. Send to:

Professor Kanji Ono, Editor - JAE
6531 Boelter Hall, MSE Dept.
University of California
Los Angeles, California 90095-1595 USA
FAX (1) 818-990-1686
e-mail: ono@ucla.edu

Authors of any AE related publications are encouraged to send a copy for inclusion in the AE Literature section to:

Mr. T.F. Drouillard, Associate Editor - JAE
11791 Spruce Canyon Circle
Golden, Colorado 80403 USA

Only papers not previously published will be accepted. Authors must agree to transfer the copyright to the Journal and not to publish elsewhere, the same paper submitted to and accepted by the Journal. A paper is acceptable if it is a revision of a governmental or organizational report, or if it is based on a paper published with limited distribution.

Compilation of annotated data files will be accepted for inclusion in CD-ROM distribution, so that others can share in their analysis for research as well as training. ASCII or widely accepted data formats will be required.

The language of the Journal is English. All papers should be written concisely and clearly.

2. Page Charges

No page charge is levied. One copy of CD-ROM will be supplied to the authors free of charge.

3. Manuscript for Review

Manuscripts for review need only to be typed legibly; preferably, double-spaced on only one side of the page with wide margins. The title should be brief. An abstract of 100-200 words is needed for Research and Applications articles. Except for short communications, descriptive heading should be used to divide the paper into its component parts. Use the International System of Units (SI).

References to published literature should be quoted in the text citing authors and the year of publication. These are to be grouped together at the end of the paper in alphabetical and chronological order. Journal references should be arranged as below. Titles for journal or book articles are helpful for readers, but may be omitted.

H.L. Dunegan, D.O. Harris and C.A. Tatro (1968), Eng. Fract. Mech., 1, 105-122.

Y. Krampfner, A. Kawamoto, K. Ono and A.T. Green (1975), "Acoustic Emission Characteristics of Cu Alloys under Low-Cycle Fatigue Conditions," NASA CR-134766, University of California, Los Angeles and Acoustic Emission Tech. Corp., Sacramento, April.

A.E. Lord, Jr. (1975), Physical Acoustics: Principles and Methods, vol. 11, eds. W. P. Mason and R. N. Thurston, Academic Press, New York, pp. 289-353.

Abbreviations of journal titles should follow those used in the ASM Metals Abstracts. In every case, authors' initials, appropriate volume and page numbers should be included. The title of the cited journal reference is optional.

Illustrations and tables should be planned to fit a single page width (6.5"). For the reviewing processes, these need not be of high quality, but submit glossy prints or equivalent electronic files with the final manuscript. Lines and letters should be legible.

4. Review

All manuscripts will be judged by qualified reviewer(s). Each paper is reviewed by one of the editors and may be sent for review by members of the Editorial Board. The Board member may seek another independent review. In case of disputes, the author may request other reviewers.

5. Electronic Media

This Journal will be primarily distributed electronically by CD-ROM. In order to expedite processing and minimize errors, the authors are requested to submit electronic files or floppy disk copy of the paper. We can read Macintosh and IBM PC formats. On the INTERNET, you can send an MS Word file or the text portion to "ono@ucla.edu".

6. Color Illustration

We can process color illustration needed to enhance the technical content of an article. With the new format, authors are encouraged to use them.

ACOUSTIC EMISSION EXAMINATION OF MODE I, MODE II AND MIXED-MODE I/II INTERLAMINAR FRACTURE OF UNIDIRECTIONAL FIBER-REINFORCED POLYMERS

JÜRGEN BOHSE and JIHUA CHEN *

BAM, Federal Institute for Materials Research and Testing,
Unter den Eichen 87, D-12200 Berlin, Germany
* Technical University of Berlin, Institute of Nonmetallic Materials
Englische Strasse 20, D-10587 Berlin, Germany

ABSTRACT

The interlaminar fracture behavior of unidirectional fiber-reinforced GF/Epoxy and GF/Polyamide-12 laminates is evaluated by mode I, mode II and mixed-mode I/II fracture mechanics tests combined with acoustic emission (AE) monitoring. New fracture criteria of the micro-crack initiation point ($INIT_{locAE}$) and the start of macroscopic delamination ($INI-PROP_{locAE}$) propagating along the whole crack front are defined by means of time-dependent linear location of AE sources. Furthermore, by AE examination, the length l_D of the damage zone around the delamination tip is determined. From the analysis of the frequency power spectra of individual AE signals, matrix cracking and fiber/matrix debonding are identified as micro-failure mechanisms and the energy contribution of these mechanisms in specific fracture stages is calculated. The damage zone geometry is calculated by finite element (FE) modeling of the elastic strain-energy distribution around the delamination tip using the critical strain-energy W_c. The critical strain-energy was determined experimentally with three-point bending tests by means of AE monitoring. Results indicate that the micro-failure mechanisms are induced by the delamination process itself as well as by compression of the flexure-loaded cantilevers. The height of the damage zone is approximated by $2r_D \approx l_D/10$.

1. INTRODUCTION

According to the standard procedure [1], crack initiation is characterized by the onset of visually recognizable delamination growth on the edge of the specimen (VIS-point) or by the onset of non-linearity on the load-displacement curve (NL-point). However, the visual determination of the initiation point and the NL-point is operator-dependent. Sometimes it is difficult to find out the NL-point in the load-displacement curve. Besides, the NL-point is not well defined from the fracture mechanics point of view. Another problem arises from friction between the cantilever surfaces under mode II and mixed-mode I/II loading conditions, which lead to an overestimation of the delamination toughness by use of standard methods. A theoretical calculation of the fracture toughness on the basis of micro-mechanical dissipation mechanisms requires information on which failure mechanisms are activated and on the size of the damage zone [2, 3]. The AE monitoring is a powerful tool for evaluation and interpretation of fracture stages by characterizing (a) the failure on a microscopic scale, (b) the mechanisms involved and (c) the size of the damage zone. In this article, AE results from different interlaminar fracture modes are discussed and a micro-mechanical interpretation of the damage zone is presented.

2. EXPERIMENTAL

Specimens and Materials

Double Cantilever Beam (DCB: mode I), End Notched Flexure (ENF: mode II) and Mixed-Mode Bending (MMB: mixed-mode I/II) fracture mechanics tests on specimens with 120 mm total length, 20 mm width, about 4 mm total thickness and initial delamination length a_0 were performed to measure the critical energy release rate under mode I, mode II and mixed-mode I/II crack loading conditions. A load-introduction with a crosshead speed of 2 mm/min (DCB) and 0.5 mm/min (ENF and MMB) was used. Starter cracks were produced by double layers of Al-foil insert with 20 µm total thickness. The delamination growth was observed visually with an optical microscope on one edge of the specimen as well as by the located AE sources.

Unidirectional continuous reinforced glass-fiber/epoxy (GF/Epoxy) laminates (42% fiber volume; 20-µm fiber diameter) were fabricated by using a hot press and wet impregnation process. Glass-fiber/polyamide-12 (GF/PA-12) laminates (34% fiber volume; 20-µm fiber diameter) were manufactured by special dry powder impregnation of tapes and following hot press process [4].

Delamination Modes and AE Sensor Position

Figure 1 characterizes the loading conditions and the positions of the AE sensors at the examined delamination modes. The vertical arrows show the loading points and directions, *a* is the actual delamination length, *Y* is the thickness direction and *X* is the length direction of the specimen, which also indicates the direction of crack growth and the position of located AE events.

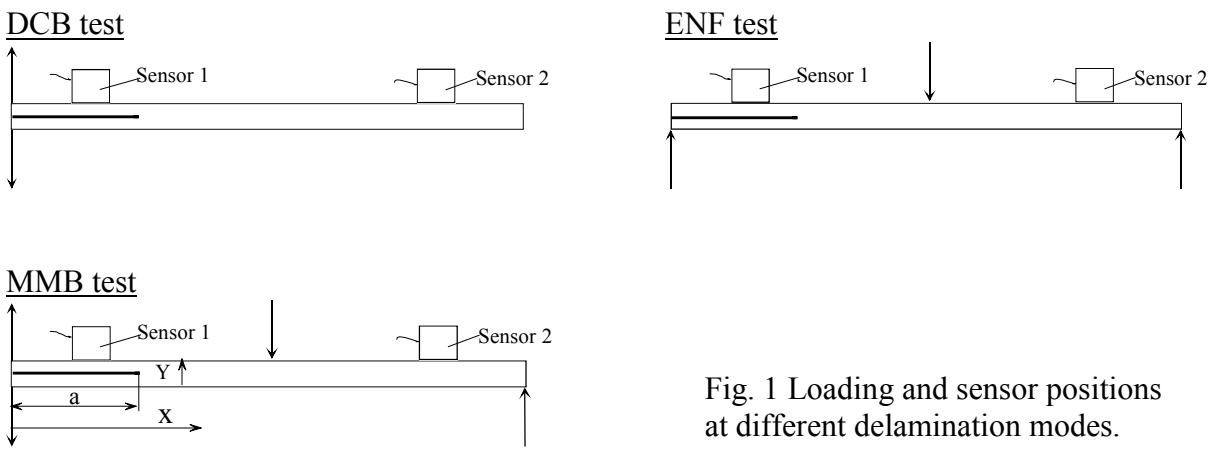

Fig. 1 Loading and sensor positions at different delamination modes.

AE Instrumentation

A two-channel MISTRAS 2001 system (Physical Acoustics Corp.) was used for the determination of AE events and AE sources in a linear-location setup during delamination tests. AE signals were monitored by two wideband transducer (PAC WD) with a sensor spacing of 75 mm, preamplifiers (PAC 1220A) with 40 dB gain and bandpass filters (20 to 1200kHz), fixed thresholds of 40 dB_{AE} and a transient waveform recording with a sampling frequency of 4 MHz.

3. RESULTS

Delamination Behavior and AE Characteristics

The AE examination characterizes microscopic and macroscopic aspects of the delamination. Figure 2a shows the detected AE signals from a DCB fracture test. The characterization of the damage zone length l_D is realized by time-dependent linear location of AE sources around the tip of the delamination (Fig. 2b and Fig. 3). The crack speed has been quantified from the slope.

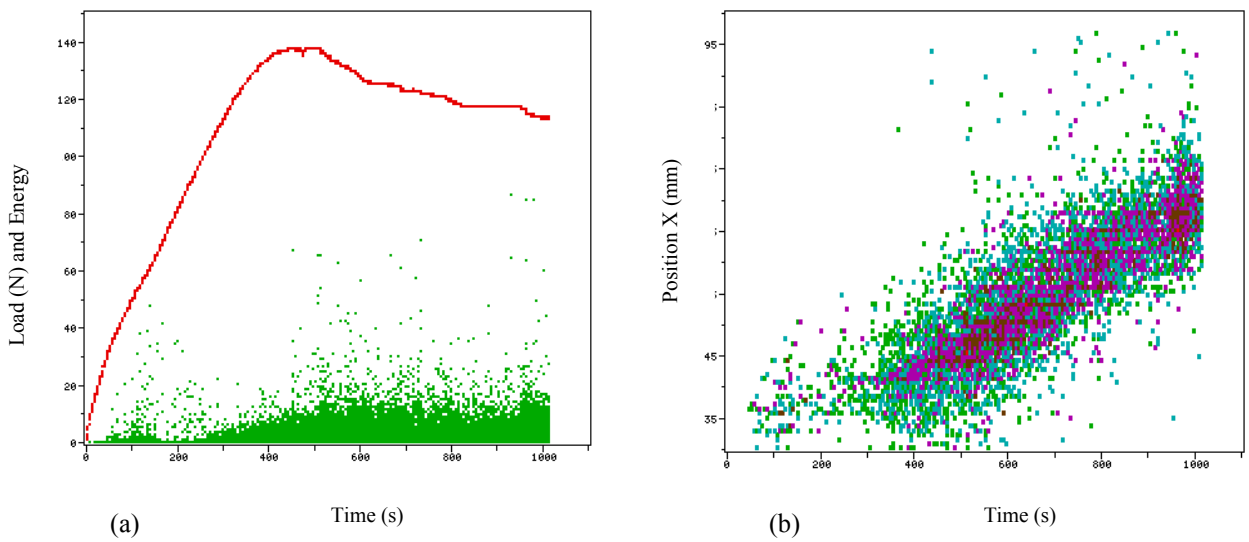

(a) (b)

DCB test (a_0 = 40 mm)

Fig.2 (a) Delamination load (line) and AE signal energy (rel. units, points) and (b) time-dependent position and size of the damage zone determined by location of AE sources with amplitudes at the sensor ≥ 60 dB_{AE} under mode I loading of GF/PA-12.

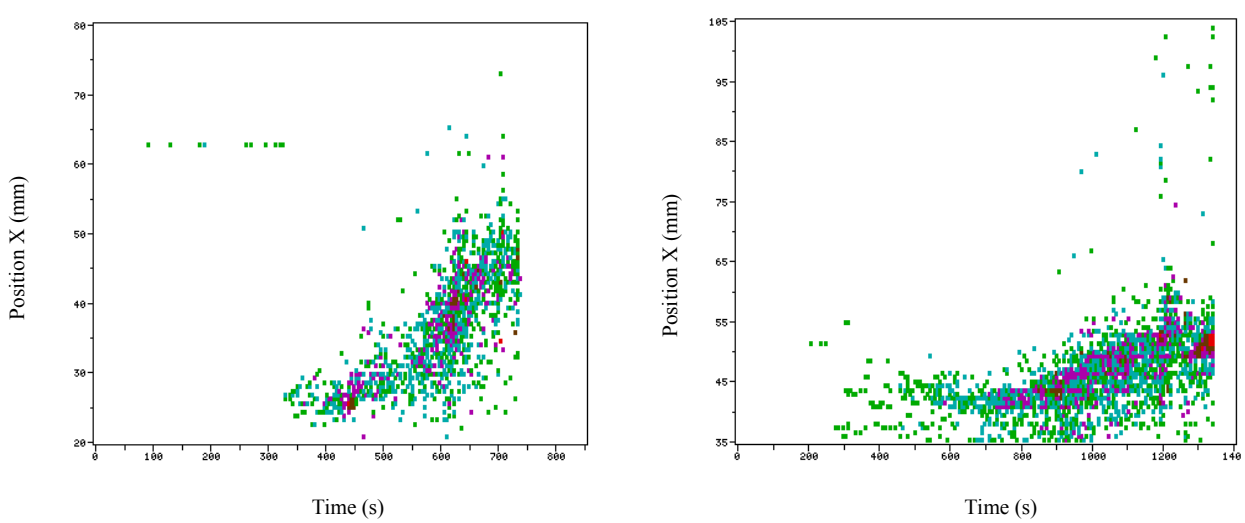

(a) ENF test (a_0 = 25 mm) (b) MMB test (G_I/G_{II} = 4/1; a_0 = 40 mm)

Fig.3 Time-dependent position and size of the damage zones (AE events with amplitudes at the sensor ≥ 60 dB_{AE}) under (a) mode II and (b) mixed-mode I/II loading of GF/PA-12.

The analysis of AE signal parameter combined with a linear location of AE sources gives a higher reliability that recorded signals are emitted really from the delamination process zone. First AE events located near the delamination tip ($X = a_0$) characterize the start of micro-crack initiation ($INIT_{locAE}$). AE location plots also show the movement of the damage zone. This can be used for the determination of the initiation of macroscopic delamination ($INI\text{-}PROP_{locAE}$) propagating along the whole crack front before the maximum load is reached. Fracture criteria derived from location of AE sources reflect an improved definition of the stages of delamination initiation and propagation than the visual criterion and the NL-point.

Calculation of the Interlaminar Fracture Toughness

If criteria derived from the AE event location are applied, the critical energy release rate values, G_{IC}, G_{IIC} and $G_{I/IIC}$ given in Table 1 are calculated. These results are compared with G_C values from NL-points and stable delamination growth (PROP) according to the standard methods [1].

Table 1: Interlaminar fracture toughness calculated from different fracture stages at mode I, mode II and mixed-mode I/II loading conditions.

Composites - Toughness	a_0 mm	B mm	$INIT_{locAE}$ * J/m^2	NL *** J/m^2	$INI\text{-}PROP_{locAE}$ ** J/m^2	PROP *** J/m^2
GF/EP - G_{IC}	40	20	28±4	195±20	388±70	379±53
GF/PA 12 - G_{IC}	40	20	1028±84	3454±161	4801±365	5213±493
- G_{IIC}	25	20	160±36	1700	1512±62	-
- $G_{I/IIC}$ (4/1)	40	20	450±20	1862	2031±276	-
- $G_{I/IIC}$ (1/1)	40	20	510	1228	1251	-

* Calculated with the Corrected Beam Theory from load-displacement point where first AE sources with amplitudes at the sensor ≥ 60 dB_{AE} are located near the delamination tip using a_0 as delamination length.

** Calculated with the Corrected Beam Theory from that point where located AE sources (amplitudes at the sensor ≥ 60 dB_{AE}) indicate a propagation onset of the complete delamination tip using a_0 as delamination length.

*** Average values calculated with the Corrected Beam Theory using a_0 as delamination length for NL-point and actual delamination length for PROP values.

The initiation values $G_C(INIT_{locAE})$ calculated from AE results agree with the theoretically expected tendency: $G_{IC} > G_{I/IIC} > G_{IIC}$. In contrast to NL-points or PROP values according to standard methods, the AE evaluation is based on the delamination initiation on a microscopic level where the friction between the cantilever surfaces is low and hence, the fracture toughness results are not falsified by the friction energies. Besides, it is not possible to determine a $G_C(PROP)$ by the standard methods under mode II and mixed-mode I/II in consequence of the flexure load introduced in front of the delamination tip. However, the $G_C(INI\text{-}PROP_{locAE})$ values based on the AE analysis is able to characterize the beginning of the macroscopic crack propagation under these delamination modes. Table 1 shows that the $G_C(NL)$ values are lower than the $G_C(INI\text{-}PROP_{locAE})$ values. A reason for this phenomenon is damages around the delamination crack surface and in the compression zones of the flexure-loaded cantilevers ($X <$

a_0 in Fig. 2b and Fig. 3b), which yields a non-linear load-displacement curve without delamination propagation. Additional damage is detected at the upper load point ($X \approx 62.5$ mm) during ENF tests (Fig. 3a).

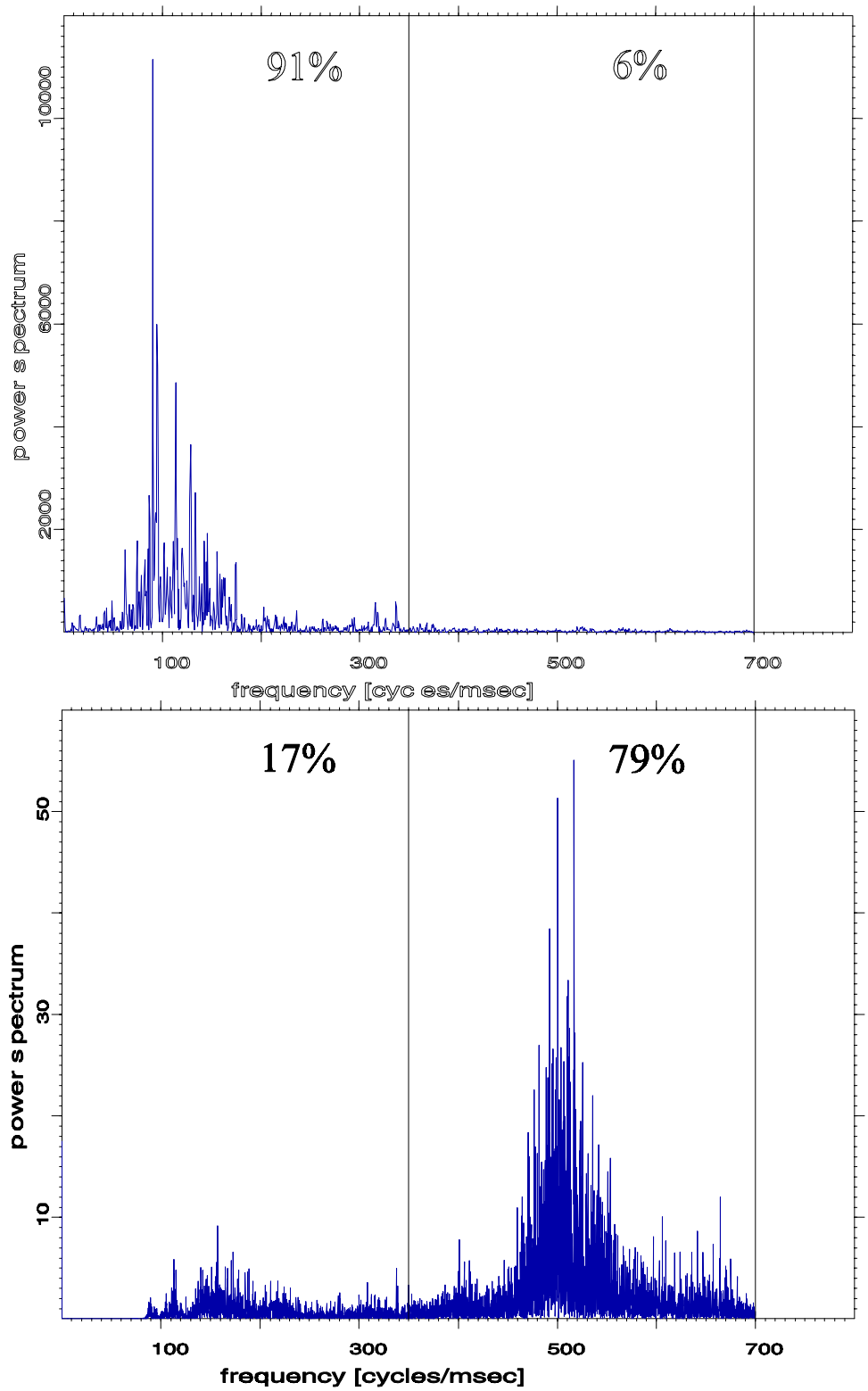

Fig. 4. Averaged AE power spectra of matrix cracking (top) and fiber breakage (bottom) in single fiber CF/Epoxy.

Identification of AE Source Mechanisms

A micro-mechanical fracture model was developed to approximate the contribution of matrix and interface mechanisms to the interlaminar fracture energy. A correlation of the AE energy rate with the delamination energy release rate was found [2, 3].

By means of model specimens, we stimulated different AE source mechanisms. Characteristic relaxation frequencies in the ranges between 100 to 350 kHz (matrix cracking) and 350 to 700 kHz (fiber break) are good candidates for distinguishing the mechanisms by a power spectrum analysis of the AE waveforms (Fig. 4).

For the assignment of AE waves to single failure mechanisms a 70%-power criterion was applied. It is assumed that matrix cracks have at least 70% of the signal power in the 100 to 350 kHz and fiber break in the 350 to 700 kHz frequency interval. All signals in-between are expected to be released from fiber/matrix debonding processes. The procedure of selection and classification of AE signals is described elsewhere [5]. AE signals from micro-cracks at the initiation of delamination process belongs to matrix cracking (Fig. 5). Fiber/matrix debonding is detected if the whole delamination front propagates.

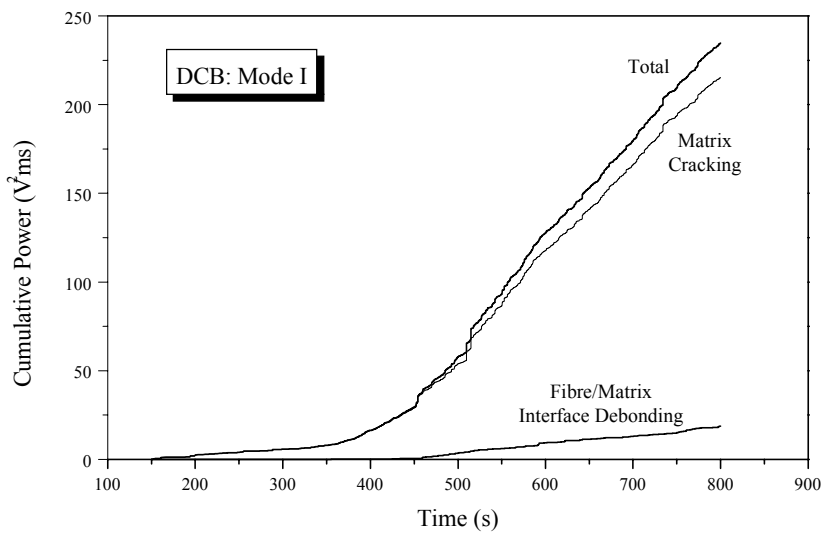

(a)

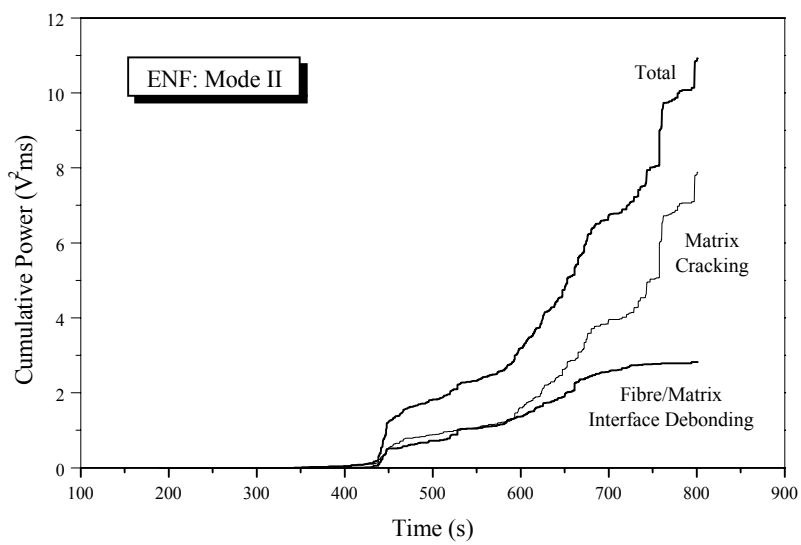

(b)

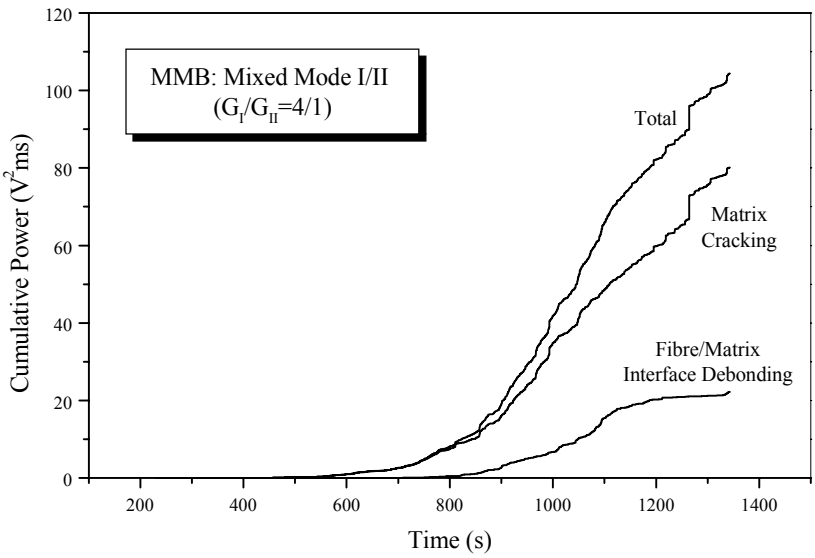

(c)

Fig. 5 Accumulated AE power from specific micro-failure mechanisms in GF/PA-12 under different delamination modes. (a) DCB; (b) ENF; (c) MMB.

The results in Fig. 5 show that fracture modes with components of shear failure (mode II and mixed-mode I/II) reduce the AE power absolutely but cause relatively higher interfacial energies. The power from fiber breakage is negligible in all cases.

Micro-Mechanical Interpretation of the Damage Zone Geometry

From the stress intensity concept of linear-elastic fracture mechanics, equation (1) calculates the size $2r_D$ of damage zones as:

$$2r_D^{(i)} = 2\beta \frac{G_{Ic} E_c}{(\sigma_c^{(\mathrm{int})})^2} \qquad (1)$$

with mode I delamination energy G_{Ic}, Young's modulus E_c of the composite and a material specific factor β. The critical stress $\sigma_c^{(\mathrm{int})}$ for initiation of fiber/matrix debonding depends on the interface adhesion and has been quantified by AE examination [3].

By FE modeling the elastic strain-energy distribution around the delamination tip was calculated (Fig. 6). In Fig. 6 (only one cantilever is shown), two density maxima are observed. One is near the crack surface around the delamination tip and the other one is in the opposite compressive zone of the flexure-loaded cantilever.

From three-point bending tests combined with AE measurements (Fig. 7) the critical strain-energy density W_c for initiation of damages by equation (2) was determined:

$$W_c = \frac{\sigma_c^2}{2E_f} \qquad (2)$$

with flexure modulus E_f and critical stress σ_c in the tensile zone of flexure-loaded specimens where AE signals with defined amplitudes are detected.

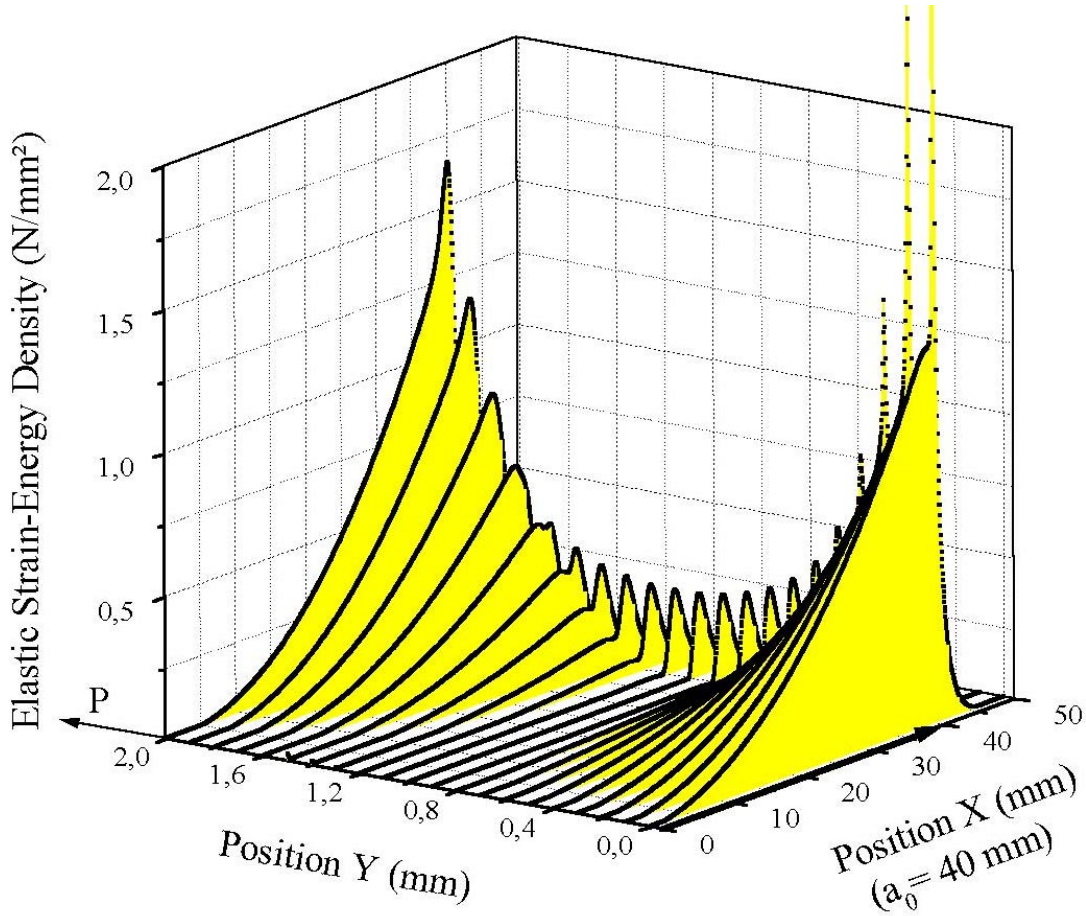

Fig. 6 Results of FE calculation of the elastic strain-energy density distribution for stable mode I delamination propagation of GF/PA-12.

This bending test simulates the damage behavior resulting from the flexure of cantilever during the DCB fracture test. The critical strain-energy density for damage initiation results from the critical stress in the tensile zone of the deflected specimen where AE signals with defined amplitude threshold are detected. Normally, the damage starts where the load is introduced and the strain in the tensile zone reaches a maximum. Damages occur within areas where the calculated strain-energy density is higher than the critical value W_c. By this value mode I fracture damage zones around the delamination tip and in the compression areas of the cantilevers were estimated (Fig. 8).

The height of the damage zone is approximated by $2r_D = h_D \approx l_D / 10$ from the contour of the delamination tip zone. As above discussed, matrix cracking and fiber/matrix debonding processes define the geometry of the damage zones.

ACKNOWLEDGEMENT

The authors wish to thank Dr. Linan Qiao for the FE modeling of the strain-energy density.

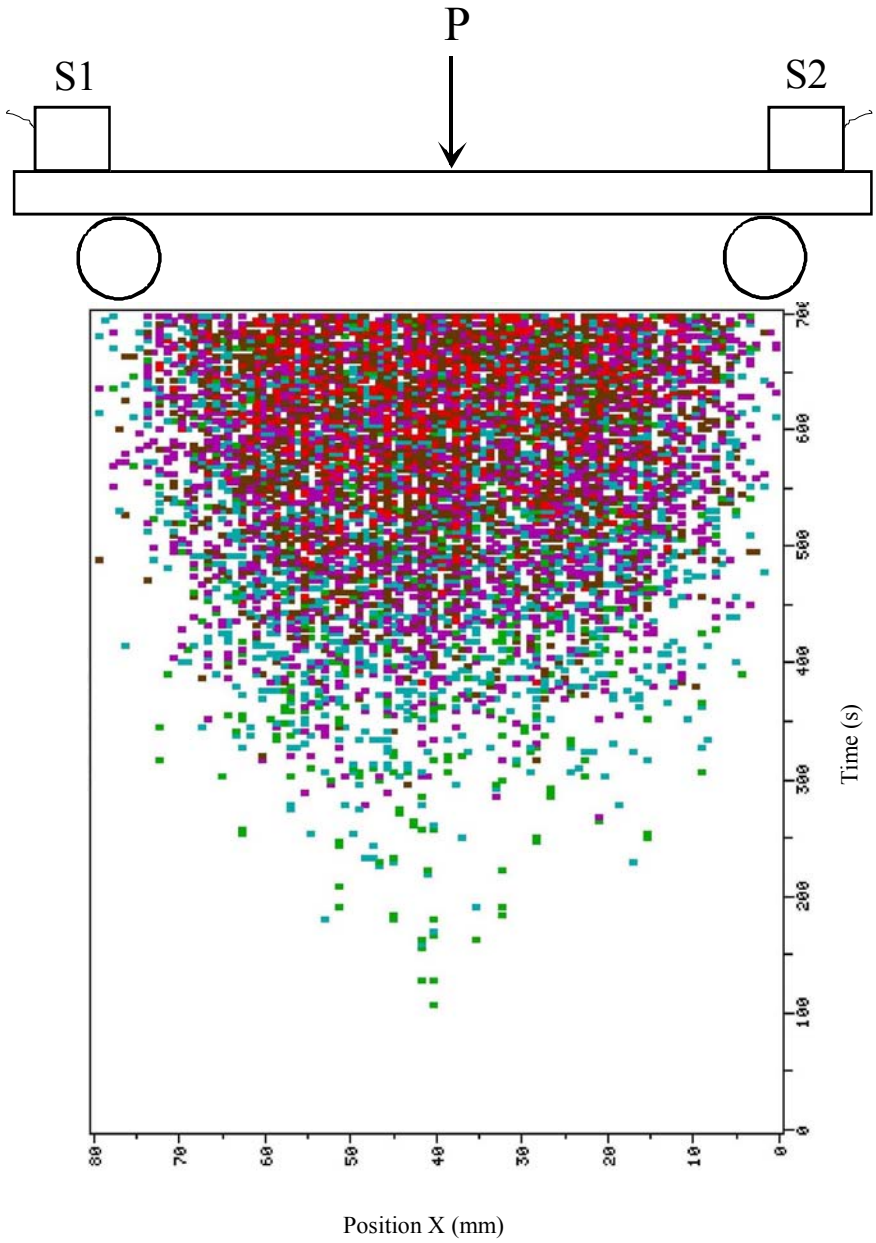

Fig. 7 Time-dependent location of AE sources during 3-point bending tests.

REFERENCES

1. Peter Davis, ed., (1993), „Protocols for Interlaminar Fracture Testing of Composites“, ESIS, September, Marine Materials Laboratory, IFREMER, Centre de Brest, BP 70, 29280 Plouzane, France.

2. J. Bohse, T. Krietsch, J.H. Chen and A.J. Brunner, (2000), „Acoustic emission analysis and micro-mechanical interpretation of mode I fracture toughness tests on composite materials“,

3. J.G. Williams & A. Pavan, eds., *Fracture of Polymers, Composites and Adhesives*, ESIS Publication 27, Elsevier Science Ltd, pp. 15-26.

4. J. Bohse and T. Krietsch, (1998), „Interpretation of fracture toughness in unidirectional glass-fibre/polypropylene composites by acoustic emission analysis of damage mechanisms“, *Progress in Acoustic Emission IX*, Big Island, Hawaii, USA. August 9-14, pp. V55-V62.

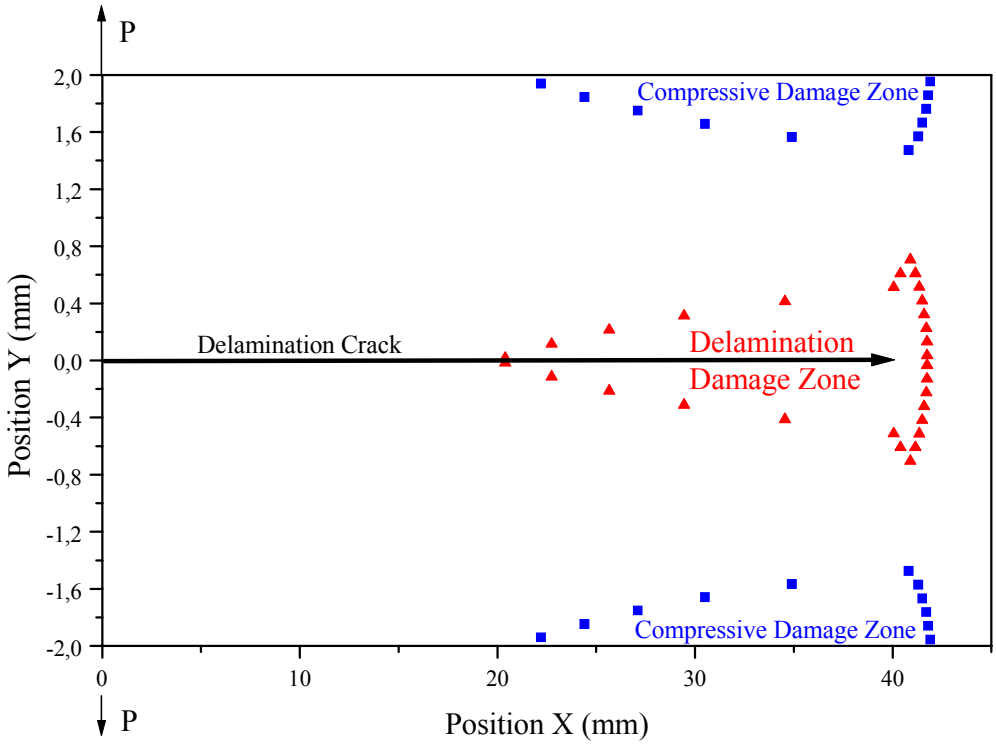

Fig. 8 Damage zones in GF/PA 12 at stable mode I delamination propagation.
(W_c = 0,38 N/mm²; AE amplitudes ≥ 46 dB_{AE})

5. J. H. Chen, E. Schulz, J. Bohse and G. Hinrichsen, (1999), „Effect of fibre content on the interlaminar fracture toughness of unidirectional glass-fibre/polyamide composite“, Composites Part A, **30A**, 747-755.
6. T. Krietsch and J. Bohse, (1998), „Selection of acoustic emissions and classification of damage mechanisms in fibre composite materials“, *Progress in Acoustic Emission IX*, Big Island, Hawaii, USA. August 9-14, pp. IV30-IV39.

FRACTURE DYNAMICS IN NOTCHED PMMA PLATES BY LAMB WAVE ACOUSTIC EMISSION ANALYSIS

KENJI NAGASHIMA, HIDEO NISHINO, MIKIO TAKEMOTO and KANJI ONO*

Faculty of Science and Engr., Aoyama Gakuin University, Setagaya, Tokyo 157-8572, JAPAN
* Dept. Materials Science and Engr., UCLA, Los Angeles, CA 90095-1595, USA

ABSTRACT

We studied the dynamics of unstable fracture and crazing in PMMA plates by using the source simulation analysis of Lamb wave AE. Speed of unstable crack propagation estimated by the waveform simulation agreed well with those measured by the surface film method (SFM) for cracks below 3 mm. Crack volume and source rise time of an unstable crack jump were 4.3 x 10^{-10} m^3 and 16 μs for 3 mm long crack. For monitoring AE from crazing, other AE systems with higher amplification were used. Craze expansion volume of mechanical craze under a constant extension test is estimated as 1.5 to 4.6 x 10^{-16} m^3, and 1000 times smaller than those of unstable crack jump. Expansion volume and source rise time of environmental craze by acetone are estimated as 1.9 to 4.5 x 10^{-16} m^3 and 0.21 to 0.35 μs. Crazes in stressed PMMA plates induced by 50 vol.% methanol have the expansion volume of 7 x 10^{-17} to 2.3 x 10^{-16} m^3 and rise time of 0.3 to 0.6 μs. The present results represent the first determination of craze microdynamics.

1. INTRODUCTION

Fracture dynamics of polymethyl-methacrylate (PMMA) have been extensively studied by using laser holography and shear-wave modulation methods [1]. Crack velocity is reported to be independent of molecular weight, specimen shape and test temperatures (-50 to 40˚ C) and loading speed. Takahashi [2] reported that the crack propagation speed abruptly changes from a few tenths m/s to several hundred m/s. Real time monitoring of crack velocity by AE monitoring is generally difficult due to fast alternation of small metastable cracking to large-scale unstable cracking. The main goal of our research is to quantify the propagation velocity of unstable cracks by AE. The crack velocity estimated by the waveform simulation of Lamb So-packet was compared with those measured by the surface-film method (SFM) [3]. For this purpose, we used a special specimen with a crack-arresting hole in front of single notch. The crack propagation distance was controlled by the holes.

Amorphous thermoplastics like PMMA tend to suffer crazing prior to unstable cracking. AE monitoring of craze generation is particularly important for the integrity evaluation of plastic containers [4-6]. AE has been correlated to cracking and to splitting of spherulites [7,8]. However, no clear evidence of AE from crazing of PMMA has been reported. AE due to crazing is weak, and could not be monitored simultaneously by an AE system suitable for crack detection. With higher amplification, we succeeded in monitoring weak AE from crazing and analyzed it with the source simulation analysis method of detected Lamb waves. We examined both mechanical and environmental crazing.

2. EXPERIMETAL METHOD

Figure 1 shows a specimen and AE monitoring method. A PMMA plate (3 mm thick, 40 mm wide and 160 mm long) with a single notch and a through-wall hole was loaded in tension. The hole was machined at 1, 3 or 8 mm from the notch tip and stops the crack propagation. On the surface, aluminum film was vapor-deposited over 10-mm width on one side of the specimen as a crack gage. Resistance change caused by the film fracture indicating crack propagation was measured by using Wheatstone bridge (WS) circuit. The output of the WS bridge was digitized by digitizer A. We used two independent AE monitoring systems. One consists of two resonant-type AE sensors (channel 1 and 2, PAC Type PICO) and an A/D converter (digitizer B). This system is called System B and has no preamplifier. It was used to monitor strong AE signals from unstable cracks. System C uses two PICO sensors, 40-dB preamplifiers and digitizer C. System C monitors weak AE signals from crazing. Digitizer A operates at 1-μs sampling interval with 4096 points at 10-bit resolution. Digitizers B and C work at 50-ns interval with 1024 points at 10 bit. All AE signals and resistance changes were synchronized by digitizer A and fed to a work station.

3. RESULTS AND DISCUSSION

Unstable Crack

We first show experimental results of 3-mm long unstable crack. Figure 2(A) shows the load vs. displacement curve with AE timing. We recorded five weak AE events (event count or EC 1 to 5) by System C prior to a pop-in at 0.4 kN, and a strong AE signal (EC 6) recorded by System B. A sudden resistance change was also observed upon the pop-in (see (B)). Resistance increased with a rise time of 77 μs and decreased afterward due to closing of the fractured aluminum film. Crack propagation velocity is estimated from the resistance change as 125 m/s. AE waveforms shown in Fig. 2(C) to (E) represent typical Lamb wave features, with first arrival P-wave and trailing So- and Ao-mode components. Note that the amplitude of EC 1 - 5 are as low as 5 μV (at preamplifier input), while that of EC 6 by an unstable crack reaches 1 V without amplification. The So- and Ao-components of EC 6 are also stretched in time, compared to weak events, probably due to slow source rise time.

We next estimated the source dynamics of these waves by the waveform simulation analysis of P- and So-components. As shown in Fig. 3, we used a PZT element to determine the overall transfer function of the system (Fig. 3(c)). The displacement of the element was directly measured by a heterodyne laser interferometer. The procedure used the time-domain deconvolution of the detected wave (a) with the source function (b), which was simplified from the measured. The crack dynamics (crack opening volume change, approximated by a $\sin^4$ step-wise function with effective rise time ΔTr^*) were estimated by iteration so that the first portion of computed waveform best matches the detected one. Shown in Fig. 4 are the examples of waveform simulation for EC 2 and 6. Source parameters for EC 2 were estimated as $\Delta Tr^* = 0.21$ μs and $\Delta V = 4.8 \times 10^{-15}$ m^3, and those for EC 6, 13.3 μs and 4.3×10^{-10} m^3. Both the rise time and crack volume of EC 2 are far smaller than those of EC 6. Other weak AE signals monitored for 1 and 8 mm long crack specimens showed ΔTr^* of 0.2 - 0.35 μs and ΔV of $1.5 - 4.8 \times 10^{-15}$ m^3. Smaller expansion volume, generally 10^4-10^5 times smaller than that of EC 6, suggests that crazing produced these weak AE events. Small cracks are also possible sources, but these appear unlikely as will be discussed later.

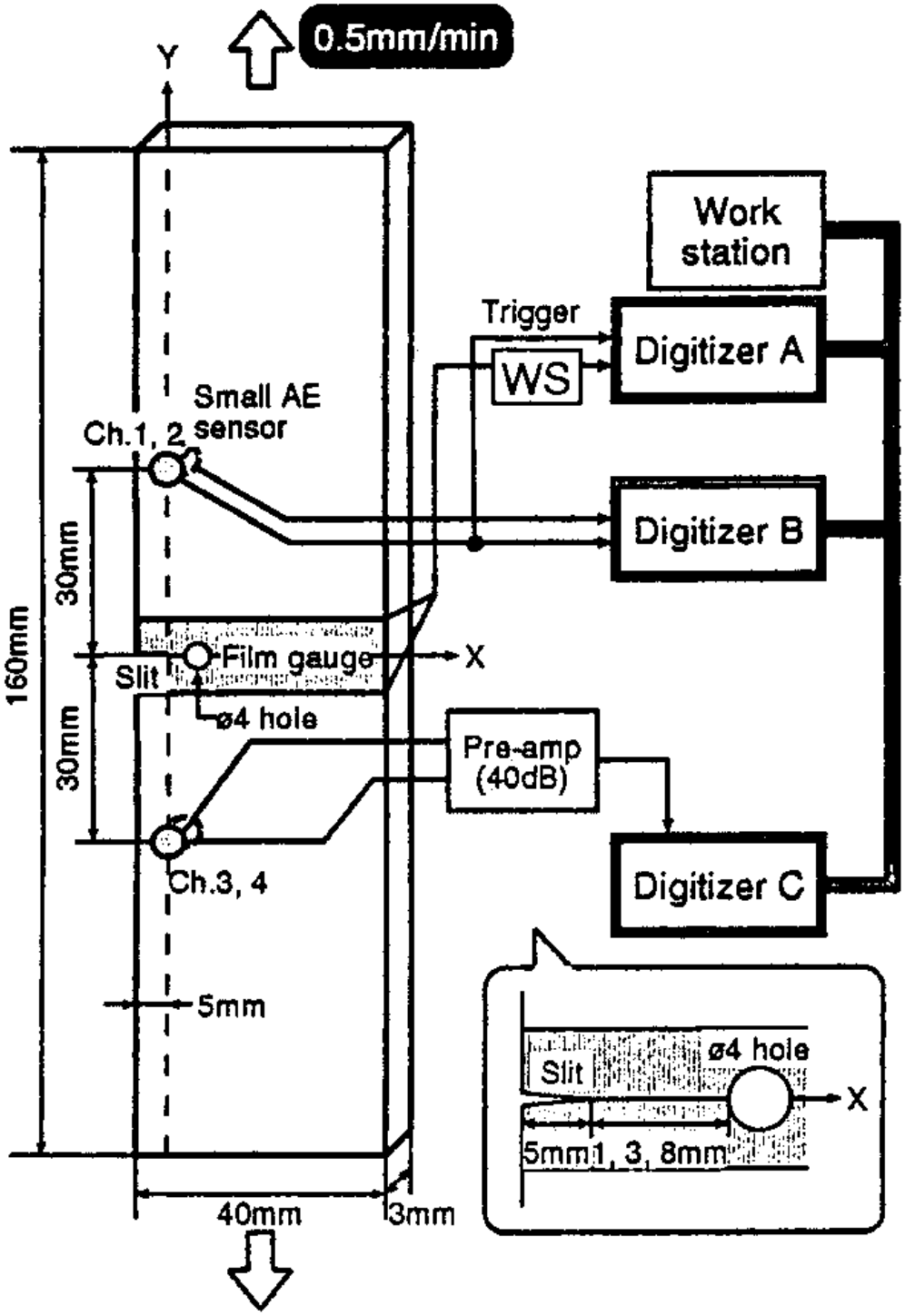

Fig. 1 Experimental setup of tensile testing. WS indicates Wheatstone bridge.

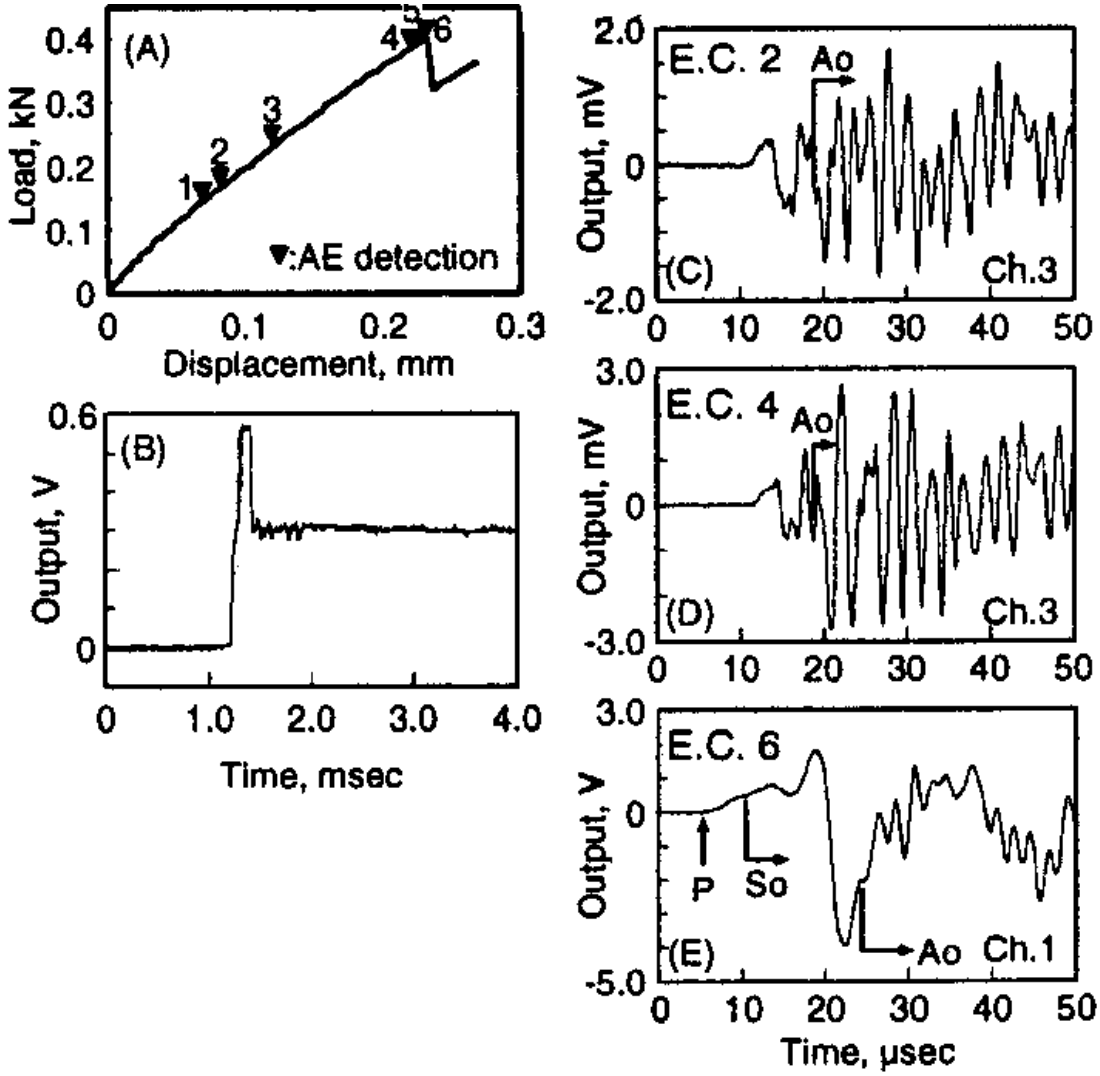

Fig. 2 (A) Load vs. displacement curve with AE timing indicated by arrowhead. (B) Crack gage output. (C-E) AE signals for event count (E.C.) 4 to 6. Start of wave components P, So, Ao shown.

Table 1 Summary of fracture dynamics results.

Crack length	Tr*(μs)		ΔV
	Waveform Sim.	SFM	(10^{-10} m^3)
1 mm	6.3	5.1	1.2
3 mm	13.3	16	4.3
8 mm	10.2	23	2.6

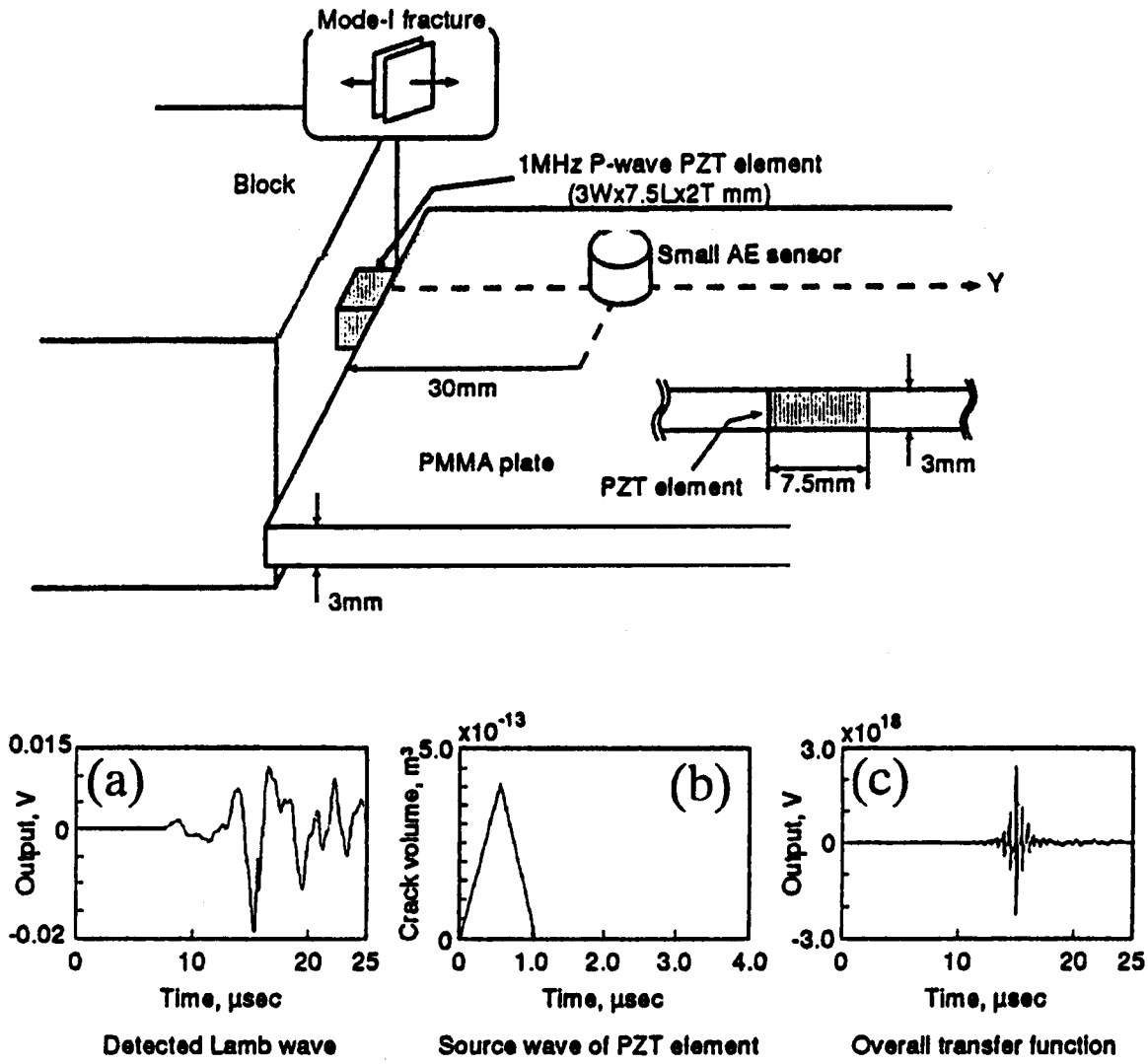

Fig. 3 Simulation of Lamb waves from Mode-I fracture using a PZT element and back-up mass.

Table 1 compares ΔTr* estimated by the waveform simulation method and SFM for large crack jump from 1 to 8 mm. ΔTr* (and the propagation velocity of the unstable crack) agreed fairly well with SFM for shorter cracks below 3 mm, but showed a large difference for 8-mm crack. This arises from the following: Fractographic observation revealed multiple cracks for 8-mm crack. As AE system detected only one AE signal during the pop-in while the SFM measured the resistance change of the entire jump.

AE from Environmental Crazing under Constant Extension Rate Test

In order to identify whether the weak AE monitored before the unstable crack jump are from crazing or micro-cracks, we recorded AE from environmental crazing by using different AE systems. Figure 5 shows the setup for craze monitoring. Specimen is the same as that of Fig. 1 without the surface film and crack-arresting hole. We monitored the radiation pattern of So-amplitudes by using 7 PICO sensors mounted on a semi-circle of 30-mm radius. Outputs of the sensors were amplified by 40 dB and fed to a digitizer/work station. We also monitored changes in the transparency of PMMA by using a laser detection system. A He-Ne laser beam passing at the crack tip was continuously monitored by a photo-diode.

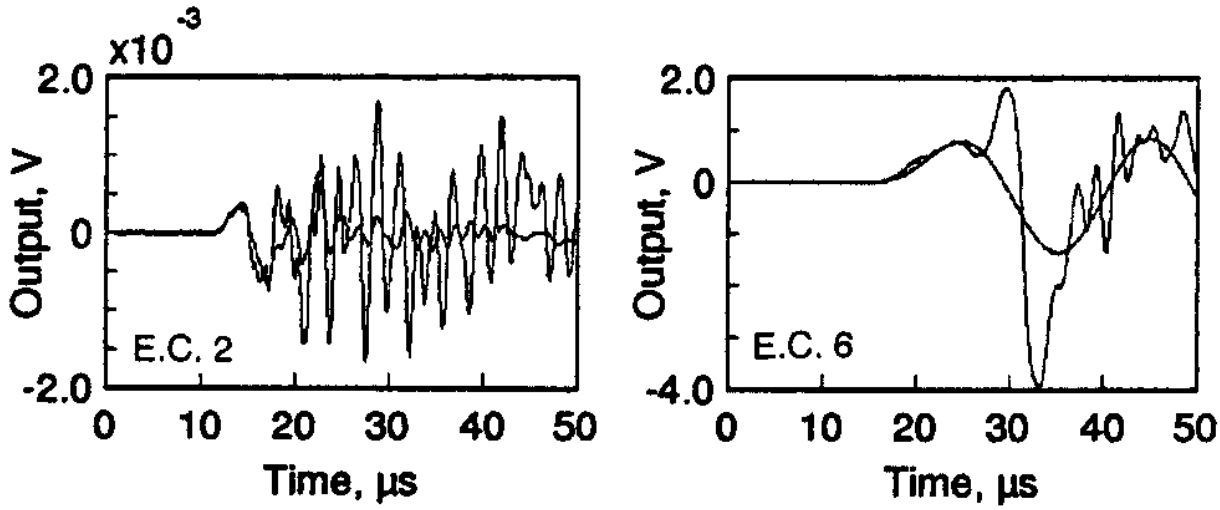

Fig. 4 Comparison of detected AE and simulated waveforms with less oscillations. Left: EC 2; right: EC 6. Note that initial 6 to 12 μs of the waveforms match well.

Figure 6 shows the load–displacement curve with AE timing. A small amount of acetone was injected into the crack tip at load of 0.4, 0.55 and 0.61 kN. At about 1 s after the first acetone injection at 0.4 kN, the photodiode detected a sudden decrease in the transmitted light intensity over a period of 4.7 μs. We visually observed radially spreading lines, and color change at the notch tip. Since no crack was observed until the second acetone injection, AE events monitored at loads below 0.55 kN are believed to be produced by environmental crazing. Upon the second acetone injection at 0.55 kN, fine cracks with small opening were also observed as clear white lines. Figure 7 shows the surface photograph around the notch tip after the test. This damage pattern is quite different from single unstable crack jump observed during mechanical loading in air. Twenty-two weak AE events were monitored below 0.7 kN, but no unstable crack was visible.

Both the kinetics and kinematics of craze were analyzed by the waveform simulation and radiation pattern analysis. Craze normal **n** and opening vector **b** were determined by the method proposed by Sato et al. [9]. Figure 8 show the profile of first peak amplitude of So-mode and two typical waveforms (EC 1 and 4). Radiation profile of EC 1, observed at 0.3 kN before any acetone injection, suggests crack-opening (Mode-I) type fracture with **n** and **b** in the loading (Y-) direction. The craze volume is estimated as 4.5 x 10^{-16} m^3 and ΔTr^* is estimated as 0.33 μs. This opening volume is smaller than any we have observed. ΔV and ΔTr^* of EC 4 are calculated as 1.9 x 10^{-15} m^3 and 0.33 μs, respectively. The EC 4 results, observed upon the first acetone injection, suggest a slant craze with **b** in the direction of 40° to the loading axis. This kinematics can explain the crazes spreading in radial directions. Among the first 13 events, 80 percent of the events showed Mode-I type opening. AE from crazing appears to be produced by the rapid formation of fibril in the direction of maximum principal stress. Relatively large amplitude of the So-mode wave in Fig. 8, in spite of extremely small source volume, appears to be due to fast source rise time. These craze events are surprisingly fast and their ΔTr^* values are comparable to carbon- or glass-fiber fracture.

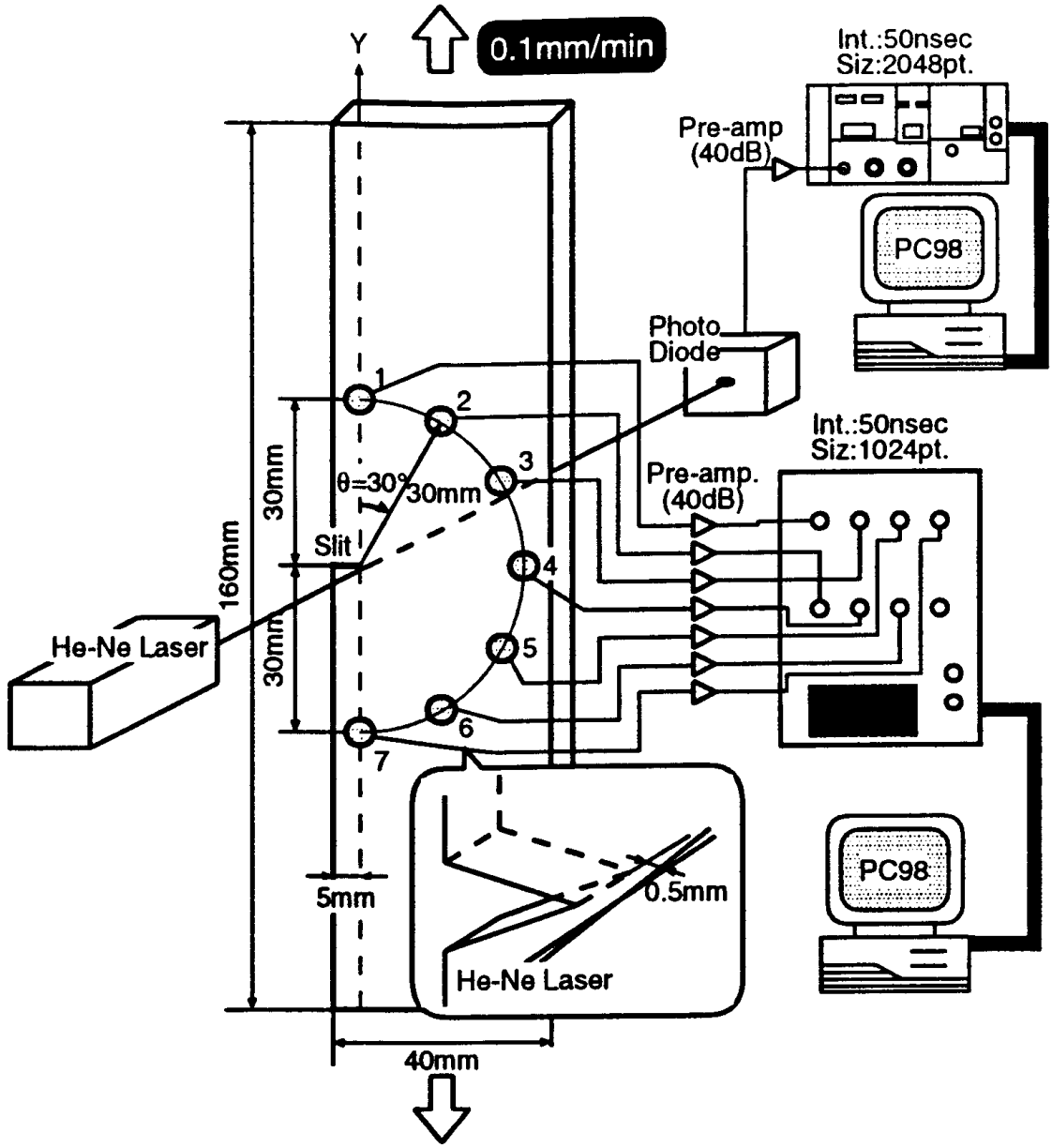

Fig. 5 Experimental setup of AE monitoring during acetone-induced crazing under tensile loading.

AE from Environmental Crazing under Constant Strain Test

Using a new AE system composed of a PICO sensor, a 60-dB pre-amplification by PAC 1220A amplifier and a PAC Mistras board, we monitored AE from environmental craze in a PMMA plate under three point bending (initial fiber stress of 25 MPa). This test is a stress-relaxation type, and gives a moderate stress condition compared to constant extension rate test. Acetone was also changed to a less aggressive aqueous solution of 50% methanol by volume. Upon the spraying of the solution, we observed 5 events over a 63 ms interval. These waves are only several times the noise level as shown in Fig. 9. Waveform simulation was attempted for some waves after removing the base line fluctuation and noise by using the epsilon–filtering and cosine-taper windowing. We obtained small values of $\Delta V = 7 \times 10^{-17}$ to 2.3×10^{-16} m^3 and fast

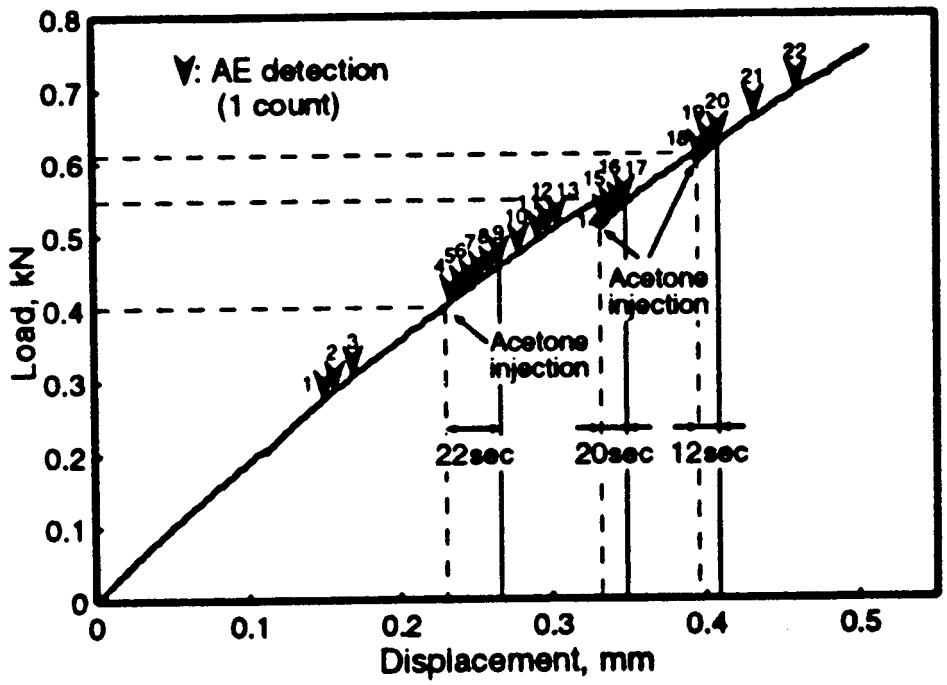

Fig. 6 Tensile load vs. displacement. Arrows indicate the timing of AE due to acetone-induced crazing.

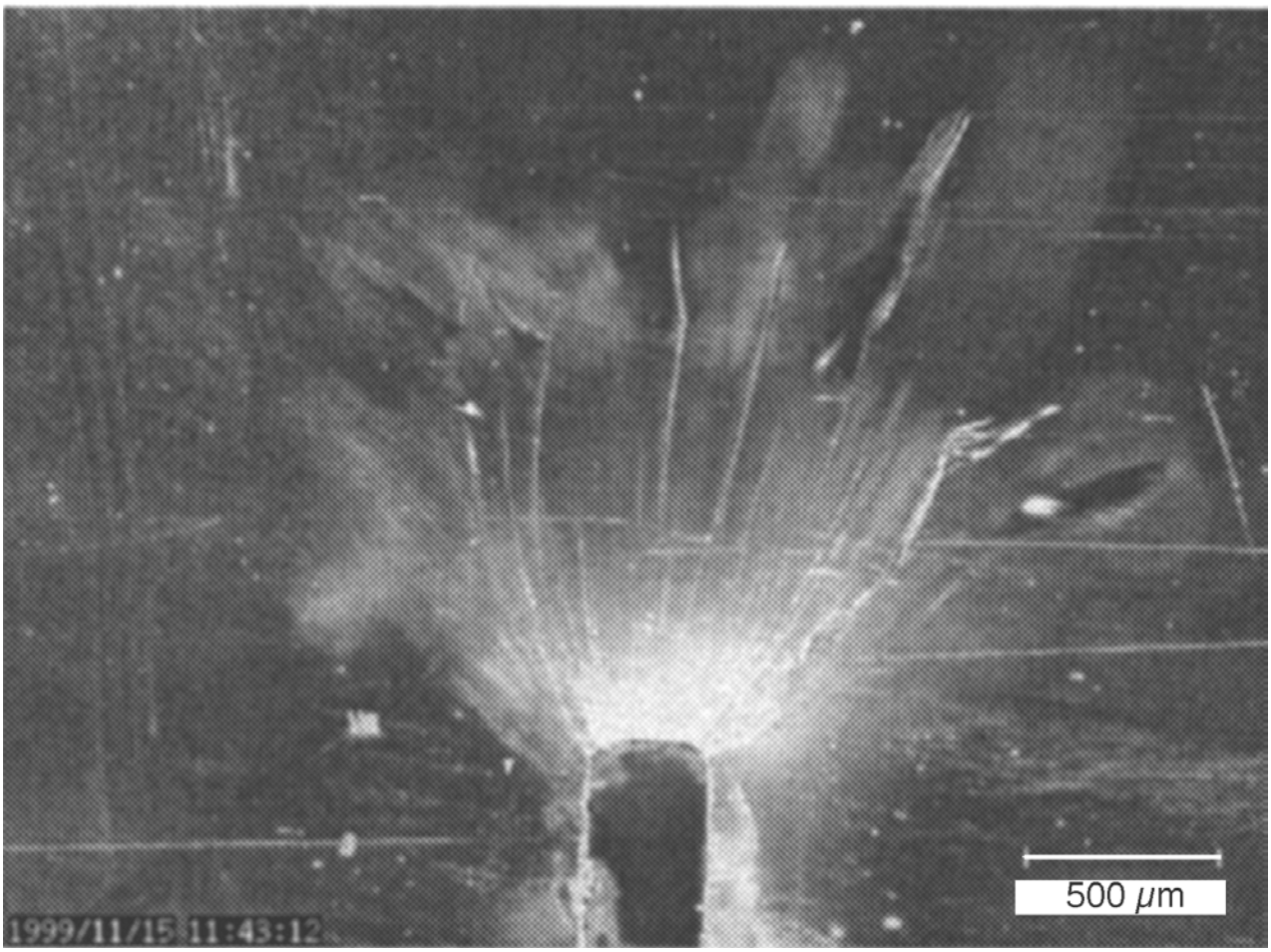

Fig. 7 Photograph of crazing near the slit tip following the test.

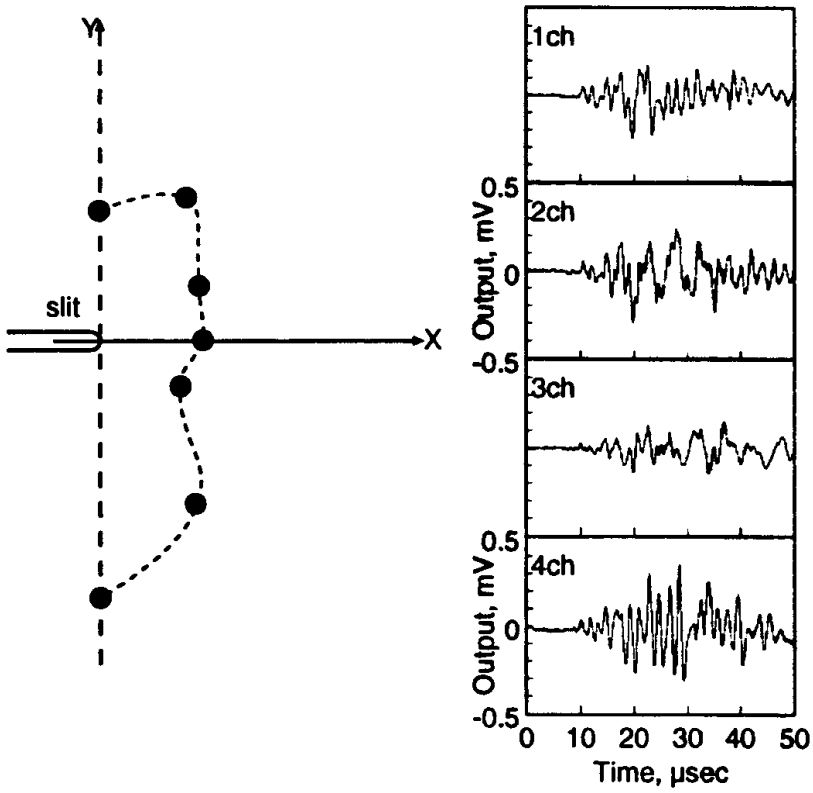

(a) EC 1

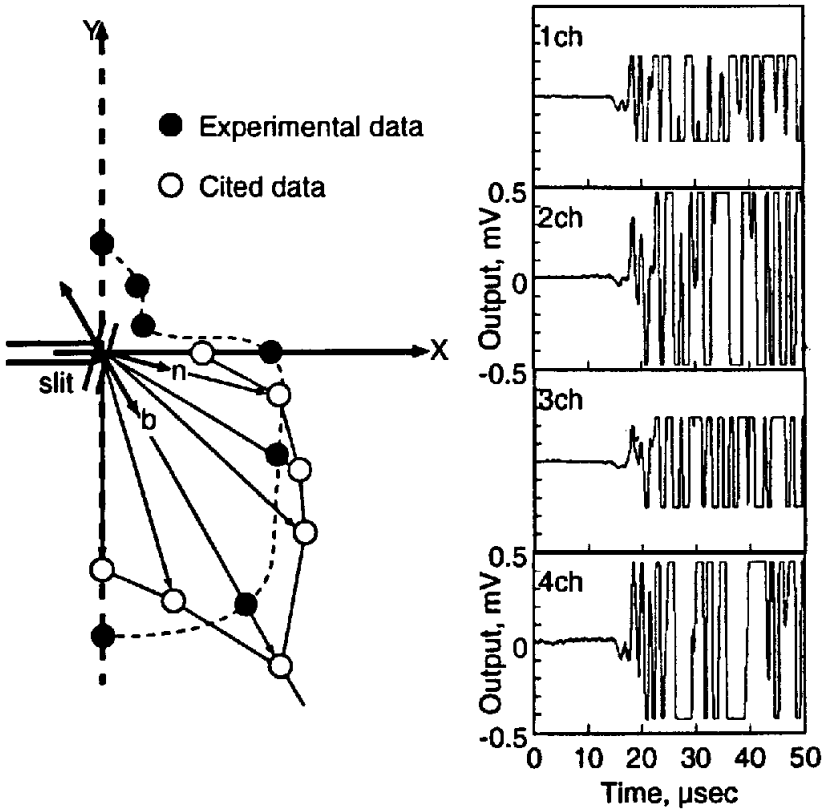

(b) EC 4

Fig. 8 Radiation patterns observed for EC 1 (top) and EC 4 (bottom). Note that the crack opening vector for EC 4 appears to incline 40° from the Y- (vertical) axis.

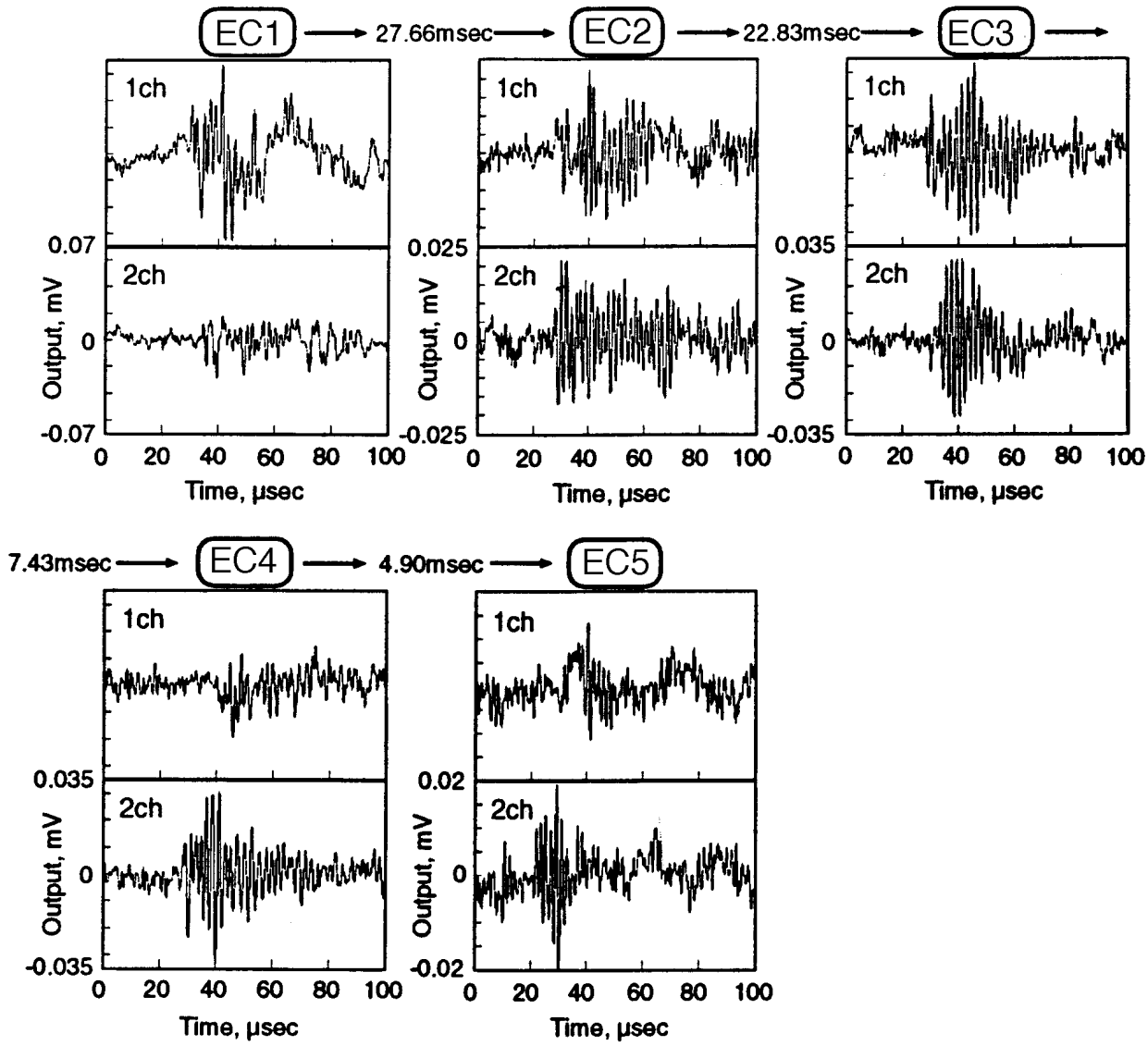

Fig. 9 Detected AE waveforms due to crazing. Five events (event count 1 to 5) occurred over a 63-ms interval.

rise times of $\Delta Tr^* = 0.3$ to 0.6 μs. The crack volumes and source rise times are comparable to those obtained in the previous section. We observed needle-shaped crazes of 2 to 5 mm long (Fig. 10(a)) in the specimen. Some surface fibril in a grown craze (Fig. 10(b)) appears to be broken, but the most fibrils retain small voids among them (cf. Fig. 10(b, c)). No open crack was observed in the present test and the observed AE signals are concluded to be from the craze formation.

4. CONCLUSIONS

Utilizing both Lamb waveform simulation analysis and surface film method, we studied the dynamics of unstable fracture and crazing in PMMA plates with single-edge notch and crack-arresting hole. Crack propagation velocity (125 - 158 m/s) estimated by the Lamb waveform simulation agreed well with those measured by the surface film method for shorter cracks.

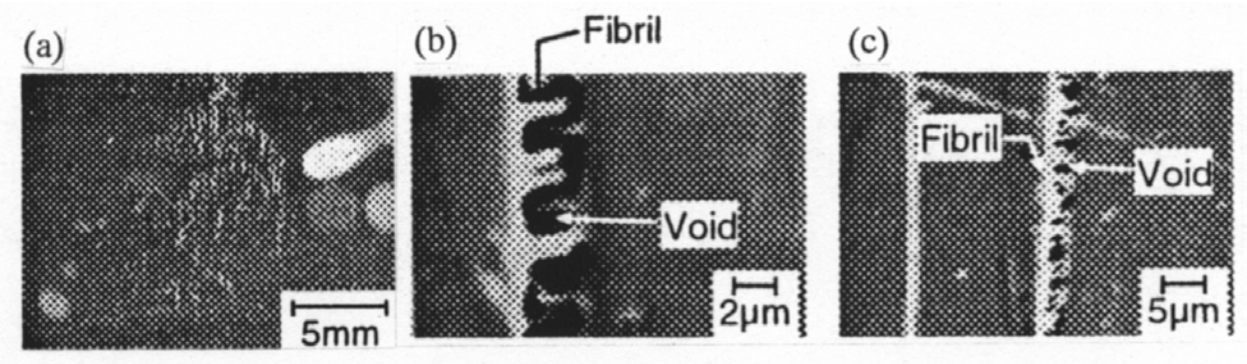

Fig. 10 Optical micrograph (a) and SEM photos (b,c) of surface crazing due to the spraying of methanol solution.

We also monitored weak AE signals from mechanical and environmental crazing using separate AE systems. AE signals from crazing were also analyzed by Lamb waveform simulation. Expansion volumes of mechanical craze under constant extension test are estimated as 1.5 to 4.6 x 10^{-16} m^3, which are 10^5 times smaller than those of unstable cracking (4.3 x 10^{-10} m^3 for 3-mm crack). The source rise times are fast and in the range of 0.21 to 0.35 μs. Similar expansion volumes and source rise times of environmental crazes by acetone and by 50 vol.% methanol are observed.

This study established that crazing in PMMA occurs with short rise times, and produces detectable AE. However, AE amplitude is small because of their small volume expansion.

REFERENCES

[1] S. Suzuki, H, Honma and R. Kusaka, J. Mech. Phys. Solids, **36** (1998) 631.
[2] K. Takahashi, K. Matsushige and Y. Sakurada, J. Mater. Sci., **19** (1984) 4026.
[3] T. Ogawa and S. Suresh, Eng. Fracture Mech., **39** (1991) 629.
[4] C. Ishiyama, T. Asai, M. Shimojo and Y. Higo, Proc. 7th Int. Fatigue Congress, **3** (1999) 1766.
[5] C. Ishiyama, T. Sakuma, Y. Bokoi, M. Shimojo and Y. Higo, Proc. 2nd ESIS TC4 Conf. Polymers and Composite, (1999) 142.
[6] M. Kobayashi, T. Asai, Y. Bokoi, C. Ishiyama, M. Shimojo, Y. Higo, Proc. 2nd ESIS TC4 Conf. Polymers and Composite, (1999) 144.
[7] M. Gakumazawa, M. Akiyama, C. Ishiyama, J. Hu, K. Takashima, Y. Higo and C. Nojiri, J. Acoustic Emission, **16**, (1998) S150.
[8] C. Ishiyama, T. Sakuma, Y. Bokoi, M. Shimojo and Y. Higo, J. Acoustic Emission, **16**, (1998) S196.
[9] T. Sato, M. Takemoto and K. Ono, Jpn. J. Appl. Phys., **38** (1999) 3193.

MONITORING OF MICRO-CRACKING DURING HEATING OF HYDROGEN DOPED GERMANIUM AND SILICON SINGLE CRYSTALS BY ACOUSTIC EMISSION METHOD

K. YOSHIDA, Y. WANG, K. HORIKAWA, K. SAKAMAKI AND K. KAJIYAMA*

Faculty of Engineering, The University of Tokushima, Tokushima 770-8506, Japan.
* Ion Engineering Research Institute Corporation, Hirakata-shi, Osaka 573-0128, Japan.

ABSTRACT

Acoustic emission activity was measured at constant heating speeds in hydrogen-doped germanium and silicon single crystals. Ion-implanted hydrogen in these crystal lattices are changed into hydrogen molecules, piled up near 1 μm depth from the surfaces and cause the micro-cracking due to hydrogen-induced embrittlement. It is apparent that the acoustic emission (AE) could be detected during this process in the semiconductor materials. As a result, it is possible to determine the temperature of the hydrogen-induced cracking. AE is effective to monitor the smart cutting in these materials.

1. INTRODUCTION

Recently, the development of silicon on insulator (SOI) wafers has been active for their low electric power consumption, low voltage operation and large-scale integration of high density. Although some manufacture methods have been already suggested for the SOI wafer with the sub-micron thick single crystal thin layers stacked on each insulator layer, the practical use of SOI is not accomplished now. There is a smart cutting method using ion implantation and is one of the most effective methods so far. Oxygen and hydrogen are considered as doping ions. In the oxygen-doping method, difficult problems still exist because of a large amount of oxygen needed and higher annealing temperature over 1300˚C (1). On the other hand, the hydrogen-doping method is more useful with less difficulty (2). The method is to separate single crystals of sub-micron thickness from a semiconductor substrate such as silicon and germanium using the hydrogen embrittlement that fortunately brings about by hydrogen molecules along defects induced by ion implantation after annealing (3). Now there does not seem to be any effective method to measure in-situ the generation of micro-cracks due to the hydrogen induced embrittlement.

Several papers have reported that acoustic emission (AE) signals generated during heating/cooling process can be applied to the material evaluation, such as the determination of glass transition temperature for dental porcelain (4), the polymorphic transformation temperature in Au-Cu and Pd-Cu alloys and the activation energy of the transformation (5, 6), and the generation of micro-crack in the investment mould for dental casting (7, 8).

Objectives in this paper are to detect hydrogen-induced micro-cracking during heating in hydrogen ion-implanted silicon and germanium single crystals by acoustic emission method and to reveal the temperature and conditions for the micro-cracking to initiate and grow.

2. EXPERIMENTAL PROCEDURES

Materials used were a p-type silicon wafer with (100) surface orientation (0.25-mm thickness) and a p-type germanium wafer with (100) surface orientation (0.40-mm thickness). After the formation of oxide film on the surface of the materials with thickness of 100 nm, hydrogen ion-implantation in 40 x 40 mm^2 silicon and germanium wafers were performed at 100 keV with the dose of 5 x 10^{16} and 1 x 10^{17} ions/cm^2, respectively. The size of specimen for AE testing was 10 x 10 mm^2. Ion implanted specimens were annealed at constant heating rates to 700˚C in vacuum and nitrogen gas atmosphere in an electric furnace for acoustic emission measurement as shown in Fig. 1. Acoustic emission generated in these specimens was detected using a 2-channel AE monitoring system of which block diagram is shown in Fig. 2. Detected AE signals were transmitted to the AE system through a waveguide that was made of an austenitic stainless steel rod with diameter of 4 mm and length of 330 mm, transformed into electric signals by an AE transducer with resonant frequency of 200 kHz. They were amplified by constant gain of 100 dB through a band-pass filter of 0.1 to 1.0 MHz and stored by a computer as AE event and amplitude above the threshold level of 58 dB that corresponded to 25 μV at input voltage of the preamplifier.

The composition of the gases discharged during heating was analyzed by a thermal desorption spectroscopy (TDS) device. Fracture appearances in these specimens were determined by cross-sectional SEM micrographs after the heating test.

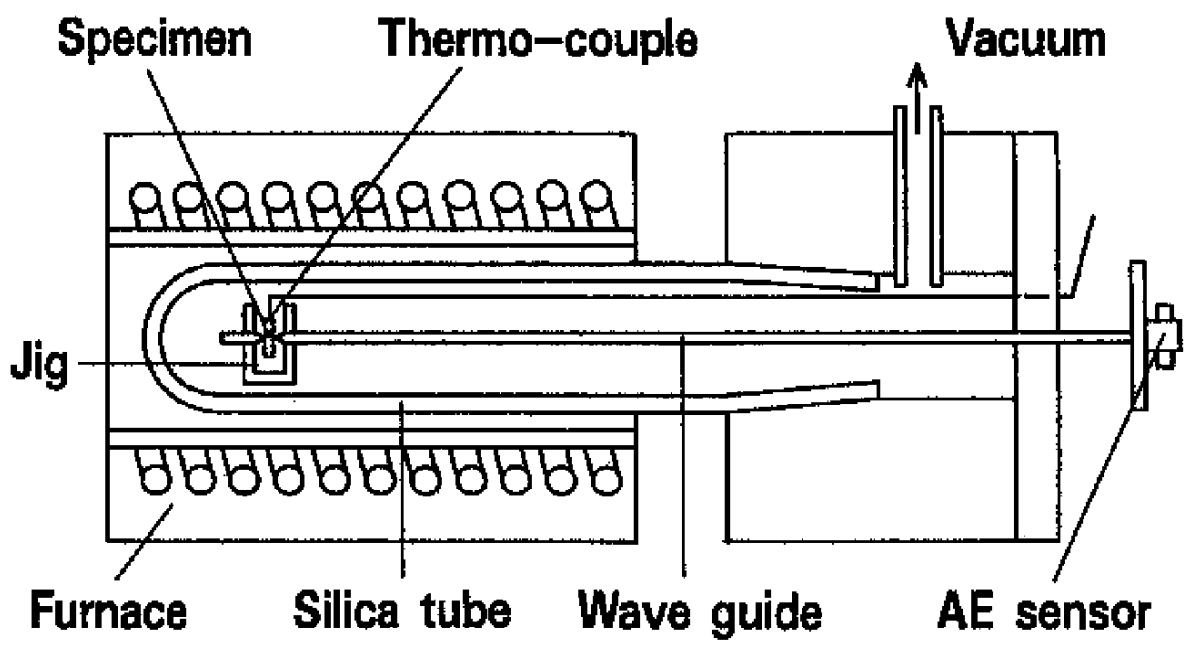

Fig. 1 System of suspending the specimen for detecting AE signals in an electric furnace.

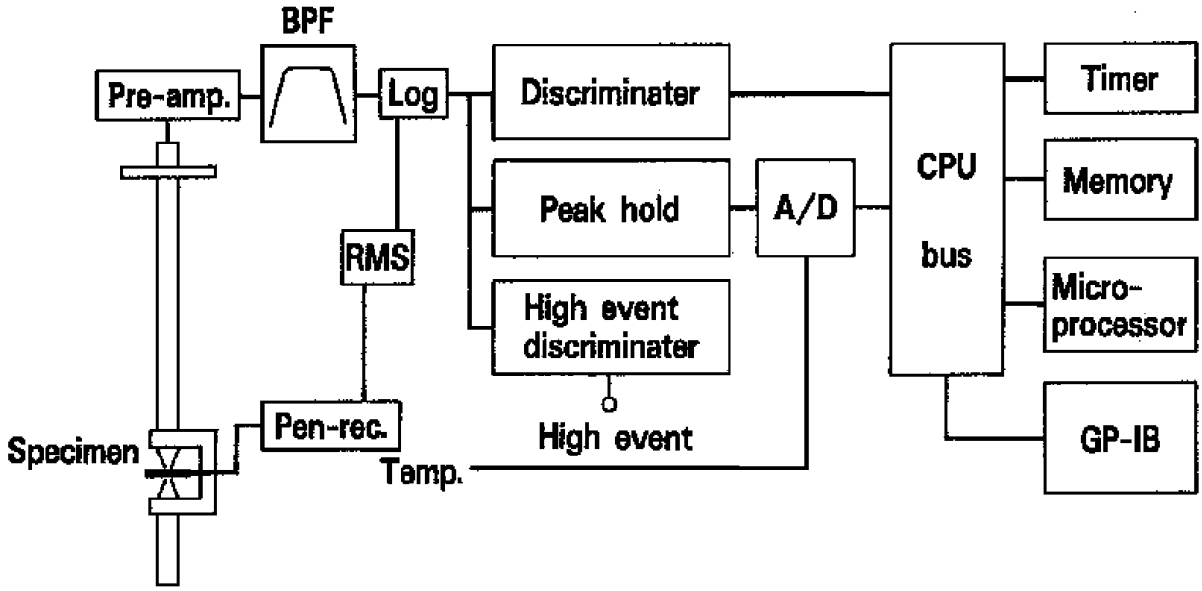

Fig. 2 Block diagram for AE measurements.

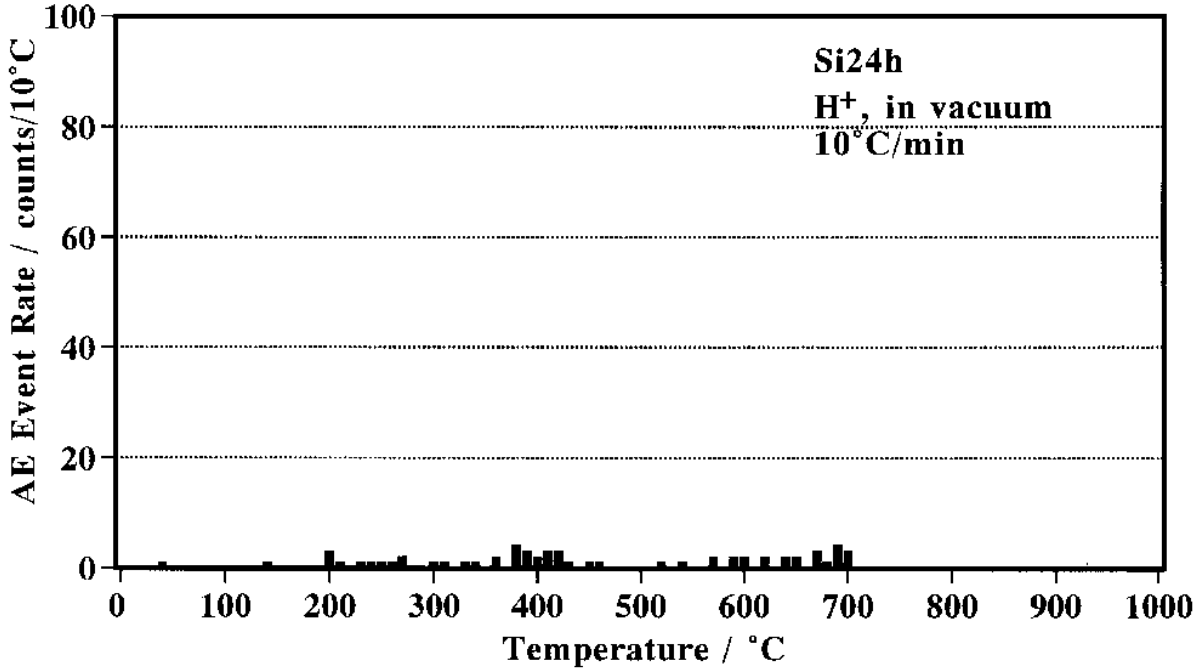

Fig. 3 AE behavior during heating at 10°C/min in vacuum in the H^+ implanted Si single crystal. (a) AE event rate.

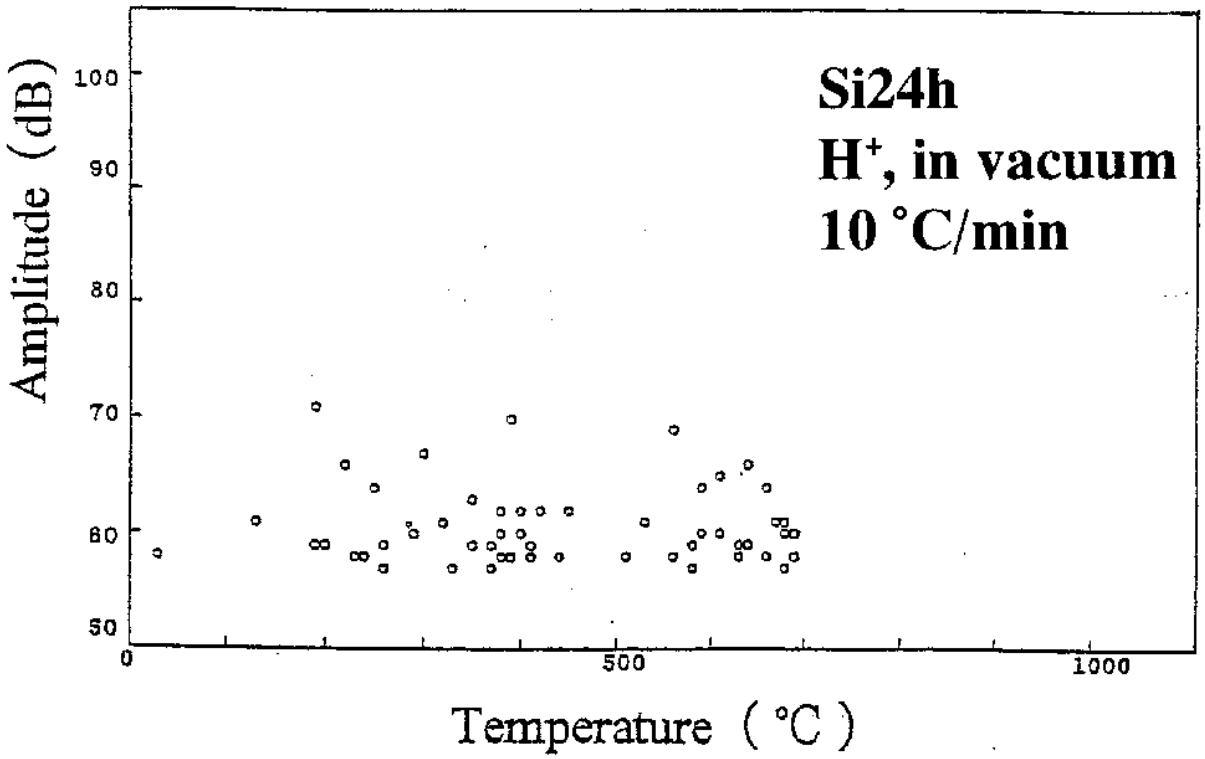

Fig. 3 AE behavior during heating at 10˚C/min in vacuum in the H^+ implanted Si single crystal. (b) AE amplitude

3. RESULTS AND DISCUSSION

Detection of Hydrogen Induced Micro-cracking in Silicon Wafers

Figure 3 and 4 show AE behaviors in hydrogen implanted silicon single crystal wafers from room temperature to 700˚C at heating rate of 10˚C/min in vacuum and nitrogen gas atmosphere, respectively. The AE event rate in vacuum indicates two peaks in Fig. 3(a). The detected amplitude of AE is low as shown in Fig. 3(b). On the other hand, the event rate in nitrogen gas atmosphere increases in the range of 600 to 700˚C and indicates a peak at 650˚C, as shown in Fig. 4(a). The dominant medium amplitude in this temperature range is detected as shown in Fig. 4(b). Total AE event counts in vacuum are smaller than in nitrogen gas atmosphere, but the AE event rate in both atmospheres increases in the range of 600 to 700˚C. It is suggested that structural changes occur in the specimen, while AE sources depress the activity because of more escape of hydrogen gas through the surface in vacuum.

Figure 5 shows the dependence of the heating temperature at 10˚C/min on the desorbed hydrogen gas intensity in argon gas atmosphere. The intensity indicates two peaks at 450˚C and 650˚C. Acoustic emission data that is consistent with the result is shown in Fig. 6. The cause of this behavior has been considered to be the structural change of composite defects formed by the hydrogen ion-implantation in the silicon single crystal (9). Accordingly, Si-Si bonds are cut off by the hydrogen ion implantation with high energy. Implanted hydrogen ions are attracted to the separate bonds. These hydrogen ions become saturated with progress of the implantation time. Then hydrogen and silicon atoms constitute a tetrahedral structure that denotes SiH_4. Hydrogen ions are precipitated at 405˚C during heating process.

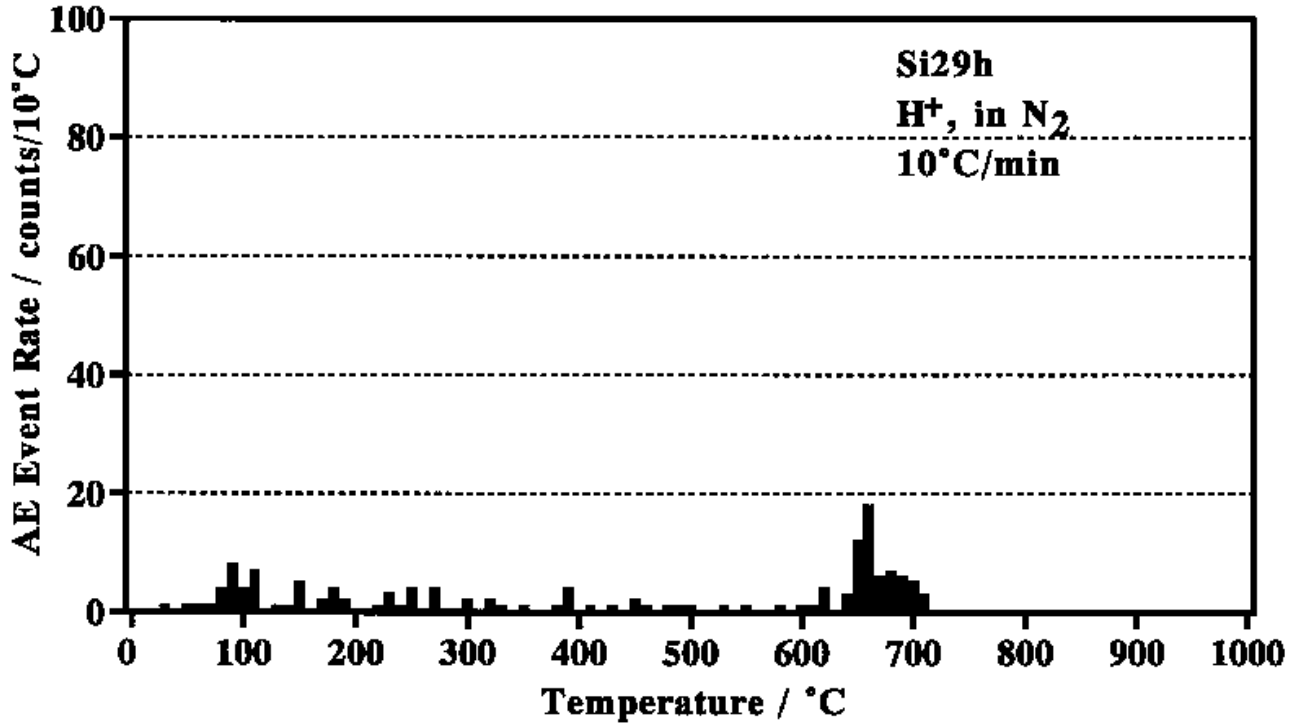

Fig. 4 AE behavior during heating at 10˚C/min in nitrogen gas in the H^+ implanted Si single crystal. (a) AE event rate.

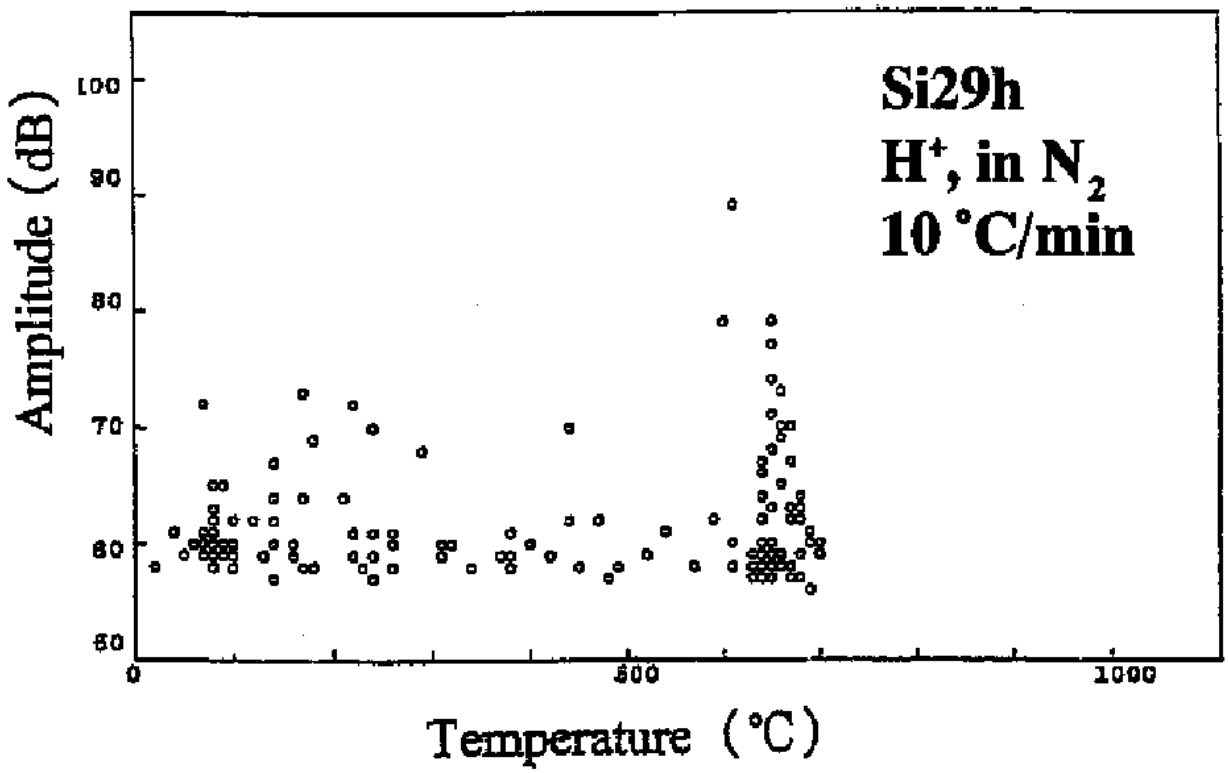

Fig. 4 AE behavior during heating at 10˚C/min in nitrogen gas in the H^+ implanted Si single crystal. (b) AE amplitude.

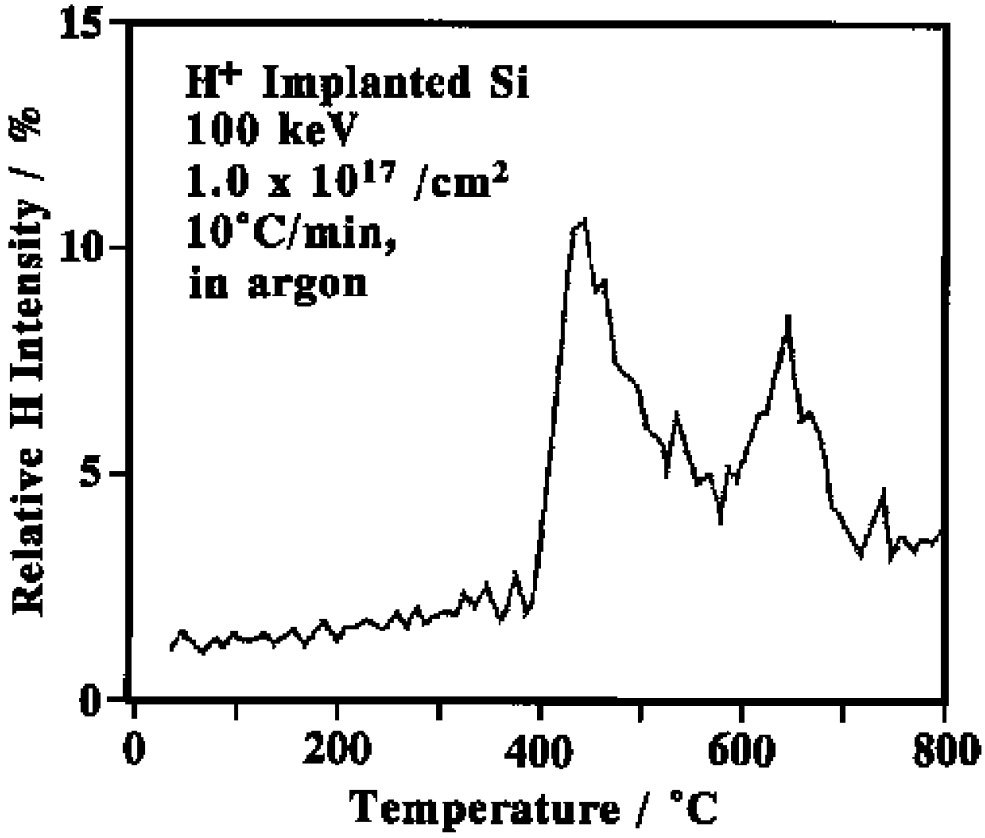

Fig. 5 H_2 desorption curve in Si single crystal wafer.

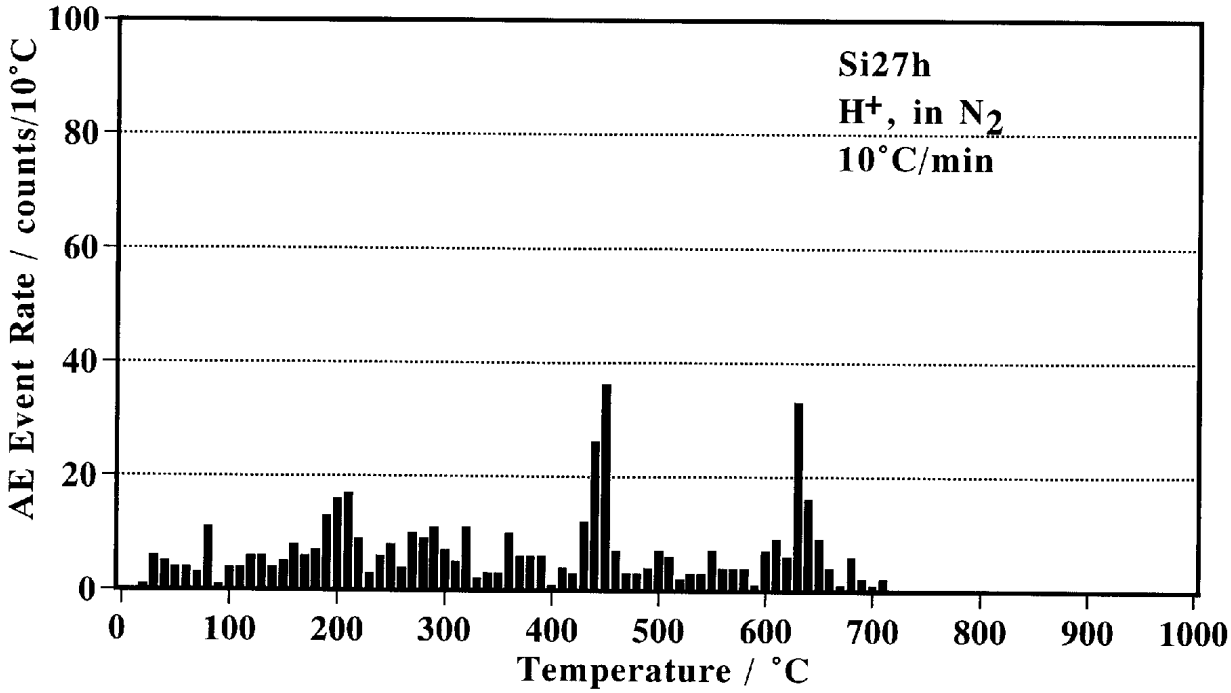

Fig. 6 AE event rate corresponding to Fig. 5.

The structure of defects changes into relatively unstable triangle structures that denote SiH_3 or Si_2H_6. Excess hydrogen ions react to form hydrogen gas. The hydrogen gas is released out of the specimen and shows the peak of intensity. With the temperature increased further, Si-H bonds are cut again at 650˚C. Similarly the hydrogen gas shows second peak of intensity. As a result, it is suggested that at 450˚C micro-cracks may be initiated partially in the specimen and at 650 ˚C they are extended all over the specimen.

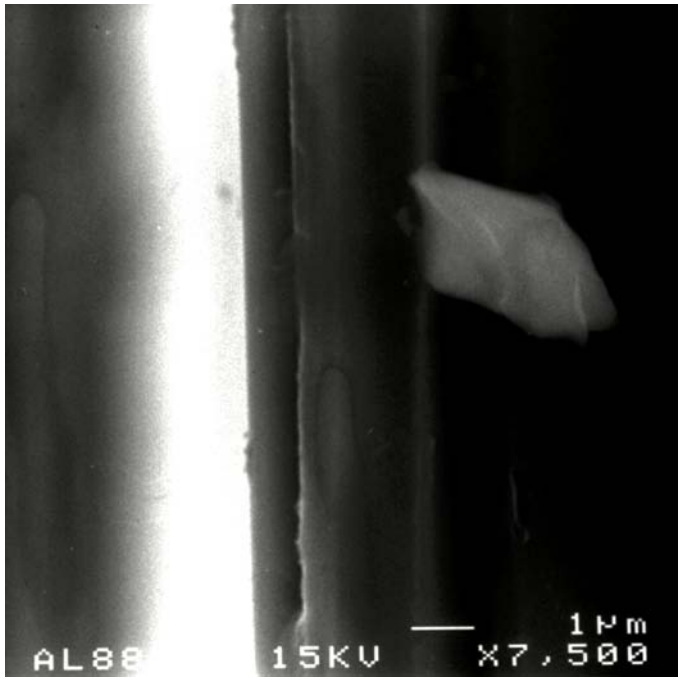

Fig. 7 A typical cross-sectional SEM micrograph in H^+ implanted silicon wafer.

A typical example of cross sectional SEM photograph in the silicon wafer is shown in Fig. 7. A uniformly fractured layer at the depth of 0.85 μm from the surface can be observed, indicating the evidence of hydrogen-induced embrittlement. The depth of the layer was almost similar to 0.87 μm in the previous paper by Kajiyama et al. (10).

Detection of Hydrogen-Induced Micro-cracking in Germanium Wafers

Figure 8 shows AE behavior in hydrogen-implanted germanium single crystal wafers from room temperature to 700˚C at three heating rates of 10, 5 and 2.5˚C/min in nitrogen gas atmosphere. In 10˚C/min heating, the AE event rate indicates two peaks at 330 and 390˚C, and decreases gradually with increase of the temperature as shown in Fig. 8(a) and (b). The detected amplitude of the AE event is very high at 330 and 380˚C, and changes into the extremely low level with increase of the temperature. This trend is identical in all heating rates. These temperatures are consistent with those in two peaks of the AE event rate. In 5˚C/min heating, the AE event rate increases steeply near 290˚C, indicates a remarkable peak at 310˚C, and decreases steeply and gradually with increase of the temperature as shown in Fig. 8(c) and (d). The detected amplitude of the AE event is very high near 300˚C. In 2.5˚C/min heating, the AE event rate also increases steeply near 280˚C, indicates a remarkable peak at 300 ˚C, and decreases similarly in the case of 5˚C/min as shown in Fig. 8(e) and (f). The amplitude also is very high near 280˚C. As for the gases desorbed during heating, the intensity of the hydrogen gas is much more active than that of other gases and has a peak value at 280 ˚C as shown in Fig. 9. After that it decreases steeply but continues to increase gradually to 520˚C, and finally decreases gradually

to null at 600˚C. The fact is well correlated with the behavior of the AE event rate. However, the peak temperature of the desorbed hydrogen intensity is lower by 30 ˚C from that of the AE event rate. It appears that the hydrogen induced micro-cracking takes a time lag to the hydrogen desorption, possibly meaning a delayed fracture.

A typical example of cross sectional SEM photograph at heating rate of 10˚C/min in the germanium wafer is shown in Fig. 10. A uniformly fractured layer at the depth of 1.0 μm from the surface can be also observed. Irregularity near the macro-crack of the germanium wafer is much more obvious than in the silicon wafer because of lower fracture strength in germanium. It is suggested that the fact may be related to the more active AE behaviors such as the event rate and the amplitude in the germanium wafer.

When these specimens were reheated under the same experimental condition, the AE events were almost absent because of no micro-cracking occurring again in these specimens. Therefore, it is apparent that the hydrogen-induced cracking ceased after only one heating/cooling process.

The temperature of the peak value in the AE event rate increases gradually with increase of the heating rate as shown in Fig. 11. On the contrary, the AE total event counts decrease fairly drastically as shown in Fig. 12. The generation of the hydrogen-induced embrittlement seems to include in part some activated processes.

4. CONCLUSIONS

Acoustic emission monitoring during heating process in the hydrogen implanted silicon and germanium wafers has been carried out to reveal the generation and growth conditions of micro-cracking by hydrogen-induced embrittlement. Results obtained are as follows.

1. The cracking by hydrogen-induced embrittlement was confirmed in the hydrogen implanted silicon and germanium wafers.
1. The temperature to complete the micro-cracking should be more than 600 ˚C in the silicon wafer, while it was in the range of 280 to 350 ˚C in the germanium wafer. It shifted to a higher temperature with an increase of the heating rate.
3. The fractured layer surface in the silicon wafer was uniform and linear. Its depth from the surface was 0.85 μm.
4. The fractured layer surface in the germanium wafer was uniform, but less linear. Its depth from the surface was 1.0 μm.
5. Acoustic emission method is considered to be a useful means to do the in-situ monitoring in the hydrogen implanted silicon and germanium wafers.

REFERENCES

1. K. Kajiyama: Appl. Surf. Sci., **85** (1995), 259.
2. N. M. Johnson, F. A. Ponce, R. A. Street and R. J. Nemanich: Phys. Rev. **B35** (1987), 4166.
3. T. Hara, Y. Kakizaki, S. Oshima, T. Kitamura, K. Kajiyama, T. Yoneda, K. Sekine, and M. Inoue: Electrochem. Soc. Proc. **97**-23 (1997), 33.
4. K. Asaoka, K. Yoshida and K. Sakamaki: J. Mat. Sci., **27** (1992), 3118.
5. K. Yoshida, K. Sakamaki, K. Asaoka and M. Yamanaka: Proc. 9th National Conf. AE, Japan, **9** (1993), 277.
6. K. Yoshida, K. Asaoka, M. Yamanaka and K. Sakamaki: J. Japan Inst. Metal, **59** (1994), 989.
7. K. Kim, K. Asaoka and K. Yoshida: Dental Materials Journal, **17** (1998), 11.

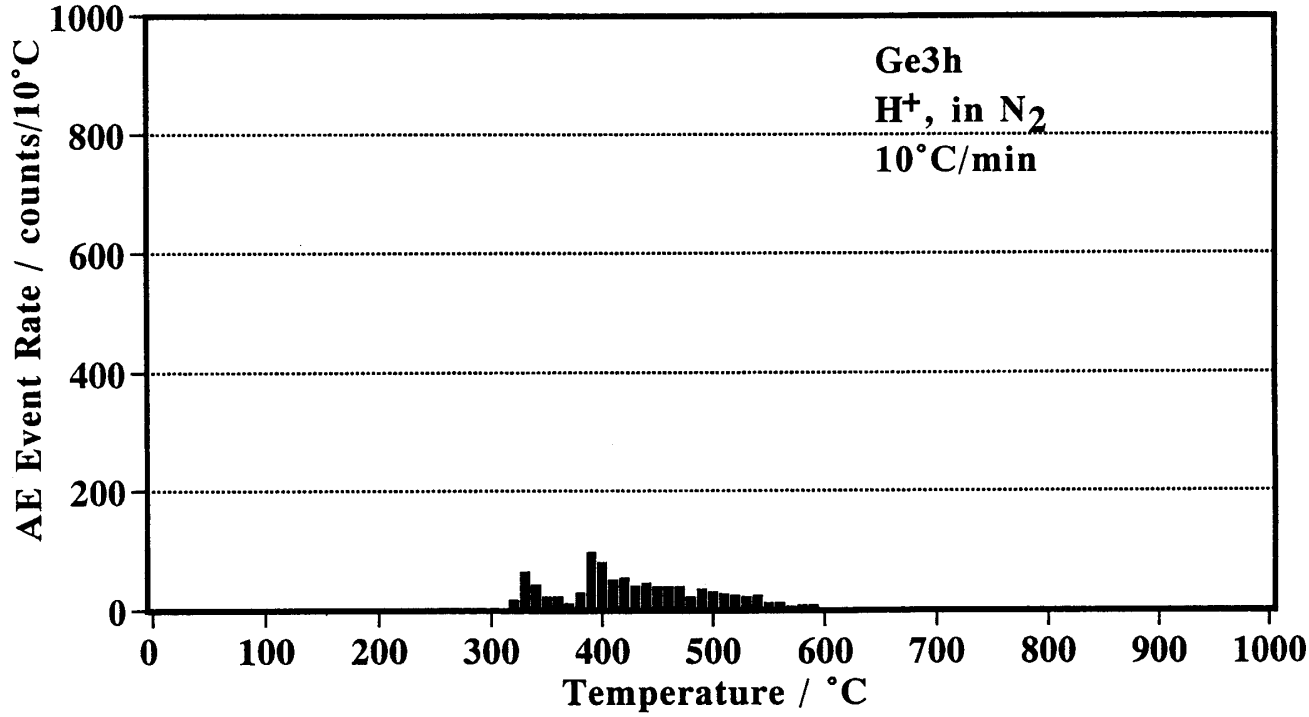

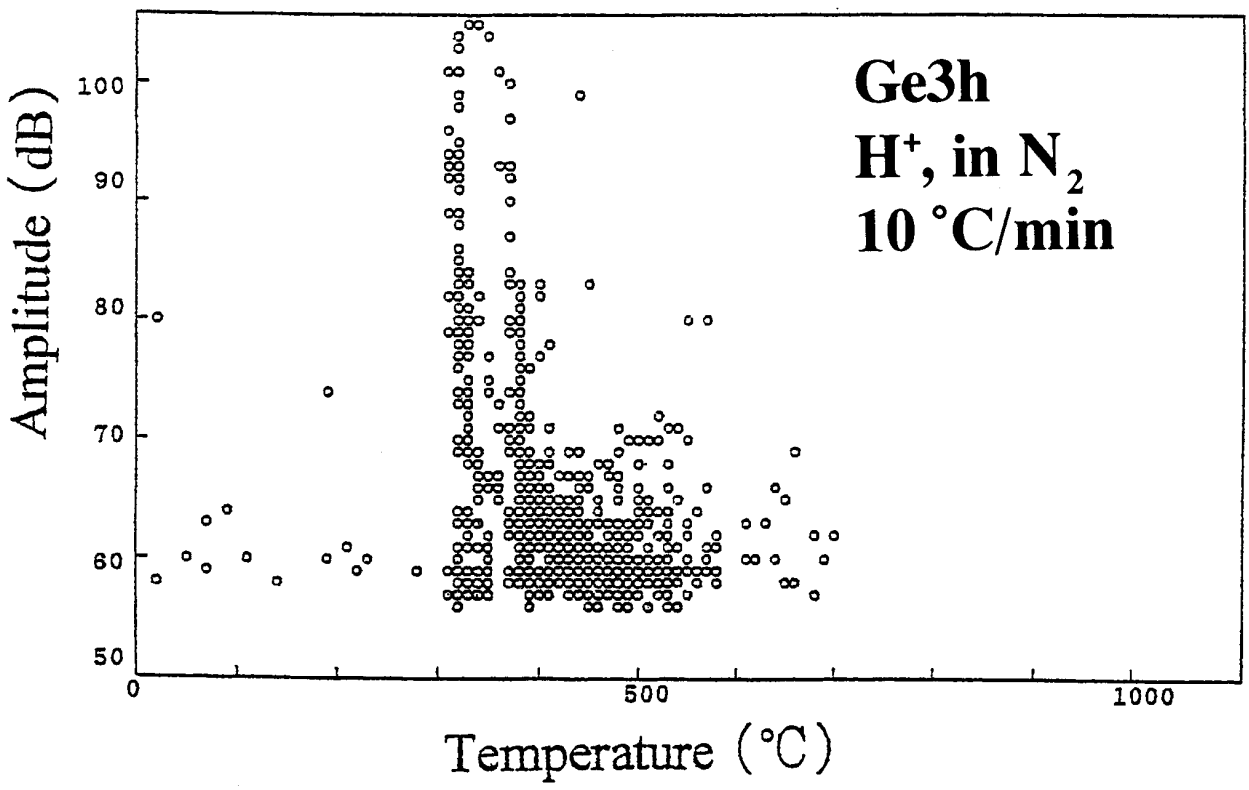

(a, b) AE event rate and amplitude: 10˚C/min.

Fig. 8 AE behavior during heating at three rates in nitrogen gas in the H^+ implanted Ge single crystal.

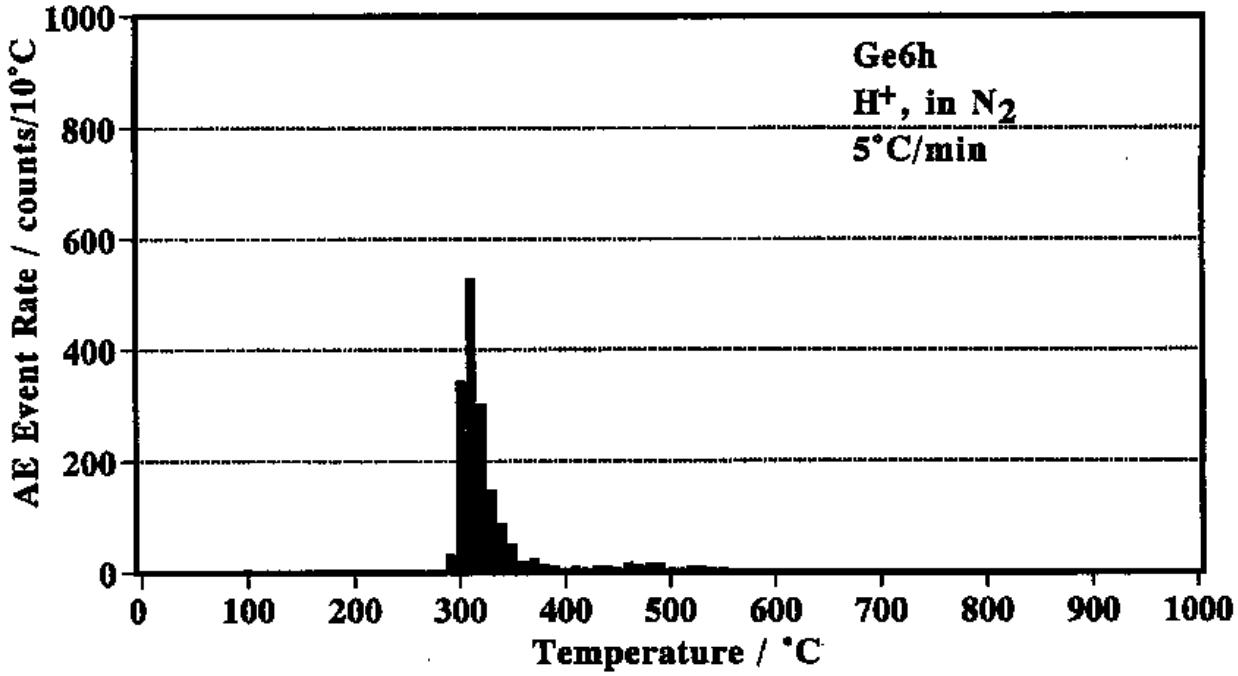

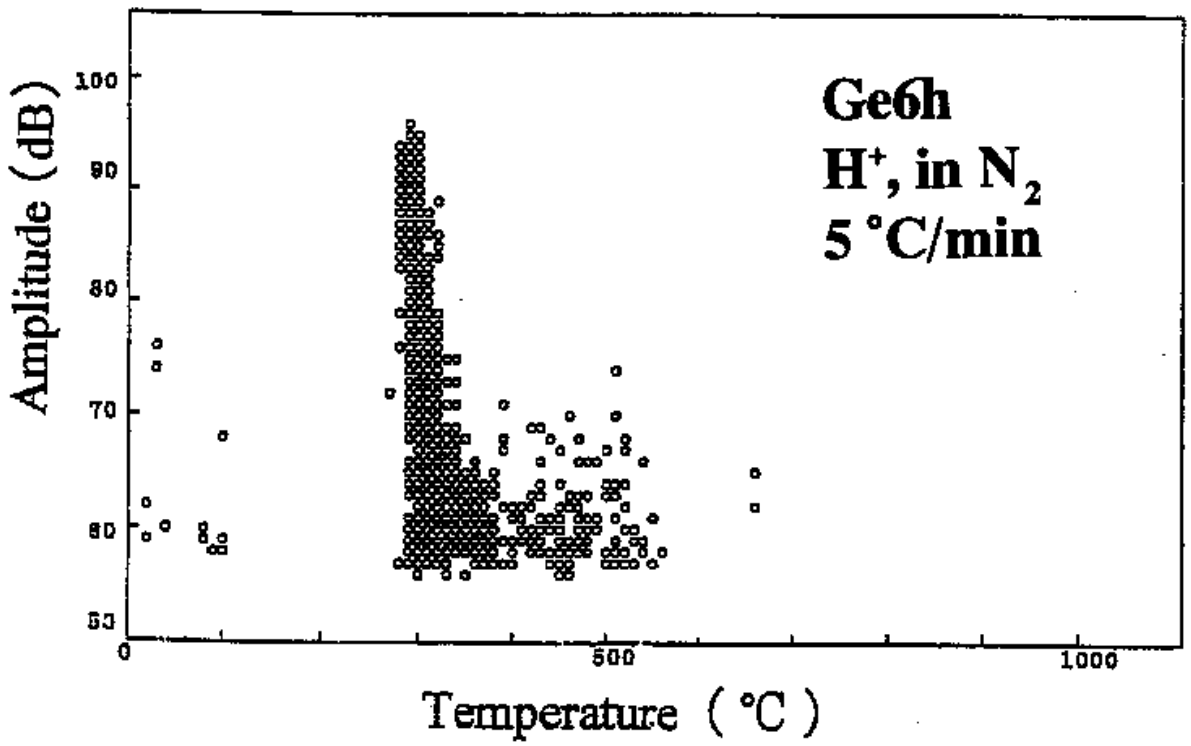

(c, d) AE event rate and amplitude: 5˚C/min.

Fig. 8 AE behavior during heating at three rates in nitrogen gas in the H^+ implanted Ge single crystal.

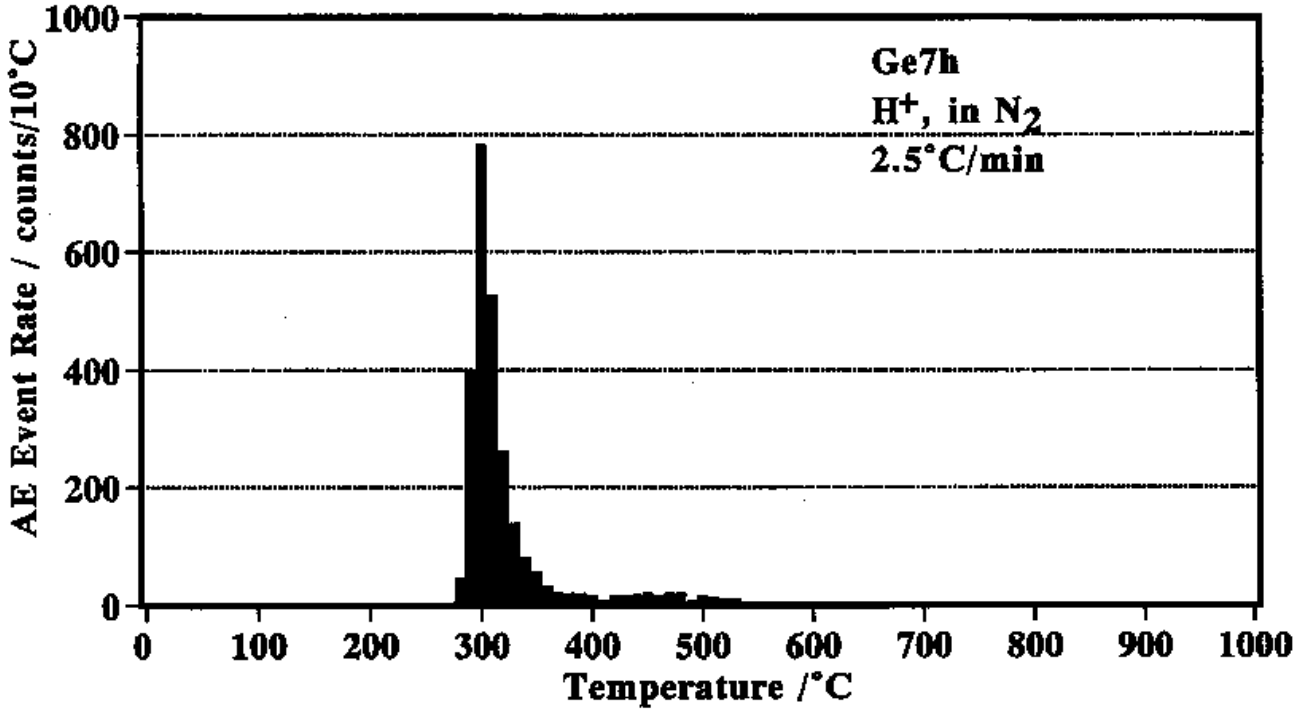

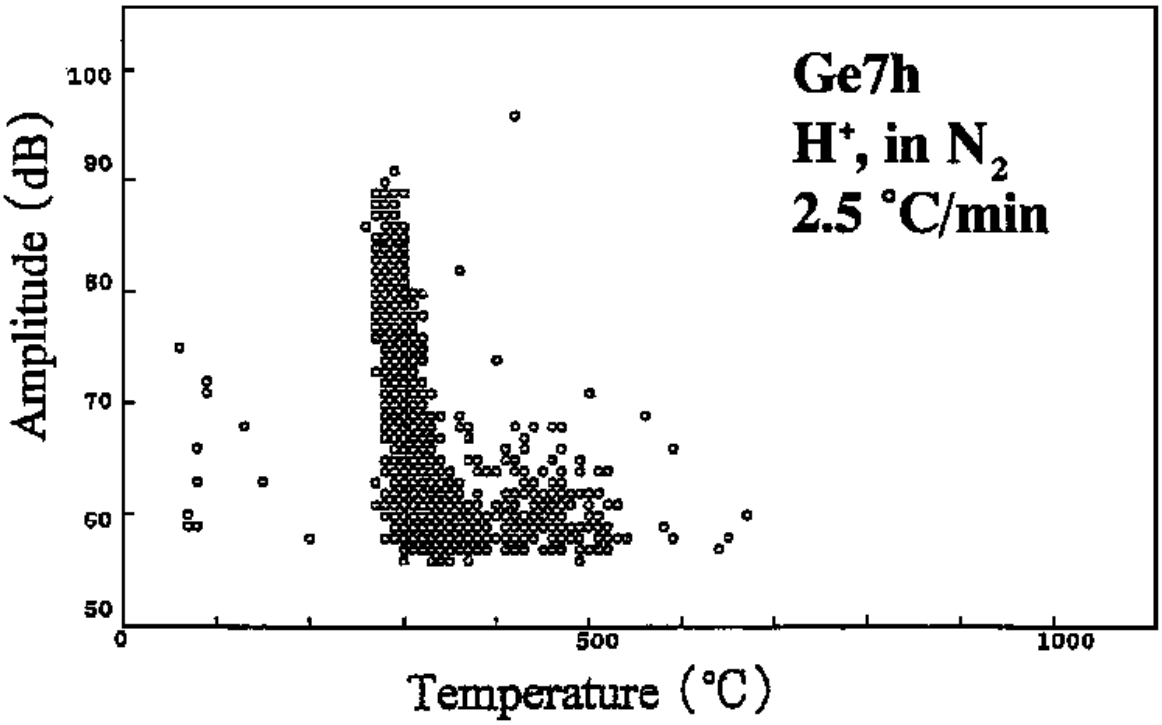

(e, f) AE event rate and amplitude: 2.5˚C/min.

Fig. 8 AE behavior during heating at three rates in nitrogen gas in the H^+ implanted Ge single crystal.

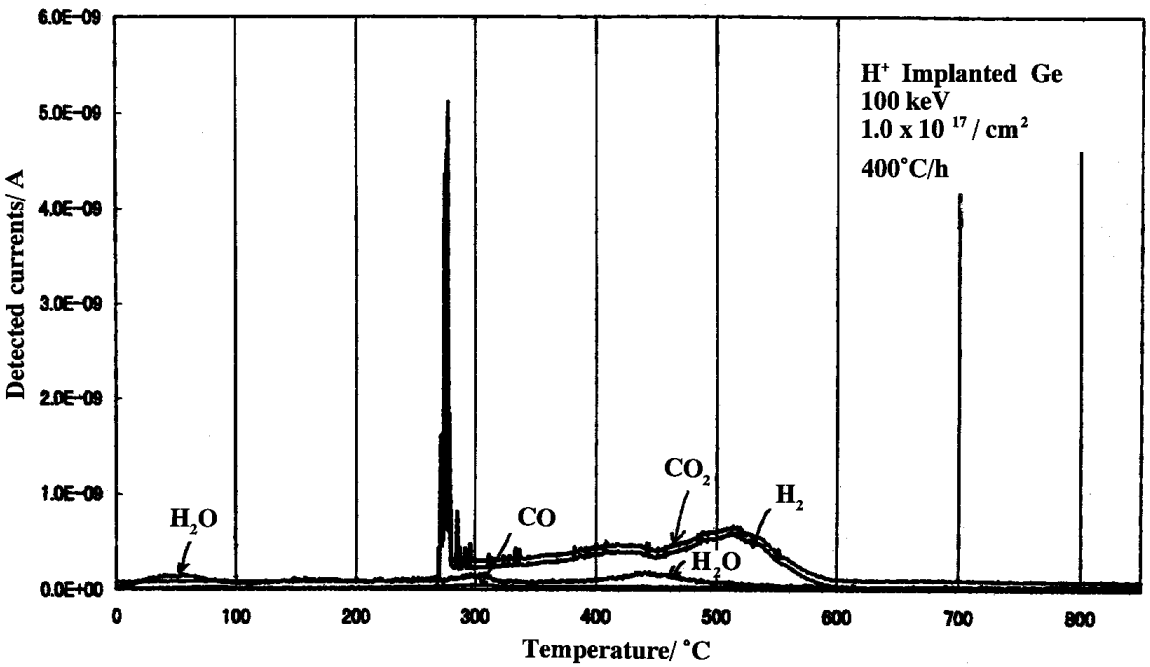

Fig. 9 Desorption curves of various gases in a H^+ implanted Ge single crystal wafer.

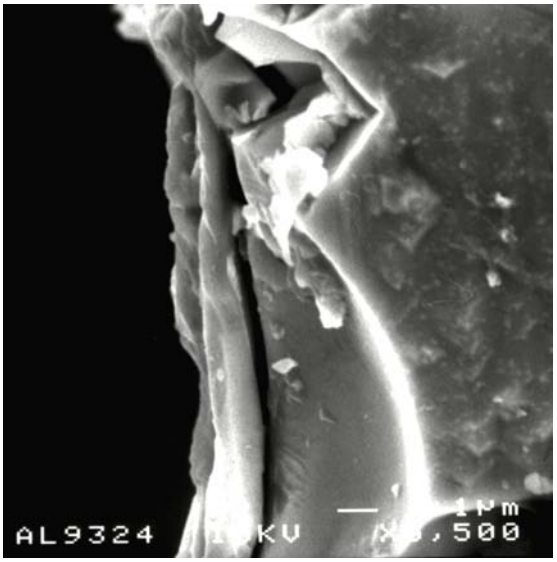

Fig. 10 A typical cross sectional SEM micrograph of hydrogen implanted Ge wafer (10˚C/min).

8. K. Asaoka, K. Yoshida, K. Hamada and M. Kon: Dentistry in Japan, **35** (1999), 89.
9. M. F. Beaufort, H. Garem and J. Lepinoux: Phil. Mag. A, **69** (1994), 881.
10. K. Kajiyama, T. Yoneda, M. Inoue and T. Hara: Technical Report of IEICE, SDM **96**-161 (1996-12), 31.

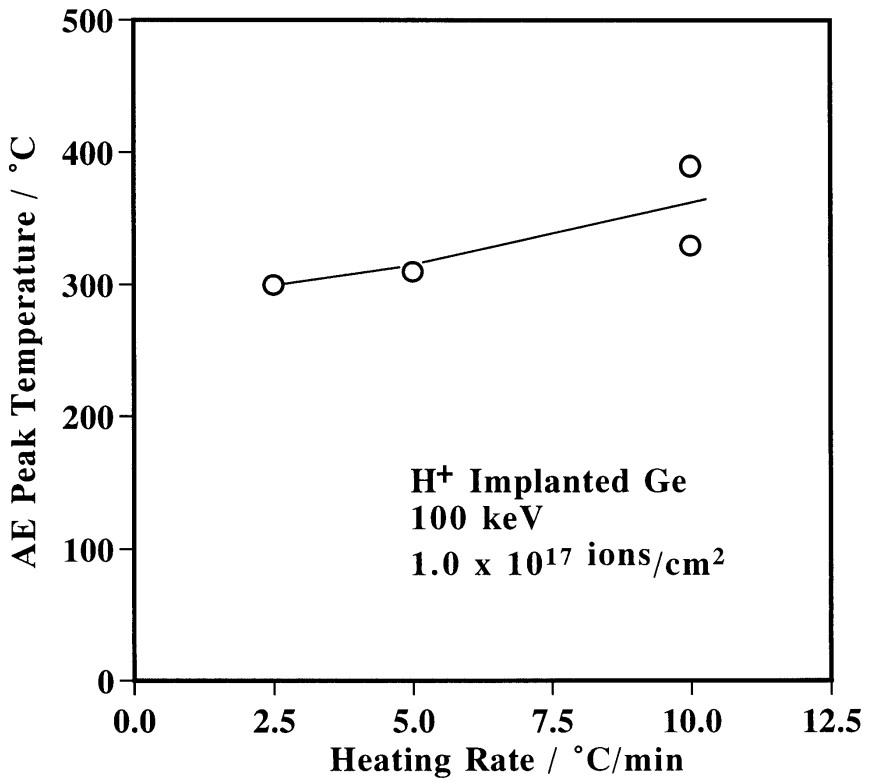

Fig. 11 Effect of heating rate on the temperature for the maximum AE event rate.

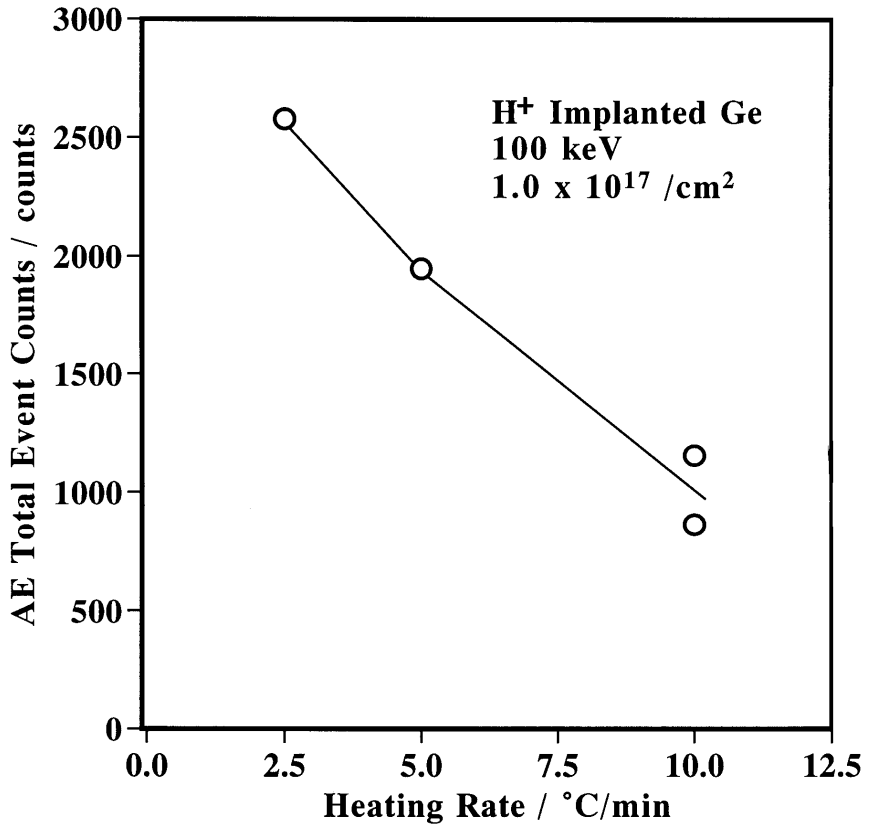

Fig. 12 Effect of heating rate on total AE event counts.

DAMAGE DETECTION IN A FIBER-REINFORCED CYLINDER (FISHING ROD) BY GUIDED WAVE ACOUSTIC EMISSION ANALYSIS

YOSHIE HAYASHI, YOSHIHIRO MIZUTANI, HIDEO NISHINO, MIKIO TAKEMOTO and KANJI ONO*

Faculty of Science and Engr., Aoyama Gakuin University, Setagaya, Tokyo 157-8572, Japan
* Dept. of Materials Science and Engineering, UCLA, Los Angeles, CA 90095-1595, U.S.A.

ABSTRACT

We propose an AE source location method in a fiber-reinforced composite cylinder on the basis of guided waves. The composite has a complex lay-up; a fishing rod composed of glass fiber mat in the inner surface, 5 layers of unidirectional carbon fiber and a spiral carbon fiber in the outer surface. We first quantified the velocity dispersion of L(0,1) and F(1,1) mode cylinder waves using a pulse laser and an AE sensor. Artificial AE sources were next excited by a point YAG laser and detected by two sets of three AE sensors attached at 120° step on the surface. Waveform similarity and arrival time difference of F(1,1) mode at 225 kHz were utilized for locating the circumferential zone (split thrice into 120° zone) and axial zone (length direction in 7 mm step), respectively. Most artificial sources were identified into a correct zone. Utilizing the location algorithm developed, the initiation and progression of local damage during axial–compression of the rod were studied. The source locations estimated agreed with the location of fiber delamination revealed by post-test dye-penetrant examination.

1. INTRODUCTION

Fiber-reinforced composite cylinders and cylindrical containers are widely used as sporting goods, corrosion resistant pipes, cryogenic vessels and so on. These composites have complex lay-ups of reinforcement, and possess excellent mechanical characteristics. Drawback lies in the buckling and impact damage. Damage detection by AE monitoring is valuable for the integrity evaluation of newly developed equipment. However, the source location of AE in hollow cylinders is difficult compared to those of bulk-mode and Lamb-wave AE, since signals in a cylinder propagate as multi-mode guided waves (or cylinder waves). Complex nature of cylinder waves is complicated by anisotropic reinforcement. We recently developed new source location methods of Lamb waves in anisotropic CFRPs [1] and of the cylinder waves in metallic pipes [2]. For the Lamb-wave AE, we utilized group velocities at a selected frequency obtained by the wavelet transform of Ao-mode waves. The source location was accurately identified within the error of the wall thickness. A source location method of cylinder waves is also given in this symposium [3].

In this paper, we introduce a new and simplified source location method of cylinder wave AE in a fiber reinforced composite. It is applied successfully to the source location of local damage during axial compression of the composite.

2. TEST SPECIMEN AND SOURCE LOCATION

Specimen is a fishing rod (5 m long, 14.6 mm diameter at grip end, for fresh-water fishing), reinforced with a mix of 96 mass% carbon fiber and 4% glass fiber. As shown in Fig. 1, it is

composed of glass-fiber mat in the inner surface, 5 layers of unidirectional carbon fiber and spiral carbon fibers in the outer surface. Young's modulus: E and Poisson's ratio: ν in the axial direction, measured for as-received rod with spiral carbon fibers, are 30 GPa and 0.24, respectively. Those for the rod without spiral carbon fibers are 10 GPa and 0.26, respectively.

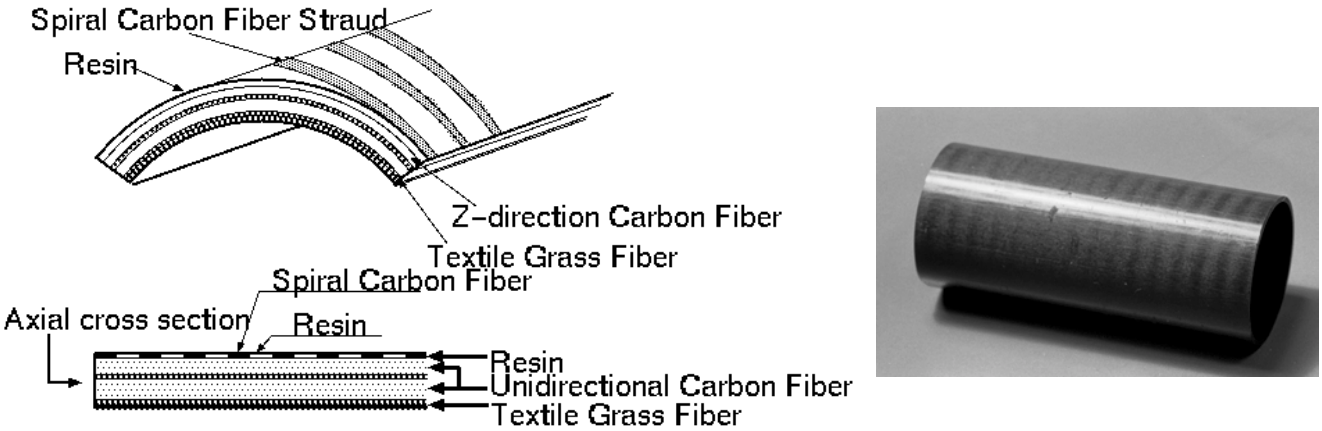

Fig. 1 Ply lay-up and a photo of a pipe section.

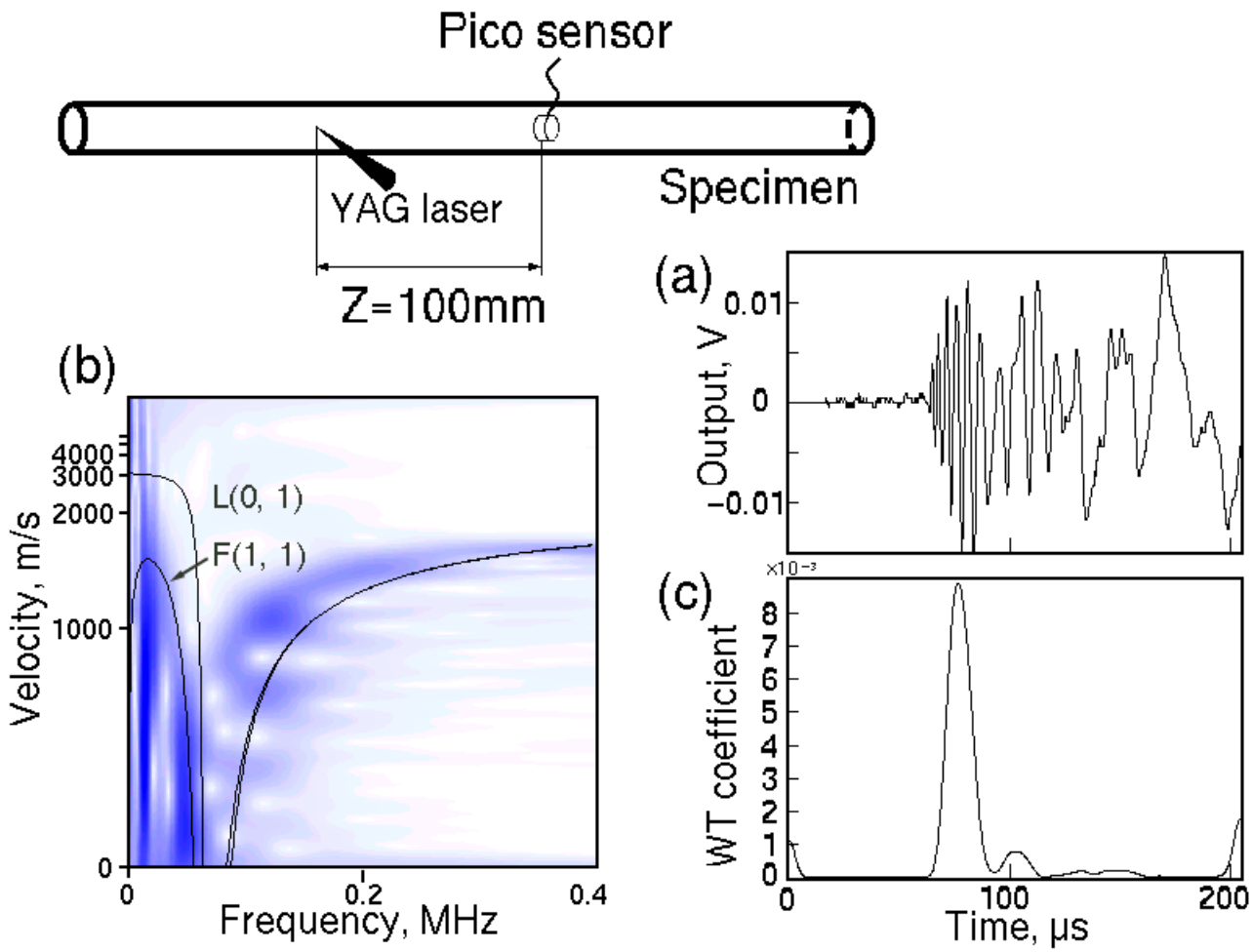

Fig. 2 Experimental setup. (a)Lamb wave AE signal produced by pulse YAG laser. (b) The contour map of wavelet coefficients and group wave dispersion curves for cylinder waves.
(c) The wavelet coefficient at 225 kHz vs. arrival time.

Due to the difficulty in measuring the anisotropic elastic properties by mechanical testing, we first quantified the characteristics of cylinder waves propagating in the rod. As shown in Fig. 2, we excited cylinder-waves by directing a point-focused YAG laser pulse on the rod surface. The arriving waves were monitored by an AE sensor (PAC Type PICO). Detected waves, Fig. 2(a), show characteristic features of cylinder waves, with small amplitude L(0,1) mode arriving at around 20 μs, followed by large amplitude F(1,1) mode. Group velocity dispersions, constructed from the contour map of wavelet coefficients and time-of-flight method, are shown in Fig. 2(b). Theoretical group velocity dispersions of the L(0,1) and F(1,1) modes, computed by using E=20 GPa and ν=0.25, are superposed in the figure. These elastic constants are average of two values measured for the rod with and without outer spiral fiber. Due to strong anisotropic properties of the rod, ridges (higher wavelet coefficients) of the contour map do not completely coincide with the computed group velocity dispersions. Therefore, we measured the group velocity at selected frequency and utilized them for source location. Figure 2(c) is an example of time transient of wavelet coefficient at 225 kHz. The main peak at ~80 μs corresponds to the arrival of large amplitude wave.

3. SOURCE LOCATION ALGORITHM AND ACCURACY

We first measured the axial distribution of group velocities as a function of frequency. As shown in Fig. 3, cylinder wave AE signal was excited by a laser pulse on the rod surface, and monitored by two sets of three PICO sensors attached at 120° step on the surface 110 mm apart. The origin of the axial (z-) coordinate was at the left sensors and angle θ was measured from ch.1 sensor. AE signals were excited at (z mm, 0°) and monitored by ch.-1 sensor at (0 mm, 0°). Figure 4 shows the distribution of group velocities at frequencies from 150 to 350 kHz. Variation of group velocity is smallest at 225 kHz. Large amplitude of F(1,1) mode at 225 kHz is also useful for the source location (see Fig. 2(b)).

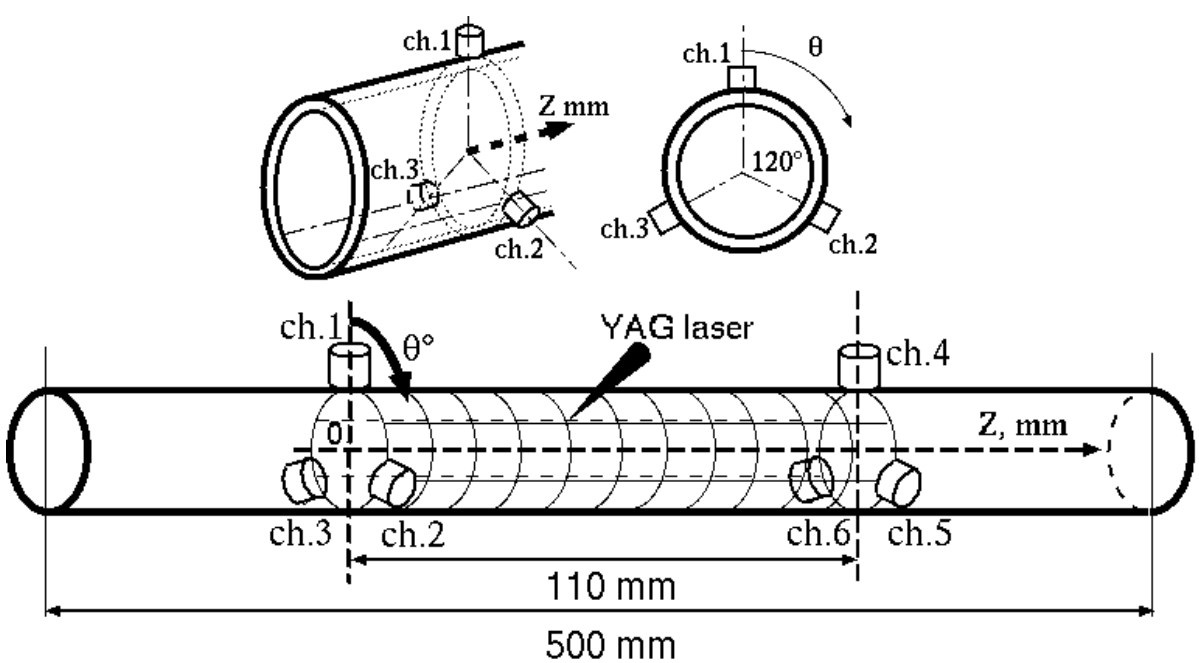

Fig. 3 Setup for cylinder wave generation and monitoring system with the cylindrical coordinate.

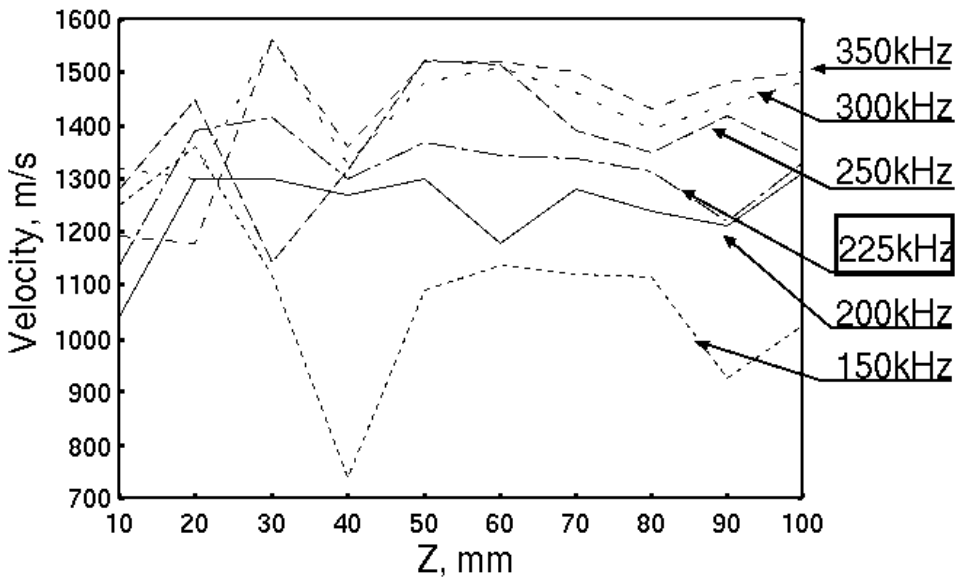

Fig. 4 Changes in the axial group velocities of cylinder waves at different frequencies.

Source location was performed in three steps. First, a rough z-location of the source was identified by using the average arrival time of 225-kHz component at two sets of the sensors. Next, a correct circumferential zone is identified by using similarity coefficient g_{ij} among waveforms detected [4]. The coefficient g_{ij} represents the similarity of dominant F(1,1) mode. An example is given with AE data in Fig. 5. The waves shown in the middle column are excited at position (40 mm, 180°) and monitored by six sensors (ch.1 to 6). Corresponding wavelet coefficients at 225 kHz are shown in the right column. We identify the circumferential zone by comparing the similarity coefficient g_{ij} of the three waves monitored by a set of 3 sensors furthest from the source location. Here, it is the right set. For this case, g_{ij} was highest between ch.5 and 6, and the source was identified to the zone from 120 to 240˚.

For the axial source location, or the third and final step, we select two AE sensors closest to the previously estimated circumferential zone. These sensors are ch.2 or ch.3 in the left set, and ch.5 or 6 in the right set. From the arrival times of 225 kHz component to these sensors, the source location is identified into one of axial zones by using a linear location algorithm. Here, we set the axial zone width of 7 mm since the group velocity slightly varies with z (Fig. 4). The axial position was located as z = 31 mm, from the arrival time 56.4 μs and 29.2 μs to ch.5 and ch.2, respectively. Location error from the exact position (40 mm) was 9 mm.

Location accuracy was examined by using a point-focused YAG laser. Result is shown in Fig. 6. The top figure shows the located zone (dark mesh) for sources placed along sensor-connecting lines (indicated by ●). Eight of ten sources were correctly located. The bottom figure gives the located zones for the sources midway between two sensor-connecting lines (or at $\Delta\theta$ = 60˚). Here, four sources were misplaced to another zone near-by. Incorrect location was due to misreading of the first arrival time of weak 225kHz component. The present location algorithm seems to have a drawback of misplacing the axial zone when the circumferential zone is incorrectly located.

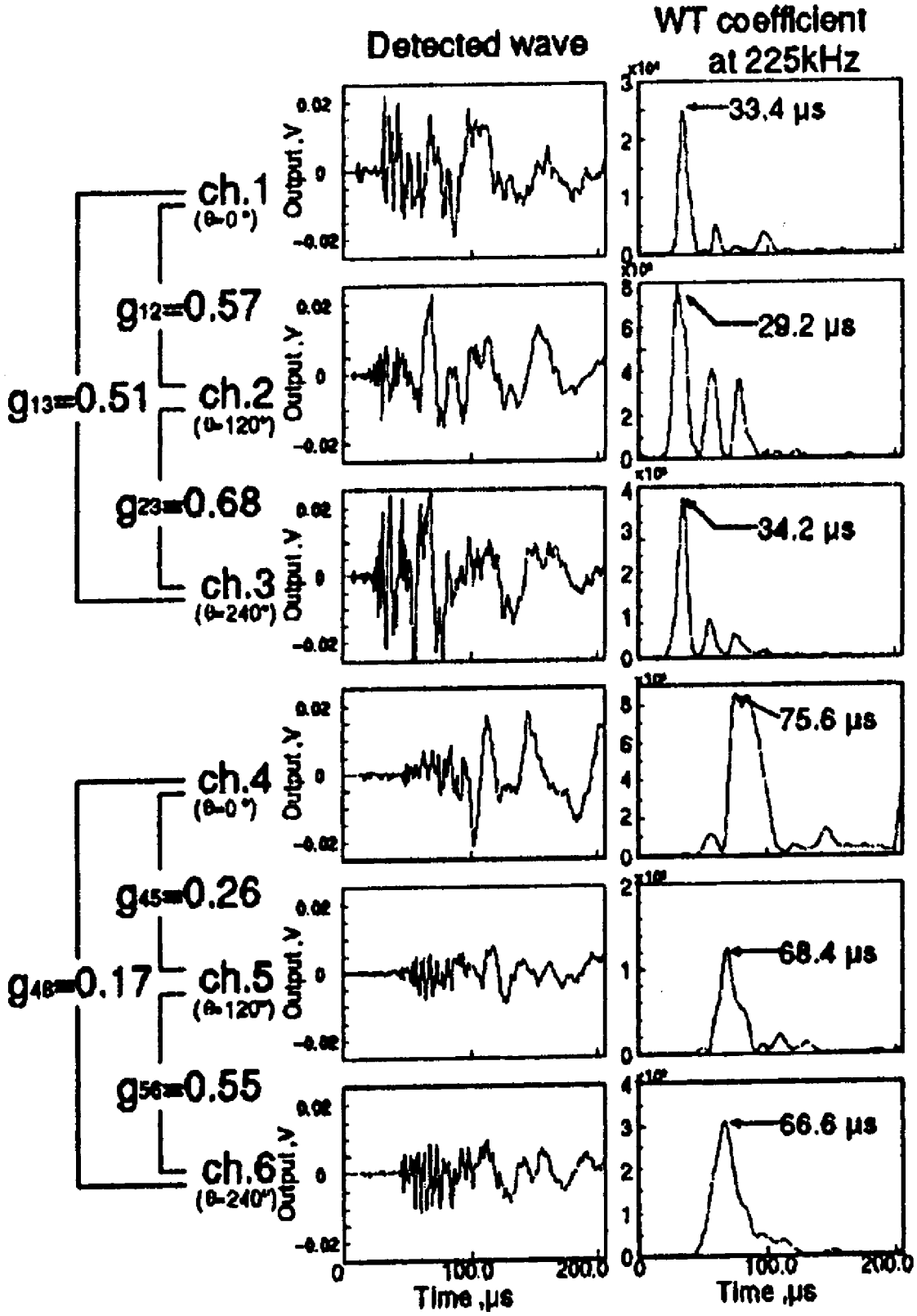

Fig. 5 Finding the source location using similarity coefficients, g_{ij}.

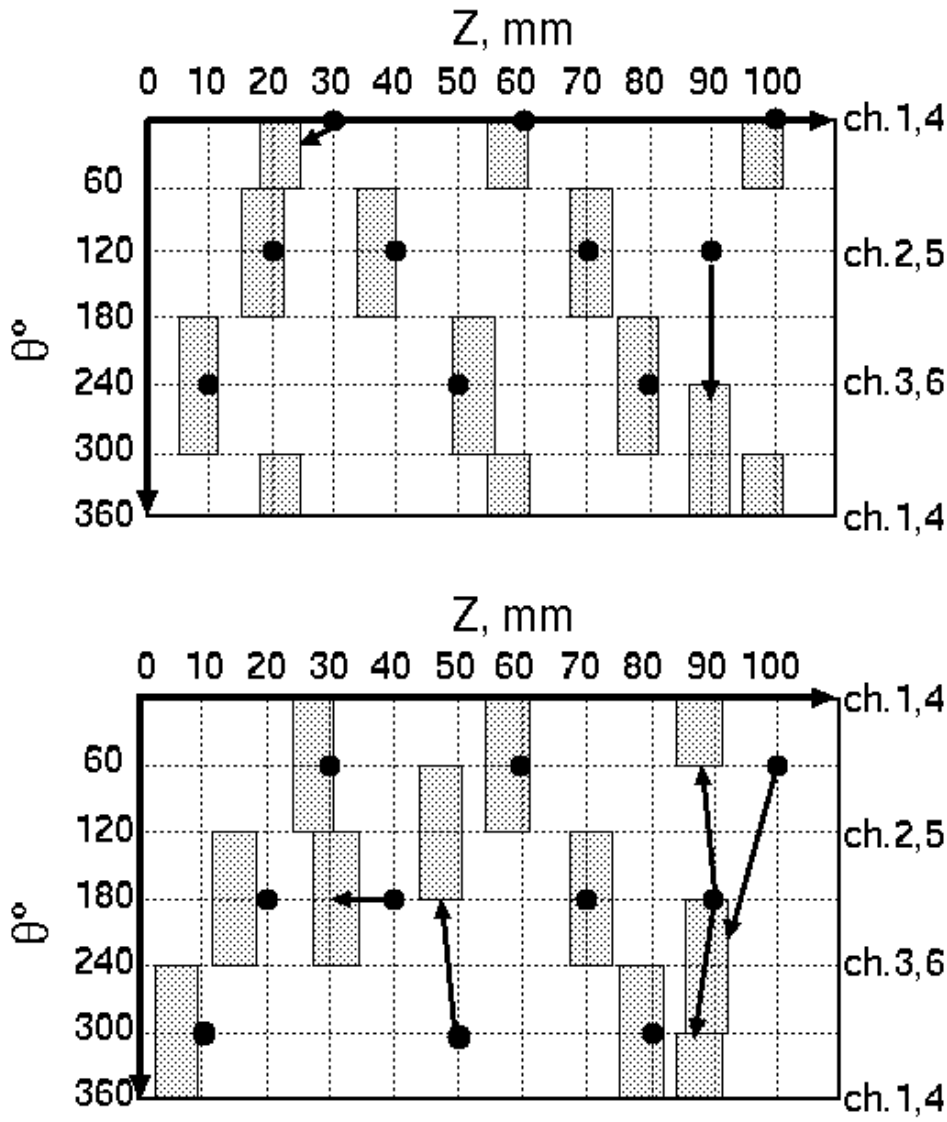

Fig. 6 Estimated source zones and true source positions (●). Top: sources on the sensor-connecting lines. Bottom: sources between two sensor-connecting lines.

4. DAMAGE LOCATION DURING COMPRESSION

Using the test method shown in Fig. 7, we monitored AE during axial-compression of a 210-mm long composite rod. Both ends of the rod were protected by polyester resin skirts from buckling. Figure 8 represents the load vs. displacement. The first AE event was monitored at around 0.7 mm displacement. The amplitude of 12 events (indicated by black arrows) was too weak. At 1.3 mm displacement, a large pop-in was observed and accompanying AE exceeded the monitoring range. Among 27 events monitored below 5 kN, the source location analysis of only 10 events, indicated by white arrows, were possible.

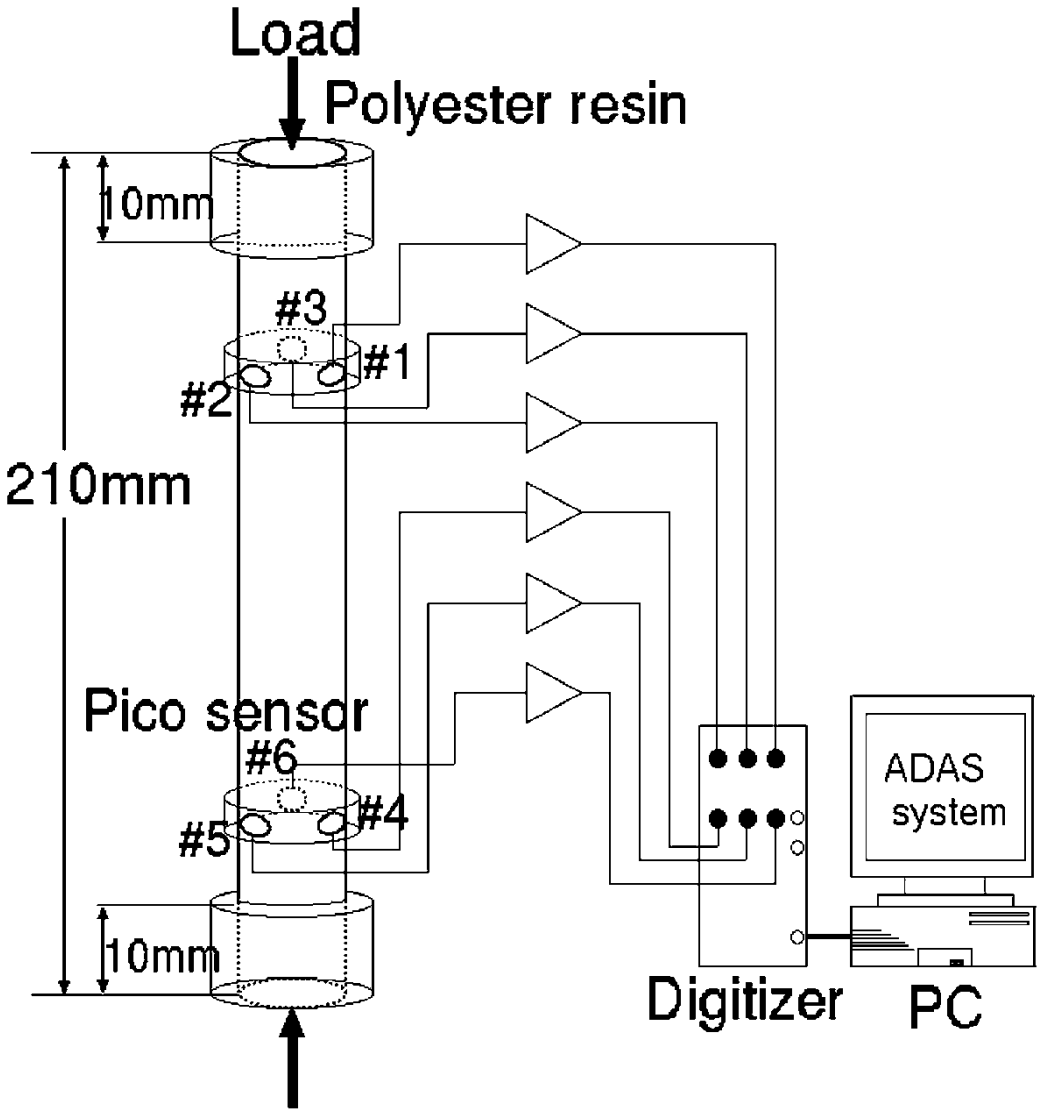

Fig. 7 Setup for axial compression of composite cylinder.

Figure 9 shows AE event count (EC) 16 observed at 1.14 mm displacement. The arrival times are similar for ch.2-6 waves, and the high g_{ij} values between ch.2-3 and ch. 4-5 are at 0.33. This led to the location at (49-56mm,120-240°). Using the arrival time of 42 and 45.6 μs to ch.2 and 5, and 50.2 and 52.6 μs to ch.3 and ch.6, the source was located near the rod center, i.e., z = 49-56 mm.

Progression of source locations is shown with event numbers in Fig. 10. Here, the dark zones at (50-70 mm, 180°) designate that several sources were located there, suggesting the concentrated damage initiation. These locations agreed with the axial fiber-delamination revealed by the post-test dye-penetrant examination (Fig. 11). The fiber delamination, as a precursor of buckling, occurred at z= 50 to 70 mm and θ=180°.

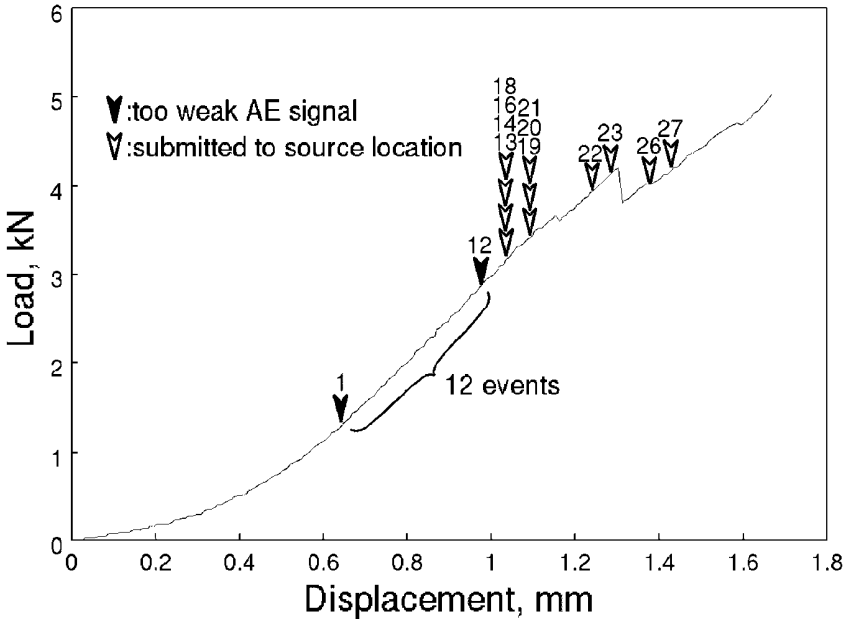

Fig. 8 Load-displacement curve with timing for AE signals indicated by arrows.

5. CONCLUSION

We propose a new and simplified source location method of cylinder-wave AE from a fiber-reinforced composite cylinder. Utility of the developed method was demonstrated for a fishing rod with complex lay-up. Results are summarized below:

1) Wavelet transform makes it possible to determine the group velocity at a selected frequency. We used the axial group velocity of 1350 m/s at 225 kHz for the composite rod.
2) We devised a source location method using the AE signals monitored by two sets of three AE sensors attached on the surface. Source location was conducted in three steps. First, a rough z-location of the source was obtained, then a circumferential zone was identified by using the similarity coefficients of three AE signals (F(1,1)-mode waveform) away from the source. Finally, an axial zone was determined by using the axial velocity at 225 kHz. Most artificial sources (YAG laser ablation) are correctly identified.
3) Sources of AE signals monitored during axial-compression of a 200-mm long composite cylinder were located to zones, in which the fiber-delamination was revealed by the post-test dye-penetrant examination.

REFERENCES

[1] H. Yamada, Y. Mizutani, H. Nishino, M. Takemoto and K. Ono, "Source Location on Anisotropic Plates Using Lamb Waves", 42nd AEWG Meeting, June 15-16, Princeton, USA, (1999).

[2] H. Nishino, F. Uchida, S. Takashina, M. Takemoto and K. Ono, "A new method of source location in Pipes using cylindrical guided waves", 24th EWGAE 2000-European Working Group on Acoustic Emission, May 24-26, France, (2000).

[3] F. Uchida, H. Nishino, M. Takemoto and K. Ono, "Cylinder Wave Analysis for AE Source Location and Fracture Dynamics of Stress Corrosion Cracking of Brass Tube", paper at 15th International Acoustic Emission Symposium, September 11-14, Tokyo, Japan, (2000).

[4] William R.Uttal, "Real-Time Computers", Harper & Row Publishers, (1967), p.185.

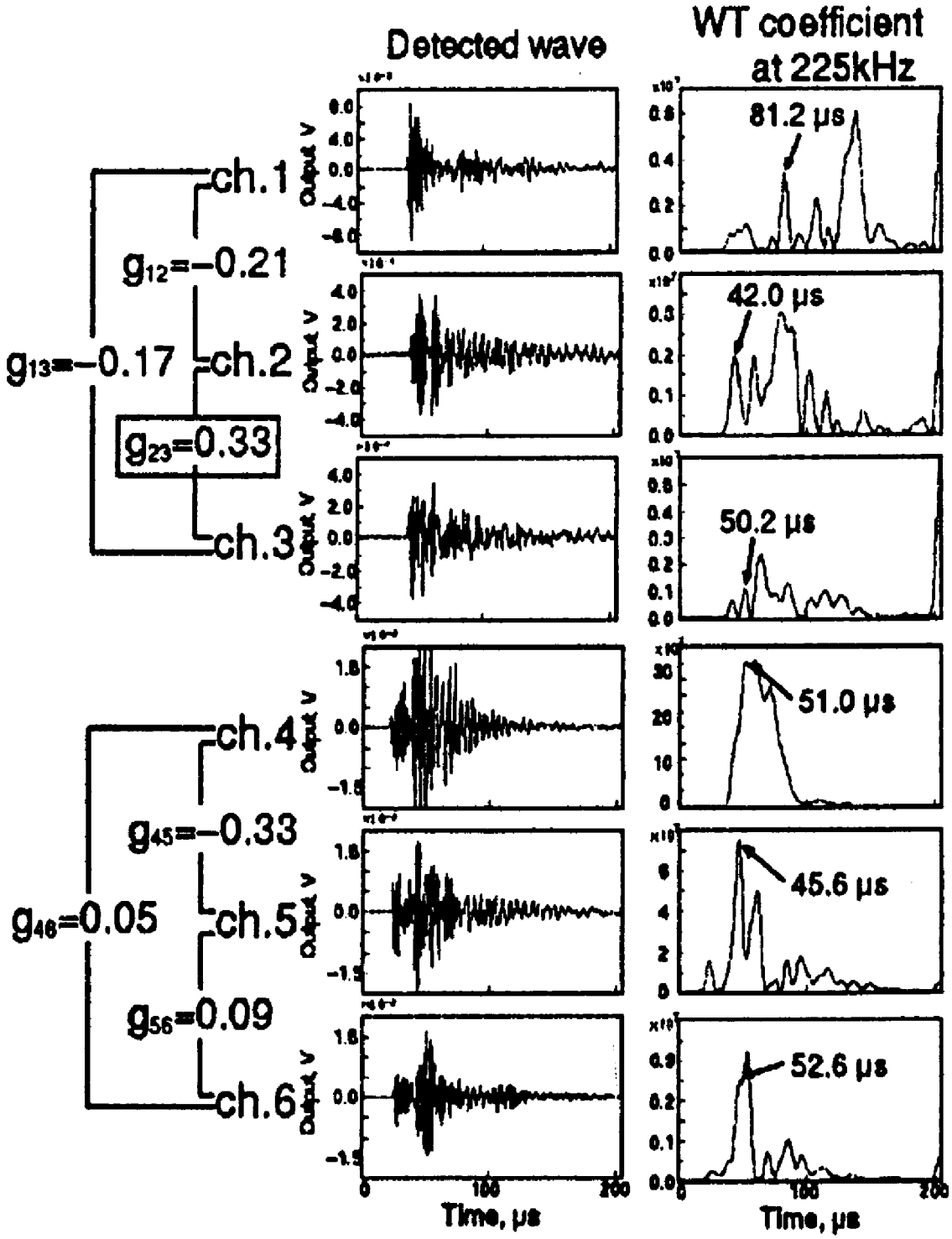

Fig. 9 Cylinder waves (EC 16) monitored during compression (middle), their similarity coefficients (left) and wavelet coefficients at 225 kHz vs. time (right).

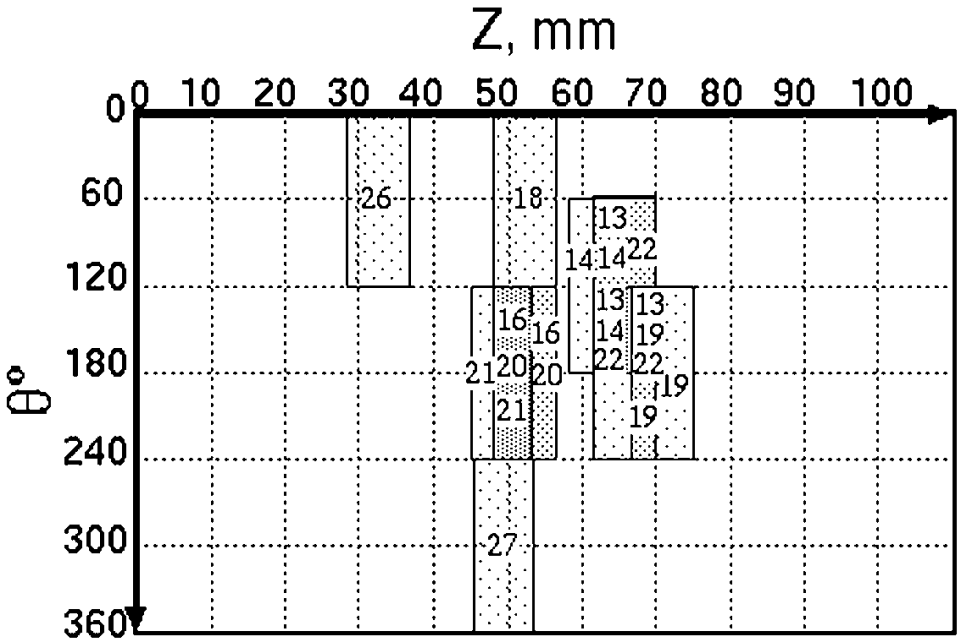

Fig.10 Estimated source location of AE events.

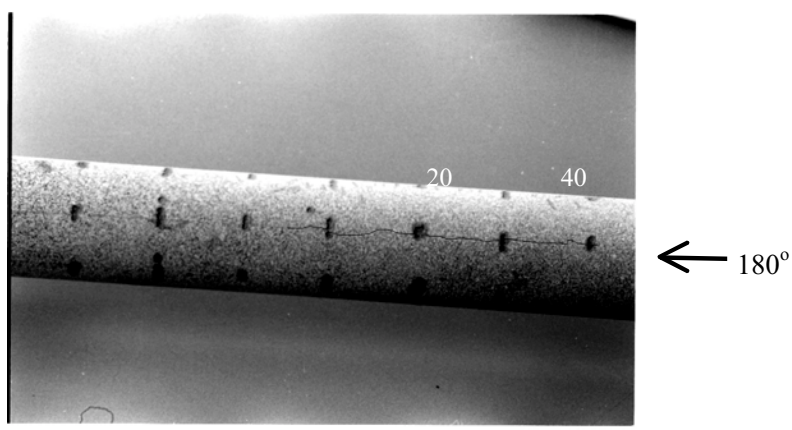

Fig.11 Surface photograph of the rod after the dye-penetrant examination.

ACOUSTIC EMISSION CHARACTERIZATION AND NUMERICAL SIMULATION OF INTERNAL DAMAGE PROGRESSION IN CFRP MULTI-DIRECTIONAL SYMMETRIC LAMINATES

ISAMU OHSAWA, ISAO KIMPARA, KAZURO KAGEYAMA, SATOSHI ABE, and KAZUO HIEKATA*

Department of Environmental and Ocean Engineering, The University of Tokyo, Bunkyo, Tokyo 113-8656, Japan, *SWG, IBM Japan Ltd., Yamato, Kanagawa 242-8502, Japan

ABSTRACT

Acoustic emission characteristics and internal damage progression of multi-directionally reinforced carbon/epoxy symmetric laminates were investigated by applying tensile loads on coupon specimens, which were composed of 0-, 45-, and 90-degree layer. The initiation of transverse lamina crack in 90- and 45-degree layers and the onset of edge delamination in the interlaminar region were monitored by acoustic emission. The monitored results were compared with the results of numerical simulation based on our proposed theory of internal damage progression in multi-directional laminates. The internal cracks were observed by microscopy, and the interlaminar delamination was detected by using ultrasonic C-scan technique. Predicted stress of crack initiation by the proposed theory agreed well with critical stress observed by acoustic emission.

1. INTRODUCTION

It is well known that two kinds of damage, namely transverse lamina crack and interlaminar delamination occur in case of tensile loading of a multi-directional laminate [1], which is composed of extremely anisotropic uni-directional CFRP, at an early stage before ultimate failure. Therefore, the prediction of reduction in stiffness of a laminate due to damage is important in the application of laminated composites to real structures. This damage progression is also likely to influence the ultimate failure strength.

To clarify the damage mechanism of laminates, a large number of damage models have been proposed and analytical simulations have been performed for relatively simple laminated structures such as cross-ply laminates [2] . However, many problems still remain to be resolved, and it appears that no damage prediction method has been established yet. The initial damage occurs in stable progression in such laminated composites. If the damage phenomenon exhibits stable progression, then it is possible to set the allowable stress for composite laminate design at a higher value. However, for setting the allowable design stress at initial damage, it is essential to thoroughly understand the mechanism of damage progression in laminated composites to be used in structures. This requires the establishment of a damage prediction method especially for general-purpose multi-directional laminated composites.

In the present study, AE techniques are used for studying the damage progression of cross-ply laminates. The correlation between crack initiation in 90-degree layer and AE characteristics under tension are discussed first. Next, damage due to transverse lamina cracks is modeled for multi-directional laminates, a theory for internal damage progression is proposed and the influence of stacking sequence on the damage behavior is analyzed by numerical simulation.

Damage progression during tensile tests is monitored using acoustic emission (AE) techniques and the correlation between predicted stress of crack initiation by the proposed theory and AE behavior is discussed.

2. MATERIALS AND SPECIMENS

Cross-ply laminates and multi-directional symmetric laminates were molded using TR340H150 prepreg sheets (0.3 mm/ply and 0.6 mm/ply). Table 1 shows the laminates used for tensile tests. The tensile test specimens were cut from laminated plates using a diamond wheel. The coupons were 300 mm long and 20 mm wide. The specimen edges were polished by waterproof emery paper of #1000 for microscopic inspection of transverse cracks. During the tensile tests, #1000 sand paper followed by #600 sand paper were wrapped around the end of the specimens instead of bonding end-tabs. This measure prevented unnecessary AE generation from the grip area, and proved to be a useful and easy technique for AE measurements during the tensile tests.

3. AE INSTRUMENTATION

AE signals were detected by two 150-kHz resonant-type piezoelectric AE transducers (PAC.R-15), which were attached 150 mm apart at the mid-length of a specimen. A standard pencil lead (JSNDI-006, dia. 0.5 mm, HB) recommended by the Japan Society for Non-Destructive Inspection (JSNDI), was used to confirm adequacy of contact between the AE sensor and the specimen, and also for checking the sensitivity of the AE sensor. The AE instrumentation consisted of Physical Acoustic Corporation (PAC) MISTRAS-2001, filtered through a 20-dB amplifier set for the frequency range of 100 kHz to 300 kHz. The threshold level of the AE system was 1.7 mV at the sensor. The dead time was set at 300 μs.

Table 1 Cross-ply and multi-directional laminates for tensile specimen.

Stacking sequence	Plies	Thickness (mm)
$[0_2/90_4/0_2]$	8	1.2
$[45_2/-45_2/0_2/90_2]_s$	16	2.4
$[45_4/-45_4/0_4/90_4]_s$	32	4.8
$[45_2/0_2/-45_2/90_2]_s$	16	2.4
$[45_4/-45_4/0_4/90_4]_s$	32	4.8

4. RESULTS AND DISCUSSION

Tensile specimens were loaded at the crosshead speed of 0.5 mm/min. Mean strain was measured using an extensometer with a gage length of 100 mm to exclude strain due to local damage.

Cross ply symmetric laminates

The strength of the 90-degree layer is extremely small compared to that of a 0-degree layer. The stress in the 90-degree layer is in a tensile state because of the influence of thermal residual stress. It is well known that transverse lamina cracks easily occur in 90-degree lamina when a

tensile load is applied on the specimen. To correlate cracks in the 90-degree lamina with AE activity, tensile load was increased progressively in steps of 2 kN, the specimen was removed from the testing machine at each step, and the number of cracks on the specimen edge was observed.

Figure 1 shows point plots of AE amplitude vs. time, energy vs. time and tensile load vs. time. Until the maximum load of about 14 kN, most of the data can be clearly classified into AE groups with high amplitude of more than 80 dB, and into regions of no AE activity in the amplitude range of 60 to 80 dB.

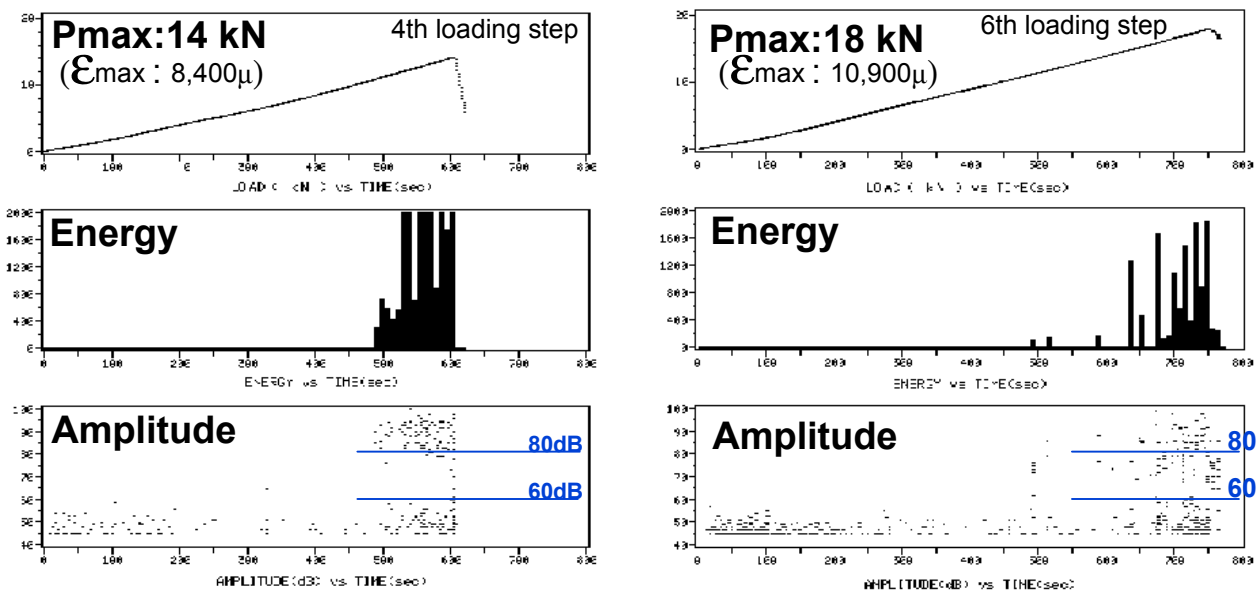

Fig. 1 Diagram of AE output of $[0_2/90_4/0_2]$ cross-ply laminates.

The high amplitude AE corresponds to transverse lamina cracks in the 90-degree lamina [3], and shows a trend similar to that of the number of cracks observed on the specimen edge after removal of the specimen from the testing machine. The plot of load vs. time increased linearly with practically no discontinuities even when AE with high amplitude occurred.

It is concluded, therefore, that the influence of cracks in the 90-degree layer on the reduction in stiffness is extremely small for cross-ply specimens. At loads greater than 14 kN, AE activity began to occur in the range of 60-80 dB, while the number of AE data over 80 dB decreased gradually. Cracks with high AE energy are considered to have occurred initially until a load of 14 kN, while damage modes at low energy started subsequently.

Multi-directional symmetric laminates

In these experiments, load was applied until 90% of the failure strain, the specimen was removed from the testing machine after unloading, and crack density on the specimen edge was measured. Figure 2 shows the point plots of load vs. time, energy vs. time and AE amplitude vs. time for a monotonic static tensile test. The amplitude distribution increased rapidly from about 650 s indicating AE behavior totally different compared to the AE behavior in cross-ply laminates in spite of similar AE measurement conditions, probably because of the inclusion of different damage modes.

After the rapid increase of AE, the plot of load vs. time became discontinuous, indicating that the reduction in stiffness was strongly influenced by the damage. AE activity also showed a peak and included high amplitudes after the rapid increase. The results evidently indicate a transition from the occurrence of cracks requiring high energy to damage phenomenon at low energy such as interlaminar delamination.

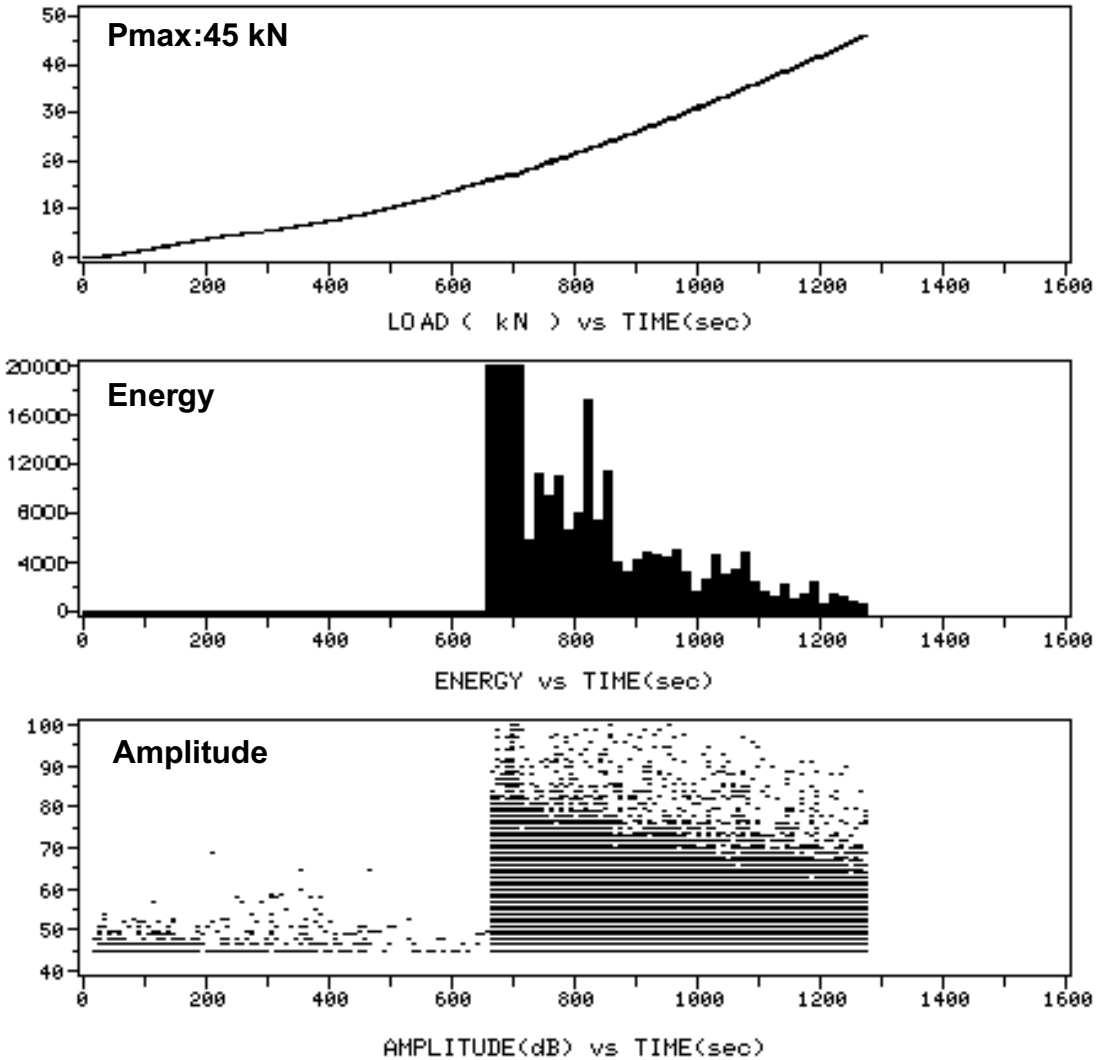

Fig. 2 Diagram of AE output of $[45_4/-45_4/0_4/90_4]_s$ laminates.

5. NUMERICAL SIMULATION AND COMPARISON WITH EXPERIMENT

Prediction of cracks in transverse lamina and internal damage progression

The theory proposed here attempts to predict the occurrence of transverse lamina cracks and the progression of damage in multi-directional laminates using the energy release rate. The prediction of damage is expressed schematically in Fig. 3. An overview of the proposed theory is as follows. An imaginary damage progression of Δc (crack density) is considered for each lamina. The reduction in stiffness, which is the change in potential energy of laminate, indicated by the area with oblique lines in the figure, is assumed to be equal to the energy expended for generating a crack. The stress in each lamina at damage progression is calculated using the energy balance described above. Assuming that damage progresses in each lamina, in which this

stress becomes a minimum, the stress-strain relationship is obtained by repetitive calculations of Δc.

The degradation in tensile stiffness and shear stiffness is obtained by calculating the stress field and the strain field numerically after dividing the symmetrical part in the layer damaged by transverse lamina cracks into elements as shown in Fig. 4.

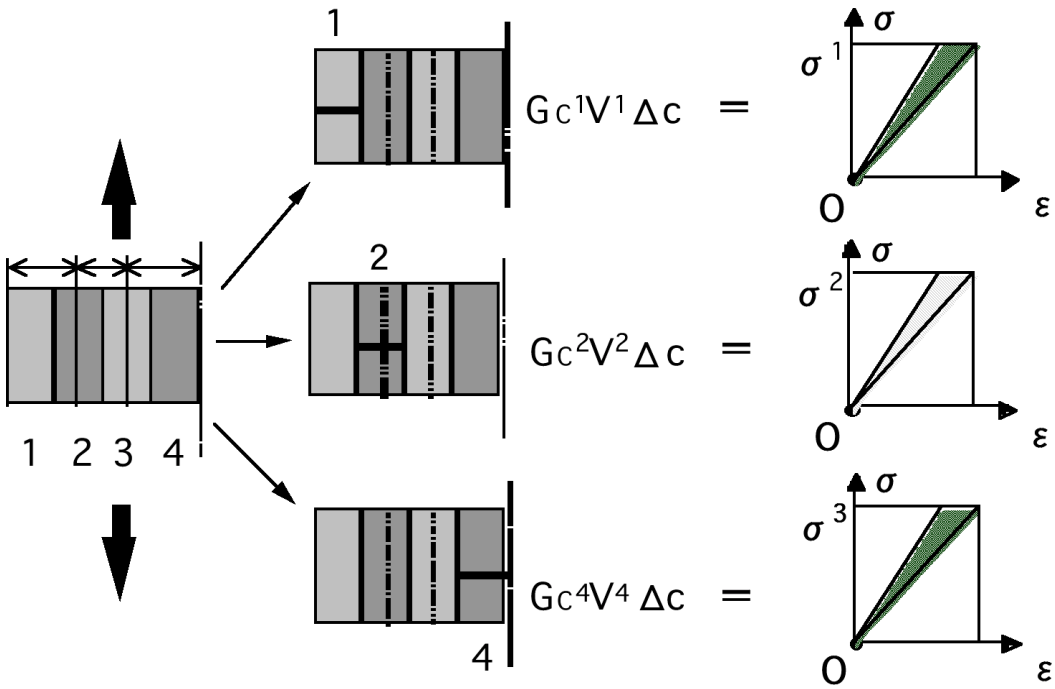

Fig. 3 Schematic illustration of damage estimation using the energy criterion.

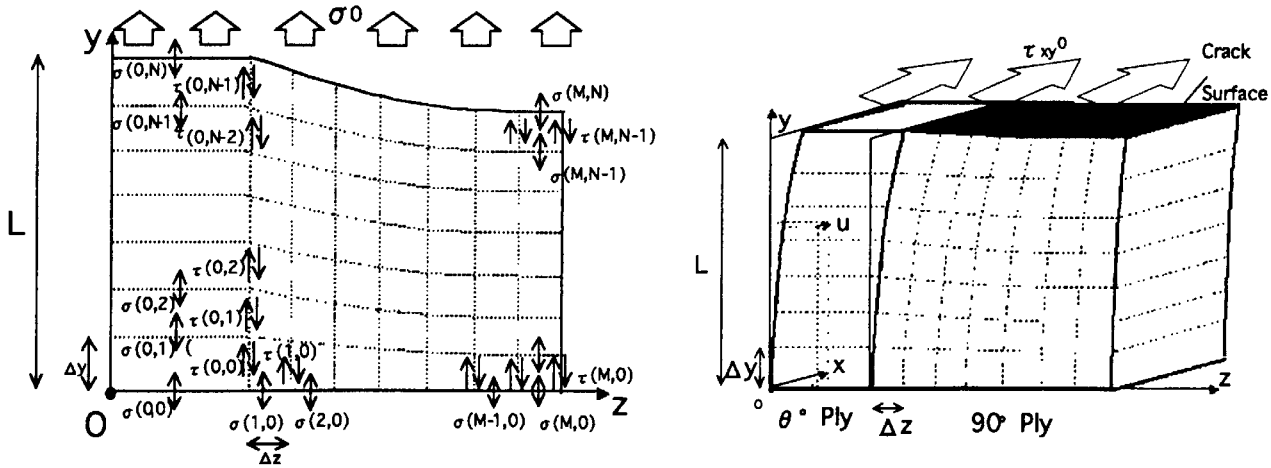

Fig. 4 Schematic illustration of degradation model of tensile and shear modulus.

Comparison with tensile tests

Figures 5 and 6 indicate the comparison of results of numerical simulation and results of tests on multi-directional symmetric laminates. The thermal residual stress was calculated by using the coefficient of thermal expansion and the theory of laminated plate, and then correcting the thermal residual stress of the 90-degree layer. The black arrow in the figure indicates the

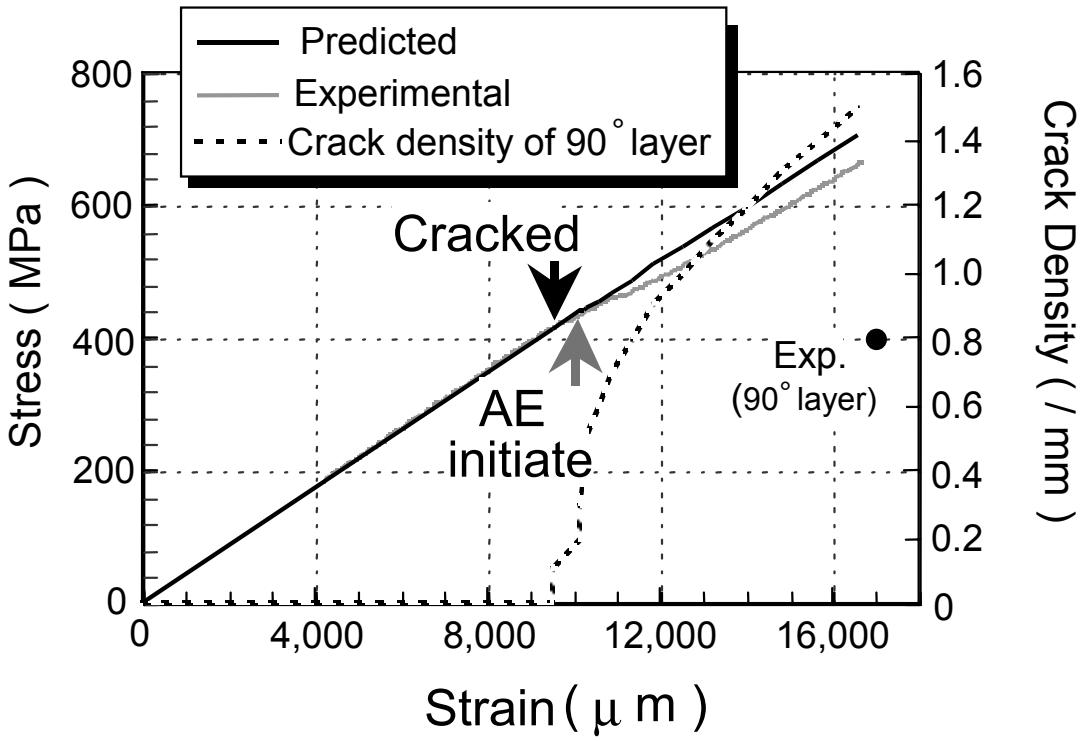

Fig. 5 Comparison of numerical simulation and AE results of $[45_2/-45_2/0_2/90_2]_s$ laminates.

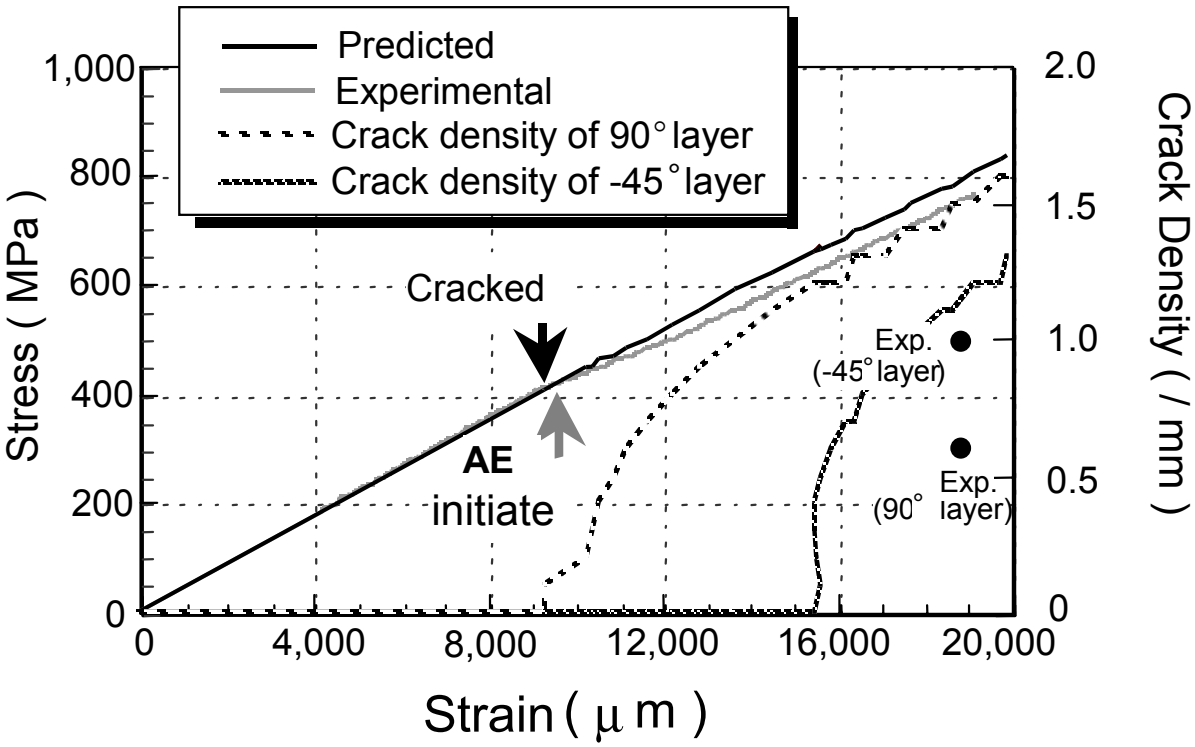

Fig. 6 Comparison of numerical simulation and AE results of $[45_2/0_2/-45_2/90_2]_s$ laminates.

initiation of damage due to crack (crack density equal to 0.1/mm) by simulation, and the gray arrow indicates the point, at which AE starts increasing rapidly.

The results of two kinds of laminates showed that good correspondence for the stress at initiation of damage. However, experimental data of crack density (given in Figs. 5 and 6 as ●) showed low values compared to simulation results. This is because only transverse lamina cracks were considered in the simulation, whereas in the tests, other damage modes such as interlaminar delamination and filament breakage are likely to have occurred after transverse lamina cracks were saturated.

Figure 7 indicates the reduction in stiffness under tension. Experimental values were extremely low compared to the simulation results. Again, this is attributed to the influence of other damage modes, such as interlaminar delamination. Figure 8 shows the C-scan image of a specimen after test. It can be confirmed from this figure that interlaminar delamination originating at the edge of the test specimen extends to the center of the specimen.

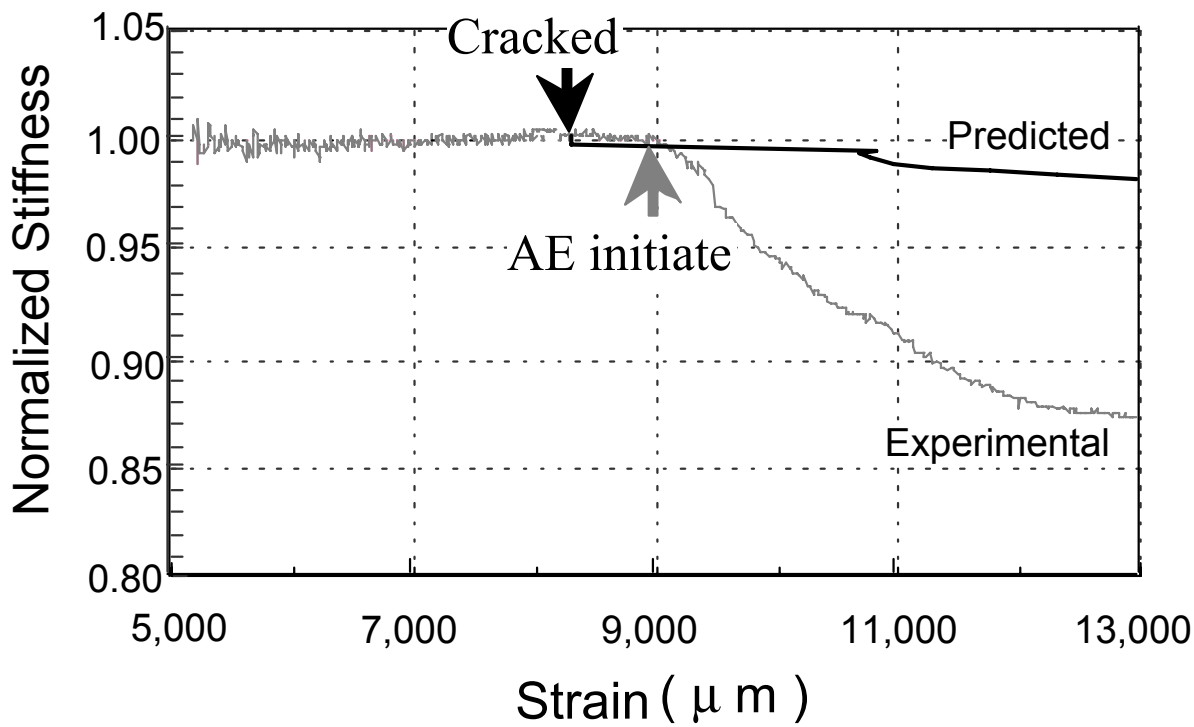

Fig. 7 Comparison of stiffness reduction of numerical simulation and experimental results of $[45_2/0_2/-45_2/90_2]_s$ laminates.

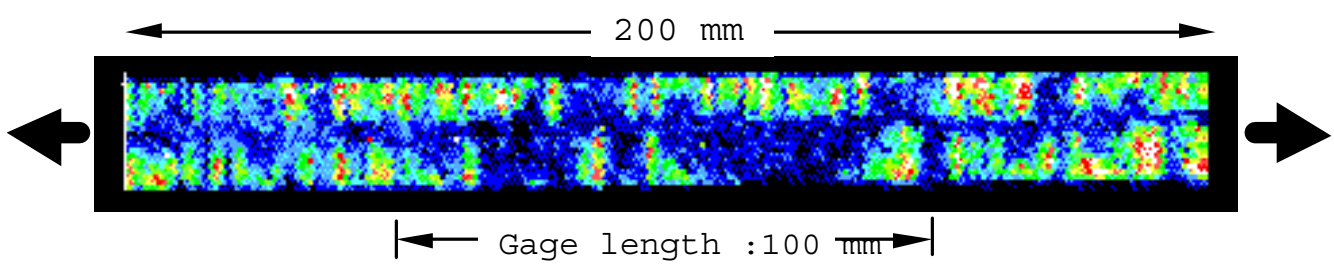

Fig. 8 C-scan image of $[45_4/-45_4/0_4/90_4]$s laminates including interlaminar delamination.

6. CONCLUSIONS

Acoustic emission technique was used during tests on cross-ply and multi-directional laminates, and the behavior of transverse lamina cracking mainly in 90-degree lamina was monitored. It was confirmed that the two kinds of laminate tested showed entirely different AE characteristics. Based on the proposed theory for multi-directional laminates, good correlation between predicted stress at crack initiation and AE initiation stress caused by cracking was observed. However, the actual damage included other damage modes such as interlaminar delamination and extension of crack to the adjacent layer. Accordingly, a new simulation approach using an advanced model that considers the damage modes mentioned above is considered to be essential.

REFERENCES

1. T.K. O'Brien, M. Rigamonti and C. Zanotti, " Tension Fatigue Analysis and Life Prediction for Composite Laminates," NASA Technical Memorandum 100549; Avscom Technical Memorandum 88-B-015 (1988).
2. K. Tohgo, K. Akizuki and Y. Sugiyama, "Ply Cracking Damage Theory and Damage Behavior in CFRP Cross-ply Laminates," Proceedings A of JSME, **64** (621), (1998), 30-37. (in Japanese)
3. I. Ohsawa, I. Kimpara, K. Kagayama and T. Suzuki, "Acoustical Analysis of Transverse Lamina Cracking in CFRP Laminates under Tensile Loading," Proceedings of 4th International Symposium on Acoustic Emission from Composite Materials, (1992), pp. 55-64.

SCC MONITORING OF ZIRCONIUM IN BOILING NITRIC ACID BY ACOUSTIC EMISSION METHOD

CHIAKI KATO and KIYOSHI KIUCHI

Japan Atomic Energy Research Institute, Department of Nuclear Energy System,
Tokai, Ibaraki 319-1195, Japan

ABSTRACT

Zirconium has been used as structural materials for heavily corrosive devices in recent commercial reprocessing plants. Although it has excellent corrosion resistance against nitric acid solutions, the susceptibility to stress-corrosion cracking (SCC) increases with increasing the concentration of nitric acid and temperature. We attempted to monitor the initiation and propagation of the trans-granular type SCC by measuring acoustic emission (AE). AE signals were monitored during the slow strain-rate tensile test (SSRT) with notched specimens. Two AE sensors were mounted for reducing boiling and mechanical noise. The SSRT was pursued in a boiling nitric acid with 3 to 12 in normality, comparing with the reference tests in silicone oil at the same temperature. The stress level for detecting the AE signals due to TGSCC was decreased from near the tensile strength to 0.2%-proof strength with increasing the concentration of nitric acid. The practical possibility of AE method for monitoring the SCC was established from a good correlation between the AE signals and the fraction of surface area fractured by SCC on the SSRT.

1. INTRODUCTION

Sufficient corrosion resistance against boiling nitric acid solutions including oxidizer ions of TRU and FP elements is required for the materials used in commercial reprocessing plants for spent oxide fuels (1). Austenitic stainless steels with ultra-low carbon grade such as types 304L and 310Nb had been developed for this purpose. However, these materials have suffered from inter-granular attacks due to trans-passive corrosion mainly at heat transfer surfaces with high oxidation potential. In the recent design, the application of these steels is limited to devices operated at low boiling point of less than 70˚C at low pressures for inhibiting the trans-passive corrosion (2). On the other hand, zirconium has been used as one of the alternative materials applied for devices operated in the normal pressure like a dissolver and Pu evaporator. This metal without trans-passive behavior shows excellent corrosion resistance in heavily oxidizing nitric acid solutions. However, it shows high susceptibility to transgranular-type stress corrosion cracking (TGSCC) in nitric acid solution (3). Our previous study has shown that the susceptibility to SCC depends strongly on the concentration of nitric acid and the crystallographic texture of zirconium, because it is easy to propagate along the closed packed

planes like (0001) of hcp crystal structure (4). The SCC mechanism is interpreted as the quasi-cleavage type cracking controlled by the film rupture mechanism. The appropriate monitoring method for the SCC of devices made of zirconium would be required to confirm the reliability during the operation.

In this study, the practical applicability of AE measurement for monitoring the SCC of zirconium was examined using the slow strain-rate tensile test (SSRT) in boiling nitric acid solutions.

2. EXPERIMENTAL PROCEDURES

(1) Test Specimens

Test specimens were prepared from zirconium metal plates with the chemical composition of ASTM 702 pure grade as shown in Table 1. This material was refined by vacuum arc remelting (VAR), hot rolled to 8 mm in thickness and annealed in the alpha-phase stable temperature. The mechanical properties of this material are shown in Table 2. In the present test, round notched specimens have been employed for confirming AE signals at the cracking position. The shape and dimension of this specimen are shown in Fig. 1. The susceptibility to SCC of the notched specimen in nitric acid solutions was confirmed in another report (5). The notch was machined parallel to the hot rolling direction, which is easy to propagate SCC. The AE sensor was directly contacted to specimens to obtain high sensitivity. Two AE sensors were attached for getting AE signals at two different locations. Type A with the notch position set on the equal distance from each sensor was used in oil and in boiling nitric acids with 8 and 12 in normality. However, the noise level reduction was not adequate in this setting. Therefore, type B with the notch position set on difference distance from each sensor was used in boiling nitric acids with 3 and 6 in normality. The noise level was markedly suppressed due to the time lag of AE signals input between each sensor.

(2) AE Measurement

A block diagram for the AE measurement used in the present study is shown in Fig. 2. The MISTRAS-2001 system made by the Physical Acoustics Corporation (PAC) was used. The outline for AE measurement was described in Table 3. The resonance-type AE sensor having the center frequency at 150 kHz (PAC, R15) was used. The AE parameters, time, rise time, amplitude, counts to peek, duration, total counts and AE waveform, were measured for each AE event. The sampling rate of AE waveform is 4 MHz. AE signals obtained from the sensor were amplified at 80 dB and filtered to pass signals with the frequency range from 10 to 400 kHz. This system consisted of a pre-amplifier and main amplifier with band-pass filter. The threshold of AE signals was set at 10-20 mV. The front-end filter was used in order to reduce the electrical-noise-like impulse. In addition, the location of objective AE source was clarified by comparing the time lag of AE signals at each position for eliminating noises caused from bubbles or mechanical contact. The difference-time filter (delta-T) of input signal from each sensor was

Table 1 The chemical composition of zirconium plate. (wt.%)

H	C	N	O	Fe+Cr	Hf	Zr+Hf
<0.0004	0.02	0.005	0.14	0.08	0.8	>99.2

Table 2 The mechanical properties of zirconium plate.

Temperature	0.2% proof strength	Tensile strength	Elongation	Reduction of area
373 K	204 MPa	410 MPa	27.6 %	47.8 %
523 K	89 MPa	244 MPa	46.4 %	64.4 %

Table 3 The setting condition of AE measurements.

AE Sensor type	R15 150kHz resonance
Amp-gain	40 dB
Preamp-gain	40 dB
Wave Sampling rate	4 MHz
High pass filter	10 kHz
Low pass filter	400 kHz
Threshold	40 ~ 45 dB
Peak definition time	300 μs
Hit definition tume	600 μs
Hit lockout time	1000 μs
Front end filter	> 3 counts
Delta-T filter	<10 μs (12,8N HNO3,OIL) >2,<7 μs (6,3 HNO3)

set within 10 μs for type-A specimens. The same AE event would be monitored at 42 mm away from the notch center by assuming the velocity of AE waves of 4200 m/s. However, the setting condition was unable to reduce the noise due to boiling bubbles. Therefore, the setting condition of delta-T filter was changed to 2 to 7 μs for type B specimens.

(3) Slow Strain-Rate Tensile Test (SSRT)

The susceptibility to SCC of zirconium depends on the concentration of nitric acid as reported in the previous study. The present experiment examined SSRT in boiling nitric acids with 3 to 12 in normality. The reference data was obtained by the same SSRT in chemically non-active silicone oil at 115˚C (6). The crosshead speed on the SSRT was controlled at 1.67 x 10^{-6} mm/s, which correspond to the appropriate strain rate for detecting the susceptibility to film-

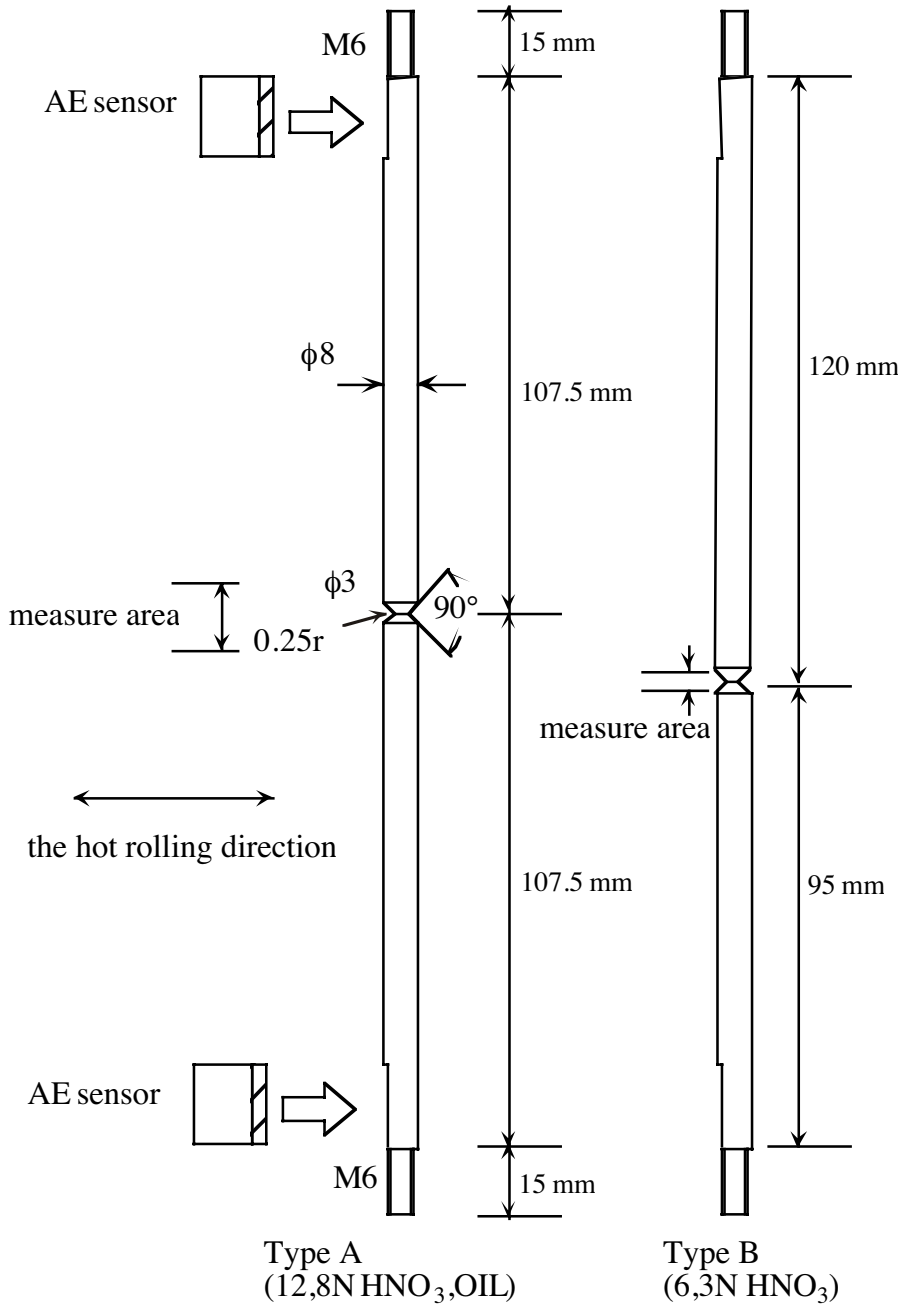

Fig. 1 The notched specimen used for the SSRT.

rupture-type TGSCC. The test cell consists of the see-through type double glass wall with the evaporated metal film heater and hard Teflon flanges. The internal glass diameter is 70 mm. The test solution was used without renewal during the SSRT, because the solubility of zirconium in boiling nitric-acid solutions is lower than several ppm. After the SSRT, the morphology of the fracture surface was examined in detail by a scanning electron microscope (SEM) for fractographic analyses.

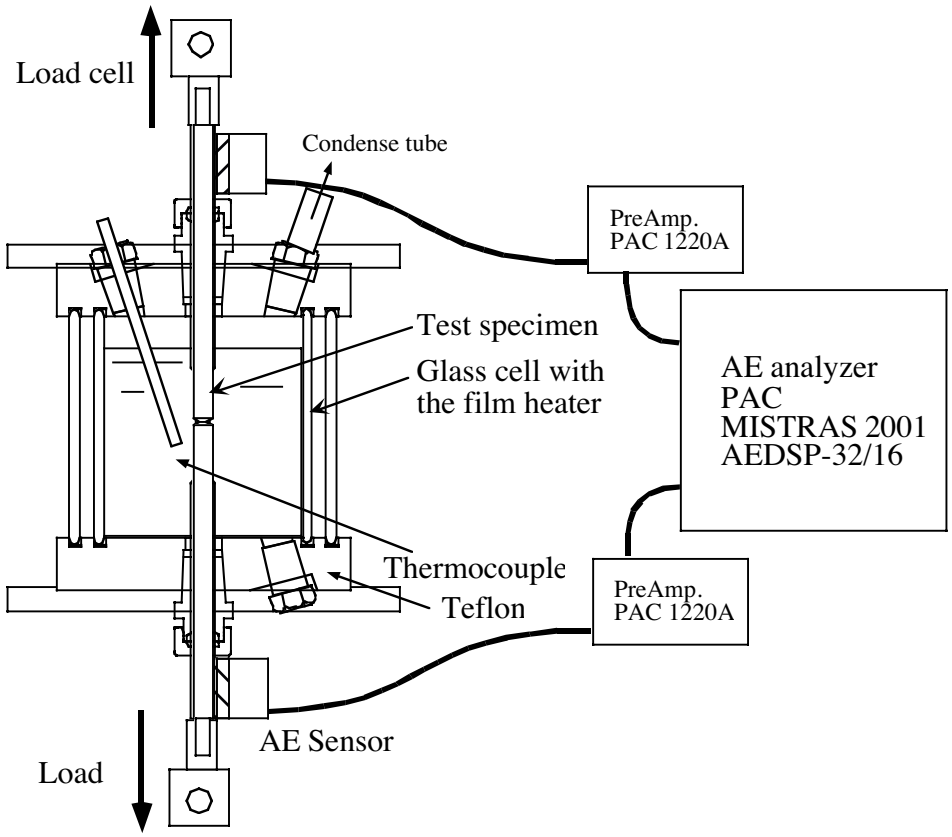

Fig. 2 The schematic diagram of the AE measurement system.

3. RESULTS AND DISCUSSION

Figure 3 shows the stress-time (strain) curves obtained by SSRT in boiling nitric acid and in silicone oil at 115˚C, respectively. Figure 4 shows the histograms of AE hits obtained in boiling nitric acids and silicone plotted against time. Compared with silicone oil, the time to failure is reduced with increasing nitric-acid concentration as expected from the previous SCC reports (6). The reduction rate of rupture time in nitric acids to that in silicone oil were 19%, 21%, 22% and 25% in 3N, 6N, 8N and 12N HNO_3, respectively. It shows the sensitivity to SCC increases with increasing the concentration of nitric acid. In the present analysis condition, the AE event due to the SCC was only obtained in nitric acid solutions, because that due to the plastic deformation was not detected. The background noise on the event of AE signals was detected in a wide range of stress–strain curves, even if the low stress region in 8N and 12N HNO_3. It was expected to come from noise caused by the formation and annihilation of boiling bubbles. The difference in the initial AE counting rate between 8N and 12N HNO_3 would be dependent on the boiling condition as the background noise level was different.

In 12N HNO_3, the rising time of AE hits is nearly 35 hrs and the stress level reaches 215 MPa. In 8N HNO_3, the rising time of AE hits is nearly 52 hrs and the stress level is 305 MPa. In 6N HNO_3 there are two points of rising AE hits. The first rising time of AE hits is nearly 57 hrs

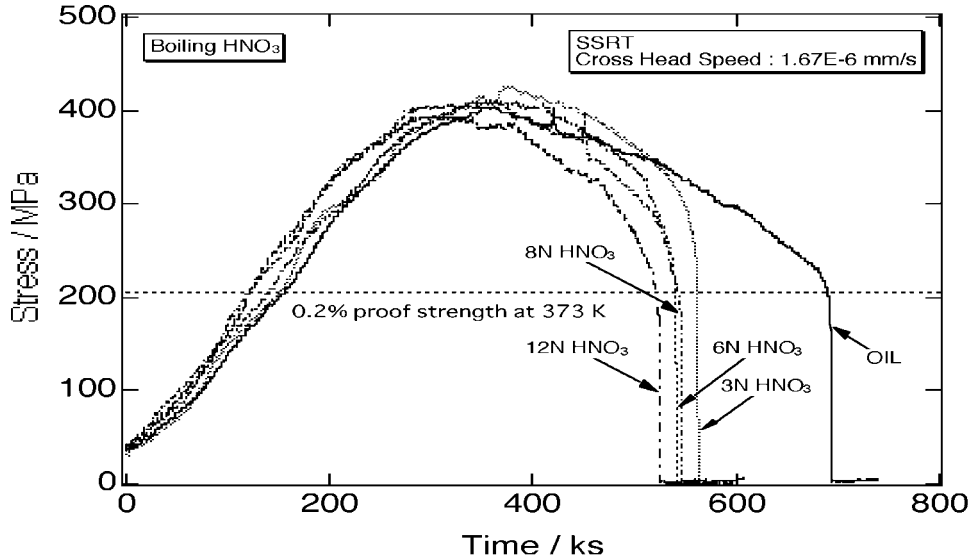

Fig. 3 The stress-time(strain) curves of SSRT.

and the stress level is 293 MPa. In 3N HNO_3, the rising time of AE hits is extended to nearly 109 hours and the stress level becomes 420 MPa. This stress level is comparable the ultimate tensile stress of zirconium at 373 K (see Table 2). The rising time is clearly shortened by increasing the concentration of nitric acid. The stress level of AE event increase due to SCC in 12N HNO_3 was decreased to 0.2%-proof stress level of zirconium at 373 K. In 6N HNO_3, the second peak is arising at close to the tensile stress. This AE hits behavior is similar to that in 3N HNO_3. The present observation shows that the difference of the AE generation mechanisms depends on the concentration of nitric acids.

The optical photographs of the fracture surface after SSRT are shown in Fig. 5. The surface morphology fractured in silicone oil showed the metallic luster and ductile fracture. On the other hand, fracture surfaces in boiling nitric acids showed dark color and quasi-cleavage-type fracture along circumference of notch groove. The area ratio of the quasi-cleavage-type fracture increase with increasing the nitric acid concentration, as 38%, 38%, 65% and 80% in 3N, 6N, 8N and 12N respectively. It depends on the susceptibility to SCC. SEM photographs of the fracture surfaces of SSRT specimens are shown in Fig. 6. On specimens fractured in boiling nitric acids, the ductile fracture is only observed in the center of the fracture surface due to mechanical tearing at the final stage on tensile tests. Figure 7 summarizes the relationship between the susceptibility to SCC, the area ratio of the quasi-cleavage-type fracture and the nitric acid concentration. The fracture surface area by SCC was coincident with the generation rate of AE signals. It is clear that the susceptibility to SCC increases with increasing the concentration of nitric acids to more than 6 in normality.

The waveforms of AE signals were analyzed in order to discriminate the AE signals due to SCC from noise due to bubbles. Figure 8 shows typical AE waveforms and power spectra originated from the bubble and SCC, respectively. The amplitude value of the two conditions is

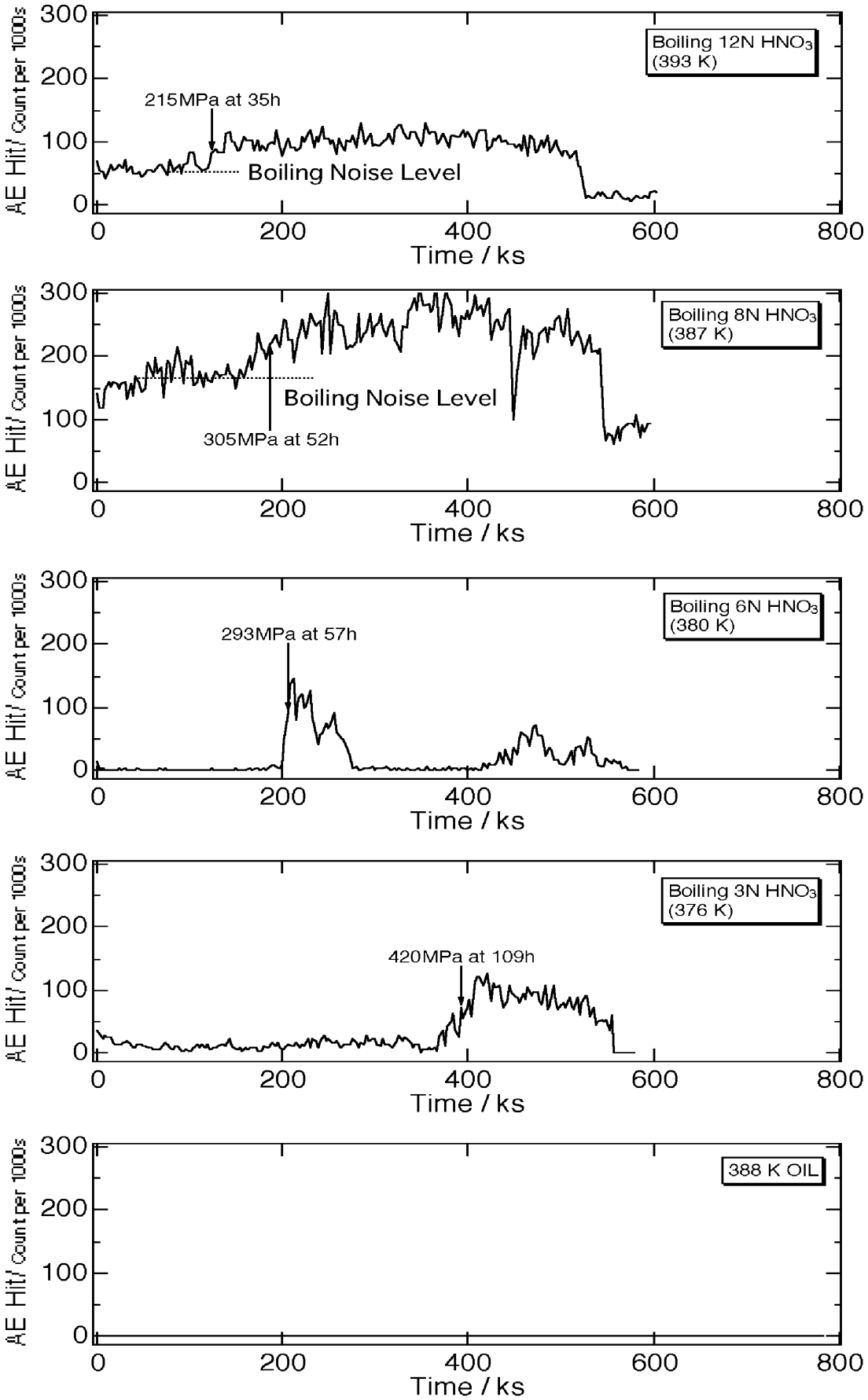

Fig. 4 The histograms of AE hits rate of SSRT.

	OIL	3N HNO_3	6N HNO_3	8N HNO_3	12N HNO_3
optics macroscopic photographs	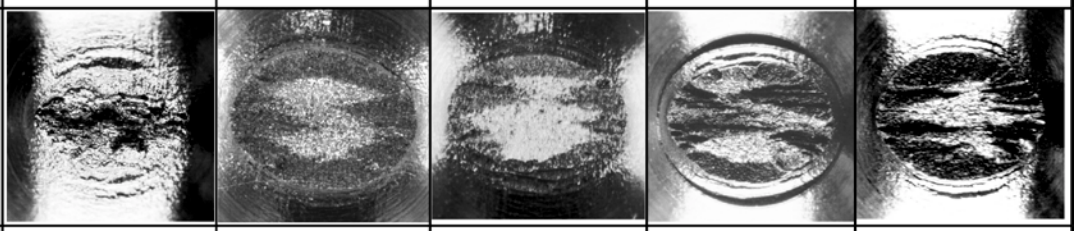				
Area of quasi-cleavage fracture (%)	0 %	38 %	38 %	65 %	80 %

Fig. 5 Optical photographs and the area ratio of quasi-cleavage fracture after SSRT.

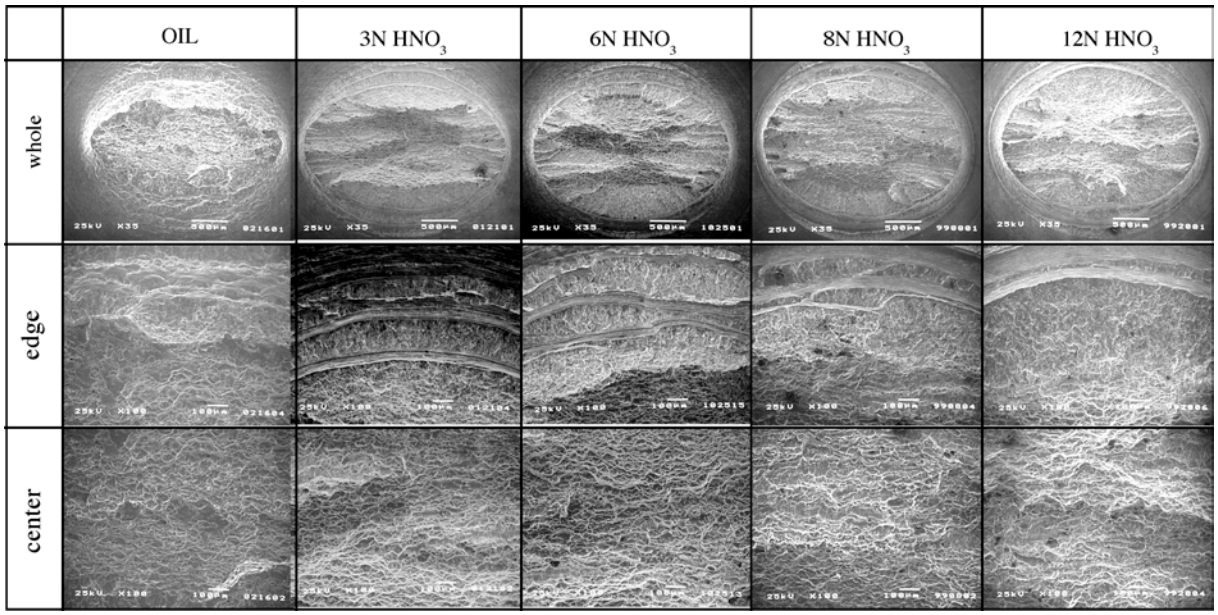

Fig. 6 SEM photographs of the fracture surfaces after SSRT.

not clearly different. Therefore, it is difficult to separate the AE signal due to the SCC from the noise by amplitude discrimination. However, the AE waveform due to the bubbles obtained by two sensors located at two different positions did not show any similarity. On the other hand, the AE waveforms by SCC detected at two sensors coincide with each other. In addition, the rise time of AE parameters showed the difference between the bubble and SCC. Accordingly, it appears possible to separate the AE signal due to SCC from the noise by analyzing the similarity in waveforms measured at different locations.

4. CONCLUSION

The applicability of AE monitoring method for detecting the transgranular-type SCC of zirconium in boiling nitric acid solutions was examined and following results were obtained.

(1) The AE method is one of the most promising methods for clarifying the crack initiation and

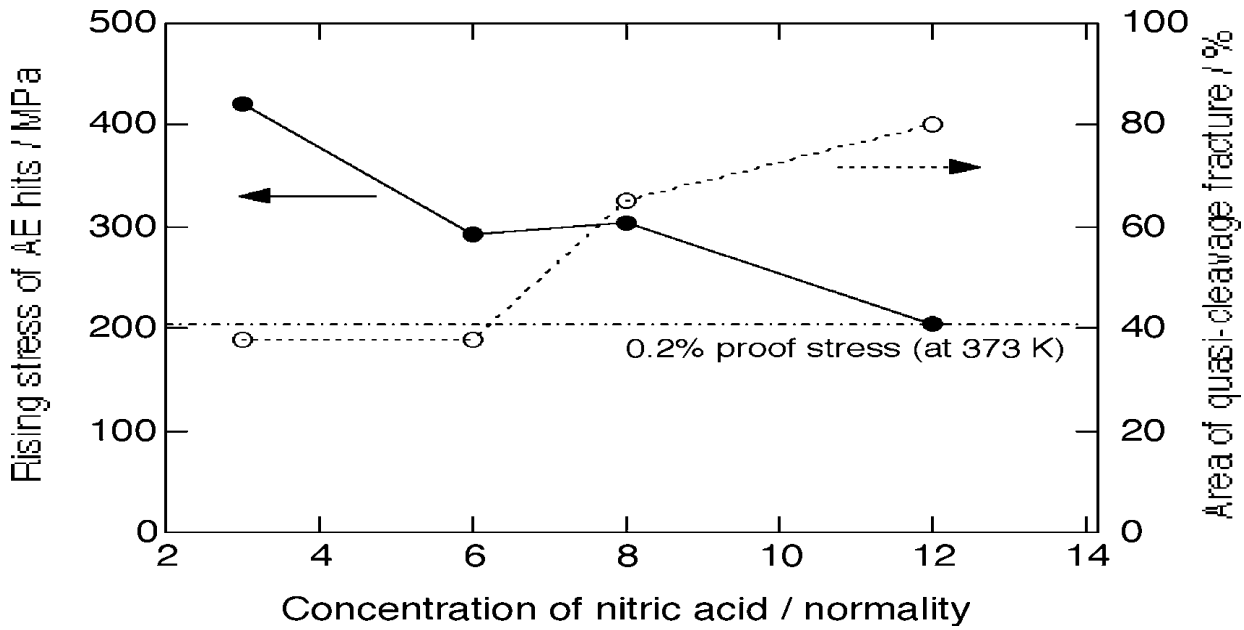

Fig. 7 The relationship between the susceptibility to SCC and the nitric acid concentration.

propagation of SCC of zirconium.

(2) Both the AE hits and the susceptibility to SCC increased with increasing the concentration of nitric acid. The stress level for generating the AE event due to the SCC was decreased to the 0.2%-proof stress in boiling 12N HNO_3.

(3) The AE signals derived from the SCC can be separated from the noise of bubbles, by analyzing the waveforms obtained from a pair of sensors at different positions. A similar waveform was only obtained with the AE signals due to the SCC.

REFERENCES

(1) K. Kiuchi; J. Atomic Energy Society of Japan, **31** (1989), 229.

(2) K. Kiuchi, N. Yamanouchi, M. Kikuchi and Y. Kuriki; Proc. RECOD'91, Vol. 2**,** (1991), p. 549

(3) J.A. Beavers, J.C. Griess and W.K. Boyd; Corrosion, **36** (1981), 292.

(4) P. Fauvet and G. Pinard Legry; EUROCORR'92, Espoo, Finland.

(5) C. Kato, Y. Takagi, K. Kiuchi; Proc. International Symp. on Plant Aging and Life Predictions of Corrodible Structures, 1995, Japan, p. 883.

(6) K. Kiuchi, M. Hayashi, H. Hayakawa, M. Sakairi and M. Kikuchi; Proc. RECOD'94, Vol. 3, (1994).

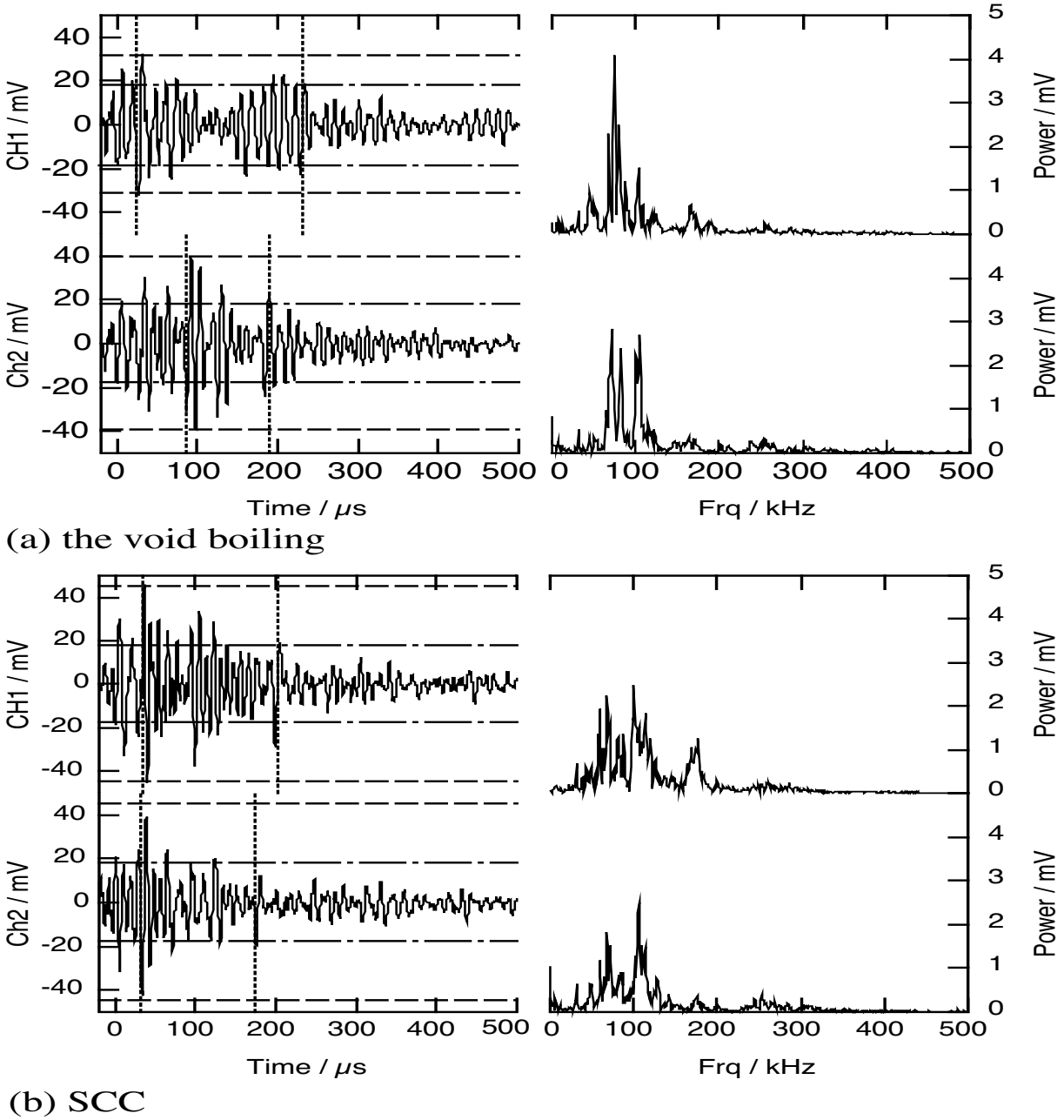

Fig. 8 The typical AE wave pattern and power spectra derived from the bubbling void and SCC respectively.

ACOUSTIC EMISSION MONITORING OF CHLORIDE STRESS CORROSION CRACKING OF AUSTENITIC STAINLESS STEEL

SHINYA FUJIMOTO, MIKIO TAKEMOTO and KANJI ONO*

Faculty of Science and Engr., Aoyama Gakuin University, Setagaya, Tokyo 157-8572, JAPAN
* Dept. of Materials Science and Engineering, UCLA, Los Angeles, CA 90095-1595, USA.

ABSTRACT

We analyzed the fracture dynamics of chloride-SCC of austenitic stainless steel AISI 304 by AE source simulation method. Using the varied mechanical and thermal loading systems in 35-38 mass % $MgCl_2$ solution at 95 to 98˚C, we produced transgranular (TG) and intergranular (IG) type SCC. We monitored no AE from the transgranular (TG) type SCC even by using an AE monitoring system with 80 dB amplification, but did monitor a large amount of AE by using 40 dB amplification system, from intergranular (IG) type SCC. Source dynamics estimated by unique waveform simulation of Lamb So-packet revealed grain-size fractures with fast source rise time of 0.17 to 1.05 μs. Though the mechanism of SCC is not well-understood, it is confirmed that IG-SCC does emit detectable AE signals.

1. INTRODUCTION

Stress corrosion cracking (SCC) of austenitic stainless steel by chloride ions is a continued problem in chemical and nuclear power plants. SCC is believed to be caused by the anodic dissolution of metal along active-paths such as slip lines, strain-induced martensite and chromium-depleted zone along grain boundaries, and is called APC (active-path corrosion) type SCC. Chloride-SCC of austenitic stainless steels, typical APC-SCC, shows two types of fracture morphology, transgranular (TG) and intergranular (IG), depending on the environmental (temperature, concentration), loading (mechanical and thermal) conditions as well as the microstructure (sensitized or not). In 1970s and 80s, extensive AE research [1,2,3] of TG-type SCC of AISI304 steel in a boiling $MgCl_2$ solution (B.P.:146˚C, test solution specified by JIS G0576(79) and NACE G36(78)) had been attempted, and led to a conclusion that the TG APC-SCC did not emit AE. The use of highly concentrated $MgCl_2$ solution (42 % $MgCl_2$) with pH less than 1.6 was criticized since it could not simulate the IG-type SCC experienced in heat-exchanger tubing. At present, 30 or 35 mass % $MgCl_2$ solution with pH of about 3.5 at non-boiling temperatures are widely used as test solutions. In these solutions, IG-type SCC occurs readily by changing the temperature and loading condition as well as the sensitizing treatment. The present author [4] reported that the heat-flux and bi-axial stress state promotes IG-SCC in low concentration $MgCl_2$ solutions, as in the case of SCC in heat exchanger tubes. SCC of Inconel 600 and that of low carbon 304L and 316L steels in high temperature light water, typical IG-SCC, are serious problems in nuclear power plant. Whether such IG-SCC produces AE or not is an important and critical factor for SCC detection by AE monitoring and is the thrust of our study; in particular, whether the APC-SCC produces AE, and if so, by which fracture mechanism.

We reported previously [5] that the IG-SCC of sensitized AISI 304 steel by polythionic acid at room temperature produces numerous Lamb-wave AE signals with sufficient amplitude for detailed analysis. Fracture dynamics were determined by using an experimental transfer function

for So-mode Lamb wave. The effective source rise times estimated were in the range of 0.28 to 0.77 μs. This result indicated that the IG-SCC progresses discontinuously, with fast grain boundary fractures.

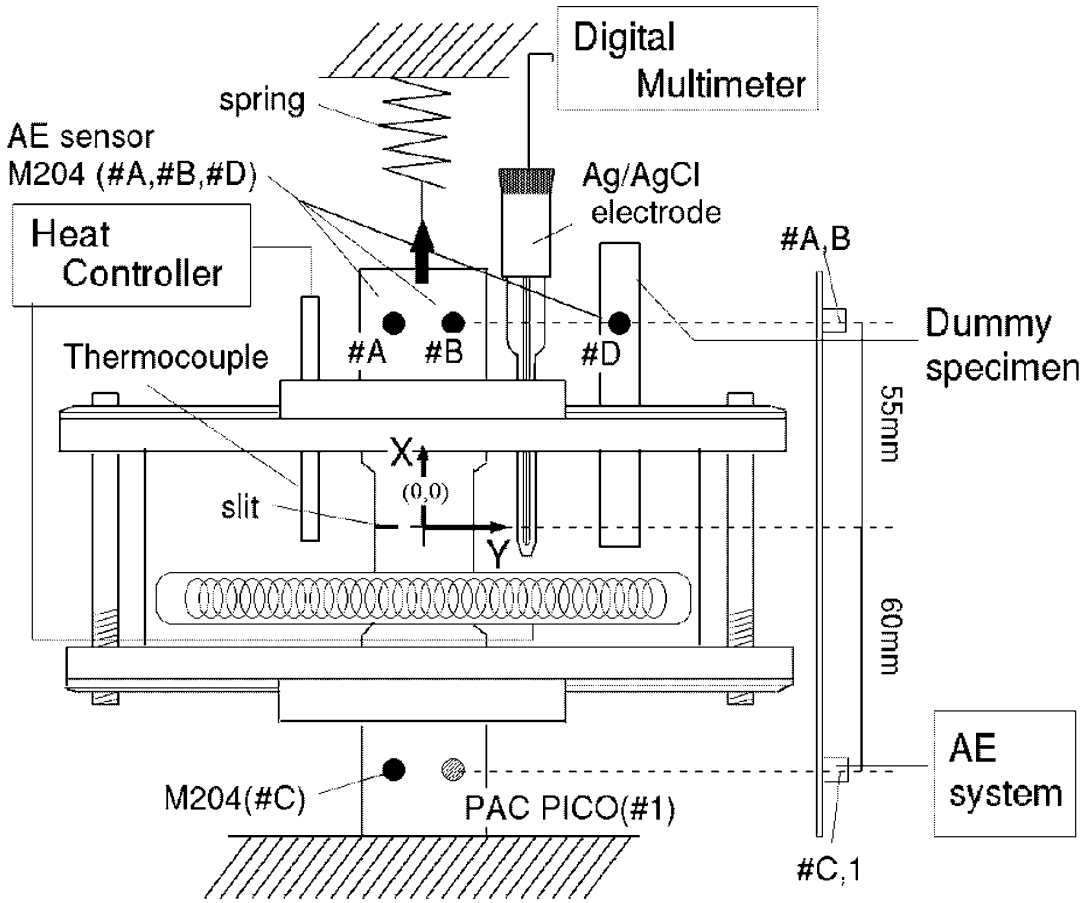

Fig. 1 Experimental setup for Type A SCC test.

In this paper, we report our recent results of AE monitoring from TG- and IG-SCC of AISI304 steel in 35 and 38 mass % $MgCl_2$ solution under various loading conditions. We observed no AE from TG-SCC, but detected frequent AE signals from IG-SCC. Fracture dynamics of IG-SCC were obtained by a unique waveform simulation method and compared with those obtained for IG-SCC due to polythionic acid.

2. TEST METHODS AND AE MONITORING

In order to stimulate the TG- and IG-SCC of AISI304 steel, we used two test methods. Figure 1 shows Type-A test, where a thin plate (0.8 mm thick) of AISI 304 stainless steel was loaded in tension in a 35 mass % $MgCl_2$ solution at 95˚C. The specimens were heated at 1050˚C for 30 min and quenched in water or furnace-cooled, The furnace-cooled specimens are slightly sensitized and more susceptible to IG-SCC than the water-quenched ones. Load was applied to the specimen using a compressed spring with through-wall double-sided slits of 10-mm depth. This method is a decreasing-stress test since the applied load decreases with SCC progression. Four AE sensors were mounted on both surfaces away from the corrosion cell. Three sensors (#A-C, JT M204) with a pre-amplification of 40 dB and one sensor (#1, PAC PICO) without

were used. Outputs of the sensors were further amplified by 40 dB, and digitized by a fast A/D converter at 50 ns interval with 1024 points at 10-bit resolution. We used highly sensitive M204 sensors since we detected no AE in preliminary SCC tests. Possible noise due to 80-dB total amplification was monitored by the same type sensor (#D) mounted on a stress-free plate immersed in the same solution. Change of corrosion potential was simultaneously measured via a reference electrode of Ag/AgCl.

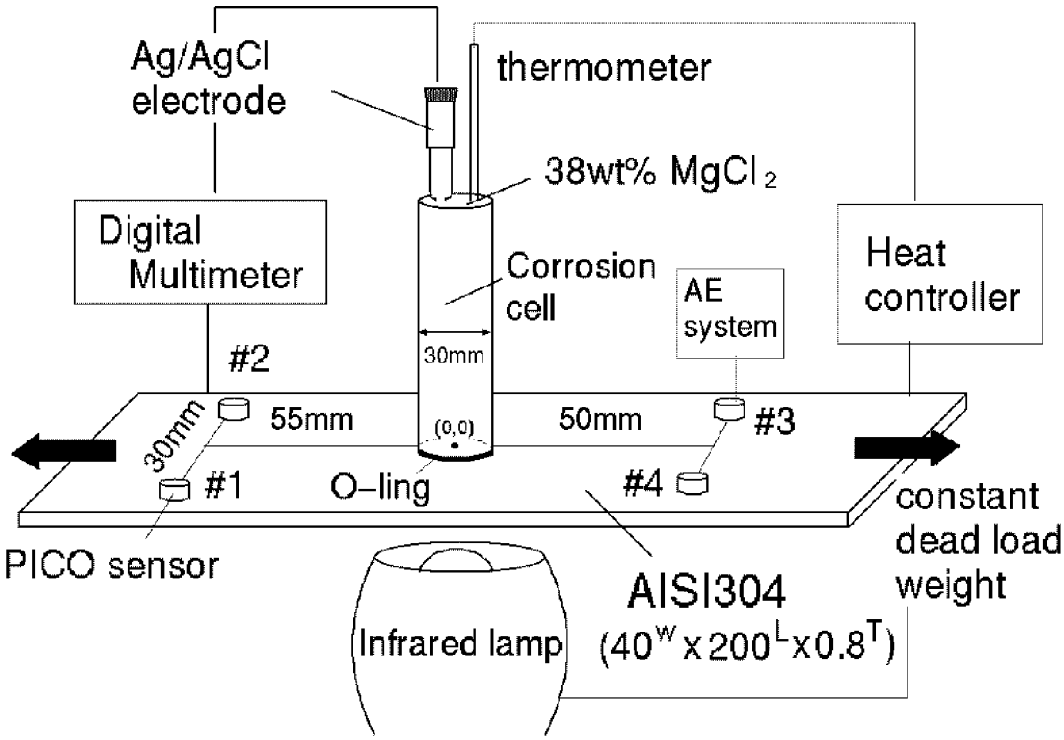

Fig. 2 Experimental setup for Type B SCC test.

Figure 2 shows Type-B test method, which can produce IG-SCC. Sheet specimen of 0.8-mm-thick 304 stainless steel was loaded in tension by a cantilever loading system with constant dead weight (increasing-stress type), and heated by an infrared lamp from the lower surface. In order to localize the SCC initiation, a shallow (0.5-mm depth) circular dimple of 4 mm diameter was machined at the center of the specimen. A 30-mm-diameter alumina tube was attached as a corrosion cell on the specimen with an O-ring. This test, using 38 mass % $MgCl_2$ solution at 98˚C, produces typical IG-SCC due to the biaxial thermal stress state and applied stress when sensitized specimens are used. Four PICO sensors, mounted separately at 50 and 55 mm from the cell center monitor Lamb-wave AE signals. Corrosion potential was monitored by the same system as shown in Fig. 1.

3. TEST RESULTS AND FRACTURE DYNAMICSOF SCC

Trasngulanular SCC by Type-A Test (decreasing-stress type)

We repeated SCC tests of both non-sensitized and sensitized specimens, but could not detect any AE in spite of SCC occurrence. When a test was interpreted, all cracks that propagated 4 mm long were found to be TG-type cracking even for sensitized specimens. A few AE signals could be observed occasionally only at the final stage of SCC. Figure 3 show the source location of

three such AE signals (E.C. 1, 2 and 3) at ligament of two main SCCs from opposite slits. SCCs started at slit corners after 20 hr at 118 MPa loading, but did not emit any AE until 50 hr at which two main SCCs propagated in parallel. AE signals were detected when SCCs connect to each other. Interesting to note is that cracks near the slit corner (a) are TG-type while that at the ligament (b) is IG-type. IG-SCC is caused by higher biaxial tensile stresses at branched crack tips.

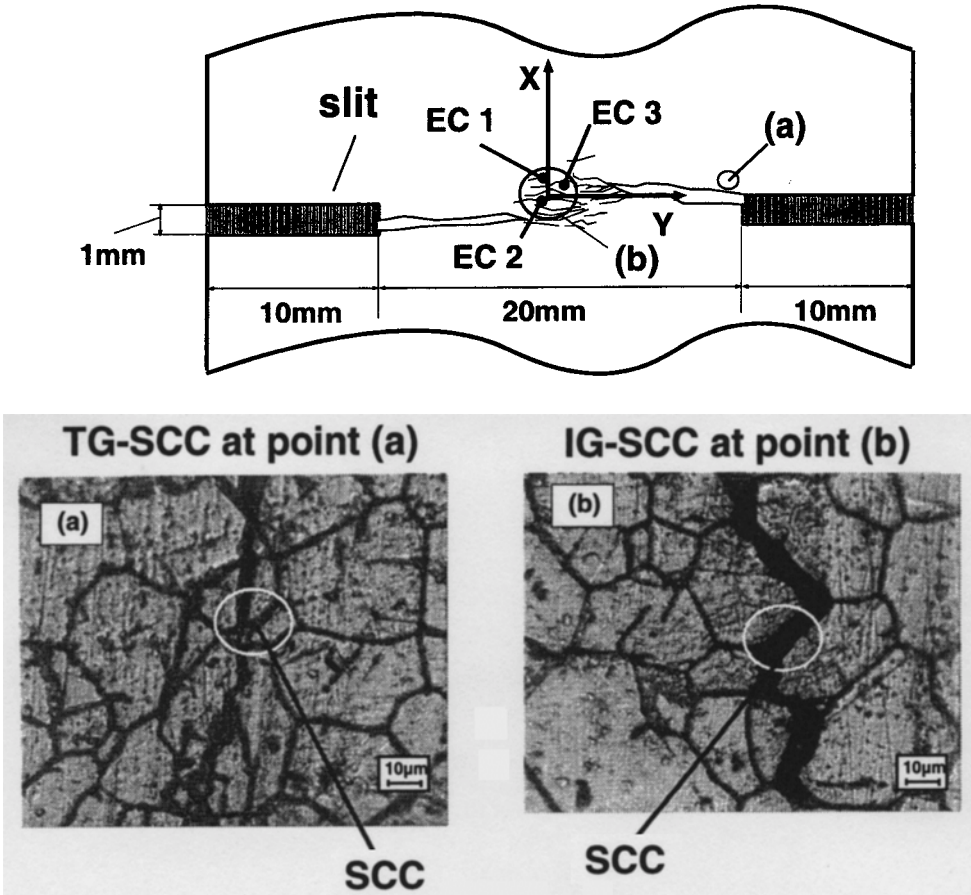

Fig. 3 The source location of three AE signals (EC.1-3). Crack morphology at (a) and (b) are shown below. SCC conditions: 115 MPa in 35% $MgCl_2$ at 95˚C. 10 μm marker shown.

Figure 4 show three AE signals (EC1-3) at around 51 hr. No noise was detected by sensor #D (M204). AE signals show typical features of the Lamb wave, i.e., first arriving weak So-mode and trailing strong Ao-mode.

We examined whether AE is produced by SCC or by mechanical fracture of 304 stainless steel, since these AE signals are monitored near the final fracture. The fracture dynamics of three events were studied by conducting the So-mode waveform simulation. The overall transfer function, including the sensor, medium and AE monitoring system, was determined by the method shown in the top of Fig. 5. Lamb-wave AE signals were excited by a compression-mode PZT element, glued to a sheet specimen (304 SS) and a steel block by epoxy, and were detected by M204 and PICO sensors. Here, the out-of-plane displacement of PZT element was monitored by a laser interferometer and converted to crack volume as shown in Fig. 5(b). The over-all transfer function, Fig. 5(c), for the So-Lamb wave due to the Mode-I crack opening was obtained by the time-domain Gauss-Zeidel deconvolution of detected wave (a) with source wave (b).

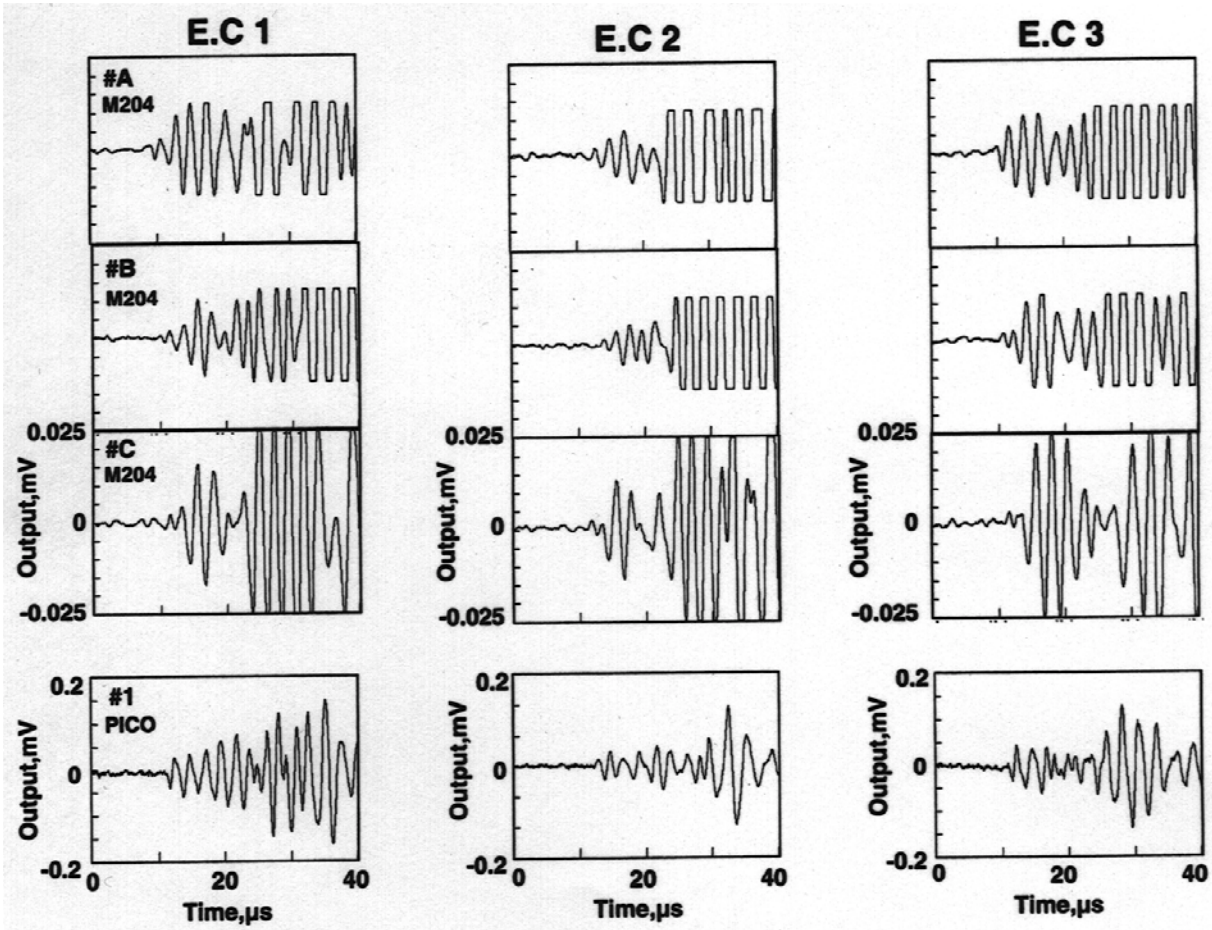

Fig. 4 Lamb wave detected by four sensors during Type-A SCC test.

Crack opening of SCC was determined by matching the simulated waveform of the So-packet to the detected ones. Detail of this method can be found elsewhere [8].

In Fig. 6, simulated So-packet is overlapped on the detected waveform. The effective source rise times are estimated as 0.7 to 0.8 μs. These times are slightly larger than those (0.3 to 0.77 μs) of IG-SCC by polythionic acid (pH = 2.0) of heavily sensitized 304 steel [9]. Crack size, estimated by assuming the crack opening of 1 μm, coincides with the grain size (about 30 μm). This indicates that the AE events observed were produced by discontinuous fast fracture along individual grain boundary.

IG-SCC by Type-B Test (increasing-stress type)

We first measured the attenuation of Lamb waves in a water-loaded thin plate, since the amplitude of Lamb-wave AE was generally low. Using the system in Fig. 7, we monitored Lamb wave AE, excited by ablation of focused YAG pulse irradiated at mid-thickness distal plane, for plate with and without corrosion cell. The left PICO sensor was used to monitor the intensity of ablation. This setup simulates the wave propagation in Type-B test. Amplitudes of the So-packet did not change with and without the cell, while those of Ao-mode was slightly decreased with the cell in place. We also measured the wave attenuation for the plate coated by silicone rubber over 10 to 40 mm long. So amplitude was unchanged, but Ao amplitude significantly decreased by rubber coating. These indicate that weak So-mode signals are not due to the energy leaking into solution, but due to the small surface crack.

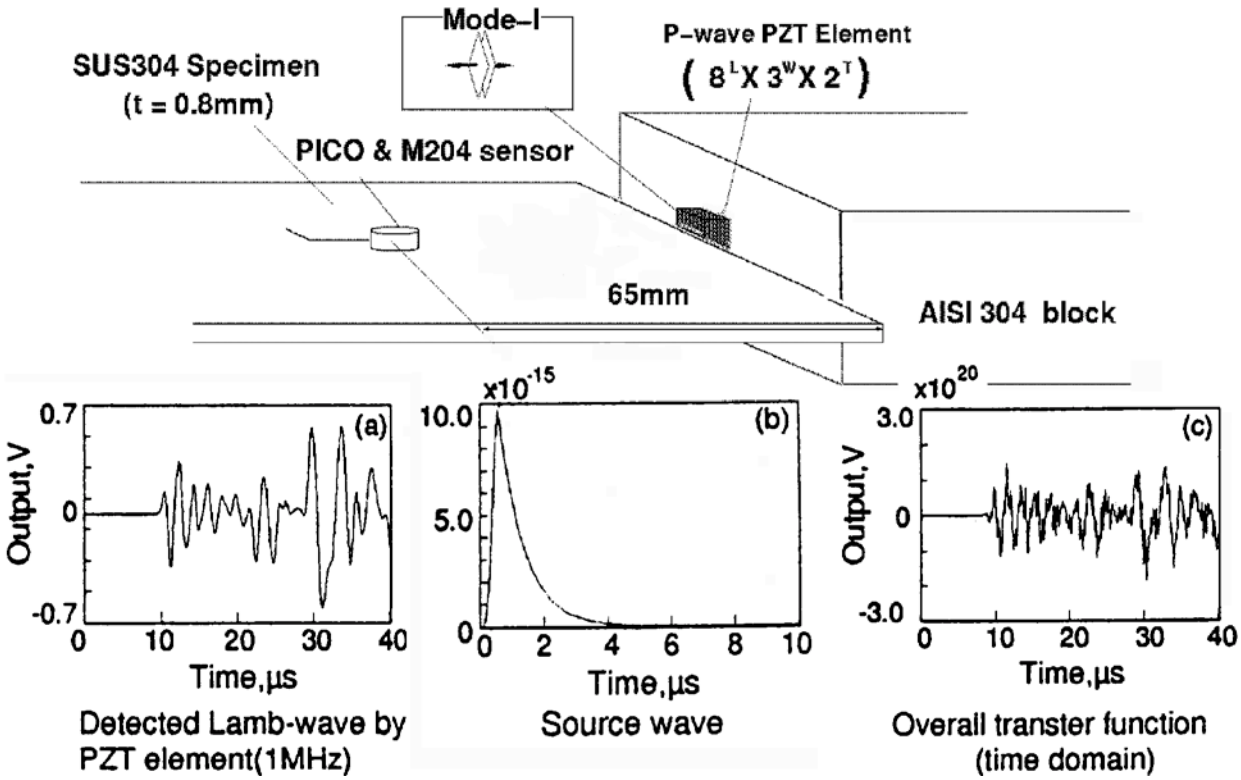

Fig. 5 Experimental setup for simulating Mode-I fracture by 1 MHz PZT-element and procedure of determining the over-all transfer function.

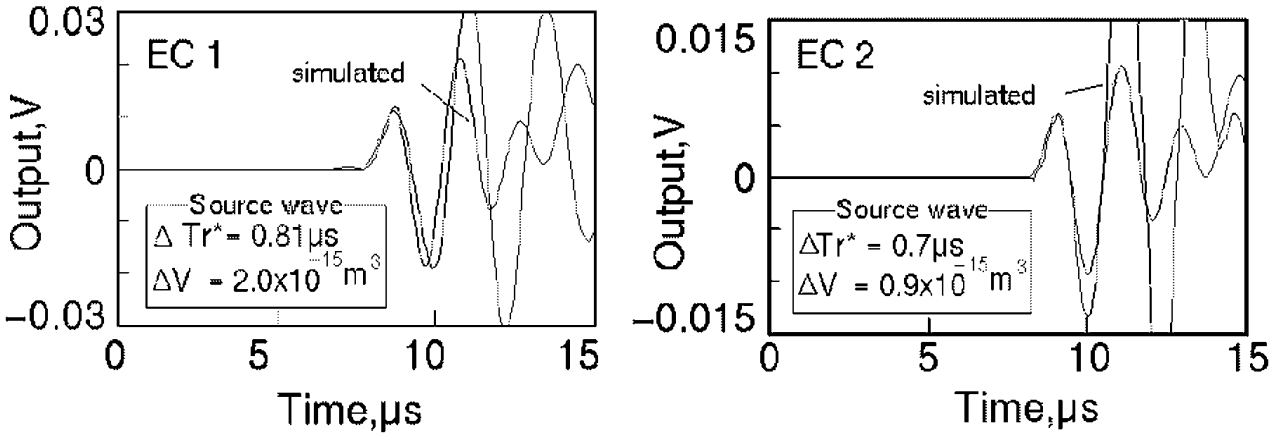

Fig. 6 Overlapping of simulated S_0-packed of Lamb wave on the waves monitored during Type A (decreasing stress) SCC test.

Using Type-B test, we observed 80 events during a test lasting 100 ks (28 hr), as shown in Fig. 8. AE counts are relatively small, since our AE system has a long dead time for storing the digitized data. Many more AE counts, almost 5 times, can be expected by using a fast acquisition system when AE occurs at a high rate [6]. SCC propagated for 17 mm long in both directions, as shown in Fig. 9. Most AE sources are located close to the main SCC. Event count (EC) number is shown in the location. Here, the source location was identified by using the frequency independent sheet velocity (first arrival time) of the So-Lamb wave, and some events

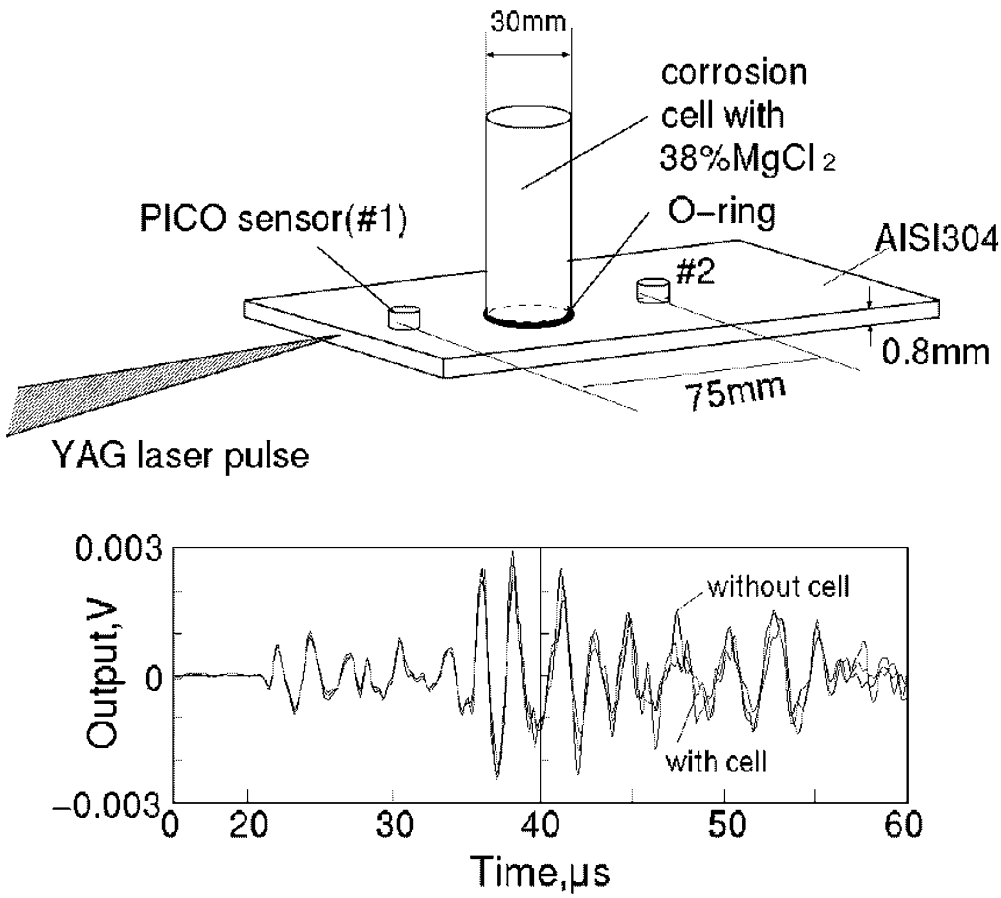

Fig. 7 Laser-induced Lamb waves monitored by #2 PICO for plate with and without corrosion cell.

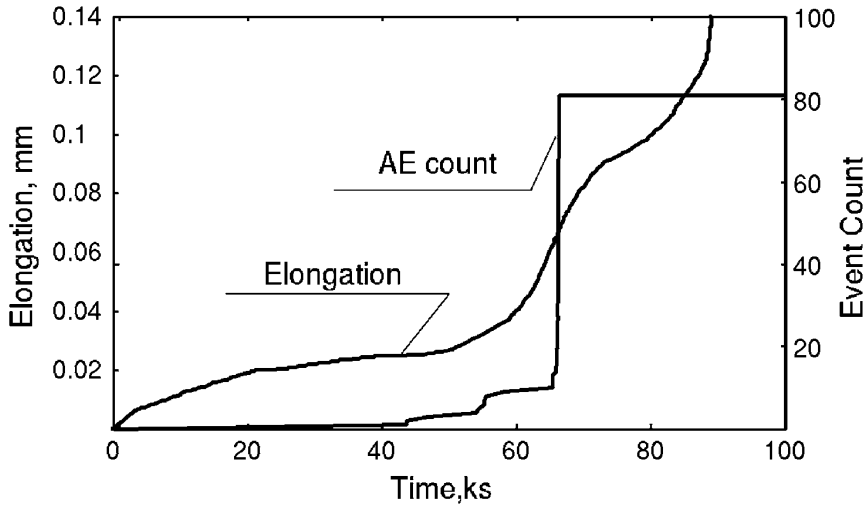

Fig. 8 Cumulative AE event counts and elongation change during Type B (increasing stress) SCC test.

with weak So-amplitude were omitted. Fractographic observation (Fig. 10) shows typical IG cracking with many secondary (or sub-) cracks along grain boundaries. Grain boundary fracture with smooth surface are locally observed. This feature is similar to that in IG-fracture produced by polythionic acid and fluoride SCC of sensitized AISI 304 steel [5,7].

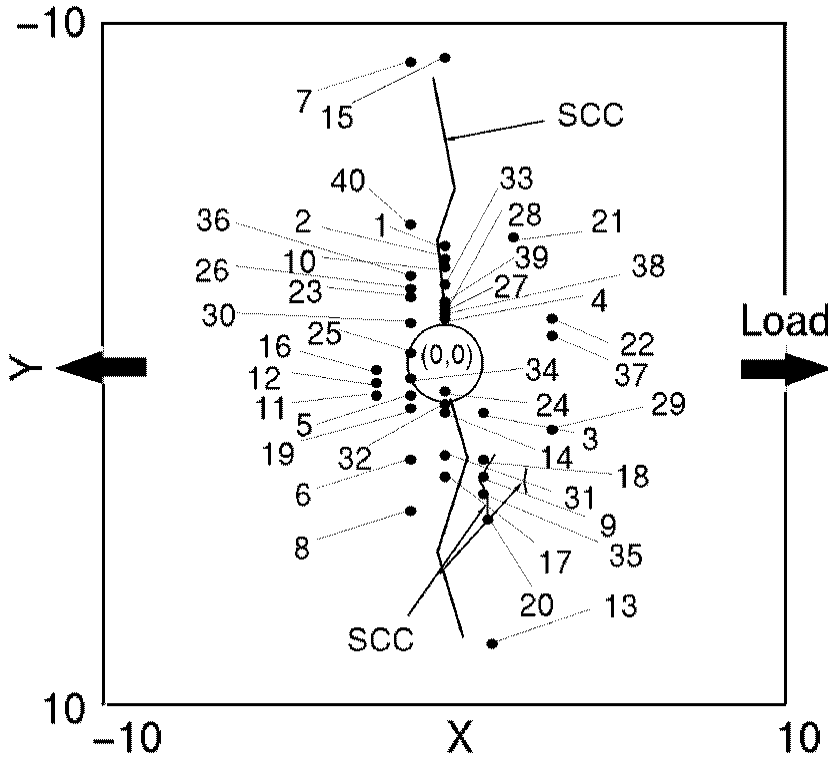

Fig. 9 Source location of Lamb wave monitored by Type B SCC test.

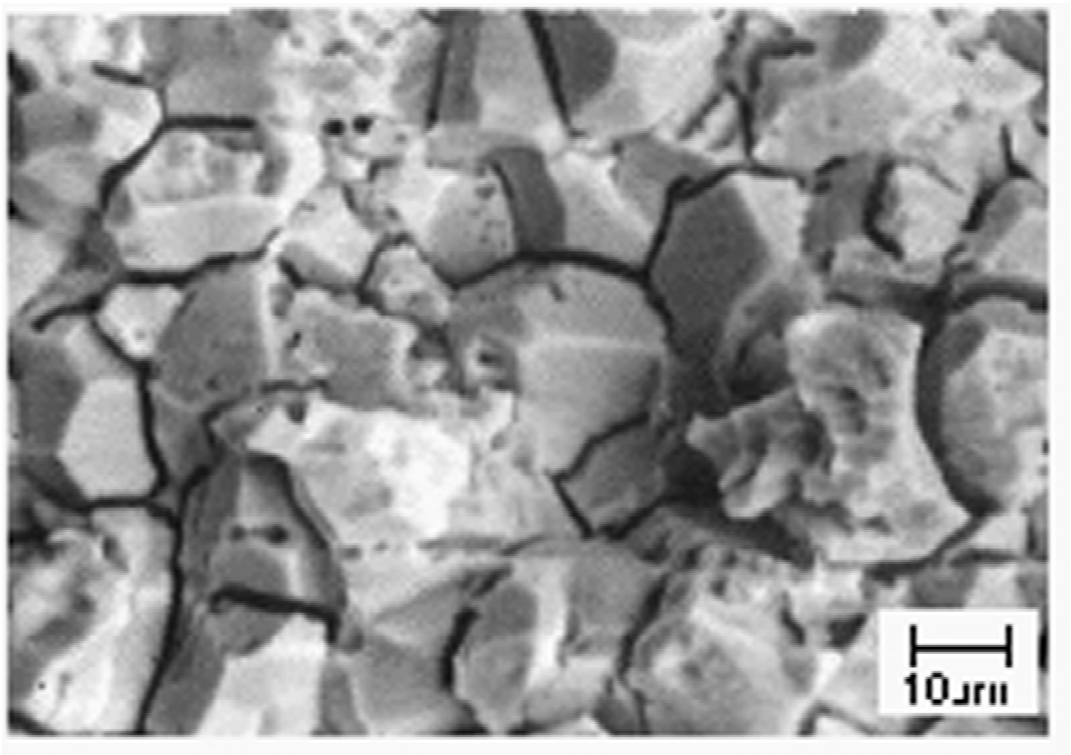

Fig. 10 Intergranular SCC by Type B (increasing-stress) SCC test with numerous secondary IG-cracks. A marker for 10 μm is shown at bottom right.

Table 1 summarizes the results of selected SCC tests among 28 runs, including those by Type-A test. No AE was detected for TG-SCC but a large number of AE events for IG-SCC are evident. Because most chloride-SCC in process plants are associated with IG-cracking, AE can be a useful monitoring method of SCC. Disputable conclusion on AE by APC-SCC has long precluded the application of AE to SCC monitoring, but the present work demonstrates beyond doubt that AE can monitor the IG- SCC. Next we studied the fracture dynamics of IG-SCC by the same method used in the previous section. Shown in Fig. 11 are the examples of AE events monitored. So-waves are generally weak, indicating grain size fracture near the surface. Analysis was applied to AE signals (11 events) with sufficient amplitude. Typical waveform simulation results are shown in Fig. 12. Source parameters are shown in Fig. 13. Estimated source rise time varied widely from 0.17 to 1.0 μs, and the crack volume was estimated in the range from $2x10^{-16}$ to $1.4\ x10^{-15}\ m^3$.

Source mechanisms of these SCC are not well understood at present. No AE produced from TG-SCC suggests that SCC silently advances by the anodic dissolution of metal along active paths in the grain. AEs from IG-SCC may be due to the hydrogen-assisted cracking or proton-induced grain boundary de-cohesion. The fact that IG-SCC is caused by neutral fluoride ions [7] suggests the grain boundary de-cohesion by specific anions. More research, using AE system with fast data acquisition, on SCC under various environmental conditions of sensitized steel is needed.

4. CONCLUSIONS

We monitored and analyzed Lamb–wave AEs from chloride-SCC of austenitic stainless steel (AISI 304) by using two SCC test methods. Results are summarized below:

1) SCC of sensitized or non-sensitized AISI304 steels in 35% $MgCl_2$ at 98˚C under decreasing-stress tests produced transgranular SCC. No AE signal was detected for this TG-SCC.
2) Dead loading (increasing-stress type) SCC test of sensitized steel under heat flux, in 38 mass % $MgCl_2$ at 95˚C, produced IG-SCC. Many AE signals were monitored during the initiation and propagation of IG-SCC.
3) Source simulation of So-Lamb AE events, monitored during IG-SCC, revealed fast, discontinuous fracture with rise time of 0.17 to 1.0 μs over an individual grain.
4) AE can be used for the detection of IG-SCC initiation and progression.

REFERENCES

[1] H. Okada, K. Yukawa and H. Tamura, Application of Acoustic Emission Technique to the Study of Stress Corrosion Cracking in Distinguishing Between Active Path Corrosion and Hydrogen Embrittlement, Corrosion, **30** (1974) 253.

[2] S. Yuyama, Detection and Analysis of Crevice Corrosion-SCC Process by the Use of AE Technique, J. Iron and Steel of Japan, **68** (1982) 2019.

[3] S. Yuyama, Fundamental Aspects of Acoustic Emission Applications to the Problems Caused by Corrosion, ASTM STP 908 (1986) p. 4.

[4] M. Takemoto and J. Nagata, Trans. J. Soc. Chemical Engineers, **12**-6, (1986) 681-687 and 675-680.

[5] M. Takemoto, O. Tamura and H. Suzuki, AE Study of Stress Corrosion Cracking Mechanism of Stainless Foil Using Quantitative Lamb Wave Analysis and Video Images, Progress in AE IX, (1998) AEWG, Hawaii, pp. 178-185.

Table 1 Test result of various chloride SCC test.

specimen	heat treatment	test method	sensor & amplification	crack type	AE
0.8mm plate with notch	as received	Type A $\sigma \leqq 147$MPa	PAC PICO 40dB	TG	No
0.8mm plate with hole	1050℃x15min furnace cool	Type A $\sigma \leqq 147$MPa	M204: 80dB	TG	No
0.25mm plate with hole	1050℃x1h furnace cool	Type A $\sigma \leqq 147$MPa	M204: 80dB	TG	No
0.25mm plate with notch	1050℃x1h furnace cool	Type A $\sigma \leqq 147$MPa	M204: 80dB	TG	No
0.8mm plate	as received	Type A $\sigma \geqq 147$MPa	PAC PICO 40dB	TG	No
0.8mm plate	1050℃x15min furnace cool	Type A $\sigma \leqq 117.6$MPa	PAC PICO 40dB	TG	No
0.8mm plate with hole	1050℃x15min furnace cool	Type B 147MPa $\leqq \sigma \leqq 205.8$	PAC PICO 40dB	IG	Yes
0.8mm plate with hole	as received	Type B 147MPa $\leqq \sigma \leqq 205.8$	PAC PICO 40dB	IG	Yes
0.25mm plate with hole	1050℃x1h furnace cool	Type B 147MPa $\leqq \sigma \leqq 205.8$	PAC PICO 40dB	IG	Yes
0.5mm plate with hole	1050℃x1h furnace cool	Type B $\sigma \geqq 205.8$MPa	PAC PICO 40dB	IG	Yes

TG

IG

[6] T. Sato, H. Nishino, M. Takemoto and K. Ono, Dynam ics of Delayed Fracture of High Tension Steel Plate by the Lamb Wave Analysis (in Japanese), Paper presented at The Annual meeting of KSMDI (2000, May) Tokyo.

[7] M. Takemoto, External Stress Corrosion Cracking (ESCC) of Austenitic Stainless Steel, Materials Performance, 24-6, (1985) 26-32.

[8] T. Sato, M. Takemoto, K. Ono, Effect of Fracture Dynamics in Thin Plate on the Waveform and Radiation Pattern of the Lamb wave, Japan. J. Appl. Phys., **39** (1999), 3193-3200.

[9] M. Takemoto, O. Tamura, A Fast Cleavage Fracture in the Polythionic SCC of Type 304 Stainless Foil Revealed by the Lamb Wave Analyses and Direct Observation, J. Japan Soc. of Corrosion Engineering, **46** (1997) 662-668.

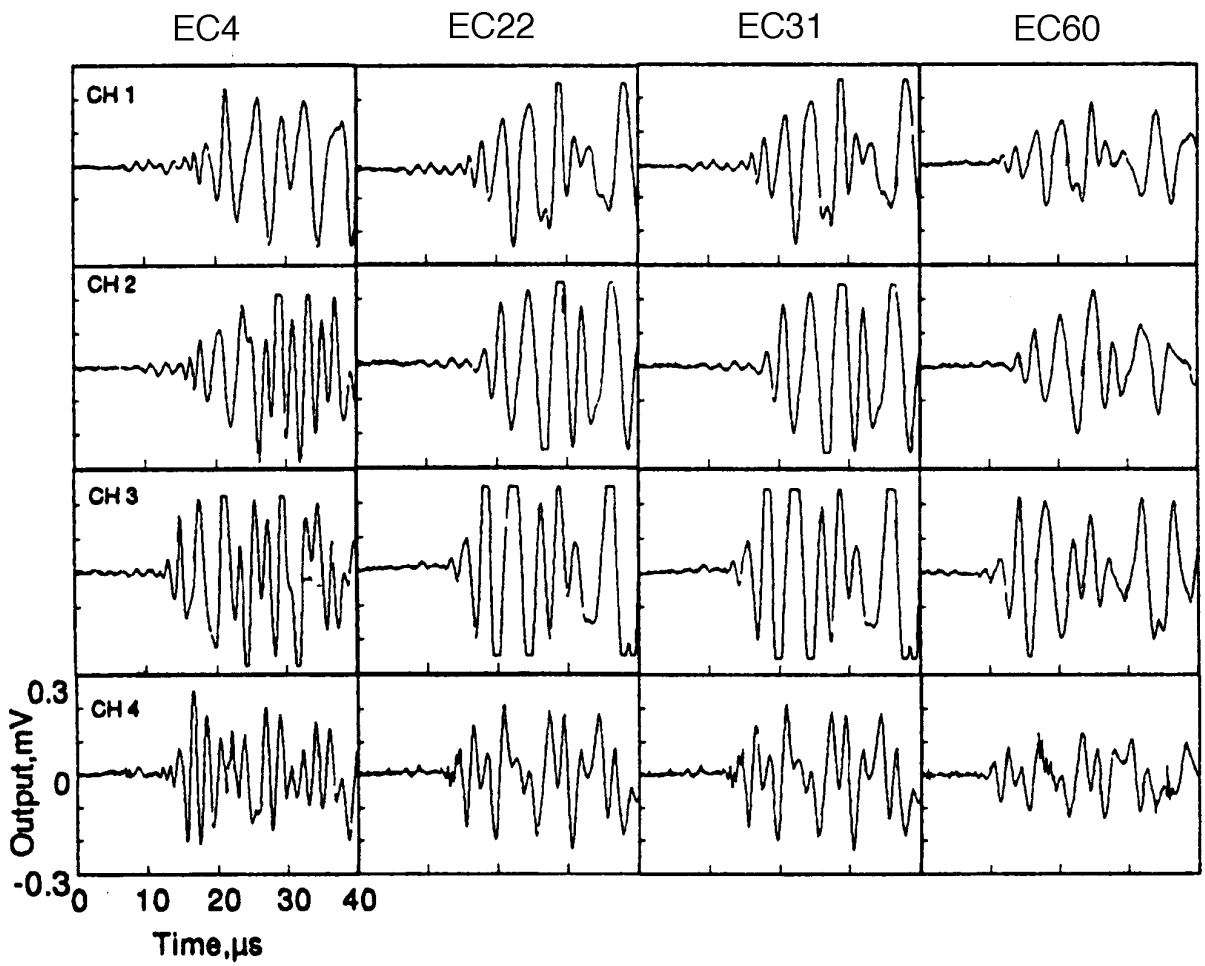

Fig. 11 Lamb wave detected by PICO sensor during Type B (increasing-stress) SCC test.

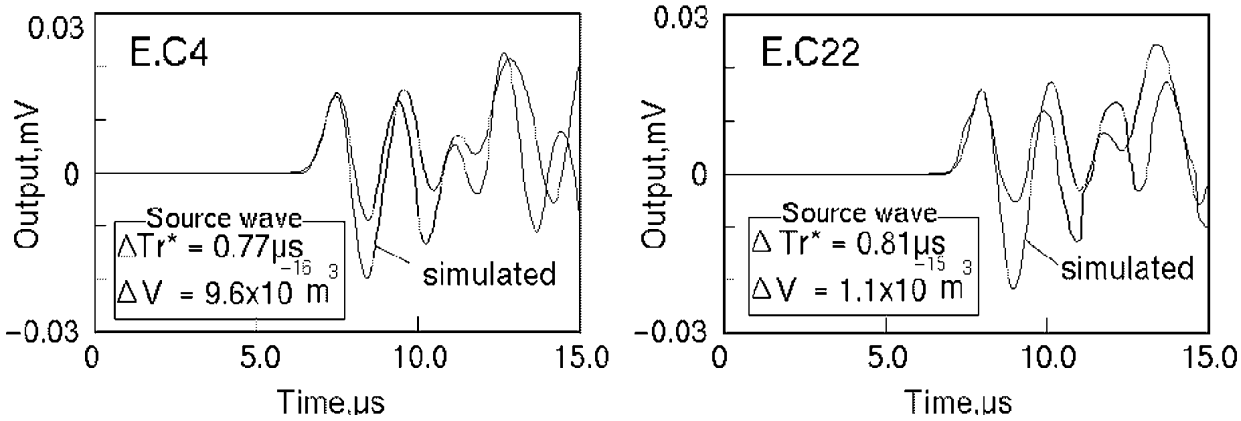

Fig. 12 Overlapping of simulated S_0-packet on the lamb waves detected during Type B SCC test.

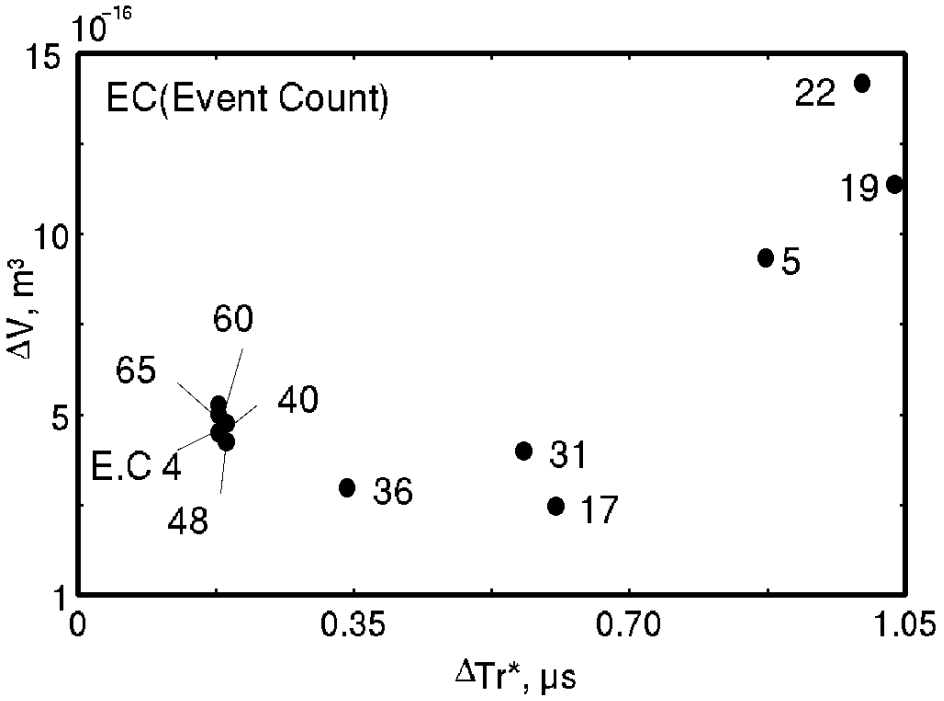

Fig. 13 Source parameters of Mode-I fracture during Type B SCC test.

CYLINDER WAVE ANALYSIS FOR AE SOURCE LOCATION AND FRACTURE DYNAMICS OF STRESS CORROSION CRACKING OF BRASS TUBE

FUKUTOSHI UCHIDA, HIDEO NISHINO, MIKIO TAKEMOTO and KANJI ONO*

Faculty of Science and Engr., Aoyama Gakuin University, Setagaya, Tokyo 157-8572, JAPAN
*Dept. Materials Science and Engineering, UCLA, Los Angeles, CA 90095, U.S.A.

ABSTRACT

Based on the quantitative modal analysis of cylinder waves, we developed new source location and fracture dynamics analysis methods. Source location along the tube axis was identified by using the arrival time differences of L- and F-modes at a selected frequency. Wavelet transform was utilized for effective determination of wave mode and frequency to be used. Source locations were identified within maximum error of 6% for propagating distance from 100 mm to 3000 mm for 5 mm diameter aluminum tube. Next we analyzed AE signals from ammonia-SCC of 5-mm brass tube exposed to Mattsson's solution. Source locations were determined, by using L(0,1) and F(2,1) modes, and the results agreed with actual position of SCC. Fracture dynamics of SCC, estimated by the L(0,1) mode waveform simulation, indicated an association of fast grain boundary fracture in ammonia-SCC of brass.

1. INTRODUCTION

Quantitative analysis of cylinder-wave acoustic emission (AE) is important for monitoring the local damage such as stress corrosion cracking (SCC), fretting, denting and pitting corrosion in heat exchanger tube and buried pipeline. AE signals in a hollow cylinder are propagated as multi-mode cylinder (cylindrical) waves. Quantitative analysis of cylinder wave poses much difficulty due to complex circumferential modes. Theoretical background of the cylinder wave was first provided by Gazis [1], who showed three modes; longitudinal (L-), flexural (F-) and torsional (T-) modes. Fitch [2] generated L- and F-modes by using annular transducers and verified the validity of Gazis's theory. Alleyne and Cawley [3] utilized certain modes of the cylinder wave in nondestructive testing application for chemical plant piping. They reported that the cylinder waves can propagate several tens of meters in a 76 mm steel pipe. Rose et al [4] analyzed attenuation of cylinder wave due to energy leakage into liquid. We recently proposed a new source location method in small size tube (5 mm diameter and 1 mm thickness aluminum pipe) by using the group velocity difference between L(0,1) and F(1,1) modes [5].

In this paper, we examined AE signals produced as cylinder waves by ammonia-SCC of brass tube. Source location and fracture dynamics were analyzed by using modal analysis and waveform simulation method, respectively. First, we briefly introduce quantitative analysis of the cylinder waves and the source location method of AE signals monitored by a single AE sensor. Source location accuracy was studied for laser generated AE signals in 5 mm diameter aluminum tubes. Both the location and fracture dynamics were analyzed for SCC-produced AE

signal. The source dynamics were estimated by unique waveform simulation of L(0,1) mode cylinder wave monitored by a single AE sensor.

2. SOURCE LOCATION OF CYLINDER WAVE AE

We computed the group velocity dispersion of cylinder waves based on the characteristic equation of a 6 x 6 matrix form [1]. Vibration mode of the cylinder wave is classified into three; L(0,m), F(n,m) and T(n,m) with vibration mode parameters (n,m) in the circumferential direction n and radial (thickness) direction m. However, we do not discuss the T-modes in this paper, because their vibration is limited in-plane and can not be monitored by a conventional AE sensor or a laser interferometer. L-mode is axially symmetric mode (n=0) and exists as L(0,m). Figure 1 shows group velocity dispersions of L- and F-modes for an aluminum pipe of diameter: d = 5 mm and thickness: t = 1 mm or t/d = 1/5. Velocity dispersions of A_0- and S_0-mode Lamb waves for 1 mm thick aluminum plate are also shown. It is noted that the shape of the dispersion curves is identical for constant t/d. Therefore, the horizontal axis is normalized by the product of frequency (f in kHz) and wall thickness (t in mm). This behavior is the same as that of Lamb wave dispersion curve.

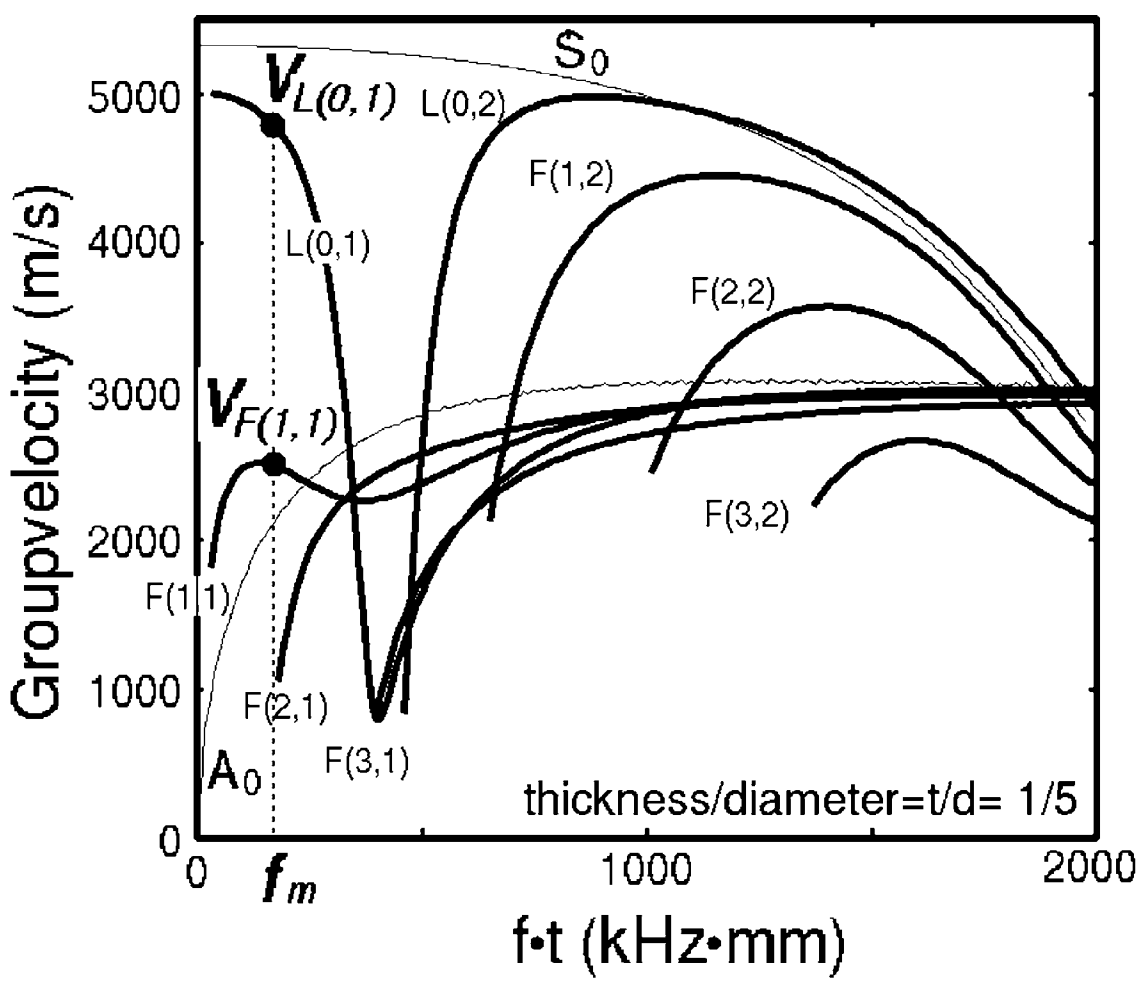

Fig. 1 Group velocity dispersion of aluminum tube with diameter 5 mm and thickness 1 mm, t/d = 1/5.

We determined the source location of AE signal monitored by a single AE sensor mounted on tube end, by using the velocity difference of the two wave modes at a selected frequency. Though different wave modes and frequency can be used depending on both the tube dimension and acoustic properties, we here show the method with the use of the L(0,1) and F(1,1) modes. As shown in Fig.1, there exists a large group velocity difference at frequency f_m (180 kHz for 5 mm aluminum tube). Utilizing the group velocities $V_{L(0,1)}$ of L(0,1) mode and $V_{F(1,1)}$ of F(1,1) mode, the source location along the z axis (z being the axial distance from the end sensor) is given by equation (1),

$$z = \{(V_{L(0,1)} V_{F(1,1)})/(V_{L(0,1)} - V_{F(1,1)})\} \Delta t. \qquad (1)$$

Δt designates the arrival time difference between L(0,1) and F(1,1) modes at the frequency f_m. This is obtained from the wavelet contour map of a detected signal.

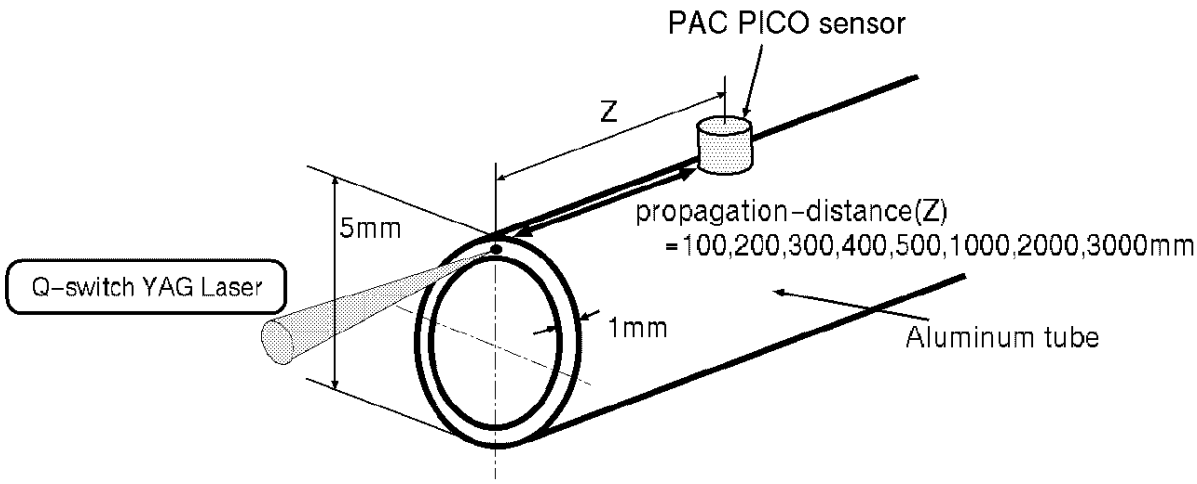

Fig. 2 Setup for cylinder-wave AE monitoring.

Experimental group velocity dispersion derived from wavelet contour maps of the detected signal guide us in selecting the wave mode and frequency. For a larger diameter tube (16 mm), we used the group velocities of L(0,2) mode and F(1,2), as reported elsewhere [5]. For 5 mm diameter brass tube, as will be discussed later, we use group velocities of L(0,1) and F(2,1) modes at f_m = 190 kHz. Location accuracy of the proposed method was studied using artificial sources. As shown in Fig. 2, we excited cylinder-wave by ablation due to pulse-YAG laser beam on the distal plane and monitored by a small resonant type AE sensor (PAC, PICO, nominal center frequency 450 kHz) mounted at 100, 200, 300, 400, 500, 1000, 2000 and 3000 mm from the tube end. Figure 3 show the waveform of a cylinder- wave signal (a) for 5 mm tube (t/d=1/5). The group velocity dispersion curves are given in (b), derived from wavelet contour map. Group velocity in the vertical axis was calculated from wavelet peak at each frequency by the time-of-flight method, and shown in logarithmic scale. Theoretical velocity dispersion curves of L(0,1), L(0,2), F(1,1) and F(1,2) are shown in (b) by solid lines. For this tube, we used arrival time difference of L(0,1) and F(1,1) at 180 kHz. Time transient of wavelet coefficient at 180 kHz is shown in (c) as a function of z. The first wavelet peak corresponds to the L(0,1) mode and and the second peak the F(1,1). Using the time difference Δt between the two peaks and theoretical group velocities of $V_{L(0,1)}$(4749m/s) and $V_{F(1,1)}$ (2490m/s) at 180 kHz, location is determined as shown in Table 1.

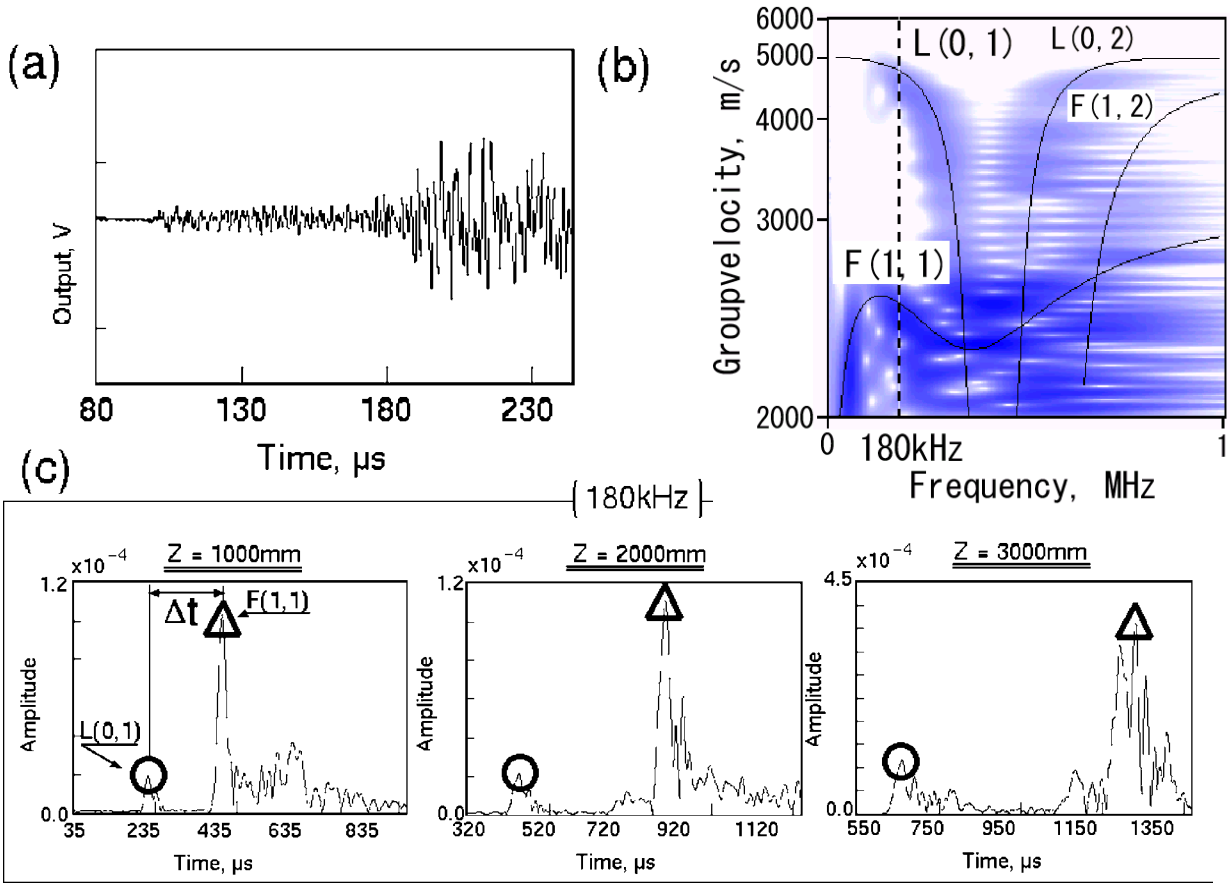

Fig. 3 Waveform (a), group velocity dispersion (b) and time-transient of wavelet coefficient at 180kHz (c).

Table 1 Error of source location.

given souce: Z(mm)	100	200	300	400	500	1000	2000	3000
estimated location(mm) (%)	100±5.3 (5.3%)	200±6.8 (3.4%)	300±3.3 (1.1%)	400±5.6 (1.4%)	500±2.0 (0.39%)	1000±46 (4.6%)	2000±118 (5.9%)	3000±0.9 (0.03%)

Large error for z =100 mm is due to the difficulty in separating the L(0,1) and F(1,1) modes. Source location errors for z =200 to 500 mm were less than 3.4 % and 5.9 % for z=1000 to 3000 mm. These errors are small enough for the source location of AE signal. Source location is possible for longer distances as long as the cylinder wave is detected.

3. ANALYSIS OF AE SIGNALS PRODUCED BY STRESS CORROSION CRACKING

Stress corrosion cracking (SCC) of brass by ammonia is an old and still continuing problem in cartridge cases, heat exchangers, condensers and automobile radiators. Ammonia is produced from ammunition (powder smoke) and decomposition of microorganism. Radiator tubes of sanitary car suffers ammonia–SCC twice every year when it is not periodically cleaned. Mattsson's solution (NH_4OH+$(NH_4)_2SO_4$+ $CuSO_4$, pH = 7.2, specified in NACE G37-73) stimulates the ammonia-SCC of brass at ambient temperature. This SCC occurs at extremely low tensile stresses below 40 MPa, and has been known to be an active path corrosion (APC)

(APC) type SCC [6 - 8]. It has not been ascertained whether AE is produced by ammonia–SCC, but we detected numerous AE signals.

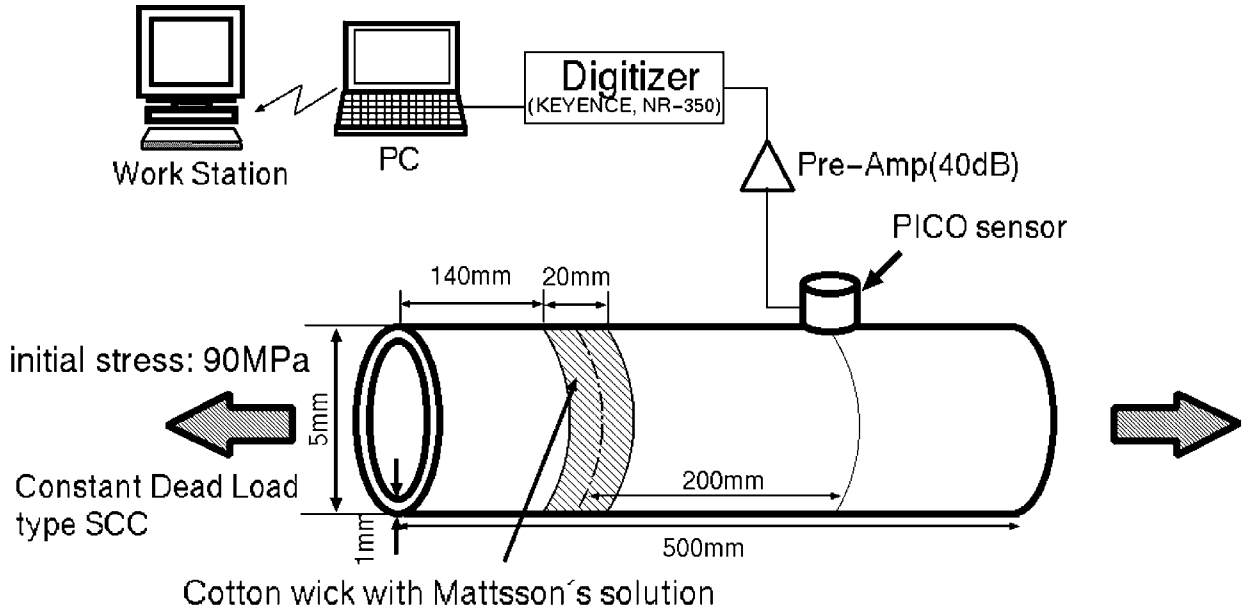

Fig. 4 Setup for AE monitoring during ammonia-SCC of brass tube.

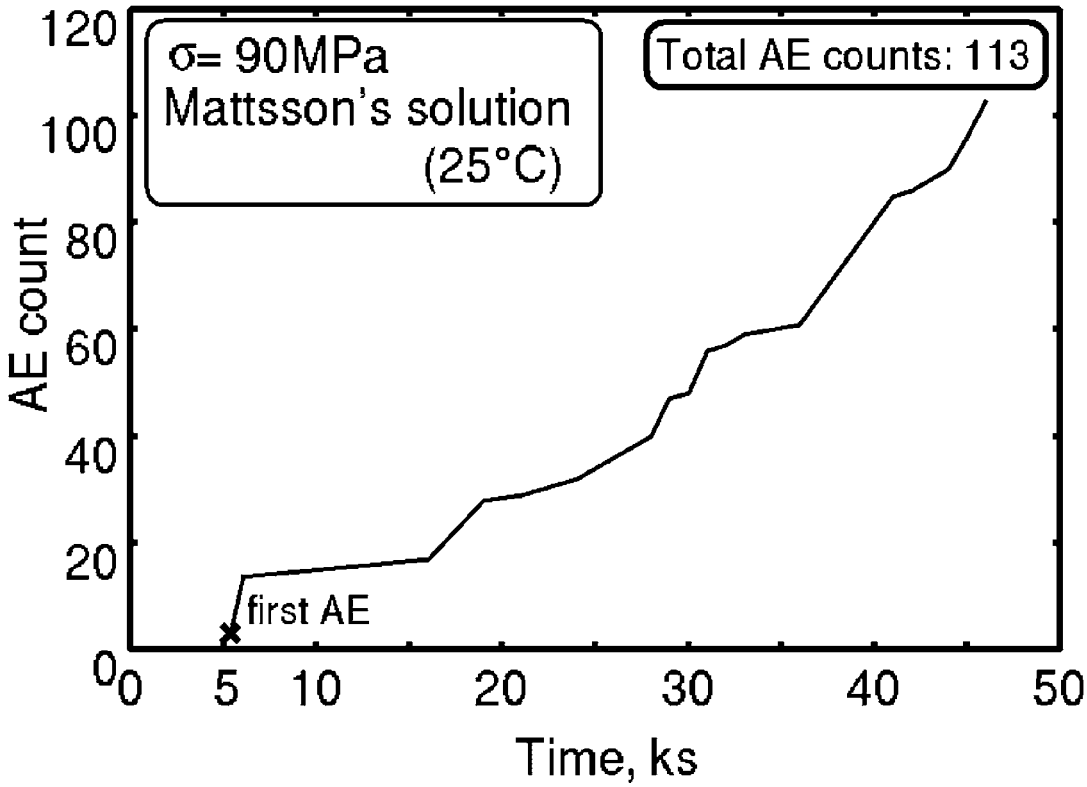

Fig. 5 Cumulative AE events detected during ammonia-SCC test..

Figure.4 shows experimental setup for AE detection from ammonia-SCC. Mattsson's solution was brought in contact to the outer surface of 5 mm diameter and 1 mm thick brass tube

using a cotton wick of 20 mm width. A PICO sensor was mounted on one end at 200 mm from the center of the wick. Output of the AE sensor was amplified by 40 dB and digitized at 40 ns sampling interval with 4096 points at 8 bit resolution, and fed to a work station. Figure 5 shows cumulative AE counts. Open cracks and many fine cracks were observed underneath the cotton wick, at position z = 200-210 mm (Fig. 6). We detected 113 events during 46-ks (13-hr) test at 90 MPa. Most of them are weak signals and only 22 events with sufficient L(0,1) amplitude, monitored at later times, were subjected to the source location analysis.

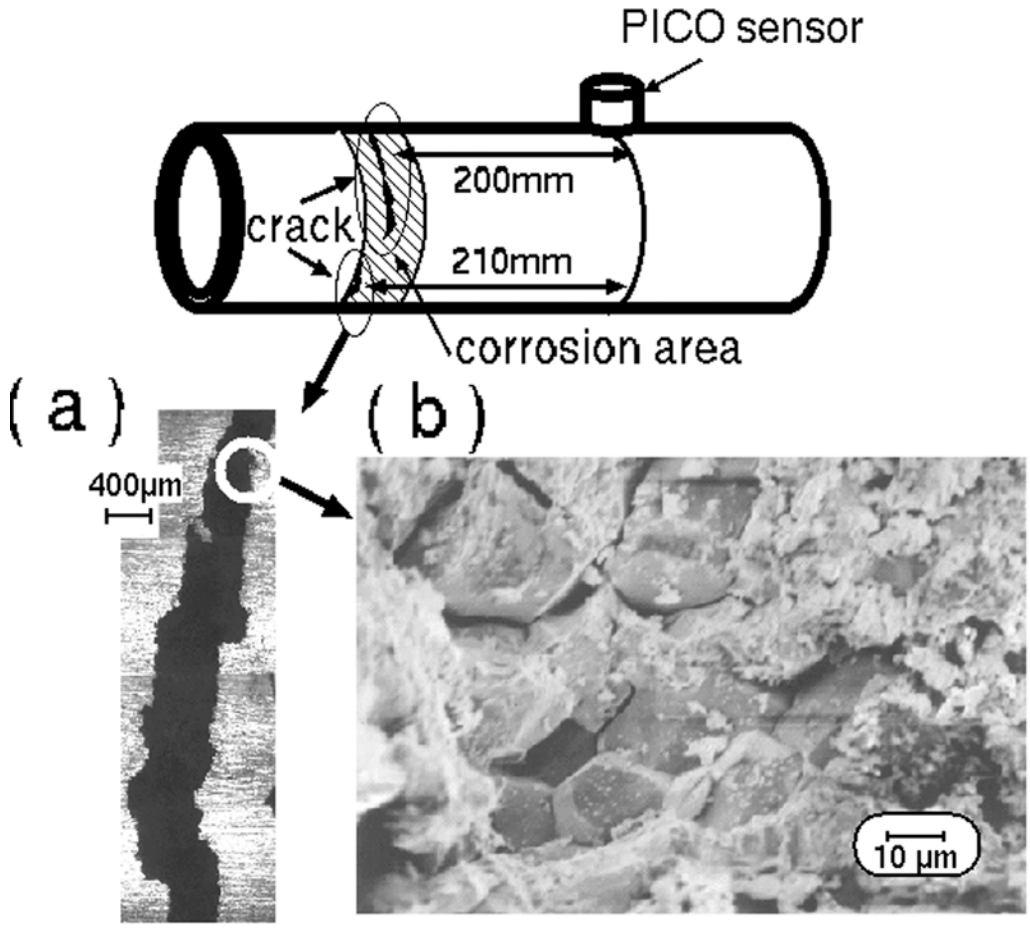

Fig. 6 IG-SCC of brass exposed to Mattsson's solution.(a)surface crack by optical and (b) fracture surface by SEM.

Figure 7 shows two AE signals (Event Count 66 and 70) and their time transient of wavelet coefficient at 190 kHz. Waveform shows the characteristic features of cylinder waves, with first arriving weak L-mode and trailing strong F-modes. Difficulty in cylinder wave AE monitoring is a large amplitude difference between L- and F-modes. We must detect entire waves of L- and F-modes over longer time period for source location using the slow sampling interval. This requirement is, however, as discussed later, contradictory to that for waveform simulation.

Group velocity dispersions of these two waves are shown in Fig. 8 with theoretical dispersion curves of L(0,1) and F(2,1) modes. Gray scale is shown in logarithmic scale to cover the entire intensity range. L(0,1) mode at low frequency is weak but F(2,1) mode is strong, indicating weak generation efficiency of F(1,1) mode. The contour map indicates the usage of L(0,1) and

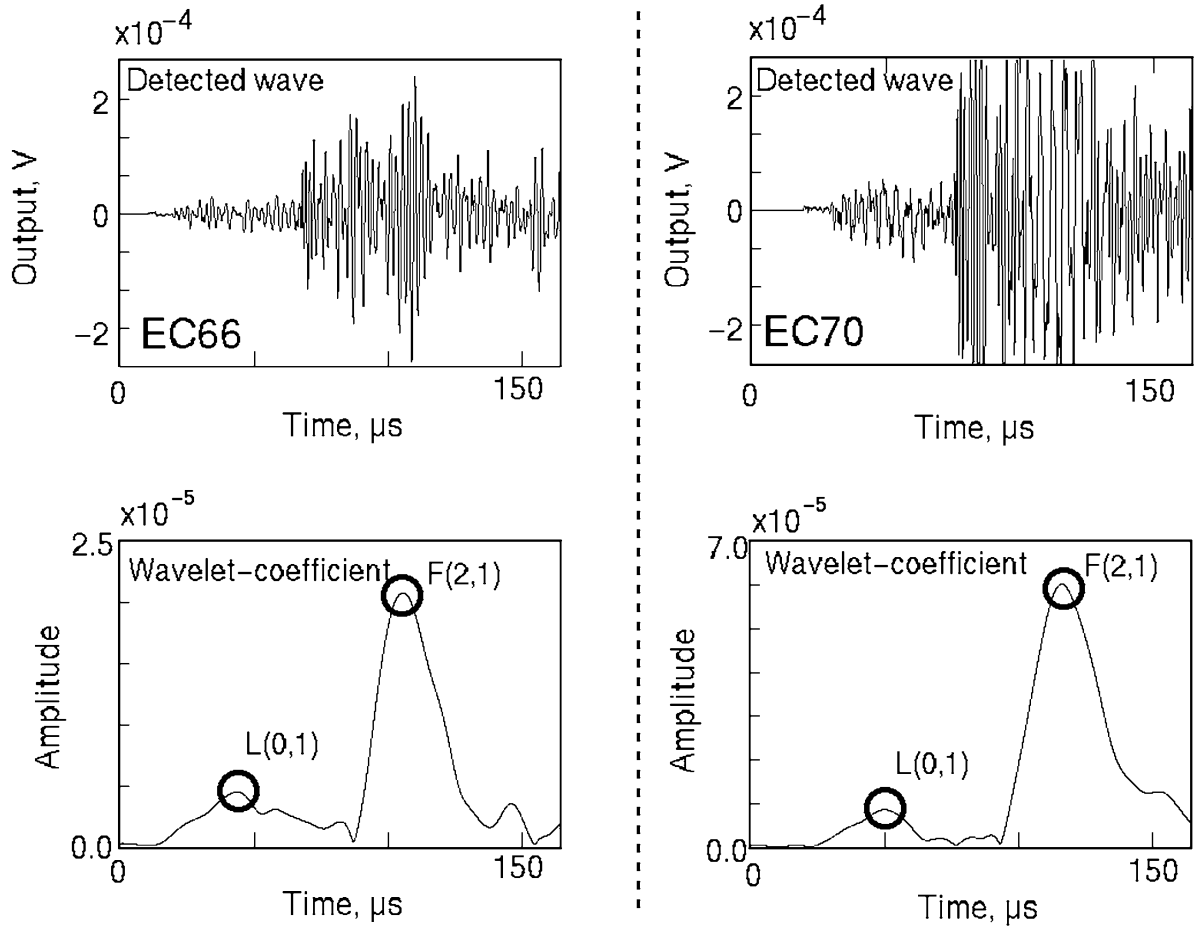

Fig. 7 Waveform (the upper) and wavelet coefficient at 190 kHz of AE signals, produced by ammonia-SCC of brass tube.

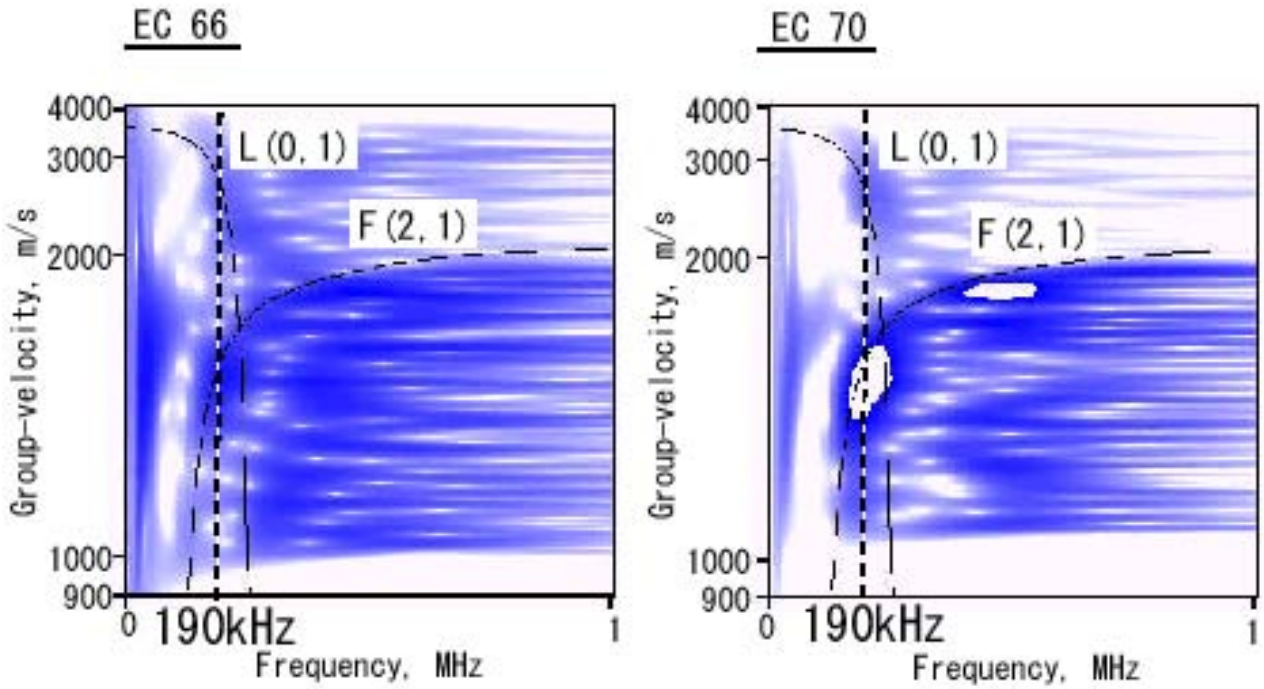

Fig. 8 Group velocity dispersion of cylinder wave AE produced by ammonia-SCC of brass tube.

F(2,1) mode velocities at the frequency of 190 kHz for the source location. The group velocity of L(0,1) and F(2,1) modes were calculated as 3935 m/s and 1320 m/s, respectively. Estimated source locations were distributed at 195 ±6 mm from the sensor position and very close to the actual position of SCC. Ammonia-SCC was intergranular (IG) type per SEM observation (see Fig. 6(b)). This indicates that the ammonia-SCC, typical APC-IG-SCC, does produce acoustic emission, as in the case of APC-IG-SCC of austenitic stainless steel by chloride ions [9].

Next we estimated the fracture dynamics of SCC by waveform simulation of first arriving L(0,1) mode wave. Here, the waveform simulation must be done to the L(0,1) mode, which shows uniform out-of-plane displacement (or velocity component of displacement) over the entire surface of the tube. We determined the overall transfer function for L(0,1) mode experimentally by using the same method for Lamb wave. As shown in Fig. 9, we excited L(0,1) mode wave by an expansion of small compression mode PZT element (1 x 1 x 2 mm). Out-of-plane displacement of the element was measured by a laser interferometer and converted to the volume opening; see Fig. 9(b). The overall transfer function, Fig. 9(c), was obtained by the time-domain Gauss-Zeidel deconvolution of the wave (a) with (b). The source parameters; effective rise time ΔTr* and crack volume ΔV, with its time dependence approximated by a 4th power sine step-wise function, were obtained by waveform matching of the first portion of the L(0,1) mode. Detected (EC 79) and simulated waveforms are compared in Fig. 10. Here, the third and fourth peaks are matched. ΔTr* and ΔV are estimated as 0.32 μs and 2.7x 10^{-15} m^3, respectively.

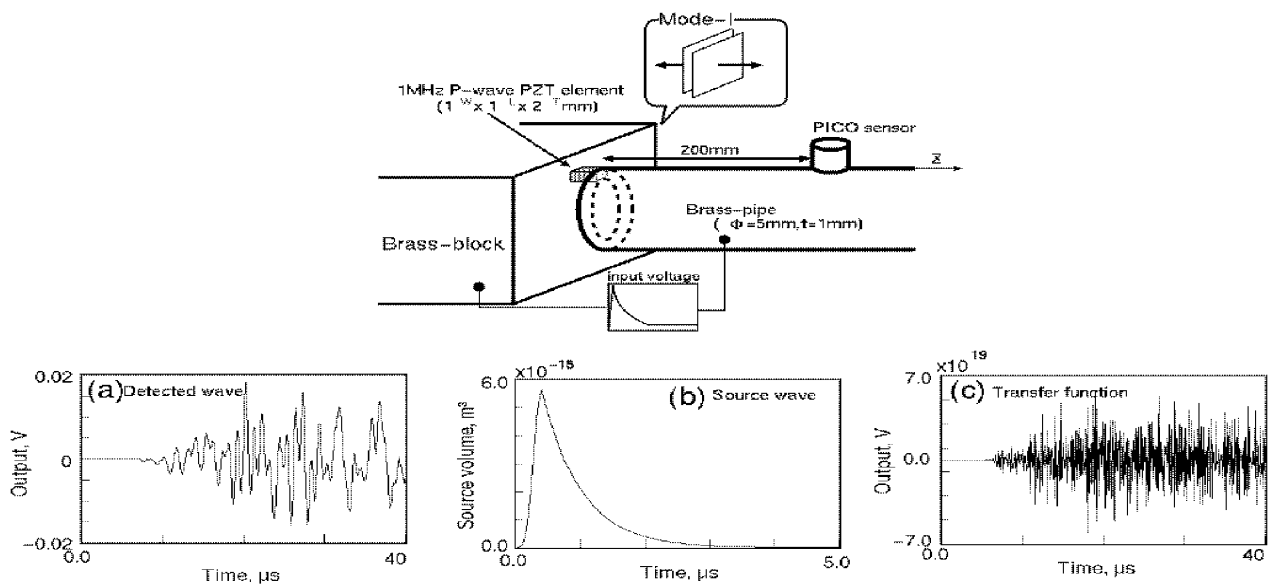

Fig. 9 Experimental setup for monitoring cylinder wave due to Mode-I fracture and procedure for preparing the over-all transfer function for the cylinder wave.

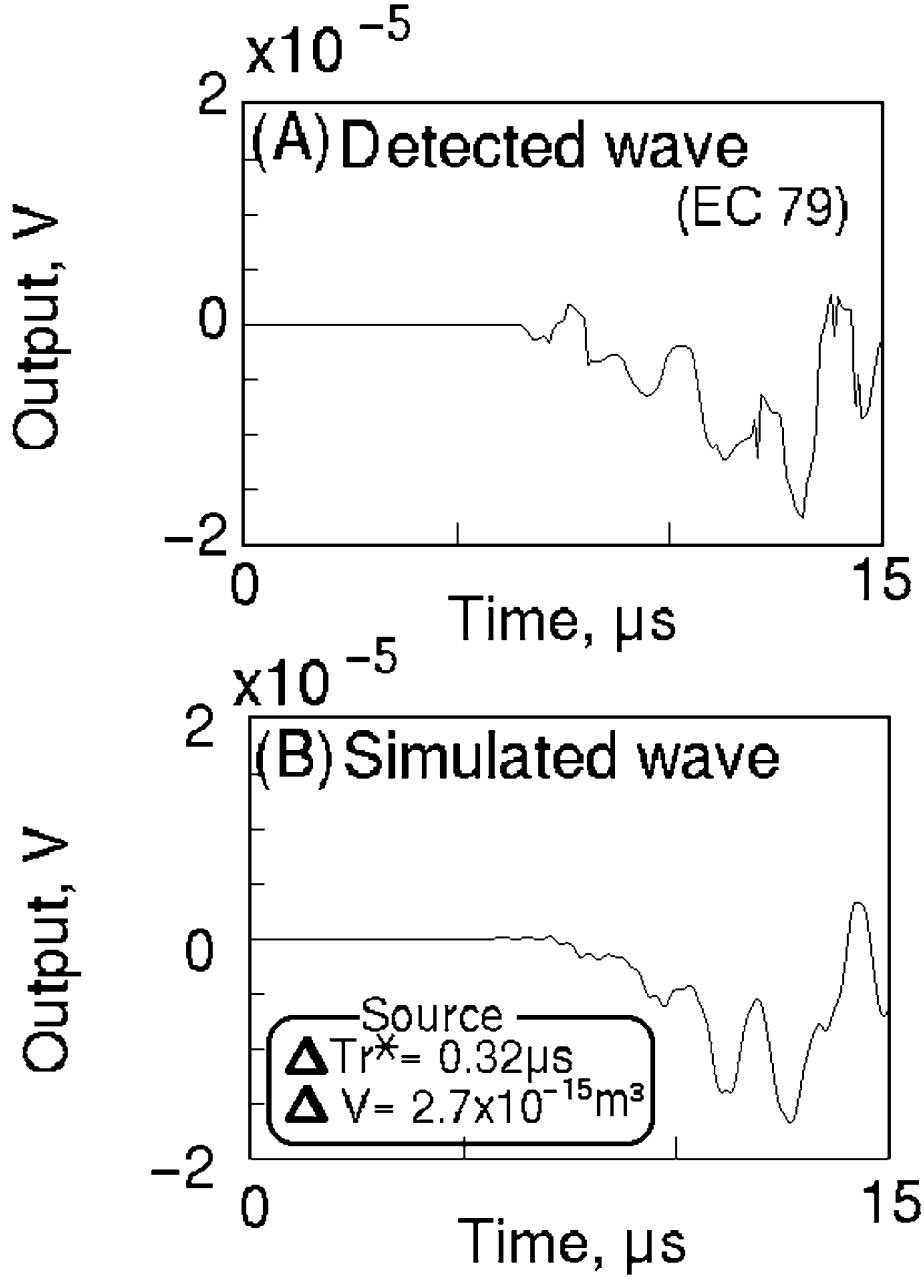

Fig. 10 Comparison of waveform detected (A) and simulated (B).

We must detect the first weak waveform of L(0,1) for the source dynamic analysis using short sampling interval and large amplification. This requirement is contradictory to those for source location (long sampling interval and low amplification). Usage of two AE systems satisfies these requirements and is needed for further research.

4. CONCLUSION

Based on the quantitative modal analysis of cylinder wave, we proposed a new source location method of AE signal monitored by a single AE sensor. We analyzed the AE signal produced by ammonia-SCC of brass tube. Results are summarized below;

1) Source location in the axial direction was obtained by using the arrival time difference between the L- and F-modes, and the theoretical group velocities at selected frequency. Wave modes and frequency are chosen using the wavelet transform of AE signal detected. Location accuracy of artificial sources for 5 mm diameter pipe was less than 5.9 % for 100 to 3000 mm distance.
2) The source location method developed was applied to AE signals produced by ammonia-SCC of 5 mm diameter brass tube. Estimated AE location agreed well with the location of SCC. Source dynamics were estimated by the waveform simulation of the first arriving L(0,1) mode, and suggested grain boundary fractures with fast source rise time.
3) Due to large amplitude difference of L- and F-mode and different sampling conditions, two independent AE systems, one with long sampling interval and low amplification and other with fast sampling interval at large amplification, are needed for both analyses.

REFERENCES

[1] D. C. Gazis, "Three-Dimensional Invenstigation of the Propagation of Waves in Hollow Circular Cylinders," J. Acoust. Soc. Am. **31**, 568-573 (1959).

[2] A. H. Fitch, "Observation of Elastic-Pulse Propagation in Axially Symmetric and Nonaxially Symmetric Longitudinal Modes of Hollow Cylinders," J. Acoust. Soc. Am. **35**, 706-708 (1963).

[3] D. N. Alleyne and P. Cawley, "The Excitation of Lamb Waves in Pipes Using Dry-Coupled Piezoelectric Transducers," J. Nondestr. Eval., **15**, 11-20 (1996).

[4] J. L. Rose, J. J. Ditri, A. Pilarski, K. Rajana and F. Carr, "A Guided Wave Inspection Technique for Nuclear Steam Generator Tubing," NDT &E Int., **27**, 307-310 (1994).

[5] H. Nishino, F. Uchida, S. Takashina, M. Takemoto and K. Ono, "A New Method of AE Source Location in Pipes Using Cylindrical Guided Waves," Proc. of EWGAE 2000.

[6] H.W. Pickering and P.J. Byrne, "Stress Corrosion of α–Brass in an Acid Sulfate Solution," Corrosion, **29**, 325 (1973).

[7] R.P.M. Procter and F.N. Stevens, "The Formation of Cuprous Oxide Films on α–Brass Stress – Corrosion Fracture Surfaces," Corrosion. Sci., **15**, 349 (1975).

[8] N.W. Polan, J.M. Popplewell and M.J. Pryor, "Mechanically Assisted Dezincification of Cu-Zn alloys during Stress Corrosion in Ammoniacal Solutions," J. Electrochem. Soc., **126**, 1299 (1979).

[9] S. Fujimoto, M. Takemoto and K. Ono, "AE Monitoring of Chloride Stress Corrosion Cracking of Austenitic Stainless Steel," Progress in AE X, Proc. 15th IAES, JSNDI, Tokyo, 2000, pp. 129-134.

DETECTION OF PRE-MARTENSITIC TRANSFORMATION PHENOMENA IN AUSTENITIC STAINLESS STEELS USING AN ACOUSTIC EMISSION TECHNIQUE

T. INAMURA, S. NAGANO, M. SHIMOJO, K. TAKASHIMA and Y. HIGO

Precision and Intelligence Lab., Tokyo Institute of Technology, Yokohama 226-8503, Japan

ABSTRACT

Acoustic emission (AE) measurements were performed on a 304 austenitic stainless steel during cooling to investigate pre-martensitic transformation phenomena of α'-martensitic transformation. Low amplitude AE signals were observed sporadically in the temperature range from 225 to 209 K, above M_s^b (=208 K) (M_s^b is the temperature, at which burst-like transformation starts, in this study). However, no visible martensites were observed above 212 K in optical microscopy observation. In contrast, low amplitude AE signals were measured only in the temperature range from 212 K to M_s^b temperature in the specimen which had been cooled down to 212 K before the AE measurement. In this temperature range, the formation of fine α'-martensite particles was confirmed in our previous study. Therefore, the source of low amplitude AE is supposed to be the formation of fine α'-martensites. AE technique is a promising method to investigate the kinetics of the pre-martensitic transformation phenomenon in this alloy.

1. INTRODUCTION

Martensitic transformation is a diffusionless transformation, which is achieved by cooperative and shear-like movements of atoms, and by a nucleation and growth [1]. It has been well known that burst-like transformation of austenite (f.c.c.) into α'-martensite (b.c.c.) is caused by simple cooling or plastic deformation in austenitic stainless steels. The formation of α'-martensite is accompanied by a large volume dilatation due to the Bain distortion. In addition, the transformation propagates at a speed of shear waves in the material and the formation of a lath or a plate α'-martensite is completed within about 10^{-8}~10^{-7} seconds [2]. Therefore, acoustic emission (AE) waves are generated during the transformation. AE waves include information of dynamic properties of martensitic transformation. AE technique is, thus, one of the most promising methods to examine dynamic properties of such an extremely fast phenomenon, and has been used to determine M_s^b (M_s^b is defined as the temperature at which spontaneous burst-like martensitic transformation occurs, in this study) and to investigate kinetics or dynamics of the transformation [2-4]. In these previous studies, it has been reported that relatively low amplitude AE signals were observed sporadically before the burst-like martensitic transformation during cooling in Fe-Cr-Ni [2], Fe-Pt [3], Ti-Ni-Fe [4] alloys. These low amplitude AE signals have been considered to be related to the pre-transformation phenomena and/or the nucleation process of burst-like martensitic transformation [3]. The pre-transformation phenomena are considered to be essential to understand the nucleation mechanisms of martensitic transformation, however the nucleation process of α'-martensite has not been investigated experimentally yet. In our previous study, low amplitude AE signals were also detected sporadically just above the M_s^b, and are deduced to be related to a pre-martensitic transformation phenomenon and/or the nucleation of the burst-like α'-martensitic transformation in a 304 austenitic stainless steel [5]. However, the source of the low amplitude AE signals have not yet

been clarified either in this alloy. The objective of the present study is to investigate the source of low amplitude AE signals which are observed above M_s^b in a 304 austenitic stainless steel.

2. EXPERIMENTAL PROCEDURE

The material used in this study was a hot-rolled 304-type austenitic stainless steel (Fe-18Cr-8Ni) rod, which is commercially available. Two pieces of disc-shaped specimens, with dimensions of 15 mm in diameter and 2 mm in thickness, were cut by a wheel cutter. The specimens were electropolished to remove the deformed layer which may be introduced during cutting, and then electro-etched using an oxalic acid solution. Microscopic observation was performed using a scanning laser microscope with resolution of less than 1 μm. One of the disk-shaped specimens was used without any pre-cryogenic treatment before the AE measurement. A pre-cryogenic treatment was performed on the other specimen at 212 K to observe the change in the frequency of the occurrence of low amplitude AE above this temperature (As mentioned in below, the temperature of 212 K is above M_s^b of this specimen). Hereafter, these specimens are termed "non-treated specimen" and "pre-cooled specimen", respectively.

AE measurements were carried out during cooling. A disc-shaped specimen was attached to the bottom of the wave-guide using vacuum grease. The wave-guide, which was made of an austenitic stainless steel, had been immersed in liquid nitrogen for 6 hours to avoid martensitic transformation during the measurements. The specimen was then cooled down from room temperature (~ 298 K) to 200 K with a cooling rate of approximately 1 K/min. The temperature of the specimen surface was measured using a Cu-Cu constantan thermocouple which was spot-welded onto the specimen surface. The AE transducer used was a piezoelectric (PZT) 140 kHz-resonant type. The detected AE signals were amplified by a pre-amplifier (NF-9917) and a main-amplifier (NF-AE922) with a total amplification of 80 dB, and analyzed by an AE analyzer (NF-AE932). The threshold level was set at 100 μV at the output of the transducer. Root mean squared (RMS) voltage of AE signals and total AE event counts were plotted as a function of specimen surface temperature.

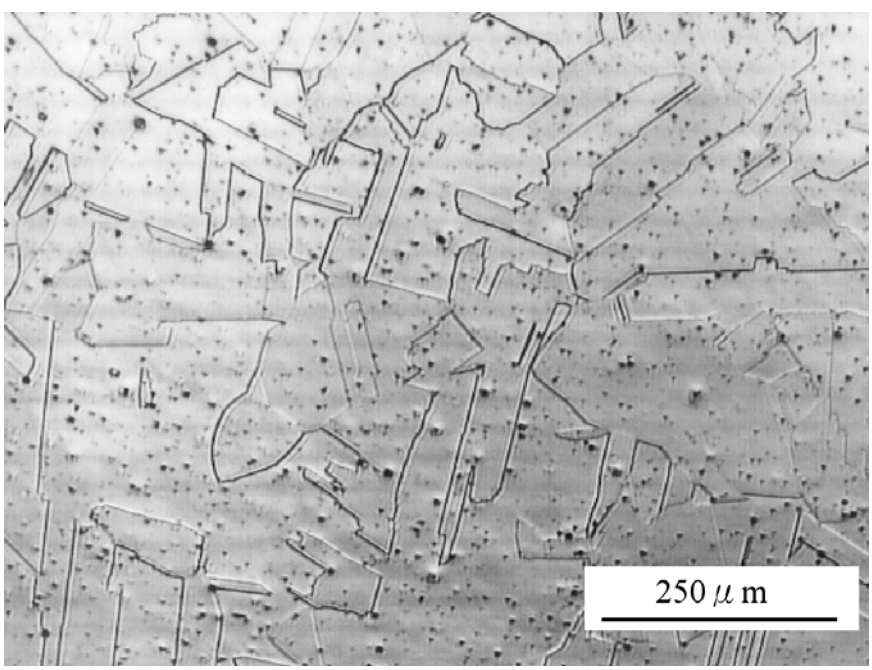

Fig. 1: Scanning laser microscope image of the specimen before the AE measurement.

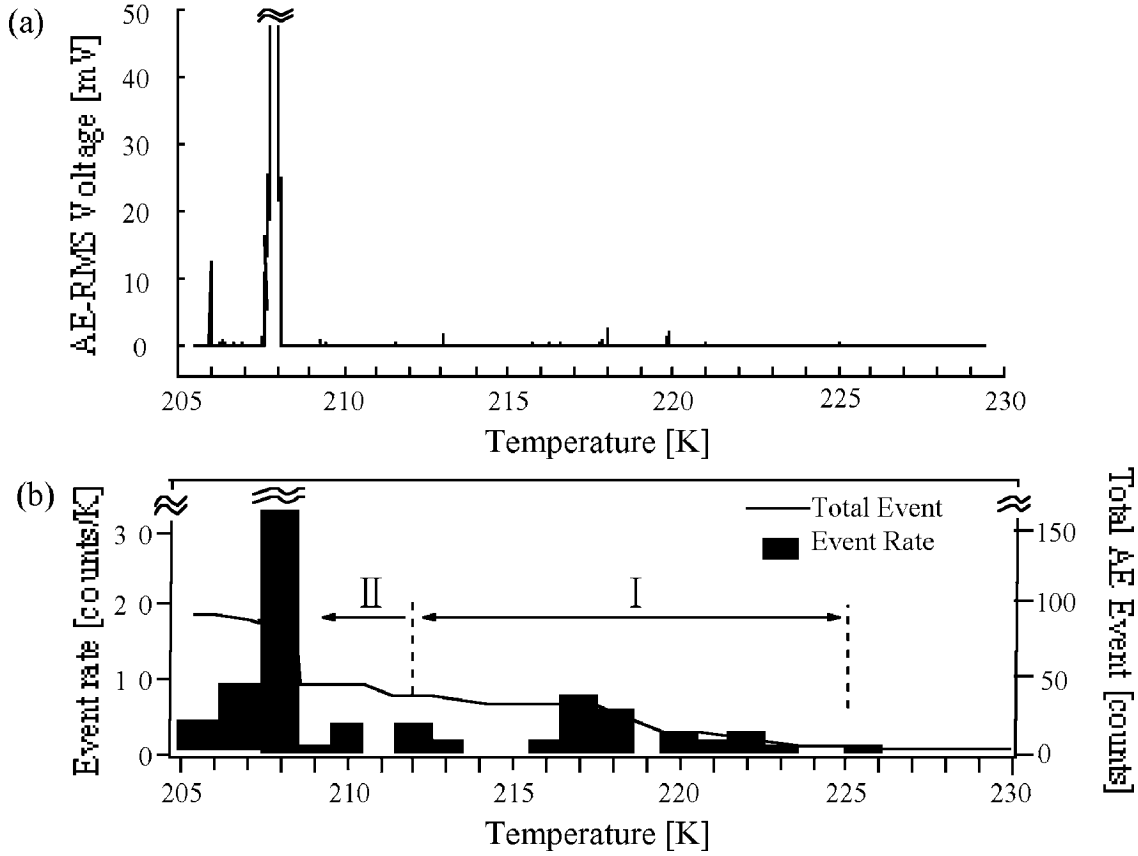

Fig. 2: (a) AE-RMS voltage during cooling of 304-type stainless steel (non-treated); (b) Total AE event count and event-rate of 2(a) as a function of temperature;

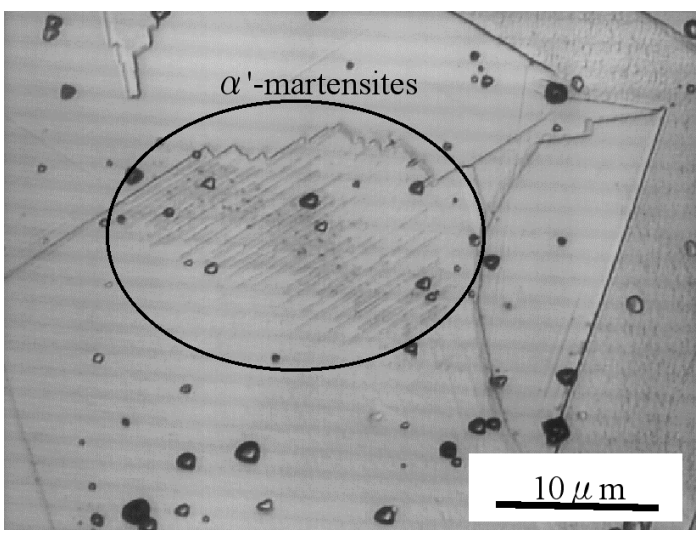

Fig. 2: (c) α-martensite plates observed in the non-treated specimen after the AE measurement (inside the ellipse, along 2 o'clock direction).

3. RESULTS AND DISCUSSION

Figure 1 shows the initial microstructure of the specimen. The specimen is fully austenite and no deformation-induced martensites are observed. Figure 2(a) shows AE-RMS voltage of the non-treated specimen during cooling and Fig. 2(b) shows the AE event rate and the total AE

event counts as a function of temperature. No AE signals were detected above 226 K during cooling. Burst AE-signals were started to be detected at 208 K and some plate-like α'-martensites were observed on the surface of the specimen after this AE measurement as shown in Fig. 2(c). According to Takashima et al. [6], the burst-like formation of α'-martensites generates burst-like AE-signals. Thus, the M_s^b of the non-treated specimen was determined to be 208 K. Low amplitude AE signals were detected sporadically in the temperature range of 226~209 K. The total event counts increased suddenly in the temperature range of 220~212 K and the event rate was extremely increased in this temperature range. Figure 3 shows scanning laser microscope image of the typical microstructure of the specimen which was cooled down to 212 K (pre-cooled specimen) before the AE measurement. No martensite was observed in this specimen. Therefore, it is considered that the low amplitude AE signals observed above M_s^b were not due to the formation of α'- and ε-martensite plates which are visible under the microscope used. This result corresponds to the results obtained by other researchers that no martensites were observed above M_s^b despite low amplitude AE signals were sporadically detected above M_s^b [2-4]. Therefore, a kind of fast phenomena, which generates AE, is deduced to occur in the temperature range from 226 K to 209 K, especially in the temperature range from 220 to 212 K.

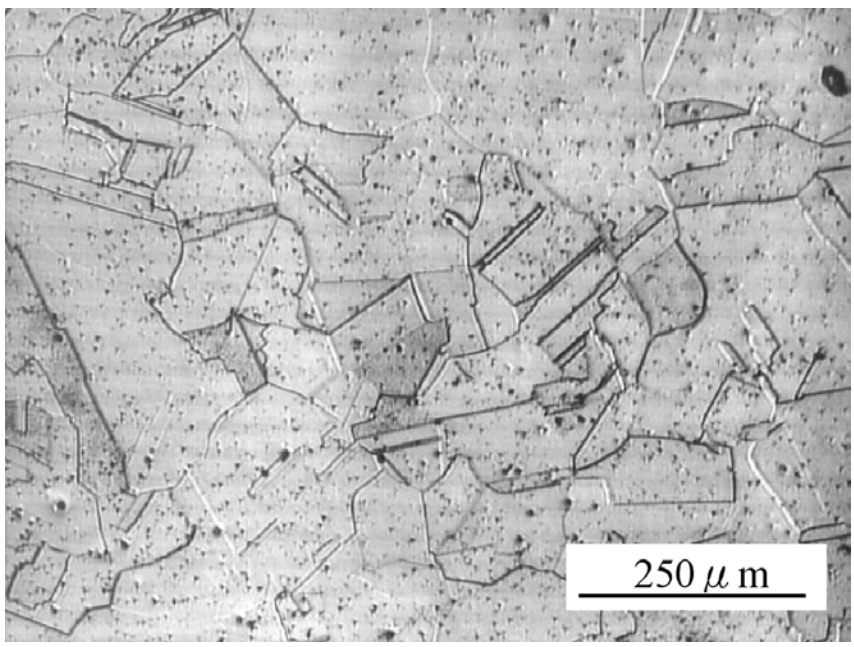

Fig. 3: Microstructure of the specimen after cooled down to 212K (pre-cooled specimen).

Figure 4 shows AE-RMS voltage and event rate and total AE event observed during the AE measurement of the pre-cooled specimen. Hereafter, the temperature range from 226 to 212 K is termed "region I" and the temperature range from 212 K to M_s^b is termed "region II" , in both Figs. 2(b) and 4(b). As mentioned above, "pre-cooled specimen" had been cooled down to 212 K and then warmed up to room temperature in the laboratory air before the AE measurement. The M_s^b of the pre-cooled specimen was determined to be 207 K (see Fig. 4(a)). The M_s^b of the pre-cooled specimen and the non-treated specimen seem to be approximately the same temperature. Sporadic low-amplitude AE signals were observed below 226 K also in the AE measurement of the pre-cooled specimen. However, the temperature range in which low amplitude AE was observed frequently was different from that observed in the non-treated specimen. In non-treated specimen, an increase in total AE event counts was mainly observed in region I as shown in Fig.

2(b). In contrast, such an increase in total AE event counts was not observed in region I in the pre-cooled specimen. In the pre-cooled specimen, total AE event counts started to increase mainly in region II, i.e., below the pre-cooling temperature. This result indicates that the generation of low amplitude AE which occurs above 212 K had been completed by the pre-cooling at 212 K before the AE measurement. The generation of AE is caused by the release of elastic strain energy in the shorter duration time. In addition, it is considered that α'-martensitic transformation is the only phenomenon which occurs during simple cooling and generates AE. Thus, the generation of low amplitude AE is considered to be related to α'-martensitic transformation.

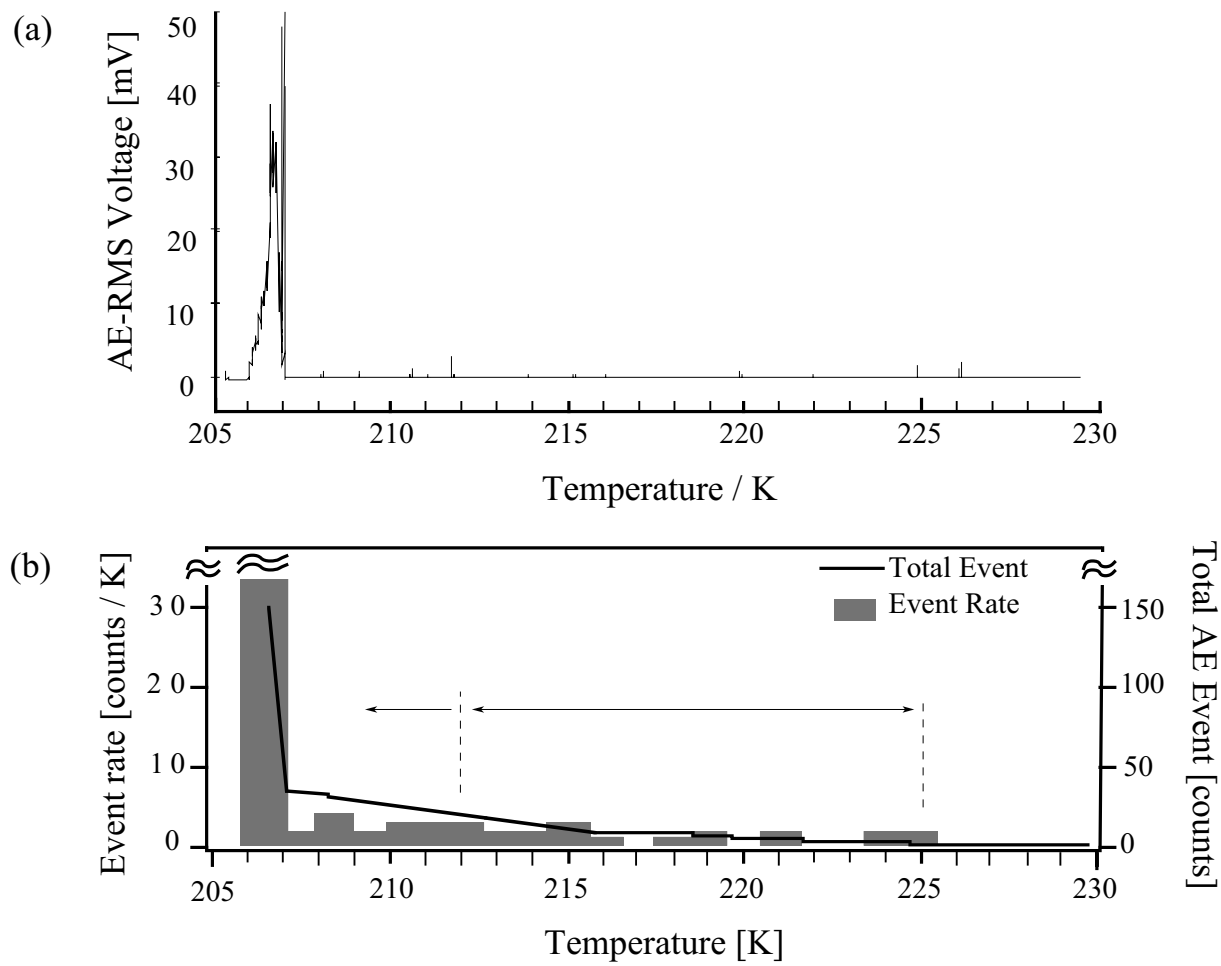

Fig. 4: (a) AE-RMS voltage during cooling of the pre-cooled specimen; (b) Total event counts and event-rate of (a) as a function of temperature in pre-cooled specimen.

In our previous study [5], the formation of fine α'-martensite particles, the diameter of which was 30~100 nm, were confirmed by transmission electron microscopy (TEM) in the 304-type stainless steel which had been cooled down to just above M_s^b. In general, the growth of α'-martensites needs driving force to deform matrix in order to absorb the Bain distortion. This driving force is provided by the free energy difference between the parent phase (f.c.c.) and martensite (b.c.c.) phase. It is considered that these micro-sized α'-martensites cannot grow into "large martensites (as shown in Fig. 2(c))", which cause plastic deformation of matrix, because the specimen used in the previous study had not been cooled down below M_s^b (The driving force for the growth of "large martensite" had not been provided above M_s^b). In addition, Bogers and

Burgers showed that two intersecting {111}<$11\bar{2}$> shears transform f.c.c. lattice into b.c.c. lattice [7]. According to this, it is reasonable to consider that intersections of partial dislocations in austenite have a b.c.c.-like stacking and to be a preferential nucleation site of α'-martensite. The atoms in the b.c.c.-like stacking region should move to b.c.c. positions with relatively lower energy barrier which can be overcome by cooling to a certain temperature above the M_s^b. It is thus suggested that the generation of low amplitude AE observed above M_s^b in this study is due to the formation of micro-sized α'-martensite particles at intersections of partial dislocations. The micro-sized α'-martensitie particles are deduced to be formed in the temperature range from 226 to 209 K, especially in the temperature range of 220 to 212 K, according to the results obtained in this study. Some of the b.c.c.-like stacking regions and the atoms around the regions in the specimens are supposed to complete the transformation into b.c.c.-stacking above 212 K. This should be the reason for that the number of the observed low amplitude AE above 212 K was smaller in the pre-cooled specimen than that observed in the non-treated specimen. These results strongly suggest that AE technique is a useful method to investigate also the pre-transformation phenomenon, and/or the kinetics of the nucleation of burst-like α'-martensitic transformation in this alloy system.

4. CONCLUSIONS

The M_s^b of the material used was determined to be 208 K and low amplitude AE signals were detected frequently in the temperature range of from 226 K to 212 K. No visible martensites were formed above 208K using a scanning laser microscope. While the generation of low amplitude AE was observed in the temperature range from 212 K to M_s^b in the specimen which had been cooled down to 212 K before the AE measurement. Then, the generation of low amplitude AE which occurs above 212 K had been completed by the pre-cooling at 212 K before the AE measurement. The formation of fine α'-martensite particles was confirmed in the specimen which had been cooled down to just above M_s^b using TEM in our previous study. Thus, the source of the low amplitude AE is deduced to be due to the formation of micro-sized α'-martensite particles at intersections of partial dislocations in this alloy system. AE technique is found to be a promising method to clarify the kinetics of the pre-martensitic transformation phenomenon of burst-like α'-martensitic transformation.

REFERENCES

[1] J. W. Christian, G. B. Olson and M. Cohen, *J. de Physique IV,* **5**, (1995), C8-3-C8-10.
[2] K. Takashima, Y. Higo and S. Nunomura, *Phil. Mag.* **49**, (1984), 231-241.
[3] H. Ohtsuka, K. Takashima and G. B. Olson, *Mat. Res. Soc. Symp. Proc*. **459**, (1997), 407-412.
[4] K. Takashima and M. Nishida, *J. de Physique IV* **5**, (1995), C8-735-C8-740.
[5] T. Inamura, M. Shimojo, K. Takashima and Y. Higo, *Proc. of 1999 National Conference on Acoustic Emission*, (1999), JSNDI, Tokyo, pp. 103-106 (in Japanese).
[6] K. Takashima, Y. Higo and S. Nunomura, *Scripta. Metall.* **14**, (1980), 489-491.
[7] A. J. Bogers and W. G. Burgers, *Acta Metall.* **12**, (1964), 255-261.

ACOUSTIC EMISSION ANALYSIS OF CARBIDE CRACKING IN TOOL STEELS

KENZO FUKAURA and KANJI ONO*

Himeji Institute of Technology, Shosha, Himeji 671-2201, Japan
*University of California, Los Angeles, California 90095-1595, USA

ABSTRACT

Fracture of hardened tool steels is expected from large carbides, although the initial state of fracture has been difficult to evaluate. We employed acoustic emission analysis during the tensile testing of two tool steels in order to determine the progression of internal damage. Steels used are 1.4C-11Cr-0.8Mo-0.23V (JIS SKD11) and 0.8C-8.1Cr-1.9Mo-0.52V (modified SKD11). Both were quenched and tempered to obtain the maximum secondary hardening. For the modified steel, a lower hardness temper was also used. In SKD11 steel, AE signals from carbide cracking started at about half the fracture stress and AE-event counts reached ~10,000 at the fracture stress. In modified-SKD11 steel, AE signals from carbide cracking started at 70-90% of the fracture stress (20% higher than that of SKD11 for similar tempering) and AE-event counts were only several hundreds near the fracture stress. (These were less than 50 at stress corresponding to the fracture stress of SKD11.) The average amplitude of pre-fracture AE signals was also reduced by 6 dB in the modified steel. These changes reflect the reduction in the amount and size of primary carbide particles. When the carbide size becomes twice larger, the stress for carbide cracking is reduced to one-half. It is thus critical to refine the primary carbide in alloy design.

1. INTRODUCTION

Hardened tool steels are an important class of steels and are used as cold-forming dies, punches, etc. under increasingly severe conditions [1,2]. For such applications, improvements of their low-cycle fatigue strength are the critical task for ferrous metallurgists [3-6]. In hardened tool steels, both primary and secondary carbides contribute to their high hardness and superior wear resistance [7]. The carbide fracture and decohesion of carbide/matrix interface have significant effects on the deformation and fracture behavior of these steels, as suggested by fractographic evidence. One of the authors has investigated a series of tool steels and identified the primary carbide fracture as the likely cause of their brittle fracture by careful analysis of fractured carbides and by the use of Stroh theory of fracture initiation [8]. However, the fracture initiation stage is difficult to examine using conventional metallurgical characterization techniques. Thus, acoustic emission (AE) is used in this work to determine the condition of fracture initiation and subsequent progression in standard and modified tool steels. Carbide cracking can be identified unambiguously with AE and crack-induced waveforms correlated to the AE source function via experimentally determined Green's function.

2. MATERIALS AND EXPERIMENTAL PROCEDURES

A conventional tool steel (1.4C-11Cr-0.8Mo-0.23V, JIS SKD11) and its modification are used in this study. The modification reduced Cr and C content and increased Mo and V, resulting in the optimized composition of 0.8C-8.1Cr-1.9Mo-0.52V (modified SKD11). The chemical composition of the steels used is given in Table 1. After hot rolling, both steels were homogenize-annealed and air-quenched from 1303 K following a carbide-spheroidizing treatment. Tempering was between 473 and 833 K. Vickers hardness after tempering is given in Fig. 1. In the as-quenched state, SKD11 has a higher hardness, but the modified steel has a slightly higher peak hardness after secondary hardening at higher tempering temperatures. Test specimens were tempered to achieve the peak hardness (tempering at 773 K for SKD11 and 793 K for modified SKD11). For the modified steel, tempering at 473 K was also used. In order to stabilize the microstructures, double tempering was used in all the specimens.

Table 1. The chemical composition of the steels used.

JIS SKD11	1.41C; 11.10Cr; 0.80Mo; 0.23V; 0.24Si; 0.41Mn; 0.023P; 0.001S
modified SKD11	0.80C; 8.10Cr; 1.90Mo; 0.52V; 0.88Si; 0.39Mn; 0.022P; 0.001S

The shape of specimens is hour-glass type. The specimen has the reduced section of 5 mm minimum diameter with the radius of 30 mm. This geometry was selected so that it can be also used for fatigue testing. The stress concentration factor is 1.406. The grip parts are threaded (M18). It has shoulder flat on both side of the reduced section. Tensile tests utilized a floor-model Instron and the cross-head speed was 0.254 mm/min. Fracture surface observation utilized a scanning electron microscope (JEOL 5200).

Two small AE sensors were coupled to machined shoulders on both sides of the reduced section. The sensors are resonant type with the center frequency of 375 kHz (AET MAC-375). The distance between the sensors was 45 mm. Two 40-dB pre-amplifiers (PAC 1220A) and two 2-channel MISTRAS systems (on 2 separate PCs) were used. One system used MI-LOC and the other MI-TRA software. Most of AE data to be presented here is from the MI-TRA system, as synchronized triggering did not function properly in MI-LOC system. The threshold level was 40 dB in reference to 1 μV as the pre-amplifier input as 0 dB. Only those AE signals from the reduced section were analyzed by limiting the arrival-time difference to 10 μs via the use of group-replay function in MI-TRA. The rms voltages from one of the channels were recorded with load on the parametric channels and by using an HP-3400A and a two-pen recorder.

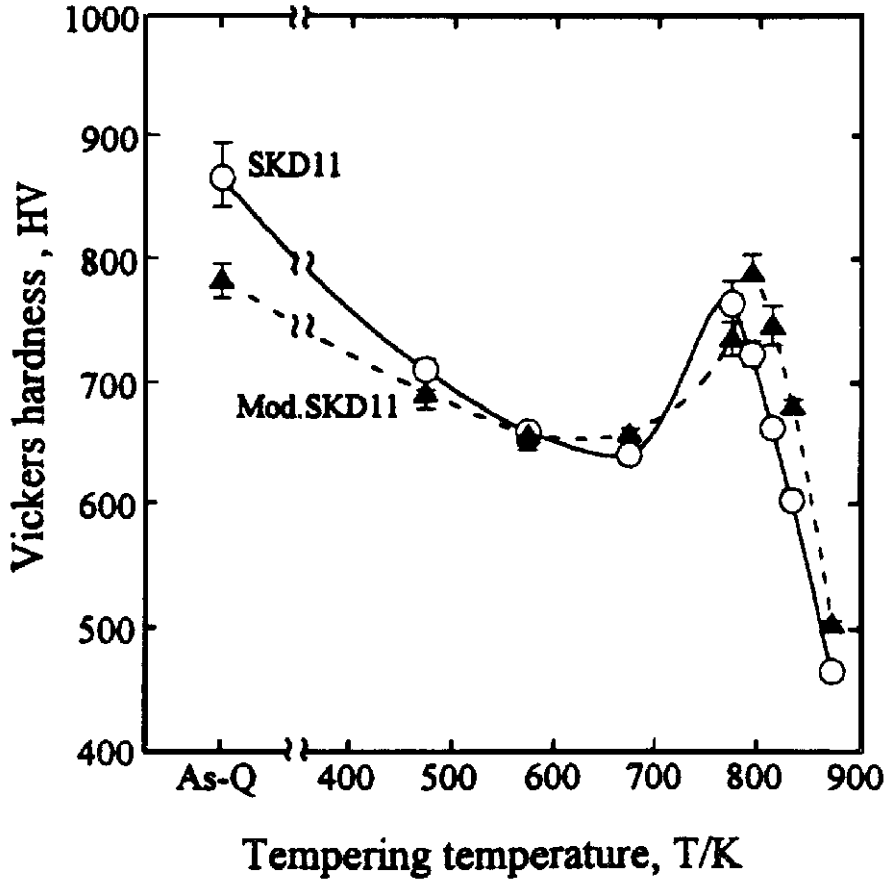

Fig. 1 Changes in Vickers hardness as a function of tempering temperature.

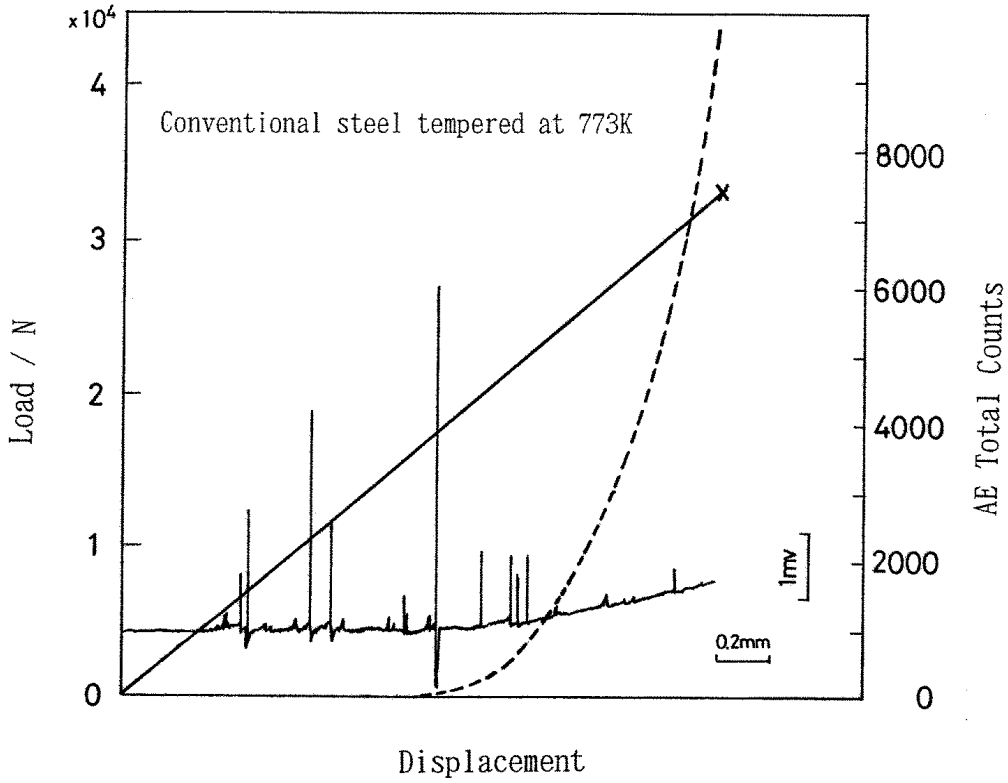

Fig. 2 Tensile and AE test results for SKD11 steel, quenched and tempered at 773 K.

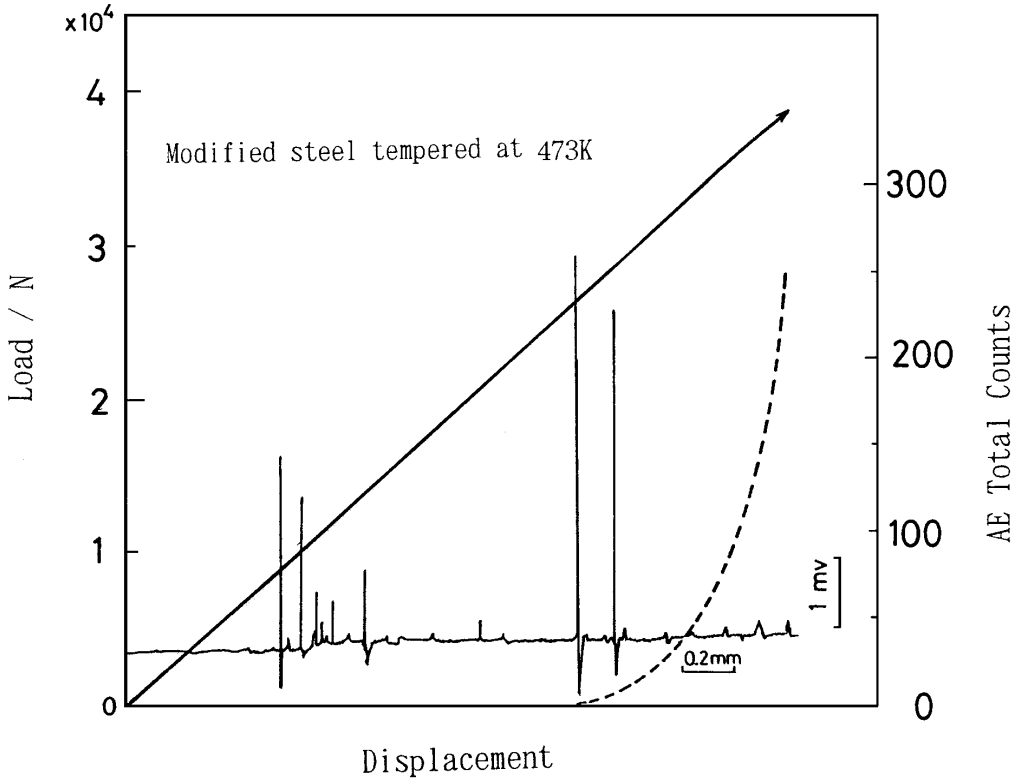

Fig. 3 Tensile and AE test results for modified SKD11 steel, quenched and tempered at 473 K.

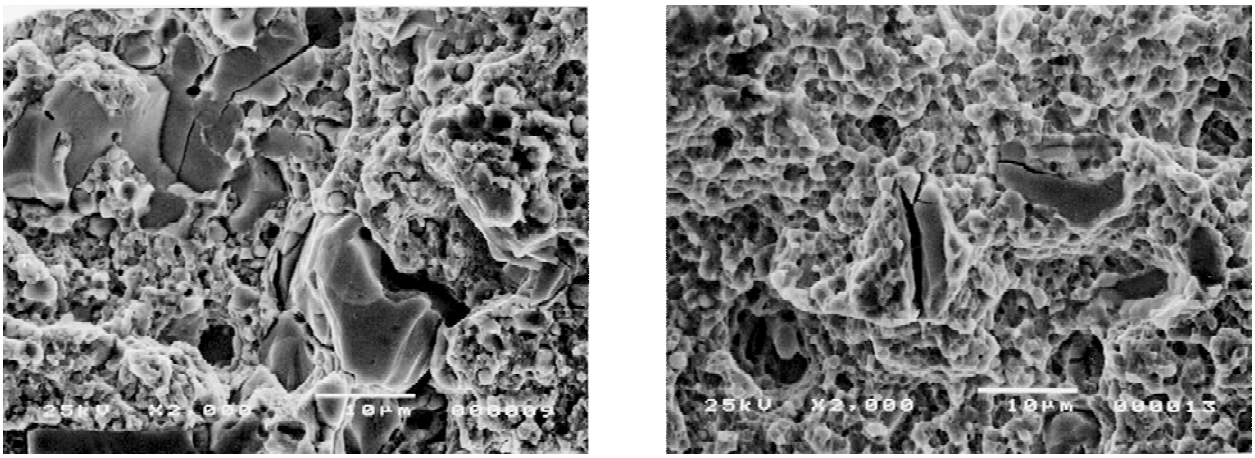

Fig. 4 Fracture surfaces of quenched and tempered steel. Left: SKD11; Right: Modified SKD11. White marker indicates 10 μm.

3. RESULTS AND DISCUSSION

Tensile and AE test results for SKD11 steel are shown in Fig. 2. Both rms voltage plot and cumulative AE event counts are given. (Note that the event count data includes only those from the reduced gage section, whereas the rms voltage plot shows large spikes that come from the grip sections. These spikes should be ignored.) The load-displacement curve is essentially linear and no

plastic yielding was recognized. AE events started at 1.01 GPa and the event rates continually increased until reaching the fracture stress of 2.41 GPa. The total AE events at fracture was ~10000. The rms voltage plot showed a slight increase from the background level starting as the AE event count curve began to rise. However, the increase was small (<0.7 mV). The waveform examination indicates that no continuous AE signals existed and the increase in the rms voltage was due to numerous burst emissions at close intervals. Typical AE signals observed from the gage section have a sharp initial rise with relatively short decay. The waveform was essentially unchanged throughout the test. Its frequency spectrum closely corresponds to that of the AE sensor used.

For the modified steel tempered at 473 K, tensile and AE test results are given in Fig. 3. The load-displacement curve is again linear and no plastic yielding was observed. AE events started at 1.84 GPa and the event rates continually increased until reaching the maximum stress of 2.74 GPa, where the test was stopped. The total AE events decreased substantially to 250. The rms voltage plot showed a slight increase from the background level near the end of the test, but waveforms showed no indication of continuous emission. Again, spikes are spurious noise and should be ignored. AE signal waveforms were similar to those in SKD11. For the modified steel tempered at 793 K, AE events started at 2.06 GPa. Similar AE behavior was observed otherwise.

When conventional tensile test specimens with uniform gage section are used, the yield strength can be determined and the values are listed in Table 2. These values are slightly different from the present experiment due to different test geometry. However, the AE start stress increases significantly by the alloy modification. In SKD11, AE start stress was 60 % of the yield strength, while that for the modified steel was comparable to or higher than the yield strength.

Microstructural test result is given in Table 3. In the modified steel, the mean diameter of the primary carbide (M_7C_3) was reduced by a factor of two and the maximum size was also reduced to 2/3. The volume percentage decreased from 7.5% to 2.2%. Effects of the modification were minor in prior austenite grain size and retained austenite content. Thus, the change in the AE start stress is believed to be a consequence of the size and volume reduction of the primary carbide. In particular, it appears that large carbides are responsible for the AE signals observed. Even though the maximum size was decreased by only a third, the reduction in overall volume and the shift to smaller average size contribute to a large drop in carbides that generate AE signals.

In Fig. 4, two fractographs are shown, indicating cracked carbides of 10+μm size. Naturally, SKD11 has more of larger carbides. Since the minimum cross sectional area is ~20 mm^2, the viewed area is approximately 1/10,000. Since either side of the final fracture surface is expected to be also the sites of carbide cracking, only a fraction of the cracked carbides are detected as AE. Thus, it is estimated that an AE signal is due to those carbides greater than 10 μm in diameter. Note that carbides that contribute to AE are those fracturing parallel to the fracture surface. The

fracture also produces secondary cracks normal to the main crack plane, but the displacement due to such secondary cracks is less effective in exciting the AE sensor.

The amplitude of AE signals was examined and the trend is shown in Fig. 5 against the load. Generally, the amplitude is low at less than 55 dB. Further, the amplitude decreased slightly as the load level increased and that the average decreased from SKD11 steel to modified steel at 473 K temper (by ~2 dB) to modified steel at 793 K temper (by ~6 dB). The lower amplitude in the modified steel is consistent with the reduced carbide size, but the effect of tempering in the modified steels is not clear at present.

Table 2. Mechanical properties and AE start stress.

	Yield strength	Tensile strength	AE start stress
SKD11 (773K temper)	1.66	2.19	1.01 GPa
Modified SKD (473K)	1.58	2.04	1.84 GPa
Modified SKD (793K)	2.04	2.62	2.06 GPa

Table 3. Primary carbide size of the steels.

	Mean dia. (μm)	Max. dia. (μm)	Volume	Austenite GS (μm)	Retained austenite
SKD11	5.3	21.5	7.5%	5.3	7% at 773K
Modified SKD	2.5	14.4	2.2%	6.9	4% at 793K

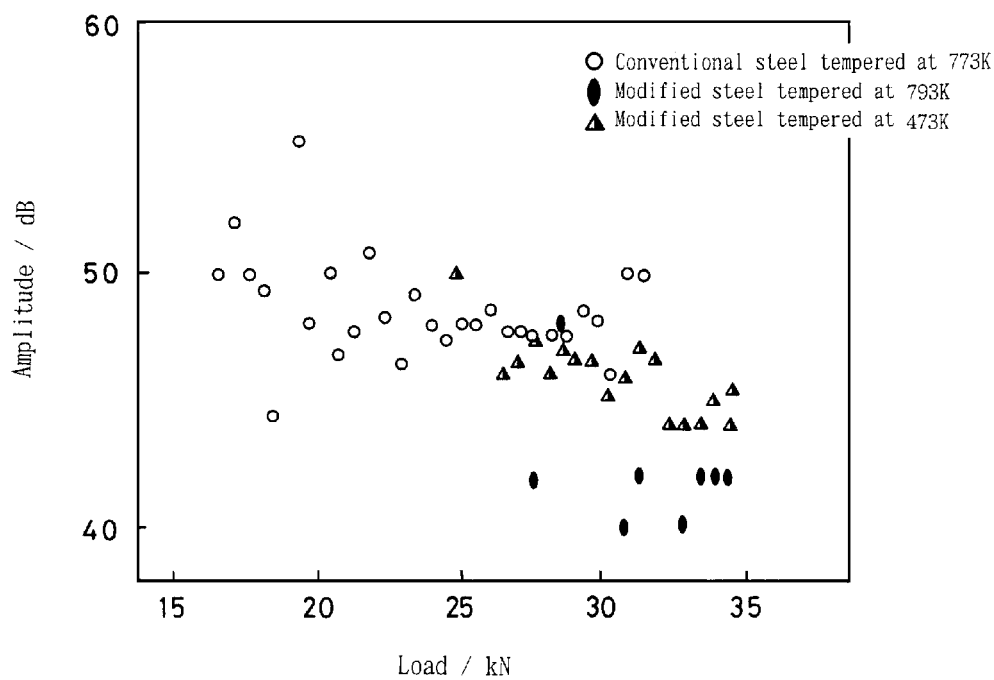

Fig. 5 AE event amplitude vs. load for the three different steels.

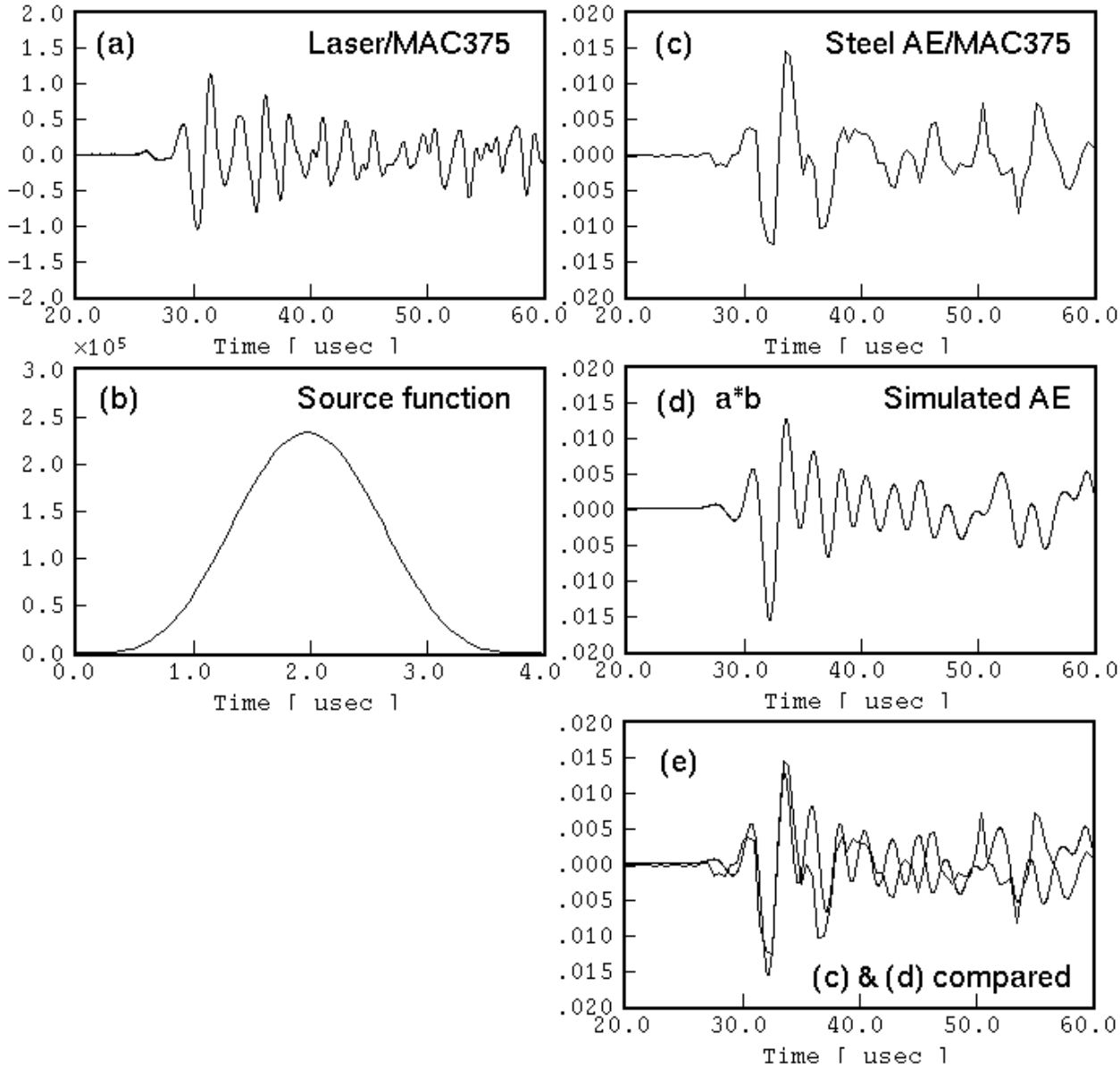

Fig. 6 (a) Experimental transfer function for a crack in tensile specimen with a resonant sensor (AET MAC375) mounted on a shoulder flat. (b) Bell-shaped source function. (c) Measured AE signal during a tensile test. (d) Simulated signal. (e) Comparison of measured and simulated signals.

Experimental determination of Green's function is possible when a force impulse can be applied and the resultant displacement can be measured with a wide-band sensor of known response. Usual impulse sources use the fracture of glass capillary or pencil lead, but these are mono-pole sources. A new laser source was recently devised. Masaki et al. [8] demonstrated the validity of using the break-down of silicone oil in a confined space by a laser beam as the source

of impulse. This source has a short rise time of 0.07 μs and is a dipole source. This method has opened a path for getting an experimental transfer function for geometry that is impossible to calculate a theoretical Green's function. We used this approach for a tensile specimen with hour-glass-shape reduced section. Here, a shallow notch was made at the smallest diameter and a laser source is excited inside the notch. A resonant sensor (AET MAC375) was mounted on a shoulder flat. The waveform obtained contains the transfer functions of the specimen and the sensor and can be compared to AE waveforms recorded from specimens of the same geometry (albeit with grip arrangement less notch).

An AE signal from a carbide crack is shown in Fig. 6c. This is a time-expanded initial portion of a typical signal. The transfer function for this geometry and sensor combination is given as Fig. 6a, which resulted from laser excitation and has the main peak at ~400 kHz, extending to 1.5 MHz. The convolution of a bell-shaped source function with 1 μs rise time (Fig. 6b) with the transfer function produces a simulated waveform (Fig. 6d). For the first two oscillations, the waveforms (c and d) match closely as shown in Fig. 6e. (The overall frequency range appears to peak at 200 kHz in the AE signal, especially when the entire signal of ~0.5 ms is used. This is probably due to the presence of grips.) Thus, the crack opening mode of brittle fracture generated the AE, and cracking process is fast (~1 μs). This result is consistent with many other studies of brittle fracture. The use of relatively low-frequency sensors, however, may be limiting the detection of faster events and future experiment using higher speed instrumentation is desirable to verify this aspect.

4. CONCLUSION

(1) This study demonstrates the utility of AE method for detecting the initiation of carbide cracking, which is critical in alloy development work for improved fracture resistance. The minimum size of the carbide is approximately 10 μm.

(2) Laser-induced impulse method simulating the crack-opening mode of fracture in hour-glass tensile sample has verified the nature of AE sources in high-strength steels to be a high-speed (~1 μs) phenomenon. An experimental system transfer function is also determined.

ACKNOWLEDGEMENT

The authors are grateful for valuable assistance of Messers. R. Masaki and Y. Mizutani of Aoyama Gakuin University (AGU) in conducting the laser experiment. One of the authors (KO) gratefully acknowledges the hospitality of Prof. M. Takemoto during his sabbatical leave at AGU.

REFERENCES

1. F.K. Kirk, Metal Tech., **49** (1982) 198.
2. S. Inoue, Tetsu-to-Hagane, **73** (1987) 1461.
3. Y. Murakami, S. Kodera and S. Konuma, Trans. Japan Soc. Mechanical Eng., **A54** (1987) 688.
4. M. Knoerr, K. Lange and T. Altan, J. Mater. Processing Tech. **46** (1994) 57.
5. T. Abe and K. Kanazawa, J. Soc. Mater. Sci. Japan, **45** (1996) 9.
6. J. Yoshida, M. Katsumata and Y. Yamazaki, Tetsu-to-Hagane, **84** (1998) 79.
7. A.M. El-Rakayby and B. Mills, J. Mater. Sci., **23** (1968) 4340.
8. K. Fukaura, H. Sunada, Y. Yokoyama, K. Teramoto, D. Yokoi, N. Tsujii, Tetus-to-Hagane, **84** (1998), 72-77.
9. R. Masaki, M. Takemoto and K. Ono, *Nondestructive Characterization of Material IX*, AIP Conference Proceeding 497, ed. R.E. Green, Jr. (1999) pp. 3-8.

SOURCE PARAMETERS OF ACOUSTIC EMISSION EVENTS IN SALT ROCK

GERD MANTHEI, JÜRGEN EISENBLÄTTER, THOMAS SPIES*, and GERNOT EILERS[§]

GMuG Gesellschaft für Materialprüfung und Geophysik, D-61239 Ober-Mörlen, Germany,
*Federal Institute for Geosciences and Natural Resources, D-30655 Hannover, Germany,
[§]Federal Office for Radiation Protection (BfS), D-38201 Salzgitter, Germany

ABSTRACT

Long term acoustic emission (AE) measurements have been carried out in a salt mine in northwestern Germany with the aim to investigate the micro- and macro-fracturing processes in a region of a high degree of excavation. The AE events were detected by a network of 24 borehole sensors. In order to get information about the source mechanisms, the moment tensor method has been applied to strong events, which were localized with good accuracy using more than 29 compressional and shear wave onsets. The selected events originated from a pillar in the vicinity of large rooms. The mechanism of each acoustic emission event has been calculated considering the first motion of at least eight clearly discernible P-wave onsets. In order to get a better fit of calculated and measured amplitudes, specific correction factors for the sensors have been applied. The moment tensor analysis indicates that a mixed mode of shear and tensile cracking occurs. For most investigated events, the P and T axes show similar orientations. Additional geomechanical data such as deformation measurements and crack opening measurements confirm the obtained results of the moment tensor analysis.

1. INTRODUCTION

Since 1995, a segment of a salt mine in northwestern Germany has been monitored by a network of 24 acoustic emission (AE) sensors [1]. The network covers a rock volume of about 150 m x 150 m x 100 m in an underground repository for low-level nuclear waste. The aim of the AE measurements is to investigate the micro- and macrofracturing processes, which are important for the evaluation of the stability of cavities and the hydraulic integrity of the rock, especially in the case of the underground disposal of hazardous waste in salt rock. The AE events are automatically located using the compressional (P) and shear (S) wave onsets. The maximum amplitudes of the signals and the location of the events are used to calculate a measure of strength of the source analogue to the magnitude in seismology.

In this paper, the measured radiation pattern of AE sources has been used to determine the fracture type and the orientation of the fracture planes utilizing the moment tensor method. This method requires a good sensor coverage of the focal sphere in all directions. In the present case, the spatial distribution of the AE sensor network was designed for source location in a large region and not for determination of source parameters. Therefore, in most areas of the monitored region the coverage of the focal sphere by the sensor network was only poor. We therefore selected AE events from a region in the center of the network where the best coverage was supposed.

2. EXPERIMENTAL SETUP

24 borehole sensors equipped with piezoelectric transducers are installed in 3 to 20 m deep boreholes. Figure 1 shows the configuration of the network in a plan view on three levels. The central unit of the measuring system consists of a transient recorder monitoring the data stream of the sensors (frequency range of 1 to 100 kHz), a personal computer controlling all actions of data acquisition and in-situ evaluation, and a modem for telecommunications. Two types of borehole sensors with different coupling have been used. Five sensors (Type W) were pressed pneumatically against the wall of boreholes of diameter 100 mm and further 19 sensors (Type S) were pressed by means of springs against the smooth face of boreholes with smaller

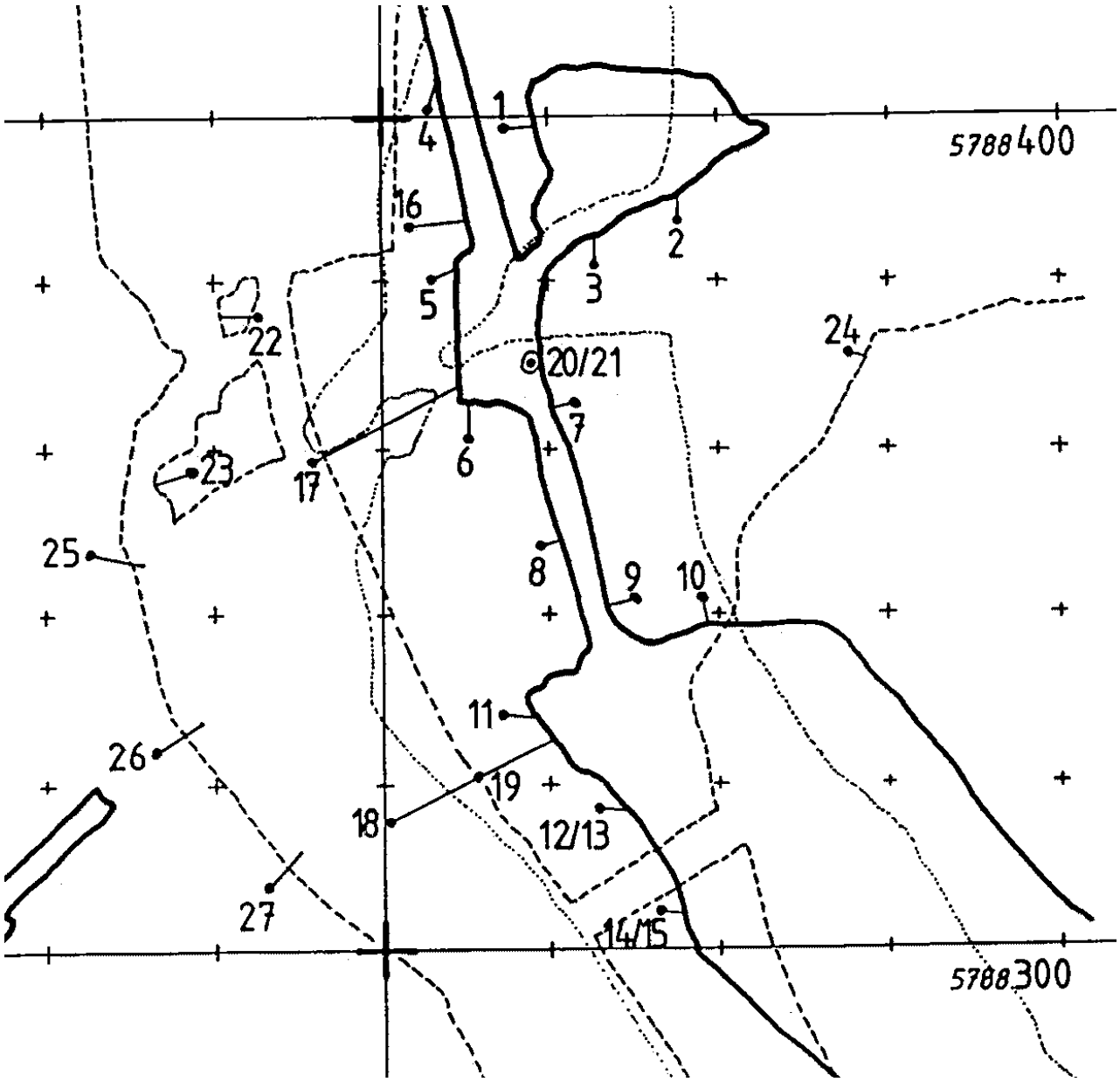

Fig. 1 Configuration of the network of sensors at three levels of a salt mine in horizontal projection one upon another. The distance between the crosses is 20 m. The upper level, the intermediate level, and the lower level are indicated by continuous lines, by dotted, and by dashed lines, respectively. Rectangular frame indicates the locations of the investigated events.

diameter 46 mm. Both types of borehole sensors were characterized in situ with respect to P-wave sensitivity as a function of incidence angle. Fig. 2 shows that the radiation patterns of both sensor types are similar at small angles up to 50°. The half width (-6 dB) is in the range of 80° to 100°. At greater angles of incidence the sensitivity shows more variations and decreases by 20 dB and 30 dB, respectively. Note that there is a polarity change for incidence angles greater than 90° (i.e. wave passes the sensor from behind). Type S is approximately 20 dB more sensitive for these angles compared to Type W.

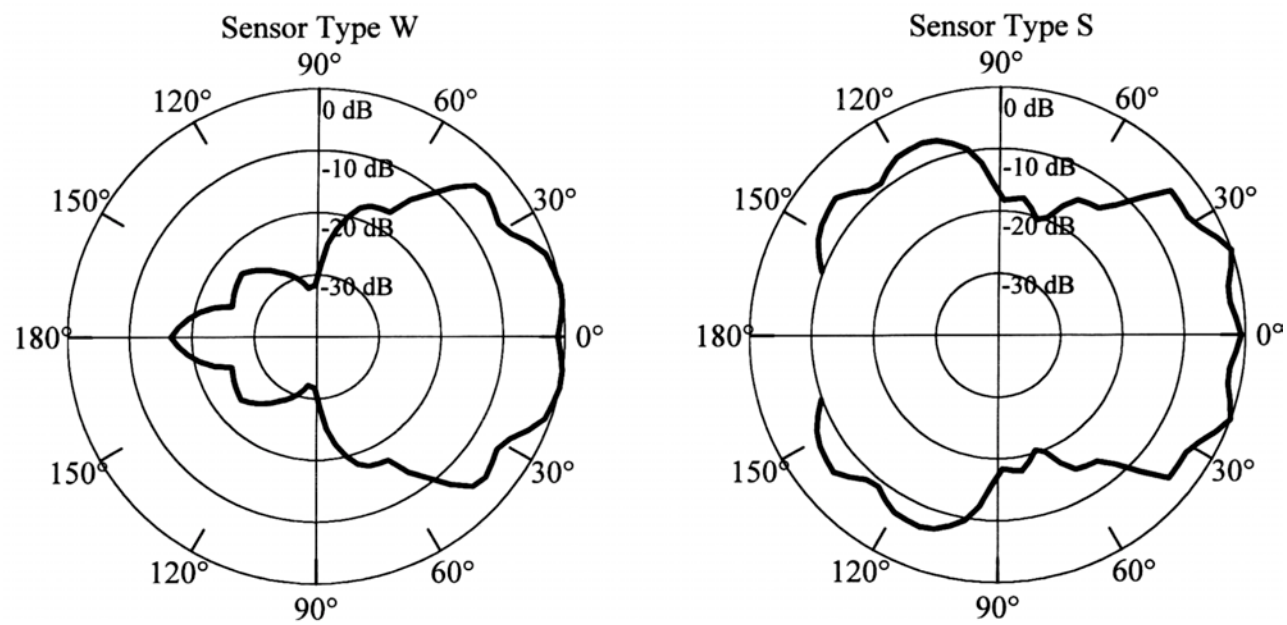

Fig. 2 P-wave sensitivity of the borehole sensors Type W (left) and Type S (right) as a function of the incidence angle.

3. APPLICATION OF THE MOMENT TENSOR METHOD

The moment tensor method has been applied to 68 events with strong signal amplitude, which were recorded in a period of 19 months. The events occurred in a pillar at the upper level (continuous lines in Fig. 1) in the vicinity of Sensors No. 9 and 10 (marked by a rectangular frame in Fig. 1). The dimension of this area is 22 m x 13 m. In vertical direction the sources lie in a small area of 5 m width, 7 m above a large room at the intermediate level. The signals of the selected events were band-pass filtered in a frequency range from 2 to 25 kHz. These frequencies correspond to wave lengths of the P wave between 2.25 m and 0.18 m. In Fig. 3, aligned P-wave onsets of an AE event are plotted. To the right hand side of the signal traces, the peak-to-peak amplitude in volt and its polarity, the distance between sensor and source in meter, and the angle of incidence to the sensor normal vector are denoted. The data were treated in the following steps:

- Calculation of the theoretical P-wave onsets utilizing the source location and P-wave velocity.
- Plotting of the signals in a small time window of 400 µs around the theoretical onsets.
- Manual picking of the exact signal onsets.
- Multiplication of the data in the time window by a Hanning window function.

- Storing of the most important event parameters like event number, peak-to-peak amplitude, polarity, onsets, and the unfiltered signal in the small time window of the P-wave onset.

Figure 3 shows that the polarities of the P waves detected at Sensors No. 1, 5, 8 and 11 are reversed in comparison to the others. In these cases the sensors were behind the source (incidence angle greater than 90°). In the case of not clearly discernible P-wave onsets, the signals have been dropped. This happened in the shown example at Sensors No. 7, 12, 13 to 16, 18, 19, 22, and 23, where the travel paths were very long or the wave radiation was disturbed ("shaded") by galleries. Note that the polarities of all P-wave onsets are positive after changing the polarities for incidence angles greater than 90°. Maybe, this fact indicates a tensile source component. The radiation pattern of a pure tensile source shows the same polarity in all directions (as for an explosion source type as well).

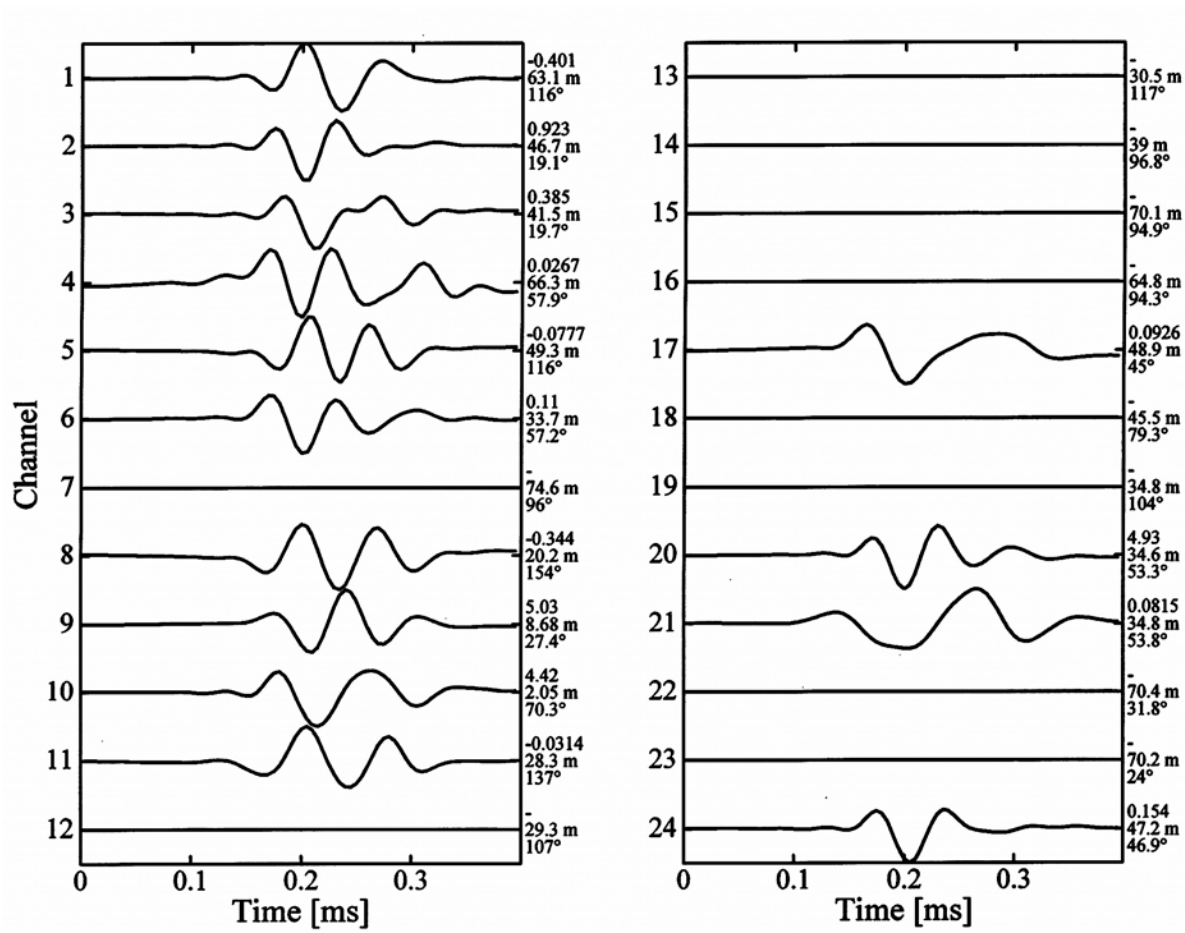

Fig. 3 Aligned P-wave onsets of an AE event located in the middle of the salt rock pillar close to a large room at the upper level.

The measured signal amplitudes are influenced by spherical divergence which is proportional to r^{-1} (r is the source-receiver distance) in the far field radiation pattern, by the radiation pattern of the borehole sensor (compare Fig. 2), by wave attenuation, and by coupling effects of the borehole sensors. The wave attenuation and the coupling effects of the sensor were investigated experimentally. The maximum amplitudes A and the distances r are used to determine the wave attenuation according to the relation

$$A \propto [\exp(-\alpha r)]/ r ,$$

where α is the attenuation coefficient. In a semi-logarithmic plot of A·r versus r for all sensors a linear relationship is obtained as expected and a straight line is fitted to the data. The slope of the line corresponds to the attenuation coefficient, systematic deviations from the fit at specific sensor positions correspond to coupling or site effects which can occur in the vicinity of the sensor location. By averaging over many events located in the whole monitored area a very low attenuation coefficient at the test site of 1.7 dB/10 m is obtained. The coupling coefficient varied in the range between -10.5 dB (Channel No. 6) and 9 dB (Channel No. 7).

Under consideration of the above-mentioned amplitude effects the results of the inversion calculation for one AE event is displayed in the upper part of Fig. 4. This figure shows the calculated radiation pattern (left hand side) in a projection to the lower hemisphere. The locations of the calculated P and T axes are indicated by black and white triangles, respectively. Projected rays are plotted as circles. Black circles indicate compressional first motion. The channel numbers are also shown. It can be seen that the polarity of the P-wave first motion is always positive.

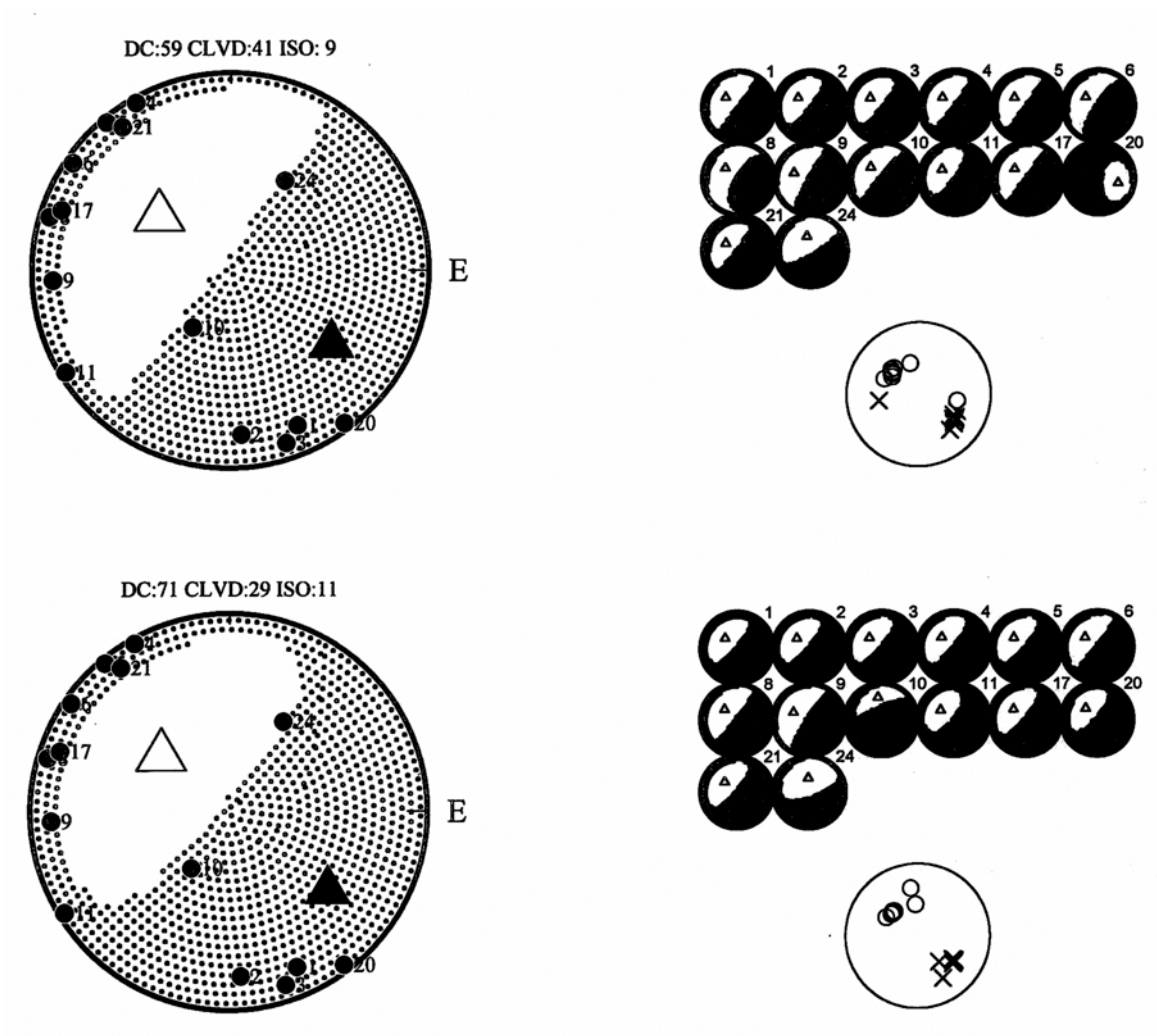

Fig. 4: P-wave radiation patterns and projected rays of an AE event projected on the lower hemisphere (equal area projection, north is on top). Black/dotted area (white) indicates compressional (dilatational) first motion. The upper and lower parts show the results of the inversion calculations without and with specific sensor correction factors, respectively.

We decomposed the momentum tensor into isotropic and deviatoric source components. The isotropic part is described by the trace of the moment tensor. It is quantifying a volume change in the source. The percentage of the isotropic part is defined by the ratio of the squared trace and the sum of squared eigenvalues e_i of the moment tensor multiplied by 100 after reference [2]. The purely deviatoric part, which is calculated by subtracting a third of the trace from each eigenvalue of the moment tensor, is further decomposed into a double couple (DC) and a compensated linear vector dipole (CLVD) with the same principal axis orientation. Here,

$$DC\% = [1 - 2(|e_3 - tr|/|e_1 - tr|)]\cdot 100\%,$$

$|e_1 - tr| \geq |e_2 - tr| \geq |e_3 - tr|$ is assumed, and $tr = (e_1 + e_2 + e_3)/3$ [3].

In the present case, the decomposition leads to a mixed mode mechanism with 59% DC component (corresponding to 41% CLVD component) and 9% isotropic component. The nodal lines indicate the two possible orientations of the crack plane. Note, that a double couple has two possible fault planes which are perpendicular to each other, the so called normal fault and auxiliary fault plane which cannot be distinguished from the focal mechanism. Additional information is necessary to find the actual fault plane, as e.g. knowledge about the stress situation in the region near the source location. In our example one possible crack plane is vertical and has a strike of 37°, measured clockwise from north.

4. RESULTS

In order to investigate the influence of single sensors on the inversion result, a jackknife test has been applied. In this test, one sensor after the other is systematically excluded from the input data. Every possible permutation was tested. The right hand side of Fig. 4 shows the resulting radiation patterns. These do not strongly vary apart from the case in which sensor No. 20 has been excluded. In this case, the locations of the P and T axes indicated by crosses and circles, respectively, differ from all other inversion runs. This indicates that the solutions are not well constrained and strongly influenced by amplitude at a single sensor (like No. 20 in the above example). Therefore, additional specific corrections for the sensors were introduced to constrain the solution and to obtain a better fit between calculated and measured data. The additional correction factors were determined by averaging the ratio of measured and calculated amplitudes of each sensor for all 68 events. This leads to relative high values of correction factors up to 4.5 for shaded sensors (No. 4 and No. 5) and to very low correction factors down to 0.15 for sensors, which are in a favourable position for most source locations. The lower part of Fig. 4 shows the result of the inversion calculation after application of the correction factors to the input data. In comparison to the results of the previous calculations, the P-wave radiation patterns and the locations of the P and T axes do not strongly vary. The DC component increases up to 71%. The jackknife test indicates that the solution is well constrained now and not influenced by the measured amplitudes at single sensors any more. Now, sensor No. 20 makes no exception.

Figure 5 displays the results of the moment tensor calculations of all 68 selected events. The left-hand side gives the spatial distribution of the estimated P-wave radiation patterns projected on the lower hemisphere (equal area projection) in a plan view (north on top). On the right-hand side of Fig. 5, the contours of the P and T axes distributions are plotted. In spite of the fact that the sources are distributed in an extended area of about 22 m in Y-direction and 13 m in X-direction, it can be seen that all events have similar radiation patterns as well as orientations of the crack planes. The distributions of T and P axes show peaks in the middle and in north or south directions, respectively. This means, the T axis is vertical and the P axis horizontal in north

direction. Figure 6 shows the probability density of the DC and isotropic components. The distributions are normalized, so that the integral over full range of possible source components is unity. Most of events show a mixed mode of shear and tensile cracking. The majority of the DC components range between 20 % and 80% with a maximum at 60%. The isotropic components show a maximum below 5%. Nevertheless, most of the events have a significant isotropic

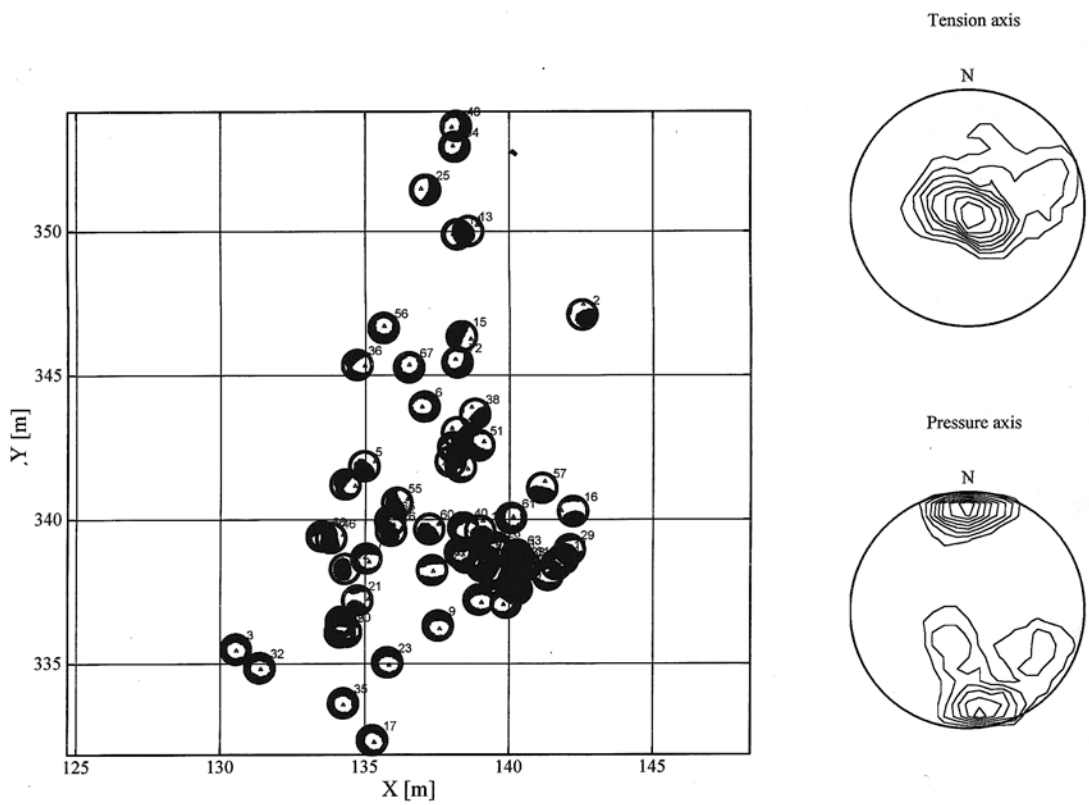

Fig. 5 Radiation pattern for all evaluated events in an equal area projection on the lower hemisphere (left). Distribution of the P and T axes (right).

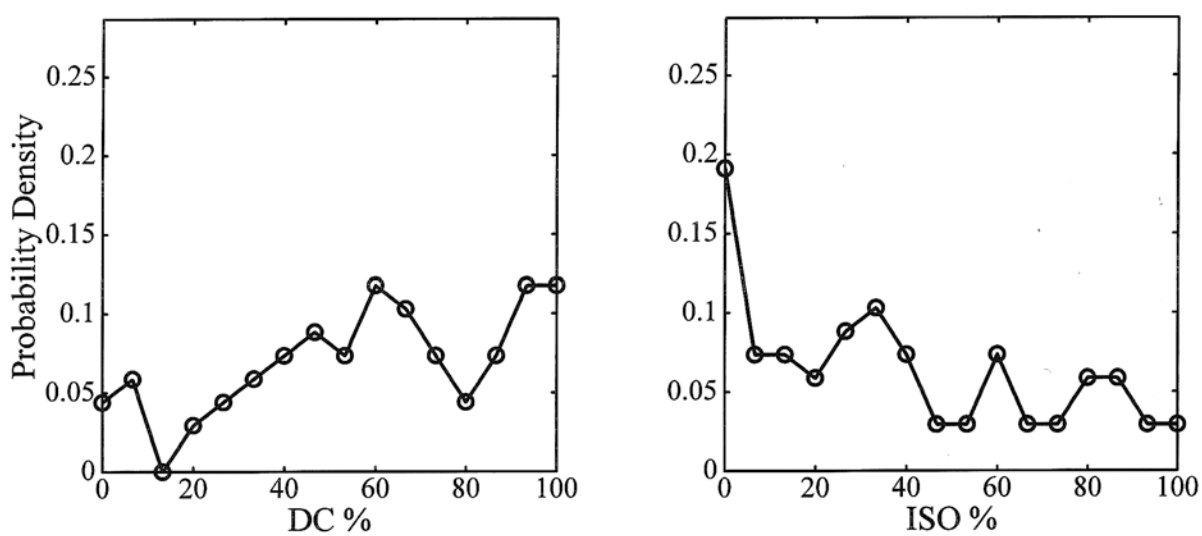

Fig. 6: Probability density of the double-couple component (DC) and the isotropic component (ISO).

component. Nine events were identified as "pure" shear cracks (DC component greater than 90% and isotropic component less then 5%). Pure tensile sources were not obtained. A pure tensile crack has 100% CLVD component and approximately 75% isotropic component.

5. DISCUSSION OF RESULTS AND CONCLUSIONS

All investigated events originated from a small region at the contour of a large room. In this region, deviatoric stresses occur, which lead to creep of salt and in longer-time consequence to microcracking and permeability increase. In the present case, the stresses were further enhanced by the fact that the stopes of two large rooms at the intermediate and lower level are situated below the area under investigation (cf. Fig. 1, location of Sensor No. 10).

The moment tensor analysis pointed out that mixed mode of shear and tensile cracking occurs. Under the consideration that the motion of both modes happened on the same microfracture plane, Fig. 7 displays the model of the source mechanism schematically. It shows a hatched area where the events originated and the location of the large rooms in a vertical cross section together with the directions of the P and T axes. The arrows parallel to the crack plane represent the shear motion and those perpendicular to the crack plane represent the tensile motion. The vertical T axis could be explained as a consequence of tensile stress release in the area of the large room at the intermediate level (Room 2 North at Level 2a in Fig. 7). In the wall of the north drift at the upper level, a large horizontal crack has been observed. The opening of this crack is monitored by displacement measurements, which show opening rates of 0.15 mm/annum (or mm/year) in vertical direction. The above-mentioned source model is in accordance with these in-situ displacement measurements.

We cannot fully explain the influence of the sensor arrangement and the coupling of the sensors. The fact that the data fit becomes better after applying specific correction factors raises some questions and needs to be further discussed. This uncertainty may be explained by the pure sensor coverage in vertical direction. In order to raise more confidence in these results, a check with an alternative method like the relative moment tensor method [4] would be helpful, where the sensor coupling effects play no role.

REFERENCES

1. T. Spies, J. Eisenblätter, *Micro- and Macrocracking at the Boundary of Rock Salt and Anhydrite,* Proc. International Society for Rock Mechanics, Paris, Eds. G. Vouille, P. Berest. A. A. Balkema, Rotterdam, 1999, pp. 1071-1074.
2. P. G. Silver, T. H. Jordan, *Optimal estimation of the scalar seismic moment,* Geophys. J. R. Astr. Soc. **70**, 1982, 755-787.
3. M. L. Jost, R. B. Herrmann, *A students guide to a review of moment tensors,* Seis. Res. Letters, **60**, 1989, 37-57.
4. T. Dahm, G. Manthei, J. Eisenblätter, *Relative Moment Tensors of Thermally Induced Microcracks in Salt Rock,* Tectonophysics **289**, 1998, 61-74.

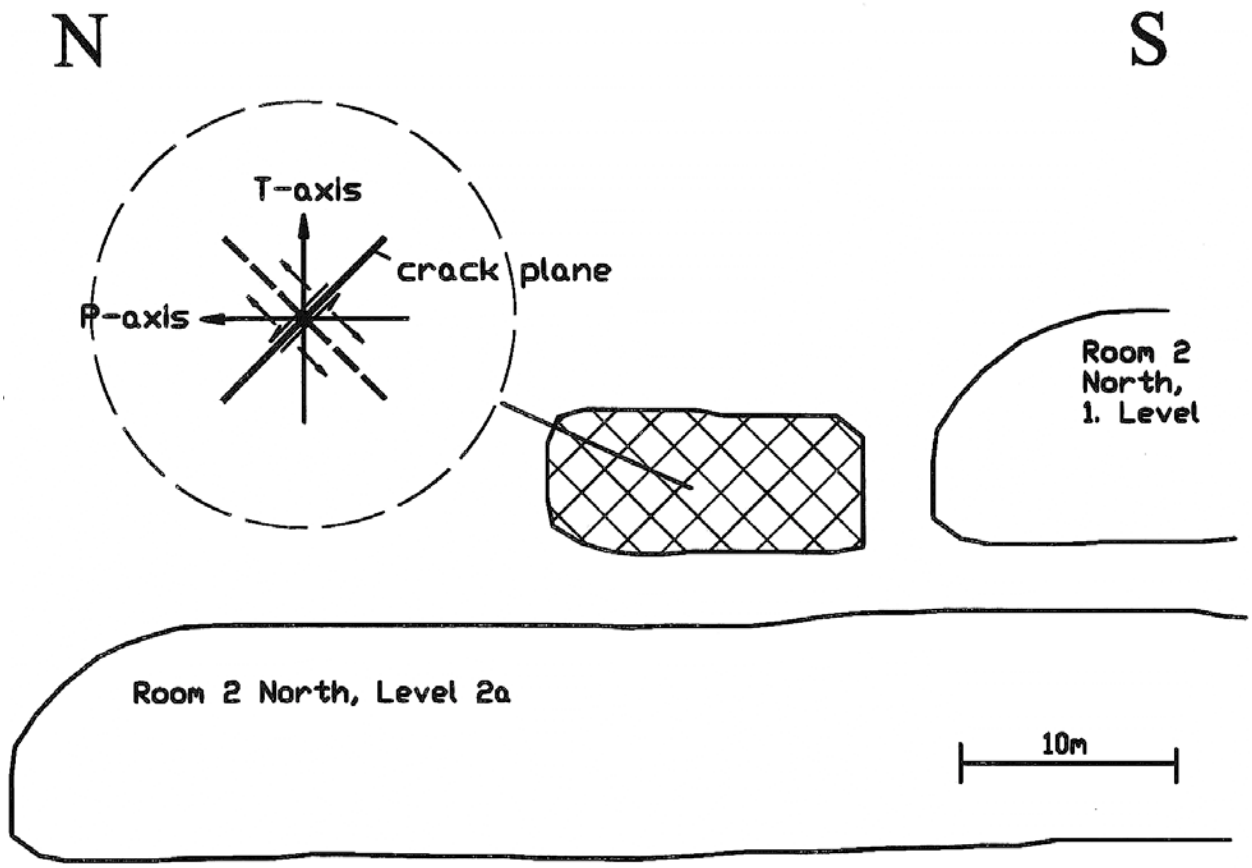

Fig. 7 Location of the crack planes where shear and tensile motion take place together with the area of AE events (hatched) and the location of the rooms.

GEOMETRICAL COMPLEXITY OF ROCK INCLUSION AND ITS INFLUENCE ON ACOUSTIC EMISSION ACTIVITY

KEN-ICHI ITAKURA, ATSUSHI TAKASHIMA, TATSUMA OHNISHI and KAZUHIKO SATO

Faculty of Engineering, Muroran Institute of Technology, Muroran 050-8585, Japan

ABSTRACT

Underground rock mass and rock slopes consist of various types of rocks with different physical properties and geometry. In such a rock-engineering site, unexpected failure tends to occur when rocks containing inclusions are affected by stress change. Depending on the geometry and the physical properties of the inclusion in matrix rock, stress concentration induces local fractures with acoustic emission (AE), and catastrophic failure can occur. To monitor an unstable rock area using AE techniques, therefore, it is important to know the relationship between the features of the inclusion rock and AE activity.

In this study, using cylindrical rock specimens consisting of andesite and tuff, Brazilian and uniaxial compression tests were carried out to determine the relationship between AE source locations and the complexity of inclusion geometry appearing on the surfaces of sliced sections of the specimens. It was found that more AE sources were present in sliced sections with a higher complexity index value of inclusion. It was thought that local stress concentration occurred in a section with a complex structure and that more micro-fracturing was therefore generated with AE.

1. INTRODUCTION

Underground rock mass and rock slopes consist of various types of rocks with different physical properties and geometry. In such a site, the volume encompassing with a discontinuity plane, such as a pore, a crack, or a lump of rock within the matrix, can be regarded as an inclusion. If stress change is exerted on rock mass with inclusions, complex and unexpected fractures might occur due to the influence of the difference in physical properties and the geometry of the inclusion. Such rock fractures can cause a disaster in a mining area or civil engineering field.

Figure 1 shows differences in AE activities of rock specimens subjected to uniaxial compression stress. The specimen shown in Fig. 1(a) includes andesite particles in a tuff matrix, and the specimen shown in Fig. 1(b) consists mainly of andesite with a tuff layer in the bottom area. In the case of the latter specimen, high AE activity is maintained for a long period from a low stress stage despite the fact that the experimental conditions were almost the same as those for the specimen shown in Fig. 1(a). Generally, in a specimen consisting of only andesite, it is known that AE activity becomes higher just before the maximum stress, though Fig. 1(b) shows a different AE activity pattern. This AE activity pattern is thought to be caused by crushing of the tuff layer at a low stress stage, which induces unstable failure of the andesite. In other words, it seems that the physical properties and the geometry of the inclusion affect the micro-fracturing activity and main failure of the specimen.

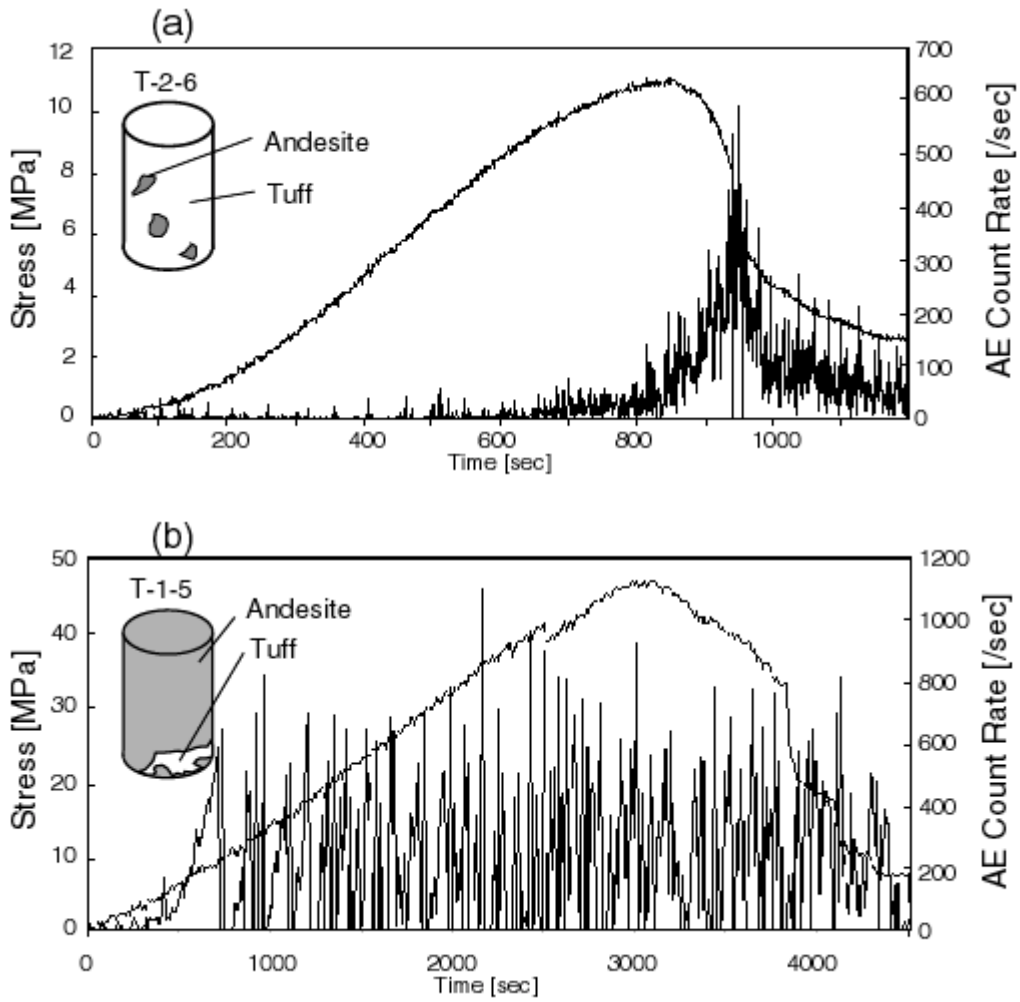

Fig. 1 Differences in rock structure and AE activities during uniaxial compression tests. (a) Specimen consisting of andesite inclusions within a tuff matrix. (b) Specimen consisting of a tuff layer within an andesite matrix.

In this study, laboratory experiments using specimens consisted of two different kinds of rock were conducted to determine the relationship between complexity of the boundary plane of a rock and AE activity around the plane. In the experiments, Brazilian tests and uniaxial compression tests were carried out on specimens that had been collected at the rock slope at Toyohama, Hokkaido. The activity of this rock slope has been monitored to try to predict large-scale rock falls. It is expected that the results of laboratory experiments, i.e., the determination of the relationship of the complexity of inclusion geometry and AE (or micro-fracturing) activity, can be applied to field monitoring techniques to determine the optimal allocation of AE sensors for effective monitoring. This paper describes the results of Brazilian tests and the relationship of the complexity of a boundary plane of rocks and AE source locations.

2. ROCK SPECIMEN AND EXPERIMENTAL PROCEDURE

Rock specimen and its inside structure

Specimens of tuff breccia rock consisting of tuff and andesite were prepared from drill cores sampled at the rock slope of Toyohama, Hokkaido. The size of the specimen used for the Brazilian test was 49.3 mm in diameter and 51.2 mm in height. Figure 2(a) shows the

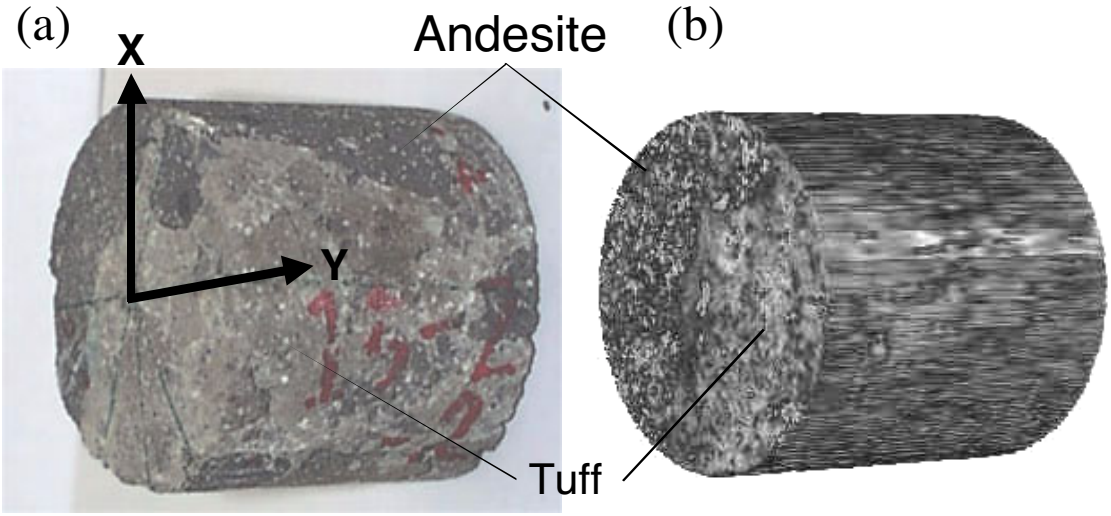

Fig. 2 Rock specimen used for the Brazilian test. (a) Photo image. (b) 3-D image reconstructed from X-ray CT data.

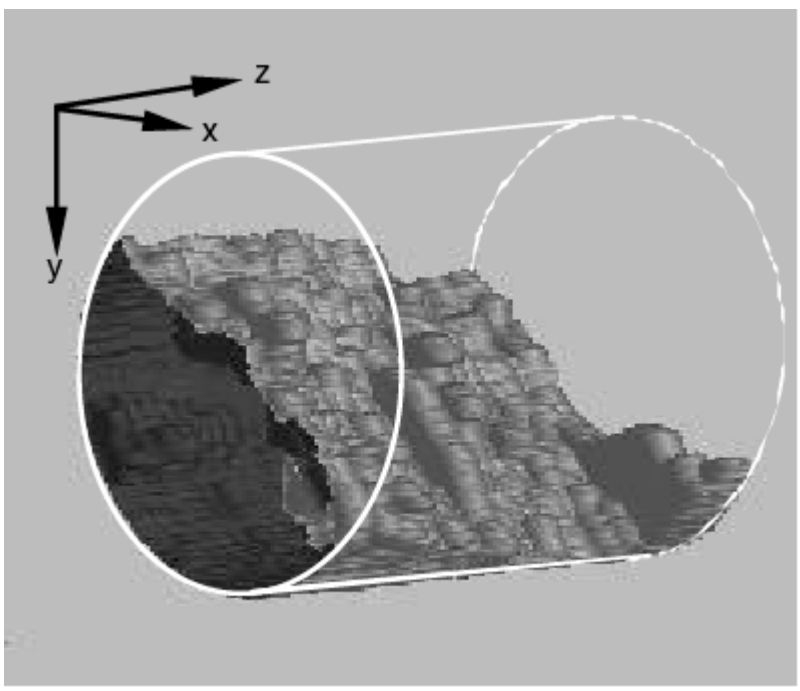

Fig. 3 Tuff region extracted from a 3-D image.

appearance of the specimen. The dark parts of the specimen shown in Fig. 2(a) are andesite, which has micro pores, and the other parts are tuff.

Before loading, sectional images of the specimens were obtained by X-ray computerized tomography (CT). Twenty-two images were taken parallel to the bottom base of the cylindrical specimen for the Brazilian test. Figure 2(b) shows a 3-D image that was reconstructed by using 22 CT data of the specimen. The whitish area shows a low-density region, i.e., a tuff region and

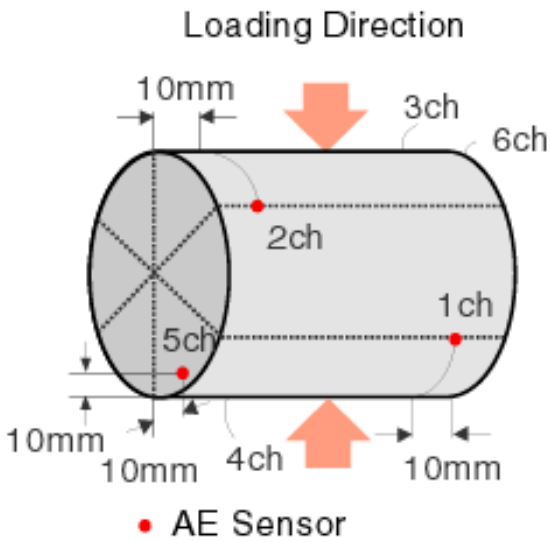

Fig. 4 Arrangement of AE sensors for a specimen.

pores in the andesite. The densities of andesite and tuff are ~2.48 g/cm^3 and 1.56-1.78 g/cm^3, respectively. Figure 3 shows the tuff region extracted from the 3-D image of Fig. 2(b). Complex changes in the boundary plane of tuff and andesite parts along the z-axis can be seen.

Experimental procedure

To detect the AE waveforms, six small-sized PZT elements were affixed on the surface of the specimen, as shown in Fig. 4. The shape of the PZT was a frustum of circular cone with an upper base of 1 mm in diameter, lower base of 4 mm in diameter, and height of 5 mm. The resonant frequency of this PZT was 320 kHz. The apparatuses used in the experiments were the same as those used previously [1, 2]. The AE waveform detected by PZT sensors is amplified up to 85 dB using a preamplifier and signal conditioner, and recorded on the hard disk of a PC with a sampling time of 100 ns. AE source locations were determined by the conventional least-squares method, and a P-wave velocity structure was assumed by an ellipsoid model with three velocity axes of 1289.7, 700.3 and 1084.2 m/s [3, 4]. In the Brazilian test, strain rate was controlled in the range of 10^{-5}/s using an MTS servo controlled testing machine. The loading direction is along the y-axis of Figs. 2 and 3.

3. EXPERIMENTAL RESULTS AND DISCUSSION

AE source location

AE source locations were determined for 8.4% (334 events) of the total number of recorded AE events. The magnitude of these AE events is relatively high, and the location error by the least-squares method is less than 5 mm. Figure 5 shows the location distribution projected onto three-axes directions of the specimen. Solid dots show the coordinates of the AE source. It can be seen that almost all of the AE sources are distributed along the loading plane (y-axis direction), which is the eventual fracture plane. However, there are a few AE sources around the area of loading points. This is thought to be because the waveforms generated around the areas of loading points attenuated on their way to more distantly located sensors, so that the source location is not determined by the lack of waveforms.

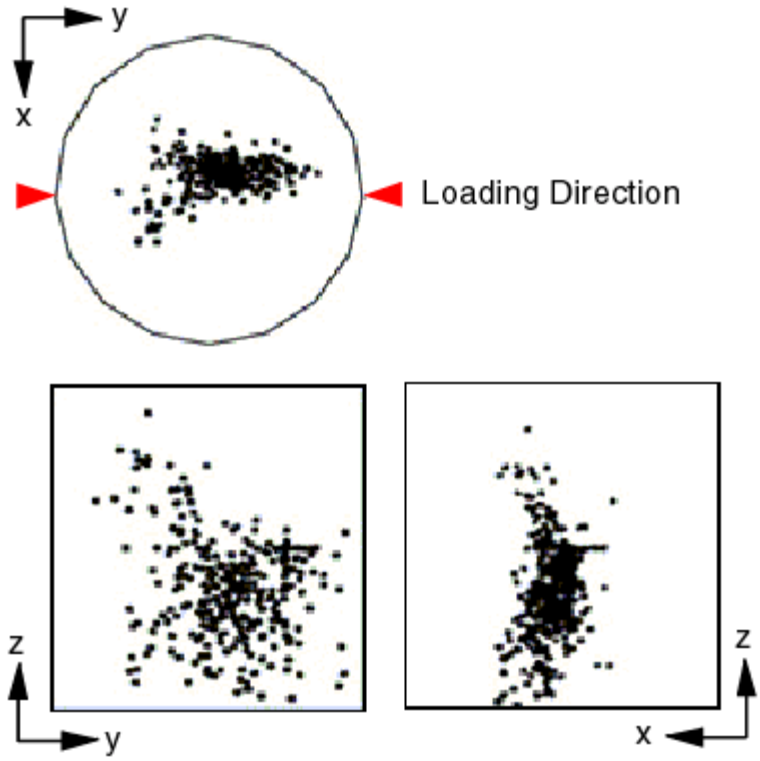

Fig. 5 AE source distribution projected into three-axes directions.

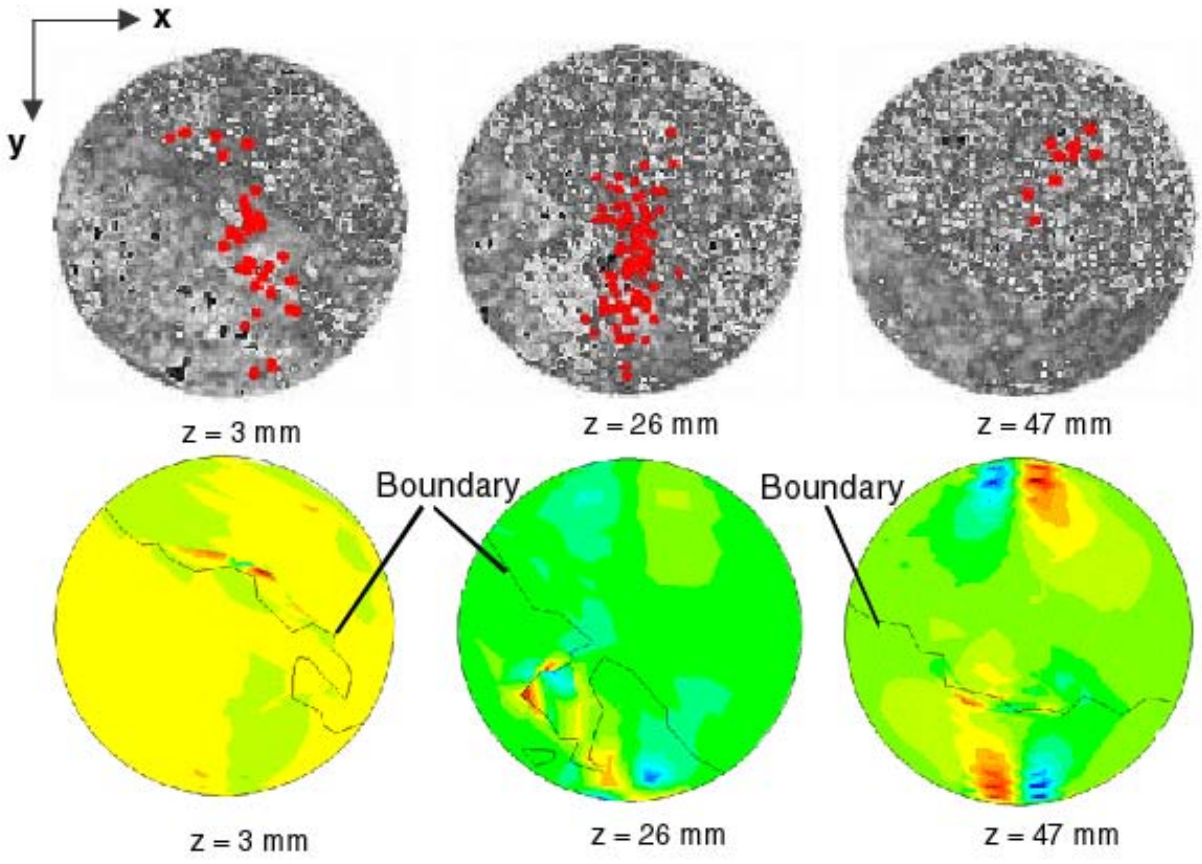

Fig. 6 Typical AE source locations and stress concentration in sections of a specimen.

Figure 6 shows typical X-ray CT sections at z=3 mm, 26 mm and 47 mm, and the results of FEM analysis of the corresponding sections. In the X-ray CT images (upper three circles), solid dots show the AE source locations determined within ±5 mm from the CT image sections, and the area with white spots of high contrast is andesite. In the lower three circles, the boundary between tuff and andesite regions is indicated by a line. Considering the differences in the physical properties of tuff and andesite regions, Young's moduli of tuff and andesite were estimated to be 3.2 GPa and 37 GPa, respectively, for elastic 2-D FEM analysis under the plane-strain conditions. The dark area in this figure shows a higher shear stress region at a load of 102 N. To emphasize the contrast and stress concentration, the gray scale levels have been changed for each section. Figure 6 shows that the stress concentration occurred in the area near the loading axis and where the geometry of the boundary was complex. The AE source is located not only along the loading axis but also in the area of stress concentration. That is, the results of FEM analysis and AE source location suggest that microfracturing and AE generation are active in the area of stress concentration, where the boundary of rocks is complex.

Geometry of inclusion and its complexity

To explain the complexity of a boundary line of rocks in a certain section, fractal dimension and some indices used in texture analysis were introduced. The fractal dimension of a boundary line was calculated by the box counting method [5]. A typical index used for representing the complexity of a binary image is Cl based on the length of the boundary line [6]:

$$Cl = L/(2^{R+1}(2^R - 1)),$$

where L is the total boundary length along the white or black binary pixels, and 2R shows the number of columns or rows for the square binary image of $2^R \times 2^R$.

Table 1 shows the values of the complexity index Cl and fractal dimension of the boundary curves of three typical sections. These results show that Cl and fractal dimension accurately reflect the complexity of the boundary curve of each section.

Table 1 Complexity index for representing boundary lines of rocks.

Location of Section(mm)	z=3	z=26	z=47
Fractal Dimension	1.15	1.18	1.13
Complexity Index Cl	0.008977	0.012745	0.007475

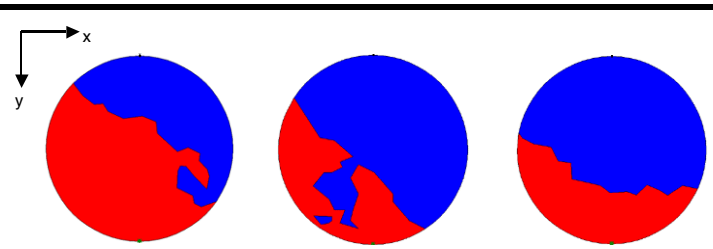

AE and complexity index of inclusion

The number of AE events was compared to the complexity index for the boundary of rocks in an X-ray CT image of each section. The thin cylinder of 11.3 mm in height was assumed to contain the number of AE events in the region at each sections of the CT images, as shown in Fig. 7. Figure 8 shows the variations in the complexity index Cl and total number of AE events inside each disk region along the z-axis. This figure shows that the region with a higher value of

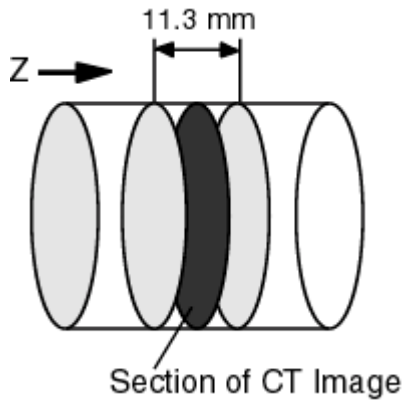

Fig. 7 Thin cylinder to count the number of AE events in the vicinity of a section of CT image.

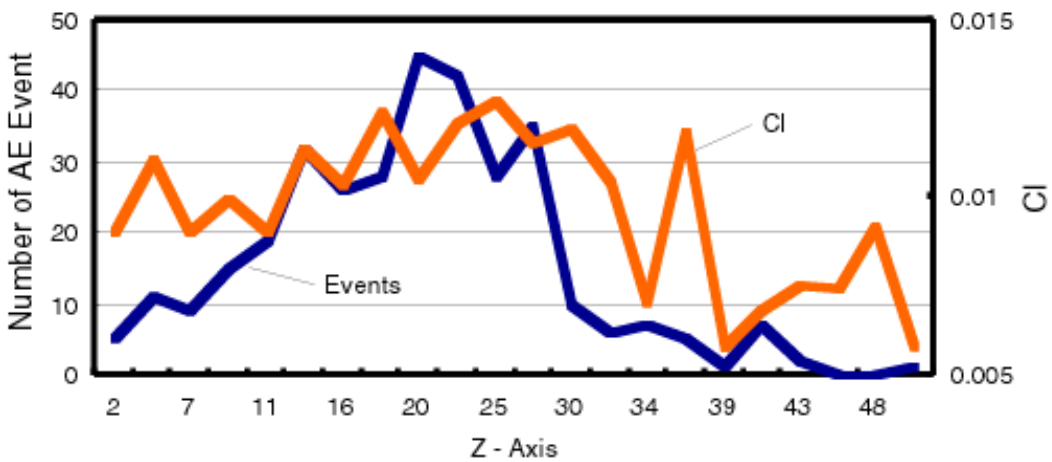

Fig. 8 Variation in the complexity index value Cl and number of AE events along the z-axis of a specimen.

complexity index almost corresponds to the region, in which more AE events were generated. Furthermore, the variation patterns of the two parameters along the z-axis were shown to be similar. Figure 9 shows the correlation between the number of AE events and complexity index Cl. Similar correlation was found for the fractal dimension and for other indices representing the complexity of an image. Also, the total relative AE energy inside the perimeter cylinder shows a similar correlation to the complexity indices.

Consequently, it was found that the more complex the boundary geometry of rocks was, the more AE events were generated in that area. These micro-fracturing activities with AE were thought to be caused by the stress concentration.

4. CONCLUDING REMARKS

Rock specimens of tuff breccia used in this study consisted of tuff and andesite with a complex geometrical structure. To examine the region of AE generation, Brazilian tests were conducted on the specimens. X-ray CT images were also taken before the loading tests to understand the complexity of the boundary geometry of rocks, and FEM analysis was carried out to confirm the region of concentrated stress inside each specimen. The experimental and

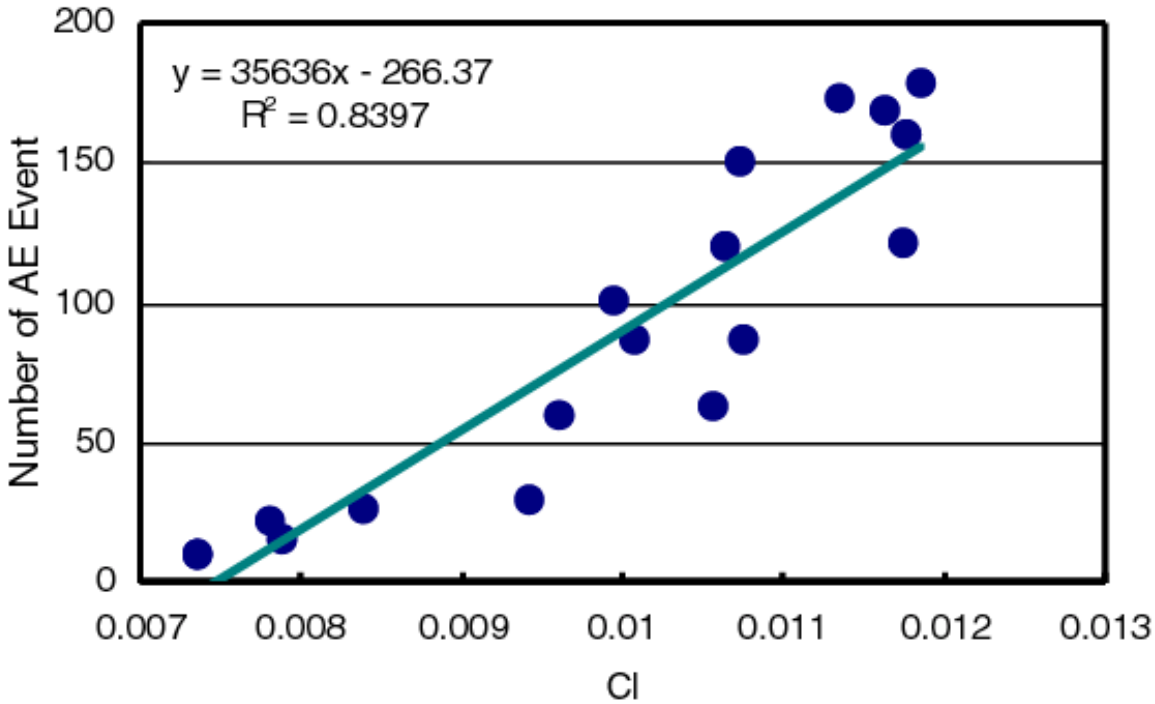

Fig. 9 Relationship between number of AE events and complexity index value Cl.

analytical results are as follows.

1) From X-ray CT images representing density distribution, the geometry of the boundary between tuff and andesite was determined. The boundary lines changed according to the section of the specimen.

2) Fractal dimension and indices used in texture analysis were found to be useful for evaluating the complexity of the boundary geometry.

3) Although most of the AE sources were located along the eventual fracture plane, some of them were located along the boundary of rocks near the loading axis. These AE sources were affected by the complexity of the boundary curve.

4) The results of 2-D FEM analysis considering the physical properties of rocks showed that stress concentration occurred in the region where the boundary geometry of rocks was complex.

5) It was found that the variation in the number of AE sources located in the vicinity of a section along the z-axis was correlated with the variation in the complexity index for boundary geometry. That is, stress concentration occurred at the region of complex boundary geometry, and then microfracturing activities were generated in the same region with AE activity.

ACKNOWLEDGMENTS

The authors would like to thank Hokkaido Engineering Consultants Co., Ltd., and Dr. T. Goto and Dr. K. Kodama of Muroran Institute of Technology for their kind assistance. Dr. K. Sugawara and Dr. Y. Obara of Kumamoto University cooperated with us to obtain the X-ray CT images of specimens. This work was supported by a grant-in aid for scientific research (No. 10650912) from the Ministry of Education, Japan.

REFERENCES

1. K. Itakura, Y. Watanabe, K. Sato, T. Goto, J. Kodama and Y. Yoshida: "Modeling Method for Cracks in Rocks based on the Fractal Structure of the AE Source Distribution", J. of the MMIJ, **114**(12), (1998), 918-924 (in Japanese).
2. K. Itakura, K. Sato, K. Nagano and Y. Kusano: "Fractals on Acoustic Emission during Hydraulic Fracturing," J. of Acoustic Emission, **13**(3/4), (1995), S75-S82.
3. K. Itakura, K. Sato and A. Ogasawara: "The Observation of Microcracking Cluster in Stressed Rock by AE and Seismic Tomography Techniques," *Progress in Acoustic Emission, V*, (1990), JSNDI. Tokyo, pp. 422-429.
4. K. Itakura, K. Sato and A. Ogasawara: " Monitoring of AE Clustering Activity Prior to Main Faulting of Stressed Rock by Acoustic Tomography Technique," Proc. 5th Conf. on AE/MA in Geologic Structures and Materials, (1995), pp. 1-17.
5. J. Feder: *Fractals*, Plenum Press, (1988).
6. R. Taniguchi and E. Kawaguchi: "On the Relation of Binary Image Complexity to Gray-Scaled Image Thresholding", Trans. Institute of Electronics, Information and Communication Engineers, **J70-D**(1), (1987), 164-173 (in Japanese).

APPLICATION OF AE IMPROVED *b*-VALUE TO QUANTITATIVE EVALUATION OF FRACTURE PROCESS IN CONCRETE MATERIALS

T. SHIOTANI, S. YUYAMA*, Z. W. LI* and M. OHTSU§

Technological Research Institute, Tobishima Corporation, Sekiyado, Chiba 270-0222, Japan
* Nippon Physical Acoustics Ltd., Shibuya, Tokyo 150-0011, Japan
§ Graduate School of Science and Technology, Kumamoto University, Kumamoto 860, Japan

ABSTRACT

In the present study, fracture processes are investigated quantitatively in four different kinds of concrete specimens by applying improved *b*-value (I*b*-value) analysis. It is observed that the variation of the I*b*-value corresponds well to the fracture process of specimens during each loading stage, independent of dimension, shape and reinforcement of the specimen. The results of the I*b*-value analysis were in good agreement with those obtained from the moment tensor analysis. Even when the moment tensor analysis may be inapplicable, the fracture process of the specimen can be evaluated by applying the I*b*-value analysis. It is concluded that the I*b*-value is a very useful parameter for quantitative evaluation of the fracture process in concrete materials.

1. INTRODUCTION

In recent years, it has been recognized that concrete structures deteriorate under various service environments. Especially, during the 1995 Great Hanshin Earthquake, many reinforced concrete (RC) structures were severely damaged due to strong ground motions. It is strongly desirable to establish non-destructive inspection methods, which can evaluate the deterioration of concrete structures quantitatively from the early stage of fracture. Since acoustic emission (AE) is effective in monitoring the initiation of cracks in concrete materials and structures, its applicability has been extensively studied in both materials (Yuyama et al., 1995a) and structures (Yuyama et al., 1994; Yuyama et al., 1995b; Murakami et al., 1993; Minemura et al., 1998).

To analyze AE data acquired, parameter analysis is widely and frequently employed. Among AE parameters, in particular, the AE peak-amplitude is considered a closely related parameter to the magnitude of fracture. Many researchers have studied *b*-value and m-value determined from a negative gradient of the peak-amplitude distribution. Recently, in order to apply the *b*-value analysis for fracture evaluation in slope failure, the method of calculating the *b*-value has been modified by incorporating statistical values of amplitude distribution (Shiotani et al., 1994; Shiotani and Ohtsu, 1999). This is now referred to as improved *b*-value (I*b*-value) analysis. In this paper, fracture processes in four different kinds of concrete specimens are evaluated by applying the new analysis. Comparison is made for the results obtained from both the I*b*-value analysis and the moment tensor analysis (Ohtsu et al., 1998).

2. ANALYSIS

2.1 Improved b-value

Because AE peak amplitude is associated with the magnitude of fracture, the *b*-value that is defined as a slope of the amplitude distribution is known as an effective index related to the states of the fracture (Mogi 1962; Sholz 1968). The *b*-value was originally defined in

seismology. In AE applications of b-value, however, there were some problems to be resolved. First, even though both earthquake and AE magnitudes are defined in logarithm, seismic activities are distributed from 5 to 8 in earthquake-magnitude, and AE activities in peak amplitude range from 30 dB to 100 dB. Second, seismic *b*-value is obtained by using seismic data in a limited period and in confined range. However, the *b*-value in AE applications is conventionally obtained by using accumulated number of AE amplitude and from whole of the specimen. Third, a maximum likelihood method, provided that M - M_z has an exponential distribution, is applied in obtaining seismic *b*-value, where M is a seismic magnitude and M_z is a minimum magnitude. In the maximum likelihood method, the *b*-value is given by,

$$b = \frac{\log e}{\overline{M} - M_z} . \qquad (1)$$

It is noted in equation (1) that, when calculating the *b*-value with the maximum likelihood method, minimum magnitude should be previously determined. Figure 1 shows AE amplitude distributions resulting from a trap door test in a sand mass. The trap door test can provide several numbers of fractures by dropping the bottom of experimental box in the sand mass. In the trap door test, the condition of passive earth pressure in the geotechnical materials can be successively reproduced. In Fig. 1, the accumulated number of AE events integrated from infinity to zero (see a blue colored line) and frequency of AE events (see a red colored line) are drawn. The blue colored line shows that a linear approximation can be applied only in a narrow range from 43 to 50 dB, although AE events distributed from 30 to 59 dB. Moreover, it is possibly expected that the amplitude distributions can be shifted horizontally due to the conditions of AE sensor response, types of couplant and so forth. Hence, the maximum likelihood method using the minimum amplitude would be inapplicable for the AE applications.

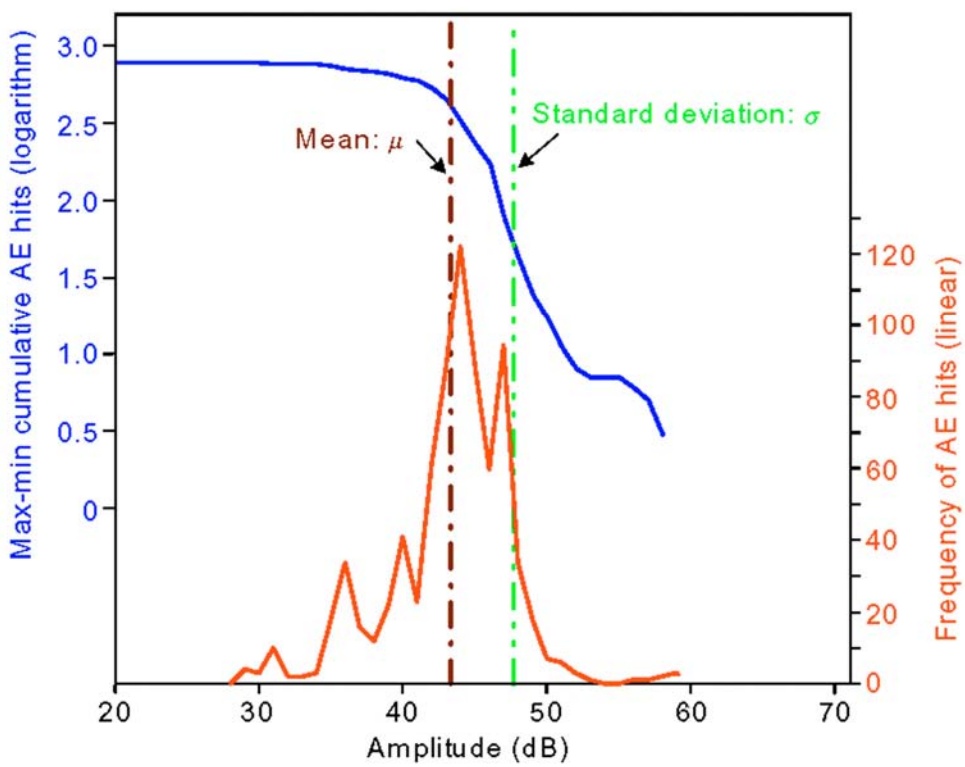

Fig. 1 AE amplitude distribution resulted from a trap door test.

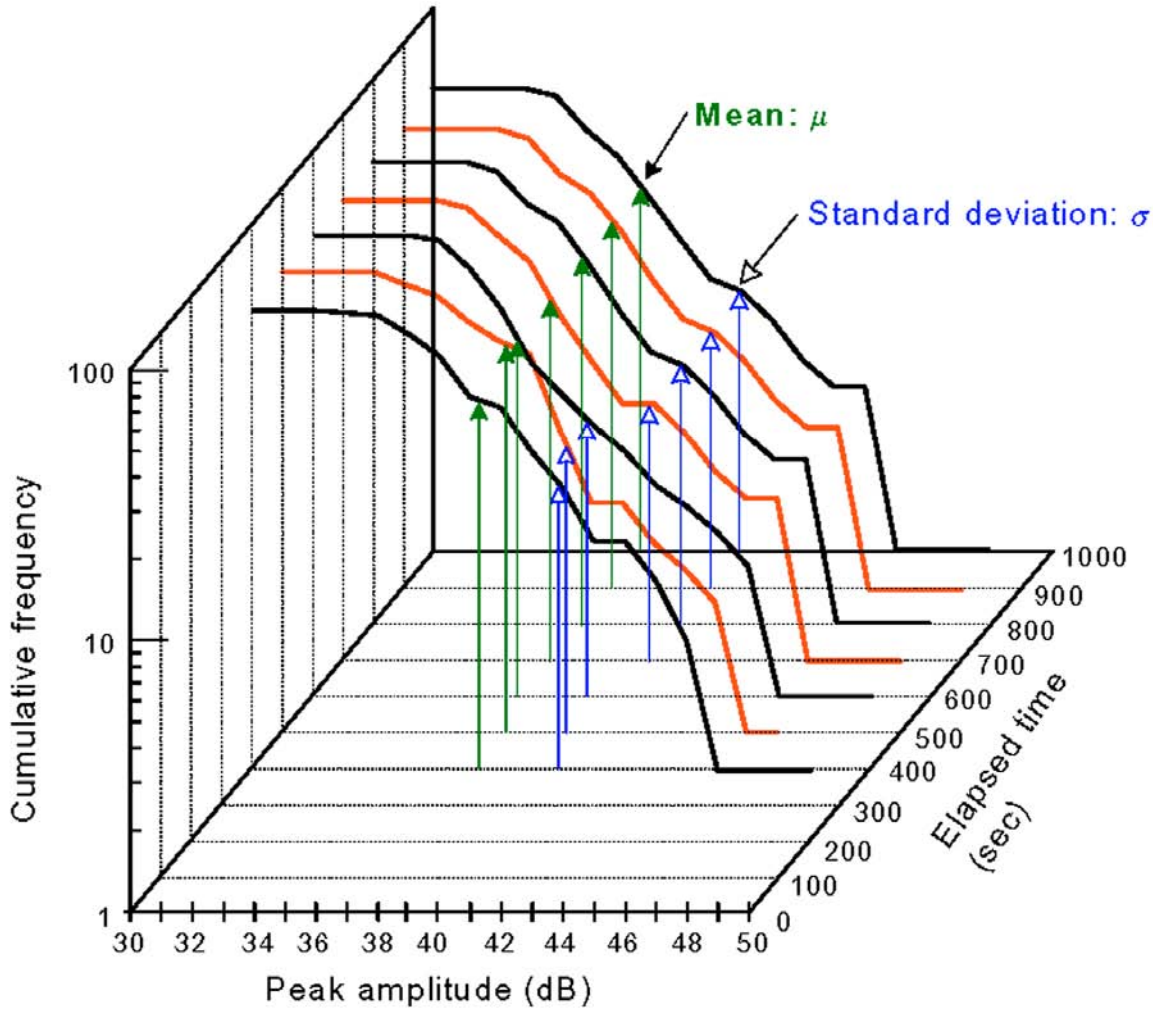

Fig. 2 3D amplitude distributions from a trap door test.

The value of AE peak amplitude is thus varied with each monitoring. In AE applications, a method for determining the amplitude range independent of the range of amplitude is necessary in order to obtain the *b*-value quantitatively. In an improved *b*-value (I*b*-value) analysis being proposed, the range of AE amplitude is determined based on such statistical values as the mean μ and standard deviation σ. Figure 2 shows three-dimensional amplitude distributions with elapsed time resulting from the trap door test. Each distribution is drawn by 100 data points of AE events, with green colored arrows showing the mean in each distribution and yellow colored arrows showing the standard deviation. It is found that the distributions between the two arrows can be approximately represented by a single straight line. When the amplitude range is thus obtained, the upper amplitude w_2 and lower w_1 are formulated as $\mu + \alpha_1\sigma$ and $\mu - \alpha_2\sigma$, respectively. Setting the accumulated amplitude over w_1 and w_2, as $N(w_1)$ and $N(w_2)$, I*b*-value (improved *b*-value) is given by,

$$Ib = \frac{\log_{10} N(w_1) - \log_{10} N(w_2)}{(\alpha_1 + \alpha_2)\sigma}, \qquad (2)$$

where α_1 and α_2 are constants.

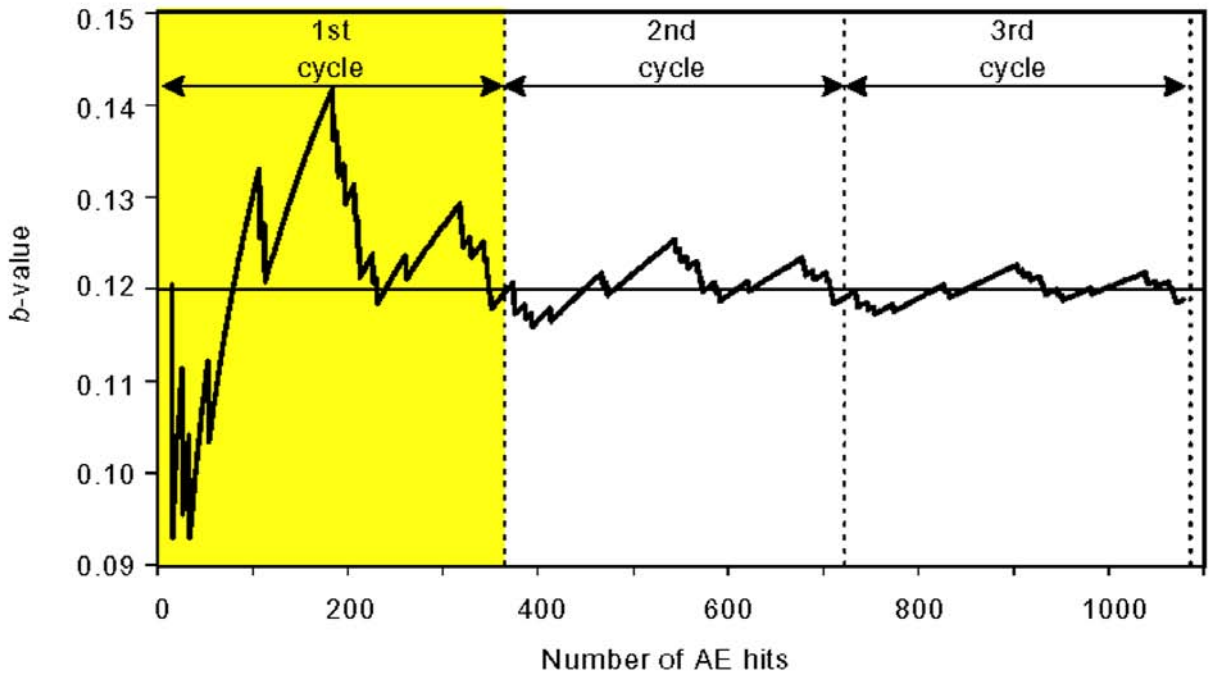

Fig. 3 The b-value resulted from a trap door test by means of accumulating AE data.

The other modification in the I*b*-value analysis over the conventional b-value is the number of AE event analyzed. In determining a *b*-value, the number of the peak amplitudes as denoted β in equation (3) should be set for the calculation. Figure 3 shows *b*-value that resulted from the trap door test by means of accumulating AE data. In this accumulation, for example, the *b*-value at *t* is calculated by using derived AE data from time zero to *t*. In Fig. 3, the *b*-value up to the final failure is intentionally repeated three times. It resulted from Fig. 3, and three different variations are observed, and *b*-value approaches 0.12 with elapsed time. This suggests that the *b*-value is highly dependent on a population parameter. This non-quantitative behavior would be also obtained for the *b*-value analysis of AE data within a fixed test period. For instance, AE activities would become higher with approaching the final failure. The population parameters would also become larger with elapsed time. Thus, *b*-value with the fixed time is also difficult to apply in AE applications. Figure 4 shows the *b*-value by means of constant number of 50 data points from the same data set as given in Fig. 3. One characteristic variation is similarly observed through the repetition. This implies that the constant number of population is so effective for performing the *b*-value analysis. To further improve the calculation of the *b*-value, the number of AE data points is formulated by,

$$\int_0^\infty n(a)\,da = \beta \quad , \qquad (3)$$

where $n(a)$ is the number of AE hits (or events) at da and β is the total number of AE hits (or events) data subjected to the I*b*-value analysis.

Figure 5 shows the correlation coefficients *r* with respect to the population (a sample number of AE amplitude data) where the data are approximated by the Gutenberg-Richter formula as given in equation (4), and the same data set as used in Fig. 2. Any number over 50 is considered

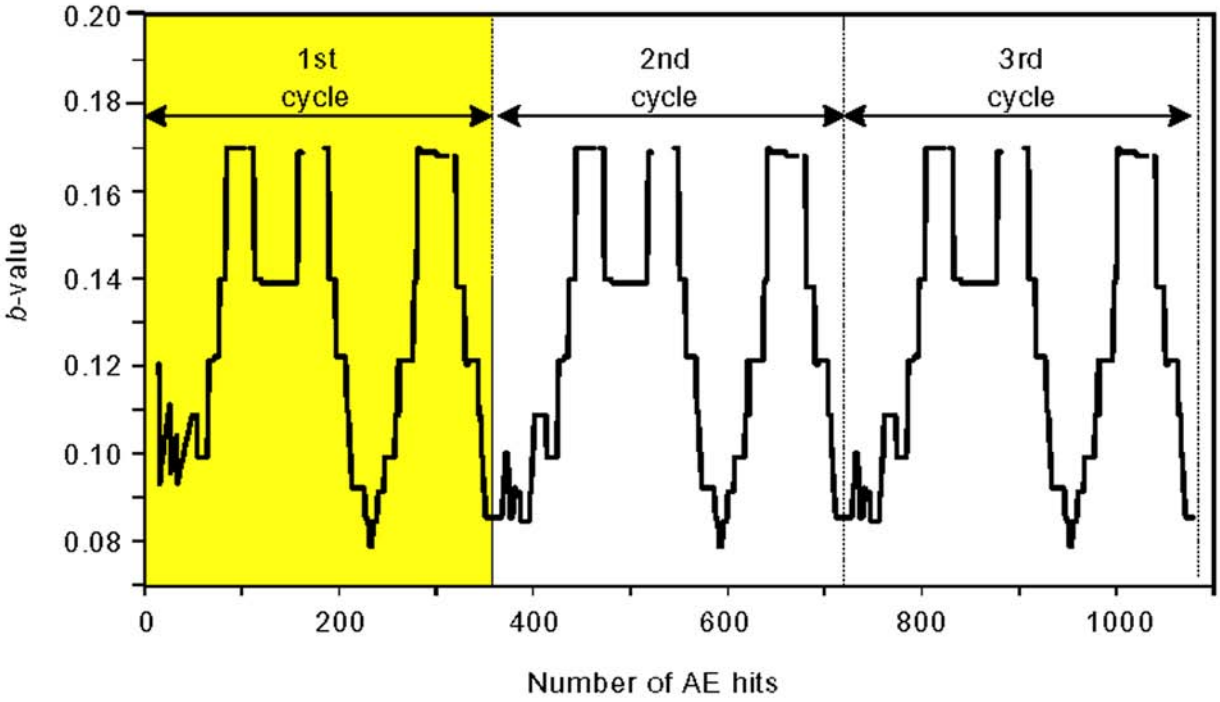

Fig. 4 The b-value by means of constant number of 50 data from the same data as Fig. 3.

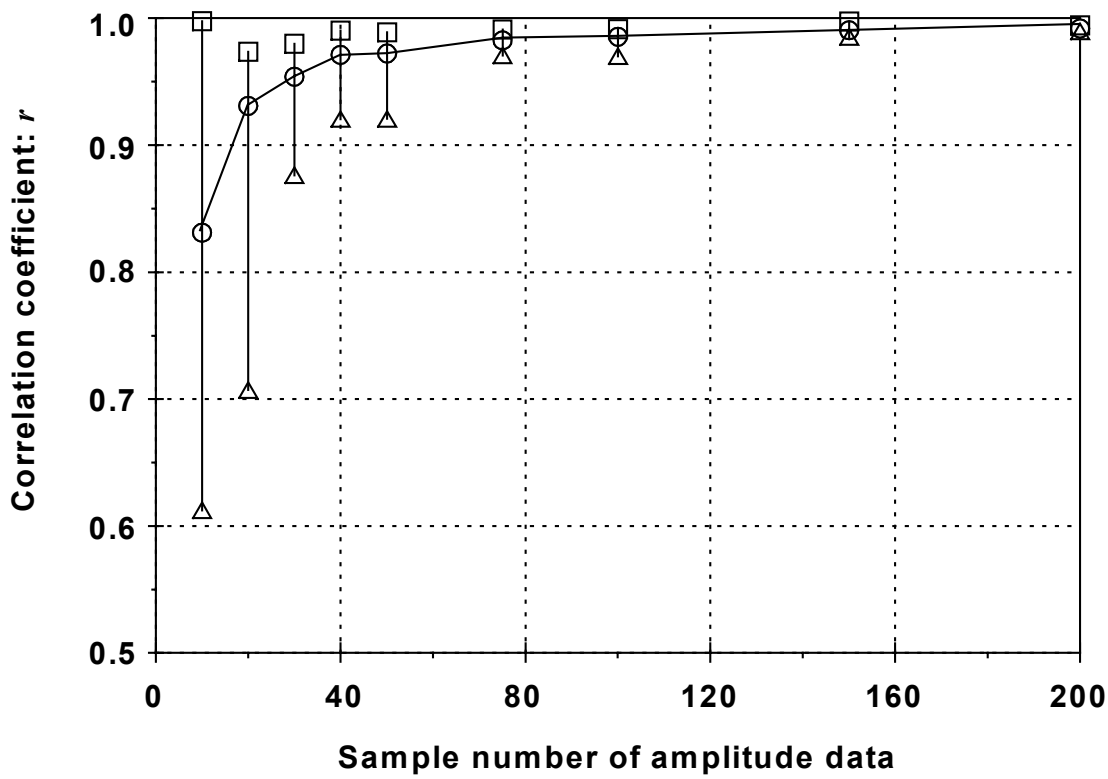

Fig. 5 Correlation coefficients approximated by Gutenberg-Richter's formula in a trap door test.

appropriate as β. In consideration of the problem in population parameters mentioned earlier, β from 50 to 100 would be an appropriate range to calculate the I*b*-value. (Shiotani et al., 1994).

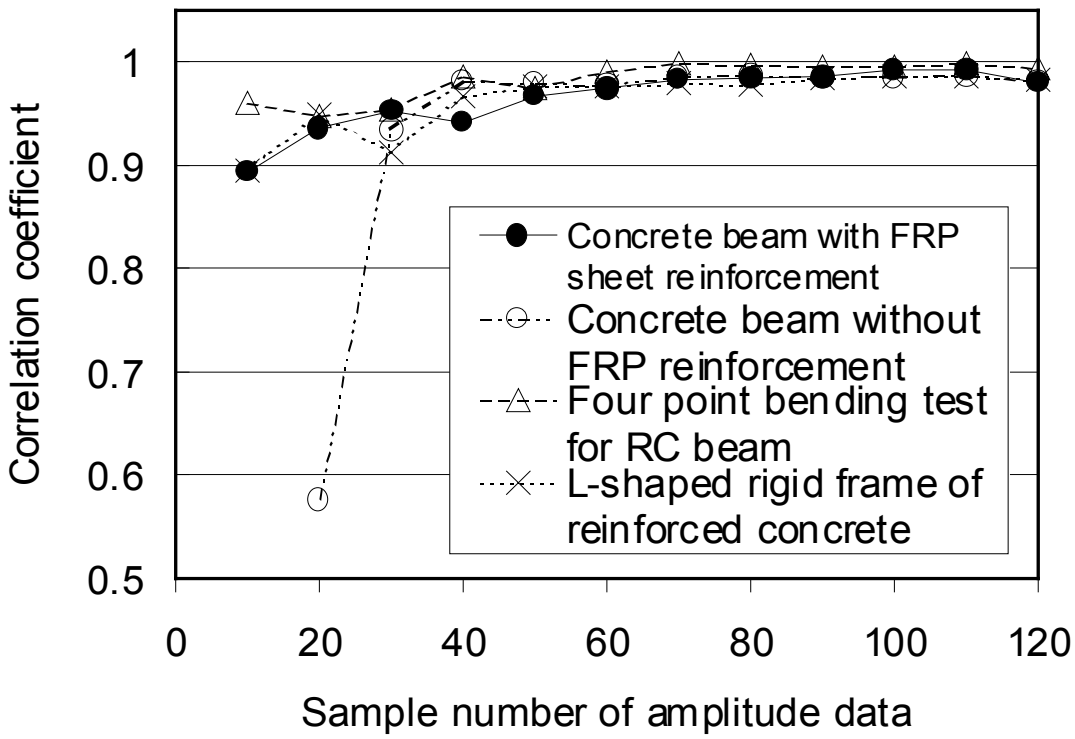

Fig. 6 Correlation coefficients approximated by Gutenberg-Richter's formula in various concrete specimens.

These results were obtained in geotechnical materials. Appropriate numbers of β in concrete materials are discussed in the following section.

2.2 Sampling number of amplitude in concrete materials for Ib-value analysis

In concrete materials, correlation coefficients with increasing the population is examined to determine the proper number of sampling data necessary for calculating μ and σ. Figure 6 shows the correlation coefficients in different specimens as noted, approximated by the Gutenberg-Richter formula of equation 4. These correlation coefficients are obtained when an approximation by the Gutenberg-Richter formula is performed.

$$\log N(M) = A - bM \ , \qquad (4)$$

Here, N is the total number of earthquake-frequency at over M and A is an empirical constant. In the AE applications, peak amplitude (dB) is substituted for M and b is the b-value. The peak amplitude is defined in dB, multiplying the log-amplitude by 20. When a comparison between the seismic b-value and Ib-value is made, the Ib-value should be multiplied by 20.

It is shown from Fig. 6 that, in all the different specimens, the relations between the logarithmic total number of AE events and the AE amplitude give a reasonable straight line when the number of sampling data becomes larger than 50. Hence, in this study for concrete materials, AE amplitude data of 50 samples ($\beta = 50$) are used to obtain the Ib-value.

2.3 Moment tensor analysis

Moment tensor analysis is a method developed for quantitative AE waveform analysis based on the measurement of very first P-wave arrivals. The procedure can give quantitative information on three-dimensional location of cracks, crack types, crack orientation and direction of crack motion. A computer code for simplified moment tensor analysis is named SiGMA (Ohtsu et al., 1991). In the SiGMA procedure, digital records of AE waveforms are analyzed, and more than six waveforms for each AE source are necessary. After experiment, each AE waveforms corresponding to one AE event are displayed on the CRT screen. Two parameters, the arrival time (P1) and the amplitude of the first motion (P2), are read on the screen. Three-dimensional AE sources are located from the arrival time differences (P1). Then, moment tensor components are determined based on the amplitudes of the first motions (P2). Finally, eigenvalue analysis is performed, and the classification of crack types and the determination of crack orientation are made. In this study, results of the moment tensor analysis are compared with those obtained from the I*b*-value analysis.

3. SPECIMENS AND TEST PROCEDURES

A four-point flexure test of reinforced concrete beams was conducted as shown in Fig. 7. Cyclic loading was applied. Locations of six AE sensors (S1-S6) are also given in the figure. A sketch of an L-shaped RC rigid frame and arrangement of six AE sensors are illustrated in Fig. 8. Tensile force was applied (see the two arrows) to expand the corner of the L-shape model. Center-notched concrete beams with and without FRP sheet reinforcement were subjected to three-point flexure load. Figure 9 gives a sketch of the specimen. The coordinate system and sensor locations are also shown in the figure. In the FRP reinforced specimen, one ply of CFRP sheet was bonded on the bottom corresponding to the tensile zone.

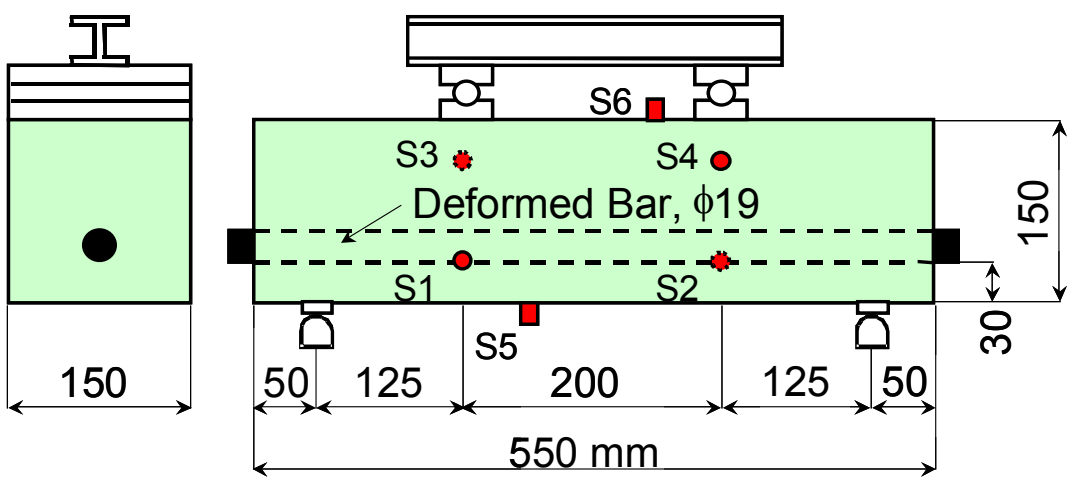

Fig. 7 Reinforced concrete specimen in flexural test and AE sensor locations.

4. RESULTS AND DISCUSSION

4.1 Cyclic flexure test of reinforced concrete beams

The loading history for the cyclic flexure test of a reinforced concrete beam specimen is shown in the top of Fig. 10. Results of the I*b*-value analysis for the Ch-5 sensor data are also

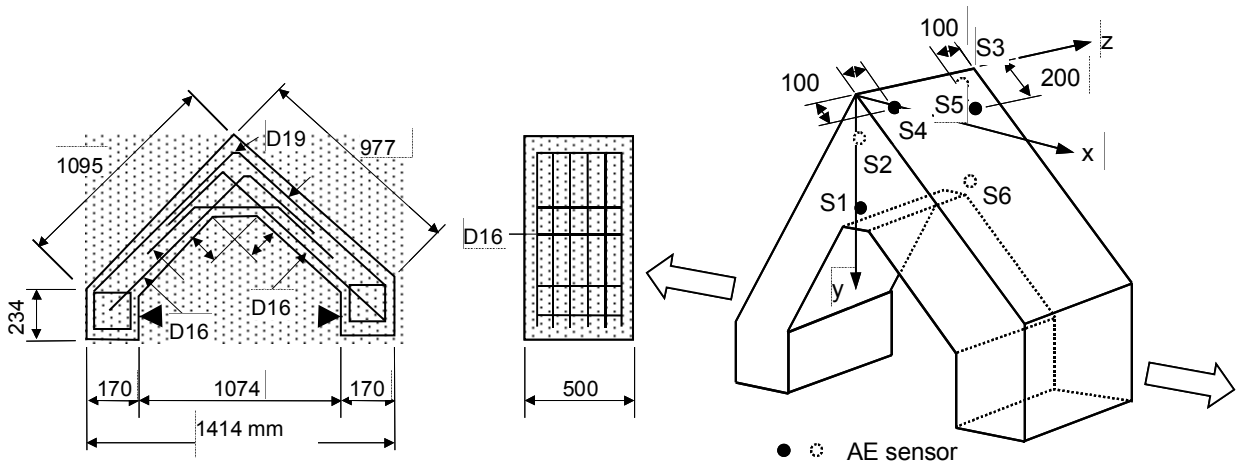

Fig. 8 Cyclic loading test of "L" shaped rigid frame.

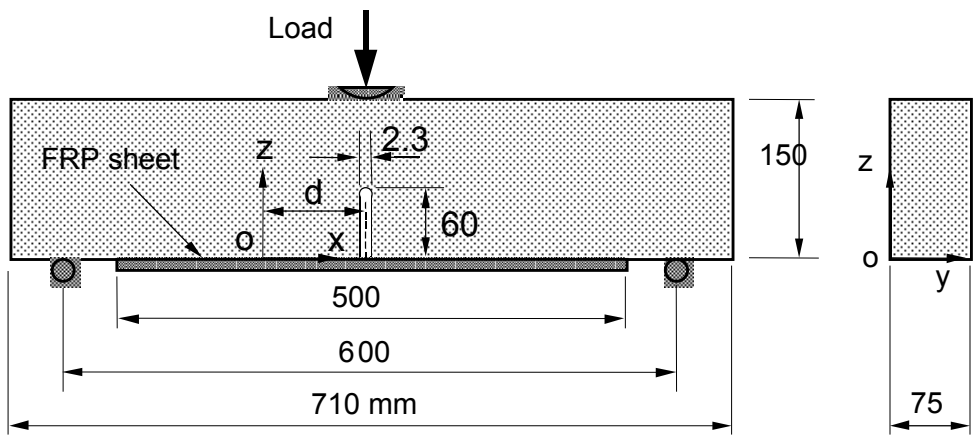

x-y-z: AE sensor coordination
d=100mm for specimen without reinforced FRP sheet
d=10mm for specimen with reinforced FRP sheet

Ch	Without CFRP sheet			With CFRP sheet		
	x	y	z	x	y	z
1	0	55	0	180	8	0
2	200	20	0	30	75	10
3	0	20	150	0	0	140
4	200	55	150	110	38	150
5	50	75	130	160	75	120
6	150	0	130	110	0	30

Fig. 9 Details of three-point flexure tests for concrete specimen with a center notch.

given in Fig. 9. This sensor was placed below the center of the specimen in the tensile zone. The dotted vertical lines represent the time of the maximum load of each stage. The maximum load was 49 kN in both stage I and stage II. Subsequently, it was increased in steps to the final load of 120 kN.

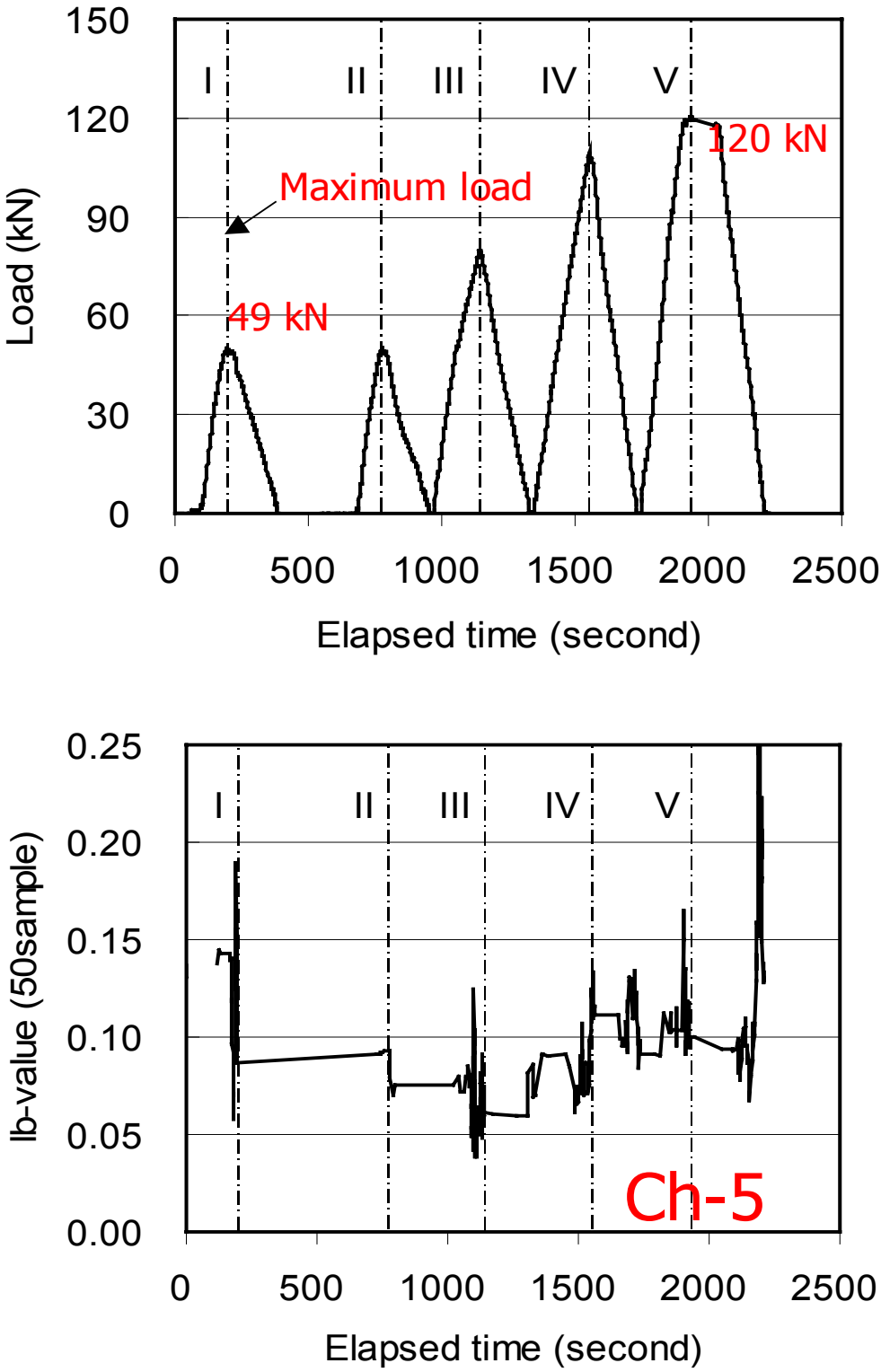

Fig. 10 Results of cyclic flexure test in reinforced concrete beam.

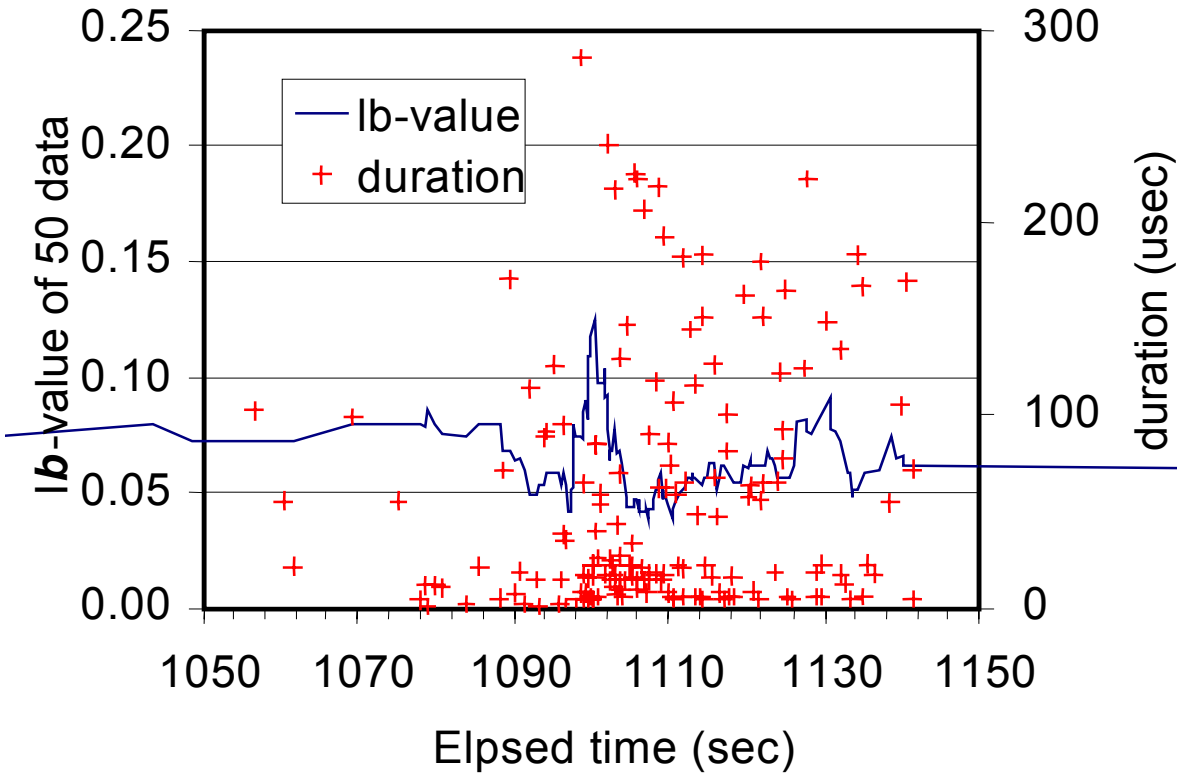

Fig. 11 Results of cyclic flexure test in reinforced concrete beam.

In stage I, the I*b*-value started at ~0.14 and varied to 0.06 to 0.19 as the load approached the maximum. This sudden variation of drop and rise in the I*b*-value appears to coincide the initiation of microscopic fracture; i.e., the generation of mortar cracks. The decrease in the I*b*-value represents the addition of high amplitude events due to cracking, while the subsequent drop implies the frictional AE of numerous high amplitude signals. In stage II, the I*b*-value was stable; it remained at 0.085-0.09 and decreased suddenly at the maximum load to 0.076. (This implies that cracks opened at the nominally the same load; presumably, the load slightly exceeded the previous maximum.) Thus, the I*b*-value exhibits the same characteristic as that of Kaiser effect. In stage III, the I*b*-value starts to increase at the previous maximum load of stage II (due to opening of crack face), and then reaches below 0.05. The I*b*-value smaller than 0.05 implies the onset of macroscopic fractures, because the specimen has experienced functional yield stress, indicated by the reduced slope of the load-time curve. In stage IV, the I*b*-value starts to decrease at the load much lower than the previous maximum load of stage III. Considering the characteristic of the Kaiser effect, this represents the severely damaged state in the specimen, in which shear type of cracks predominantly occurred within the specimen. In stage V, the I*b*-value begins to increase from the load 50% of the previous maximum load. The I*b*-value subsequently increases to over 0.15 when cracks between mortar and reinforcement were possibly grown, and abruptly decreases near the peak load. While the load was kept close to the maximum, the I*b*-value decreases gradually, representing continual crack development. Final unloading increases the I*b*-value close to 0.3 reflective of closure of crack face from unloading. Figure 11 shows an enlarged view of the I*b*-value in stage III. Every AE event is plotted with its event duration in the figure. The process of increase in I*b*-value corresponds to the prevailing generation of AE events with short event duration (see the cluster of 0 - 25 μs), while in the process of decrease it reaches the bottom of 0.04, and AE events with long event duration are predominantly observed (see the

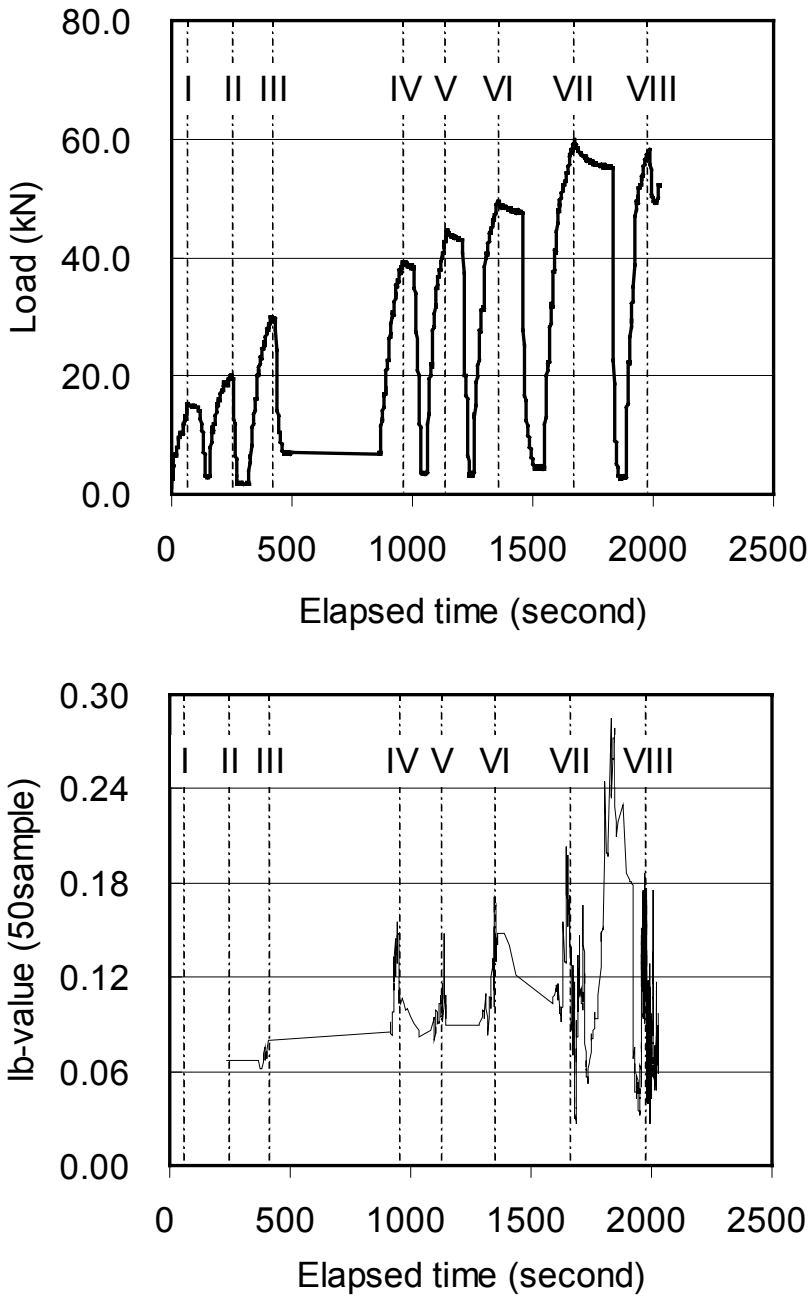

Fig. 12 Results of cyclic loading test in L-shape rigid frame.

cluster around 200 μs). Fracture phenomenon with short event duration means the microscopic fracture of the tensile type, and that with long duration implies the generation of shear type of fracture or frictional slip along the crack interface. Interpretation of the I*b*-value behavior is thus feasible.

In the moment tensor analysis, AE events obtained are 8 (I), 2 (II), 32 (III), 25(IV) and 9 (V) through the test. The parentheses denote the stages. AE events become the largest at stage III, which conforms the consideration of the I*b*-value. In stage V, only 9 events are obtained from the moment tensor analysis, although the I*b*-value changed between 0.09 and 0.16. In order to perform the moment tensor analysis, sets of waveforms consisting of at least six readable

waveforms are required. In the latter period of fracture, since there exist many cracks generated in the specimen, it is very difficult to obtain sets of waveforms with six valid waveforms. Thus, the moment tensor analysis may not be applicable to the latter period of fracture where macroscopic cracks of shear type are dominant. Unlike the moment tensor analysis, the I*b*-value analysis could evaluate the progress of fracture even in a heavily damaged phase. This is because the I*b*-value analysis only requires amplitude information independently of the number of AE events.

4.2 L-shaped rigid frame

Load was applied to the L-shaped rigid frame in the step-wise manner. The loading levels are divided into eight stages as shown in Fig. 12. The maximum loads are reached at times indicated by the dotted vertical lines. The I*b*-value analysis for the Ch-1 sensor data, giving representative behavior, is shown in the figure.

The I*b*-value cannot be determined in stages I and II due to low AE event totals. It stays low in stage III, then slightly drops and increases near the peak of stage III. The I*b*-values of ~0.15 are obtained at the end of stage IV, V and VI. In these stages, however, I*b*-value reduction to 0.05 is not observed. The I*b*-value smaller than 0.05 implies the onset of macroscopic fractures, where the specimen has experienced functional yield stress. Thus, the specimen reaches the yield point only past the stage VI, although the load-time curve shows significant non-linearity. In stage VII, because it is obviously recognized that the I*b*-value grows up to 0.20 and then falls to the bottom of 0.03, the specimen has possibly been subjected to the functional yield load. In stage VIII, at the load smaller than the previous maximum load, the specimen has reached the final failure. It suggests that the specimen has already experienced the functional yield stress during the previous stage VII. Thus, it appears that progress of fracture in the previous stage VII, evaluated from I*b*-value analysis, is reasonable.

Meanwhile, among a total of 1024 sets of waveform data, only 19 sets could be subjected to the moment tensor analysis. This is because the size of specimen is so large and with a quite complicated shape. No comparison was feasible between the I*b*-value and moment tensor analysis.

4.3 Center-notched concrete beams with and without FRP sheet reinforcement

In center-notched concrete beam specimens without FRP reinforcement, brittle nature of fracture is expected. Figure 13 shows results of the three-point flexure test of such a sample. The top shows the loading history and the bottom shows the I*b*-value for Ch-1 AE data against elapsed time. In the top figure, results of the moment tensor analysis are also shown, where arrows denote cracks of tensile type and cross symbols exhibit those of shear type. Both directions of the symbols correspond to crack orientations. The results of the moment tensor analysis could be classified into two stages.

In Fig. 13, the I*b*-value starts to increase at around 32 s (80% of the maximum load) and reaches 0.14. The I*b*-value gradually decreases to 0.07 at the maximum load and beyond. The I*b*-value successively decreases below 0.05 during strain softening. The increase may be caused by nonlinear deformation of the specimen, while the decrease may be due to catastrophic failure. On the other hand, the fracture process of the specimen could be divided into two stages by the moment tensor analysis. The first stage is determined to be until the maximum load, where the

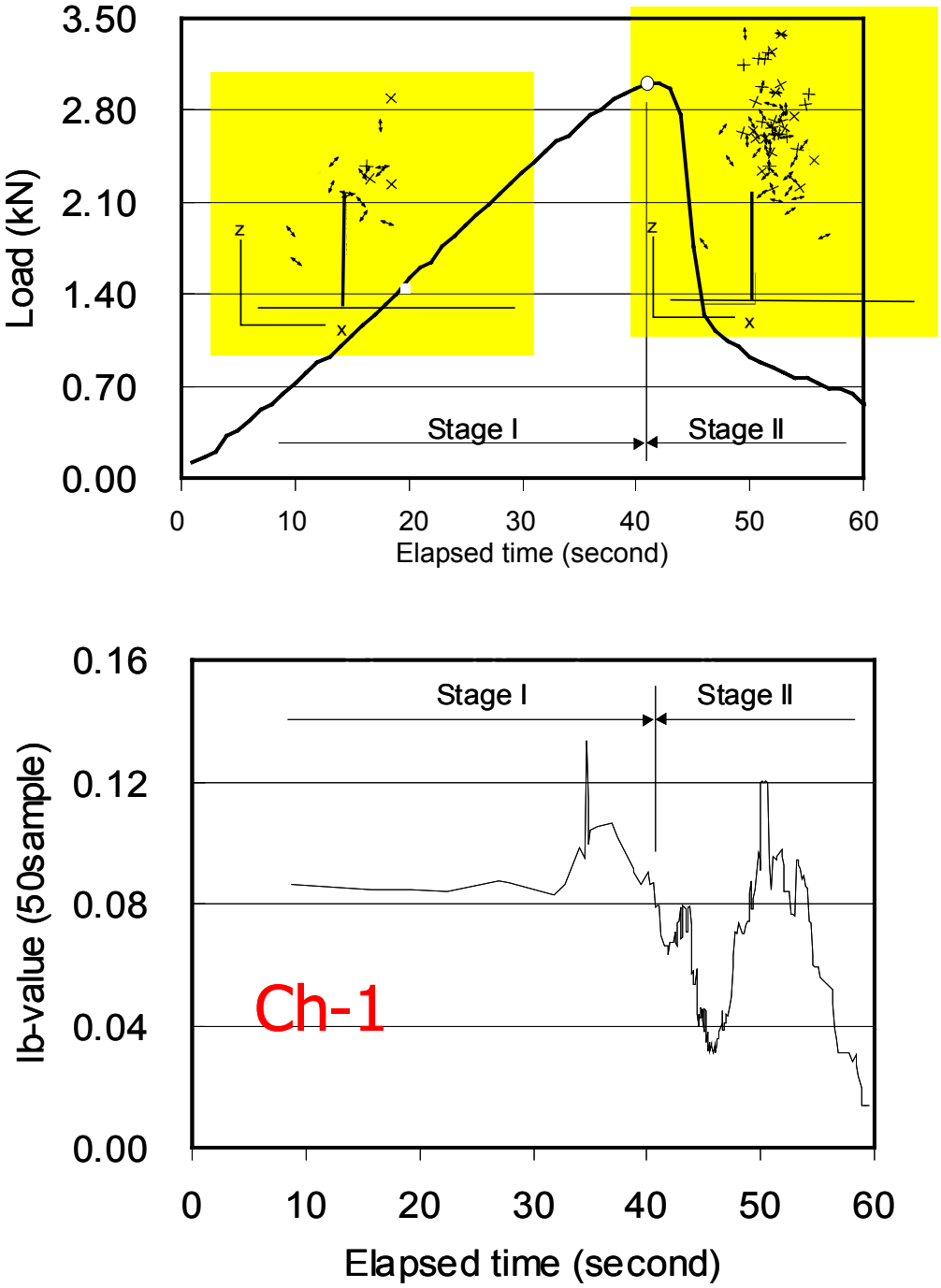

Fig. 13 Results of center notched concrete beam without a FRP sheet reinforcement.

cracks occurred only at a narrow area near the notch tip. After the maximum load, as the second stage began, cracks grew rapidly upward and the specimen failed right away. Thus, the results of I*b*-value analysis were in good agreement with those obtained from the moment tensor analysis.

Figure 14 shows results of load (top) and the I*b*-value (bottom) in the concrete beam reinforced with a CFRP sheet. Figure 15 shows results of moment tensor analysis. Also in the figure, a photo corresponding to fracture stages is given.

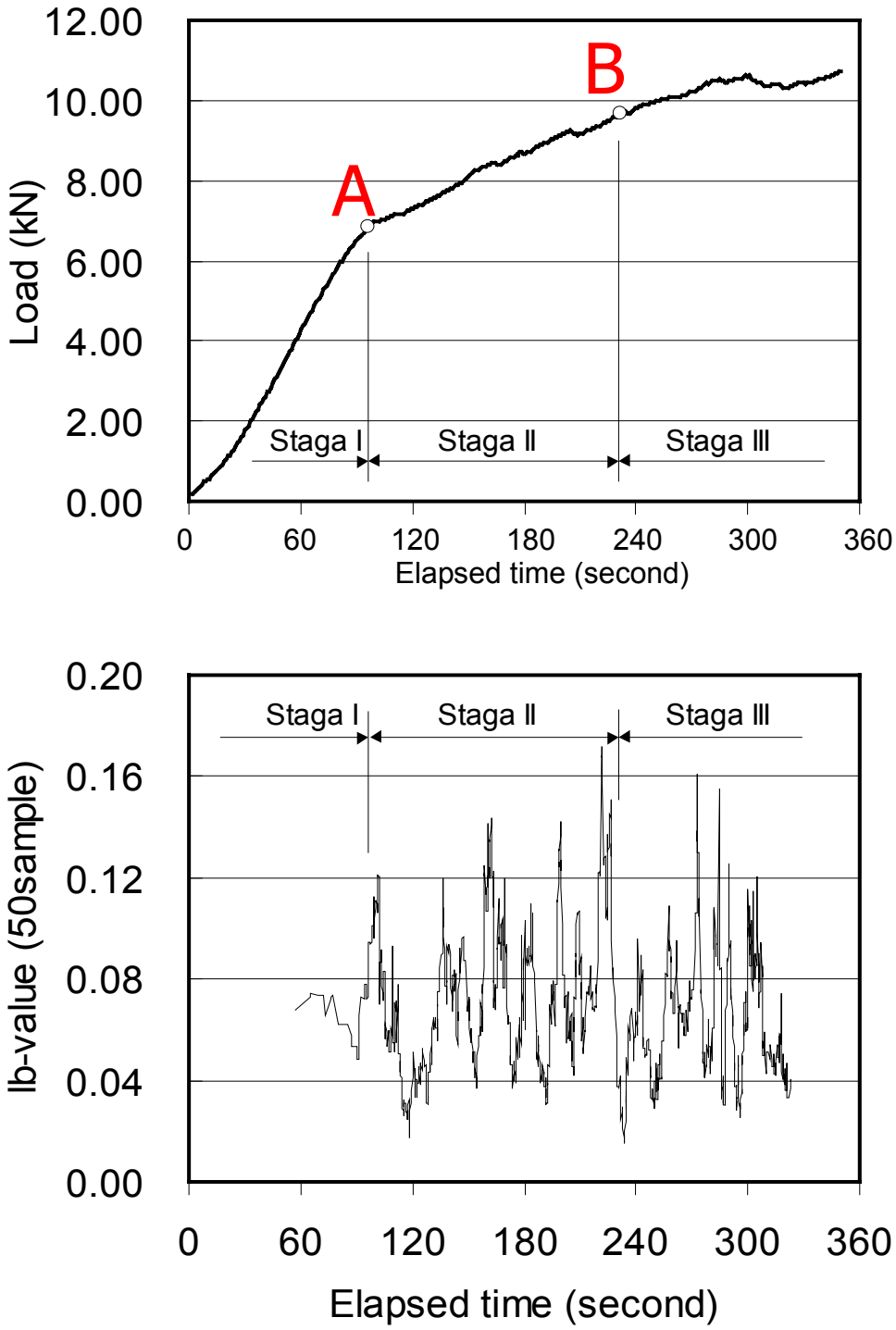

Fig. 14 Results of center notched concrete beam with a CFRP sheet reinforcement.

The fracture process is divided into three stages by the moment tensor analysis. Each stage is denoted as in Fig. 14. In the first stage corresponding to the loading level before point A, cracks are observed only within the area close to the notch tip as shown in Fig. 15(a). This is the same behavior as in the first stage of the specimen without reinforcement. Therefore, the loading point A can be regarded as the functional maximum allowable load in this type of specimen. The second stage is determined between loading point A and loading point B, where the main cracks ahead of the notch tip grew rapidly as shown in Fig. 15(b). Also in this stage, a diagonal crack

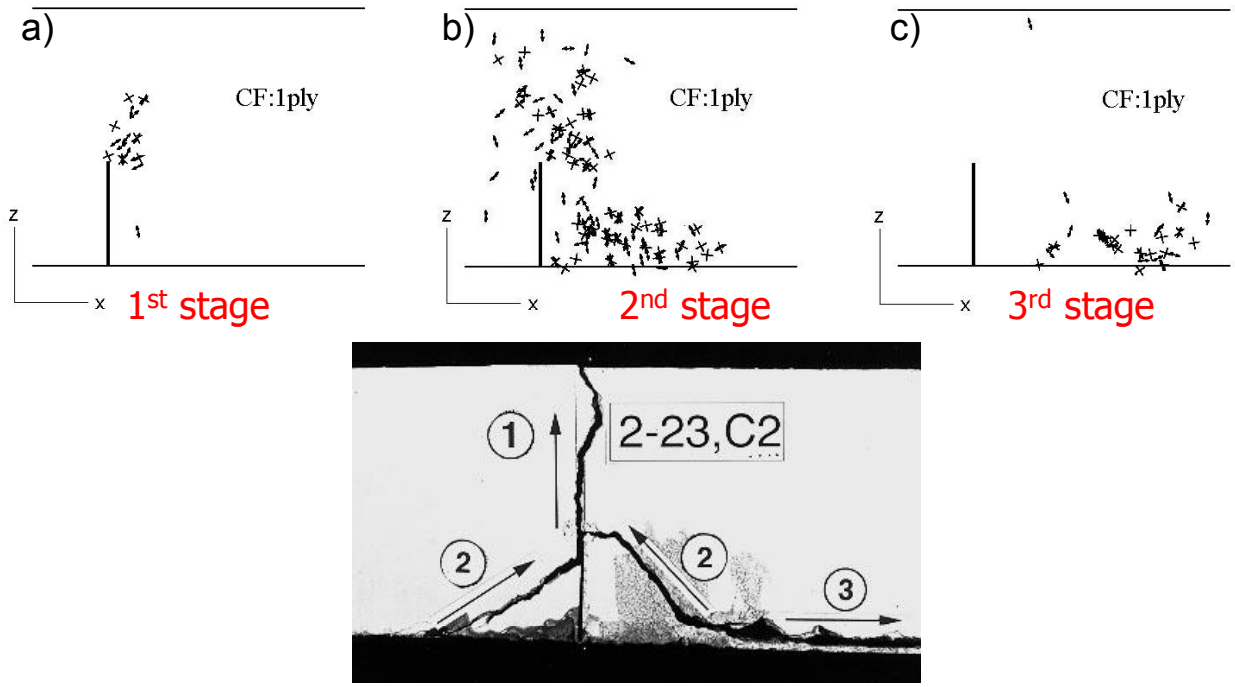

Fig. 15 Results of center notched concrete beam with a CFRP sheet reinforcement.

initiates from the bottom of the specimen toward the notch tip and a bottom crack propagates near the interface between the CFRP sheet and the concrete. After the loading point B or the third stage, cracks are only observed in the bottom of the specimen, continuing to propagate towards the supports. Thus, it is obvious that, during the second stage, the main crack had already reached the upper surface of the specimen.

From Fig. 14 (bottom), it is seen that the I*b*-value starts to decrease at about 80% of loading point A in the first stage. This is just the same behavior as that from the specimen without reinforcement. After loading point A, during the second stage, the I*b*-value increases and decreases repeatedly over a large range (0.03 to 0.17). Furthermore, the I*b*-value is observed to reach below 0.05 many times in this stage. This implies that the similar magnitude of large fracture is consecutively generated in the specimen during the stage. As the load approaches the point B, the I*b*-value changes most drastically and reaches as low as 0.02. It is thought that this resulted from the rapid propagation of the main crack up to the upper surface of the specimen. Consequently, the coincidence between the results of the I*b*-value analysis and the moment tensor analysis is further confirmed.

5. CONCLUSIONS

Fracture processes in four types of concrete specimens were evaluated by the I*b*-value analysis. Comparing the results with those obtained from the moment tensor analysis, the followings are concluded:

1. The I*b*-value analysis can evaluate the fracture process of concrete specimens with different dimensions, shapes and reinforcement arrangements. Thus, the I*b*-value is a useful feature to characterize fracture process in concrete structures.
2. Fracture process can be reasonably evaluated by the I*b*-value analysis even when the moment tensor analysis is inapplicable due to specimen size and shape.

REFERENCES

O. Minemura, N. Sakata, S. Yuyama, T. Okamato and K. Maruyama (1998), "Acoustic Emission Evaluation of an Arch Dam during Construction Cooling and Grouting," Construction and Building Materials, **12**, 385-392.

K. Mogi (1962), "Magnitude Frequency Relation for Elastic Shocks Accompanying Fractures of Various Materials and Some Related Problems in Earthquakes," Bulletin of Earthquake Research Institute, **40**, 831-853.

Y. Murakami, S. Yuyama, T. Shimizu, H. Kouyama and M. Matsushima (1993), "Deformation Behavior and AE Characteristics for Anchorage Pulling Tests on the Foundations of Power Transmission Pylons (Part II, Moment Tensor Analysis)," Proc. the 9th National AE Conference, JSNDI, pp. 143-150 (in Japanese).

M. Ohtsu, T. Okamoto and S. Yuyama (1998), "Moment Tensor Analysis of Acoustic Emission for Cracking Mechanisms in Concrete," ACI Structural J., **95**(2), 87-95.

M. Ohtsu, M. Shigeishi, S. Yuyama and T. Okamoto (1991), "SiGMA Procedure for AE Moment Tensor Analysis," J. JSNDI, **42**(10), 570-575.

T. Shiotani, K. Fujii, T. Aoki and K. Amou (1994), "Evaluation of Progressive Failure Using AE Sources and Improved *b*-value on Slope Model Test," *Progress in Acoustic Emission VII*, eds. T. Kishi, Y. Mori and M. Enoki, JSNDI, Tokyo, pp. 529-534.

T. Shiotani and M. Ohtsu (1999), "Prediction of Slope Failure Based on AE Activity," *Acoustic Emission: Standards and Technology Update*, ASTM STP 1353, ed. S. J. Vahaviolos, ASTM, pp. 156-172.

H. Sholz (1968), "The Frequency-Magnitude Relation of Microfracturing in Rock and Its Relation to Earthquakes," Bulletin of Seismological Society of America, **58**(1), 399-415.

S. Yuyama, T. Okamoto and S. Nagataki (1994), "Acoustic Emission Evaluation of Structure Integrity in Repaired Reinforced Concrete Beams," Materials Evaluation, **52**, 86-90.

S. Yuyama, T. Okamoto, M. Shigeishi and M. Ohtsu (1995a), "Quantitative Evaluation and Visualization of Cracking Process in Reinforced Concrete by a Moment Tensor Analysis of Acoustic Emission," Materials Evaluation, **53**, 751-756.

S. Yuyama, T. Okamoto, M. Shigeishi and M. Ohtsu (1995b), "Acoustic Emission Generated in Corners of Reinforced Concrete Rigid Frame under Cyclic Loading," Materials Evaluation, **53**, 409-412.

EVALUATION OF FRACTURE PROCESS IN CONCRETE JOINT BY ACOUSTIC EMISSION

T. KAMADA, M. ASANO, S. LIM, M. KUNIEDA and K. ROKUGO

Department of Civil Engineering, Gifu University, Yanagido 1-1, Gifu 501-1193, Japan

ABSTRACT

Fracture process in concrete joint between old and new concrete was investigated thorough AE procedures. Both bending and shear tests were conducted at each specimen with concrete joint. The joint surfaces were treated with different surface preparation methods. AE measurements were performed during tests and the AE features were examined. The results presented that the AE characteristics had strong correlation with surface roughness at joint. This method would be an effective tool for the comparison among different concrete joints with similar strength.

1. INTRODUCTION

Mechanical behavior of a construction joint, which has interface between old and new concrete, strongly affects the performance of a concrete structure. Bonding that is improved by surface treatments is one of the important performances for construction joints. Some indices and testing methods have been proposed for evaluating the bond property. Bond strength calculated by the maximum load has been only an index at final failure, and it has not been usual to evaluate a softening region in the fracture behavior. Fracture mechanics parameters, such as tension softening diagram and fracture energy, are effective indices to evaluate the bond property including the softening region [1]. These indices, however, are estimated by using comprehensive behavior such as load-displacement relationship in the tests, and cannot monitor the fracture process.

Acoustic emission (AE) technique, which is a method to receive elastic waves due to micro-cracks in concrete, is useful to evaluate fracture processes. Especially, locations of cracks, which are changing step by step, can be also estimated by this technique. The AE hit, which is one of the parameters in AE technique, has been applied to evaluation of the fracture process of jointed specimens under bending tests [2] or direct tensile tests [3]. In this study, bending tests and shear tests for jointed specimens were carried out. The fracture process of jointed specimens was investigated by using not only the AE hit but also the characteristics of received waveform. The relationship between AE characteristics and bond properties due to different surface treatments was studied.

2. EXPERIMENTAL PROCEDURES

Bending test

Specimens The size of the jointed specimen, that had a joint at the center of the specimen, was 10x20x80 cm (width x depth x length). The mixture proportions of old and new concrete are shown in Table 1. Cement used was the high early strength Portland cement (specific gravity: 3.12), and the maximum size of coarse aggregate was 15mm. Compressive strengths of the new and the old concrete at the age of 21 and 28 days are shown in Table 2. In order to prevent a sudden crack propagation, a steel bar (D13) was embedded at compressive side (2 cm from the

upper side) in the beam specimen, as shown in Fig. 1.

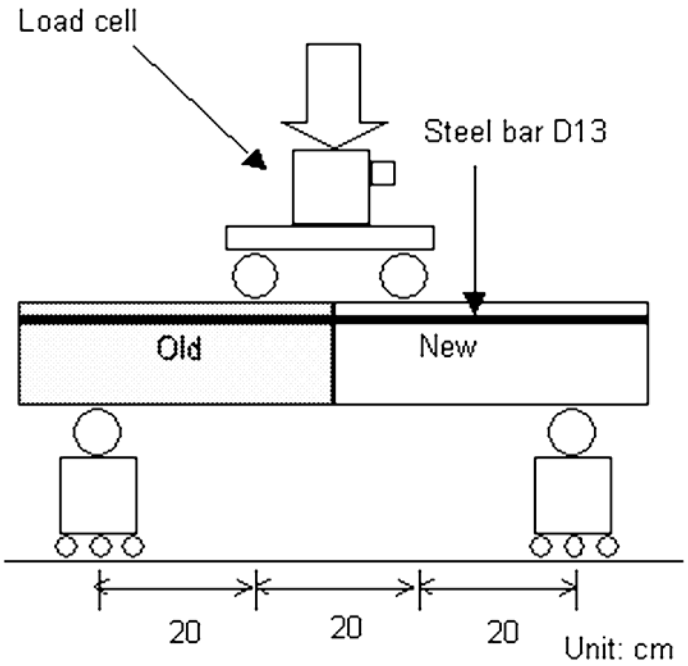

Fig. 1 Bending test setup.

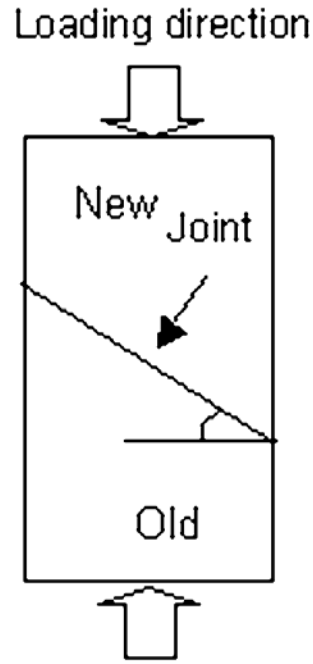

Fig. 3 Shear test setup.

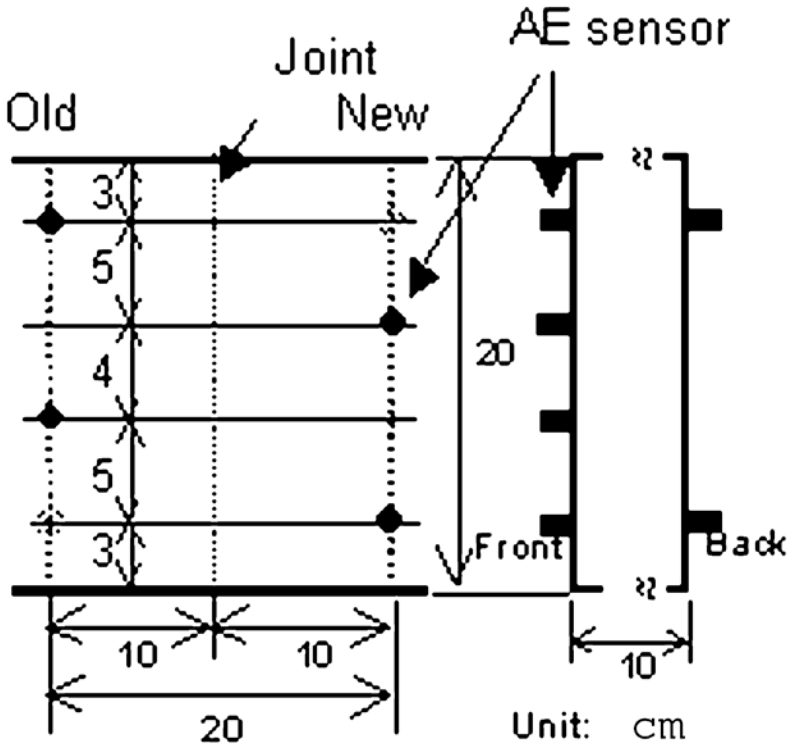

Fig. 2 AE sensor location.

Three types of surface roughness, namely a non-treatment surface after removing a formwork, wire-brushed surface, and washed-out surface (washed-out depth: 2mm and 6mm), were chosen as the old concrete surfaces. For comparison, specimens without joints were also

made. Three specimens in each series were made in this test. Four-point bending tests (span: 60 cm) were carried out as illustrated in Fig. 1. The results of strength tests were shown in Table. 2.

AE measurement The system manufactured by Physical Acoustics Corporation was used for the measurement of AE. AE signals detected by 150 kHz resonant sensors were amplified with the pre-amplifier by 40 dB, and were also amplified with the main-amplifier by 40 dB, so that the total gain was 80 dB. For the bending tests, the threshold value was 45 dB. The detected AE signals were analyzed and recorded in terms of waveform parameters. As shown in Fig. 2, six sensors were attached on the front (four sensors) and back (two sensors) of the specimen. Rubber pads and teflon sheets were inserted in order to eliminate the noise due to contact of the specimens with the loading apparatus.

Shear test

Specimens As shown in Fig. 3, compressive load was applied to the rectangular specimens with a joint, of which angle was 45 or 60 degrees. The size of specimens was 10x10x40 cm (width x depth x length). The mixture proportions of old and new concrete are shown in Table 1. Compressive strengths of the new and the old concrete at the age of 103 and 106 days are shown in Table 2.

Two types of rough surfaces (washed-out depth: 2 mm and 4 mm), which are treated by using washed-out method, were chosen as the old concrete surfaces. In addition, specimens without joints were also made. Casting direction was taken at right angle with the longitudinal axis of the specimen. Test series for the slope-angle and surface roughness of the old concrete are shown in Table 3. Three specimens were made in each series.

AE measurement Four sensors were attached on the surface of a specimen, as shown in Fig. 4. The procedure for AE measurement was the same in the bending test.

Table 1 Mixture proportions

Test	Concrete	Air (%)	W/C (%)	Unit weight (kg/m^3)				
				W	C	S	G	Ad
Bending	Old & New	1.7	50	170	340	756	1002	1.02
Shear	Old	4.3	55	172	312	793	1002	0.927
	New	4.2	55	171	310	793	1002	0.927

Ad: AE water reducing agent

Table 2 Properties of concrete

Test	Concrete	Strength (MPa)		Young's Modulus (GPa)	Age (days)
		Compressive	Flexural		
Bending	Old	44.5	5.6	30.5	28
	New	43.8	4.8	28.1	21
Shear	Old	48.8	4.1	28.1	106
	New	46.8	5.3	28.5	103

Table 3 Test series.

Series	Slope angle α (degrees)	Surface preparation
A0	-	-
A64	60	Washed-out 4 mm
A62	60	Washed-out 2 mm
A44	45	Washed-out 4 mm
A42	45	Washed-out 2 mm

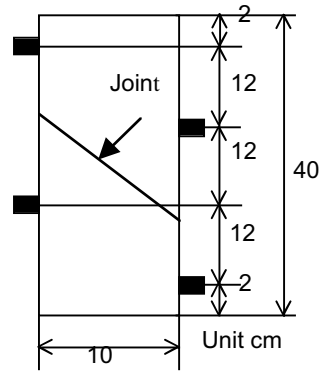

Fig. 4 AE sensor location.

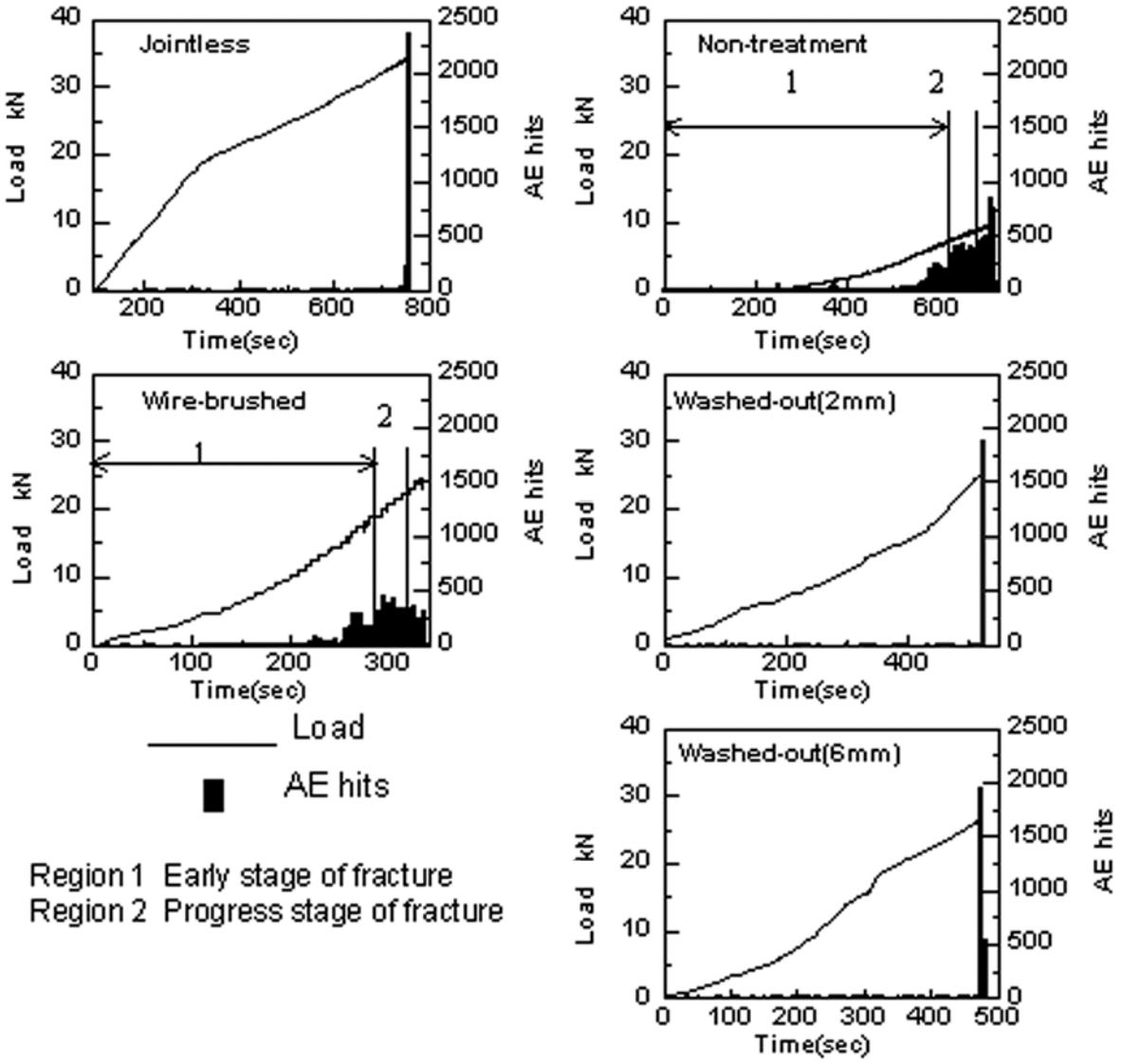

Fig. 5 Load and AE activity under bending tests.

3. RESULTS AND DISCUSSIONS

Bending test

AE hits Figure 5 shows the relationship between applied load and AE hits in the bending test. The maximum load of the specimen without joint was the highest in these specimens. For the specimens with the joint, the maximum loads of the specimens, in which old concrete surfaces were washed-out (6 mm and 2 mm) or wire-brushed, were higher than that of the specimen with non-treatment surface. Especially, the AE signals in the specimen without joint and the washed-out specimen were hardly detected up to the maximum load. However, they suddenly increased on reaching the maximum load. On the other hand, in the case of the specimens with wire-brushed and non-treatment surface, AE activities, which are thought to indicate occurrence of micro or macro crack, could be found before the maximum load. Although the maximum loads of wire-brushed specimens were as high as those of the washed-out specimens, it seems that debonding at the joint occurred in the low load level. These micro or macro cracks in low load levels might change the transport characteristics for water or chloride ion, which affect a corrosion of steel reinforcing bar or esthetics of concrete structures. Therefore, it can be concluded that AE parameters are effective indices for a quantitative evaluation of these cracks.

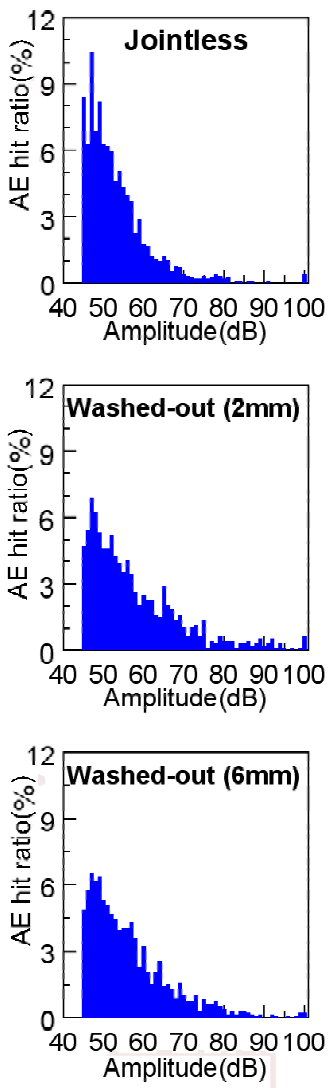

Fig. 6 Amplitude distribution (Group 1).

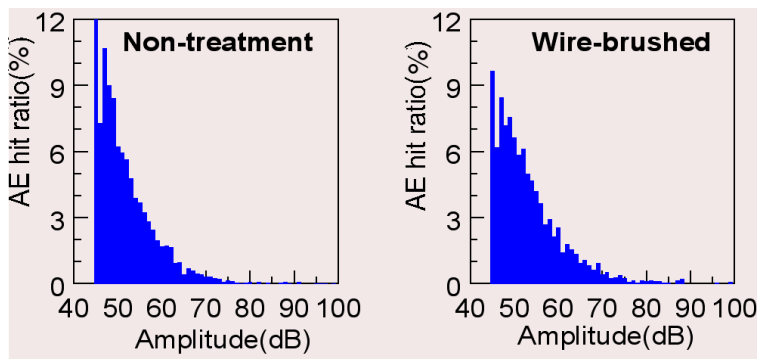

Fig. 7 Amplitude distribution (Region 1,Group 2).

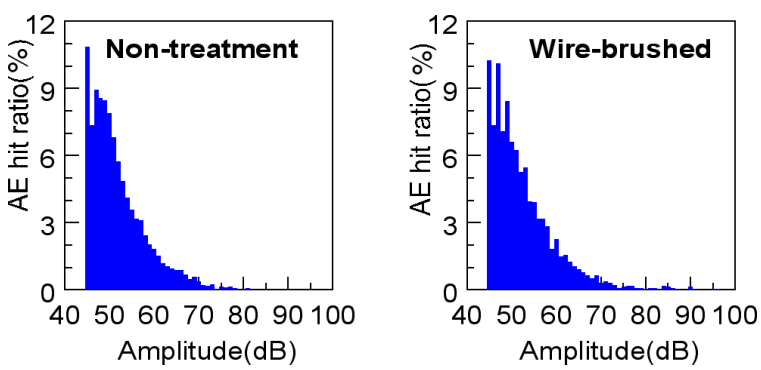

Fig. 8 Amplitude distribution (Region 2,Group 2).

Maximum amplitude In this study, the test results were classified into two groups from the viewpoint of the AE hits. One was Group 1 that consisted of the jointless and washed-out (2mm and 6mm) specimens. The other was Group 2 that consisted of the non-treatment surface and the wire-brushed specimens. In the investigation for Group 1, the amplitude distribution obtained from the test-start to half of the total measurement time, was adopted because of removing the AE due to the compression failure or the

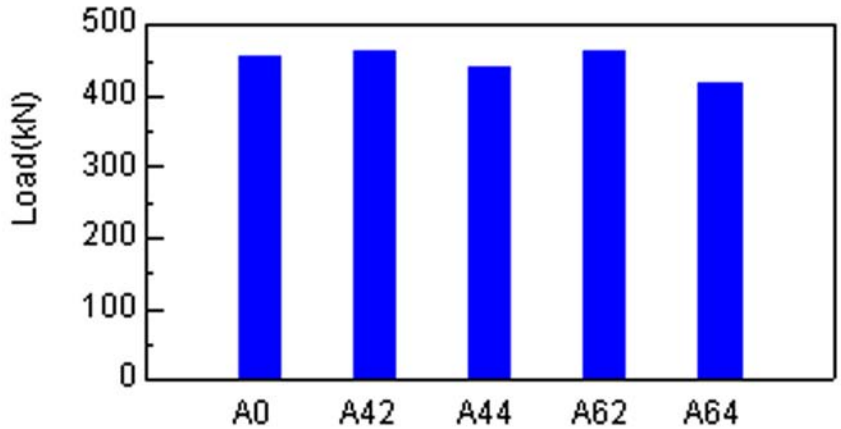

Fig. 9 Maximum loads in shearing tests.

debonding between the concrete and the steel bar. The amplitude distributions for the Group 1 are shown in Fig. 6. The ratio of the AE hits with lower amplitude (45~50 dB) to the total AE hits in the jointless specimens was larger than that in the washed-out specimens (2 mm and 6 mm). Although AE behavior of the jointless specimens that evaluated by AE hits was similar to that of washed-out specimens, the failure process that was revealed by the amplitude characteristics was different from that of washed-out specimens [4]. It seems that the energy due to crack generations at the joint is larger than that of cracks in plain concrete. The influence of washed-out depth on the AE behavior is not clear in this experiment.

In the investigation for Group 2, the amplitude distributions in the Regions 1 and 2 (which are defined in Fig. 5) are shown in Fig. 7 and 8, respectively. For the non-treatment surface specimens, the amount of AE signals with lower amplitude (45 ~ 50 dB) in the Region 2 became larger than that in Region 1. For the wire-brushed specimens, the difference of amplitude distributions between the Regions 1 and 2, however, was not clear. In the case of the wire-brushed specimens, the ratio of the AE hits whose amplitude were over 50dB to the total AE hits was relatively larger than that of non-treatment specimens. Because the consumed energy for the failure of the non-treatment surface specimens was lower than that of the wire-brushed specimens, the magnitude of the AE sources of the non-treatment surface specimens became smaller than that of the wire-brushed specimens. These results indicate that the failure easily progresses afterwards, when the failure of the non-treatment surface specimens is once generated. It was clarified that not only the AE hits but also the amplitude distributions were effective indices for the evaluation of failure process.

Shear test

Comparison with maximum loads Figure 9 shows maximum loads under shear test. The effect of slope-angle or washed-out depth on the maximum loads was not observed in these tests.

Evaluation using maximum amplitude distribution Figure 10 shows the result of AE source location analysis in each specimen. The detected AE sources were located around the joint, and the failure at the joints was confirmed through this analysis. In the experiment, a crack along the joint can be observed in the specimens with the joint.

Figure 11 shows the amplitude distribution of each specimen. These results were obtained by using the data, whose locations were clarified through the AE source location analysis.

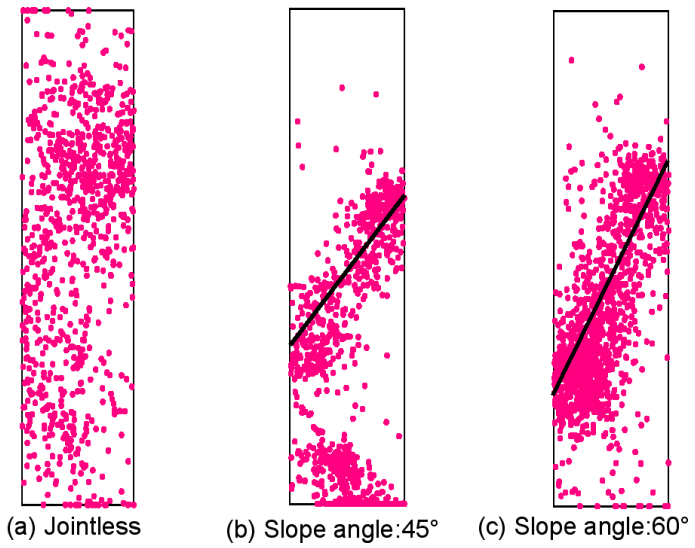

Fig. 10 Results of AE source location analysis.

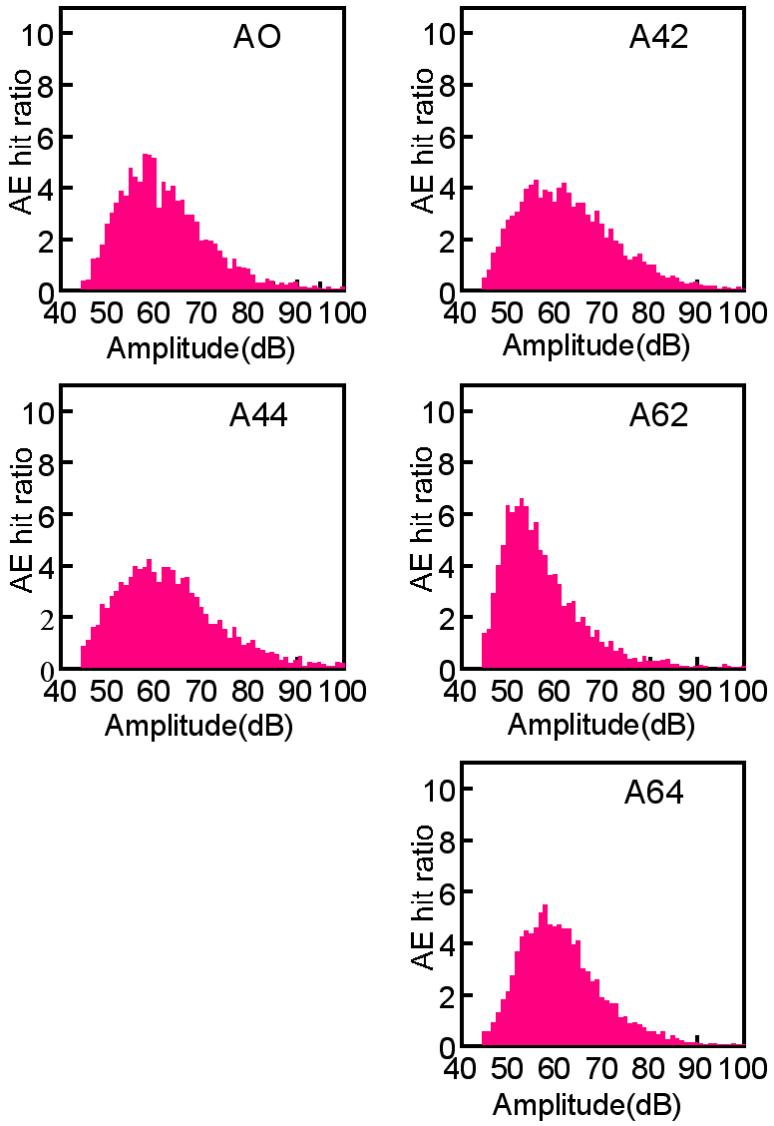

Fig. 11 Amplitude distribution of five test specimens. AE hit ratio given in %.

The shape of amplitude distributions of Series A44 and A42 were similar to that of Series A0 that was compressive failure type. Therefore, it seems that the failure of Series A44 and A42 can be also classified into the compressive failure type. For Series A64 and A62, the amplitudes at the maximum AE hits ratios in the amplitude distributions were smaller than those of Series A44 or A42. In the case of the Series A62, the amplitudes at the maximum AE hits ratios in the amplitude distribution was smaller than that of Series A64, and the ratio of AE hits whose amplitudes were over 60 dB was definitely smaller than that of Series A64. The failure of Series A62 depends on slips at interfaces under shear stress, which was clarified by referring to the previous study [5]. In the shear tests for jointed specimens, it was revealed that the roughness of old concrete surface improved the resistance against a large deformation [6]. The results of AE measurement could be also effective to evaluate the resistant properties at joint under the shear stress.

4. CONCLUSIONS

The conclusions were obtained as follows;

(1) In the bending tests of the specimens with a construction joint, AE activity was affected by the difference of surface roughness of old concrete.
(2) For the evaluation by using the amplitude distribution, the shape of amplitude distribution was affected by surface roughness. The amplitude distribution, which was affected by fracture process, was more effective index than the maximum load.
(3) In the shear tests, the relationship between washed-out depth and maximum loads was not affected by the slope-angle.
(4) For the evaluation by using the amplitude distribution, the amplitude distribution in case of smaller slope angle of 45 degrees, the shape of amplitude distribution was similar to that of jointless specimens. The amplitude distribution in the case of the larger slope-angle of 60 degrees was, however, affected by the washed-out depth of old concrete.
(5) The failure of Series A62 depends on slips at interfaces under shear stress as compared to the Series A64.

REFERENCES

1. N. Kurihara, M. Kunieda, Y. Uchida and K. Rokugo, “Bond Property of Concrete Joint and Size Effect,” Journal of Materials, Concrete Structures and Pavements, JSCE, No. 613/V-42, (1999), 309-318.
2. I. Adachi and S. Sakoda, “Acoustic Emission in the Construction Joints of New and Old Concrete,” The Proceedings of the 10th National AE conference, (1995), JSNDI, pp. 179-184.
3. K. Miyano, T. Kita, Y. Murakami and T. Kyogoku, “Evaluation of Joint Properties of Anti-Washout Concrete by Acoustic Emission,” Proceedings of Japan Concrete Institute, **12**(2), (1990), 359-364.
4. A. A. Pollock, “Acoustic Emission Amplitudes” Nondestructive Testing, **6**(5), (1973), 264-269.
5. T. Kamada, M. Iwanami and S. Nagataki, “Acoustic Emission Classification of Cracks in Concrete,” Tokyo Institute of Technology, Department of Civil Engineering Technical Report, No. 55, (1997), 1-12.
6. T. Makitani, K. Katori and S. Hayashi, “An Evaluation of Surface Roughness of Pre-Cast Panel and Experiments on Ability of Shear Transfer through Construction Joint,” Proceedings of Japan Concrete Institute, **17**(2), (1995), 171-176.

DAMAGE DIAGNOSIS OF CONCRETE-PILES BY MACHINERY-INDUCED ACOUSTIC EMISSION

T. SHIOTANI, S. MIWA, Y. ICHIMURA* and M. OHTSU§

Research Institute of Technology, Tobishima Corp., Sekiyado, Chiba 270-0222, Japan
*Public Works Research Institute, Ministry of Land, Infrastructure and Transport, Tsukuba, Ibaraki, Japan; §Graduate School of Sci. and Tech., Kumamoto University, Kumamoto, Japan

ABSTRACT

After recent strong earthquakes in Japan, it has become important to investigate the soundness of structures in the disaster areas. Investigation of the above-ground structures is easily conducted by visual observation, whereas that of substructure, especially pile-foundations installed in deep bearing strata, presents substantial difficulty. In order to investigate the structural integrity of concrete-piles, a procedure to evaluate the damage conditions of the concrete-piles by utilizing an AE technique has been studied. In this paper, the procedure is applied to actual cast-in-place concrete-piles connected with a footing. To generate AE events from the existing cracks, heavy-machinery is utilized. AE activity is monitored both directly and indirectly in the pile. One-dimensional source location is performed to identify locations of the damaged zone and existing cracks. Comparing the results from the AE technique with those of borehole camera, core samples retrieved and wave velocity sounding, it is concluded that the AE technique provides useful information, which could not be obtained otherwise. Thus, the applicability of the proposed AE technique by inducing heavy machinery is confirmed in evaluating the structural integrity of damaged concrete-piles.

1. INTRODUCTION

In pile-foundations, the degree of damage has been discussed based on the existence and width of crack, although the relation between these is still unsolved. Even in techniques for investigating cracks, however, standard techniques have not yet emerged. So far, there exist a few methods to investigate the crack conditions of the piles. The pile integrity test (PIT) (Middendorp and Reiding, 1988), which is a sort of impact-echo test, has been widely applied (Tsukada and Ichimura, 1998). Originally PIT have been developed as a test for quality control of piles after completion to check the sufficiency of design lengths. Instrumentation of PIT is modified with low frequency characteristics less than 1 kHz to apply to longer piles. As for the frequency of 1 kHz, it has not be clarified for its effectiveness in evaluating pile-damage. Consequently, the applicability of PIT is not yet confirmed in assuring the soundness of concrete-piles. Acoustic emission (AE) is known as elastic waves related directly to fracture. As for the fracture process of concrete-piles, AE signals due to both crack initiation and crack growth could be observed (Ohtsu, 1995). In damaged concrete-piles, it is also expected that secondary AE signals due to fretting at existing crack surfaces would be released (Shiotani et al., 1999a). Paying attention to the secondary AE signals, therefore, we have proposed a procedure to evaluate the damage and structural integrity of concrete-piles (Shiotani et al. 1997).

In the present paper, the AE technique is applied to actual cast-in-place concrete piles connected with a footing. The piles have already been subjected to substantial lateral loads and are expected to be heavily damaged (Ishii et al. 1994). To induce AE generation from the

existing cracks, heavy-machinery is utilized. A load is first applied from a side of the footing. Secondly, the heavy-machinery is placed on the footing and dynamic loads are driven into the piles. AE sensors attached on the pile and in a monitoring well were used to detect AE waves and these were examined primarily with respect to their arrival times. One-dimensional source location is performed to identify locations of the damaged zone. Finally, results of the damage locations identified by the AE technique are compared with those by borehole camera observation, core samples retrieved and wave velocities

2. EXPERIMENT

2.1. Site of a Pile Tested and AE Monitoring

An in-situ test was carried out at the reclaimed land of Kishiwada City in Osaka Prefecture. The land was reclaimed from the seabed of 13 m depth in 1992, and composed of sandy gravel of 5 to 10 in SPT N-value, with underlying alternation of cohesive soil and sandy soil. A footing of 9.0 m x 9.0 m x 2.3 m was made on the land on pile foundation, consisting of nine piles. A damage investigation is conducted for the pile No. 9 (1.2 m dia. and 28.9 m length), located at one corner of the footing as shown in Fig. 1. AE waves generated are directly monitored by AE sensors placed on the internal wall of a borehole P9 drilled in the pile. AE activity is also monitored by AE sensors placed in a monitoring well B1, which is excavated in the ground. The center-to-center distance between the pile and well is 1.9 m.

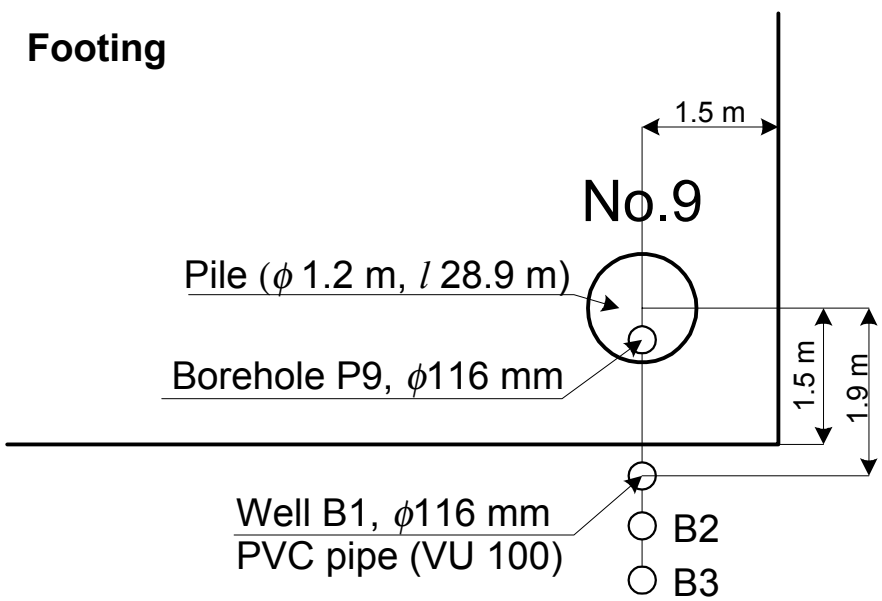

Fig. 1 Plan view of a pile foundation tested.

2.2. AE Monitoring Depth and Methods of AE Sensor Setup

Figure 2 shows an array of AE sensors and zones of AE monitoring. The depth of concern is 11.5 m from the surface of the footing. In the case of direct AE monitoring on the borehole wall, five AE sensors of 60 kHz resonance are arranged in a thin plate of 3 m long, where AE sensor is equally spaced at 50 cm. Thus, a set of AE sensors covers the range of 2 m. The array is placed in step of 1.5 m with 0.5 m overlap down to 11.0 m in stages (zone 1 to 7). For the zone 8 (the

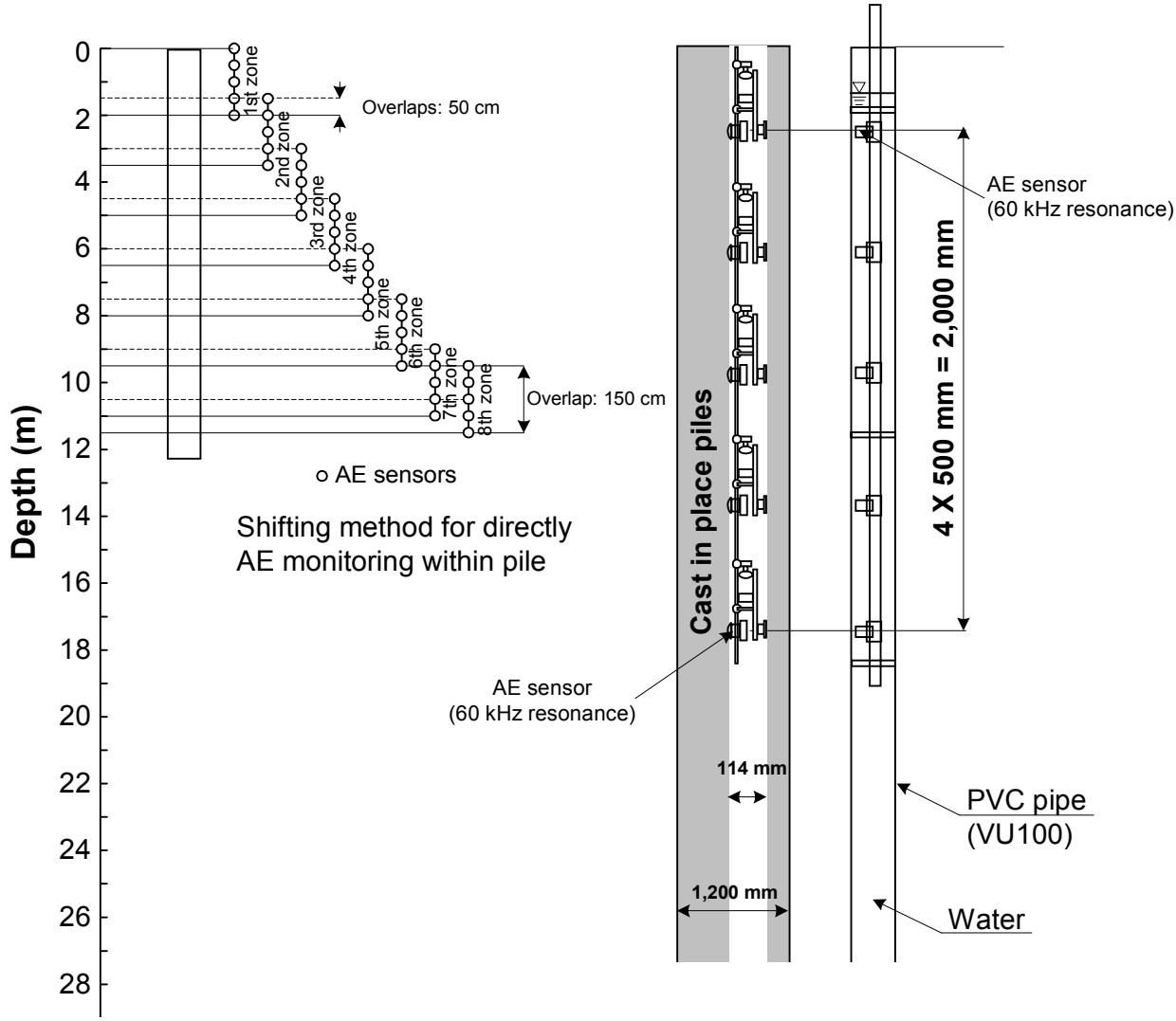

Fig. 2 Array of AE sensors and zones of AE monitoring.

bottom stage), the array is placed between 9.5 m and 11.5 m with an overlap of 1.5 m with the zone 7 immediately above. The borehole monitoring was limited, but covered the depth thought to be the location where pile is severely damaged.

To move and set the sensor array to the design depth, a special device consisting of rubber balls with shifter levers was developed as shown in Fig. 3. The rubber balls can be expanded and contracted by air pressure. The array can move in the borehole when the rubber is expanded and a pile attachment is directed downward with spring tension. To set the sensor at a proper location, the rubber is contracted and the pile attachment is directed to the pile with spring compression. Thus, the device can be firmly placed against the interior wall by the constant pressure due to the spring.

In the case of indirect AE monitoring, the monitoring well was dug and a polyvinyl-chloride (PVC) pipe was buried. Sensor arrangements and the resonant frequency of AE sensors are the same as those of direct monitoring, although the sensors are fixed in a fiberglass-reinforced bar. They are set in design depths as to keep spaces between the sensors and the wall. The indirect

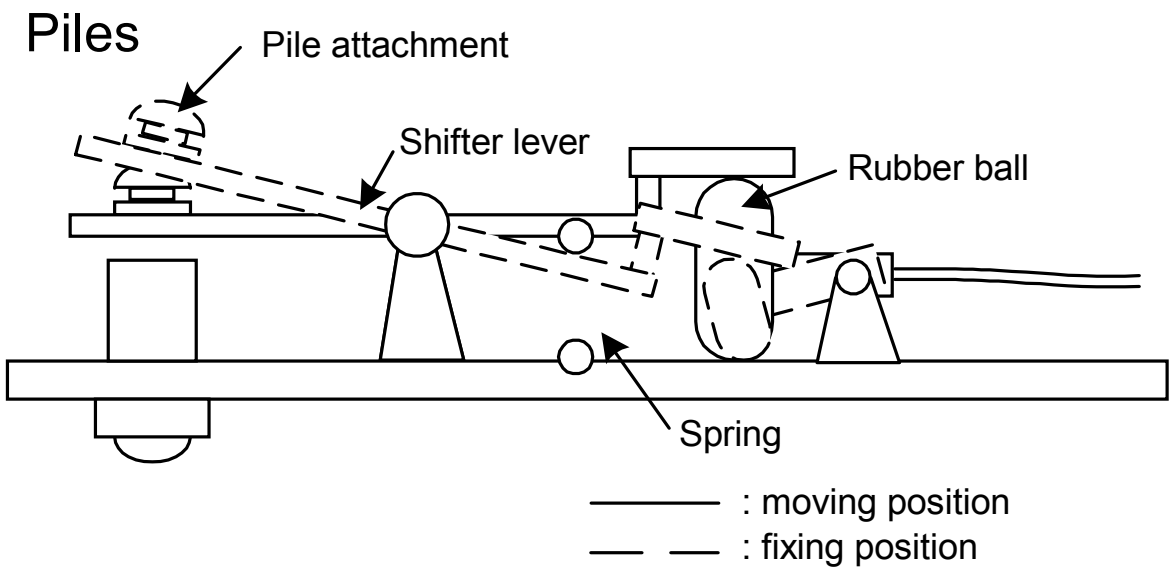

Fig. 3 A mechanical device to move and set AE array in borehole.

AE monitoring is performed by filling the remaining space with water. By adapting this procedure, AE waves detected are successively propagated through ground, PVC pipes and water up to AE sensors. It is confirmed that this sensor arrangement combining PVC pipes and water has twice the sensitivity of the conventional type of steel-waveguide (Shiotani et al, 1999b).

2.3. AE Instrumentation

Ten AE sensors of 60 kHz resonance (PAC) are employed for detecting AE signals, which are amplified by 40 dB in a sensor-integrated preamplifier. The signals of amplitude over 45 dB are processed by a 10-channel MISTRAS AE system (PAC) under the condition of 4 kwords in waveform length and 10 ms dead time.

2.4. Loading Procedure by Heavy-Machinery

To induce AE activity from existing cracks of the pile, a hydraulic excavator of 0.59 m^3 in bucket capacity and 11.8 tons in operating weight is used. A loading procedure by the hydraulic excavator is demonstrated in Fig. 4. Such static loads as in lateral, in diagonal and in perpendicular directions are first applied by putting the shovel of the hydraulic excavator on the side of the footing. Next, the hydraulic excavator is moved on the footing, applying dynamic loads into the piles by arm's expansion and contraction with up-and-down movement.

3. RESULTS AND DISCUSSION

3.1. Observation of Borehole by a CCD Camera and Core Samples Retrieved

To observe the damage state, a charged coupled device (CCD) camera is inserted into the borehole drilled in the pile. Cumulative numbers of cracks observed every 0.5 m are shown by

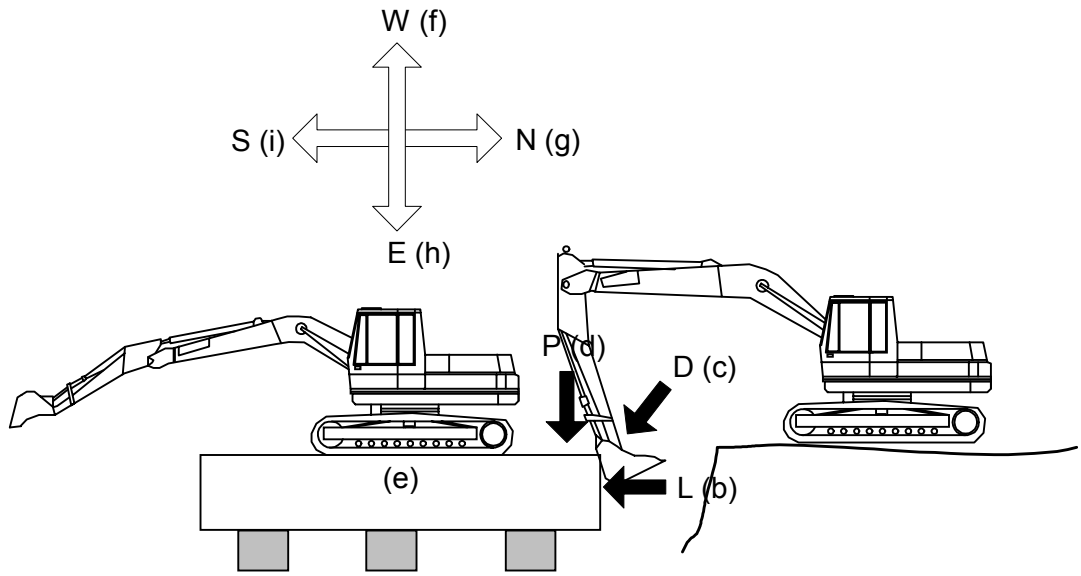

(a) BGN monitoring
(b) Lateral load
(c) Diagonal load
(d) Perpendicular load
(e) Placing machinery on footing
(f) Arm's expanding with up-and-down movements to the west
(g) ditto to the north
(h) ditto to the east
(i) ditto to the south
(j) removal from footing

Fig. 4 A loading procedure by hydraulic excavator.

broken lines in Fig. 5(a). Also given in Fig. 5(b) are pictures of core samples retrieved. It is estimated from Fig. 5(a) that the damage around the pile head is particularly serious. Cracks are also found around 5.0 m, 7.0 m and 10.0 m. Comparable locations of cracks are observed from the core samples and the camera observation. Specifically, in the footing, only two cracks of 2.2 m and 2.3 m corresponding to the pile-head are observed from the camera. From the core samples, however, further numbers of ruptures are obtained above the pile-head. The rupture of the core samples within the footing is believed to be generated when the boring is performed. By considering the fact that there are no similar ruptures due to boring below the footing, it suggests that critical microcracks, which can not be observed by the CCD camera, have already been generated in the footing due to the lateral loads applied prior to this investigation. When the

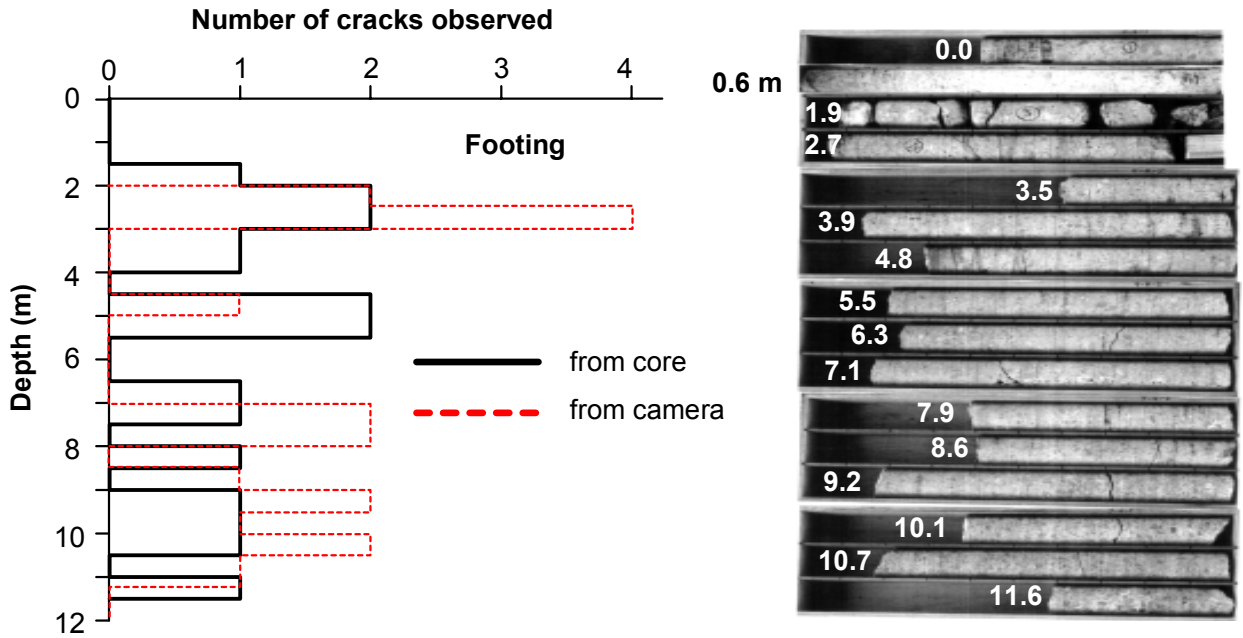

Fig. 5 Condition of cracks in the pile tested. (a) Accumulated Number of cracks with depth, (b) Core samples retrieved.

torsion by the boring was given, coalescence and progress of existing cracks were introduced into the footing. Because the accuracy of crack widths measured by the image processing system with the CCD camera is 0.25 mm, crack widths evaluated by the system are limited to larger than 0.25 mm. Incidentally, it is reported that the width of surface cracks is critically associated with assessment of the deterioration in reinforced concrete structures (Yuyama et al, 1994). According to their report, the crack widths ranging from 0.12 mm to 0.20 mm correspond to the damage degree of "light" or "medium", and crack widths over 0.5 mm correspond to "severe" in deterioration process. Thus, it suggests that the image processing system with the CCD camera adapted may not have sufficient capacity as to evaluate structural integrity of the piles.

3.2. AE Activity

Figure 6 shows AE sources computed by one-dimensional source location algorithm during loading procedure. To examine the integrity of the footing, only the depth from the surface to 2.0 m, zone 1, is evaluated. AE sources are indicated by circles where the magnitude of diameter reflects the number of AE (ringdown) count. AE sources with open circles denote results obtained by the direct AE monitoring, and solid circles show those by the indirect monitoring. It is found from the figure that AE sources are not observed in the period (a) of background noise monitoring. In the period from (b) to (e), static loads are applied to the footing, and AE sources are observed only inside of the footing (down to 2.3 m deep). However, the magnitudes of sources are relatively small. A large number of AE sources of greater magnitude are produced at the onset of dynamic loads due to arm's movement to the north in the period (g), although there are not many emissions during the previous load application (f). The north direction is compatible to that of lateral load applied prior to the investigation. AE sources are also observed under the condition of unloading (i), when the hydraulic excavator is removed. These emissions during unloading are thought to be produced from friction along the pre-existing cracks. This implies that there obviously exist macroscopic shear cracks in the pile. AE activity during unloading is thus expected to be a damage index in concrete structures (Shiotani el al., 1999a;

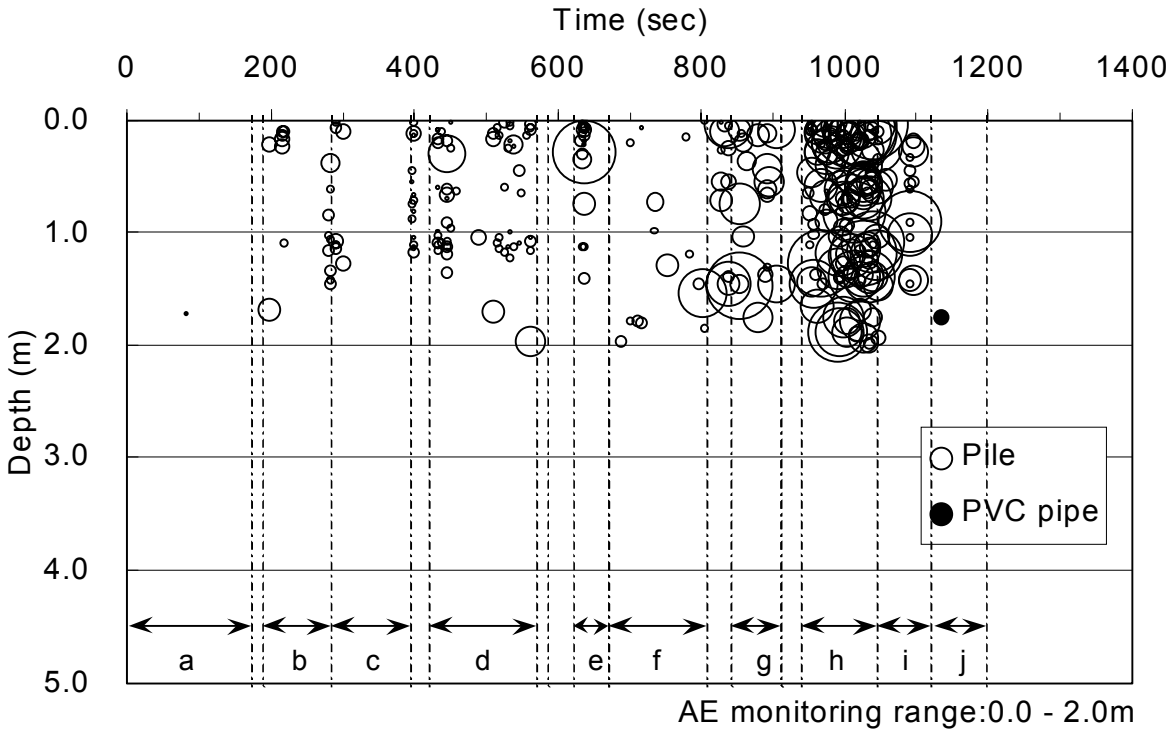

(a) BGN, (b) Lateral load, (c) Diagonal load, (d) Perpendicular load, (e) Placing machinery on footing, (f) Arm expanding with up-and-down movement to the west, (g) ditto to the north, (h) ditto to the east, (i) Removal from footing, (j) BGN

Fig. 6 One-dimensional AE sources during loading procedure in zone 1.

NDIS 2421, 2000). AE sources during dynamic loading may contain mechanical noise signals generated on the footing surface due to the motion of the hydraulic excavator. However, AE events within the footing are actively generated, and thus damage is reasonably evaluated. The degree of damage is further verified by results of core samples retrieved.

Figure 7 shows cumulative AE parameters at every 5-cm depth. Results of accumulated AE events by direct AE monitoring, AE counts by direct AE monitoring, the averaged AE count by direct AE monitoring, and the averaged AE counts by indirect AE monitoring are given. From Figs. 7 (a) and (b), it is found that AE activities are intensely observed at the locations of 1.0 m to 1.5m and around 2.0 m. Intensive AE activities are also observed from 3.0 m to 3.5 m, and around 5.0 m, although the cumulative number is relatively small. It becomes clearer by expressing the average of counts as shown in Fig. 7 (c). The averaged counts is given by, accumulated ringdown counts divided by accumulated AE events at every 5-cm depth. Large counts of AE events are remarkably generated in areas from 3.0 m to 3.5 m, 4.2 m to 5.0 m and 6.3 m to 7.0 m except for the footing. According to a result of indirect AE monitoring in Fig. 7 (d), the averaged counts are large around 1.8 m, 3.2 m and 4.8 m, although arrival time of AE waves are out of the allowable time difference between the wave velocity and the pile-AE sensor arrangement. These AE activities are supposed to be generated from ground deformation, which is strongly related to coalescence and progress of cracks in the piles due to dynamic loads. Therefore in direct AE monitoring, the monitoring well should be set in range where ground deformation due to pile-behavior with external loads could be reached.

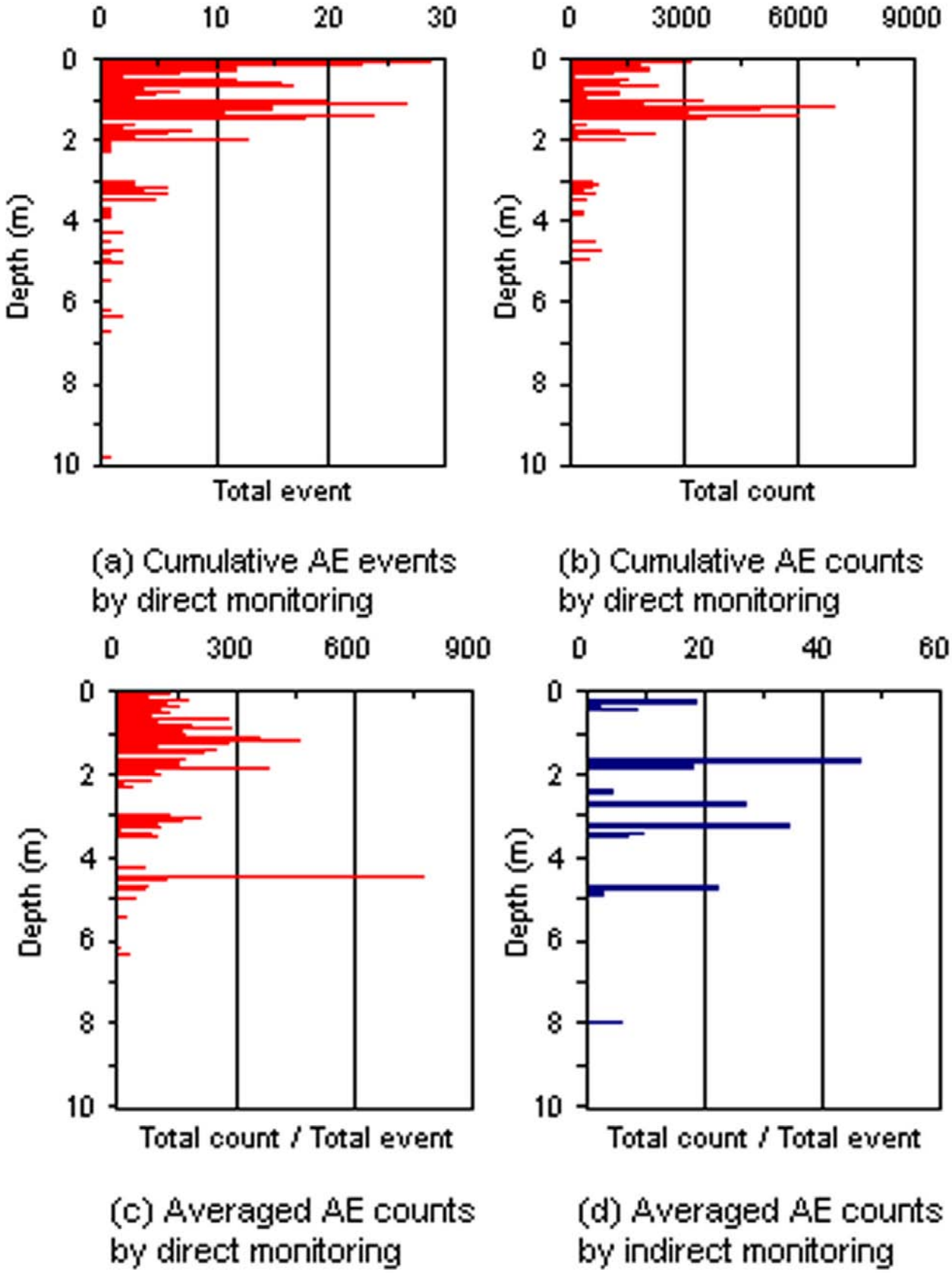

Fig. 7 Cumulative AE parameters at every 5-cm depth.

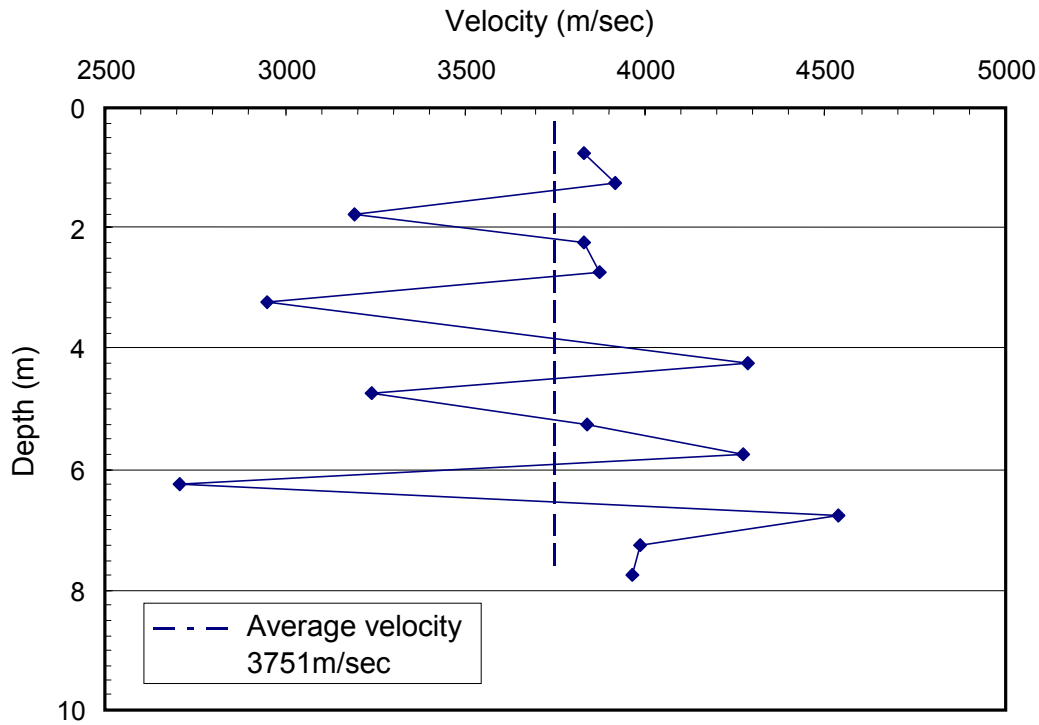

Fig. 8 Distribution of wave velocities in the pile.

A wave-velocity sounding is performed by using AE sensors placed in the pile. Elastic waves are artificially generated by hammering the surface of the footing with a steel hammer. Figure 8 shows the distribution of wave velocities in the pile, which is computed from the arrival times at the AE sensors. In the figure, the wave velocity between 1.0 m and 1.5 m, for example, is plotted at depth of 1.25 m. In general, it is well known in cast-in-place concrete piles that a zone where the lower wave velocity is obtained in the piles, the lower strength and density are expected. This is because the wave velocity is strongly related to the mechanical properties of concrete materials. Thus, the zones of the pile showing extremely low velocities are thought to be identical to those of damaged pile. It is found from Fig. 8 that portions of lower wave velocity range from 1.5 m to 2.0 m, 3.0 m to 4.0 m, 4.5 m to 5.5 m, and 6.0 m to 6.5m. These locations are judged to be damaged and in remarkable agreement with the damaged locations evaluated by AE activity.

All estimated locations of damage by several techniques are summarized in Fig. 9. The following findings are derived.

1) Damages below the pile head are observed by a CCD camera and in core samples.
2) From results of AE sources and wave-velocity sounding, existence of critical cracks within the footing is expected, although they are not possibly observed by the CCD camera. From observation of core samples retrieved, it is found that there possibly exist the critical cracks within the footing.
3) Damage is estimated at 3.0-m depth by AE sources. This location agrees remarkably with that by the wave-velocity sounding, although the CCD camera is unable to observe it.
4) Damage around 5.0-m depth is estimated by all techniques.
5) Damages ranging from 6.5 m to 7.0 m are observed from AE sources. These locations approximately correspond to those of the CCD camera and the wave-velocity sounding.

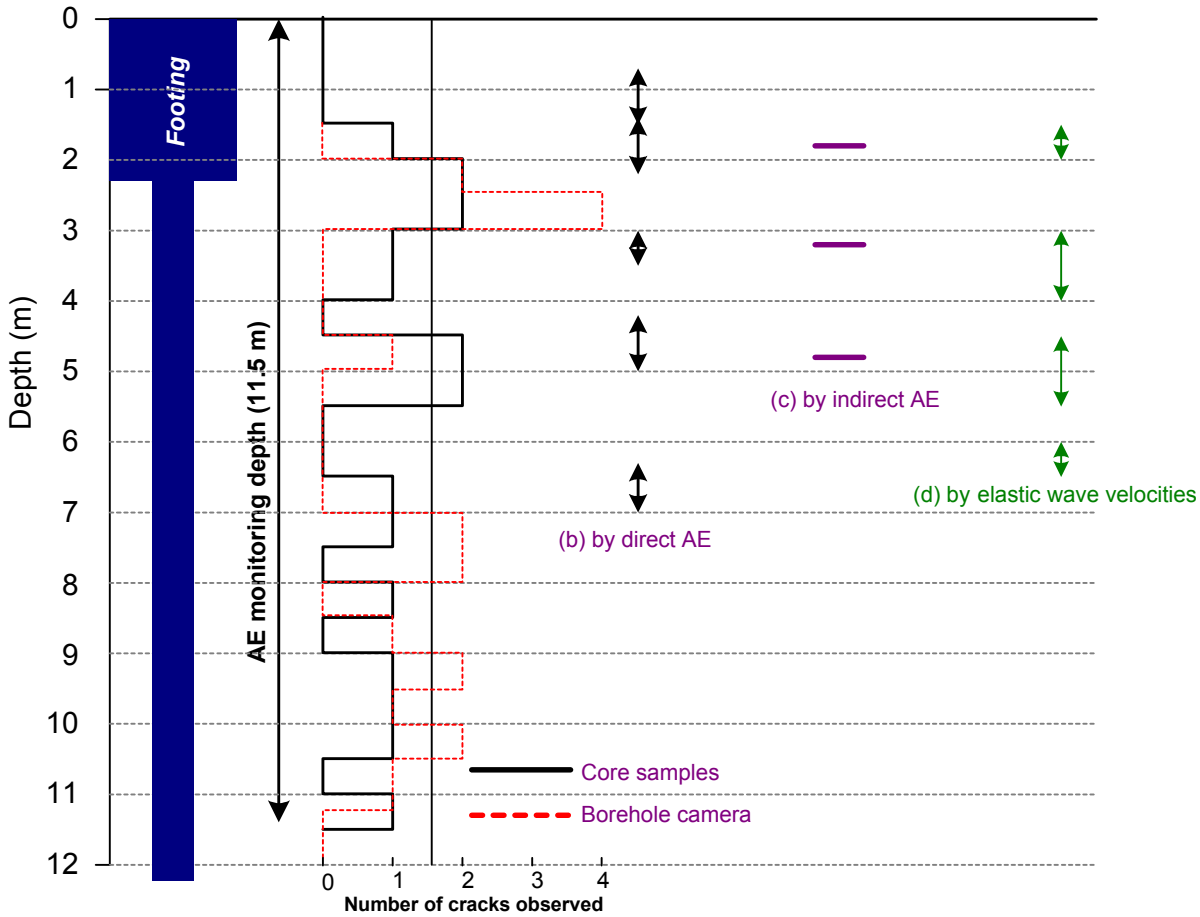

Fig. 9 Locations of damage evaluated by several techniques.

4. CONCLUSIONS

It is found that applications of static and dynamic loads by heavy-machinery is practical to generate AE events from damaged and cracked zones of concrete-piles. Results are concluded as follow:

1) For the diagnosis of damaged concrete-piles, it is necessary to develop the image processing system by the CCD camera with more than 0.1 mm resolution.
2) Because AE events within the footing are actively generated due to dynamic load, the damage of a footing could be estimated. This is confirmed by the results of core samples retrieved. It is promising to apply the AE technique to actual civil structures that potentially experienced earthquake damage.
3) Identification of damaged locations can be examined from the intensity of AE sources, along with the average of AE (ringdown) counts.
4) Zones of slow wave velocity remarkably conform to those estimated as damaged by the presence of AE sources.

As a result, it is apparent that the AE technique is effective to damage evaluation of concrete-piles. The result of the AE technique provides useful information, which could not be evaluated by the other observation. Although the damage of the footing evaluated by AE sources are not

identical to actual cracks observed by the CCD camera, there exists the zone of slow wave velocity and the ruptures of the core samples retrieved. Because the footing is firmly connected with reinforcing steel bars to the piles, the damaged zones estimated would be reasonably identified. Thus, the applicability of the proposed AE technique by vibration-inducing heavy-machinery is confirmed.

ACKNOWLEDGEMENTS

The present study has been achieved jointly with Public Works Research Institute of Ministry of Land, Infrastructure and Transport, Public Works Research Center, Hanshin Expressway Public Corporation, and 12 private companies. The authors would like to express their gratitude to the institutions and all those who were involved in this joint research.

REFERENCES

Y. Ishii, Y. Maekawa, N. Murata, K. Yonemura and H. Mizoguchi (1994), "Large Lateral Displacement Experimental Studies of Grouped Cast-in-Place Piles," Proceedings of the 29th Japan National Conference on Geotechnical Engineering, The Japanese Geotechnical Society, pp. 1603-1606. (in Japanese)

P. Middendorp and F. J. Reiding (1988), "Determination of Discontinuities in Piles by TNO Integrity Testing and Signal Matching Techniques," Proceedings of the 3rd International Conference on the Application of Stress-Wave Theory to Piles, pp. 33-43.

NDIS (Standard of the Japanese Society for Non-Destructive Inspection) 2421 (2000), "Recommended Practice for in Situ Monitoring of Concrete Structures by Acoustic Emission," The Japanese Society for Non-Destructive Inspection, 24 pages.

M. Ohtsu (1995), "The History and Development of Acoustic Emission in Concrete Engineering," Concrete Library of JSCE No. 25.

T. Shiotani, N. Sakaino, M. Ohtsu and M. Shigeishi (1997), "Damage Diagnosis of Concrete Piles after Earthquakes by Acoustic Emission," Proceedings of Forth Far East Conference on Nondestructive Testing, Korean Soc. Nondest. Testing, pp. 579-588.

T. Shiotani, M. Shigeishi and M. Ohtsu (1999a), "Acoustic Emission Characteristics of Concrete-Piles," Construction and Buildings Materials, **13**, 73-85.

T. Shiotani and M. Ohtsu (1999b), "Prediction of Slope Failure Based on AE Activity," Acoustic Emission: Standards and Technology Update, ASTM STP 1353, ed. S. J. Vahaviolos, pp.156-172.

Y. Tsukada and Y. Ichimura (1998), "Application of Integrity Tests for Quality Control of Cast-In-Situ Piles," Journal of Geotechnical Engineering, JSCE, No.603/ III-44, 139-146. (in Japanese)

S. Yuyama, T. Okamoto, M. Shigeishi and M. Ohtsu (1994), "Quantitative Evaluation and Visualization of Cracking Process in Reinforced Concrete by Moment Tensor Analysis of Acoustic Emission," Materials Evaluation, **53**, 751-756.

ACOUSTIC EMISSION MONITORING OF CLOSELY SPACED EXCAVATIONS IN AN UNDERGROUND REPOSITORY

THOMAS SPIES and JÜRGEN EISENBLÄTTER*

Federal Institute for Geosciences and Natural Resources (BGR), D-30655 Hanover, Germany
* Gesellschaft für Materialprüfung und Geophysik mbH, D-61239 Ober-Mörlen, Germany

ABSTRACT

Acoustic emission (AE) measurements were carried out as a contribution for the evaluation of the hydraulic integrity around and the stability of cavities in salt rock. The locations of AE events and their magnitudes were determined using a network of 24 sensors. High AE activity regarding the rates of events was found between the closely spaced rooms. These concentrations of locations appear in form of shear bands. The exact location of a small drift connecting two rooms in the level of their roofs could be reconstructed by the AE activity around its contour.

1. INTRODUCTION

In the field of underground disposal of radioactive waste, the evaluation of the hydraulic integrity of the rock and the stability of the cavities is an important task. Microcracking changes the microstructure of the rock so that permeability might increase. Macrofracturing can lead to stability problems. Results of laboratory experiments and geomechanical model calculations are used to derive conclusions on integrity and stability. In any case, *in-situ* measurements have to be performed to test these results and conclusions especially in complex situations regarding the geometry of cavities, the geological structure or the material behavior of the rock [1].

Acoustic emission (AE) measurements in the rock are the only method to detect micro-cracking directly by registration of high frequency seismic or acoustic waves radiated during crack generation. The present AE measurements were performed in rock salt, which is a favorable rock for radioactive waste disposal underground as it is capable of creep deformation without occurrence of fracture in a wide range of the conditions of state. Nevertheless, in presence of high deviatoric stresses microcracks are generated. Dilatancy of rock salt - the irreversible volume increase caused by microcracking - has been well investigated with laboratory experiments [2] providing the stress conditions at the onset of dilatancy (dilatancy boundary). At stress conditions above the dilatancy boundary, the progressive generation of microcracks results in an increase of permeability and in the occurrence of creep failure as long-term consequences.

AE measurements have been successfully applied to monitor dilatancy around cavities (excavation damaged zone) as well as micro- and macrofracturing at prominent geological boundaries in the rock [3], [4]. In this paper results of monitoring in a mine segment with closely spaced cavities are presented where high stress concentrations occur between the cavities.

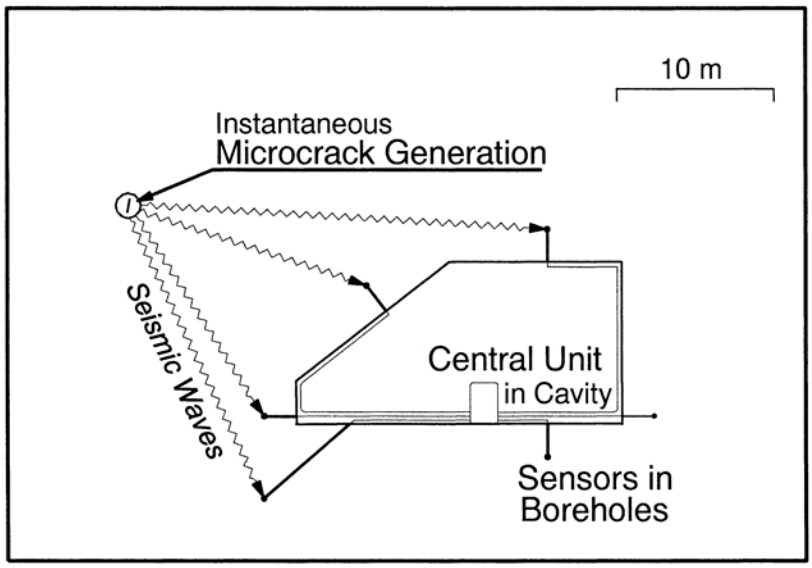

Fig. 1. Principle of acoustic emission measurements in the rock.

2. MEASURING PRINCIPLE AND ON-SITE EVALUATION OF AE EVENTS

Figure 1 displays the principle of AE measurements in a vertical cross section. The piezoelectric sensors are installed in boreholes drilled from the cavities. 24 sensors have been connected to the system used. The seismic signals are recorded in the frequency range from 1 to 100 kHz. Using this range high sensitivity and location accuracy is achieved compared to microseismic investigations in the frequency range of 0.01 to 1 kHz. Thus cracks with linear dimensions of some millimeters to centimeters can be detected.

The locations of AE events are determined on site by inversion of the travel times of P-waves and S-waves, which are extracted from the signals. This is done in different steps. After pre-processing of the signals by filtering and smoothing operations, in the first step, the P-wave onsets are automatically picked using high-quality signals only, i.e. signals with high signal-to-noise ratio. From these P-wave onsets a first estimation of the source coordinates is made using an iterative least-squares procedure. If the residual error is larger than 0.8 m, the onsets with the largest residues are stepwise eliminated and a new solution is calculated until the residual error falls below the said limit.

In order to be able to locate sources outside of the sensor network, we also consider the S-wave onsets. Therefore, we automatically pick the S-wave onsets in the time interval expected due to the result of the location using P-wave onsets only. In the second step of source location, we use the found S-wave onsets together with the remained P-wave onsets. P-wave and S-wave onsets with large residues are again eliminated until the residual error falls below 0.8 m. Locations are considered valid only if at least ten onsets (P-wave or S-wave) remain.

In spite of the complex geometric situation with AE sensors in the vicinity of closely spaced excavations and resultant masking of direct wave propagation paths, we obtain a location accuracy of about one meter in distance up to 50 m around the sensor network, using the described procedure.

A measure of strength analogue to the magnitude in seismology is determined on site as well. The maximum amplitudes A of the 24 sensor signals and the distances r of the AE source from the sensors are used for this purpose. We define the mean amplitude at a reference distance of 50 m from the source as the AE magnitude of the source. This magnitude is specified in dB with the usual reference voltage of 1 μV prior to amplification.

In the case of body wave propagation, we may presume the following relationship between amplitude A and distance r:

$$A \propto [\exp(-\alpha r)] / r,$$

where α is the wave attenuation coefficient covering the effects of intrinsic absorption and scattering. In a semi-logarithmic function of the product A·r versus r of all sensors a linear relationship is obtained as expected and a straight line is fitted to the data. The value of this straight line at the reference distance of 50 m is determined and regarded as the magnitude of the AE event. An example for the determination of magnitude is displayed in Fig. 2. The amplitudes are specified in dB, which is a logarithmic measure: $20 \cdot \log (A/A_0)$ with normalization amplitude A_0. The distance r as a factor of the product A·r is normalized as well using the reference distance. The crosses in Fig. 2 denote the maximum signal amplitudes of the single sensors whereas the rectangles denote the amplitudes after sensor corrections. The corrections for the single sensor are obtained by minimization of the deviations of its signal amplitudes from the mean trend of all sensors when a large number of AE events are considered. Thus the scatter of the amplitude data is reduced slightly. In the example of Fig. 2 the magnitude is determined to be 60 dB. It has to be emphasized that this procedure results in relative magnitude, which cannot be compared to the values of seismology.

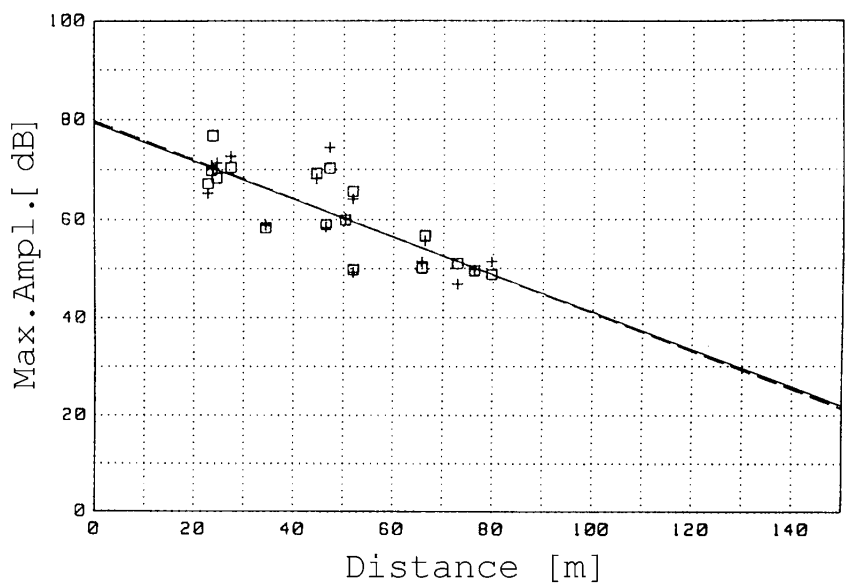

Fig. 2. Determination of magnitude of an AE event defined as the amplitude value at the reference distance of 50 m using the maximum signal amplitudes at the single sensors. In this example a magnitude of 60 dB is obtained.

3. DESCRIPTION OF OPERATIONAL SITE

The salt mine of Morsleben located between the towns of Braunschweig and Magdeburg in northern Germany is used as a repository for low level radioactive waste since 1978. It is a salt deposit with folded thick strata of rock salt in succession with strata of anhydrite, potash and salt

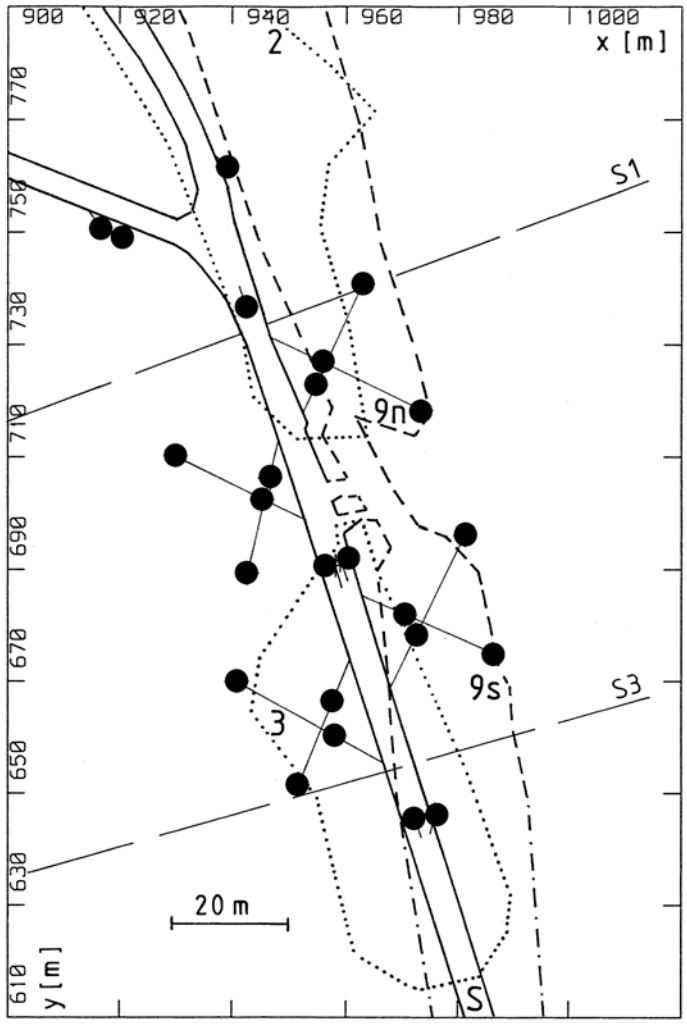

Fig. 3. Plan view of the monitored region with the projection of three levels plotted one upon another: upper level in dashed lines (Rooms 9n and 9s), intermediate level in solid lines (Drift S), lower level in dotted lines (Rooms 2 and 3). The AE sensors in the boreholes are denoted by the black dots. The profile lines of the vertical cross sections S1 and S3 through the cavities are indicated (see Figs. 4 and 5).

clay [5]. The waste is disposed of in large rooms mainly in rock salt. In specific segments of the mine, geomechanical investigations are performed to characterize the rock behavior by strain and stress measurements, hydraulic measurements and AE measurements.

Figure 3 shows a mine segment in a plan view (horizontal projection) where cavities with close spacing were mined in rock salt about 70 years ago. The orientation of the y-axis is south to north and of the x-axis west to east. In this plan view, three different levels are displayed one upon another in a rather complex arrangement: Rooms 9n and 9s at the upper level in dashed lines, the drift S at the intermediate level in solid lines and Rooms 2 and 3 at the lower level in dotted lines. To clarify this complex figure, the vertical cross-section (vertical projection in Figs. 4 and 5) along the profile line S1 shown in Fig. 3 can be used. In Figs. 4 and 5, the large Room 9n at the upper level, the drift S at the intermediate level and the large Room 2 at the lower level are displayed using the same signatures as in Fig. 3. The vertical section of profile line S3

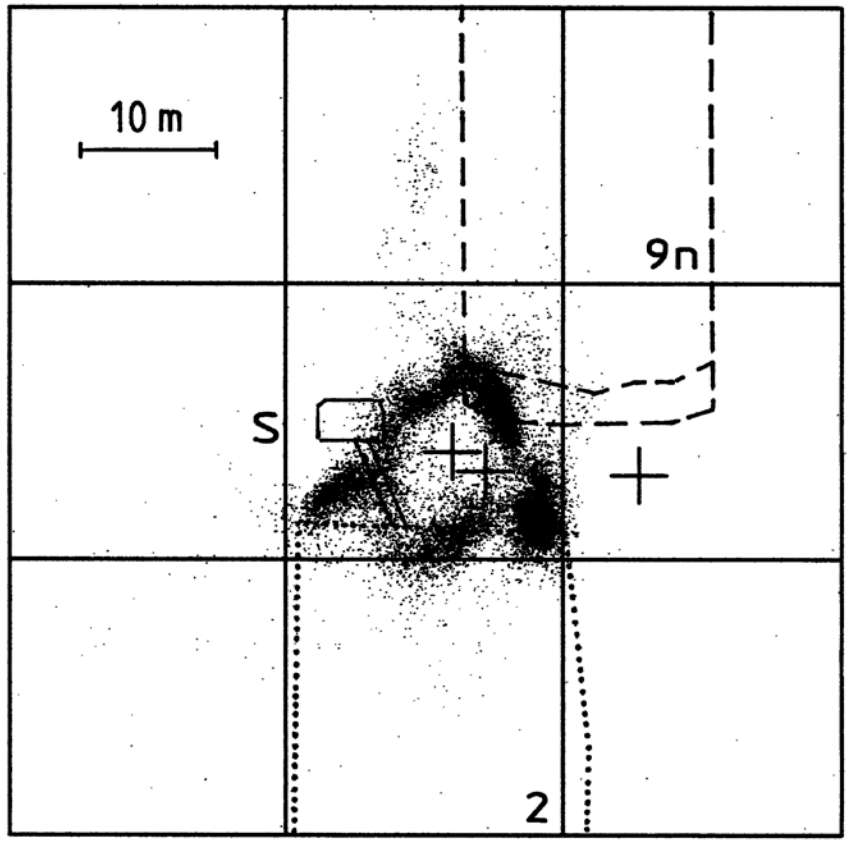

Fig. 4. Cavities in the vertical cross section S1 and locations of AE with magnitudes M > 0 dB as dots (data of one month, 17,241 events).

exhibits a similar arrangement for the southern vertical row of cavities in Fig 3. The average depth level of the cavities displayed is 500 m. In the drift of the intermediate level, fissures in the walls and floor heave are observed. The opening of the fissures is controlled by strain measurements, which result in opening rates of 0.2 mm/annum (mm/year). To monitor this situation, an AE network has been installed. The boreholes in Fig. 3 are 3 to 30 m long. The locations of the sensors are denoted by the black dots. The deeper boreholes are equipped with two sensors. All boreholes were drilled from the drift as the large rooms are not accessible with drilling equipment. So only AE events in the region between the large rooms can be located. From the geomechanical point of view, this is no disadvantage as the stress concentrations are expected between the large rooms.

4. RESULTS

As an example for the obtained AE locations, Figs. 4 and 5 show data of a spatial interval with a thickness of 20 m in the direction perpendicular to profile S1. The data of this interval is projected into the vertical cross section S1. Figure 4 contains all events regardless of magnitude whereas in Fig. 5 only larger events with magnitudes M > 40 dB are included. Some of the microcracks seem to be located inside the openings. At one hand, this can be explained by variations of the geometry of the rooms perpendicular to the profile line S1. In this 20-m horizontal interval the level of the floor of Room 9n is varying as indicated by the two lines in Figs. 4 and 5. Furthermore Room 2 has a more irregular shape of the roof compared to the

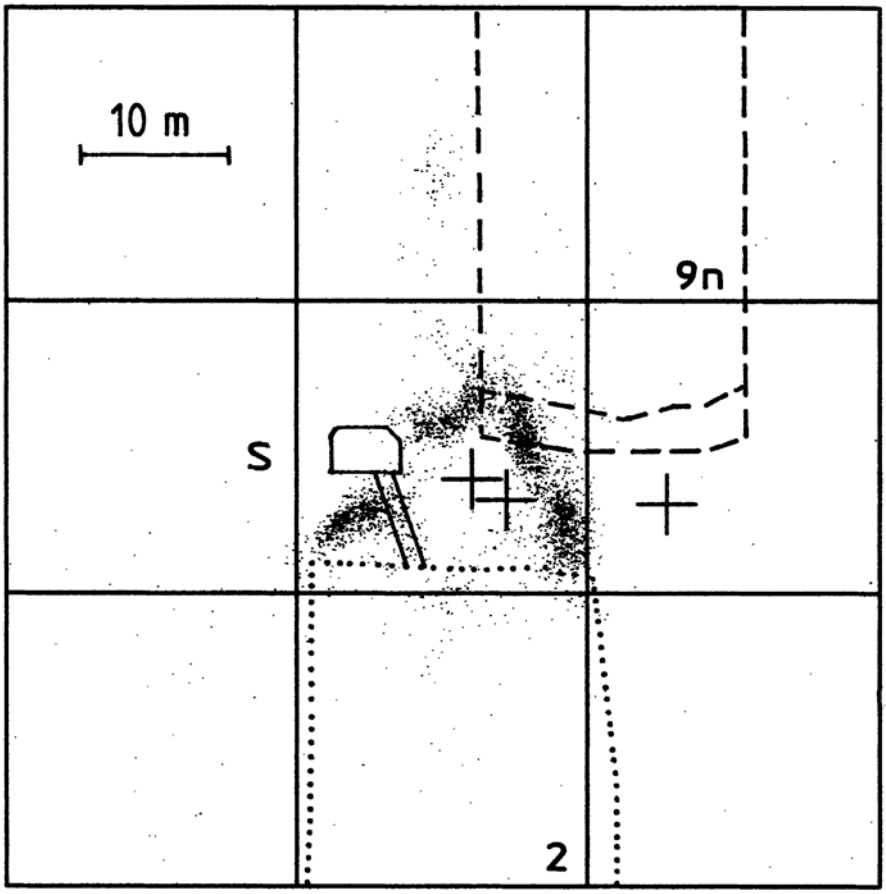

Fig. 5. Cavities in the vertical cross section S1 and locations of AE with magnitudes M > 40 dB as dots (data of one month, 3320 events).

information provided by standard mine survey. The crosses in Figs. 4 and 5 denote the locations of sensors in the horizontal interval.

The locations in Figs. 4 and 5 show dense accumulations in the shape of several narrow bands between the rooms. Outside of these shear bands no significant AE activity can be observed. In the bands intensive microcracking takes place indicating a high geomechanical load. Comparable results are obtained by geomechanical model calculations for such arrangements of cavities. Deviatoric stresses and deformations are found to be high in the region between the openings and they also show the band-like spatial distribution. The locations of events with M > 0 dB (Fig. 4) and M > 40 dB (Fig. 5) indicate that there are no or only few stronger events close to the openings. This may be explained by a high degree of damage close to the contours so that the storage of elastic energy is limited and the radiated seismic energy of crack generation is lower compared to the less damaged rock.

Figure 6 is a plan view, showing AE locations in a 2-m thick vertical interval between the roofs of Rooms 2 and 3 and the floor of Drift S. Here, only the contours of the drift at the intermediate level in solid lines and Rooms 2 and 3 at the lower level in dotted lines are given.

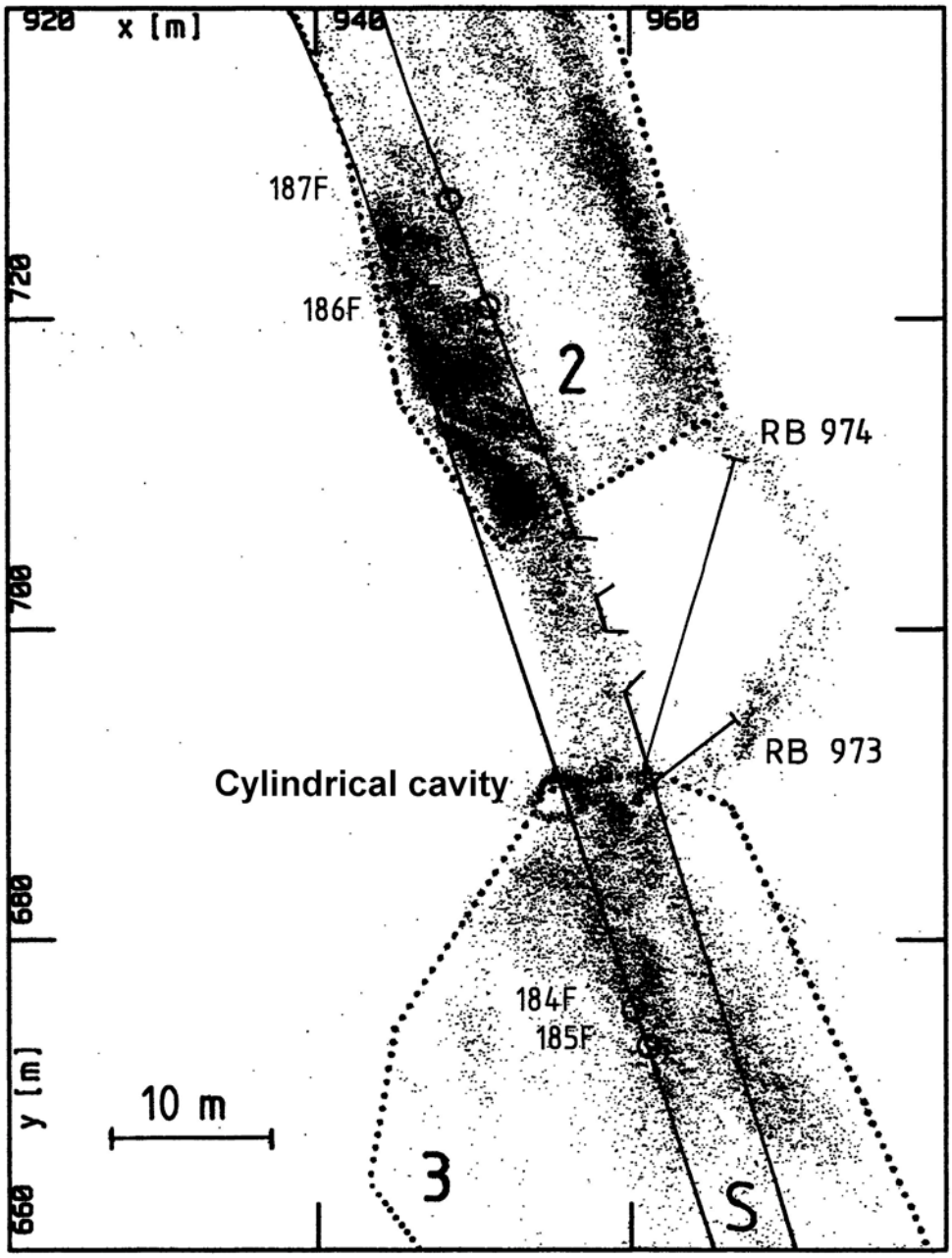

Fig. 6. Plan view of intermediate level (Drift S) and lower level (Rooms 2 and 3). The AE locations of a 2-m thick depth interval between the floor of the intermediate level and the roof of the lower level are displayed (data of one year, 72,902 events). Two boreholes were drilled from the drift to verify the existence of the bow shaped small drift. Strain measurements at fissures in the walls are marked by small circles.

The contours have been revised in comparison with the results of standard mine survey (see Fig. 3) to be consistent with the observed spatial distribution of AE. Again, it can be seen that the AE activity is limited to the rock directly above the roof of the lower rooms. The AE locations also map smaller loaded elements of the arrangement of cavities indicating the achieved accuracy of location of less than 1 m. For instance, a roughly cylindrical cavity with a vertical axis and with

a diameter of 2 m can be recognized as a ring of AE (see notation in Fig. 6). This cavity is a vertical connection from the floor of drift S down to the roof of Room 3. Furthermore specific activity outside the cavities which were documented in the mine's maps, in the shape of a bow is observed connecting the corners of Rooms 2 and 3. From detailed analysis of the locations, it was concluded that there could be another small drift causing this unexpected activity. As the lower rooms are not accessible to look for such a feature this had to be proofed by two boreholes (see notation RB973 and RB974 in Fig. 6). The boreholes reached the proposed drift in the predicted locations within the accuracy of better than 1 m.

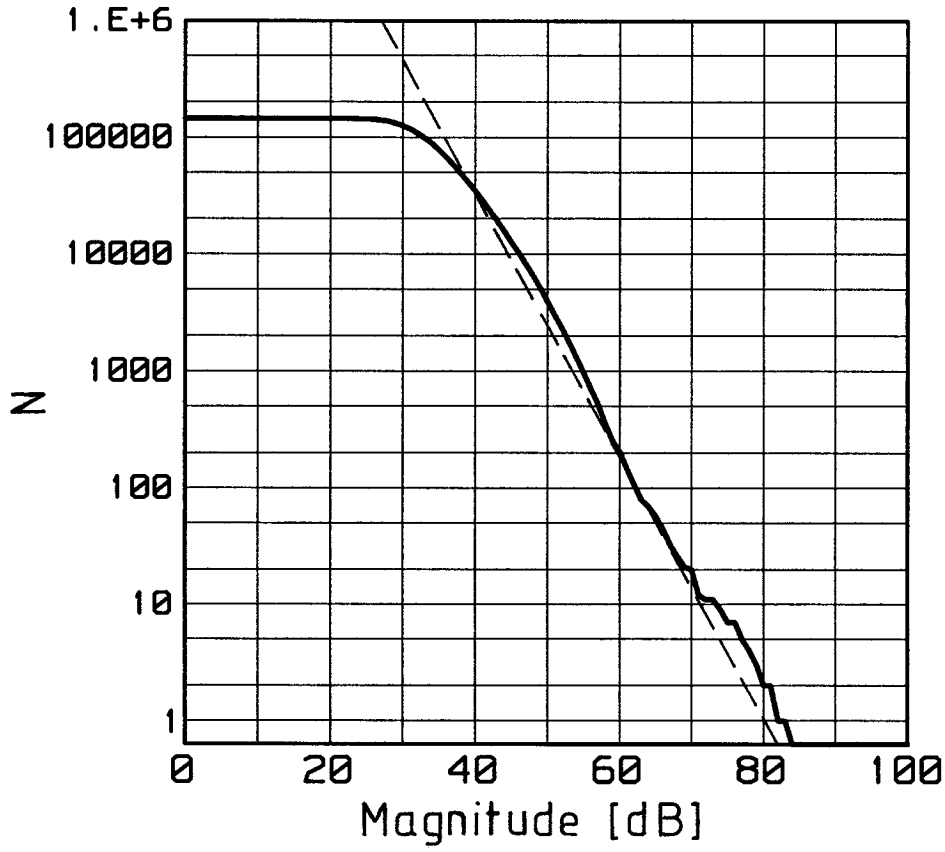

Fig. 7. Cumulative frequency distribution of magnitudes of AE events from a sub-volume of the monitored region (data of one year, about 145,000 events).

As an example for the frequency distributions of AE magnitudes, Fig. 7 displays data of the region below Drift S and the roof of Room 2. The locations of the cavities and the AE can be found in Figs. 3 and 4. The cumulative frequency distribution in Fig. 7 has a lower bound value at about 30 dB, which marks the sensitivity of the AE network for weak events. The largest recorded magnitudes are around 80 dB. Regarding the slope of the curve and the largest values of magnitude, this distribution is similar to results of other AE investigations characterizing dilatancy around cavities in rock salt [3]. At the operational site no significant change of the magnitude distributions within the monitoring period of more than two years could be observed.

5. SUMMARY AND CONCLUSIONS

AE measurements were carried out to monitor microcrack generation between closely spaced cavities in an underground repository for low level radioactive waste. The locations of AE events and their magnitudes were determined. Regarding the rates of events high AE activity is found between the large rooms. The concentrations of microcracks in form of shear bands are in agreement with the results of geomechanical calculations. The exact location of a small drift connecting two rooms in the level of their roof could be reconstructed by the AE activity around its contour.

From the obtained results on the microcrack generation, it can be concluded that permeability has increased between the large rooms and it will further increase due to continuing microcracking. The AE activity regarding the rates of AE events, their locations and their magnitudes are not varying strongly during the monitoring period of more than two years. So it is concluded that no change of the geomechanical situation took place within this period and no sudden change will take place in the near future. This is also confirmed by the results of geomechanical model calculations. On the other hand, it is concluded that the roofs of Rooms 2 and 3 have to be supported to preserve their stability permanently, e.g. by backfilling of the rooms.

REFERENCES

1. N. Diekmann, H. Schnier and T. Spies, "Geotechnical measurements for safety assessments in different development phases of radioactive waste repositories in salt," *Proc. of GeoEng2000*, Melbourne, (2000), Paper 0788.
2. U. Hunsche and A. Hampel, "Rock salt – the mechanical properties of the host rock material for a radioactive waste repository," Engineering Geology **52**, (1999), 271 – 291.
3. T. Spies and J. Eisenblätter, "Crack detection in salt rock and implications for the geomechanical situation", *Proc. 3rd Intl. Conference on Mechanics of Jointed and Faulted Rock*, Vienna, ed. Rossmanith, H., (1998), Balkema, Rotterdam, pp. 405 - 410.
4. T. Spies and J. Eisenblätter, "Micro- and macrofracturing at the boundary of rock salt and anhydrite", *Proc. 9th Intl. Congress on Rock Mechanics (ISRM)*, Paris, eds. Vouille, G., and Berest, P., (1999), Balkema, Rotterdam, pp. 1071 – 1074.
5. J. Behlau and G. Mingerzahn "Geological and tectonic investigations in the former Morsleben salt mine (Germany) as basis for the safety assessment of a radioactive waste repository," EUG 10, Strasbourg, J. Conf. Abst. **4**: 518, Cambridge, (1999), ISBN 1362-0886, and Special issue, Engineering Geology, 'Geosciences and Nuclear Waste Disposal', in press.

ACOUSTIC EMISSION MONITORING OF THE JAS 39 GRIPEN COMBAT AIRCRAFT

DAN LINDAHL and MARKKU KNUUTTILA

CSM Materialteknik AB, Box 1340, 581 13 Linköping, Sweden

ABSTRACT

JAS 39 Gripen is a lightweight multirole combat aircraft partly manufactured from carbon-fibre reinforced plastic (CFRP). With an aim to verify the strength of the airframe, an extensive test programme has been carried out at Saab Aerospace in Linköping, Sweden. This paper presents some results and experiences from two of these tests, done on two separate, almost complete airframes, which were monitored by acoustic emission (AE). The AE equipment used is a 72-channel system.

The first test was the full-scale static structural test. AE was used to monitor the wings and the vertical stabiliser, which are primary manufactured from CFRP. The main purpose of the AE monitoring was to obtain information on sub-critical damage, which might occur during loading of the wings and vertical stabiliser. With the AE system we were able to detect and localise damage at an early stage and to prevent unexpected failure occurring during testing at moderate load levels. Localised areas of damage pointed out by AE were confirmed by traditional non-destructive testing (NDT). The AE monitoring did not cause any false alarms and no additional damage was detected by other NDT techniques.

The second test was the full-scale fatigue test. Only metal parts of the airframe such as the three main wing attachment bulkheads, the side panels of the fuselage and some joints were monitored by AE. The main reason for using AE monitoring this time was to lower the risk that an undetected fatigue crack would grow critical causing failure or damages hard to repair. During testing of the originally planned 16,000 flight hours, which equals four life times, no damage have been detected in the monitored parts neither with AE nor traditional NDT. Cracks induced by a testing tool in an adjacent area were on the other hand successfully detected by AE, which clearly illustrates its potential to detect damage.

1. INTRODUCTION

JAS 39 Gripen, the world's first lightweight multirole combat aircraft, is the result of a joint development program by the Swedish aircraft industry. The designation JAS is a Swedish abbreviation for Fighter, Attack and Reconnaissance. Each JAS 39 aircraft will perform all three missions. As of September 1999, 75 JAS 39 Gripen aircraft are in service within the Swedish airforce and a total of 204 aircraft have been ordered.

With an aim to verify the strength of the airframe as demanded by the Swedish customer FMV (Swedish Defence Material Administration), an extensive test programme has been carried out from simple specimens and minor components to joints and complex structures. The testing procedures agreed on by Saab and FMV basically follows the specifications issued by the US Ministry of Defence, MIL-SPEC. As the crowning achievement, two full-scale tests were done

on two separate, almost complete JAS 39 Gripen airframes. The first test, the full-scale static structural test, was carried out in 1992-93. In Fig. 1, the test rig used to load the airframe is shown. At this overarching test a total of 35 different load cases were tested gradually to higher load levels, starting at 100 % of limit load. The second test, the full-scale fatigue test, was carried out in 1993-99. At this test a flight spectra built upon 56 different missions was used repeatedly to symbolise four lives of 4000 flight hours each.

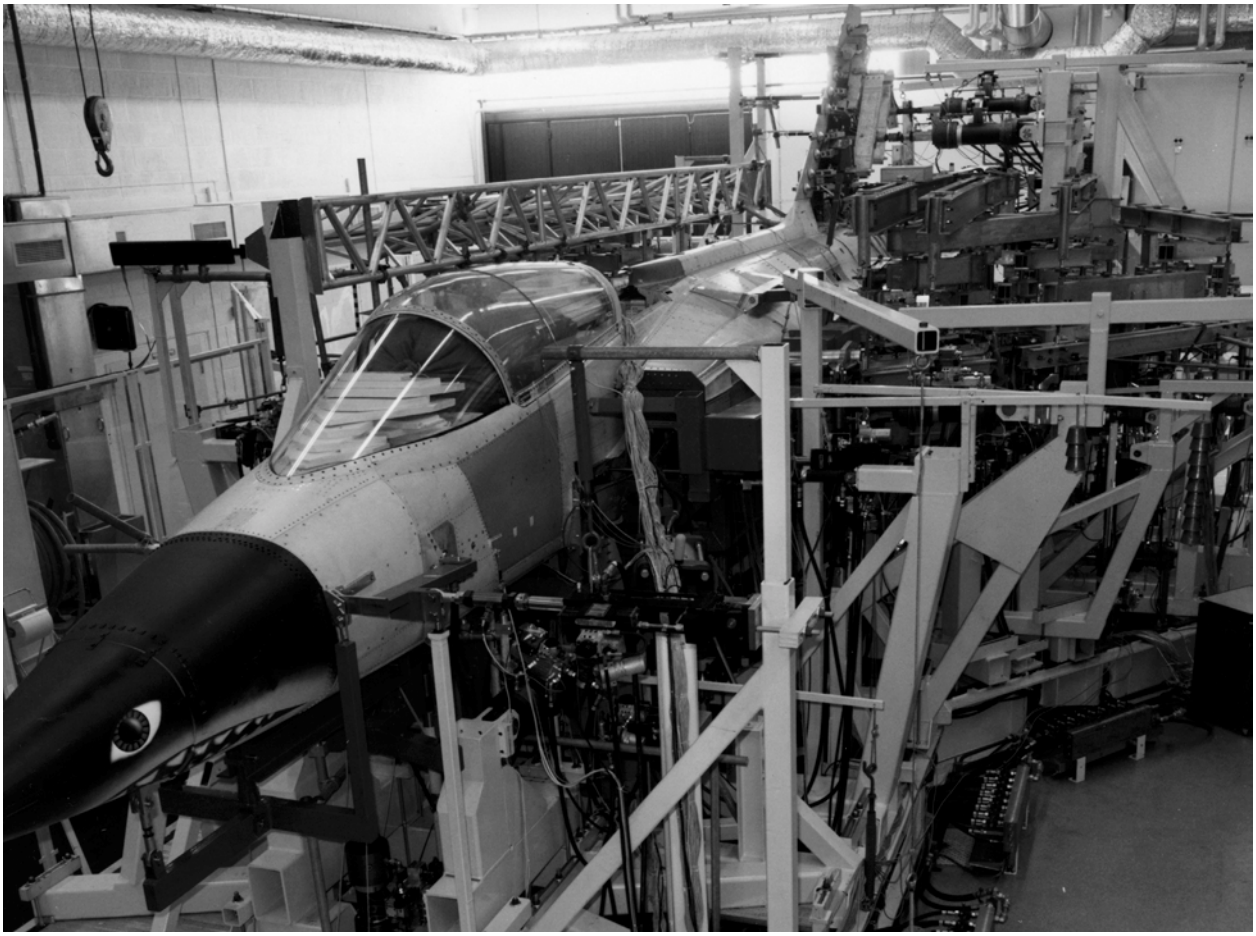

Fig. 1. The full-scale static structural test.

During these two full-scale tests acoustic emission (AE) has been used to monitor parts of the airframe. This paper presents some results and experiences from the AE monitoring of these two tests.

The full-scale fatigue testing was extended beyond the 16,000 flight hours already achieved in 1999 so that export versions of the aircraft were also tested. AE was also used during this testing and the results from the AE monitoring may be reported elsewhere.

2. AE MONITORING AT THE FULL-SCALE STATIC STRUCTURAL TEST

Objective

During the testing AE was used to monitor the wings and vertical stabiliser. The wings are CFRP skins with aluminium ribs and fittings and U-channel CFRP spars bolted together. The vertical stabiliser is made of CFRP skin and spars with aluminium honeycomb and aluminium

fittings. The main purpose of the AE monitoring was to obtain information on sub-critical damage, which might occur during loading of the wings and vertical stabiliser. A second objective was to prevent unexpected failure occurring prematurely during testing at moderate load levels.

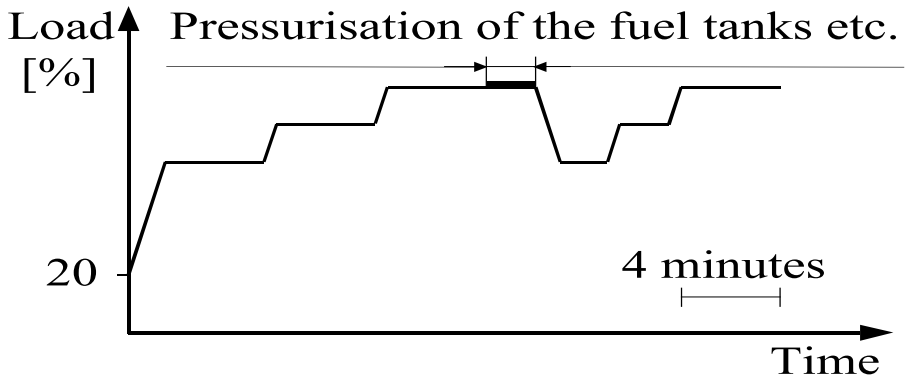

Fig. 2. Loading sequence used at the full-scale static structural test. Percent of limit load vs. time.

Equipment

A 72 channel Physical Acoustics Corporation SPARTAN-AT system and R15I integral pre-amplifier AE sensors were used at the test. The AE sensors, 30 on each wing and 12 on the vertical stabiliser, were attached in a triangular pattern to enable planar location of damage. The average distance between the sensors was approximately 0.5 m.

Testing Procedures and AE Criteria

The airframe was tested using a loading sequence such as shown in Fig. 2. In order to avoid rig noise from slack take-up the AE monitoring was not started until 20% of limit load. The load was then increased in three stages with a 4-min. hold at each test load. Any pressurisation of the fuel tanks, canopy, intakes etc. was carried out as a separate load stage after 4 min. at the maximum load. The load was then reduced and a second loading to the maximum test load took place.

For the real-time evaluation, PAL (Physical Acoustics Limited) had worked out a criteria for issuing a warning. During the testing we paid special attention to the amount of AE hits during a 10 to 20% load increase. Continuing AE activity during the last 2 min. of a 4-min. hold was also of particular interest as it indicates creep in the structure. We also looked for local areas with concentrated AE or high energy events. Finally we checked the Felicity ratio; i.e. the load, at which AE recommences during the second loading divided by the previous maximum load. In CFRP a low Felicity ratio indicates that the material is in poor condition or close to failure. [1]

Results from the Testing

More than 100 real-time AE tests were performed successfully. With the AE system we were able to detect and localise damage at an early stage and to prevent unexpected failure occurring during testing at moderate load levels. Below four cases are discussed that illustrates the use of the AE monitoring at the full-scale static structural test.

Case 1. Incipient deformation of honeycomb core:

At this particular load case, representing a yaw, large amount of AE was detected at a sensor on the leading edge of the vertical stabiliser. The target load at the test was 180 % of limit load

but high AE activity already during loading to 160 % followed by a slow decay in activity during the hold resulted in a recommendation to stop the test and unload the airframe. This was when AE was new to the Structural Testing Crew and the people at the Stress Office so they trusted only readings from strain gauges and load cells. Additionally, the AE monitoring was not allowed to interfere with the testing schedule. So when all readings except the AE monitoring showed nothing alarming the testing was continued. During the loading to 170 % of limit load an even higher AE activity was observed and the PAL criteria for issuing a warning was well exceeded. At this point the structural testing people agreed to make a longer hold at 170 % to see how the AE activity developed. After approximately five minutes at constant load the AE activity suddenly increased dramatically and a few minutes later we decided to stop the test and unload the airframe. The AE activity versus time and load during the test is shown in Fig. 3.

At a visual inspection afterwards one could clearly see that the CFRP skin underneath one of the loading pads was cambered inwards. The high AE activity during the test was mainly caused by deformation of the honeycomb core underneath the same loading pad. Due to the AE monitoring the test was stopped in time to avoid major damage. If the testing had continued to 180 % of limit load, the leading edge of the vertical stabiliser had most likely been wrecked. Now it was possible to replace the loading pad by a larger one and continue according to the original testing schedule.

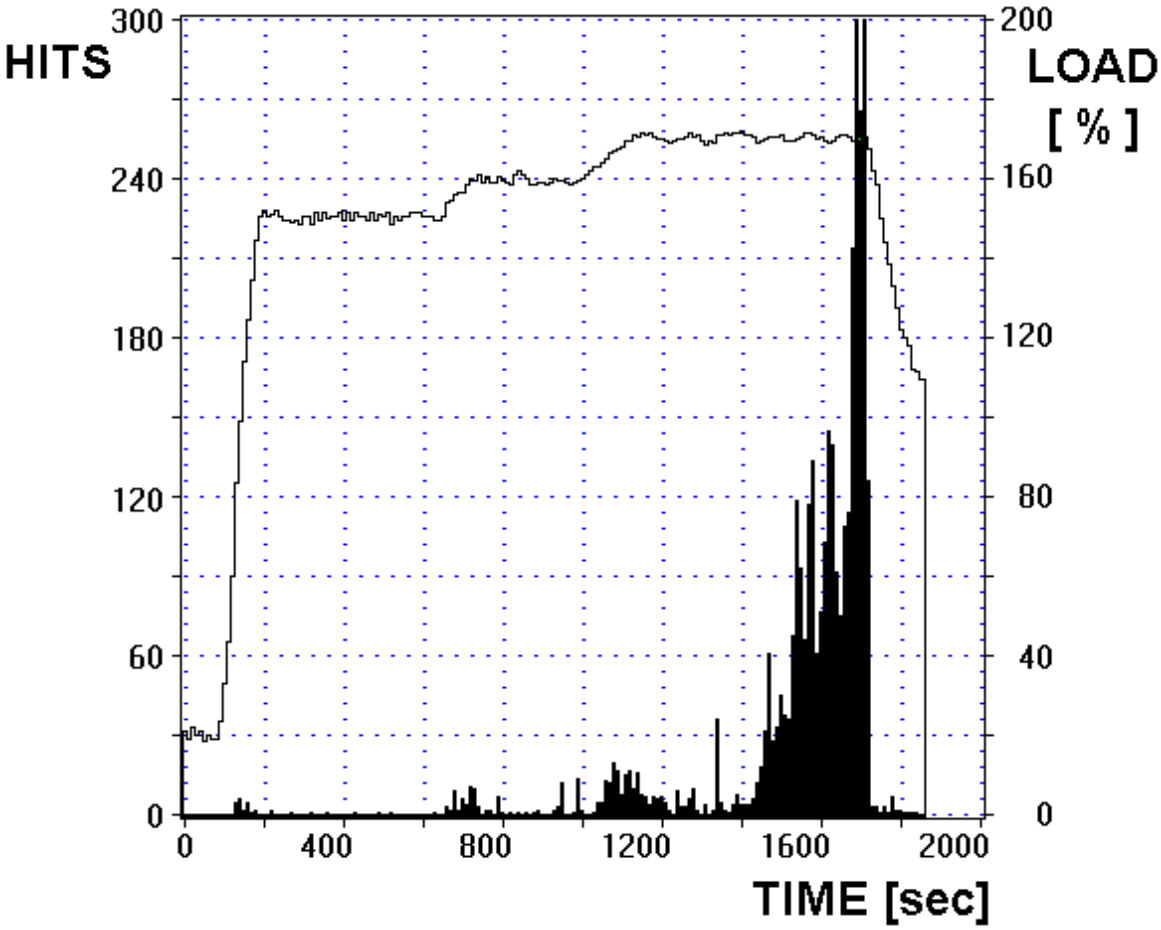

Fig. 3. AE activity versus time and load. The increase of AE hits at approximately 1400 s marks the onset of the honeycomb core deformation.

Case 2. Oblique loading at one of the loading pads on the vertical stabiliser:

At this particular load case, representing a supersonic roll, concentrated AE was located at a loading pad on the central part of the vertical stabiliser. The AE activity was first observed after a test to 180 % of limit load and the zone underneath the specific loading pad were examined by ultrasonics. The ultrasonic test, however, could not confirm any damage in the area. Furthermore, the load was not very high at this attachment point and damage of the honeycomb core due to high pressure was not very likely to occur according to people at Stress Office.

During further testing at higher load levels a continuously increasing amount of concentrated AE was observed in the area. A recommendation to replace the specific loading pad by a larger one was issued after a 220 % test. The loading pad was, however, not replaced and during testing to 230 % of limit load the AE activity increased tremendously and did not drop during the hold. After this test, a second inspection by ultrasonics was carried out and the damage was then confirmed. The NDT inspection pointed out that the damage was caused by oblique loading as showed in Fig. 4. This oblique loading gave rise to local damage of both the CFRP skin and the aluminium honey-comb core as a consequence of high local stresses already at low loads on the hydraulic jack.

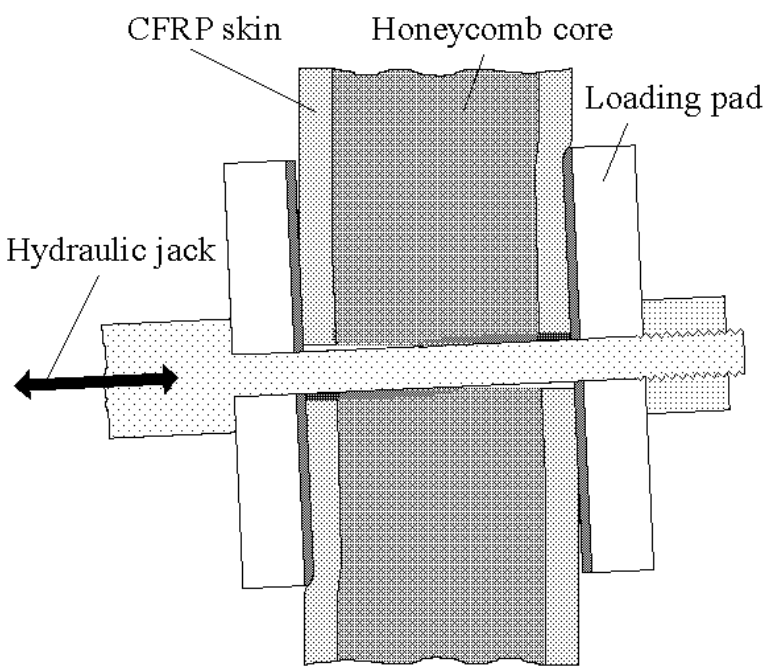

Fig. 4. Oblique loading of the vertical stabiliser resulting in high local stresses.

Case 3. AE activity due to an uneven load distribution of the airframe:

In this particular test exceptionally high AE activity was observed at load levels which had previously been exceeded using the same load case. At that earlier test the airframe was loaded to 200 % of limit load with no indications of damage. This time the target load was 220 % with holds at 200-, 210- and 220 %. Because this load case had already been tested to 200 % we expected insignificant AE activity during the first load step. The AE activity, however, was very high during the load increase and we decided to make a hold at 190 %. During the hold the actual load on each hydraulic jack was checked and compared to the set point adjustments. No discrepancy was found but the load was decreased to 80 % in order to find the reason for the AE-activity. A visual inspection of the linkage was performed. It turned out that parts of the linkage for some unknown reason had hooked on to one another causing an uneven load distribution of

the airframe. The linkage was easily adjusted and the test was later carried out to 220 % without any problem.

Case 4. Concentrated AE caused by high contact pressure during unloading of the wing:

In this particular case the actual test was already completed and the airframe was being unloaded when we noticed some strange AE activity from a local area on the left wing. The unloading was stopped immediately and a visual inspection showed that one of the loading pads had slipped over its holder as shown in Fig. 5. This resulted in a high local contact pressure during the unloading hence the AE activity. The loading pad was put back in place and the airframe could be unloaded without substantial damage.

Besides the four cases discussed above significant AE was only observed at very high loads where minor damage is expected and at the final testing of the vertical stabiliser where the intention was to test until failure. At this final testing the same load case was used as discussed in case 2 and a lot of AE early at the test clearly pointed out the previously accumulated damages. This time we were not supposed to stop the test but a tremendous increase in AE activity about 40 seconds before the final failure made it obvious that the vertical stabiliser was definitely going to fail.

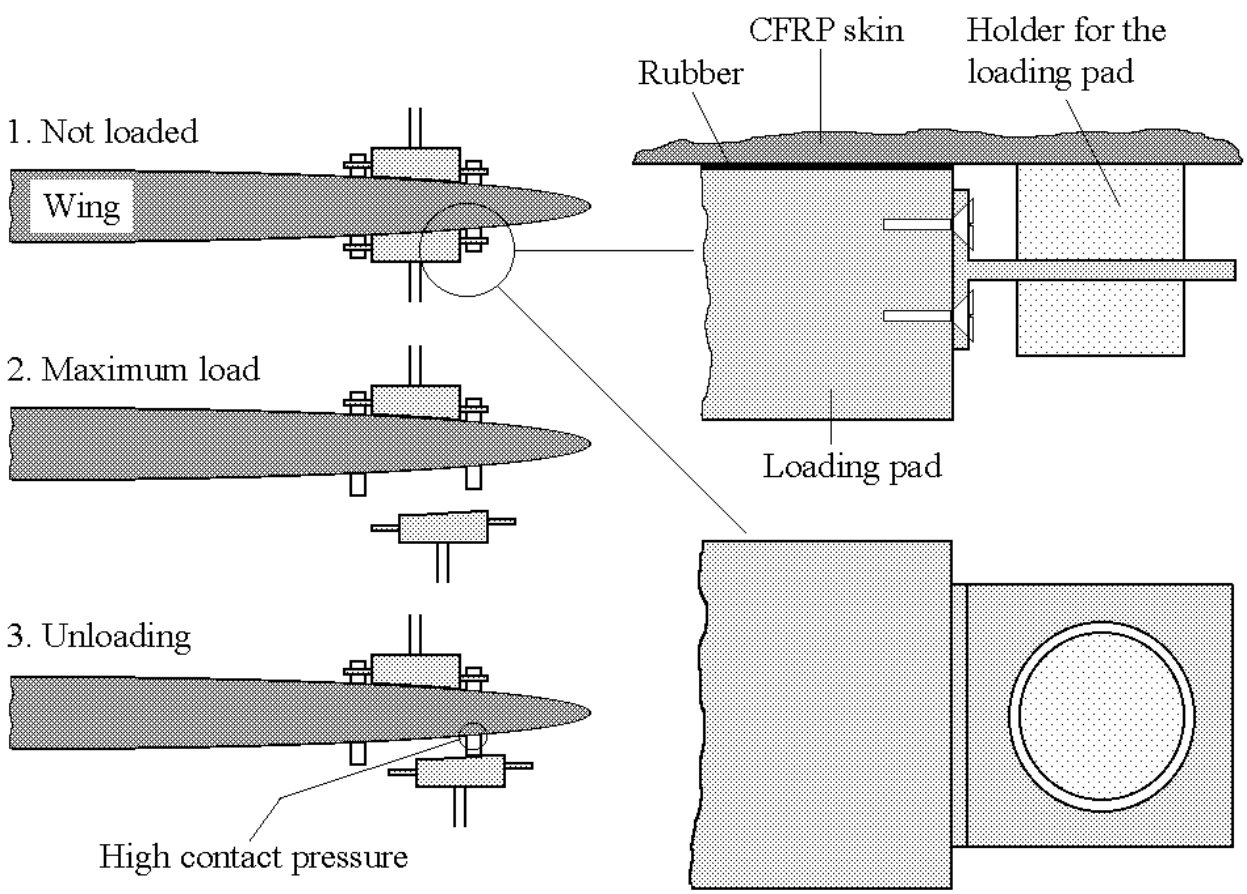

Fig. 5. Scenario causing local AE due to high contact pressure during unloading of the wing.

Summary

The AE monitoring has well fulfilled its purpose, i.e. to detect sub-critical *damage* and to prevent a total failure.

- The AE monitoring made it possible to detect and locate damage at a very early stage.
- The AE monitoring did not cause any false alarms.
- No damage of interest was missed by AE and later detected by other NDT-technique.

Because of its high ability to detect sub-critical damage in real time, AE have later been used during static tests of several structure parts such as the canard and the outboard wing elevon. These measurements have also been carried out with great success.

3. AE MONITORING AT THE FULL-SCALE FATIGUE TEST

Objective

The main reason for using AE monitoring during the full-scale fatigue testing was to lower the risk that an undetected fatigue crack would grow critical causing failure or damages hard to repair. For such complex testing there is always a risk of unexpected damages in areas difficult to inspect with ordinary NDT, or worse, in areas not inspected at all. Because AE, in opposite to most traditional NDT technique, is a real time global monitoring technique, the chances to detect such unexpected damage is increased and at the same time a better prediction of the occasion of the initiation is given. The main purpose of the AE monitoring therefor was to detect damage, if any, early during the testing and guide ordinary NDT inspection to interesting areas. A second objective has been to build up our knowledge and proficiency aiming to future inspections of ageing aircraft both on the ground and during flights.

Monitored Parts

Only metal parts of the airframe such as the three main wing attachment bulkheads, the side panels of the fuselage and some joints were monitored during the testing. The wings and vertical stabiliser, which were monitored during the static testing, have not been an object of AE monitoring since they are not considered sensitive to fatigue.

Equipment

The 72-channel AE system that was used at the full-scale static structural test has also been used during the full-scale fatigue testing with some modifications. First, mini-30S sensors in conjunction with 1220A preamps equipped with 200-400 kHz bandpass filters have been used for most parts instead of the R15I sensors. The mini-30S sensor has a higher resonant frequency, 300 kHz compared to 150 kHz for the R15I, and is more suitable to reject loading machine noise, which can be a problem when monitoring metal parts. Second, the SPARTAN AT was upgraded so that each channel could be inhibited individually depending on the actual load in the part monitored by that channel. For this purpose we used a strain gauge at each monitored part connected to a 9100A Voltage Time Gate and an Inhibit Select Box. Finally, a custom-made software was developed by PAC that allowed linking of the fatigue test control system to the AE system so that the AE data could be correlated precisely to a specific flight number and flight segment. The software has a built in feature called *Noise Mask* which allows real time filtering of events based on location and signal features. According to PAC this facility was needed to reject most of the noise so that we would not get drowned in data.

Evaluating Procedures

In order to reduce the amount of data only those parts of the load spectra having the highest probability for crack growth have been monitored, i.e. at high loads. In spite of this we have received a lot of noise from both the airframe and the test rig. The PAC software was supposed

to filter most of this noise on-line without a risk of filtering interesting AE caused by real crack growth. This was the reason why the noise mask facility was developed. PAC, however, could not find any AE parameter to separate a growing crack from external noise and fretting when trying to apply the noise mask on AE-data obtained from test samples subjected to controlled crack growth. We have therefor been forced to collect all AE data at high loads. This large amount of data has been analysed as follows: First all the AE-data are divided into blocks of 200 flight hours originating from recurrent loading sequences. Out of each of these blocks a reduced amount of AE-data are picked from a large number of specially selected loading sequences that are considered as particularly interested from a crack propagation point of view. This reduced amount of AE-data is then plotted in a number of location graphs (MS EXCEL 3D-Graphs) which are compared to location graphs originating from corresponding loading sequences from earlier testing. If increased AE-activity is detected locally, further analysis of this additional AE is done manually from the signal features as well as time and place of origin. If the AE by this means can not be rejected as external noise or fretting, the area of interest is examined by traditional NDT. In areas where we do not see any distinct signs of additional AE during the testing, the AE in fact present is considered as the natural level of background noise and no further analysis is performed.

Results from the Testing

During the testing to 16,000 flight hours, no damage has been detected in the monitored parts neither with AE nor traditional NDT. Locally increased AE activity has been observed at some occasions but often the AE has been rejected as slack take-up or buckling in adjacent structure. A few times, however, we have had some indications of fretting in rivet- and screw-joints where crack propagation in combination with fretting could not be excluded. These areas have later been examined by traditional NDT but no cracks have been found in any of the cases mentioned above.

Damage has on the other hand been successfully detected by AE at two holes through the wall of the air-channel where a sealing end is attached via two pegs. These holes only exist as a test adaptation in this test aircraft. The spots are actually outside the monitored structure but near to the aft bulkhead, which has been monitored by AE, Fig. 6. The sealing end itself is a part of the testing equipment needed to allow pressurisation of the air-channel (not shown in Fig. 6). At the two holes we noticed a substantial increase in AE activity during the testing from 11,000 to 12,000 flight hours. From the signal features we made the judgement that most of this activity was caused by slack take-up and that a minor part could have been caused by crack propagation or fretting. Our observations were reported and cracks were later indeed confirmed by a visual inspection at 12,000 flight hours. After the damages have been repaired the AE activity got back to a *normal* level during the continued testing, Fig. 7. Even though a testing tool in this case induced the damages the potential to detect damage with AE is clearly illustrated.

Summary

On the whole, the AE monitoring at the full-scale fatigue test has performed well. Inadequate hardware/software tools for filtering most of the noise from the test rig and the airframe itself have made it difficult and time consuming to evaluate the data from the AE monitoring. On the other hand, the only proven damage within or close to the monitored structure has in fact been detected by AE. This has strengthened our confidence in finding cracks by AE, if any, during the testing beyond 16,000 flight hours.

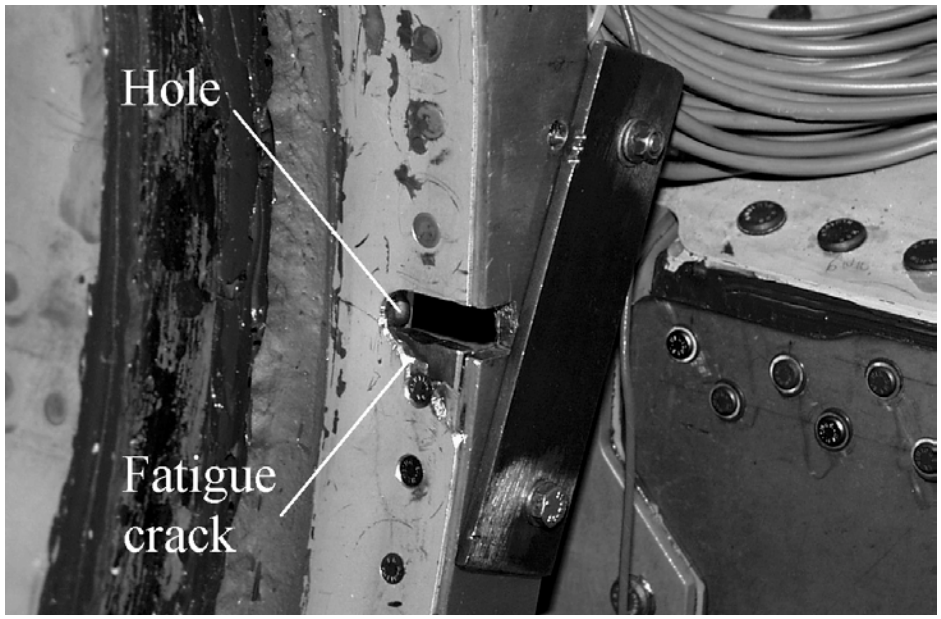

Fig. 6. Damage at one of the two holes through the wall of the air-channel.

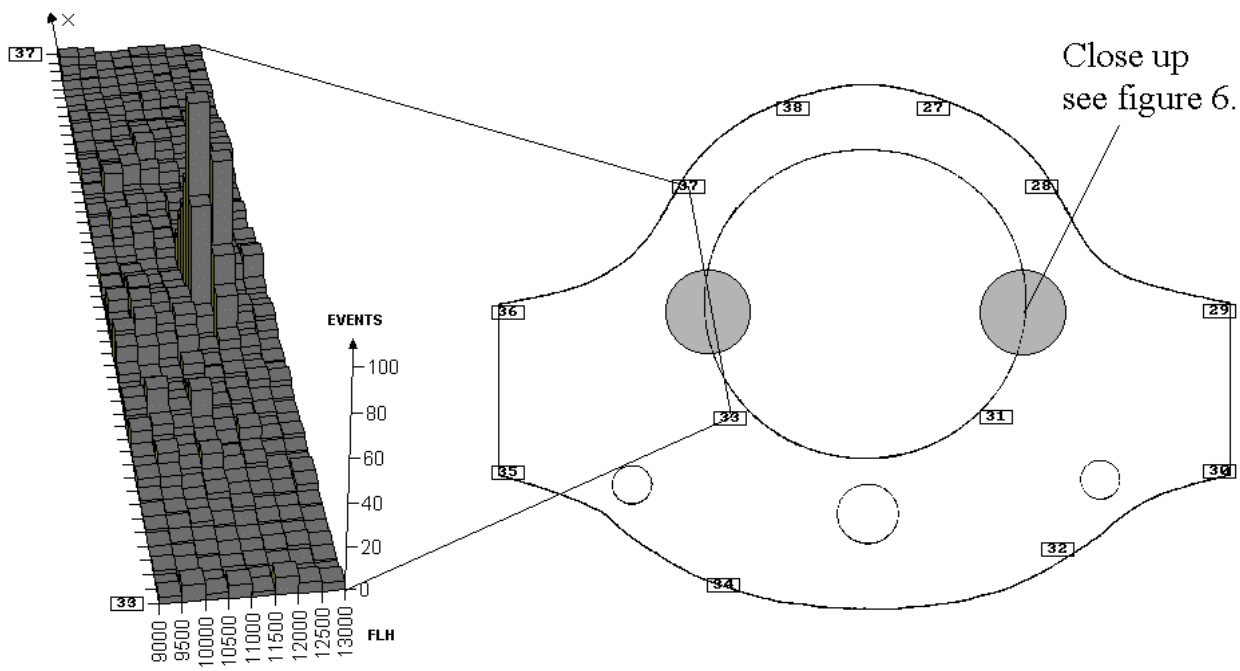

Fig. 7. Increased AE activity due to the damage incurred during the testing from 11,000 to 12,000 flight hours.

4. DISCUSSION

The way we have been evaluating the AE data have a few disadvantages. First, because the stress wave from an active crack must reach at least two sensors in order to be located, the sensors have to be closer together. To cover all appointed areas we therefore needed 102 AE sensors instead of the 72 sensors planned from the beginning. Because we only had a 72-channel AE system at our disposal some of the sensors were divided in two groups and each group

was monitored half the time. This was done by switching between the two groups every 200 flight hours of testing. Second, because the AE data had to be sorted and compared with corresponding blocks of sequences from previous testing, the AE monitoring could no longer be considered as ”real time” in the strict sense of the word. The probability, however, that a crack would initiate and grow critical in this short period of time was regarded as insignificant. Natural variations in the amount of background noise was then of greater concern as this makes it more difficult to detect real damage at an early stage. Finally, it has been a very time consuming way of evaluating the AE data even though most of the data processing has been made automatically.

Despite the disadvantages mentioned above we believe this has been the safest and most efficient way of evaluating the AE data. A great amount of the noise could probably have been rejected during acquisition but far from all the noise could have been filtered on-line without running the risk to also filter interesting AE from real damage. Hence, it has been necessary to limit the detailed analysis to local areas with increased AE activity.

Even though we feel a great confidence in our way of evaluating the AE data from the full-scale fatigue test, no guaranties can be given that all cracks have been detected. High acoustic attenuation in local areas may have caused growing cracks to remain undetected. Our chances to detect active cracks are also influenced by which of the loading sequences we have chosen to monitor. Even if a crack has in fact been physically detected we may still have missed it during the evaluation. In spite of all this, we consider the likelihood that we have missed ”significant” damage to be small, which was fortified by laboratory tests on smaller but similar structure. Our judgement is therefore that the AE monitoring have fulfilled its purpose and that the monitored parts are still at 16,000 flight hours without any damage. The AE monitoring has, however, been a lot more complicated than first expected.

5. CONCLUSIONS

AE has shown to be a very useful tool for finding cracks and sub-critical damage early during full-scale structural testing of military aircraft. During the static tests of CFRP structure, AE is often the only reliable NDT method for detecting significant damage and for preventing unexpected failure. AE monitoring of metal structure exposed to fatigue demands an experienced operator to sort out significant information out of AE data mainly consisting of mechanically induced noise. In both cases AE should be considered as complementary to traditional NDT that lowers the risk of unexpected damages during the testing. Many times, however, the AE monitoring may justify a reduced number of time-consuming inspections with traditional NDT.

REFERENCES

1. Nondestructive Testing Handbook, Acoustic Emission Testing, 2nd edition, Volume 5, ASNT, Columbus, OH, 1987, p. 18.

DETECTION AND LOCATION OF CRACKS AND LEAKS IN BURIED PIPELINES USING ACOUSTIC EMISSION

S. J. VAHAVIOLOS, R. K. MILLER, D. J. WATTS*, V. V. SHEMYAKIN§, and S. A. STRIZKOV§

Physical Acoustics Corp., Princeton Junction, NJ 08550-5303 USA; * New Jersey Institute of Technology, Newark, NJ 07102-1982 USA; § PAC Russia, Moscow, Russia;

ABSTRACT

Studies in both Russia and the United States indicate that buried pipeline testing with acoustic emission is feasible. Whether performing defect detection or leak detection, it has been shown that the ideal sensor is a resonant device directly coupled to the outer surface of the pipe and operating somewhere between 10 kHz and 40 kHz. Source location for all applications begins with traditional linear location but requires special algorithms in order to achieve the highest accuracy and to avoid false calls. This is illustrated for the case of near simultaneous emissions from defects. Also shown are leak detection cases where an adaptable threshold is required to sequence hits for proper event definition. Field studies have proven that testing can be performed online, if required, with the test procedures tied to operating conditions. Off line static testing is still shown to be the best testing environment.

1. INTRODUCTION

Studies performed in the United States and Russia demonstrated the use of acoustic emission (AE) for testing buried pipes. The work presented in this paper is a review of these efforts, which have led to the development of new hardware, software, procedures and analysis tools for detecting both cracks and leaks in buried pipelines.

The efforts in the United States (1,2) focused on the development of AE for leak detection and location in liquid-filled, buried pipelines. This effort addressed the major objective of annual testing as defined by the U.S. Environmental Protection Agency (EPA) with the additional objective of maximum sensor spacing as defined by the U.S. Army and Navy. This paper will present the highlights of this study in terms of the equipment and sensors developed to improve detection sensitivity as well as the tuned linear location technique, which was presented as the most attractive method for performing leak location.

The efforts in Russia (3) have focused on the development of the AE testing technique to be used in pre-service periods to avoid incipient accidents when a pipeline is excavated for visual inspection and re-coating. The major defects, which are detected by AE method in this case, are flaws in butt welds. For this application, linear location is also a very useful technique to detect the flaws. In order to extract the true data from a great number of recorded AE hits, a special correlation technique has been developed and will be discussed.

2. DETECTION AND LOCATION OF CRACKS IN BURIED PIPELINES USING AE

The total length of pipelines for gas, oil and product transportation in Russia is several hundred thousand kilometers. Numerous pipelines are buried with many lying in swamps (which are

nearly frozen all year long) and located in northern Siberia. The most familiar method of in-service pipeline inspection is internal diagnostics by means of special inspection "pigs". A lot of pipelines cannot be inspected with “pigs” because the pipe has a specific diameter or curvature, which does not allow the pig to pass through the pipe. In addition, many crack-like flaws go undetected (for reasons we will not discuss) after pig inspection. It is well known that AE testing has been successfully used on vessels and tanks. It can be effectively used on pipelines as well.

AE testing can be conducted during different periods of the pipeline’s life: when the pipeline is in operation; when the pipeline is being lowered after field fabrication (to define its plasticity during the lifting); during hydro-test and before major repair; for integrity checking; when segments of the pipe are being lifted from the ground for isolation change. In the last case, the pipe may fail due to a flaw that was deformed during the lifting.

One of the main requirements specified by our customers was the demand to carry out AE testing when their pipeline was in operation. This means that the load cannot exceed the working pressure during the AE test. The only way to stimulate flaws was to quickly raise the pressure, hold it and then let it reduce to the operational value. When the operational pressure is as high as possible, the sequence of steps is the opposite: the pressure is reduced, held and then raised back to the operational value. It turned out that the AE testing results were almost the same for both procedures. Flaw stimulation (for generating AE signals) is accomplished with the help of the pressure wave which spreads along the pipeline when the pressure changes as a result of a valve opening or closing or by changing the operational regime of the pump. The two pipeline load schemes (Load/Hold/Unload or Unload/Hold/Load) are shown in Fig. 1. The correspondent total AE in one channel of AE system is shown on Fig. 2.

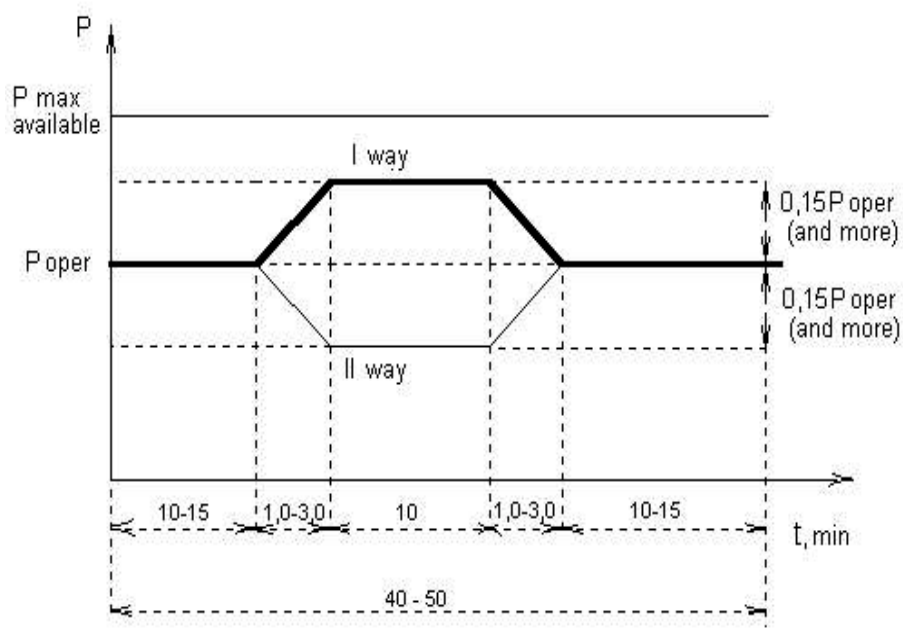

Fig. 1 Loading scheme.

The structure defects that can be defined by AE are cracks, lack of penetration, undercuts, inclusions, edge displacements in butt welding, corrosion, laminations, leaks and ice plugs, but the most frequently found defects are flaws in butt welds. The most important parameters of the

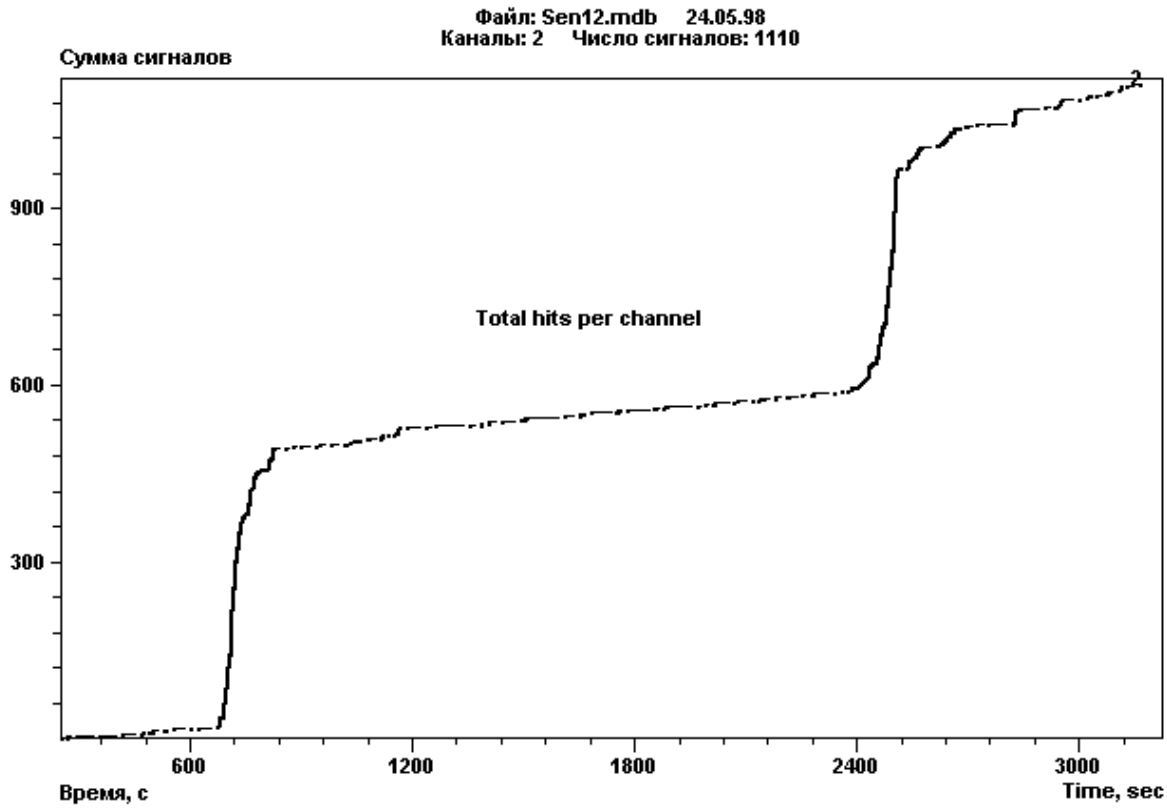

Fig. 2 Total AE during loading.

test are the distance between the sensors and the frequency band. Typically we use LDS-1 sensors with a distance between sensors of about 100 m and a frequency band from 10 kHz to 100 kHz. A lot of experimental measurements of attenuation and wave propagation in pipes with different diameters, wall thickness (empty and filled with water) were carried out. Several measurements were carried out on real buried pipelines with oil and gas. A few examples of the results are shown in Fig. 3 to Fig. 8.

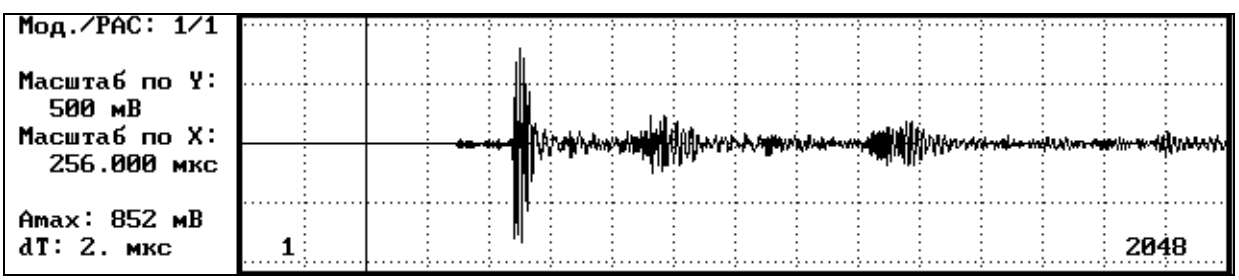

Fig. 3 The distance between source and sensor is 2 m. Empty pipe.

The figures illustrate that the wave speed used for event location for gas filled pipe is 3.3 m/ms, and for liquid filled pipes is about 1.5 m/ms (speed in the water). The attenuation graphs show that in both cases, attenuation of the highest amplitudes modes is about 0.6 dB/m. All the measurement of the waveforms and amplitude attenuation were made using the Hsu-Nielsen pencil-lead break (PLB) method. Figure 9 shows the comparison of the waveforms captured by the same type of sensors for PLB's and the case where the source of the wave was a real crack.

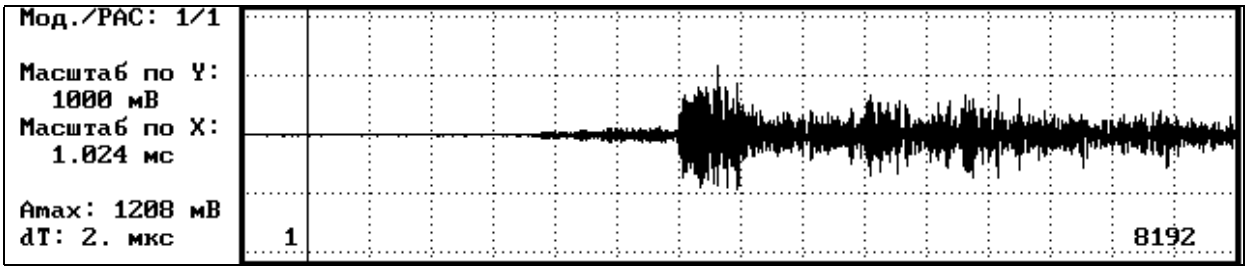

Fig. 4 The distance between source and sensor is 20 m. Empty pipe.

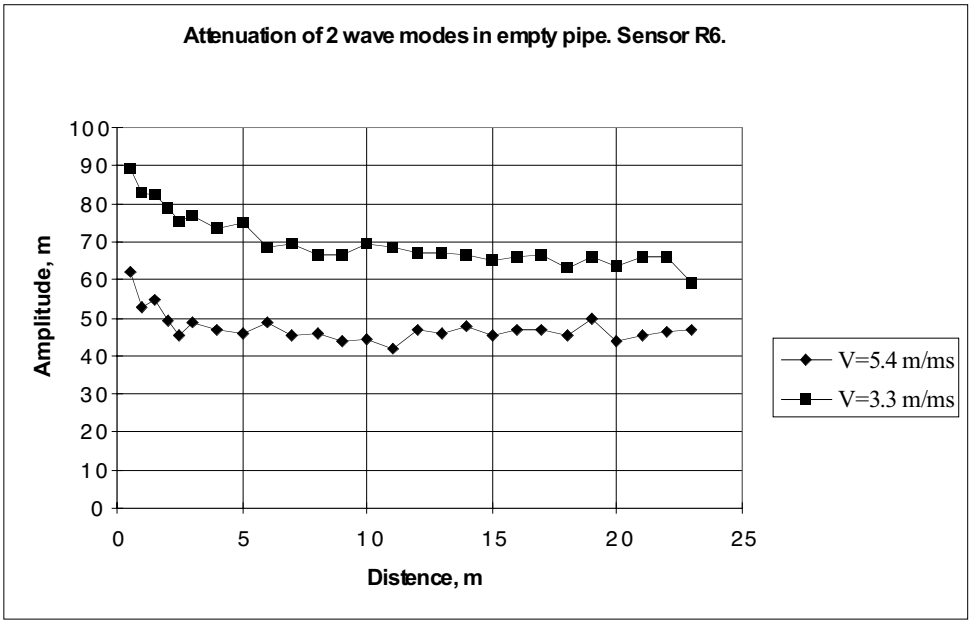

Fig. 5 Attenuation curves for two types of the wave in empty pipe.

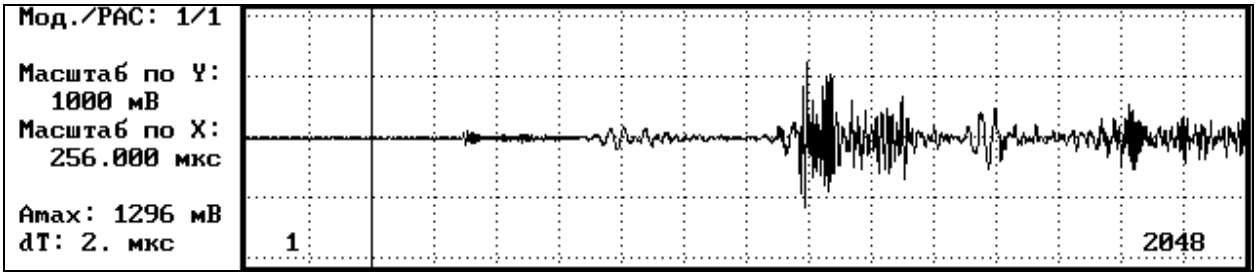

Fig. 6 The distance between source and sensor is 2 m. Pipe filled with water.

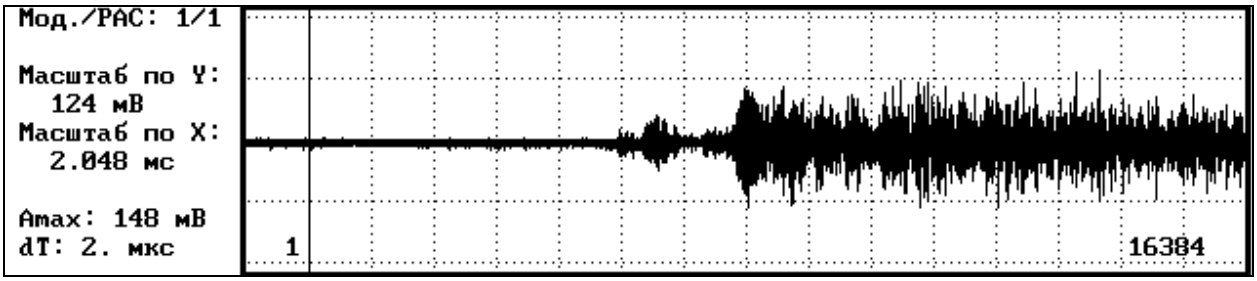

Fig. 7 The distance between source and sensor is 21 m. Pipe filled with water.

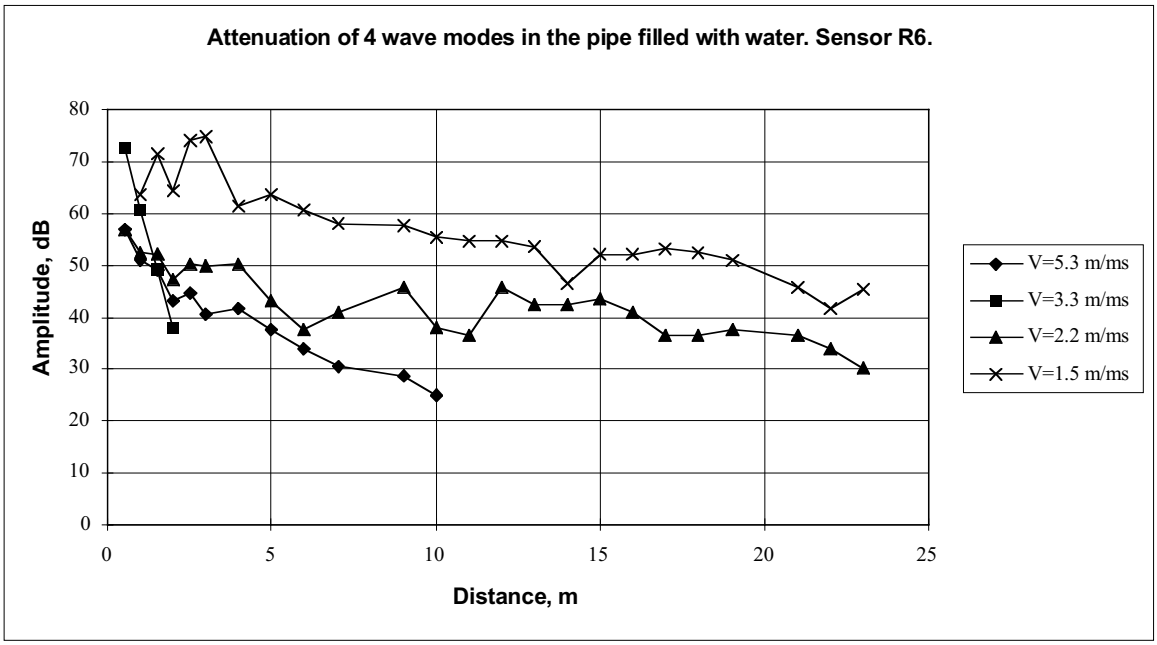

Fig. 8 Attenuation curves for several modes of wave in pipe filled with water.

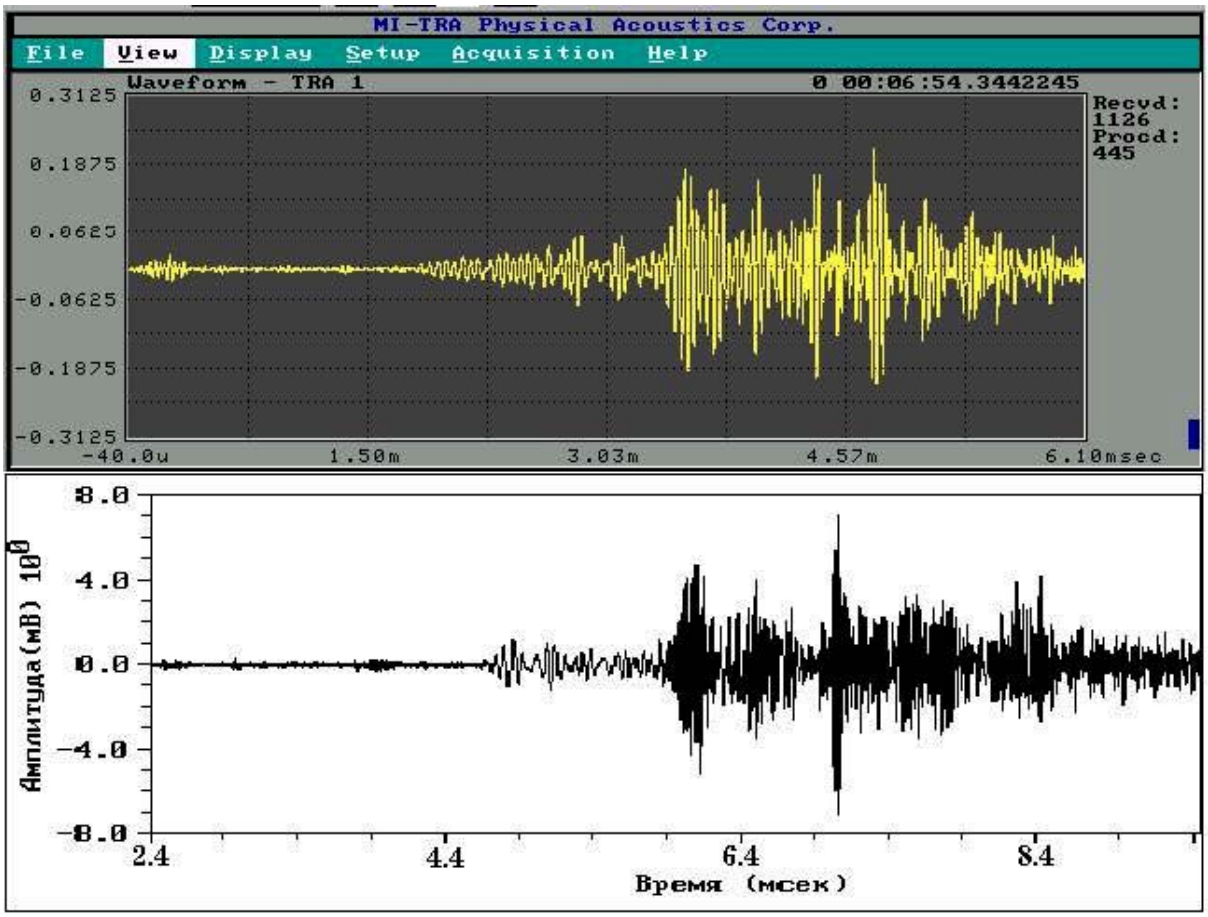

Fig. 9 Signals from real and artificial AE sources in pipe filled with water. The distance between sensor and source is 9 m.

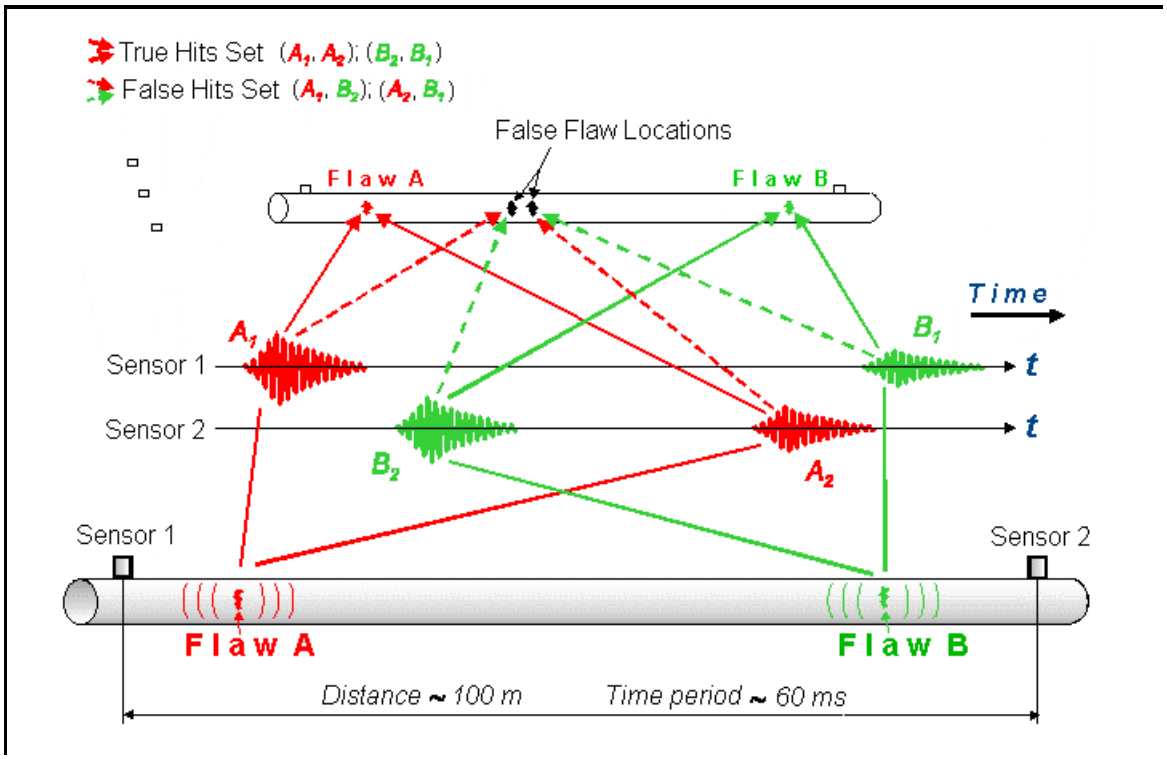

Fig. 10 The principal of correlation location.

When the distance between the sensors is about 100 m, a big problem arises. The period of time, which is equivalent to this distance (if we use wave velocity 1.2 or 1.5 m/ms) is about 80 ms. If we take into account that the loading time is several minutes and the AE activity is very high, a mixing of hits on the sensors takes place. It means that the location of real AE sources can be false. The location in this case is the only way to define the flaw. That is why the problem of mixing the hits becomes very serious.

To solve this problem, special programs (that locate sources by mean of cross correlation of the hits from neighbor sensors) were developed. Figure 10 illustrates the concept of correlation location. The program works with files that were made by Malachite AS-12, SPARTAN 2000, MISTRAS and DiSP systems. The number of properly defined flaws has grown significantly since we started to use this program.

The procedure of AE testing is as follows. The team moves in a car along the pipeline with excavated pits in order to test a segment which is about 500 m long. Six sensors are attached and sensitivity calibration is carried out. Attaching more sensors would require longer cable lines thus requiring more setup time and exposing the test to electromagnetic interference (EMI). After 10 minutes of AE data acquisition at the operational pressure, an order for pressure change is given through walkie-talkie and data acquisition continues as the pressure changes. The test is terminated after a second sensitivity calibration is performed. Then the team moves to the neighboring 500-m segment. When the team is well organized and do not encounter any delays, they can test about 2 km of pipeline per day.

3. DETECTION AND LOCATION OF LEAKS IN BURIED PIPELINES USING AE

The interest in evaluating AE was based on previous studies by the U.S. EPA, on sensitivity requirements found in federal regulations, and the needs of various agencies. Sensitivity is defined by the U.S. EPA as reliable detection of 0.1 gallon/hour (1 gph ≈ 1 ml/s) leaks during annual testing. A sensor spacing objective of 150 m was added for this program based on an understanding of conventional access to buried pipelines such as manholes, hydrants, inspection pits and valves pits.

Detection of a 0.014 gph leak was demonstrated with AE at the SERDP Test Pipeline Facility (STPF) located at the U.S. EPA in Edison, New Jersey. This demonstration was performed using a gas enhancement technique developed under SERDP funding. This technique mixes an inert gas with the liquid contents of the pipe to generate two phase flow through the leak. This small leak was accurately located (see Fig. 11) to within 0.3 m of its actual location, using sensors spaced at 7.5 m. Off-the-shelf equipment and sensors were used and a modification to a conventional location technique, tuned linear location, was introduced to improve the location accuracy. Without the gas enhancement and the improved location technique, detection of the leak would not have been possible.

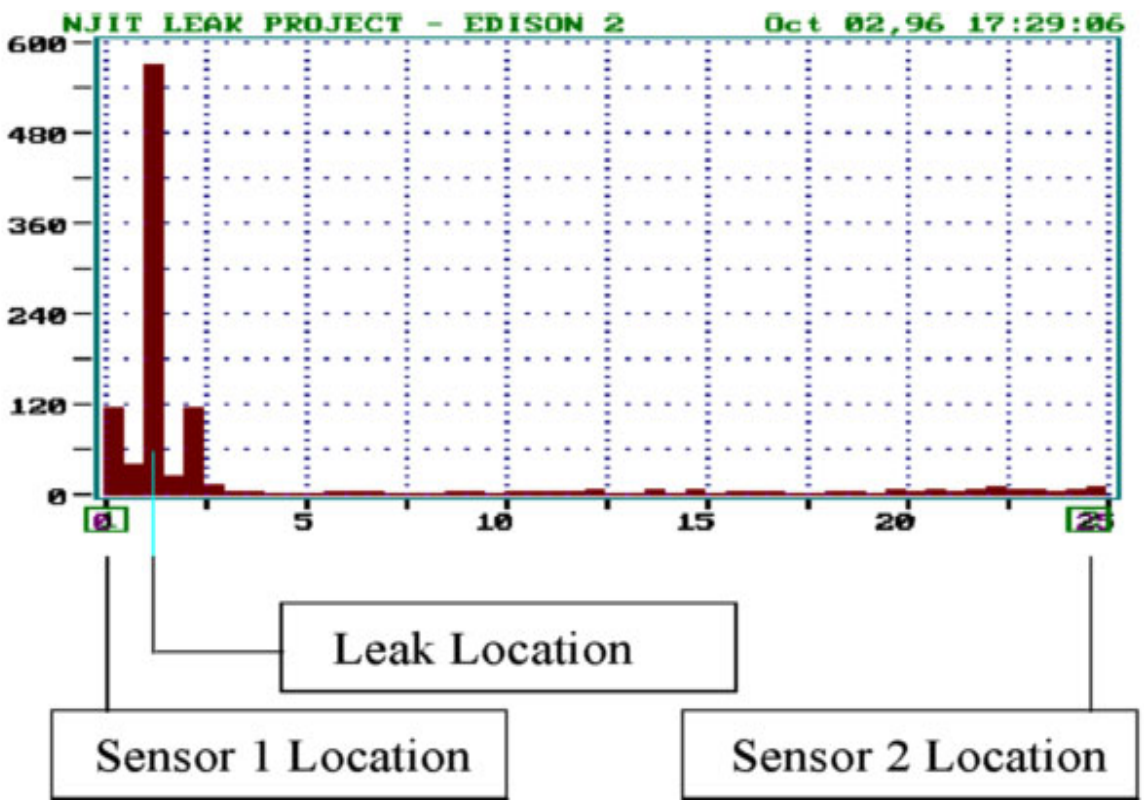

Fig. 11 Leak location on the EPA Test Loop for a 0.014 gph leak. The high frequency setup was used with 25 foot sensor spacing on a 2 inch diameter pipe.

Large sensor spacing and detection of multiple leaks were demonstrated on a High Temperature Hot Water (HTHW) systems, operated by the U.S. Army and located in Fort Drum. Multiple leaks were detected and located (see Fig. 12) during a single test using 271 m sensor spacing, while testing this system during normal operation. Confirmation of the leak locations in

Fig. 12 Location peaks from 874 foot run containing three expansion loops and problem areas corresponding to the sections of melted snow.

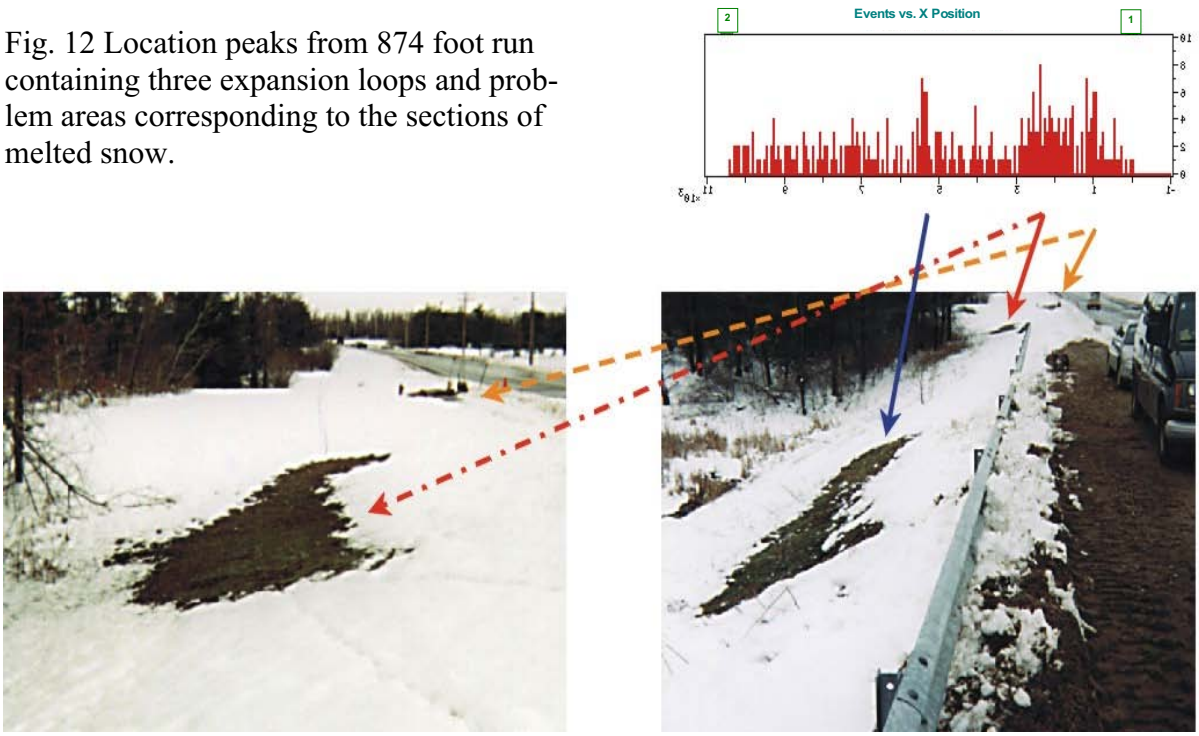

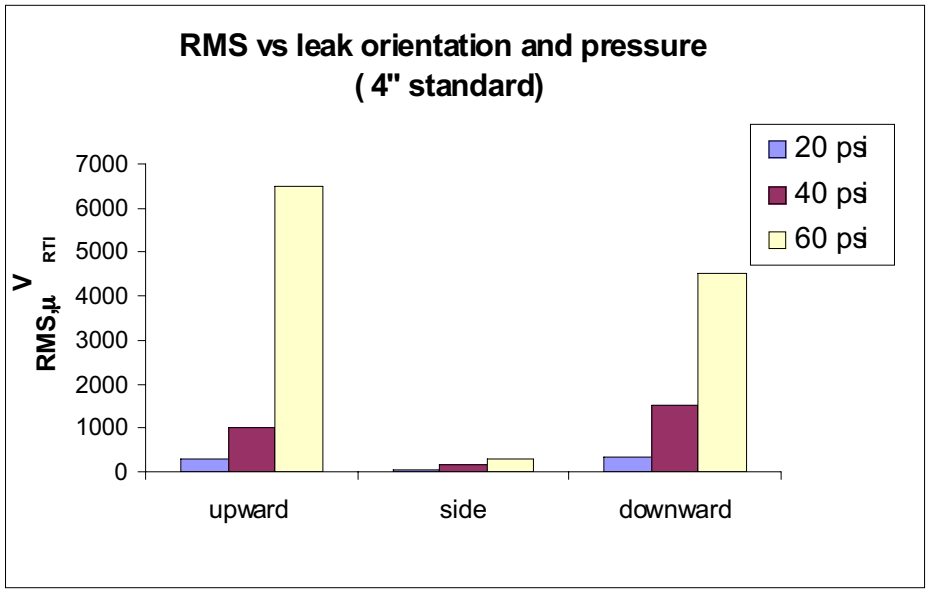

Fig. 13 Leak rate as a function of sensor spacing for various sized leaks.

this double-wall piping was made possible by melted snow and comparison with the known history of the HTHW system.

The combined objective of detecting 0.1-gph leaks with 150-m sensor spacing remains as a goal for future studies. On the Navy Test Loop (simulating a 30.5-cm diameter, aviation fuel hydrant systems) at the STPF, we were able to demonstrate leak detection sensitivity and accurate leak location for 1.0-gph leaks using 21-m sensor spacing and 20-gph leaks using 61-m sensor spacing (see Fig. 13) during normal hydrostatic testing.

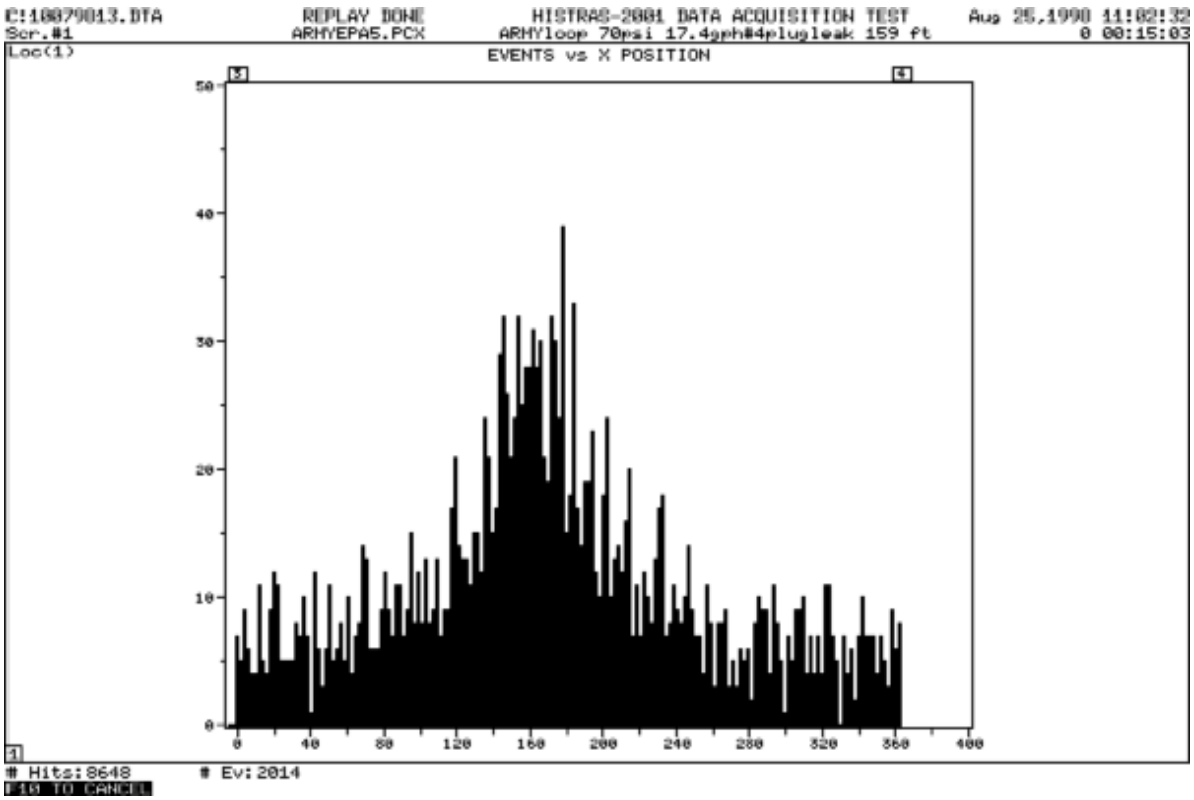

Fig. 14 Results for tuned linear location for 17.4 gph leak using 111-m sensor spacing on the Army Test Loop.

Gas enhancement techniques were also used on the Navy Test Loop in order to extend the sensor spacing limits. The results showed that the gas enhancement technique cannot take full advantage of the water-borne signal and should be restricted to cases where very small leaks are suspected and the pipe can be accessed every 15.3 m (maximum) for sensor placement.

The Navy Test Loop was also used for the demonstration/validation task at the end of the program. A test procedure was developed and refined for use on several blind tests. Based on the success of the validation effort, this procedure has been recommended for use in the proposed transition program. It was also found that the same procedures could be used on the double-wall design (of interest to the U.S. Army), as long as we could access the inner carrier pipe with our sensors. Coatings were of prime interest because they are typically part of the outer cathodic protection. Coal tar, one of the most typical coatings, was found *not* to attenuate the signal as anticipated. Coupling of the sensors to the outside surface of the pipe *did not* disturb this protective layer.

Elbows and tees were investigated for comparison with straight pipe. It was found that they can create problems leading to false leak locations. It was also determined that these problems can be overcome using elbow and tee as locations for mounting sensors (see Fig. 14).

Leak orientation and the effects of soil loading were studied in both the laboratory environment and at the STPF facility. The results show that vertically oriented leaks (up or down) produce the highest AE signals and therefore are more likely to be detected and located (see Fig. 15). We also determined that without the flow restriction, caused by soil loading, there would be

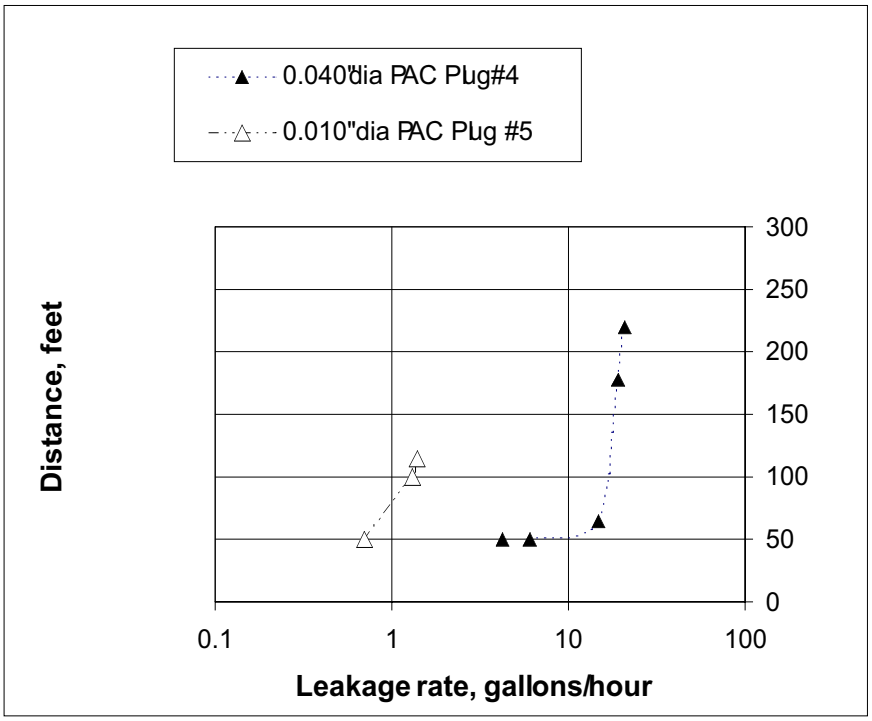

Fig. 15 Leak signal as a function of leak orientation and pressure for a 100-mm diameter pipe.

no leak signal to detect regardless of leak orientation and for the leak rates of interest. At the STPF, we determined that 0.9 m or more of backfill is required to produce the maximum AE signal at the leak.

Through laboratory studies, the work at the STPF and at Fort Drum, we were able to evaluate the effects of piping diameters in the range of 51 mm up to 410 mm. Using the test procedures developed in this program, we were able to characterize dispersion effects and determine the appropriate leak location method and characteristic wave propagation velocity.

Four different methods of performing leak location were studied. Of these four, the tuned linear location technique developed (see Fig. 16), provided a method that worked for all cases studied and yielded excellent location accuracy. The signal difference method, which was modified for this program, provided an additional means of leak location as well as a means for verifying the results of the tuned linear location technique.

Concerns about sensors with high sensitivity at low frequencies and immunity to environmental noise, were present when this program was initiated. Several sensors were delivered under SERDP funding that addressed these concerns and demonstrated excellent performance for leak detection. PAC's pipeline leak sensor (PLS-1) was integrated into a 38 mm by 1.8 m long search tube for work at the STPF. The performance of this device for leak detection and location was excellent but its diameter was deemed too big for practical use. This resulted in the development of a low profile sensor, designated as the low profile EPLS-1 (see Fig. 17), with a diameter of 19 mm and a peak frequency response of 15 kHz. The performance of the low profile EPLS-1 was evaluated during the demonstration/validation phase of this program and determined to be better than the PLS-1.

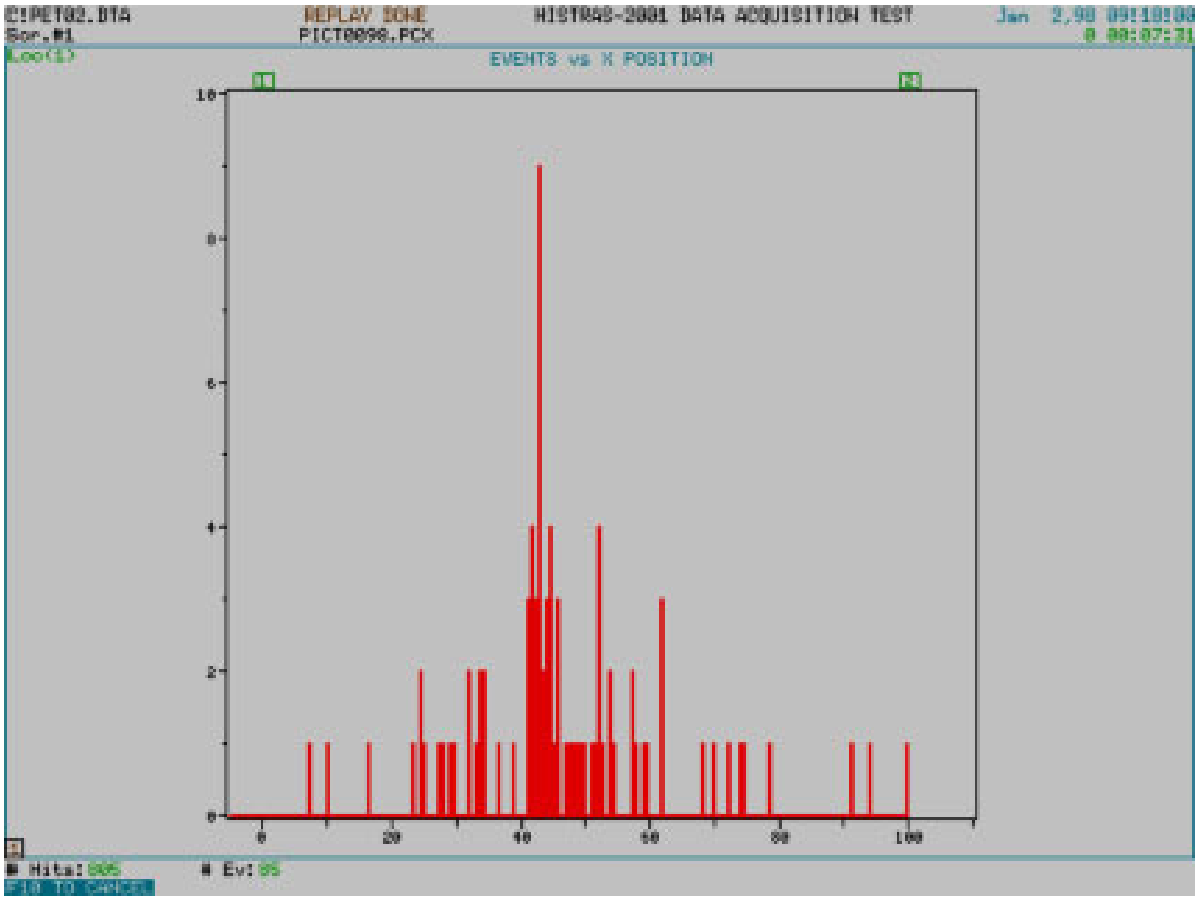

Fig. 16 Tuned linear location results for 100-foot sensor spacing and a 1.2 gph leak at the 40-foot position.

The equipment that was used was available off-the-shelf and required little modification. A PAC MISTRAS 2001 instrument was utilized in all phases of this study with only one modification. That modification extended its performance from 10 kHz down to 1 kHz allowing the evaluation of all frequency bands of interest with a single instrument. In addition, the tuned linear location technique introduced in this program, was implemented in real time using an "adaptive threshold" method called, Smart Threshold™.

4. CONCLUSIONS

Studies in both Russia and the United States indicate that pipeline testing with acoustic emission is feasible. In both countries, whether performing defect detection or leak detection, the ideal sensor is a resonant device operating somewhere between 10 kHz and 40 kHz. Source location for both applications required special algorithms in order to achieve the highest accuracy and to avoid false calls when near simultaneous events are generated.

REFERENCES

1. Miller, R.K., Pollock, A.A., Finkel, P.E., Watts, D.J., Carlyle, J.M., Tafuri, A.N., Yezzi, J.J., "The Development of Acoustic Emission for Leak Detection and Location in Liquid Buried

Pipelines," *Acoustic Emission: Standards and Technology Update*, ASTM STP 1353, ed. S.J. Vahaviolos, American Society for Testing and Materials, 1998, pp. 67-78.
2. Miller, R.K., Pollock, A.A., Watts, D.J., Carlyle, J.M., Tafuri, A.N., Yezzi, J.J., "A reference standard for the development of acoustic emission pipeline leak detection techniques," NDT&E International, **32**(1), 1999, pp. 1-8.
3. Samoilov, B.V., "In-line inspection, repairs used on ageing Russian product lines," Oil & Gas Journal, International Petroleum News & Technology, Nov. 1998, pp. 42-46.

Fig. 17 The low profile EPLS-1 as it is coupled to the buried pipeline through an access tube.

ACOUSTIC EMISSION FROM ACTIVE CORROSION UNDER THE INSULATION OF A SULPHUR TANK

PHILLIP T. COLE and STEPHEN N. GAUTREY

Physical Acoustics Limited, Over, Cambridge, CB4 5QE, UK

ABSTRACT

Iron, in the presence of water, combines with atmospheric oxygen to form a hydrated iron oxide, commonly called rust. This simple definition describes the one chemical reaction, which probably costs industry more in losses and maintenance costs than any other. This brief paper describes an extreme case of corrosion on a sulphur tank and the acoustic emission that resulted from this.

1. INTRODUCTION

The detection of corrosion activity by acoustic emission (AE) has largely focussed on phenomena such as stress-corrosion cracking, corrosion fatigue, and other "esoteric" forms of corrosion. For some reason, listening to plain old rusting has never been regarded as interesting, possibly because rust is very visible and usually easy to detect. Nevertheless, there are situations where remote detection can be useful, as in the case of under-insulation corrosion, and this paper describes one such case in detail. The basic principles and fundamentals of the use of AE, including metallurgical details, for a range of corrosion monitoring applications is described in reference 1.

2. DETECTION PRINCIPLE

Most acoustic emission applications concern emission resulting from yielding and crack growth as materials and structures are locally over-stressed. These stress-waves are detected by surface-mounted piezoelectric sensors, and the resulting electrical signals conditioned and analysed using an appropriate method.

The present authors consider the source of the AE detected from significant rusting of steel to be primarily the result of fracture and de-bonding of the scale, while many researchers mention hydrogen evolution and other mechanisms, which are usually very minor sources and low amplitude signals. These are unlikely to be detected in the field. As metal corrodes away the resulting scale has a volume of approximately twelve times that of the original metal, this means that as the scale forms it is forced to repeatedly fracture and de-bond. This results in significant AE, providing a means of detection, and monitoring for the rate of corrosion.

3. SULPHUR TANK TEST

This carbon steel tank was 23-metres circumference and 7-metres high, fully insulated, and operating at up to 120˚C. The owner was concerned about the condition of the tank wall under the

insulation, and had decided to conduct an AE test. Small holes were cut in the insulation for sensor mounting, and the sensors attached using magnetic clamps and high temperature acoustic couplant. Normal practice with AE testing is to calibrate the sensor sensitivity in-situ, then check background noise levels prior to commencing the test, which normally consists of raising the level in a tank or the pressure in a pressure vessel. In this case, however, there was such a high level of AE activity due to active corrosion under the insulation that normal integrity test procedures became irrelevant. The vessel had "failed" all the evaluation criteria without changing the stress. In the words of the operator, "on a scale of A to E, (A is "good", E is "bad"), this vessel rates as a K".

After reducing the product level substantially, subsequent inspection involved removal of all the insulation. The vessel was quickly de-commissioned and scrapped, the rust and insulation being the main component of the structure.

The AE data detected from the tank over a one hour period is shown in Figs. 1-5. In reference, the amplitude of a Hsu-Nielsen source, the European standard "field" calibration, which consists of the fracture of a 2H 0.5-mm pencil lead, is approximately 90dB on the amplitude scale, and considered a large signal by AE standards. Figure 1 shows hundreds of signals exceeding even this level. Expanding the time scale to look more closely at a 20-s period shows the pattern of activity more clearly, as shown in Fig. 2.

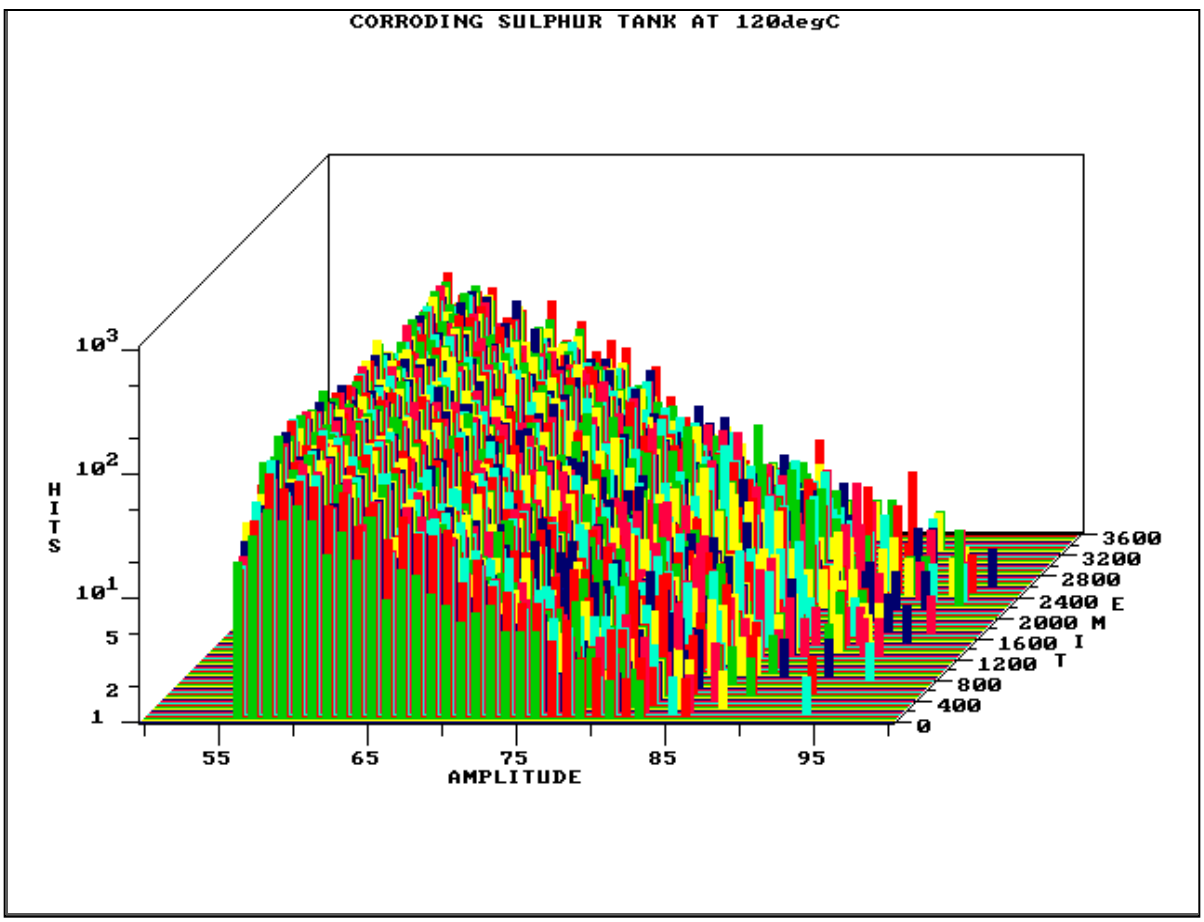

Fig. 1 AE data detected from the tank over a one-hour period.

Analysing the distribution of AE activity as a function of height up the tank wall, having obtained source locations first by 3D analysis, gave the main sources as just above the bottom knuckle and about half way up the tank coinciding with an insulation support ring. General AE activity decreased with height. This result, which showed excellent correlation with corrosion damage, is probably a function of water-retention under the insulation. See Fig. 3:

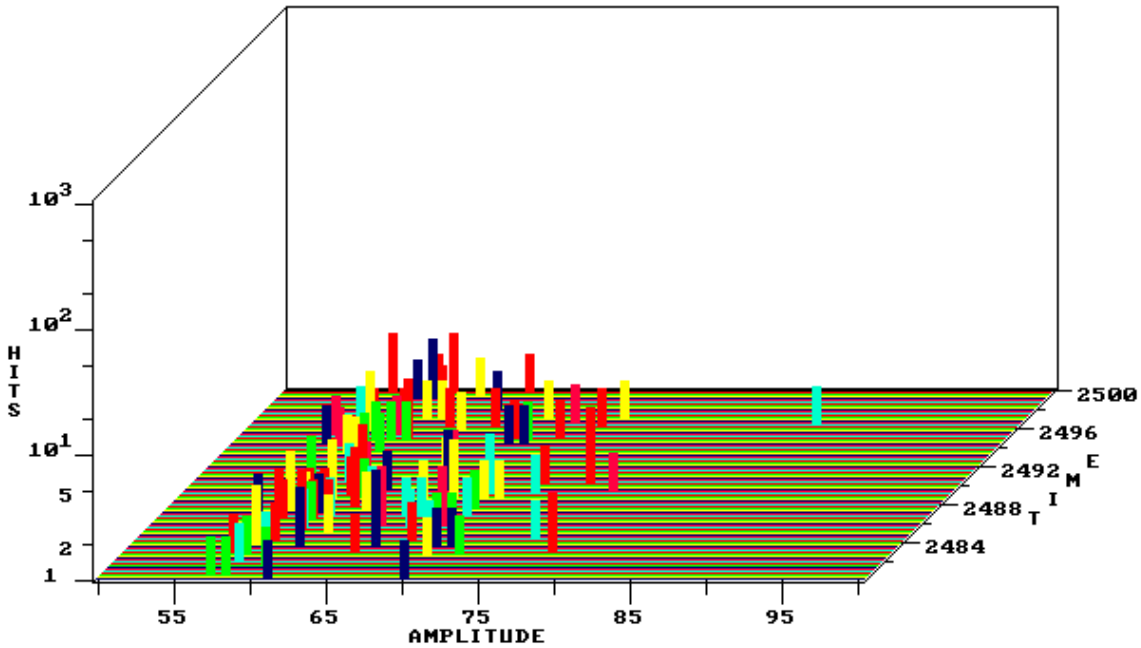

Fig. 2 Expanded AE data detected from the tank over a one hour period.

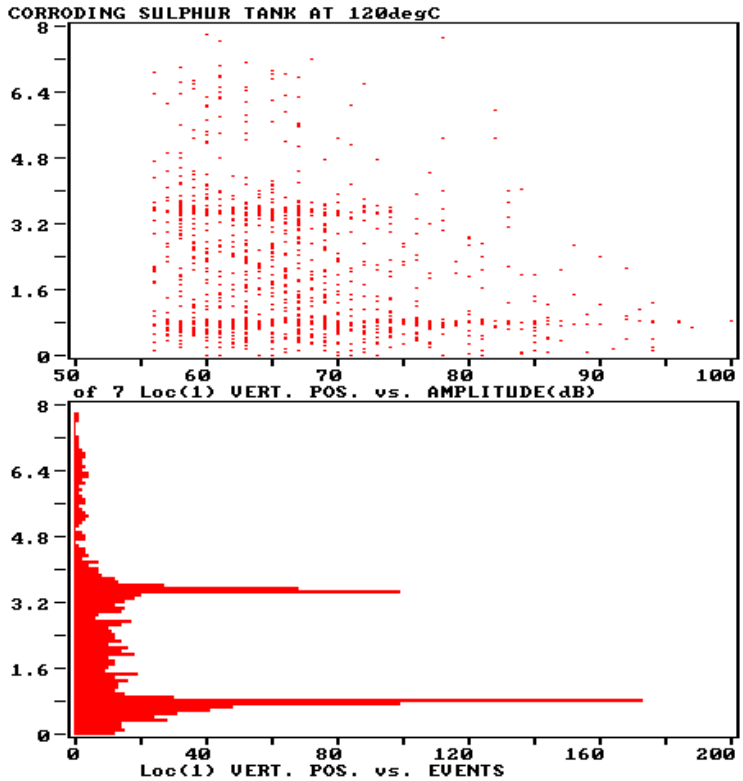

Fig. 3 AE data of corrosion damage.

The top plot of Fig. 3 shows signal amplitudes as a function of height, and the largest signals came from the most active areas. The lower plot shows number of events as a function of height in metres. The rate of activity was variable over a range of about five to one in energy terms, and two to one in hit rate. Figure 4 shows these together with amplitude as a function of time:

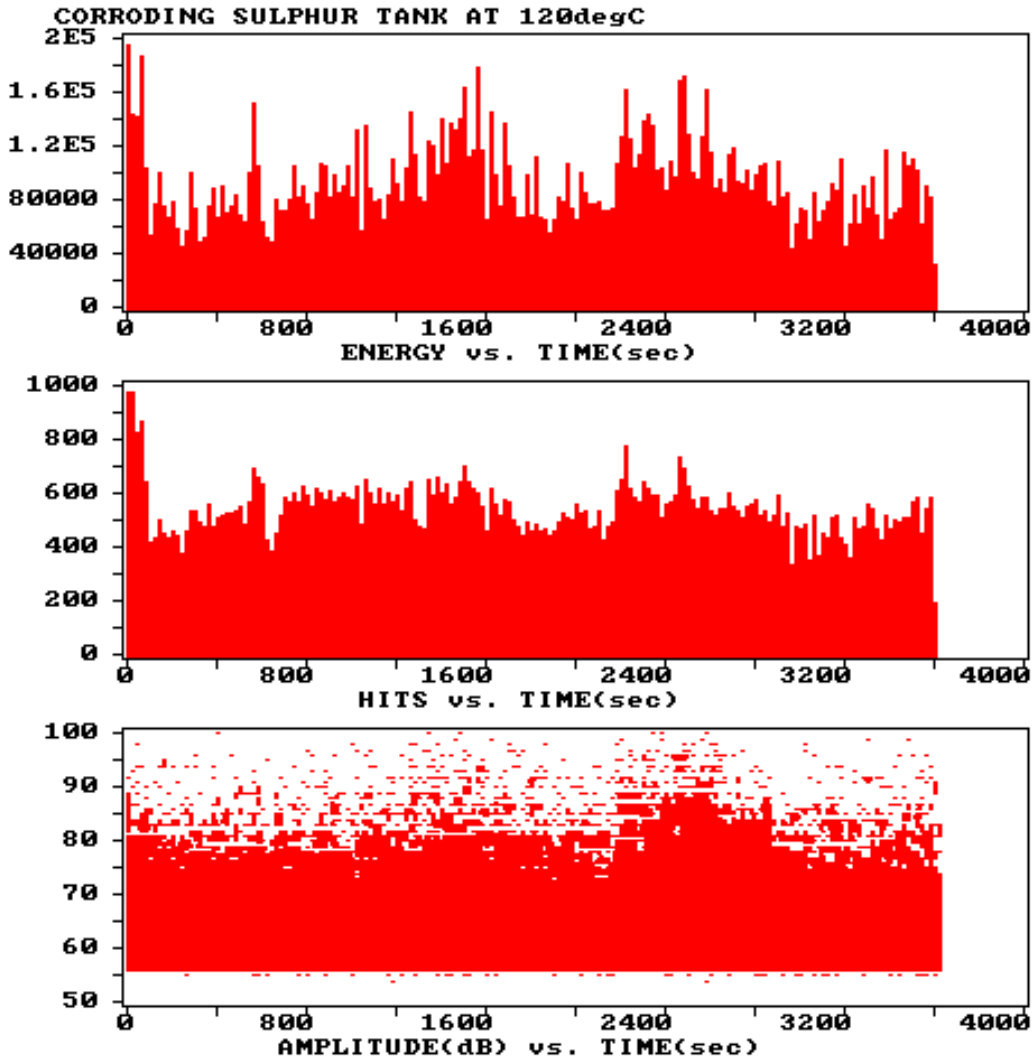

Fig. 4 AE energy and hit rates with amplitude as a function of time.

In terms of AE signal shape, there was nothing particularly special about the emissions. They were "classic" acoustic emissions, fast rise-time relative to duration, (10x), counts/duration related to sensor frequency, except for small numbers "corrupted" by overlapping events, and reflections, together with multiple transmission paths (through fluid and in structure). The planar location of sources on the unwrapped wall, with top and bottom reversed for clarity, is shown in Fig. 5:

4. CONCLUSIONS

Active rusting of carbon steel results in acoustic emission. In extreme cases, copious numbers of high amplitude AE signals are observed, which may be located by their relative time arrival.

REFERENCE

1. S. Yuyama, Fundamental Aspects of Acoustic Emission Applications to the Problems Caused by Corrosion, ASTM STP 908 (1986) p. 4.

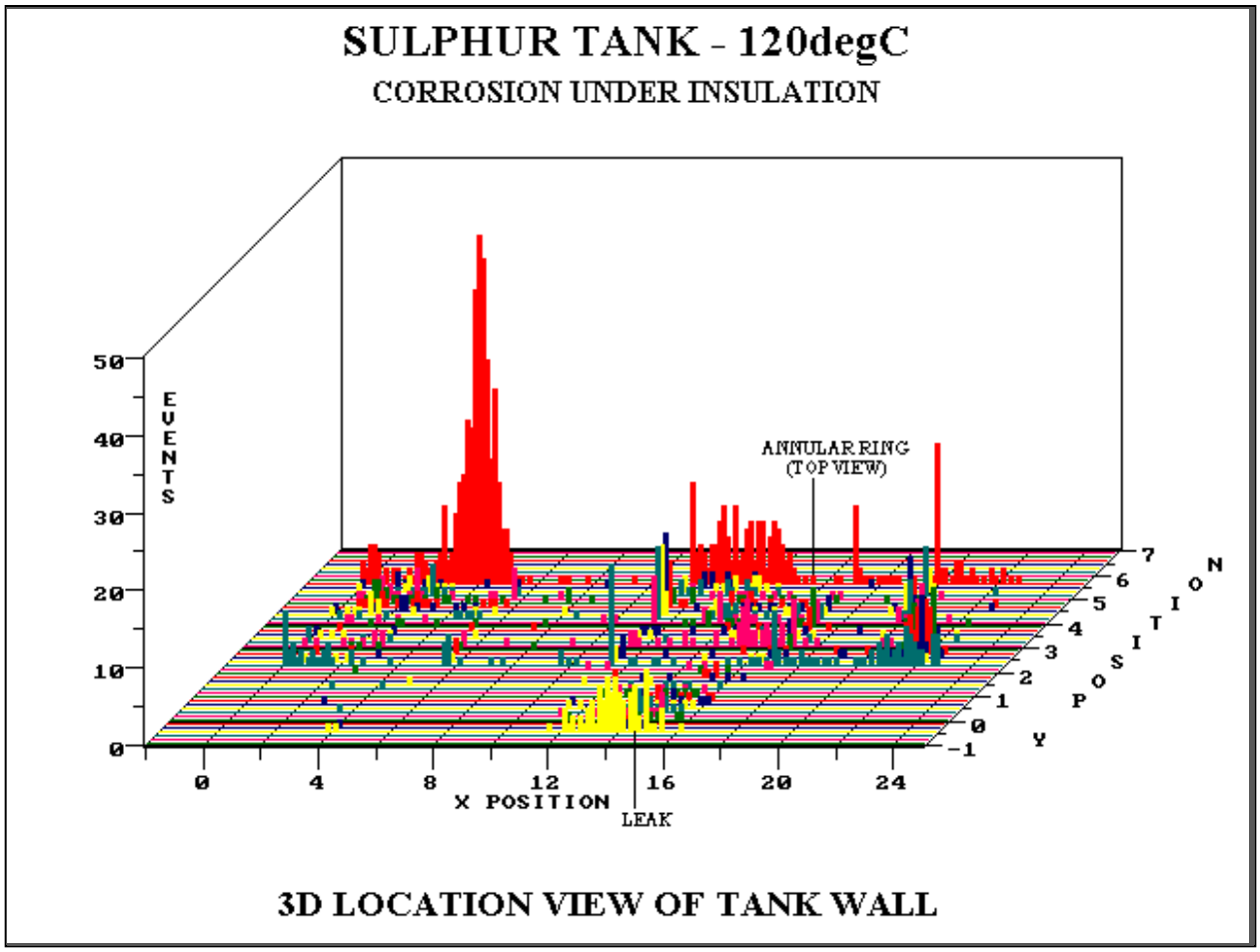

Fig. 5 The planar location of sources on the unwrapped wall.

A NEW SYSTEM FOR MACHINERY DIAGNOSIS USING AE AND VIBRATION SIGNALS

ATSUSHI KORENAGA, SHIGEO SHIMIZU[a], TAKEO YOSHIOKA, HIDEHIRO INABA[b], HIDEMICHI KOMURA[c] and KOJI YAMAMOTO[d]

Mechanical Engineering Laboratory, MITI, Tsukuba, Ibaraki, 305-8564 JAPAN,
[a] Meiji University, Tama, Kawasaki, Kanagawa, 214-8571 JAPAN,
[b] Fuji Ceramics Corporation, Fujinomiya, Shizuoka, 418-0111 JAPAN,
[c] RION Co., Ltd., Kokubunji, Tokyo, 185-8533 JAPAN,
[d] NF Corporation, Kouhoku, Yokohama, Kanagawa, 223-8508 JAPAN

ABSTRACT

Diagnostic monitoring of machinery usually involves detecting separately acoustic emission (AE) and vibration. We have developed a new diagnostic system that detects simultaneously AE and vibration from machinery and provides useful information for diagnosis in order to improve the reliability of machinery diagnostic technique. This diagnostic system comprised a sensor, a measurement unit, a computer and analysis software. The sensor, which is made by an advanced sensor fusion technique and is called a *multi-sensor,* can detect a signal that contains both ingredients of AE and vibration. The measurement unit and the software decomposed the signal into the AE and vibration and converted them into diagnostic information.

1. INTRODUCTION

Maintenance of industrial machinery usually involves time-based maintenance rather than condition-based maintenance. The result is not only the futility in having to replace machine elements that can be used for a longer time, but also the disruption in having to do periodic checks. Now, condition-based maintenance is being introduced into the industry; for example, vibration-based condition monitoring is often done for rotating machinery. However, vibration techniques cannot predict failure even if the detection of failure is possible, and the detection of failure is also difficult in low-speed rotating machines. AE-based diagnostic monitoring systems also have been developed for early prediction of failure (1). Such systems separately analyze AE and vibration, but no system that simultaneously analyzes AE and vibration by using only one sensor has yet been reported.

In 1998, the Research Group on Multiple Sensing Techniques for Machinery Diagnosis (MSD Research Group) was established by 29 organizations that include a bearing manufacturer, a bearing user, a diagnosis equipment manufacturer, a university, and a public institute. The purpose of this research group is to establish higher reliability diagnostic systems used to monitor bearings by analyzing multiple information, such as AE and vibration. The first prototype of a system designed by the group consists of a multi-sensor, a measurement unit, a computer and analysis software. The development process involves members of the research group using and evaluating the prototype. After evaluation, the system will be modified and used in practice in the future.

This paper describes the development of the multi-sensor, outlines the diagnostic system that simultaneously analyzes AE and vibration signals, and describes rolling fatigue tests done to

evaluate the performance of the system. The multi-sensor acts as a vibration sensor and AE sensor. The diagnostic system simultaneously analyzes vibration and AE, and outputs the result as a digital file in a computer.

2. MULTI-SENSOR

Description

The appearance and sectional view of the multi-sensor are shown in Fig. 1. The detecting faceplate is made of alumina, same as that of ordinary AE sensors. The detection element of a piezoelectric acceleration sensor is bonded to the detection faceplate. The electrode plate is held between two piezoelectric ceramics, and the signal from this plate passes through the connector to the measurement unit (described in the next section). Load mass above the second piezoelectric ceramic is the damper material. The two piezoelectric ceramics and damper material are ring-shaped, whose outer diameter is 9 mm, inner diameter is 3.6 mm, and thickness is 2 mm. In our experiments to optimize the multi-sensor (discussed later in this paper), we used damper material of various thickness (1.6, 2.6, and 5.6 mm). A cover is screwed on over the damper material at sufficient torque because it is easy to be transformed. The multi-sensor has a stainless steel case that is 20 mm in diameter and 30 mm high. Future versions of the multi-sensor will include a preamplifier in the upper space.

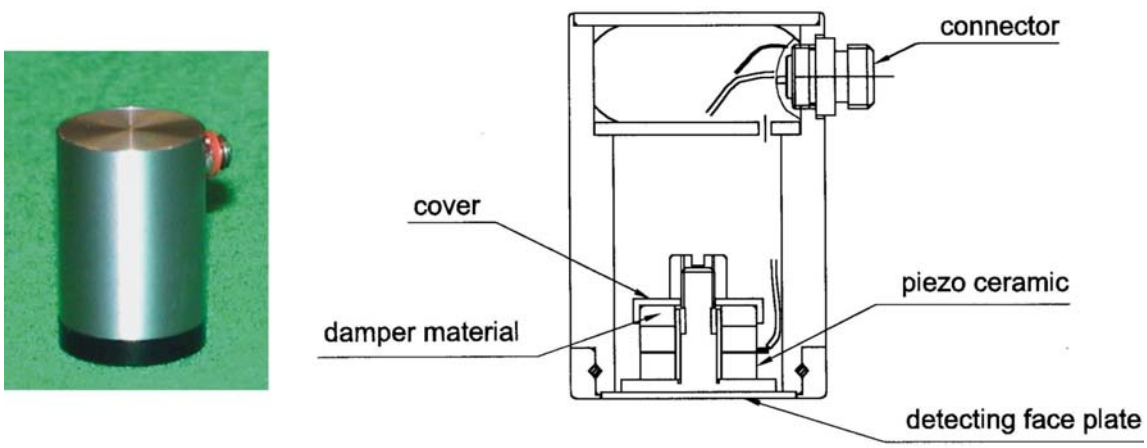

(a) Appearance (b) Sectional view

Fig. 1 The multi-sensor.

Principle of Detection

The multi-sensor has both a piezoelectric acceleration sensor and damper material of the wide-band type AE sensor as a load mass. To miniaturize the sensor, high-density tungsten alloy whose density is 17.1 Mg/m^3 is used as the load mass of the acceleration sensor. While the damper material of the wide-band type AE sensor acts as the load mass of the acceleration sensor, this sensor also operates as an acceleration sensor because the damper material functions as a load mass in the low-frequency range. Furthermore, the damper material initially functions in the high-frequency range. Thus, this sensor operates as a compound sensor for both vibration and AE.

Evaluation of the Acceleration Sensor

Frequency characteristics were measured by a comparative calibration method in order to evaluate characteristics as an acceleration sensor component of the multi-sensor. Figure 2 shows

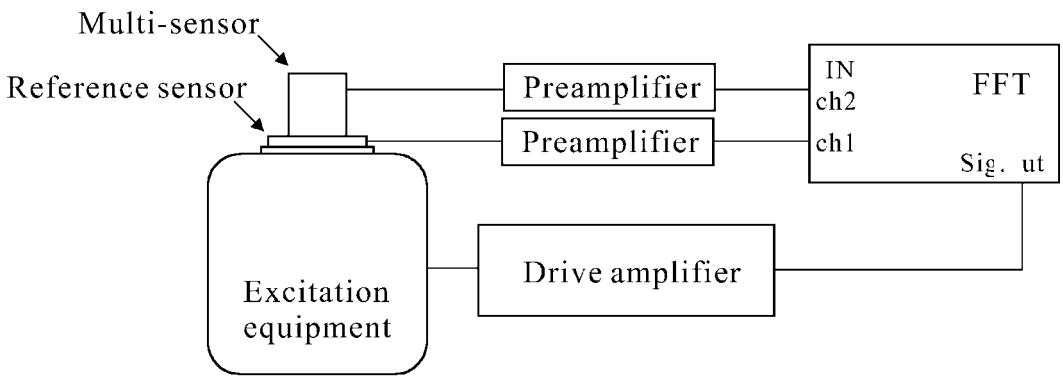

Fig. 2 Block diagram of the calibration apparatus.

a block diagram of the calibration apparatus. The multi-sensor was fixed on a pre-calibrated reference sensor, which was fixed on the excitation equipment. Vibration from the excitation equipment was applied to both sensors simultaneously, and each output was analyzed by using fast Fourier transform (FFT), and the sensitivity of the multi-sensor was obtained by comparing the output of the multi-sensor with that of the reference sensor. The units of the sensitivity are in m/s^2, and the sensitivity at 100 Hz is shown as 0 dB in frequency characteristic data. The resonant frequency of the reference sensor is about 100 kHz.

Evaluation of the AE Sensor

Characteristics of the AE sensor component of the multi-sensor were evaluated by measuring the longitudinal wave sensitivity of the multi-sensor with a secondary calibration method of the reciprocity method. The multi-sensor and the reference sensor were installed on opposite surfaces of a calibration block (0.6 m in diameter, 0.36-m thickness). The sensitivity was calculated from both the transmitting sensitivity of the reference sensor and the output of the multi-sensor. The units of the sensitivity are m/s, and 0 dB corresponds to 1 V/m/s.

Evaluation Results

Table 1 shows the sensor characteristics and Fig. 3 shows the frequency characteristics for the different thickness of damper material.

Table 1 The sensor characteristics.

Thickness of damper material	Sensor	Sensitivity	Frequency band	Resonant frequency
5.6mm	Acceleration	4.75mV/m/s^2	~20kHz	35kHz
	AE	59.7dB(966V/m/s)	100~520kHz	
2.6mm	Acceleration	3.22mV/m/s^2	~20kHz	32kHz
	AE	56dB(631V/m/s)	100~544kHz	
1.6mm	Acceleration	2.46mV/m/s^2	~50kHz	60kHz↑
	AE	55dB(562V/m/s)	110~666kHz	(62kHz)

The sensitivity of the acceleration sensor improved and the resonant frequency decreased when the thickness of the damper material was increased (Table 1). The reason is that resonance originates from the spring-mass system of the damper material and piezoelectric ceramics.

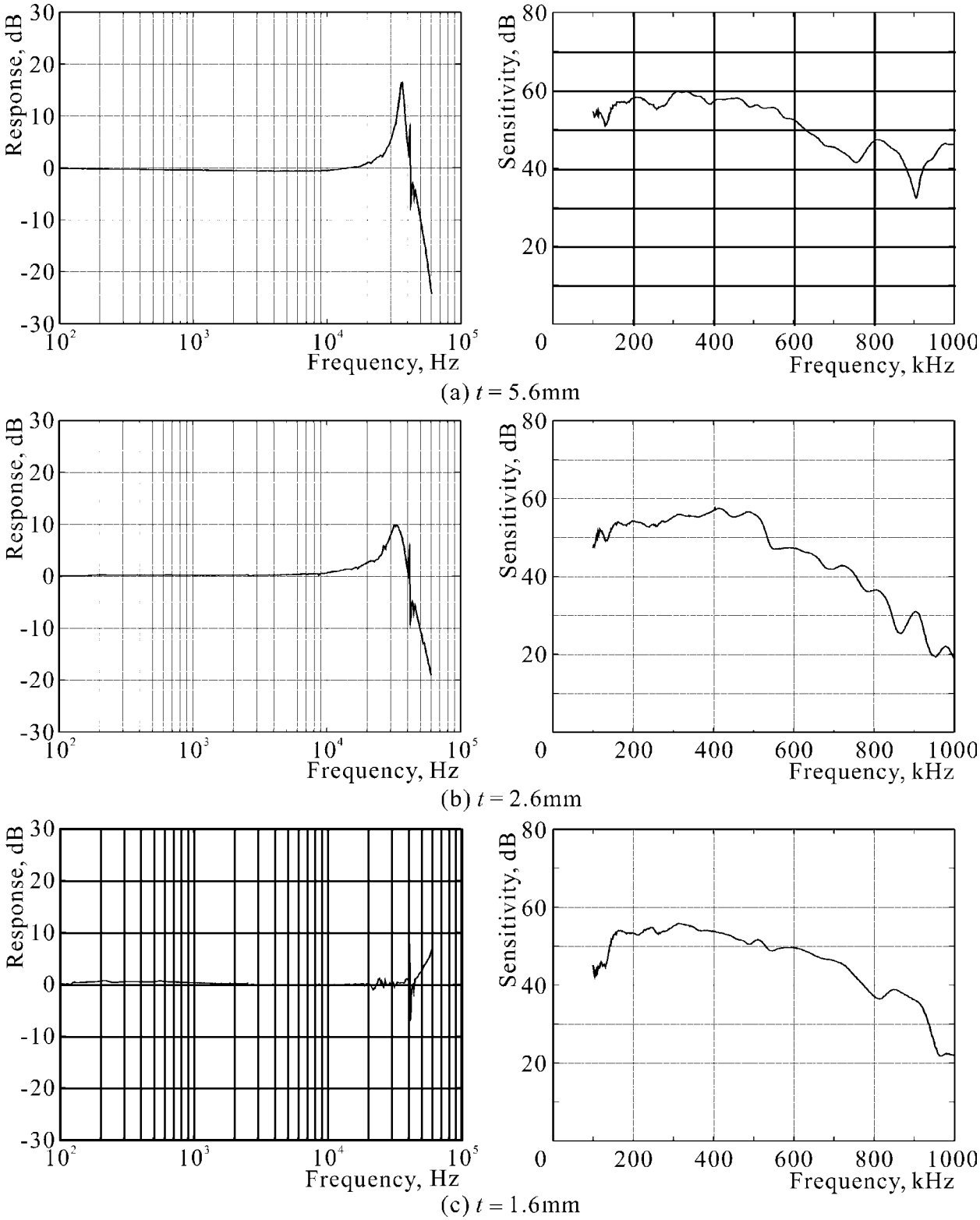

Fig. 3 Frequency characteristics of sensors.

However, the resonant frequency for the 2.6-mm-thick damper material was slightly lower than that for the 5.6-mm-thick damper material due to the junction condition of the damper material and piezoelectric ceramic. When a thinner damper material was used, the sensor could be used at a higher frequency. But the sensor using thinner damper material is difficult to use as an AE

sensor, because the sensitivity of the sensor decreases and the resonant frequency shifts into the AE region. Furthermore, when a thinner damper material was used (1.6 mm or less), the wide-band characteristics of the sensor deteriorated because the damping of the AE wave decreased. Based on these evaluation results, the optimum thickness of the damper material is 1.6 mm because the sensor can then be used at 50 kHz as an acceleration sensor and at 110~660 kHz as an AE sensor.

3. DIAGNOSTIC SYSTEM

The diagnostic system (Fig. 4) consists of a multi-sensor, a measurement unit, a computer, and analysis software.

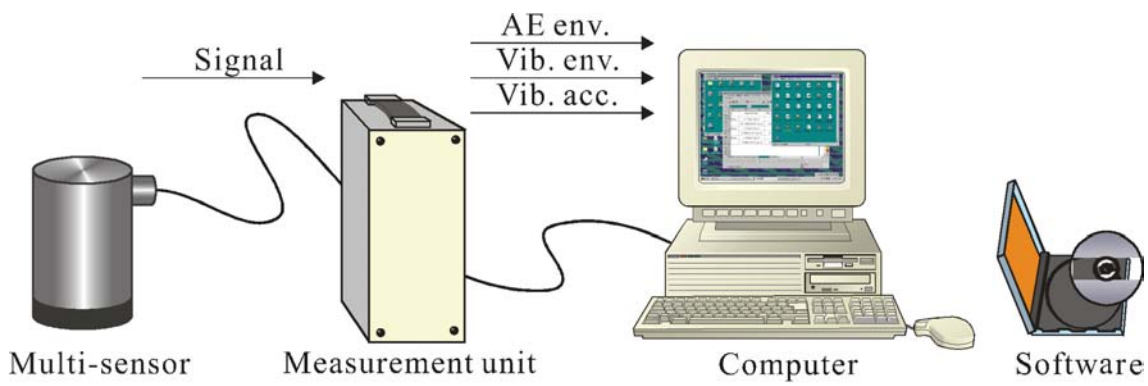

Fig. 4 Composition of the new diagnostic system.

Measurement Unit

The measurement unit contains a high-pass filter (20, 50, 100 kHz), low pass filter (100, 200, 500 kHz), amplifier (0~60dB), and signal processor. The measurement unit receives a signal from the multi-sensor, and then processes it by dividing it into AE and vibration, both of which are then processed into enveloped waveforms assuming a time constant of 1ms. The output signals are AE signal envelope, vibration signal envelope and vibration acceleration wave. These waveforms are transferred to the computer for storage and analysis.

Computer and Analysis Software

The computer receives processed signals from the measurement unit through an A/D converter and analyzes the signal by using the software we developed. The software runs on a DOS/V, Pentium® 133MHz computer. The analysis software counts AE events, calculates basic statistics (i.e., $S_i = \sum x_i^i$, $i = 1\sim6$), and does the FFT analysis for the AE and vibration signals. The sampling time is 100μs. The software creates a digital data file and outputs the count of AE events and the calculation result to a file at 1 minute intervals.

4. EXPERIMENT

As one of the experiments to evaluate the performance of the diagnostic system, rolling

fatigue test of bearing has been carrying out. The test bearing simulated a thrust ball bearing #51205. To accelerate the fatigue test by increasing the stress in the contact area, three balls were rolled on the outer raceway without a groove shoulder. The hertzian maximum stress induced in the outer raceway was 5.9GPa. To confirm the performance of the multi-sensor, AE and vibration signals were measured by conventional sensors which are on commercial base and by the multi-sensor.

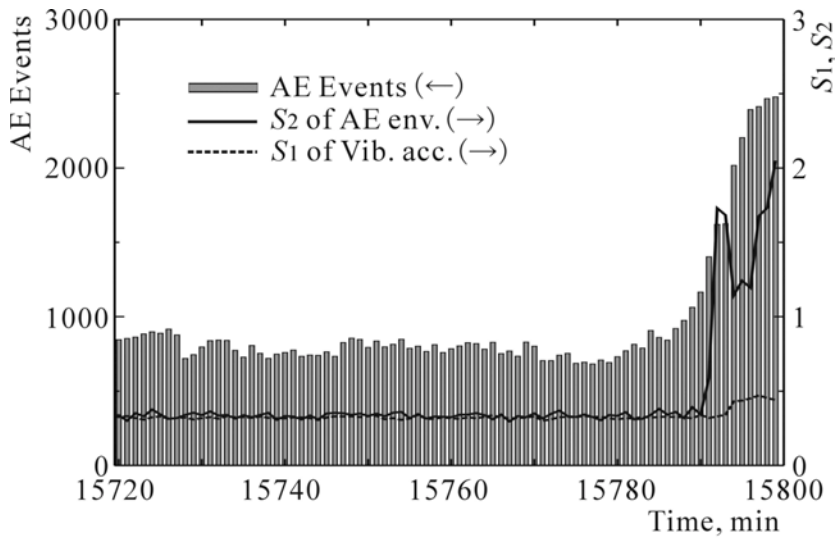

Fig. 5 Trend of AE events and basic statistics.

Figure 5 shows the trend of AE events, basic statistics S_2 of AE enveloped waveform and S_1 of vibration acceleration waveform. This test was stopped at 15799 min because of the spalling on the outer raceway. It seemed to generate the spalling at 15794 min, because the S_1 of vibration acceleration increased. Before that, AE Events and S_2 of AE enveloped waveform increased by originating from the propagation of the crack.

5. SUMMARY

We have proposed a predictive system with high reliability of the bearing diagnosis by monitoring multiple information of AE and vibration, and produced an experimental system. The 17 of the 29 organizations that belong to the MSD Research Group are making the demonstrational experiments using this system. These experiments will provide insight into the effectiveness of this system. When successfully implemented, the combination of the multi-sensor and the monitoring of multiple information will significantly improve the maintenance of industrial machinery.

REFERENCE

1. T. Yoshioka and H. Mano, “Relationship between Acoustic Emission Source Position and Spalling Position in Radial Rolling Bearings” *Tribology for Energy Conservation*, Elsevier Science B.V., (1998), p. 413.

DEVELOPMENT OF ABNORMALITY DETECTION TECHNOLOGY FOR ELECTRIC GENERATION STEAM TURBINES

AKIHIRO SATO, EISAKU NAKASHIMA, MASAMI KOIKE, MORIHIKO MAEDA*, TOSHIKATSU YOSHIARA* and SHIGETO NISHIMOTO*

Research Laboratory, Kyushu Electric Power Co., Minami, Fukuoka 815-8520 Japan
*Research Institute of Safety, Non-Destructive Inspection Co., Nishi, Osaka 550-0014 Japan

ABSTRACT

At thermal power plants that have been in service for more than 5,000 hours, steam-oxidized scales peel off inside the pipes of the boiler super-heater and flow into the steam turbine, causing erosion damage to the blades and nozzles. In order to avoid such damage, the nozzles are coated by boron and the particle levels are controlled in the condenser. Japanese electric power companies are facing an amendment of the Electric Utility Industry Law, which requires voluntary maintenance practices for longer intervals between periodic repairs and for life-extension of the existing plants. Therefore, a new technique is urgently needed to detect erosion damage at an early stage for effective maintenance. Acoustic emission (AE) has been monitored continuously for two years at a main turbine of Ainoura thermal power station. It was demonstrated that damage of the turbine nozzle can be detected by AE at an early stage. This paper reports on the procedures and evaluation criteria to detect erosion damage in the turbine.

1. INTRODUCTION

The collision of oxide scale in a steam flow causes the erosion of steam turbine blades, which may affect stable operation of the power generation plant by unexpected shut-down of steam turbines. It is necessary to detect the progress of damage of the turbine blades due to erosion as early as possible. However, the monitoring technique for the erosion of turbine blades in operation has not been established. Acoustic emission (AE) techniques have been regarded as useful for on-line monitoring of abnormal phenomena of industrial equipment. Thus, we applied an AE technique to detect the erosion of turbine blades at a thermal power plant.

At first, we obtained the characteristics of simulated AE at the collision of oxide scale with the steam turbine blades [1]. Furthermore, taking into consideration of AE measurement conditions, it was concluded that the AE technique enables us to detect erosion of the steam turbine blade. In this study, we examined AE from the erosion of steam turbine blades at an actual operating power plant.

2. AE MEASUREMENT DEVICE AND MEASUREMENT CONDITIONS

AE Measurement System

We designed a measurement system, which allows stable long-term evaluation of AE signals originated from a turbine. The block diagram of the system is shown in Fig. 1. The locations of the AE sensors and cables are shown in Fig. 2. AE sensors (wideband; AE-1544WA), are installed near each turbine bearing using glue and magnetic holders. Evaluation of AE from the turbines was conducted, mainly in sensors I, III, and V, while sensors II, IV and VI were paired with sensors I, III and V, respectively, and used to evaluate the origin of AE signals.

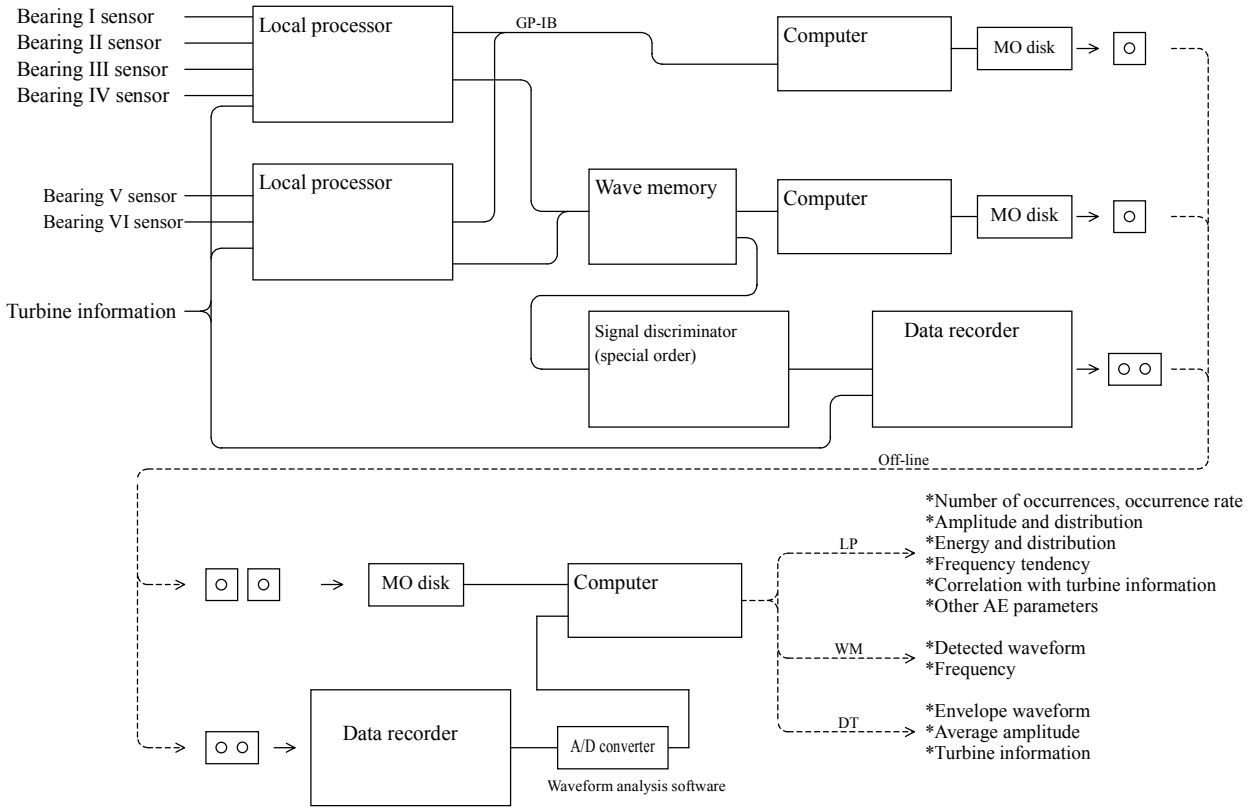

Fig. 1 Measurement system block diagram.

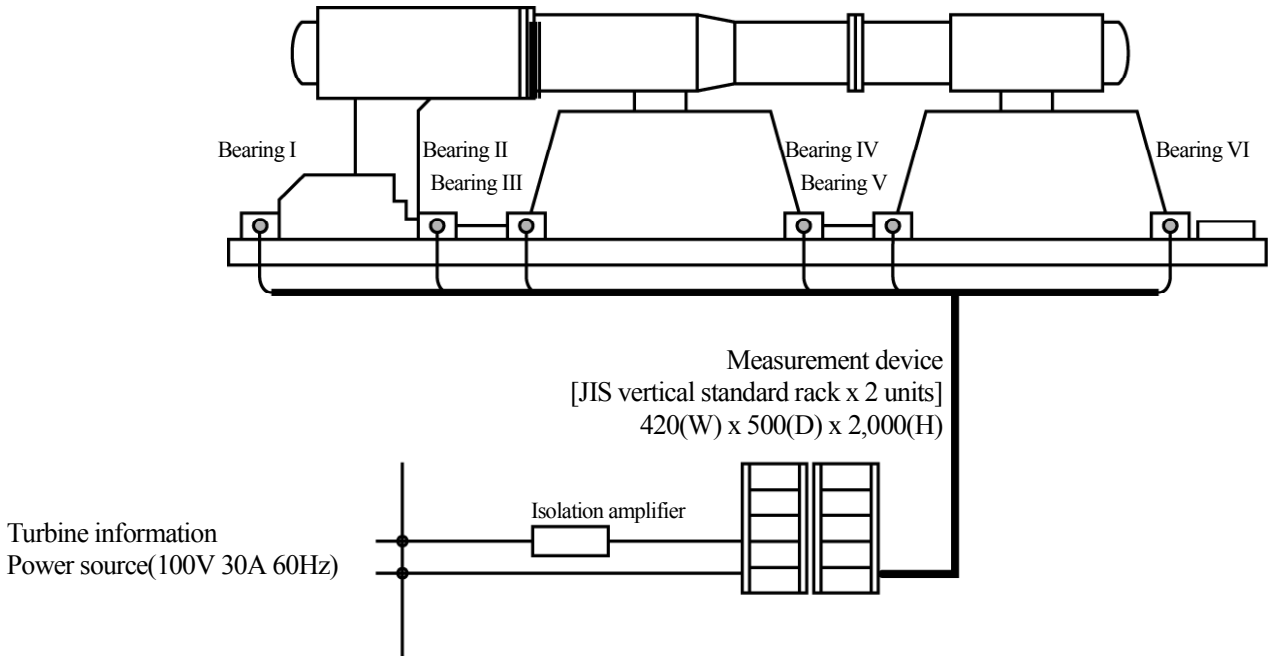

Fig. 2 AE sensor installation location and measurement device installation.

AE signals detected at each sensor were analyzed, extracting waveform parameters using a local processor, and the data were stored in the MO disk of the computer. The detected waveforms themselves were first recorded in the wave memory, and transferred to the MO disk of the computer, and recorded. The envelope waveforms were recorded on DAT tape of the data recorder. Detailed analysis on the AE parameters stored in the MO disk and the detected waveforms were made using a computer. The envelope waveforms recorded on the DAT tape were analyzed after A/D conversion.

Measurement Conditions

It has been confirmed through laboratory tests and other means that, at the time of turbine damage, we observed AE signals with amplitudes of 100 dB or more (in reference to 10 μV at 0 dB) and frequency components with the first moment (or the center of frequency spectrum) of 200 kHz or higher. However, the amplitude of an AE signal can be high depending on the type of a fracture source. Therefore, we used wideband sensors, which can withstand a wide range of temperature and vibration. Other conditions are shown in Table 1.

Figure 3 shows the wave propagation study being conducted by inputting simulated AE signals using an impulse-force hammer into the high-pressure (HP) and intermediate-pressure (IP) turbine blades. Signal level was attenuated by 20 dB. This measurement found that the AE generated inside the turbine can be evaluated by the sensors placed outside the turbine. The threshold value for each sensor installed at each bearing was set in advance. Signals that exceeded the respective threshold values were collected as AE signals.

Table 1 Measurement conditions.

Items	Conditions
HPF	200 kHz
LPF	1 MHz
Amplification factor	LOGARITHMIC
Threshold values	77 dB – 97 dB
AE sensors	Wide-band type AE-1544WA

Fig. 3 Wave propagation measurement with simulated AE signals.

Signal Analysis Parameters

As a method for evaluating turbine damage, it is necessary to examine the change in the waveforms and frequency components of AE. In conducting the evaluation, the elements below are particularly important:

1. waveform (detected waveform)
2. waveform (waveform envelope)
3. frequency (analysis of detected waveform frequency)
4. interval of AE generation
5. amplitude
6. number of AE events

3. TEST RESULTS

Outline of the Tests

AE measurement was conducted on a 500-MW supercritical steam power unit during daily start-ups and shut-downs. Note that the plant had been in service for over 120,000 hours. The general information on the facilities is shown in Table 2. The operation status of the test unit was as follows:

- Period of measurement: November 29, 1996 to October 9, 1998
- Operation hours during AE monitoring: 6,483 hours
- Number of start-ups and shut-downs: 57 (cold start 15)

Prior to testing, the following two points were checked to confirm the absence of abnormalities:

1. Electro-magnetic waves were to have no effect on the electric generation equipment, nor on existing vibration sensors
2. Conditions of sensor coupling and cables.

Separation of Background Noise

Background noise from the steam in-flow and that from the high-speed revolutions during operation were separated according to threshold values set for each bearing. The number of AE hits and the AE amplitude (energy) detected from the collision of particles and damage on the facilities were continuously monitored. Figure 4 shows the background noise and AE signals with high amplitudes.

Table 2 Unit 2 Facilities.

Commissioning			October 1976	
Accumulated operation hours			126,662 hours (as of September 29, 1996)	
Output			500 MW	
Fuel			Heavy oil, crude oil	
Specifications	Boiler	Model	Mitsubishi through CE Combined circulation boiler Radiative reheat divided furnace	
		Max. evaporation	1,720 T/H	
	Turbine	Model	Toshiba tandem-compound 3 casing 4 flow Exhaust air reheat condenser type	
		Steam pressure	246 kg/cm^2	
		Steam temperature	Main steam	811K
			Reheated steam	811K

AE Generated from the HP and IP Rotors (Cold Start)

It was found that the location of AE generation could be identified from the difference in propagation speed (time difference) between AE sensors installed on the 1st and 2nd bearings. Particles in the steam flow move from the HP first stage nozzle (center in Fig. 5), through the HP turbine, then, after being reheated in the boiler, head towards the LP turbine from the center part of Fig. 5 through the IP turbine.

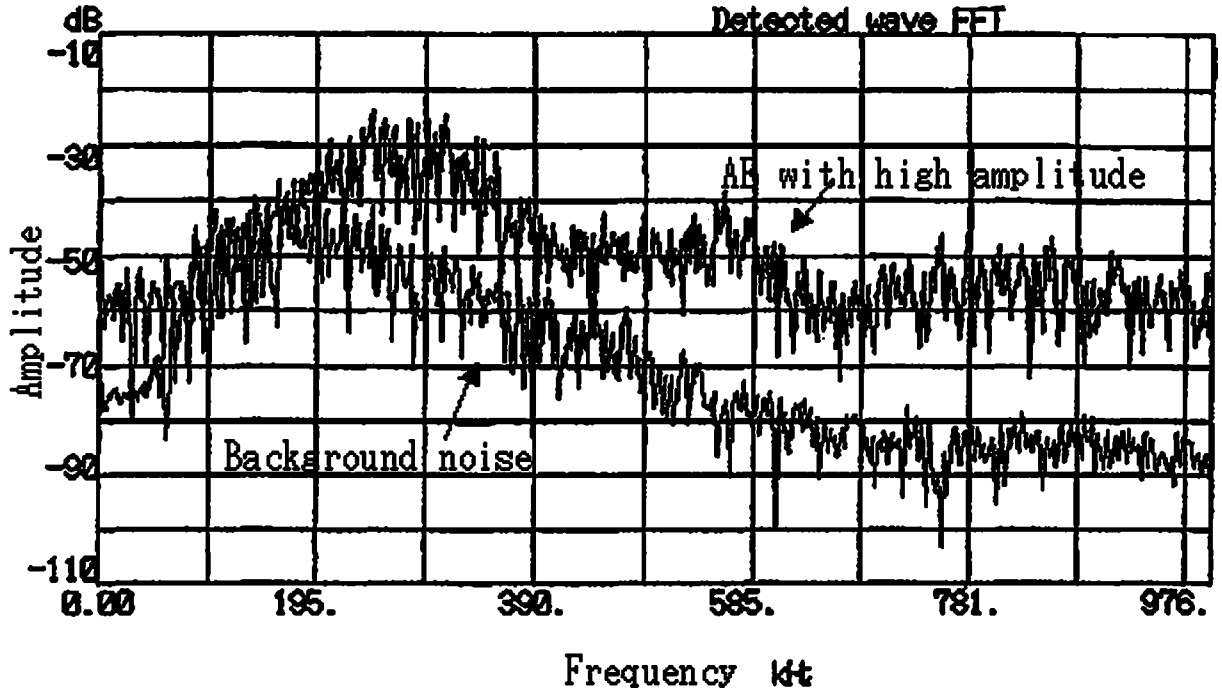

Fig. 4 Background noise and AE signals

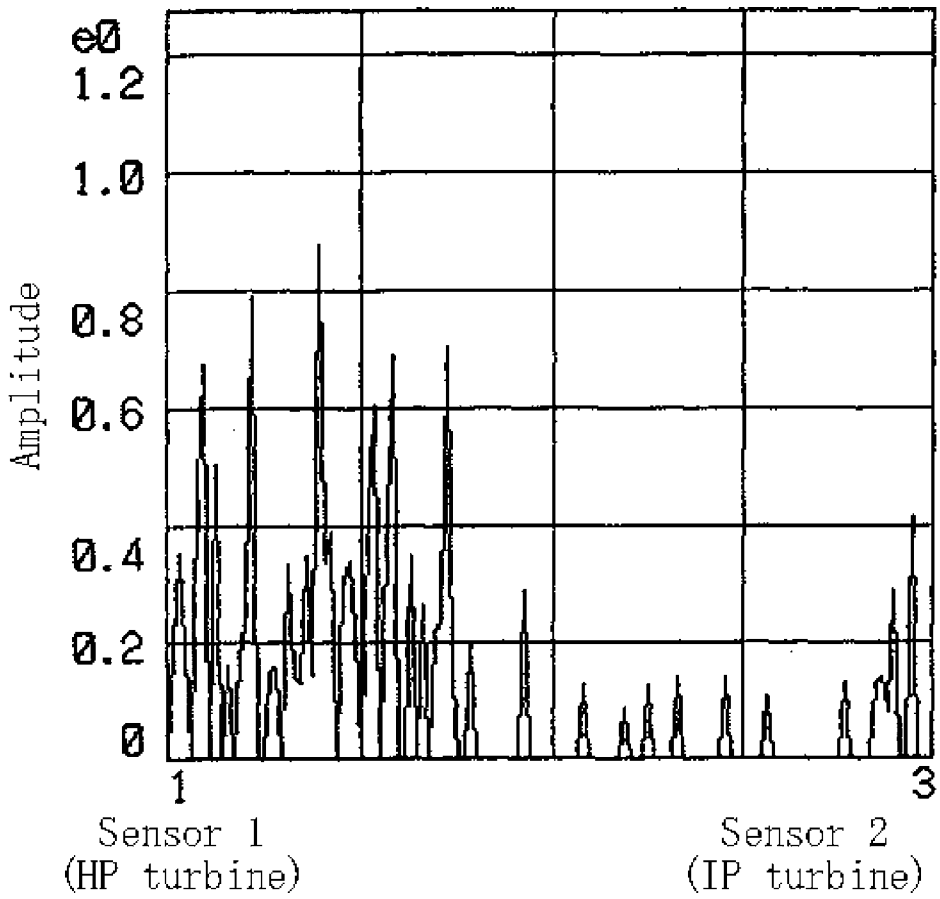

Fig. 5 Locations of AE generation.

Figure 5 shows the AE amplitude generated by the collision of solid particles in the HP and IP rotors (between the 1st and 2nd bearings) during a cold start. AE is concentrated on the HP side due to its high steam energy level. It also shows that the locations of AE amplitude agrees well with the locations of the rotor blades.

AE Wave during Normal Operation

Figure 6 shows AE generation for one typical month (August 1997) which includes daily start-ups and shutdowns during the measurement period.

- The detected AE signals show the highest value of 90 dB, immediately after start-up; the first moment of 250 kHz or more was found in the range of 80-90 dB.
- There was no problem in turbine operation during this period as shown by the value on the existing shaft vibration meter. It is 15-25 µm, which is significantly lower than the control value of 50 µm.

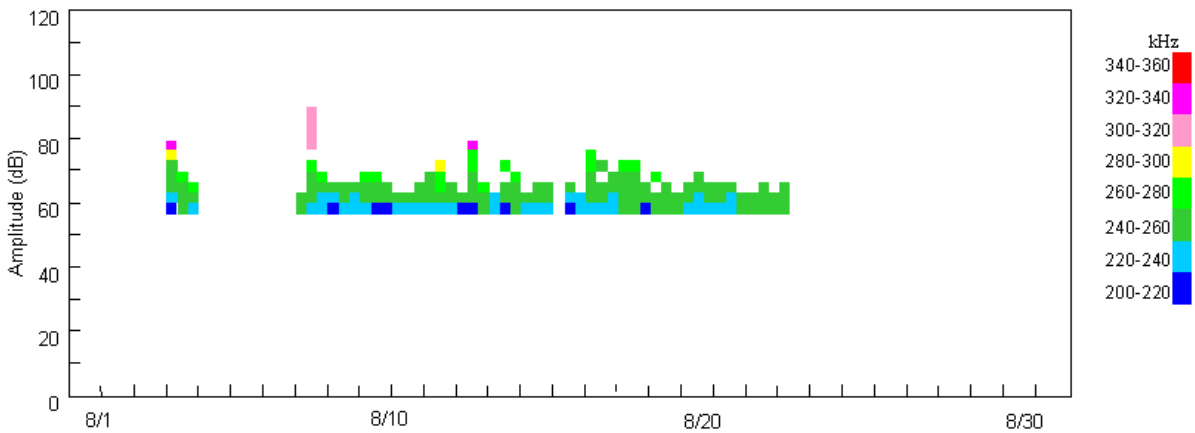

Fig. 6 AE wave during normal operation (August 1997).

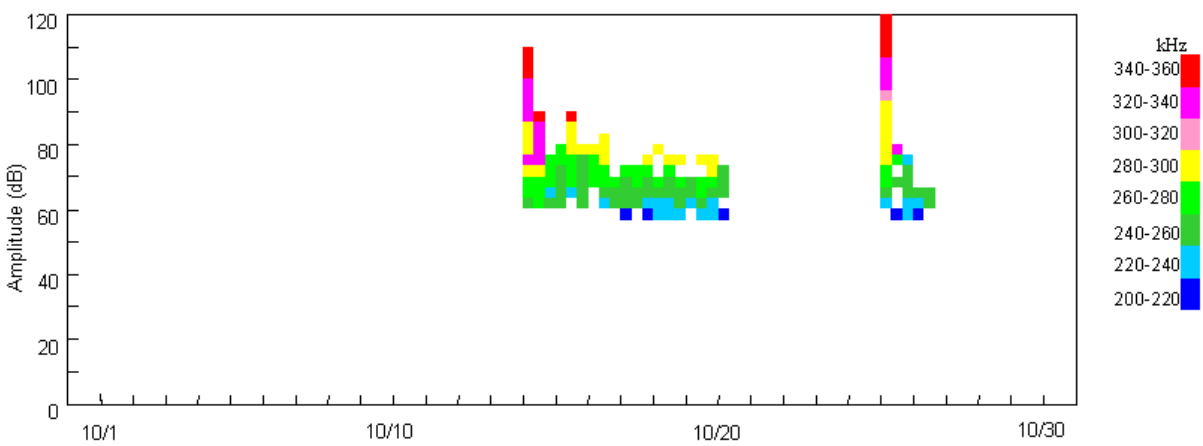

Fig. 7 AE wave at signs of turbine abnormality (October 1998)

AE Wave at Signs of Turbine Abnormality

Figure 7 shows AE generation immediately after a cold start (October 1998) and immediately after a restart. The axis of ordinates represents the amplitude and first moment; the axis of the abscissas represents the passage of time.

- AE signals with an amplitude of 80 dB or more are observed during and after the speed-up between turbine revolutions of 800-3,600 rpm. Especially upon a load increase from the parallel mode to 250 MW, the highest amplitudes of 120 dB or more are detected. First moment at this time varied in excess of 300 kHz.

• The 120 dB amplitude detected at this time should correspond to the damage which is larger than 30-100 times amplitude of 80-90dB, seen during the normal cold start.
• After this large amplitude is detected, the occurrence of unstable turbine vibration was observed at a load range of 400 – 500MW. The values measured by the existing shaft vibration meter registered 45-60 μm, exceeding the control value of 50 μm.
• At the time of the overhaul (October, 1998), cracks and damage, which are considered to be caused by the collision of particles, were observed on the turbine nozzle blades as shown in Fig. 8.

Fig. 8 HP first-stage turbine nozzle damaged by solid particles.

4. DISCUSSION

After examination of AE propagation characteristics on actual turbines, a system capable of long-term stable detection of AE was developed. This technology utilizes the AE sensors installed near the bearings for the detection of AE signals due to turbine damage.
• It detected AE waves from an actual turbine on a continuous basis for two years.
• Analyses and evaluation of collected data revealed that an examination of the amplitude variations of the waveform and first moment is effective to detect turbine damage.
• It was confirmed that high amplitude AE signals are observed prior to the onset of unstable vibration caused by turbine nozzle damage. Therefore, it is possible to detect turbine failure in the early stages by monitoring AE.

5. CONCLUSION

AE behavior was studied during the operation of a main steam turbine. The results suggest that AE is a promising technique for effective diagnosis to detect turbine failure in its early stages and found to be effective for practical maintenance program. In the future, further study will be made to develop a reliable AE system to evaluate turbine conditions in real time.

REFERENCE

1. M. Maeda, T. Yoshiara, T. Imanaka, S. Nishimoto, A. Sato, E. Nakashima, and M. Koike, *Progress in AE X*, eds. T. Kishi et al., JSNDI, Tokyo (2000), pp. 395-398.

ACOUSTIC EMISSION SIGNAL CLASSIFICATION IN CONDITION MONITORING USING THE KOLMOGOROV-SMIRNOV STATISTIC

L. D. HALL, D. MBA and R.H. BANNISTER

School of Mechanical Engineering, Cranfield University, Bedfordshire, UK

ABSTRACT

Acoustic emission (AE) measurement at the bearings of rotating machinery has become a useful tool for diagnosing incipient fault conditions. In particular, AE can be used to detect unwanted intermittent or partial rubbing between a rotating central shaft and surrounding stationary components. This is a particular problem encountered in gas turbines used for power generation. For successful fault diagnosis, it is important to adopt AE signal analysis techniques capable of distinguishing between various types of rub mechanisms. It is also useful to develop techniques for inferring information such as the severity of rubbing or the type of seal material making contact on the shaft.

It is proposed that modelling the cumulative distribution function of rub-induced AE signals with respect to appropriate theoretical distributions, and quantifying the goodness of fit with the Kolmogorov-Smirnov (KS) statistic, offer a suitable signal feature for diagnosis. This paper demonstrates the successful use of the KS feature for discriminating different classes of shaft-seal rubbing. A hierarchical cluster algorithm was employed for grouping extracted KS values. AE rub signals were simulated with various metallic seals and measured at the journal bearings of a test rig rotating at approximately 1500 rev/min. Also, the KS classification results were directly compared with more established AE feature vectors.

1. INTRODUCTION

Measurement of high frequency acoustic emissions (AE) has become a viable technique in the condition monitoring of many types of rotating machinery (McFadden and Smith, 1983; Sato, 1990; Holroyd and Randall, 1992; Mba and Bannister, 1999; Choudhury and Tandon, 2000;). Due to its superior sensitivity over conventional low frequency vibration analysis, AE measurements can provide an earlier indication of incipient faults such as fictional rubbing. In addition, time-synchronous measurement from more than one AE transducer often allows the location of rubbing to be estimated.

However, in real operational machinery it is often only practical to take AE measurements from non-rotating members, at or on the bearing housing. Consequently, AE signals originating from the rotating shaft will incur significant perturbation across the transmission path to an AE receiver attached at the bearing housing. This can be related to inhomogenities and scatterers within the structure, reflections at acoustic boundaries, interference and attenuation effects across the bearing interfaces. Moreover, the AE signal will be further coloured by the characteristic frequency response of the AE transducer itself. In light of these factors, interpretation of the AE signals is not trivial and often departs from the classic AE signal model (Mitrakovic and Grabec, 1985; Venkatesan, 1996).

In recent years various signal processing and pattern recognition techniques have been successfully applied to AE signals for diagnosing the severity and location of defects in various types of rotating machinery. Notably artificial neural networks (ANN) (Li, 1989) and clustering (Ono and Huang, 1994) have been adopted for AE signal classification. Regardless of the classification engine employed, it is invariably identification of the key resolving features or descriptors within the AE signal that is paramount for successful classification. Generally, the size of the feature vector chosen depends upon the specific application and recognition requirements. Previous studies (Chan, 1985) employed relatively large feature vectors for the AE signal classification problem. However, for discriminating between different classes of rub signatures, it was considered useful to define a feature vector with a minimum number of parameters (often assessed by a quality index). This can be related to the stability of the classification result in a clustering algorithm and is justified by 'the curse of dimensionality' (Bishop, 1999) within an ANN approach.

Typical features extracted from AE signatures in condition monitoring include peak or total energy, standard deviation, median, AE counts, RMS voltage and duration. However, these are all related to absolute energy levels of the measured waveform or rely upon pre-set amplitude thresholds. As such, the quantities exhibit considerable variability from one bearing measurement to the next and are thus extremely dependent upon factors such as background noise, in addition to AE transducer positioning and coupling. Consequently, it is believed that such features are not ideal for AE waveform classification, especially in cases where several measurement positions are required.

Alternative features more related to the amplitude statistics of the measured AE waveforms and independent of absolute energy levels have also been considered. Notably, the fourth statistical moment known as kurtosis and the ratio of peak to RMS voltage known as crest factor have been applied for condition monitoring in rotating machinery. However, laboratory tests conducted as part of this research have indicated both of these quantities to be unsuitable for classification.

Spectral analysis techniques, such as the FFT have found numerous applications in acoustic signal classification (Chan et al., 1985; Liangand and Dornfeld, 1987). Although some success has been reported in using certain spectral information within specified bands for AE classification, it is not generally believed to provide robust classification results. This is primarily because of the intrinsic broadband nature of measured AE activity and the frequency characteristics of the measurement system. Alternatively, transformations that do not involve a total averaging of time information such as wavelet transforms, spectrograms or the Wigner-Ville distributions could yield more suitable AE signal features.

In contrast, it has been shown that modelling an AE signal as an autoregressive stochastic process, as described by Melton (1982) and later Mba (1999), can provide good AE classification results. However, the use of AR coefficients as signal features approximating the shape of the signal has some disadvantages. Primarily, it is always necessary to determine the number of AR coefficients necessary to adequately represent each AE signal. Although numerous algorithms exist for determining the model order, it should be noted that the classification results could be sensitive to the AR model order. Secondly, it was evident from this study that AE signal classification using AR model coefficients was severely impaired when the measured AE signals was modulated by small levels of background acoustic noise.

In light of this discussion, it is postulated that a robust AE signal feature based upon amplitude statistics and independent of absolute energy levels or pre-defined thresholds, and less effected by pre-signal processing, can be a useful addition to AE signal classification. This paper proposes that the standard Kolmogorov-Smirnov statistic can provide such an AE waveform feature parameter for classifying different types of rubbing in rotating machinery. To demonstrate this, classification results are presented from rub experiments conducted on a journal bearing test rig that rotates at 1500 rev/min (rpm). In addition, classification performance of this technique was tested by modulating the measured AE signals with background noise taken from bearings of an operational 550 MW turbine unit.

2. ACOUSTIC EMISSION AND RUBBING IN ROTATING MACHINERY

The AE approach to condition monitoring in slow-speed rotating machinery is well-established (Choudhury and Tandon, 2000). Reasons for this include the obvious unsuitability of conventional vibration analysis at very low rev/min, the relatively low levels of background noise in such plant and the possibility of direct measurement upon the shaft. In contrast, application of AE to faster rotating machinery (i.e. >1000 rpm) has been less researched. This can be attributed to the proven success of vibration analysis and potentially higher levels of background noise. However, Sato (1990) reported that AE measurement can provide a valuable complementary tool for diagnosing rubbing in fast rotating plant such as turbine generators. For this investigation, signatures were measured at frequency bands greater than 100 kHz, overcoming mechanical background noise whilst increasing the probability of direct rub detection.

Fundamentally, a light frictional rub between the central shaft and surrounding stationary components, such as the seals within a turbine, will cause microscopic perturbation and a transient release of broadband strain energy referred to as stress waves (SW). Although originating from a different mechanical process, this wave motion is in practice extremely similar to the wave energy that propagates from microscopic cracks within solid structures, known as acoustic emissions (AE). Hence rubbing, although strictly a pseudo-AE source, is invariably associated with this term.

A number of reasons can be identified for the onset on light rubbing in a rotating plant. These include thermal effects, foundation movement, component movement, rotor unbalance or misalignment. Regardless of the exact relationship between cause and effect, the existence of rubbing is unwanted as it can often develop into more significant mechanical distress. Two main categories of light rubbing can be identified. Primarily partial rubbing constitutes distinct or intermittent rub events occurring instantaneously within the period of the shaft rotation. Secondly continuous rubbing involves more sustained contact between shaft and surrounding components. Although the mechanisms by which rub phenomena escalate are complex, it is suggested that for machinery of higher rotational speeds, a high concentration of partial rub events can lead to more sustained rubbing, which in turn can induce more serious vibration via mechanisms such as thermal bending of the shaft. Consequently, it is considered in this paper that an AE system capable of diagnosing individual partial rub events might promote the early diagnosis of impending mechanical distress.

Unlike the AE waveforms measured from continuous rubbing, partial rub events induce time-resolved AE waveforms. Propagation of such discrete rub signals departs from the elementary

theory of plane wavefronts and they are considered to approximate discrete accumulation of point source transients that can propagate via both the metallic volume and surface. The latter of these modes is considered to be predominant in propagation along the shaft and is known as Rayleigh surface waves. This elliptical wave motion is slower than both longitudinal and transverse modes and penetrates to only a few wavelengths (Pollard, 1977).

To detect rubbing using AE, it is generally advantageous to minimise both the physical distance and number of interfaces between the location of rubbing and the AE receiver. This is because significant acoustic attenuation will occur, especially at higher frequencies (>100 kHz), due to frequency-dependent absorption, geometric spreading losses and reflection at interfaces. In some slow rotating cases, it is possible to place transducers directly on the rotating shaft, (Mba and Bannister, 1999). However in many types of operational rotating machinery, such as in turbine-generators, it is only practical to make measurements remotely at the bearing housing. In such cases, AE signals produced by rubbing on the shaft will incur considerable attenuation as the signatures propagate along the shaft surface to the bearing, across an oil film and into the bearing housing. This attenuation issue is considered to be the limiting factor for AE in many examples of large-scale machinery.

Both commercially available resonant and wideband piezoelectric ceramic transducers are primarily used to measure the AE response from mechanical rub events on account of their sensitivity. Although resonant devices possess some advantages in terms of sensitivity and cost, it is considered that broadband ceramic devices are generally more suited to partial rub signal classification and are used in this paper. The primary reason for this is the superior fidelity achieved by broadband transducers allowing the motion of the impinging acoustic wave to be reproduced as a voltage signal more accurately and less influenced by the transducer response. Finally, AE techniques have significantly benefited from the exponential improvement in signal acquisition and computing power.

3. THEORY

Figure 1 shows an example AE signal measured at the bearing housing of the test rig whilst rotating at ~1500 rpm. This signature was a result of simulating a partial rub on the shaft with a steel seal fixture. Clearly, the AE burst shows some resemblance to the shape of a classic AE waveform produced by crack propagation or a Hsu-Nielson source, although it is not possible to identify individual extensional and flexural wave modes as can be often obtained by the Modal AE approach in thin plates. A notable feature of this rub waveform is the initial onset of acoustic energy through the succession of initial high energy peaks prior to the exponential decay. Therefore, it might be inferred that useful signal features might include kurtosis or crest factor as they describe the extreme values in the amplitude distribution. However, investigation of numerous rub signatures has shown considerable inconsistency in these parameters under stable experimental conditions. Consequently, they are not considered suitable parameters for classifying rubbing.

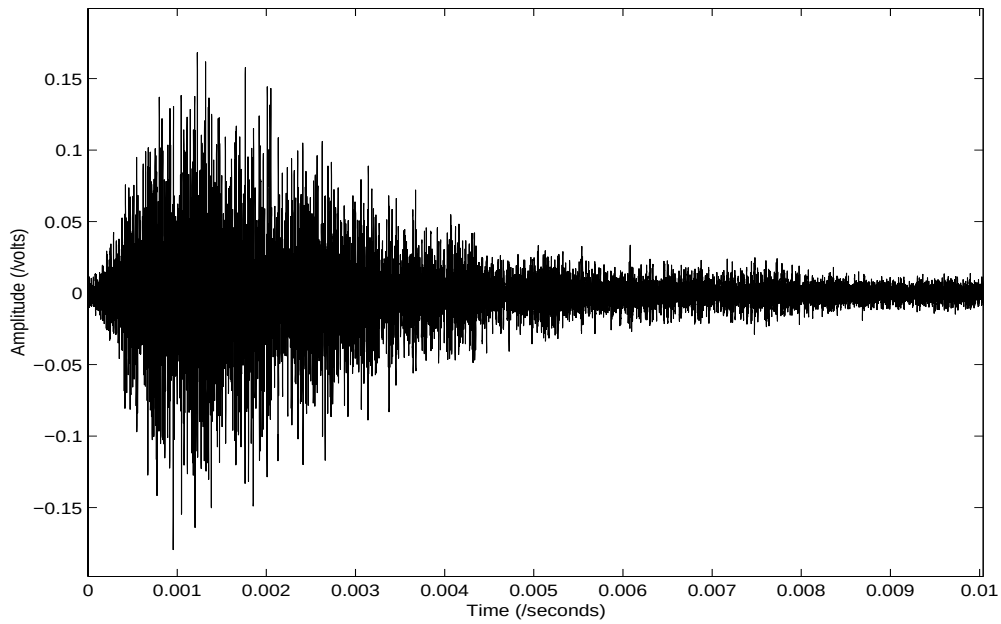

Fig. 1 A shaft-seal rub induced AE signal measured at the journal bearing of a test rig.

Alternatively, it is conceived that the Kolmogorov-Smirnov (KS) test statistic (Press et. al., 1993) might provide a more appropriate feature vector for classifying AE rub signals. In essence, this standard goodness-of-fit test quantifies the difference between the amplitude statistics of the measured AE signal and a specified theoretical distribution function model. It can be defined in equation (1) as the maximum absolute difference (D) between the empirical cumulative distribution function $S_{N2}(x)$ and a hypothesised theoretical distribution function $S_{N1}(x)$.

$$D = \max_{-\infty<x<\infty} \left| S_{N1}(x) - S_{N2}(x) \right| \qquad (1)$$

As $S_{N1}(x)$ and $S_{N2}(x)$ are non-decreasing and $S_{N2}(x)$ is considered to be constant between the defined values of amplitude x, as illustrated in Fig. 2, the maximum deviation between the two curves will occur at one of the defined observation points $x_1, x_2, x_{3\ldots} x_n$. It should also be noted that the distribution of D, in the null hypothesis, can be calculated to give the significance of any observed non-zero value of D. Moreover the statistic is invariant under reparametrisation of x. For example, the same significance exists under x as for log (x).

The basic algorithm devised for this paper is summarized in Fig. 3 and was implemented using MATLAB V5 and incorporated functions from the Statistics Toolbox. Primarily, each digital AE signal was decimated by a factor of 5 to reduce the KS computation time. However, it should be noted that this decimation in AE information was not expected to degrade classification results because of the high initial sampling rate used in the analogue-to-digital converter (ADC) (4 MHz). Following this stage, theoretical Gaussian distribution models for each of the AE signals were derived, assuming the null hypothesis that each signal belongs to this candidate family of distributions. These theoretical cumulative distribution function (CDF) curves were derived directly by the method of moments as opposed to a maximum likelihood approach. That is to say, the mean μ and variance σ^2 of each input signal was determined and the model estimate of the CDF evaluated using the two parameter equation for the Gaussian distribution family given in equation (2).

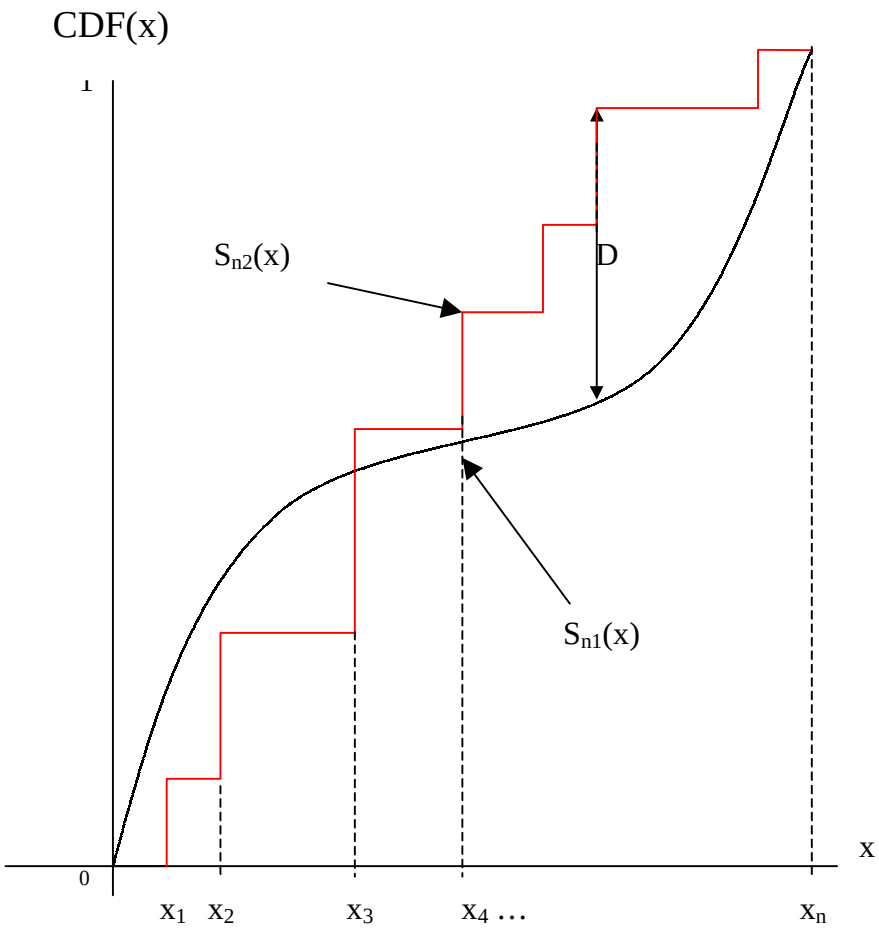

Fig. 2 D is the greatest distance between an empirical distribution $S_{n2}(x)$ and the theoretical distribution model $S_{n1}(x)$.

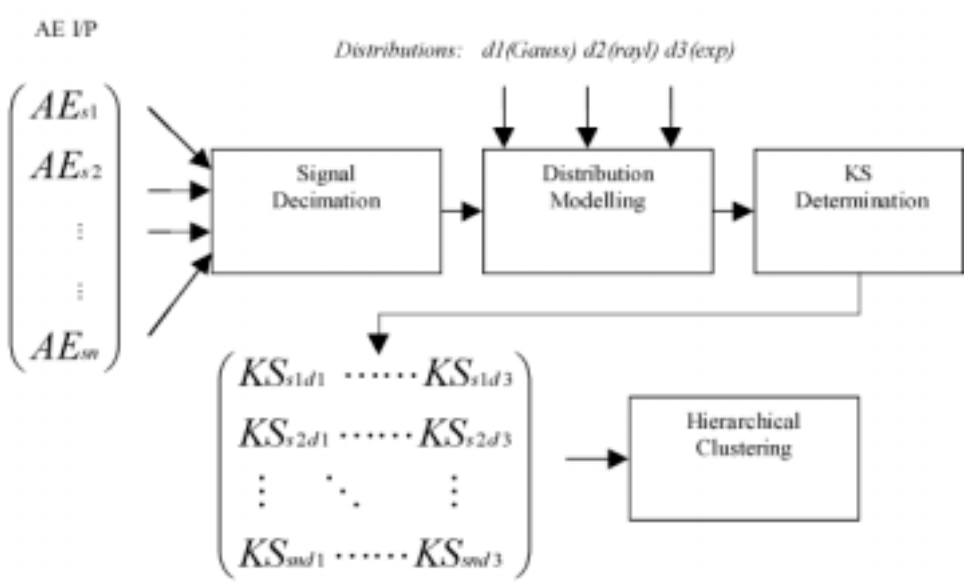

Fig. 3 A schematic for the AE classification algorithm.

$$f(x \mid \mu, \sigma) = \frac{1}{\sqrt{2\pi}\sigma} \int_{-\infty}^{x} e^{\frac{-(t-\mu)^2}{2\sigma^2}} dt \tag{2}$$

In addition to the Gaussian fit, each AE signal was modelled using theoretical Rayleigh and exponential distributions (D'Augostino and Stevens, 1986). as defined in equations (3) and (4), respectively. Therefore, it was possible to evaluate three D values for each of the AE signals, which in effect constituted three independent measures of amplitude statistics for an AE signal as illustrated in Fig. 4. These values provided the feature vector input used for classification.

$$f(x \mid b) = \int_{0}^{x} \frac{t}{b^2} e^{\left(\frac{-t^2}{2b^2}\right)} dt \tag{3}$$

where f(x|b) is Rayleigh CDF with parameter b derived from the mean or variance.

$$mean = \frac{4-\pi}{2} b^2 \quad or \text{ var } iance = b\left(\frac{\pi}{2}\right)^{\frac{1}{2}}$$

$$f(x \mid \mu) = \int_{0}^{x} \frac{1}{\mu} e^{-\frac{t}{\mu}} dt \equiv 1 - e^{-\frac{x}{\mu}} \tag{4}$$

where f(x|μ) is the exponential CDF with parameter equal to the standard deviation (μ).

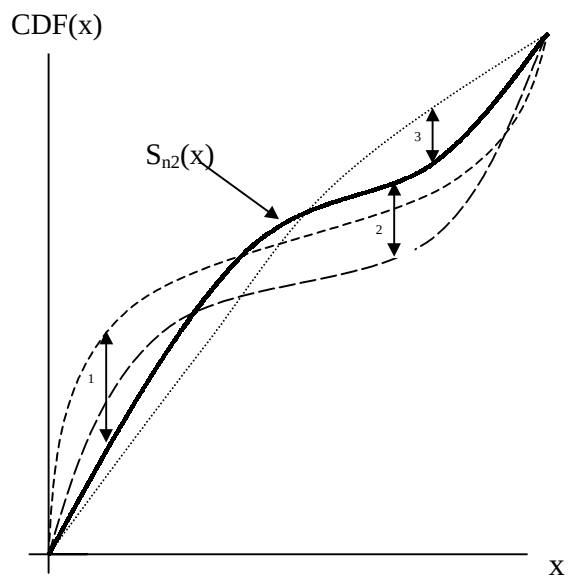

Fig. 4 Modelling the CDF of an AE signal with respect to three distribution families.

As shown in Fig. 3, rub signal classification involved hierarchical clustering (Chan, 1985; Murthy, 1987; Bently, 1988; Anastassopoulos and Philippidis, 1995), although it is believed that other approaches could equally demonstrate the use of the KS descriptor. Clustering describes *the action of partitioning a set of objects into natural groups so that the profile of the objects in*

the same cluster are very similar and the profiles of objects in different clusters are quite distinct. It is proposed that AE signatures from the same rub category (e.g. partial steel rubbing, partial brass rubbing, etc…) could be clustered in well-defined groups. This involves sequential stages of:

I Similarity, in which the Euclidean distance between every pair of KS signal vector was determined within the similarity matrix and

II Binary Linkage; in which a series of binary clusters of increasing size are made using the information in the similarity matrix, starting with the closest two signal objects, until all the objects are linked together in a hierarchical tree.

This is represented graphically within this paper using an agglomerative dendrogram plot, in which individual signals are labelled on the x-axis whilst the distance between the centroids of clusters are shown on the y-axis. The classification procedure described was used to assess whether KS features associated with AE signatures was sufficiently robust to cluster known rub classes into the correct natural groups. It should be noted that hierarchical clustering can be susceptible to undesirable early combinations involving class outliers and this can lead to spurious results.

4. EXPERIMENTAL

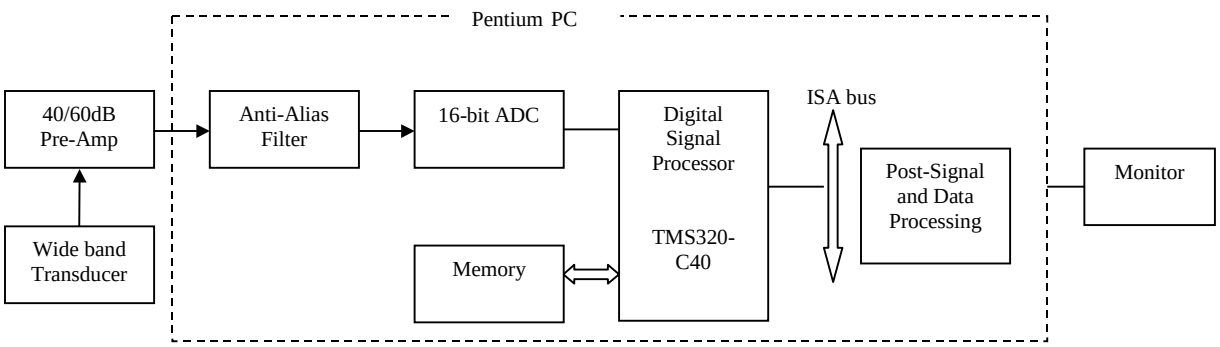

Fig. 5 A schematic of the AE measurement system.

The AE signal measurement system employed for this study is shown schematically in Fig. 5. The broadband piezoelectric transducer was a commercially built WD device from PAC© with a measurement bandwidth of 100 kHz-1 MHz. This ceramic sensing element was differentially connected to a 40-dB gain pre-amplifier, in order to effect an immediate improvement in the measured signal level and to reduce electromagnetic noise through common mode rejection. Moreover the separate pre-amplifier incorporated a plug-in analogue high-pass filter to suppress low frequency acoustic noise components and exhibited better temperature performance than could be achieved using an integral pre-amplifier. The signal output from the pre-amplifier was connected (i.e. via BNC/coaxial cable) directly to a commercial data acquisition card that occupies one of the ISA slots within a Pentium host PC. This AEDSP card also from PAC provided up to an 8 MHz sampling rate and incorporates 16-bit precision ADCs giving a dynamic range of more than 85 dB. Moreover, an extended local memory allowed the sequential recording of signals containing up to 256,000 samples. This corresponded to the continuous measurement over more than 0.06 s at a sampling rate of 4 MHz. Prior to the ADC, the card employs anti-aliasing filters that can be controlled (i.e. the band-pass altered) directly in software.

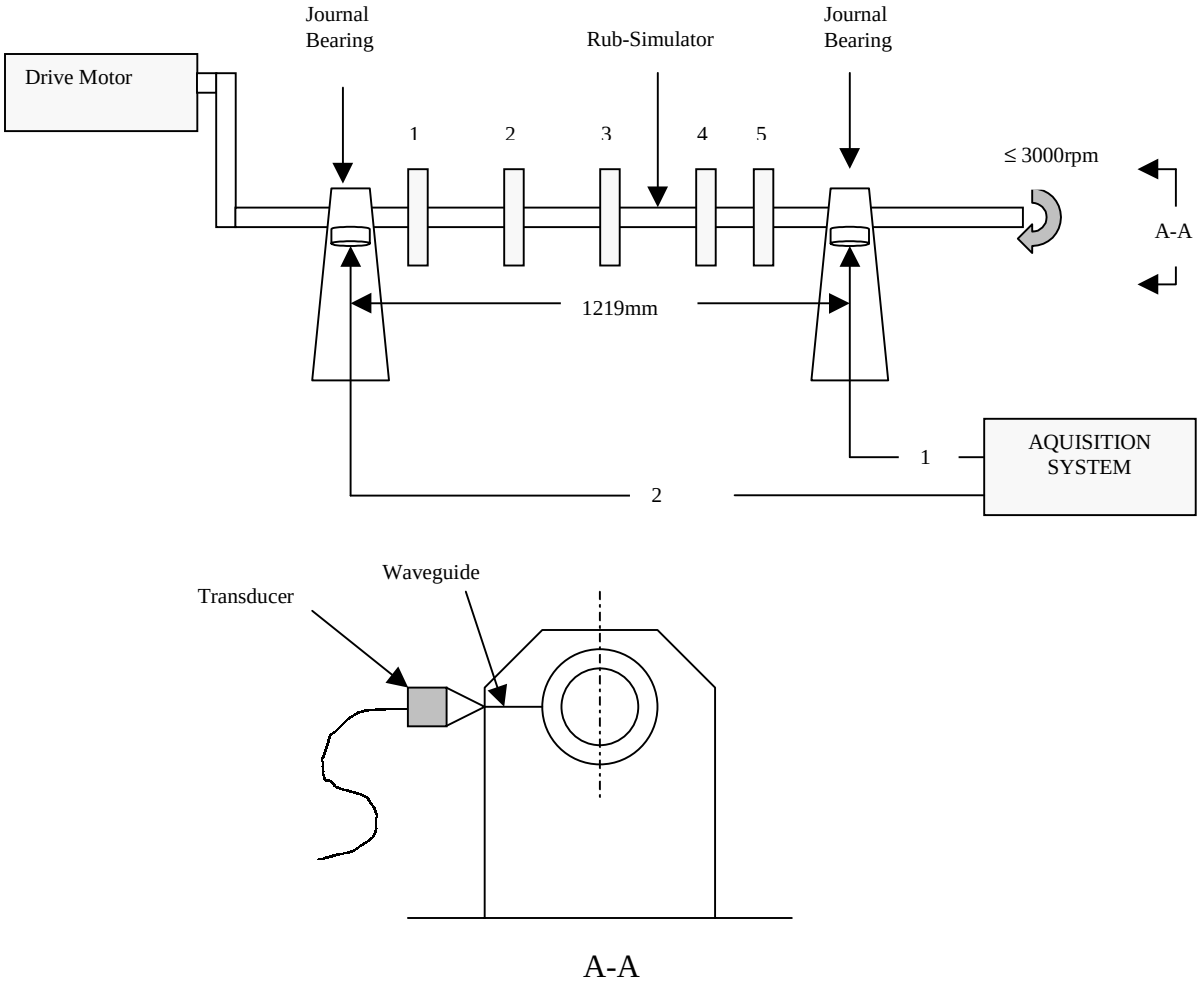

Fig. 6 (a) The journal bearing test rig,

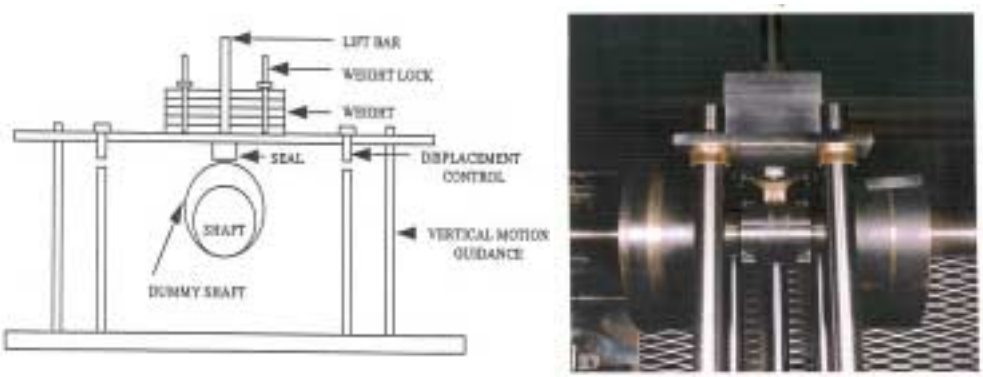

Fig. 6(b) The rub simulation mechanism.

Figure 6(a) depicts the rotating test rig. As shown, the shaft is supported by two journal bearings. A wave-guide made contact with the inner bearing housing and the receiving AE transducer was attached to the other end, ensuring a direct transmission path. Throughout the experimentation high temperature acoustic couplant was applied to ensure a good acoustic contact between transducer and the wave-guide and between wave-guide and the bearing housing. The rub simulation mechanism is positioned between the third and forth of five steel

discs shrink-fitted on to the central shaft that rotates at up to ~3000 rpm. Figure 6(b) illustrates how partial rubs are simulated using this device. Essentially, a non-concentric dummy shaft fixture is attached to the rotor so as to rub against a supported seal fixture on every shaft rotation. The seal fixtures employed were initially machined in mild steel or brass. The reaction pressure[1] exerted by the seal upon the incident shaft was set by masses applied to the rub fixture as shown in Fig. 6(b). These masses applied a force of approximately 140 N throughout the measurements.

5 RESULTS AND DISCUSSION

Using the aforementioned system, AE signals were recorded from different types of partial shaft-seal rubbing. Primarily burst signals from the partial rubbing of steel and brass seal fixtures were taken. Secondly, partial rub signals were taken from three steel seal fixtures exhibiting different states of wear. This section presents results pertaining to the use of the KS statistic to classify the defined rub classes by employing hierarchical clustering. By comparing the results to alternative AE feature extraction methods, the potential of the KS statistic is demonstrated.

a. Seal Material Classification

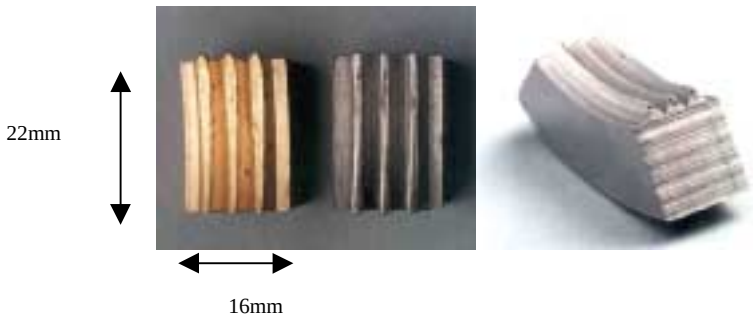

Fig. 7 Steel and brass seal fixtures.

In condition monitoring of rotating machinery, a technique that predicts the types of material rubbing on the shaft is potentially useful. Specifically, it might infer whether rubbing on the shaft is significant and should be acted upon or could provide information pertaining to the location of rubbing. To illustrate the use of the KS statistic in discriminating between rubbing from different materials, partial rub AE signatures were measured from the test rig using the identically shaped brass and steel seal fixtures shown in Fig. 7. In each case, fifteen AE signatures are recorded under the same experimental conditions, i.e., the shaft period and the load applied to the rub simulation mechanism remained constant. Examples of the AE signals produced from steel and brass seal rubbing are shown in Fig. 8.

Table 1 lists mean and standard deviation values for extracted AE features for the example steel and brass signals, see Appendix for full table. The KS values were obtained using the Gaussian, Rayleigh and exponential distribution families. Gaussian KS values for each of the signals multiplied by two were also shown and it should be noted that these values are not significantly different to the Gaussian KS values obtained from the original signals. Although

[1] Calculation of the normal reaction pressure applied by the seal upon the rotating shaft is not trivial. It depends upon:- the incident forces of the rotating shaft, the weight distribution of the entire upper section of the rub simulator (the moving components), the contact area of the seal-fixture and the supporting screws and the coefficient of friction between the vertical motion guidance posts and the upper section.

many established AE signal features were considered, only the RMS, median, kurtosis and autoregressive (AR) coefficients are represented in Table 1 as they proved more significant rub indicators.

Table 1 KS values for brass and seal rubbing.

SIGNAL /MATERIAL	KS-Gauss	KS-Rayl	KS-Exp	KS-Gauss ×2	RMS	Med	Kurt	AR (1)	AR (2)	AR (3)	AR (4)	AR (5)	AR (6)
Steel Mean	0.106	0.616	0.825	0.106	0.008	0.016	10.948	-1.999	1.234	0.059	-0.123	-0.030	-0.070
Steel STD	0.012	0.008	0.017	0.011	0.003	0.003	1.101	0.014	0.025	0.020	0.007	0.017	0.024
Brass Mean	0.053	0.580	0.881	0.054	0.006	0.014	7.849	-2.006	1.186	0.117	-0.100	-0.066	-0.068
Brass STD	0.008	0.004	0.009	0.008	0.002	0.001	0.617	0.017	0.040	0.028	0.010	0.016	0.031

Primarily, use of the KS values derived from the Gaussian, Rayleigh and exponential models for all thirty signals are considered as the input vector to the clustering algorithm, i.e., three values per vector per signature. The achieved clustering results are depicted using the dendrogram plot in Fig. 9. As shown, the x-axis represents the steel fixture rub signals by labels 1 to 15 and the signals produced using the brass fixture as signals 16 to 30. Moreover, the y-axis shows the Euclidean distances between the input KS values. It is evident that the two main clusters do discriminate between the brass and steel rub classes. Moreover, ignoring signal-6 and signal-12 corresponding to steel rubbing, the separation is relatively pronounced.

It should be noted that the algorithm used to determine KS values involves the generation of a random reference signal and hence produces slight changes in the result for a given AE signal over repeated calculation. However, this variability was not seen to prevent adequate separation between brass and steel signals over many independent experiments. Moreover, it was apparent that using a signal feature vector that constitutes repeated KS evaluations for a specified reference distribution could improve the clustering results. Figure 10 shows the clustering

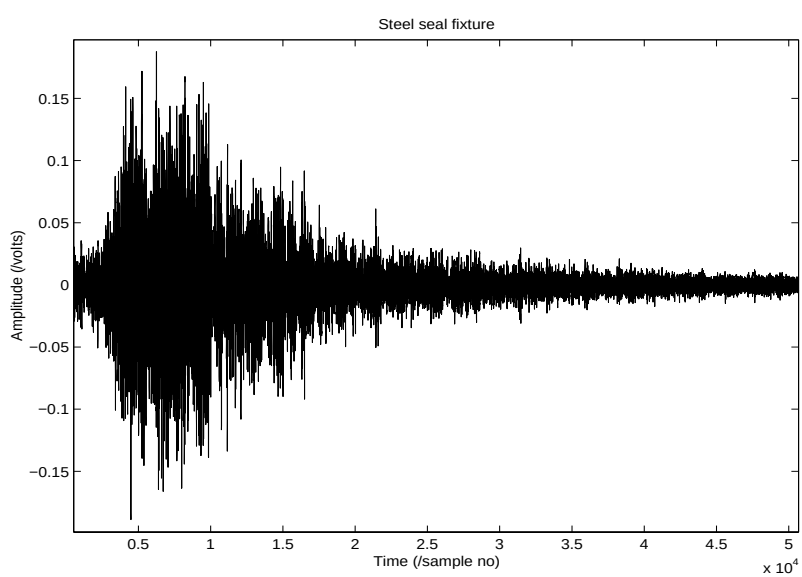

Fig. 8 (a) Examples of the AE signals produced using steel seal fixture.

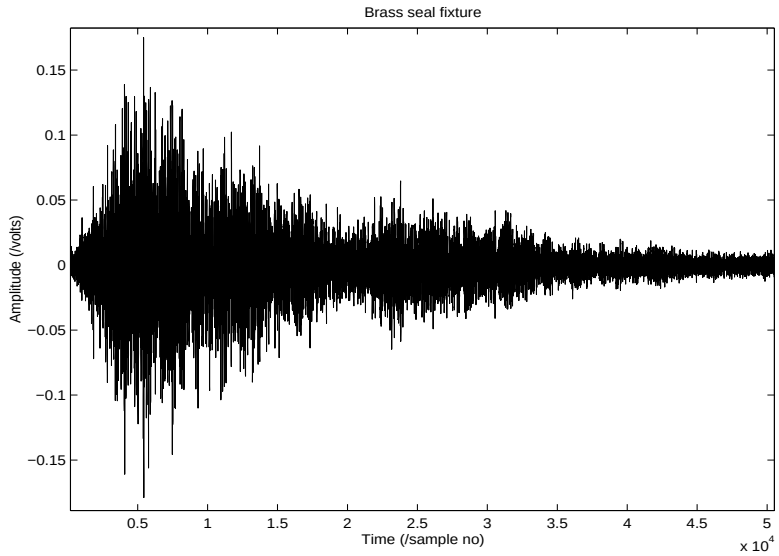

Fig. 8 (b) Examples of the AE signals produced using brass seal fixture.

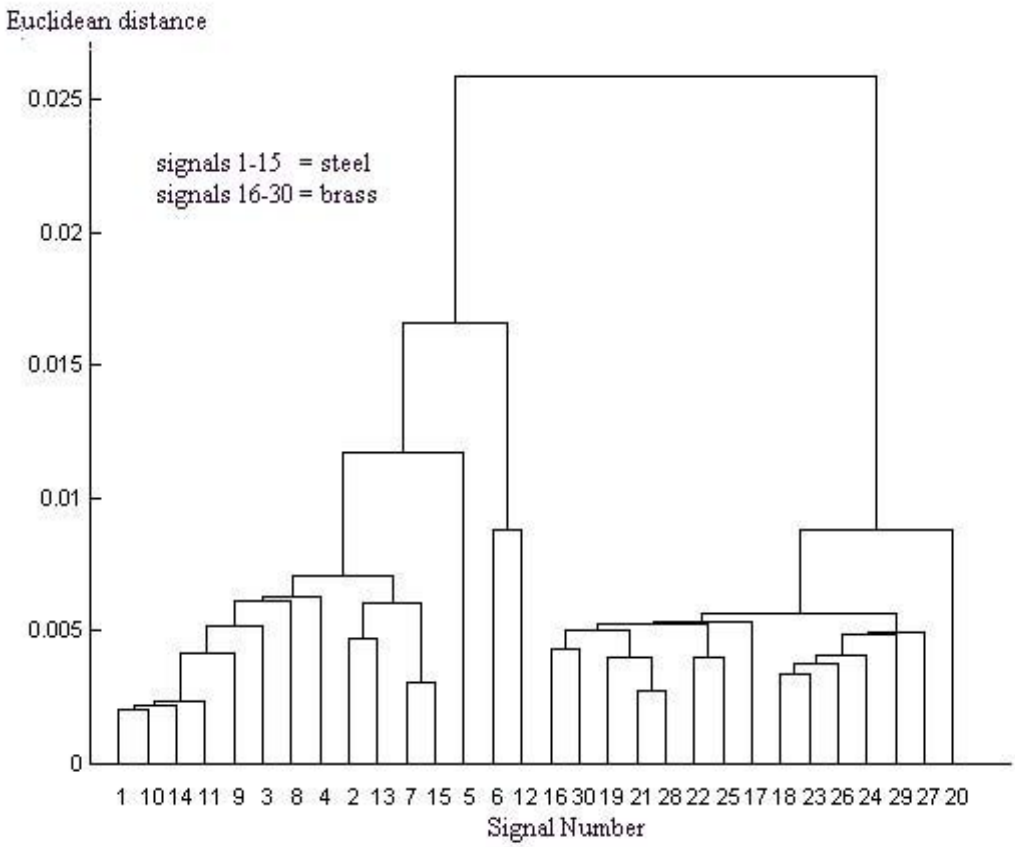

Fig. 9 Gaussian KS discrimination, single-linkage (nearest neighbour).

achieved using a feature vector consisting of four independent KS evaluations assuming the Gaussian model. In this plot, the Ward's method of clustering is employed in preference to the single-linkage (i.e., nearest neighbor). This is a procedure in which the similarity used to join two clusters is calculated as the sum of squares between the two clusters summed over all variables. It is effective in increasing the 'within cluster' homogeneity and prevents chaining.

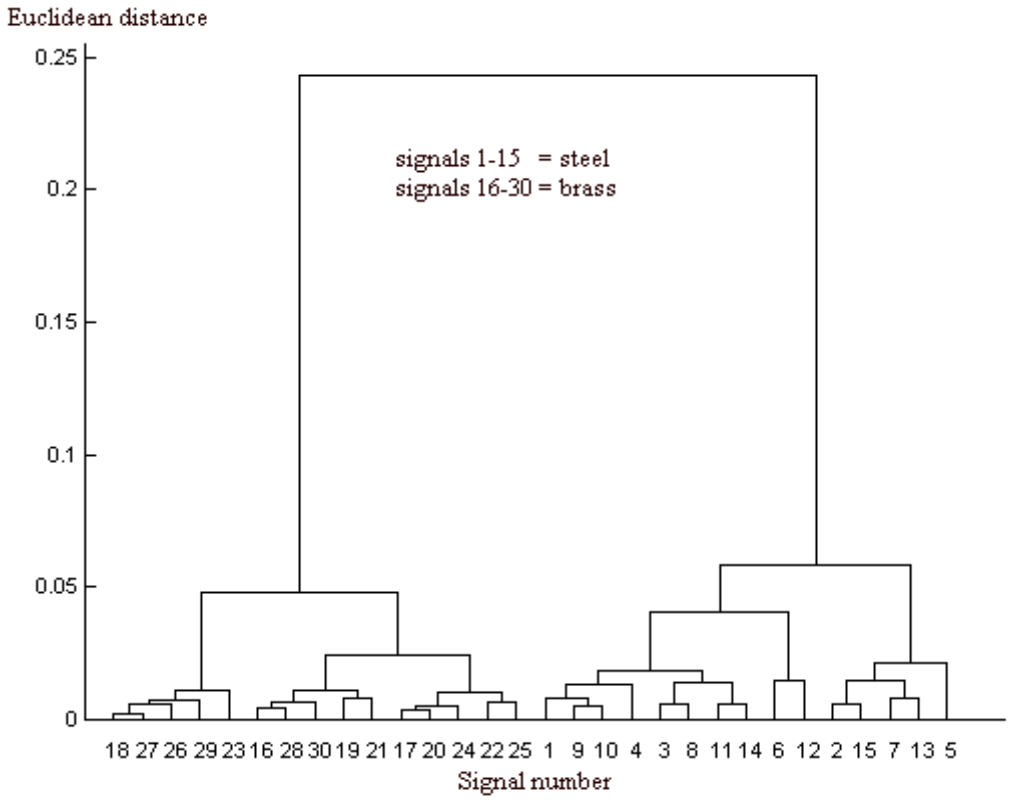

Fig. 10 Gaussian KS discrimination, Ward's method.

In contrast to the robust KS results, clustering of the thirty partial rub signals using established AE signal features such as peak energy, total energy, RMS, median, standard deviation, counts and peaks within an FFT revealed poor separation between brass and steel signals. The most appropriate of such features was the signal kurtosis. As indicated in Table 1, this energy independent measure of signal spikiness generally yielded larger values for steel rubbing signals than from brass rubbing. However, repeated tests revealed a number of spurious clustering results. This was attributed to the large spread of kurtosis values obtained across all of the AE signals measured.

Although the KS technique outperformed these established signal features dependent upon energy or extreme values within the amplitude distribution, it should be noted that application of autoregressive coefficients as input AE signal features also produced effective discrimination between brass and steel rubbing. This technique (Melton, 1982) involves modelling each AE signal as an Nth order linear stochastic process and using the subsequent AR coefficients within the clustering algorithm to represent the signal 'fine-scale' shape to within a certain accepted prediction error. The optimum order (N) for the AR model is often the lowest order at which the minimum mean-squared error becomes stationary and can be determined via the application of the final prediction error (FPE) and Akaike's information criterion (AIC) (Kay and Maple, 1981; Makhoul, 1975). However, it was considered that the success of subsequent AE signal clustering was extremely sensitive to the number of AR coefficients employed, as the optimum order varied for different classes of rub signal. In addition to this drawback, it became clear that the AR approach to partial rub classification breaks down when the measured rub signals are modulated by background acoustic noise.

To demonstrate the effect that background noise can have upon rub classification, acoustic noise from the bearings of an operational 500-MW turbine unit was superimposed upon the brass and steel rub signals. In this test, the same levels of turbine noise were added to the thirty rub signals and the same band-pass filter was applied. Figure 11 shows hierarchical clustering results achieved from fifteen noisy brass signals and fifteen noisy steel signals using a 20th order AR coefficients as the signal descriptors. This dendrogram plot clearly demonstrates that the AR approach becomes inappropriate for brass and steel classification when even low levels of background noise are present. It is interesting to note that this lack of class resolution was also observed when attempts were made to remove background noise using an appropriately designed band-pass filter. In contrast, it became clear that KS-based rub classification is less affected by the addition of real noise, see Fig. 12. As shown, AE signal classification using KS descriptors is more suitable than that based upon the more established AR technique.

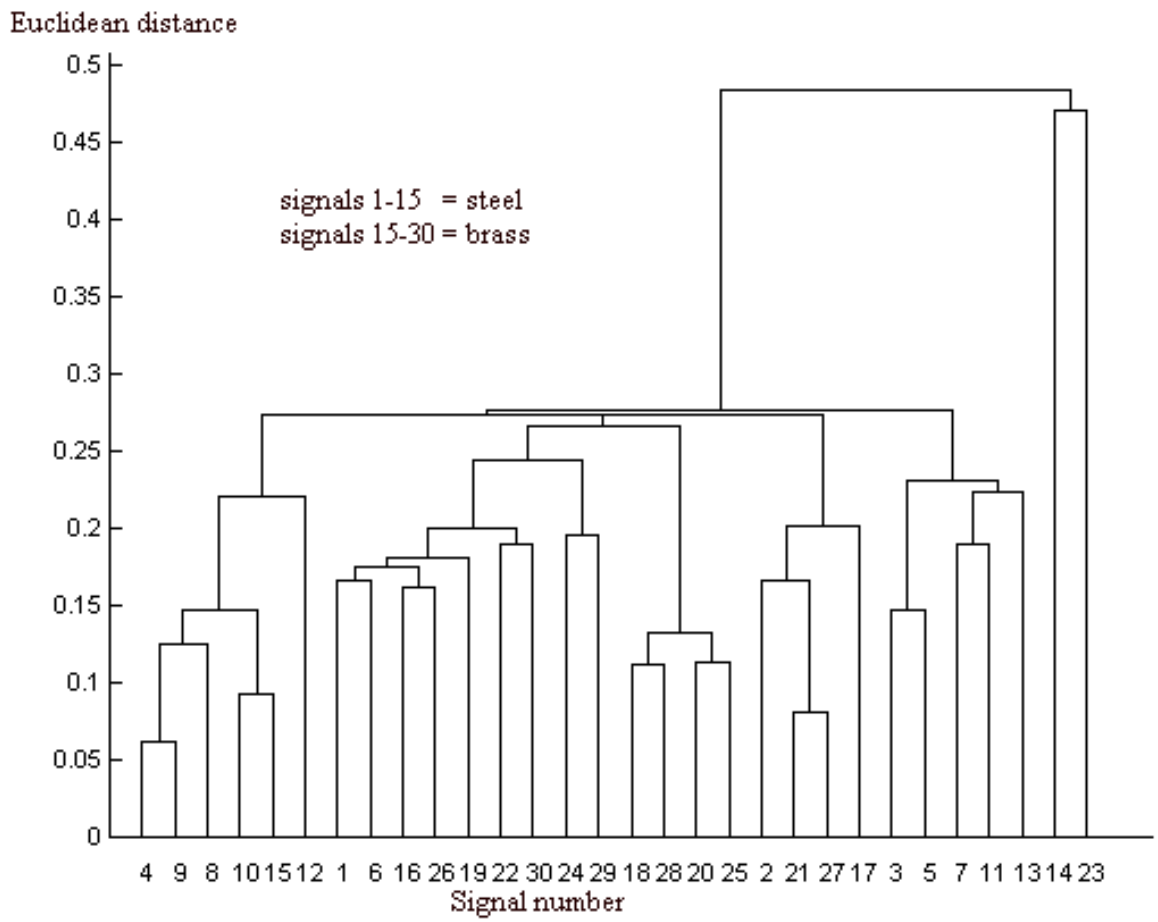

Fig. 11 AR(20) discrimination with low levels of real noise measured from a 500MW turbine.

b. Seal Wear Discrimination

It is proposed that some diagnosis of the 'wear state' of rubbing seals might be inferred from the measured AE data. Three mild steel V-groove seals at different stages of wear were prepared. These are shown in Fig. 13 and are referred to as unworn, mid-wear and worn.

Applying each of these fixtures to the partial rub simulator in turn, AE signatures were recorded at the bearings. Figure 14 shows examples of the signatures obtained for the three wear

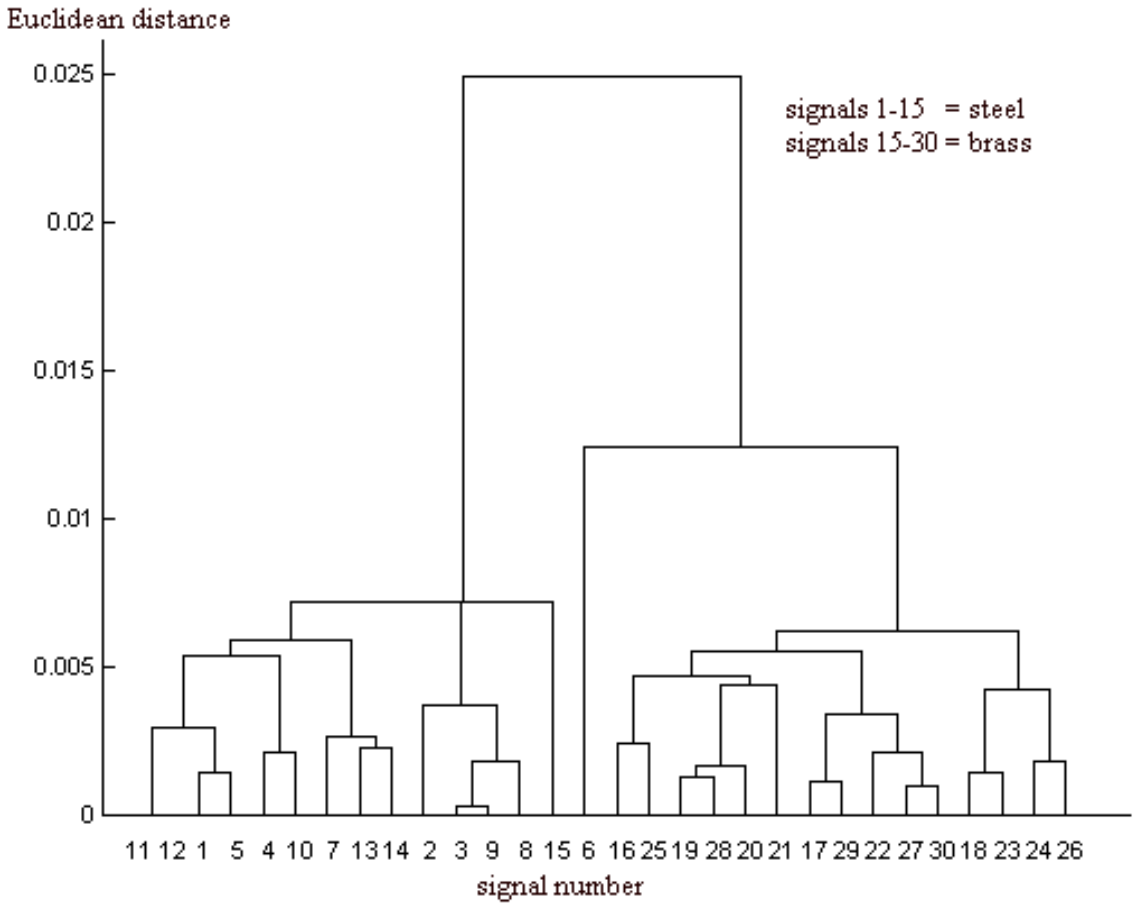

Fig. 12 KS discrimination with low levels of real noise measured from a 500MW turbine.

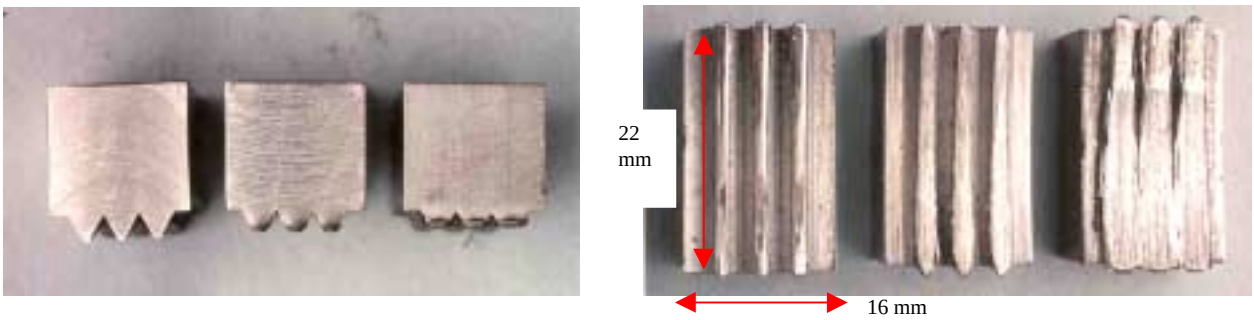

Fig. 13 The AE signatures from steel V-Groove.

states at the bearing-1. By inspection, it is obvious that the unworn signal appears to be more complex[2] than the other two wear state signals. Specifically, it is clear that two smaller bursts appear in the tail of the unworn AE waveform. However, visually identifying the difference between the mid-wear and worn state is more difficult, especially as the peak amplitudes of all three are very similar.

[2] This difference between the AE produced from 'sharp' surfaces rubbing and more planar contact is related to known asperity contact effects and is generally observed in low-speed rotating machines.

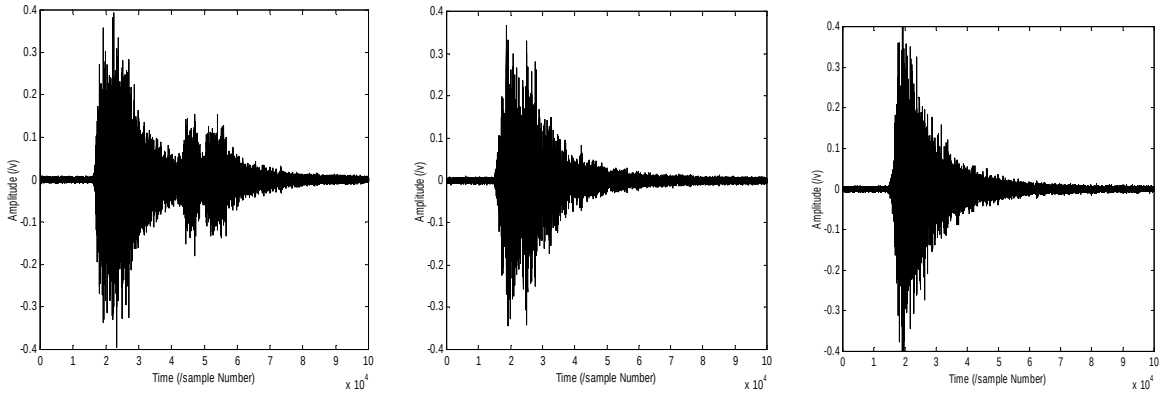

(a) (b) (c)

Fig. 14 Example AE signals from a V-Grooved steel seals exhibiting. (a) No wear, (b) Mid-wear, (c) Extreme wear.

To illustrate an automatic classification approach for these wear states, fifteen example signals were taken; five from each of the wear states. Initially, the AR model approach to clustering was applied. As in the previous section, inspection of the residual error plot, using the Akaike's Information Criterion, suggests that an AR order of 8 was sufficient to represent the signature shape. To test the applicability of the AR approach, a plot of the cluster achieved by measuring Euclidean distances between centroid values of AR coefficients associated with each signature is shown in Fig. 15. No clear pattern in the cluster was observed and it was deduced that the AR classification approach is not suitable for determination of the wear state of the rubbing seal.

To investigate using the KS statistic for distinguishing between the unworn, mid-wear and worn partial rubbing states, the same fifteen signals were used. The Gaussian distribution was used as the reference within the KS algorithm and the cluster result can be seen in Fig. 16. It is clear from this that reasonably good wear classification has been achieved. Primarily, the two major clusters discriminate between the unworn AE signals and the other two types. This can be justified in that the second and third smaller bursts within the unworn signals cause significant deviation from Gaussian amplitude statistics. Secondly, it is encouraging to observe that the Gaussian KS statistic is sensitive enough to separate mid-wear and very worn rubbing signals within the broader cluster group.

6. CONCLUSIONS

This paper introduces the use of the Kolmogorov-Smirnov (KS) test statistic as a useful signal descriptor in AE analysis. The KS results presented via hierarchical dendrograms indicate the potential of this statistic in classification of partial rubbing on shafts of fast rotating machinery. Moreover, the success of KS classification has been shown when the measured AE rub signals were modulated by background noise from a real operational 500-MW turbine.

It should be noted that the KS statistic tends to be more sensitive around the medium value (i.e., where $P(x) = 0.5$ within the CDF) and less sensitive at the extreme ends of the distribution, where $P(x)$ approach either 0 or 1. This is because the KS value does not have a probability distribution independent of amplitude (x). Therefore, it is postulated that while the KS statistic is

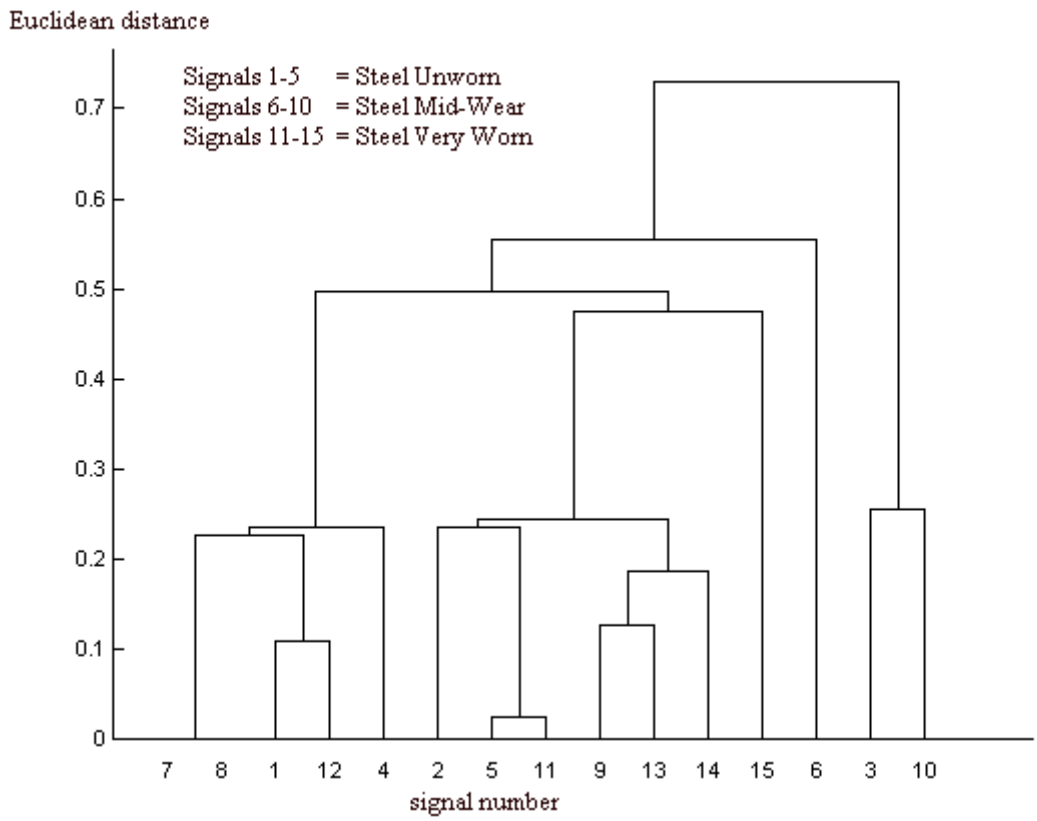

Fig. 15 Clustering achieved using 8 AR coefficients for unworn (signals 1-5), mid-wear (signals 6-10) and very worn (signals 11-15) shaft-seal rubbings.

good at finding shifts in the probability distribution, especially changes in medium value, it is not always so good at finding spreads, which more strongly affect the tails of the probability distribution. Consequently, it is concluded that the KS statistic is robust and not too sensitive to variability in amplitude outliers as is the case with the kurtosis statistic. Thus the KS statistic provides a suitably stable feature for broadband AE signals that characterises the entire amplitude statistics.

Implementation of this KS method for AE signal classification requires choosing the appropriate theoretical distribution families for reference. For the partial rub induced AE signals measured in this paper, the Gaussian distribution appeared to provide the closest fit, as indicated by the KS values given in Table 1. It is generally considered that the classification performance is increased by using reference distributions that are not rejected within the null hypothesis by exhibiting KS values that exceed the 5% significance level (Press, 1993). However, it can not be concluded from the results presented that the Gaussian distribution is the best amplitude statistics model for partial rub induced AE signals and other possible candidates include the log-normal (Lopez Pumarega et al., 1999) and t-distributions. Regardless of the distributions used for a specific classification task, it should be noted that determining the best set of reference distributions is the central consideration for the KS technique.

Interpretation of individual AE signal waveforms from partial rubbing is considered to be difficult. However, it is suggested that the general suitability of the Gaussian distribution and use of the KS statistic might infer more detailed information related to physical rub mechanisms. It is

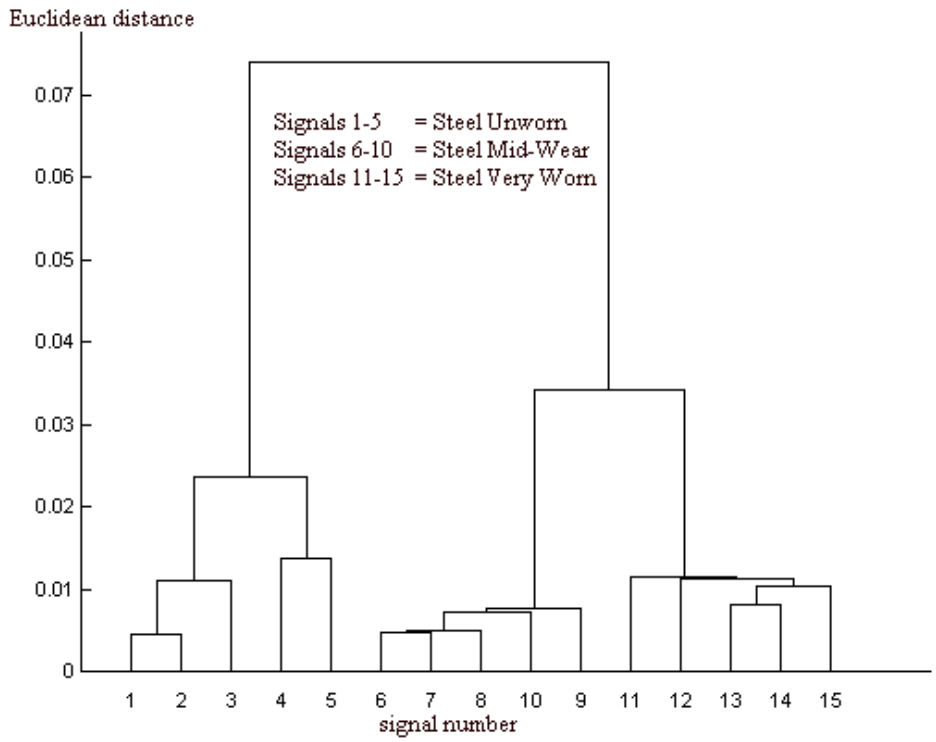

Fig. 16 Clustering achieved using the KS-statistic for unworn (signals 1-5), mid-wear (signals 6-10) and very worn (signals 11-15) shaft-seal rubbings.

postulated that the Central Limit Theorem, as used for modelling ambient noise in underwater acoustics, might be adopted in AE condition monitoring. This could state that a rub induced AE waveform, which is formed by the addition of a number of temporally close but independent asperity contacts, has a probability density function, which approaches the Gaussian distribution, as the number of contributors or AE sources increases. Consequently, it is proposed that absolute KS values, assuming a Gaussian fit, might directly classify quantities such as rub severity.

The KS statistic essentially quantifies the difference between any two distributions. Therefore, in addition to diagnosing rubbing in fast rotating machinery, it is believed that the technique might find application in other condition monitoring applications. For example, the KS statistic could be useful for diagnosing tool wear or for detecting and classifying incipient faults in low-speed rolling-element bearings. In these cases, the KS value might indicate fault severity by quantifying the deviation of a measured AE signal from a known healthy-state signature. Moreover, alternative goodness of fit statistics could be applied if required for specific condition monitoring task. For instance, one way of increasing the statistic resolution out on the tails is to replace the KS statistic with a stabilised or weighted statistic such as the Anderson-Darling statistic D^*:

$$D^* = \max_{-\infty<x<\infty} \frac{\left|Sn1(x) - Sn2(x)\right|}{\sqrt{P(x)\left[1-P(x)\right]}} \qquad (5)$$

Finally, it should be noted that these classification results were achieved using a high-fidelity wideband AE transducer. However, it is realised that the KS technique could break down using resonant devices due to low fidelity.

REFERENCES

A. Anastassopoulos and T.P. Philippidis (1995), "Clustering Methodology for the Evaluation of Acoustic Emission from Composites", *Journal of Acoustic Emission*, **13**(1-2), 11-22.

P.G. Bentley and M. J. Beesley (1988), "Acoustic emission measurement on PWR weld material with inserted defects using advanced instrumentation", Journal of Acoustic Emission, **7**(2), 59.

C.M. Bishop (1999), *Neural Networks for Pattern Recognition*, Oxford University Press. ISBN: 0198538642.

Roger W.Y. Chan, D. Robert Hay, Victor Caron, Michel Hone and R. Douglas Sharp (1985), "Classification of Acoustic Emission Signals Generated During Welding", Journal of Acoustic Emission, **4**(4) 115.

A. Choudhury and N. Tandon (2000), "Application of Acoustic Emission techniques for the detection of defects in rolling element bearings", *Tribology International*, **33**(1), 39-45.

R.B. D'Augostino and M.A. Stevens, Eds. (1986). *Goodness-of-Fit Techniques*, Marcel Dekker; ISBN: 0824774876

T. Holroyd and N. Randall (1992), "The Use of Acoustic Emission for Machine Condition Monitoring", British Journal of Non-Destructive Testing, **35**(2), 75.

S.M. Kay, and S.L. Marple, Jr. (1981), "Spectrum analysis - A modern perspective", *Proceedings of the IEEE*, **69**(11), 1380-1419.

Li (1989), "On-line bearing localized defect detection by pattern recognition analysis", ASME Trans., J. Eng. Ind, **111**, 331.

S. Liang and D. Dornfeld (1987), "Punch stretching Process Monitoring using Acoustic Emission Signal Analysis-Part-1/2", Journal of Acoustic Emission, **6**(1), 29.

M.I. Lopez Pumarega, R. Piotrkowski and J.E. Ruzzante (1999)," Discussion of the log-normal distribution of amplitude in Acoustic emission signals", Journal of Acoustic Emission, **17**(1-2), 61-67.

J. Makhoul, (1975), "Linear prediction: A tutorial review", Proc. of the IEEE, **63**(4), 561-580.

D. Mba, and R. H. Bannister (1999), "Condition monitoring of low-speed rotating machinery using stress waves: Part 1 and Part 2", Proc. Inst. Mech. Engrs., **213**, Part E, 153-185.

R. McBride, J.S. Barton, W.K.D. Borthwick and J.D.C. Jones (1993), "Fibre optic interferometry for acoustic emission sensing in machine tool wear monitoring", Meas. Sci. Technol., **4**, 1122–1128.

P.D. McFadden and J.D. Smith, (1983), "Acoustic Emission transducers for vibration monitoring of bearings at low speeds'', Report CUED/C-Mech. TR29, University of Cambridge, Cambridge.

R. Melton (1982), "Classification of NDE waveforms with autoregressive models", Journal of Acoustic Emission, **1**(4), 266.

C.R.L. Murthy, B. Dattaguru and A.K. Rao (1987), "Application of pattern recognition concepts to acoustic emission signal analysis", Journal of Acoustic Emission, **6**(1), 19.

K. Ono and Q. Huang (1994), "Pattern recognition analysis of acoustic emission signals", *Progress in Acoustic Emission*, VII, Japanese Society for NDI, Tokyo, pp. 69-78

H.F. Pollard (1977), *Sound Waves in Solids* - Applied Physics Series, Pion Limited. ASIN: 0850860539

W.H. Press, S.A. Teulosky, B.P. Vetterling and W.T. Flannery (1993), *Numerical Recipes in C*, ISBN: 0521431085.

I. Sato (1990), "Rotating machinery diagnosis with acoustic emission techniques", Electrical Engr. Japan, **110**(2), 115-127

W. Venkatesan (1996), "Detection and Modeling of Acoustic Emissions for Fault Diagnostics", *IEEE*, ISBN 0-8186-7576-4/96.

APPENDIX

SIGNAL	KS-Gauss	KS-Rayl	KS-Exp	KS-Gauss ×2	RMS	Med	Kurt	AR (1)	AR (2)	AR (3)	AR (4)	AR (5)	AR (6)	AR (7)	AR (8)
Steel-1	0.108	0.618	0.839	0.103	0.007	0.013	10.176	-2.002	1.251	0.041	-0.126	-0.011	-0.094	0.081	0.052
Steel-2	0.114	0.622	0.846	0.113	0.005	0.011	10.690	-1.989	1.219	0.066	-0.124	-0.010	-0.104	0.077	0.062
Steel-3	0.103	0.609	0.832	0.100	0.006	0.015	11.159	-2.012	1.244	0.070	-0.132	-0.040	-0.054	0.043	0.067
Steel-4	0.097	0.613	0.833	0.108	0.012	0.016	10.644	-2.007	1.259	0.022	-0.106	-0.005	-0.104	0.064	0.068
Steel-5	0.130	0.629	0.828	0.124	0.010	0.012	12.443	-2.001	1.236	0.058	-0.120	-0.047	-0.047	0.047	0.062
Steel-6	0.083	0.605	0.849	0.089	0.009	0.014	9.3301	-1.973	1.180	0.099	-0.130	-0.039	-0.055	0.048	0.065
Steel-7	0.121	0.621	0.834	0.126	0.004	0.012	13.603	-2.012	1.248	0.065	-0.126	-0.058	-0.035	0.044	0.061
Steel-8	0.098	0.615	0.834	0.097	0.008	0.016	10.462	-2.010	1.263	0.032	-0.117	-0.027	-0.068	0.052	0.065
Steel-9	0.103	0.614	0.836	0.104	0.006	0.014	11.377	-2.020	1.271	0.041	-0.119	-0.048	-0.042	0.039	0.066
Steel-10	0.107	0.617	0.819	0.107	0.010	0.017	11.894	-2.003	1.233	0.068	-0.121	-0.035	-0.068	0.051	0.067
Steel-11	0.104	0.618	0.821	0.102	0.010	0.014	10.951	-2.005	1.245	0.051	-0.130	-0.011	-0.074	0.040	0.073
Steel-12	0.088	0.598	0.806	0.086	0.005	0.024	9.953	-1.975	1.198	0.066	-0.114	-0.016	-0.107	0.092	0.052
Steel-13	0.110	0.624	0.796	0.111	0.006	0.018	10.109	-1.987	1.208	0.079	-0.119	-0.048	-0.053	0.052	0.062
Steel-14	0.107	0.616	0.794	0.107	0.006	0.019	9.958	-1.998	1.221	0.080	-0.134	-0.039	-0.057	0.056	0.058
Steel-15	0.119	0.621	0.805	0.113	0.012	0.018	11.467	-1.995	1.237	0.049	-0.121	-0.016	-0.091	0.076	0.056
Brass-16	0.048	0.579	0.893	0.047	0.007	0.014	7.536	-2.003	1.163	0.141	-0.101	-0.071	-0.079	0.055	0.065
Brass-17	0.052	0.583	0.877	0.059	0.006	0.013	8.056	-2.015	1.209	0.097	-0.098	-0.070	-0.059	0.045	0.063
Brass-18	0.063	0.582	0.872	0.066	0.006	0.015	8.793	-1.984	1.143	0.126	-0.084	-0.029	-0.143	0.089	0.058
Brass-19	0.043	0.576	0.893	0.042	0.006	0.014	7.090	-2.028	1.236	0.082	-0.095	-0.087	-0.023	0.009	0.078
Brass-20	0.054	0.570	0.882	0.059	0.006	0.014	7.494	-1.979	1.118	0.163	-0.090	-0.068	-0.089	0.049	0.073
Brass-21	0.042	0.576	0.896	0.042	0.001	0.014	6.662	-2.010	1.192	0.121	-0.109	-0.069	-0.060	0.042	0.067
Brass-22	0.053	0.578	0.873	0.048	0.007	0.016	7.880	-1.991	1.155	0.142	-0.110	-0.062	-0.070	0.045	0.067
Brass-23	0.063	0.583	0.867	0.062	0.007	0.014	8.362	-1.998	1.170	0.133	-0.106	-0.079	-0.041	0.022	0.075
Brass-24	0.059	0.577	0.873	0.055	0.007	0.015	8.032	-2.017	1.218	0.079	-0.080	-0.075	-0.058	0.036	0.069
Brass-25	0.053	0.581	0.874	0.050	0.006	0.015	7.236	-2.041	1.264	0.073	-0.118	-0.056	-0.058	0.045	0.060
Brass-26	0.061	0.580	0.882	0.056	0.007	0.014	8.643	-2.015	1.206	0.103	-0.101	-0.066	-0.065	0.046	0.063
Brass-27	0.064	0.587	0.882	0.065	0.009	0.013	8.608	-1.996	1.162	0.141	-0.103	-0.088	-0.036	0.022	0.075
Brass-28	0.042	0.578	0.886	0.044	0.005	0.014	7.448	-2.017	1.217	0.095	-0.109	-0.051	-0.074	0.049	0.064
Brass-29	0.058	0.584	0.872	0.064	0.005	0.014	8.196	-2.006	1.188	0.110	-0.091	-0.080	-0.046	0.024	0.075
Brass-30	0.044	0.580	0.888	0.051	0.006	0.014	7.700	-1.986	1.143	0.143	-0.099	-0.043	-0.120	0.078	0.061

CHARACTERIZATION BY AE TECHNIQUE OF EMISSIVE PHENOMENA DURING STRESS CORROSION CRACKING OF STAINLESS STEELS

A. PROUST*, H. MAZILLE, P. FLEISCHMANN, and R. ROTHEA+

Institut National des Sciences Appliquées, 69621 Villeurbanne, France
*Now with Euro Physical Acoustic, 94373 Sucy en Brie, France
+ Now with Rhodia, 69200 Vénissieux, France

ABSTRACT

The aim of this study is to investigate the propagation of stress corrosion cracking (SCC) with acoustic emission (AE) technique in order to better understand the cracking mechanism and develop a technique for monitoring SCC on industrial structures in service. The material/environment system is austenitic, ferritic and duplex stainless steels in a 44-wt.% aqueous $MgCl_2$ solution at 145°C. Slow strain-rate tensile tests are used to obtain well-controlled SCC conditions. Tensile tests are performed in a scanning electron microscope to correlate local deformation mechanisms with recorded AE activity. All possible AE sources are identified and characterized in order to discriminate the signals caused by SCC, allowing a good correlation between AE signals and SCC damages. The optimization of the experimental setup and of a relevant frequency parameter confirms a discontinuous mechanism of cracking including a high velocity cleavage step.

1. INTRODUCTION

Stress corrosion cracking (SCC) is an important damaging phenomenon in the oil, chemical, aerospace and nuclear industry. Unpredicted failures occur in service, which have economic, safety, health and environmental consequences. Austenitic stainless steel in chloride environment is one of the major alloy/environment system susceptible to SCC. In the last two decades, duplex and ferritic stainless steels have also been developed for service in chloride media, but they are not fully immune to SCC either. Therefore, it is worthwhile to study and compare the different grades of stainless steels.

Acoustic emission (AE) is the only non-destructive evaluation technique that allows the detection and localization of propagating cracks. Its great sensitivity is sufficient to detect stress corrosion cracks [1-7]. It can evolve into a non-intrusive method for *in situ* continuous monitoring of SCC process on critical industrial structures. AE technique can also shed light into the mechanisms of SCC.

The aim of this study is to assess the possibility of detecting and characterizing AE signals produced by SCC on three different types of stainless steels in hot chloride environment during slow strain-rate tests.

2. EXPERIMENTAL

Experiments were performed on austenitic, ferritic and duplex stainless steels, chemical compositions of which are shown in Table 1. Two different experimental setups are used [8].

a) Tensile tests either in hot chloride environment (SCC) or in inert environment (hot silicone oil) Samples are specially designed to minimize the distance between the sensors and the gauge area. The cylindrical tensile geometry of the sample with inner holes allows one to fit AE sensors at each side of the gauge area (5-mm long and 3-mm diameter) and also into the grips (Fig. 1). These samples were previously solution-annealed in argon atmosphere and water quenched in order to eliminate residual stresses and compositional heterogeneity. The corrosion cell is a glass cylinder fitted with two PTFE caps at each side, with exits for samples, the condenser, the temperature probe and the reference electrode. A resistance heater is wound around the glass cylinder. The environments are $MgCl_2$ solution for SCC tests and silicone oil as a reference medium for purely mechanical straining. The slow strain-rate experiments are carried out with a 20 kN Roël+Korthaus prototype machine, which is computer controlled. The strain is measured with a displacement transducer between the two grips. After mounting the sample in the grips, the AE instrumentation is tested with simulated AE signals. The cell is filled with $MgCl_2$ aqueous solution, which is prepared overnight to eliminate dissolved gases and to minimize bubbling during the test.

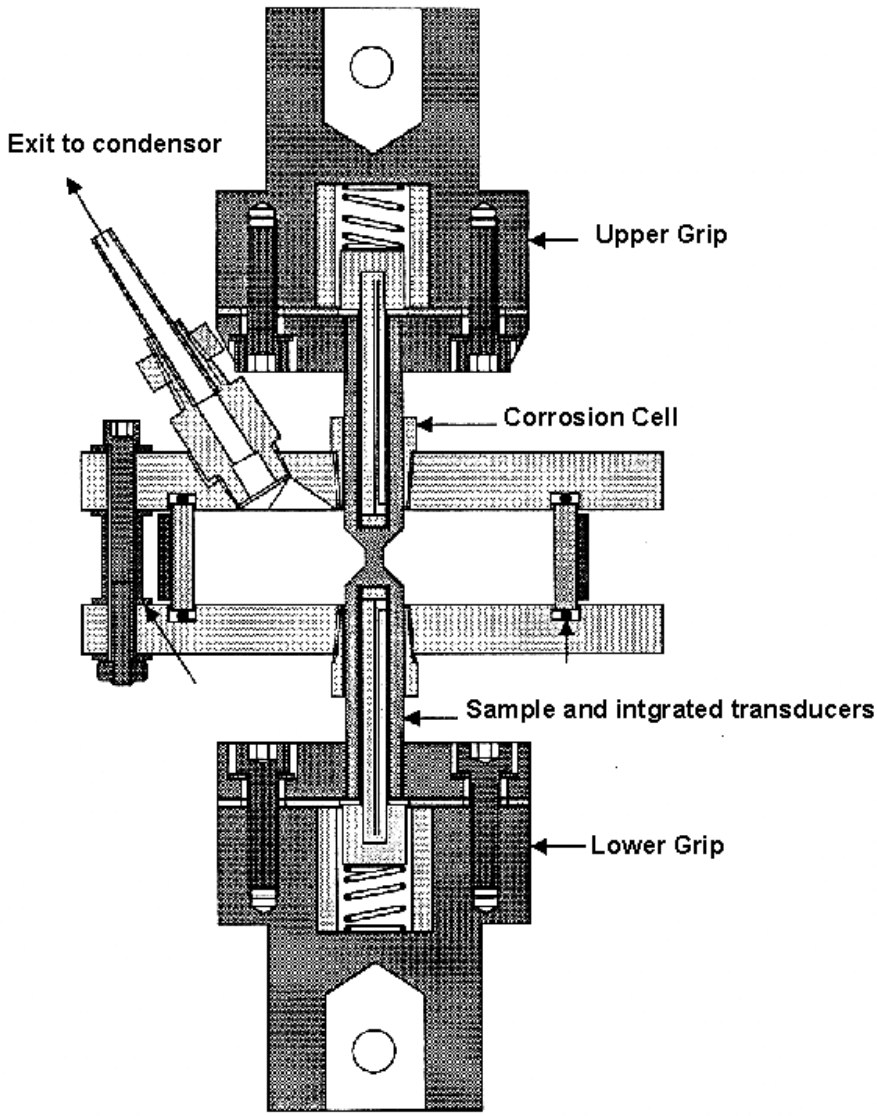

Fig. 1. Experimental setup for SCC tests.

b) Test implemented in a scanning electron microscope (SEM)

A special tensile machine has been developed in order to observe the sample surface during plastic deformation. AE sensors fixed on the sample surface allow to measure AE activity during a tensile test. The aim of these experiments is to identify the film rupture mechanism and correlate them with simultaneous AE measurements. A flat tensile sample of 1-mm thickness is used. In this case, the sample is not heat treated in order to keep it as flat as possible. After diamond polishing, a fine grid (2.5 x 2.5 µm) of gold is deposited on the sample surface. This grid acts actually as an optical extensometer [9]. An interference network, due to interaction of the grid and the electron beam, can be observed at low magnifications. The deformation of the network allows the detection and localization of a strain appearance. Then, at high magnification, these areas are identified and characterized in terms of micro-deformation.

Table 1: Composition of three types of stainless steels.

Stainless steels	Compositions (% weight)									Heat treatment (°C)
	C	Mn	P	S	Si	Cr	Ni	Mo	N	
Austenitic	0.015	1.45	0.018	0.003	0.4	17.6	14.29	2.41	0.036	30min 1050
Duplex	0.022	1.61	0.027	0.003	0.38	21.92	5.36	3.08	0.110	30min 1050
Ferritic	0.005	0.109	0.004	0.007	0.166	25.86	3.764	3.99	0.014	10min 1035

Acoustic Emission Instrumentation

The same AE acquisition system is used for all types of experiments. The two-channel AE instrumentation consists of sensors, preamplifier, filter and amplifiers (Bruel & Kjaër), and a transient recorder (Tektronix 2430A). The sensors are 150-kHz resonant PZT disks either laboratory made or commercial ones (PAC nano 30). The two channels are digitized at 10-MHz sampling rate. The acquisition system is completely computer controlled. The acquisition threshold of the oscilloscope is set up just above the background noise. The waveforms are transferred and stored on a hard disk as soon as detected, whereas all the test parameters are periodically sampled. The parameters measured by the analog-to-digital converters are stress, strain and free corrosion potential for SCC tests. AE signals are analyzed and processed after the test completion to obtain usual characteristic AE parameters: amplitude, rise time, energy and location. The frequency components are determined only with the first part of the waveform, which is more characteristic of the AE source and not of the sensor characteristics. A Blackman-weighting window is used to analyze only the very beginning of the transient. Then, the frequency parameter corresponds to the center of mass in frequency of the frequency density spectrum.

3. RESULTS AND DISCUSSION

Before analyzing the SCC process by AE, several types of tests were performed to identify and characterize the different possible sources of AE signals, related to the experimental conditions but not due to cracking propagation.

1) Electromagnetic interference and mechanical noise

AE sensors are designed to minimize their sensitivity to electromagnetic noise, but nevertheless few parasitic transients can be detected. Those parasitic transients with high frequency content (≥ 1 MHz) cannot be totally eliminated by analog filtering but they can be

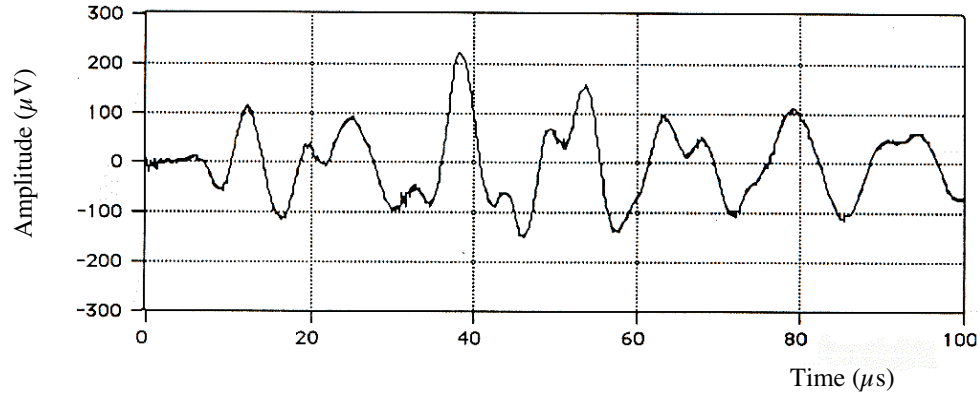

Fig. 2. Waveform relative to bubbles evolution in $MgCl_2$ solution.

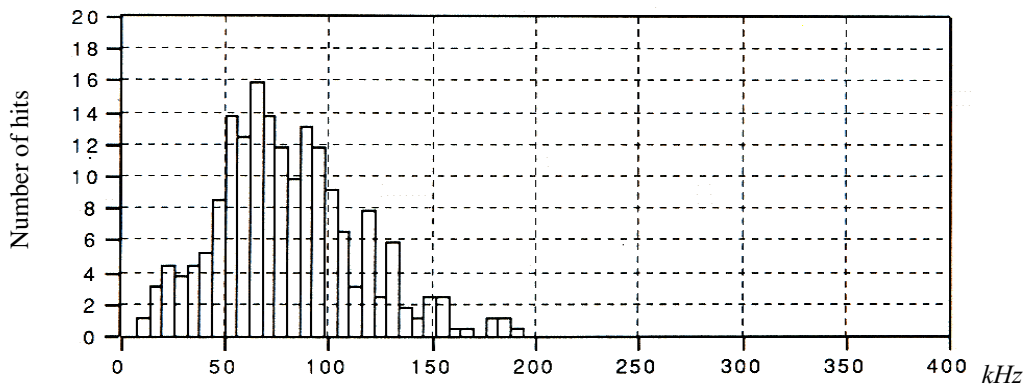

Fig. 3. Frequency parameter distribution (kHz) for boiling of $MgCl_2$ solution.

easily rejected after test completion by signal processing. No signals are detected during the crosshead motion of the tensile machine, but direct impact to the experimental device has to be avoided.

2) Physico-chemical effects due to environment

a) *Boiling and crystallization*

Bubble evolution (Figs. 2 and 3) in $MgCl_2$ induces AE signals with low frequency distribution (between 50 and 100 kHz). $MgCl_2$ crystallization produces high amplitude hits in a frequency range around 200-300 kHz (Figs. 4 and 5). The activity of these two types of AE sources can be avoided by an appropriate medium concentration and an accurate temperature control of the corrosive environment.

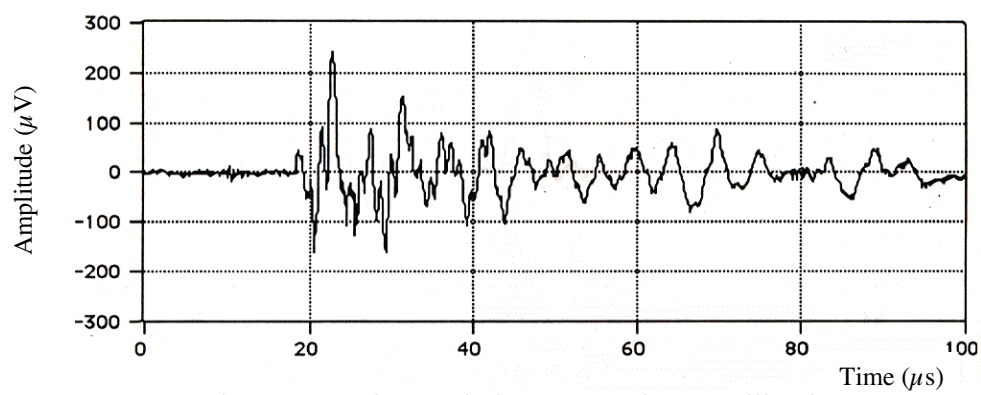

Fig. 4. Waveform relative to $MgCl_2$ crystallization.

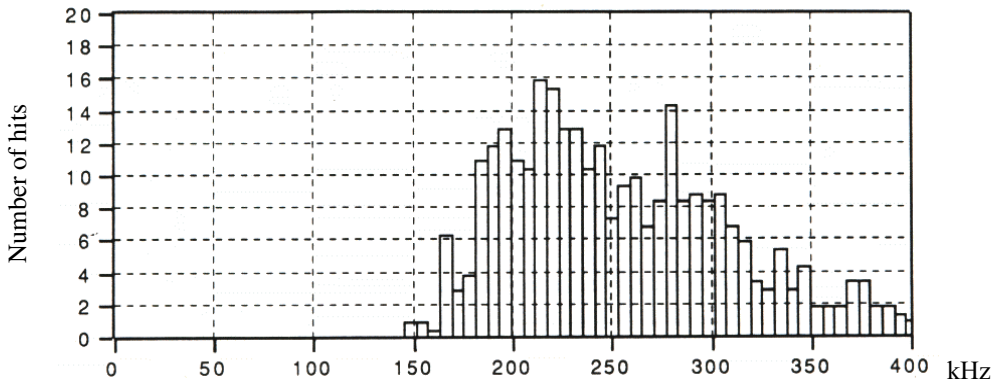

Fig. 5. Frequency parameter distribution (kHz) for crystallization of $MgCl_2$.

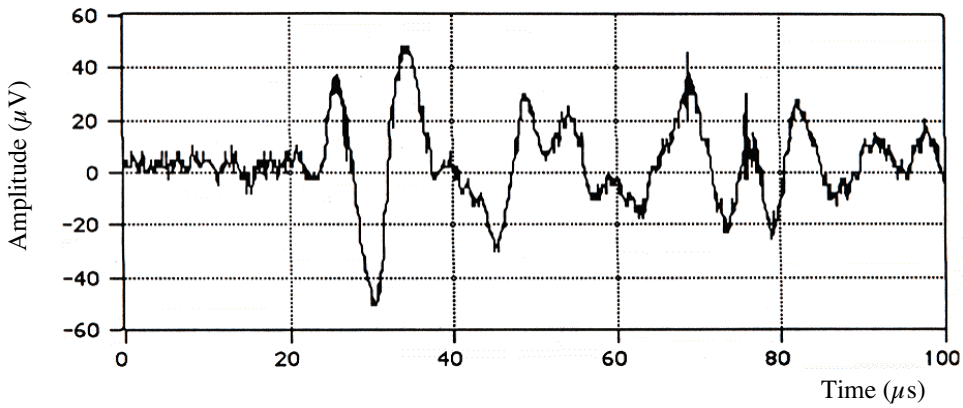

Fig. 6. Waveform detected during hydrogen evolution.

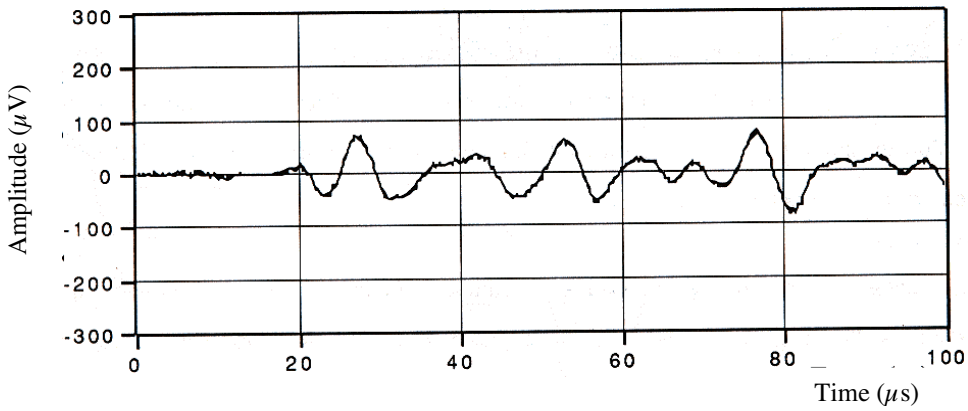

Fig. 7. Waveform detected during pitting corrosion.

b) Electrochemical effects

Electrochemical polarization tests are performed in order to analyze both pitting and/or hydrogen evolution from an AE standpoint. These two phenomena may occur during SCC tests. Hydrogen evolution is a source of low frequency (50 kHz) AE signals, as shown on Fig. 6. This source cannot be avoided because hydrogen evolution always occurs in our experimental conditions. Signals detected during pitting obtained by anodic polarization or after a long-time immersion have a low frequency content (≤ 150 kHz) and long rise times as reported on Figs. 7 and 8. At the free corrosion potential, which is the usual experimental condition for SCC tests, pitting phenomenon can be strongly reduced by an appropriate filling up of the corrosion cell in order to avoid differential aerated zone on the tested samples. Whatever the stainless steel grade

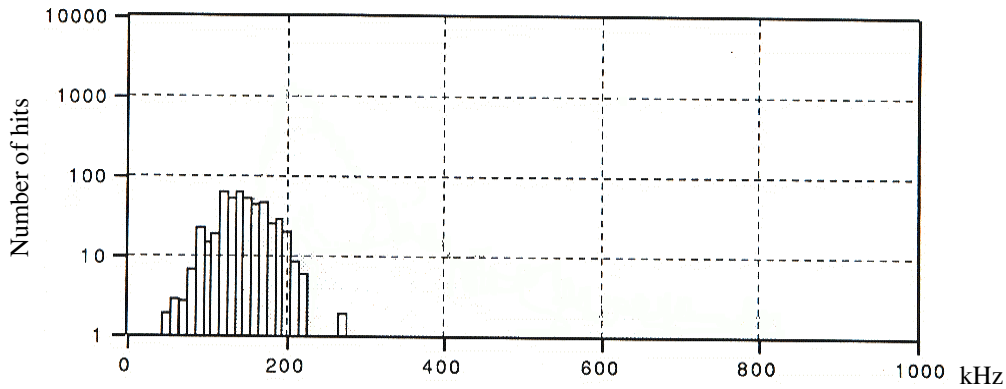

Fig. 8. Frequency parameter distribution (kHz) for signals obtained during pitting corrosion.

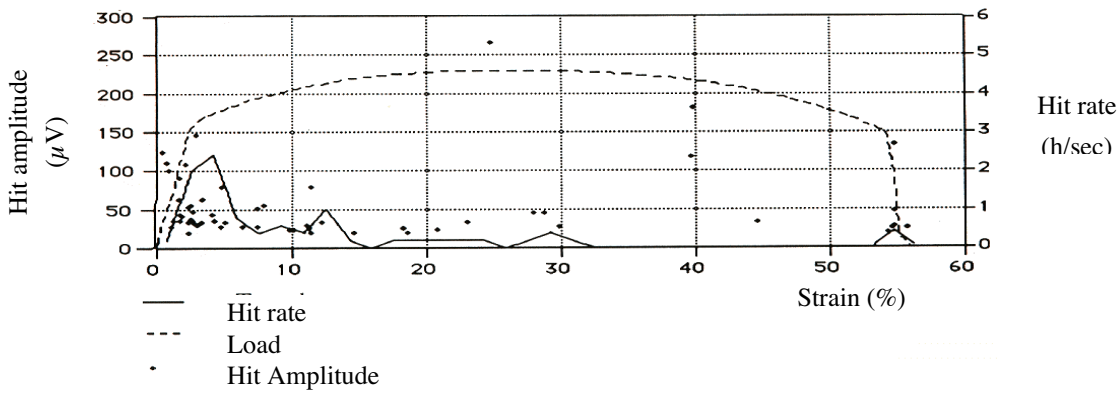

Fig. 9. Slow strain rate test on austenitic stainless steel.

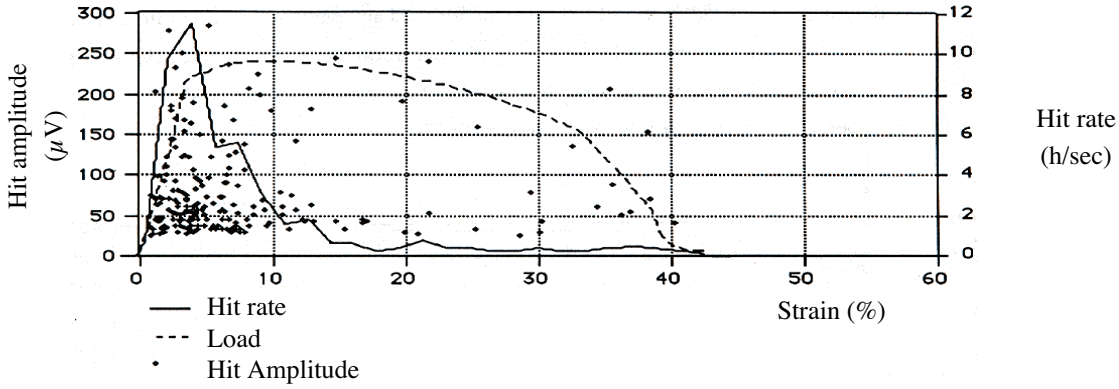

Fig. 10. Slow strain rate test on ferritic stainless steel.

tested, all the previous data are somewhat the same.

3) Acoustic emission sources related to plastic deformation

Tensile tests in inert environment have been conducted on the three types of stainless steels at different strain rates. Figures 9, 10 and 11 are relative to the three steels for the same strain rate of 3 x $10^{-3}s^{-1}$.

For austenitic and duplex stainless steels, the main AE activity appears around the yield point. However, for ferritic stainless steel, early high amplitude AE signals occur from 20% up to

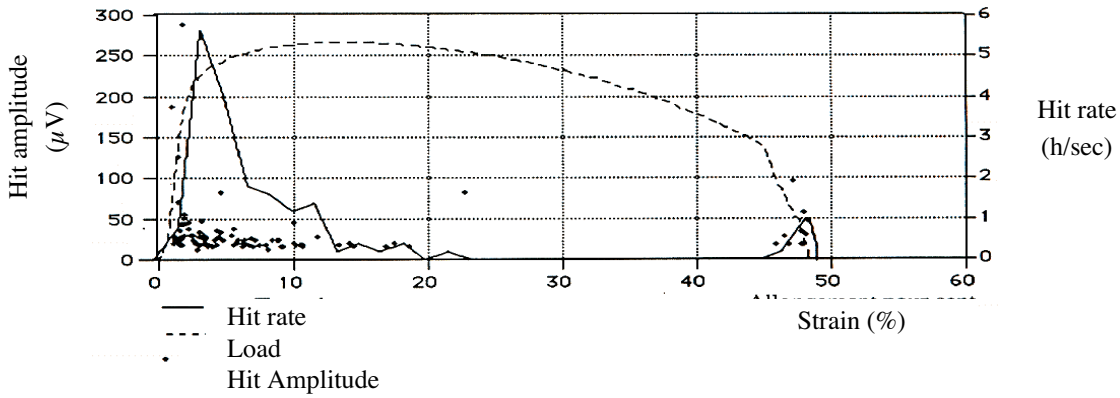

Fig. 11. Slow strain rate test on duplex stainless steel.

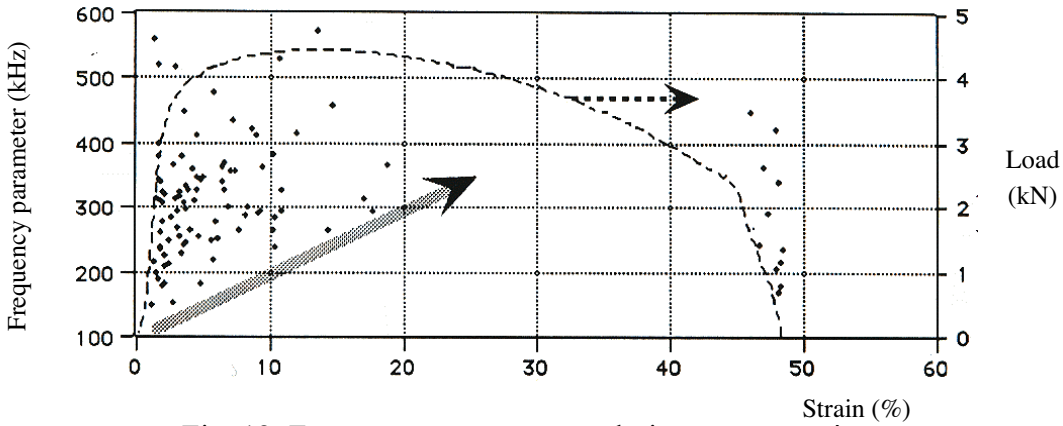

Fig. 12. Frequency parameter evolution versus strain.

100% of the yield point. AE signals are mainly detected in a frequency range from 150 kHz to 300 kHz with a shift toward high frequencies as deformation increases (Fig. 12). For the three types of stainless steel, from the ultimate tensile stress up to the final rupture, no or very few AE signals are detected. The final rupture provides some high amplitude signals in the same frequency range as in the yield stress area. With the same acquisition threshold, more hits are detected on ferritic than on duplex stainless steel. In comparison, austenitic stainless steel is far less emissive. This classification is the same whatever the strain rate [5].

With the tensile machine implemented in the SEM, the sample surface can be observed during plastic deformation. The aim of this set of experiment is to clearly identify local deformation mechanisms, responsible of the passive film rupture and correlate them with AE. Two tensile tests are performed on each type of stainless steels. The first test is carried out with crack-free samples in order to study general plastic deformation. The second is performed with pre-cracked samples (through a preliminary SCC test in $MgCl_2$) in order to observe the strain evolution at the crack tip. In all cases, AE from pre-cracked samples appears at the very beginning of the loading because of the Kaiser effect (load exceeding the load used for pre-cracking).

For austenitic stainless steel, the slip-band formation is well correlated with the beginning of the first AE signals. Nevertheless, the overall activity on the crack-free samples is quite low because the plastic deformation is very homogeneous. For pre-cracked sample, the AE activity is higher due to localized strain at the crack tip (Fig. 13). AE signals are related to the cooperative

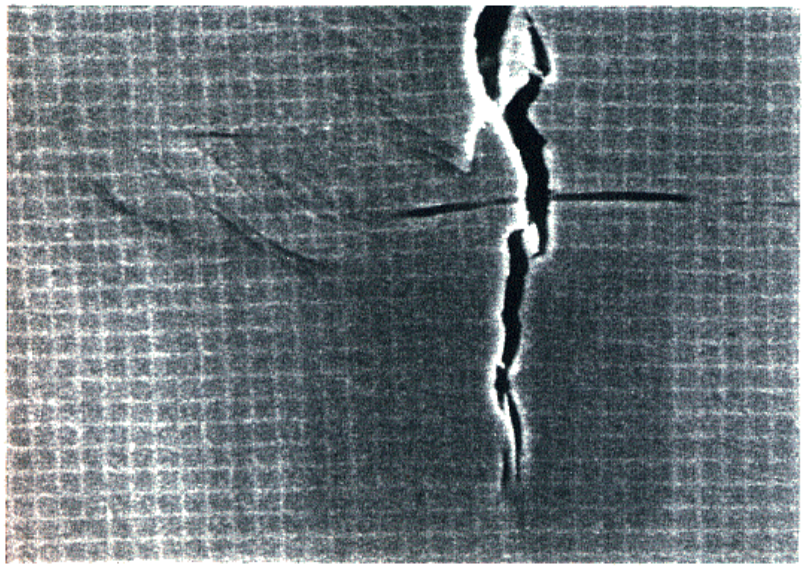

Fig. 13. First appearance of slip band at the crack tip (grid 2.5 x 2.5 μm).

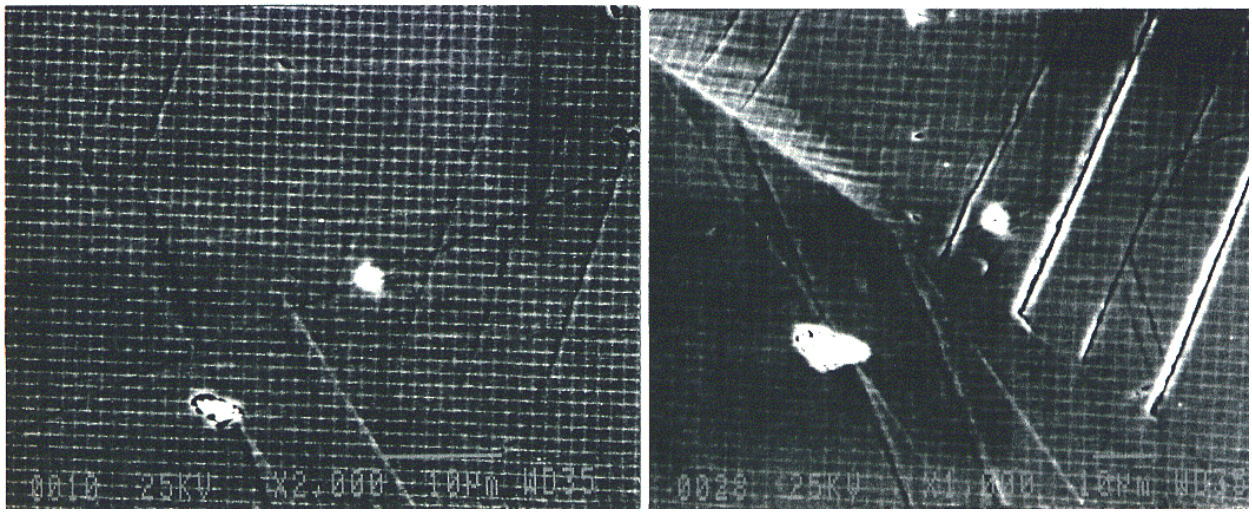

Fig. 14 (a) Microtwinning of ferritic stainless steel. (b) Glide process at grain boundary and microtwinning opening. (grid 2.5 x 2.5 μm)

dislocation motion, such as the breakaway of pinned dislocations from obstacles [10, 11]. If the dislocation density increases or if a second slip system is activated, the free glide distance is reduced corresponding to higher frequency component and lower amplitude of AE signals. For ferritic stainless steel, micro-twinning occurs at very low stresses up to the yield point (Fig. 14a). This phenomenon is an important source of high-energy AE signals. After the yield point, neither twinning nor high-energy AE signal is observed. The plastic strain is mainly produced by the glide process at the grain boundary with a lower AE activity. Micro-twinning and glide processes are able to break down the passive film and to induce SCC (Fig. 14b).

For duplex stainless steel, some AE bursts are detected at the beginning of loading but no twinning can be observed in the ferritic phase because of the small size of each phase in the duplex stainless steel. On the pre-cracked sample, the crack tip appeared to be located at interphase boundaries. The cracks were mainly transgranular, but at each interphase they

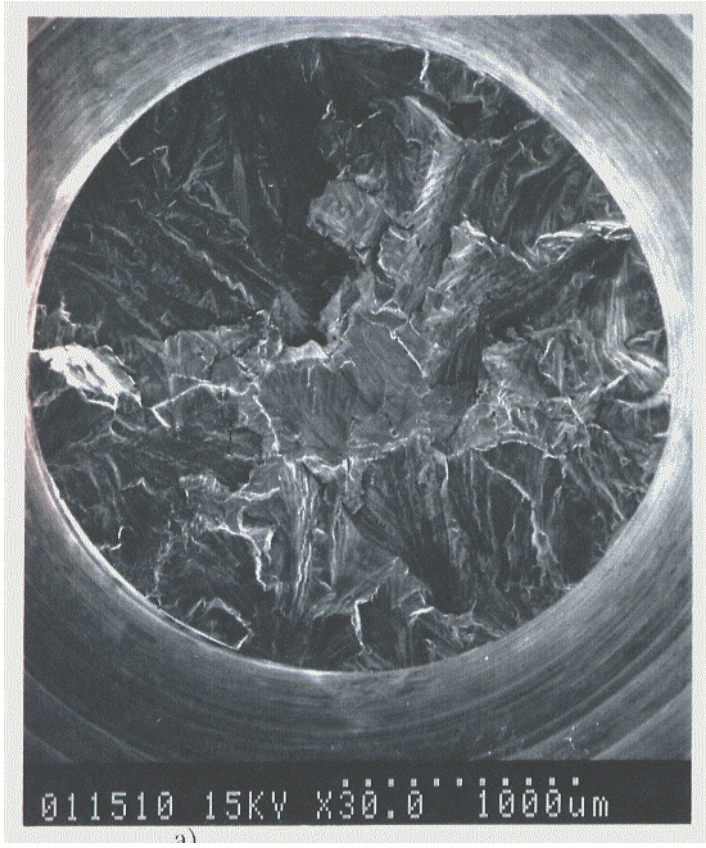

Fig. 15. Fractograph of rupture surface of ferritic stainless steel after SCC.

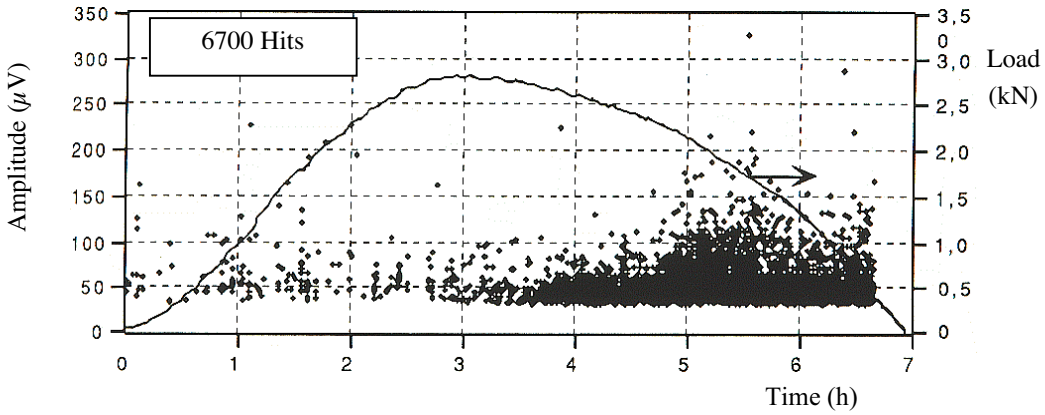

Fig. 16. AE Evolution during SCC test for a duplex stainless steel (strain rate = 3.3 x 10^{-6} s^{-1}.

preferentially followed the interphase boundaries before continuing transgranular propagation. In any case, localized strain at the interphase boundary can be large enough to produce film rupture, thus explaining why duplex steels are quite susceptible to SCC at high level of applied stress.

4) Acoustic emission sources related to SCC

For the three types of stainless steels, a strain rate of 3 x 10^{-7} s^{-1} is sufficiently low to induce total brittle rupture by SCC and even with a strain rate of 3 x 10^{-6} s^{-1}, the final brittle rupture surface is around 90% (Fig. 15). SCC-propagation process produces a large number of AE signals (up to a few thousands). As shown in Fig. 16, the temporal distribution of AE is completely different from what is observed in an inert environment. AE is detected in

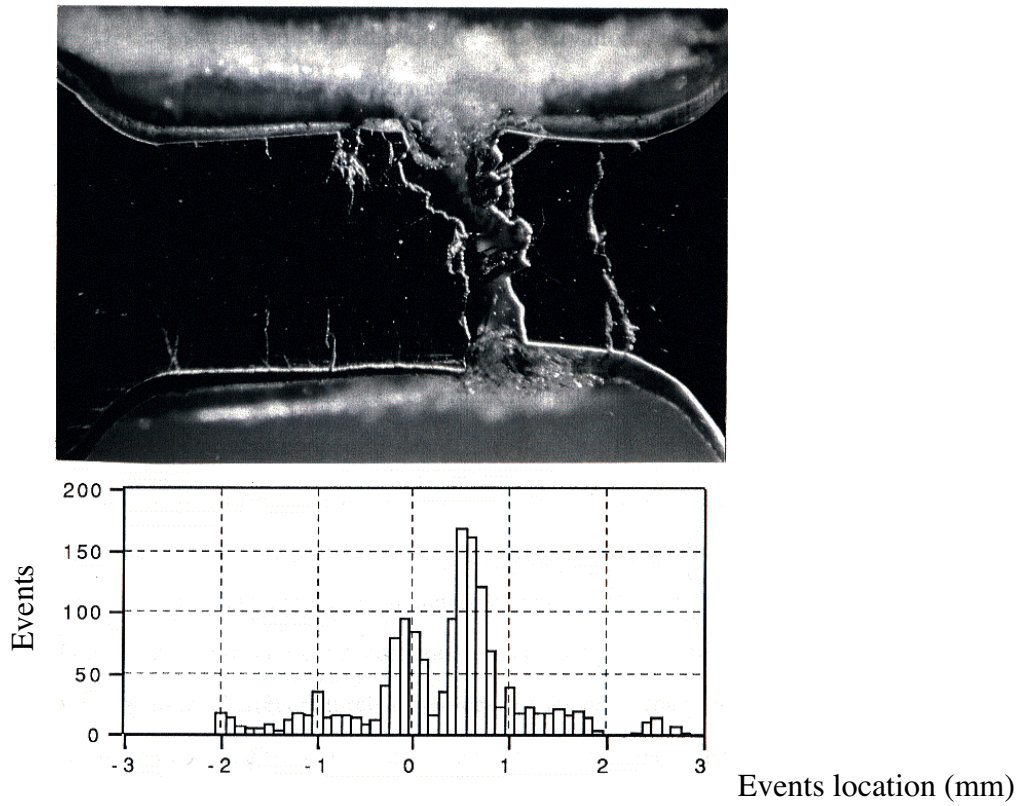

Fig. 17. Correlation between located events and actual cracks position along the sample.

experimental conditions with magnesium chloride, while very few AE signals have been found in silicone oil.

The AE sources location is in good agreement with the multi-branching and secondary cracking observed on optical and SEM micrographs (Fig. 17). Therefore, for the three types of stainless steels, the AE sources are clearly related to the SCC process. Figure 18, which summarizes the data obtained with the three types of steels, shows that the total number of hits recorded during each SCC test decreases when the strain decreases. In other words, we observe a good correlation between the AE activity and the total surface rupture.

Table 2: Characteristics of AE signals detected during SCC processes.

	Amplitude (dB)	**Energy** (µV_s)	**Frequency content** (with resonant transducer-150 kHz)	**Rise Time** (µs)
SCC process	30-70	0.01-0.3	150-600	1-30
Cooperative dislocation motion	30-45	0.01-0.2	100-400	1-30
Twinning	30-70	0.01-5	150-600	1-30
Pitting/crevice	30-45	0.01-0.2	50-200	50-70

Table 2 summarizes AE parameters, which can be processed from recorded signals during SCC test in our experimental conditions. From a practical point of view, it is worthwhile to note

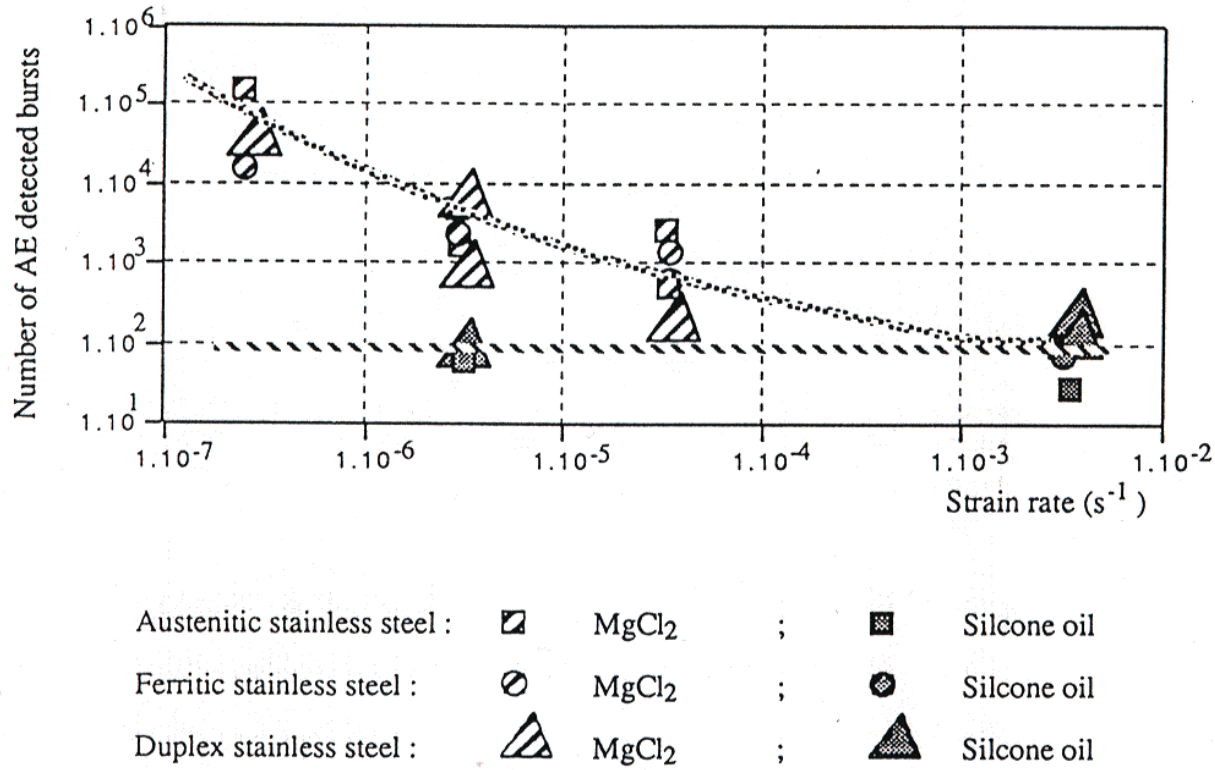

Fig. 18. Number of detected AE hits versus strain rate for three types of stainless steel during SCC tests at 145°C.

that AE hits related to pitting or crevice process are easily identified because of their long rise time [12]. The twinning process can also be easily recognized, considering the high AE energy released in this case. AE hits from SCC events have frequency components much higher than cooperative dislocations motion process. That confirms that a high-velocity cleavage phenomenon is involved during the crack propagation [13].

4. CONCLUSION

It is demonstrated that AE related to SCC can be detected during slow strain-rate experiments with three different types of stainless steels (austenitic, ferritic and duplex) in concentrated magnesium chloride solution at 145°C.

1. Several complementary experiments were necessary to perfect and optimize the AE instrumentation and testing configuration in order to detect and analyze all other possible AE sources (such as pitting or crevice propagation, twinning and co-operative dislocations motion) that can be also active during on SCC tests.

2. Pattern recognition of AE signals due to SCC events allows the monitoring of the SCC process for tested stainless steels whatever the strain rate. In particular, the analysis of appropriate frequency parameters indicates valid information on the discontinuous steps of propagation during SCC in chloride environment, even with a resonant sensor. Moreover, the high-frequency components of the SCC signals indicate that at least one high-velocity step is involved during the crack propagation with local brittle behavior of the stainless steels.

ACKNOWLEDGMENT

This study has been carried on the financial support of CEE (European Brite contract N°RI 1B-0306 C, Proposal P-2032)

REFERENCES

[1] E.N. PUGH, (1985), Corrosion, **41**(9) 517.
[2] D.G. EITZEN, and H.N.G. WADLEY (1984), NBS J. Res. **89**, 75.
[3] S. YUYAMA, T. KISHI, and Y. HISAMATSU, (1983), J. Acoustic Emission **2**(1/2), 71.
[4] R.H. JONES, M.A. FRIESEL and R. PATHANIA (1991), Corrosion, **47**(2), 105-115.
[5] A. PROUST, Etude par la technique d'EA de la corrosion sous contrainte de trois nuances d'acier inoxydable en milieu chloruré chaud. Thèse 92 ISAL 0081, INSA de Lyon (1992)
[6] R. ROTHEA, Etude par la technique d'EA de la corrosion sous contrainte des aciers inoxydables austénitiques en milieu chloruré chaud. Thèse 90 ISAL 0024, INSA DE Lyon (1990)
[7] T. CASSAGNE, D. CARON, J. DARET, A. PROUST, H. MAZILLE, G. TURLUER, and D. BOULANGER. (1999), *Ninth Intl. Conf. on Environmental Degradation of Materials in Nuclear Power Systems-Water Reactors*. Newport Beach, CA.
[8] A. PROUST, P. FLEISCHMANN, H. MAZILLE and R. ROTHÉA (1992), Intl. Conf. Corrosion-Deformation-Interactions, Fontainebleau, pp. 829 - 839
[9] A. MOCELLIN, G. THOLLET, A. PROUST, P. FLEISCHMANN, H. MAZILLE, and R. FOUGÈRES (1992), *Proc. X European Congress on Electron Microscopy*, EUREM92, Grenade
[10] C.R. HEIPLE, and S.H. CARPENTER (1987) J. of Acoustic Emission, **6**(3), 177.
[11] D. ROUBY, P. FLEISCHMANN, and C. DUVERNIER (1983) Phil. Mag. A, **47**(5), 671.
[12] M. FREGONESE, H. IDRISSI, H. MAZILLE L. RENAUD and Y. CETRE. (submitted to Corrosion Science August 1999).
[13] A. PASKIN, K. SIERADSKY, D.K. SOM, and G.J. DIENES (1983), Acta Met. **31**, 1253-1265

INVESTIGATION OF ACOUSTIC EMISSION WAVEFORMS ON A PRESSURE VESSEL

MULU BAYRAY

Institute of Pressure Vessels and Plant Technology, Vienna University of Technology
Gusshausstr. 30, A – 1040 Vienna, Austria

ABSTRACT

In this paper, acoustic emission waveforms due to simulated sources and during pressure tests on a pressure vessel will be presented. Lamb wave theory has been utilised to predict the propagation of the extensional mode S_0 and the flexural mode A_0. Electrical pulse was used as simulated AE source to investigate dispersion of the S_0 and A_0 modes. Experimentally measured dispersion plot has been found to be in close agreement with that predicted by Lamb theory. Pencil-lead breaks were used to simulate in-plane and out-of-plane type of sources. Window Fourier Transform was applied to analyse the waveforms. Results of simulated tests were employed to investigate AE signals during pressure tests of the vessel. It was found that some in-plane type AE waveforms have been recorded during each pressure test.

1. INTRODUCTION

One of the recent developments in acoustic emission (AE) testing is the use of modal analysis technique. The knowledge of the modes of the elastic waves due to an AE source has paramount importance in the analysis of AE data. This paper will present results of an investigation of AE waveforms on a pressure vessel. The aim of the paper is to show the observation of AE waveforms due to simulated sources and during pressure tests of a vessel.

In the next section, the theory of elastic waves, specifically the extensional mode S_0 and the flexural mode A_0 will be briefly discussed. Some literature on experimental work and comparison with theoretical predictions will then be given. In the following section, the Windowed Fourier Transform (WFT) method of analysing waveforms to identify the two modes will be presented, followed by the investigation of AE waveforms due to simulated AE sources. The last section deals with the investigation of AE waveforms during pressure tests. Finally, some concluding remarks will be given.

2. THEORY OF ELASTIC WAVES

Lamb waves

Lamb waves refer to elastic perturbations propagating in a solid plate with free boundaries, for which displacement occur both in the direction of wave propagation and perpendicular to the plane of the plate. Results of Lamb wave discussion from Royer [2000] will be utilised here. Assuming a plane harmonic Lamb wave propagating in a plate of thickness 2h in the positive x_1 direction, as shown in Fig. 1a, there are two possible wave modes. Those are the symmetrical Lamb wave (also called extensional wave) or S-mode and the anti-symmetrical Lamb wave (also called flexural wave) or A-mode, shown in Fig. 1b. The respective mode displacements can be obtained by considering the boundary condition $\sigma_{13} = 0$ and $\sigma_{33} = 0$ at the faces $x_3 = \pm h$. The phase and group velocities can then be determined from numerical solution of the characteristic equations.

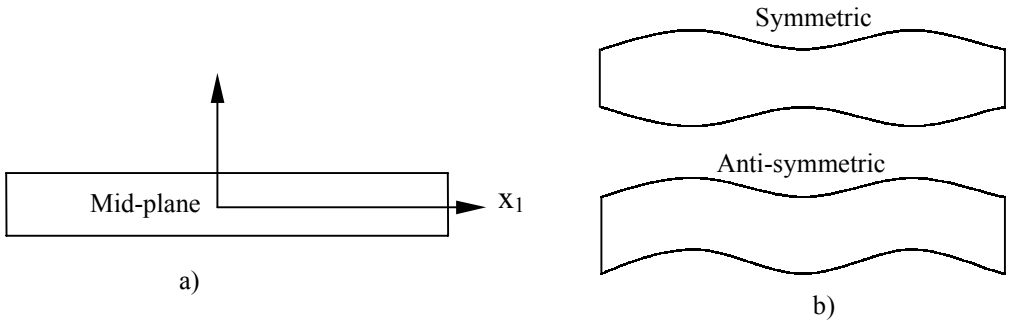

Fig. 1 a) Definition of axes and b) the two possible wave modes.

The Lamb-Rayleigh equation for an isotropic material, which relates the frequency ω of a wave with its wave number k, is given by:

$$\frac{\omega^4}{V_T^4} = 4k^2q^2\left[\frac{1-p\tan(ph+\alpha)}{1-q\tan(ph+\alpha)}\right]$$

with $\alpha = 0$ or $\pi/2$, (1)

where $\alpha = 0$ for symmetrical mode and $\alpha = \pi/2$ for anti-symmetrical mode, and

$$q^2 = \frac{\omega^2}{V_L^2} - k^2 \text{ and } p^2 = \frac{\omega^2}{V_T^2} - k^2$$

Equation 1 is commonly plotted as dispersion curve, phase velocity $V_\varphi = \omega/k$ and group velocity $V_g = d\omega/dk$ as a function of the product (frequency x plate thickness). Refer [Royer, 2000] for plot of the dispersion curve including higher order modes. In this paper, only part of the dispersion plot for the zero order modes will be considered. Figure 2 shows the dispersion curve, for carbon steel material (E = 209 GPa, $\nu = 0.3$ and $\rho = 7850$ kg/m^3), with frequency x plate thickness ranging 0.35 – 2.45 MHz x mm. This is the range of interest appropriate for plate thickness 3 – 6 mm and frequency 100 – 400 kHz. In this range, it could be noted that, S_0 is highly dispersive while A_0 is slightly dispersive.

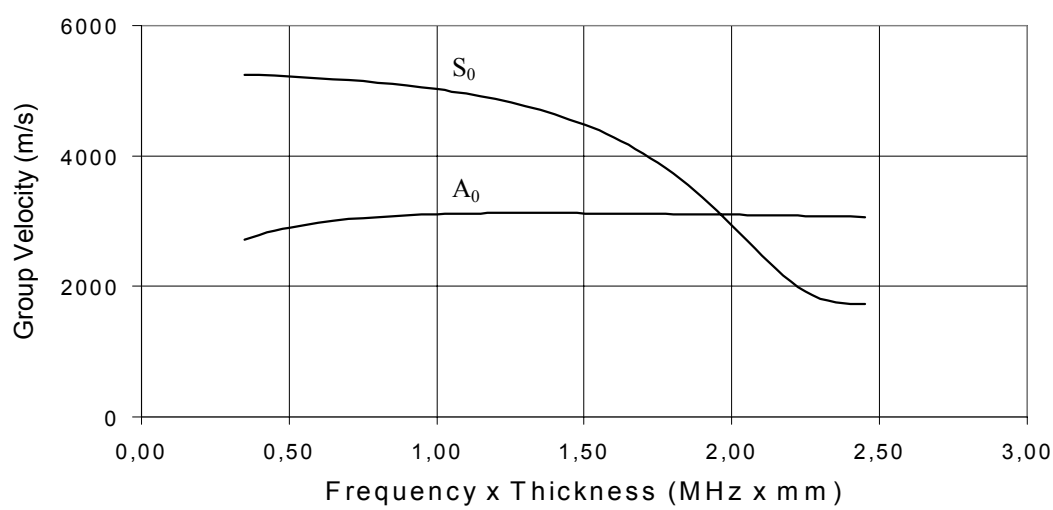

Fig. 2 Dispersion of S_0 and A_0 wave modes.

Figure 2 shows that the low frequency component of S_0 arrives earlier than its high frequency component. Also, the high frequency component of A_0 arrives earlier than its lower frequency component. It is expected that AE waves would have the propagation characteristics represented on the figure. This will be the basis on which the AE waveforms will be analysed.

Wave theory and AE signals

Plate wave theory (for the case $h/\lambda << 1$) was used in Gorman [1991] to discuss the AE phenomena in aluminium and composite plates. Pencil Lead Break (PLB) was used as source of AE and the resulting waves were detected with a broadband ultrasonic transducer. Comparisons were made between the velocity predicted by the theory and experimental measurements. It was found that the symmetrical mode velocity was in close agreement with the theory while the flexural mode velocity was in discrepancy with the theory.

Another work that considered plate wave theory with experimental measurements was reported in [Dunegan, 1997]. In this work the specimen were steel bars with different thickness. In-plane and out-of-plane PLB were used as AE source and broadband transducer was used to detect the waves. The measured velocities were found to be in good agreement compared with theoretical solutions described in the form of dispersion curves. It was also shown that the relative amplitude of the extensional mode was the highest in the mid-plane of the bars.

Theoretical discussion on Mindlin's plate theory was reported in Huang [1998]. A detailed discussion and derivation of both the extensional and flexural motions for a finite plate were presented. A comparison of the theoretical AE waveform with experimentally recorded signal was made. The experiment was conducted on aluminium plates using PLB as AE source and broadband transducer to detect the signal. The experimental waveform was in good agreement with predicted waveform. The experimental AE waveform clearly showed the two wave modes. The frequency in the S_0 mode increased as the time arrival increased, while in the A_0 mode it decreased as the arrival time increased.

3. WINDOWED FOURIER TRANSFORM (WFT)

Definitions

Fourier transform (FT) is often used in AE data analysis to extract the frequency spectral information. FT generates a frequency domain data out of a time domain data. Generally, FT is defined as:

$$S(\omega)=\int s(t)\exp(i\omega t)dt, \qquad (2)$$

where $S(\omega)$ is the FT of a time signal $s(t)$, ω is the frequency and $\exp(i\omega t) = \cos(\omega t) + i \sin(\omega t)$ is the basis function.

Windowed Fourier Transform also known as Short Time Fourier Transform (STFT), is a mathematical tool by which a signal is analysed considering a fixed width window centred at a certain time, τ. The window is shifted at intervals throughout the whole signal data. Fourier Transform is carried out at every interval to obtain an estimate on the frequency-time dependence. WFT is well known in signal processing literature [Carin, 1997]. It was also mentioned in [Suzuki et al., 1996] while discussing wavelet transform of AE signals.

Considering a window function $W(t - \tau)$, centred at time τ, the WFT is defined as:

$$WFT(\omega,\tau) = \int s(t)\, W(t-\tau)\, \exp(i\omega t)dt \qquad (3)$$

$WFT(\omega,\tau)$ yields spectral density as a function of frequency, at time τ. The window function is shifted in time over the whole signal producing frequency spectrum of the signal as a function of time. A commonly used window function is the Gaussian function, given by:

$$W(t-\tau) = \exp[\mu-(t-\tau)]^2 / (2\pi)^{1/2}\sigma^2 \qquad (4)$$

where μ (mean) and σ (standard deviation) are constants of the Gaussian normal distribution.

Results of the WFT calculation can be plotted in three-dimensional contours of Power Spectral Density (PSD) versus Frequency versus Time. (as will be shown in Figs. 11 –12.)

WFT in identifying arrival of flexural wave mode

Consider a signal having wave characteristics shown previously in Fig. 2. Its frequency-time dependence would reveal the arrival of the flexural wave mode. The arrival time could be estimated as the time, at which the frequency reaches maximum and starts to decrease. This estimated time of arrival of A_0 mode after a trigger by S_0 mode will be designated by t_{A0}.

A simple algorithm, which is employed to extract t_{A0} out of the WFT data, will be utilised in section 4 and 5. In this algorithm, instead of analysing the whole frequency spectrum at each interval of time, the centre of gravity of the spectrum (F_{cg}) is evaluated and considered as a representative frequency. When the value of F_{cg} is plotted with time, a maximum is expected to occur. The time at which a maximum F_{cg} has been reached, gives an estimate of t_{A0}. The extensional mode amplitude (A_{S0}) could then be estimated as the maximum amplitude data before time t_{A0}. Similarly, the flexural mode amplitude (A_{A0}) could be estimated as the maximum amplitude after time t_{A0}.

4. INVESTIGATION OF WAVEFORMS DUE TO SIMULATED AE SOURCES

Test vessel and AE instrumentation

Pencil lead break (PLB) and electrical pulse input (PI) were used as simulated AE sources. The tests were carried out in two phases. The first phase was conducted prior to failure of the vessel and it was only possible to simulate out-of-plane perturbation, using PLB and PI. The tests were conducted when the vessel was empty (air medium) and filled with water. In the second phase, the vessel was cut out partly to access the edge of the vessel and simulate in-plane perturbation.

A sketch of a section of the vessel and instrumentation is shown in Fig. 3. The vessel has an outer diameter of 600 mm and a thickness of 5 mm. The AE instrumentation consists of a pulser (Panametrics V103), a trigger sensor (SE900) and AE sensors (VS150 and SE375) arranged as shown in Fig. 3. All transducers were coupled to the vessel with silicone grease. The signals from the trigger and sensors were pre-amplified by 40 dB and a 100-kHz built-in filter was used. Vallen Systeme AMS3 was used to acquire and analyse the signals. Other acquisition parameters employed were a threshold of 34 dB and a rearm time of 3.2 ms.

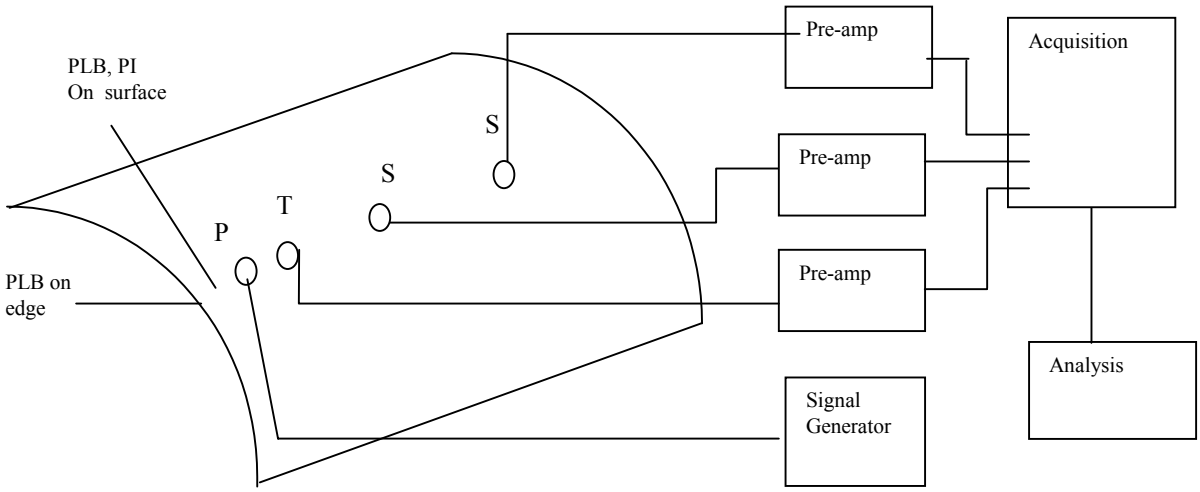

Fig. 3 Section of the test vessel and AE instrumentation. Sensors were also arranged along the circumference. P: pulser; T: trigger; S: sensors.

4.1 Experimental procedure

Phase I Narrow-band pulse input tests

In order to study the dispersion of the two modes, narrow-band pulses 100-400 kHz at intervals of 10 kHz were transmitted via the ultrasonic transducer (Panametrics V103) on to the surface of the vessel. A signal generator was used to produce the pulses. The amplitude of the pulses were 120 dB (referenced to 1 μV) for empty vessel tests and 126 dB for the full vessel tests. A trigger (SE900) at about 100 mm and a sensor (VS150 or SE375) at about 600 mm from

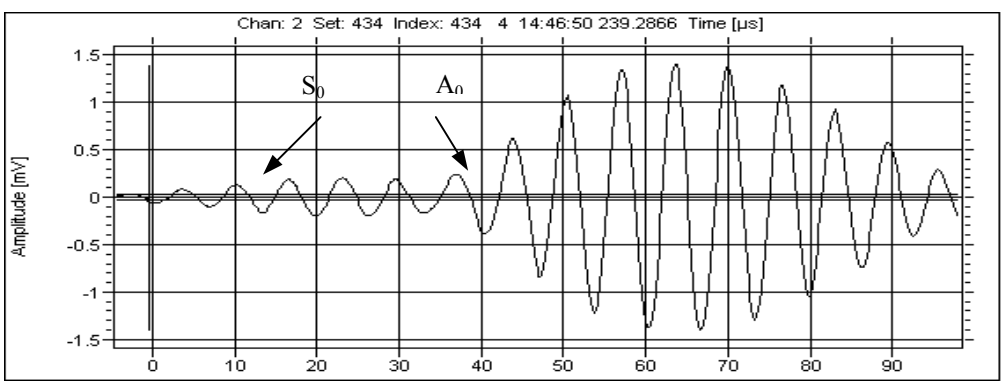

a) PI source with constant frequency

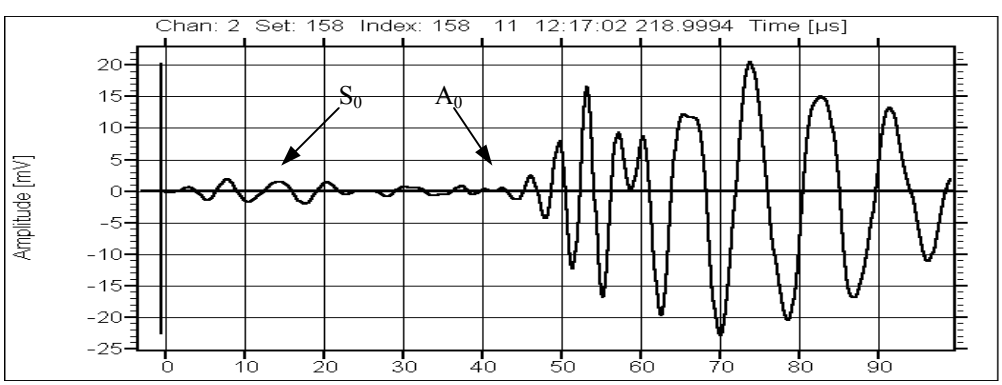

b) PLB source

Fig. 4 Arrival of S_0 and A_0 modes.

the pulser were used to record the AE signal. Investigating the transient record of the AE signal the velocities of the respective modes were determined from the arrival times. Figure 4a shows a single transient record with the arrival times labelled for the PI source.

Phase II Pencil-lead break tests

In-plane and out-of-plane sources were simulated by breaking pencil leads (0.3 mm, 2H) on the edge and on the surface of the vessel respectively. A trigger (SE900) at about 150 mm and a sensor (VS150 or SE375) at about 400 and 600 mm from the PLB were used to record the AE signal. Out-of-plane PLB source was made on the inside (z = –2.5 mm) as well as the outside (z = 2.5 mm) of the vessel. In-plane PLB source was made at three different positions on the edge of the vessel. The three positions were at about 1.25 mm above the inside surface (z = –1.25 mm), at mid plane (z = 0) and at about 1.25 mm below the outside surface (z = 1.25 mm). The transient records were then investigated for the extensional and flexural modes. The arrival time of the low frequency and high frequency component of each mode was identified. Figure 4b shows one of such records.

The two modes were identified, as mentioned earlier, from the velocity of arrival. Extensional mode arrives earlier than the flexural mode. A second characteristic used to identify the two modes was the arrival of the low and high frequency components. For the extensional mode, its low frequency component arrives earlier than its high frequency component. For the flexural mode, its high frequency component arrives earlier than its low frequency component. This is clearly observed in Fig. 4b.

Another simple test was carried out to confirm the identification of the two modes. Two sensors were mounted one outside and the other inside of the vessel at equal distance from PLB source. Referring Fig. 1, for the extensional mode, the two sensors would record signals that are in phase. However, for the flexural mode the two sensors would record signals that are out of phase. Figure 5 shows waveforms of such a test, confirming the identification of the two modes.

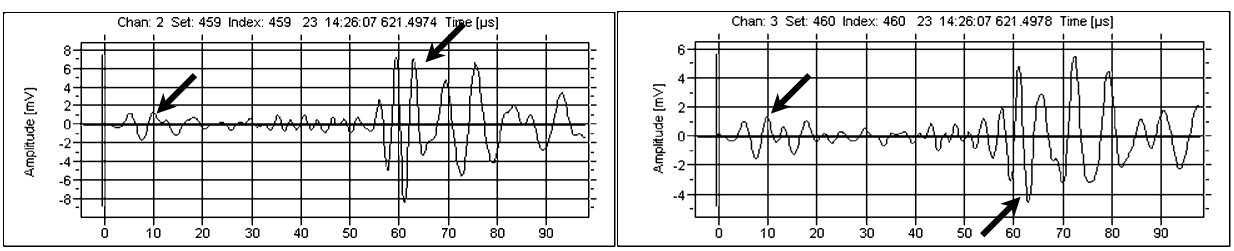

Fig. 5 PLB at z = –1.25 mm, Channel 2 VS150 sensor on outside surface and Channel 3 VS150 sensor on inside surface, both at 400 mm from source.

4.2 Experimental Results and Discussion

Dispersion

The tests described in Phase I (see section 4.1) were used to study the dispersion of the wave modes. Transient record of hits at selected frequencies, (100 – 400 kHz, at 10 kHz interval), were evaluated and the arrival time of the modes was read. The velocities were calculated using the distance between the trigger and sensor and the respective arrival time. Figure 6 shows the plot of the velocity versus frequency. Theoretical predictions discussed in the first section are included in the figure.

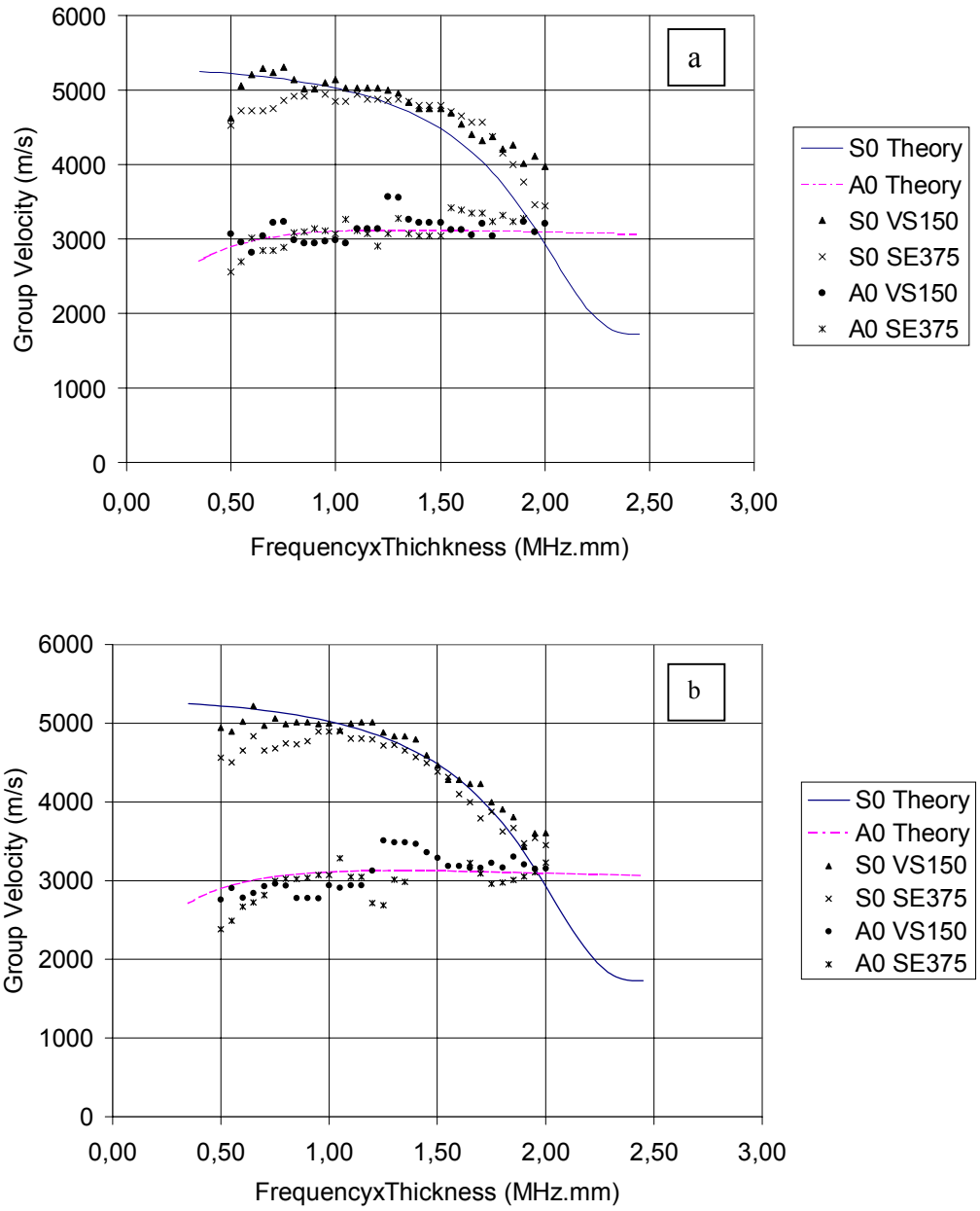

Fig. 6 Dispersion plot. a) Empty vessel. b) Vessel with water.

The measured velocities of the two modes agree with theoretical predictions. The average error was about 7%.

IP and OOP simulation

In order to simulate a crack growing from inside of the vessel to the outside surface, PLB at five different positions on the edge of the vessel were made. Figure 7 shows representative waveforms at three different positions. The amplitude ratio A_{S0}/A_{A0} is the highest when PLB was made at the mid-plane. The ratio is the lowest when PLB was made at the inside as well as the outside surface. The amplitude ratio decreases as the PLB position is shifted away from the mid-plane towards the inside and outside surfaces.

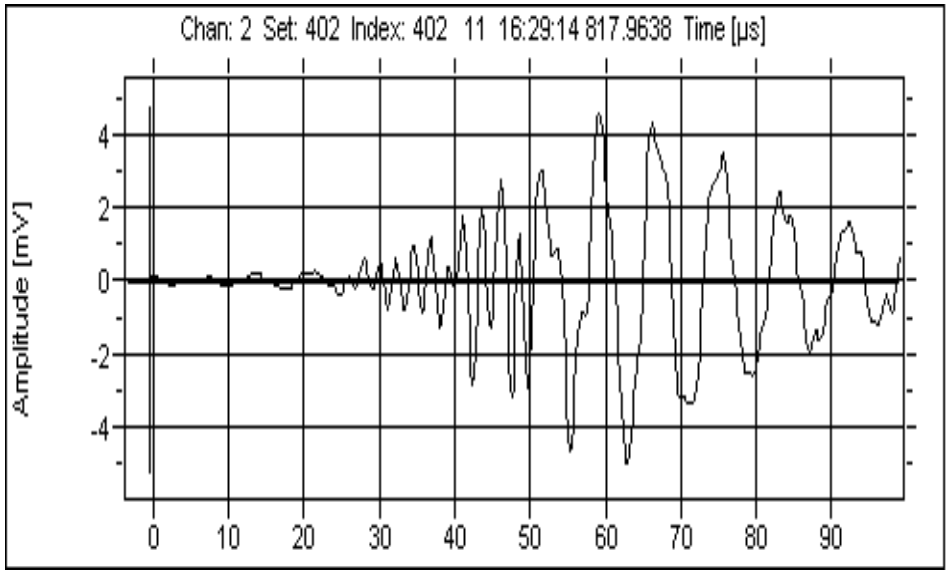

(a)

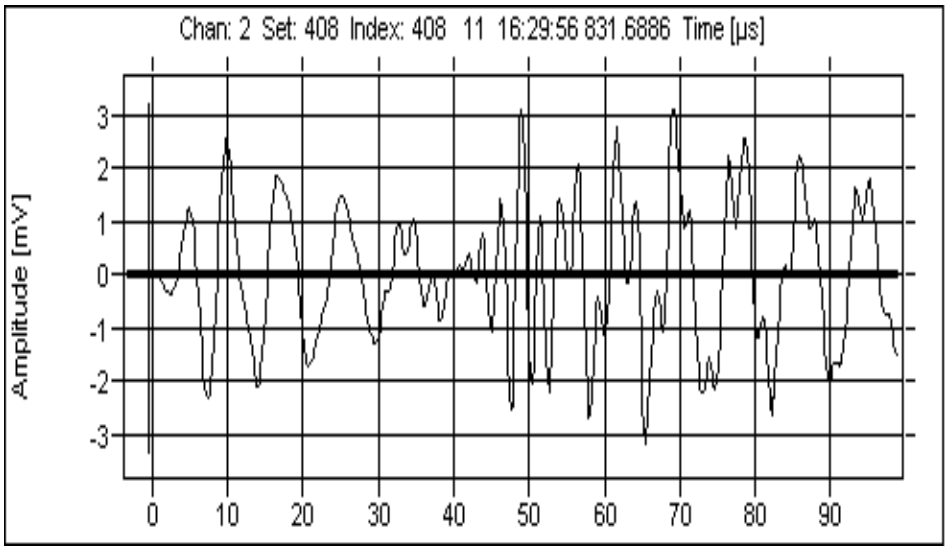

(b)

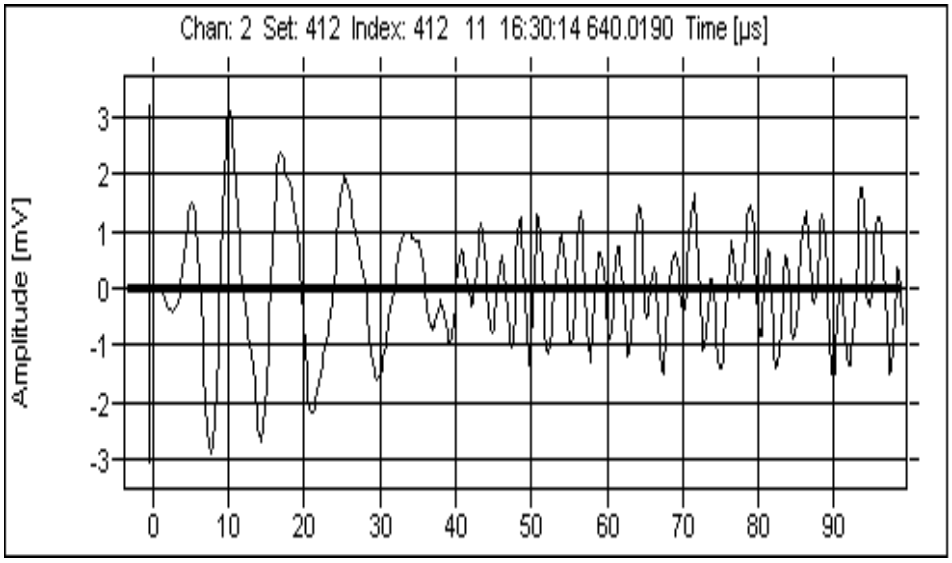

(c)

Fig. 7 Waveforms, SE375 sensor at 400 mm from source. a) PLB at z = –2.5 mm, b) PLB at z = –1.25 mm, c) PLB at mid plane.

Table 1 shows a summary of results obtained on waveforms from PLB simulated sources. Theoretically predicted values for t_{A0} at distance of 400 and 600 mm are, t_{A0} = 53.3 μs and t_{A0} = 80.0 μs, respectively. Those values are for extensional velocity of 5000 m/s and flexural velocity of 3000 m/s, which are valid for the frequency range of 100-300 kHz. The percentage error between the estimation from the WFT and predicted value is included in Table 1. The percentage error was high in some of the cases. It was possible to identify the type of the PLB sources by examining the amplitude ratio A_{S0}/A_{A0}, specially, for the OOP and IP at mid plane.

Table 1 Results of WFT for waveforms from PLB source.

Sensors : model VS150

TRA	PLB position Z (mm)	Source-Sensor Distance (mm)	t_{A0} (μs)	% error	A_{S0}/A_{A0}
1726	-2.5	400	44.8	15.9	0.077
1727	-2.5	600	57.6	28.0	0.076
1731	-1.25	400	50.4	5.4	0.480
1732	-1.25	600	69.6	13.0	0.553
1737	0	400	53.6	0.5	1.349
1738	0	600	71.2	11.0	1.426

Sensors : model SE375

TRA	PLB position Z (mm)	Source-Sensor Distance (mm)	t_{A0} (μs)	%error	A_{S0}/A_{A0}
1906	-2.5	400	50.4	5.4	0.298
1907	-2.5	600	53.6	33.0	0.243
1909	-1.25	400	35.2	33.9	0.478
1910	-1.25	600	74.4	7.0	0.642
1915	0	400	-	-	> 2.0
1916	0	600	-	-	> 1.2

5. INVESTIGATION OF WAVEFORMS DURING PRESSURE TESTS

Set-up and Instrumentation

The test vessel, with outer diameter of 600 mm, overall length of 2000 mm and thickness of 5 mm, was made of steel. The vessel was manufactured with a 1600 mm long cylinderical shell with a longitudinal weld, and two toro-spherical heads. The vessel rests on two pairs of feet, at a distance of 1300 mm from each other. A check hole, with elliptical shape of 200 mm by 150 mm size, is situated at the centre of the shell. A hydraulic system was utilised to pump water into the vessel providing controlled internal pressure.

Five AE sensors (one SE375 and four VS150) and three strain gauges were mounted on the vessel. The AE sensors, pressure sensor and strain gauges were connected to the Vallen Systeme AE data acquisition instrumentation. The test vessel and part of the set-up are shown in Fig. 8. The general AE instrumentation was similar to the tests conducted previously and reported in Rauscher [1999]. Similar acquisition parameters to that used during the simulated tests were employed.

Test Procedure

Cyclic pressurisation and intermittent pressure tests were conducted to initiate crack growth on the vessel. According to a finite element analysis conducted previously, the expected failure region would be around the check hole. The cyclic pressurisation was conducted in the range 2 bar - P_c, at frequency of 0.1 Hz. Specification of a single pressure test is shown in Fig. 9. Pressure tests were carried out intermittently every few number of cycles. Different load intensities were employed, namely type A, B, and C. Table 2 shows these three types of loading.

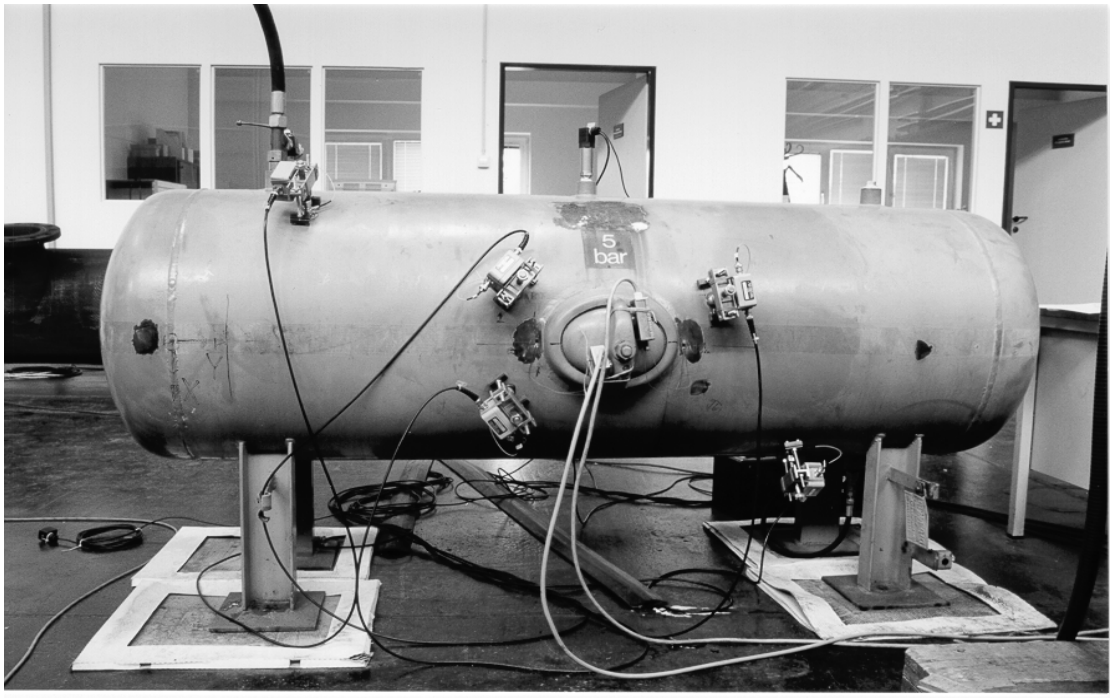

Fig. 8 Test vessel and set-up of sensors.

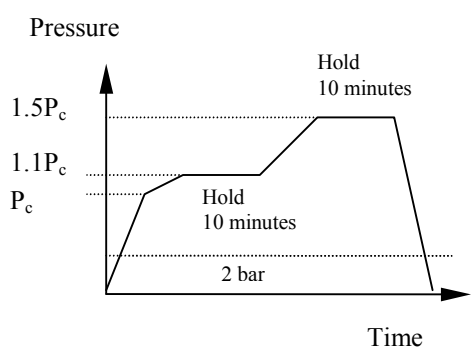

Fig. 9 Pressure test specification.

Table 2 Load levels (in bar).

Type	P_c	1.1 P_c	1.5 P_c
A	11	12	16.5
B	16	18	24
C	22	24	31

After conducting 5 pressure tests and 8000 cycles of type A, 4 pressure tests and 23360 cycles of type B, 1 pressure test and 10000 cycles of type C, without failure, it was decided to introduce a notch to accelerate the initiation and growth of crack. The notch was a saw cut made on inside of the check hole. The vessel was further loaded for 3 pressure tests and 10350 cycles of type B until leakage. The vessel failed during cyclic pressurisation, when a crack initiated at the root of the notch grew to the outer surface of the vessel.

5.1 Experimental Result and Discussion

Noise Filtering

Possible sources of noise identified during the test were:

- Electrical interference (EMI) due to a sudden starting and stopping of an oil pump used in the hydraulic system. The hits from the EMI noise were recorded with less than 1 μs difference in arrival time.
- Mechanical vibration from the oil pump mentioned above was also transferred via the vessel support from the ground.
- Noise due to friction and slight movement of a rubber gasket used to seal the check hole. Also some movement of the inlet pipe due to variation of pressure created noise. Noise due to these two cases was significant especially during cyclic pressurisation.

The following filters were utilised to minimise noise in analysing AE data:

1. Amplitude filter: Hits with amplitudes less than 40 dB were filtered out. Such low amplitude hits are likely not to be properly located.
2. Arrival time filter: Hits due to EMI noise were filtered using arrival time filter. Hits due to EMI noise were recorded as almost arriving at the same time on all channels. Therefore, events with arrival time difference between first and third hit less than 5 μs (dt13 < 5 μs) were filtered out. Only those events with dt13 ≥ 5 μs were considered for further analysis. Since the arrangement of the sensors could not possibly acquire an event arising on the vessel with dt13 < 5 μs.
3. Location filter: To avoid some hits due to mechanical noise and other hits located from the area outside the region of interest a location filter was used. The expected area of crack growth, where a notch was introduced, was located in the region: $-100 \leq X \leq 100$ and $900 \leq Y \leq 1100$ mm. Events located inside this region were considered for further analysis.

Table 3 below shows the AE events acquired during the three pressure tests. The first, second and third pressure tests were conducted 800, 7000, and 9000 cycles, respectively, after introducing the notch. The table shows the number of events before and after utilising the three filters outlined above.

Table 3 Number of events before and after filtering.

Pressure Test	**Total no of located events**	**No of events after filters 1, 2 and 3**	**% total**
First	87	19	21.8
Second	71	22	31.0
Third	24	7	24.2

The distribution of the amplitude of the first hits after filtering is summarised in Table 4. The amplitude of most of the hits (> 70%) were between 50 – 70 dB. Most of the events occurred during pressure increase from the 18 bar hold until the end of 24 bar hold. Few events (about 14%) occurred during pressure increase until 18 bar and after the end of 24 bar hold.

Table 4 Distribution of amplitude of first hits.

A (dB)	First Pressure Test	Second Pressure Test	Third Pressure Test
40 – 45	1	-	1
45 – 50	3	2	-
50 – 55	2	3	2
55 – 60	3	6	-
60 – 65	6	5	1
65 – 70	3	2	2
70 – 75	1	3	1
75 – 80	-	-	-
>80	-	1	-
Total	**19**	**22**	**7**

5.2 Fracture Surface Investigation

Part of the vessel (BM-01) was cut out, to investigate the crack growth and its fracture surface. Figure 10a shows a picture of the cut out during magnetic particles inspection of the crack. The picture shows the crack length as seen on the reinforcement of the check hole. The crack initiated at the root of the notch and the final length of the crack was about 10.5 mm.

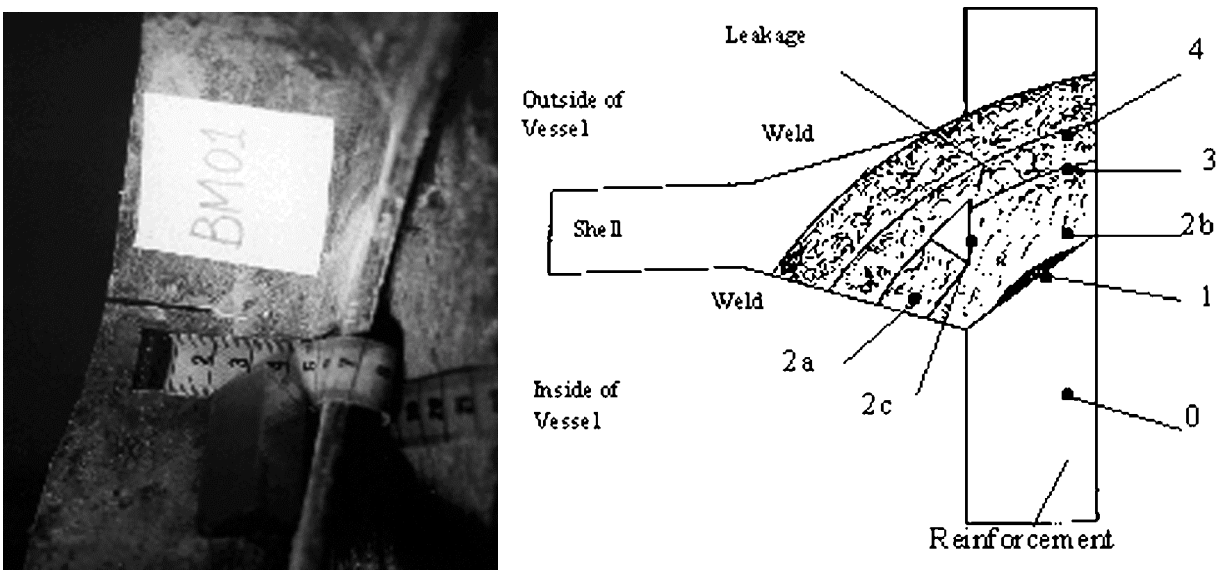

Fig. 10 a) A view of the crack on BM-01 vessel. Scale shown is in cm unit. b) Sketch of the fracture surface (not to scale).

A piece was cut out for further microscopic analysis. The fracture surface was a typical elliptical crack profile. Figure 10b shows a sketch of the fracture surface as seen under a microscope describing the different stages of the crack growth. The first pressure test occurred at early stage of the crack growth. The last two pressure tests are clearly observed on the fracture surface. The explanations of the different regions of Fig. 10b are given below.

Region 0: This region is the saw cut notch on the reinforcement of the check hole.

Region 1: A small area distinctly seen close to the root of the notch. This region is crack growth of the first 800 cycles and a crack blunting mark of the first pressure test.

Region 2: In this region the crack front is about 5.5 mm from the root of the notch. Areas 2a and 2b are fracture surfaces but at different planes. Area 2c is void due to incomplete penetration of the outside and inside welds. A crack blunting at the second pressure test is clearly seen. This region represents the crack growth during 800 – 7000 cycles.

Region 3: In this region the crack grew for further 3 mm. A crack blunting at the third pressure test is clearly seen. This region represents the crack growth during 7000 – 9000 cycles.

Region 4: In this region the crack grew for another 2 mm. The crack front reached the outside of the surface of the vessel, causing leakage. This region represents the crack growth during 9000 – 10350 cycles.

5.3 Waveform Analysis

The previous section explained the fracture surface and the different stages of the crack growth. During the pressure tests crack blunting was clearly observed. It is expected that the crack blunting would give rise to acoustic emission. Since this phenomenon occurs at the plane of the joint between the shell and the reinforcement, it is expected to produce waves similar to IP type of sources. However, the source of the AE could be from one end of the elliptical mark onto the other end along the fracture surface. Hence, the amplitude of the extensional mode would be expected to vary depending on the position of the source.

The AE events of the three pressure test were examined using the WFT discussed in previous section. Results of some selected waveforms are shown in Tables 5, 6 and 7. All the waveforms were hits recorded on sensor 2 (VS150), which was located about 400 mm from the crack. After the WFT calculations the waveforms were visually examined for any corrections overlooked by the relatively simple WFT algorithm. Those adjusted are marked on the comment column on the tables. The Transient record index (TRAI) is modified to include the prefix p1t, p2t and p3t to identify the first, second and third pressure tests.

Some of the events will be further discussed below. In addition to the WFT results of hits on sensor 2, the waveforms of sensor 1 (SE375) will also be analysed. Sensor 1 was located at about 100 mm from the crack. This distance is very short to look in to arrival time of the flexural mode. But the frequency content of the waveform on sensor 1 will provide additional information on the source type. Table 8 shows summary of six selected events. Figures 11 and 12 are waveforms of event 1 and 6, respectively.

Table 5 WFT results of events during First Pressure Test. (Hits on sensor 2)

TRAI	t_{A0} (μs)	A_{S0}/A_{A0}	Comment
P1t20645	50.4	0.096	
P1t20679	36.0	0.134	
P1t20701	20.0	0.454	Adjustment was needed
P1t20706	26.4	0.184	
P1t20757	50.0	0.280	
P1t20790	53.6	0.204	
P1t20860	50.0	1.259	Adjustment was needed
P1t20871	18.4	0.287	
P1t20906	100.0	0.290	
P1t20981	50.4	0.913	

Table 6 WFT results of events during Second Pressure Test. (Hits on sensor 2)

TRAI	t_{A0} (μs)	A_{S0}/A_{A0}	Comment
p2t54	45.6	0.191	
p2t100	45.0	0.094	
p2t114	20.0	0.300	Adjustment was needed
p2t195	45.6	0.400	
p2t233	39.2	0.612	
p2t305	37.6	0.076	
p2t340	20.0	0.300	Adjustment was needed
p2t357	50.0	0.500	Adjustment was needed
p2t363	30.0	0.100	

Table 7 WFT results of events during Third Pressure Test.(Hits on sensor 2)

TRAI	t_{A0} (μs)	A_{S0}/A_{A0}	Comment
p3t26	58.4	0.703	
p3t38	20.0	0.445	
p3t53	45.0	0.300	
p3t56	50.0	0.670	Adjustment was needed
p3t85	32.0	0.700	
p3t105	20.0	0.087	

Table 8 Summary of events.

Event	Channel	TRAI	Frequency	A_{S0}/A_{A0}	Figure number
1	1 2	p1t20678 p1t20679	Low (200-275 kHz)	0.134	11
2	1 2	p2t98 p2t100	Low (200-300 kHz)	0.094	
3	1 2	p3t104 p3t105	Low (150-200 kHz)	0.087	
4	1 2	p1t20858 p1t20860	High (350-400 kHz)	1.259	
5	1 2	p2t231 p2t233	High (250-325 kHz)	0.612	
6	1 2	p3t54 p3t56	High (200-325)	0.670	12

In summary, events 1, 2 and 3 have relatively low frequency content on sensor 1 and the ratio A_{S0}/A_{A0} , on sensor 2, is low. These events might have been produced from AE source near the surface of the vessel. Events 4, 5, and 6 have relatively higher frequency content on sensor 1 and the ratio A_{S0}/A_{A0}, on sensor 2, is close to unity or higher. Such events might have a source close to mid plane of the vessel. The above waveform analysis was limited to sensor 1 and sensor 2 only. Sensor 3 (model VS150) was close to the AE source. Only the frequency information of Sensor 1 was considered, as it was also very close to the AE source. The location of sensor 2 was also not ideal with respect to the notch. The reinforcement of the check hole had shading effect on the waveform arriving at sensor 2. With a change in the sensor arrangement better results would be expected.

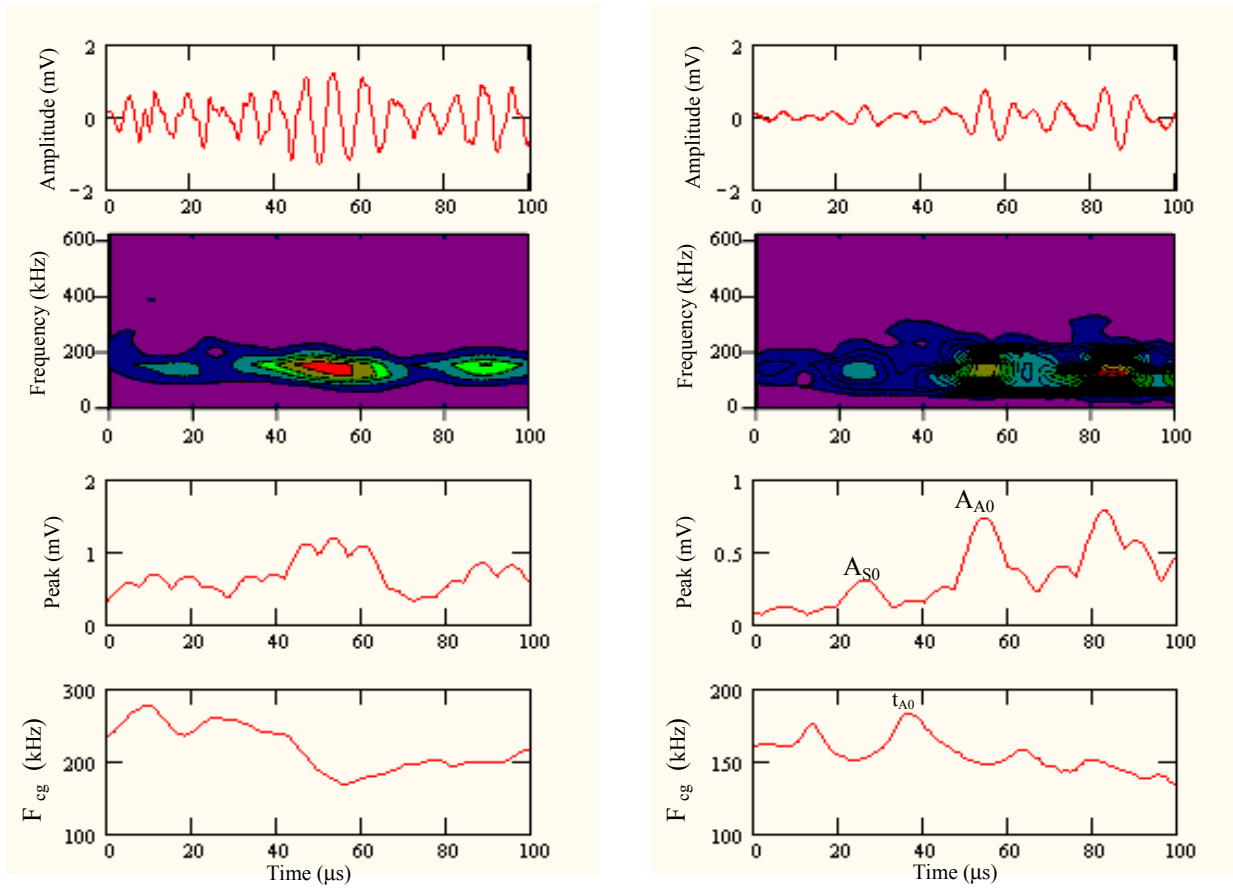

Fig. 11 Event 1, a) showing low frequency on sensor 1 and b) A_{S0}/A_{A0} = 0.134 on sensor 2.

6. CONCLUSION

Dispersion characteristics of the two modes were experimentally measured and compared with theoretical prediction. The measured group velocities of the extensional and flexural mode were in good agreement with the predictions.

It was possible to observe the IP and OOP simulated sources and their respective signals. IP sources generate a strong extensional wave mode but a weak flexural wave mode. Especially, when IP perturbation was made at mid plane the amplitude of the extensional mode was higher than that of the flexural mode. OOP sources generate a weak extensional mode but a strong flexural mode.

WFT was utilised as a tool in identifying extensional and flexural modes. WFT was used to estimate the arrival of the flexural wave and the amplitude ratio A_{S0}/A_{A0}. Results of the WFT on waveforms from PLB sources were good enough to differentiate between OOP and IP sources. The percent error in estimating the arrival time as compared to that predicted in theory was high in some of the cases. However, the accuracy could be improved by employing better mathematical algorithms.

WFT was utilised to identify the possible source of AE (OOP and IP) during pressure tests. Some events were identified during the three pressure tests as an IP source employing the WFT.

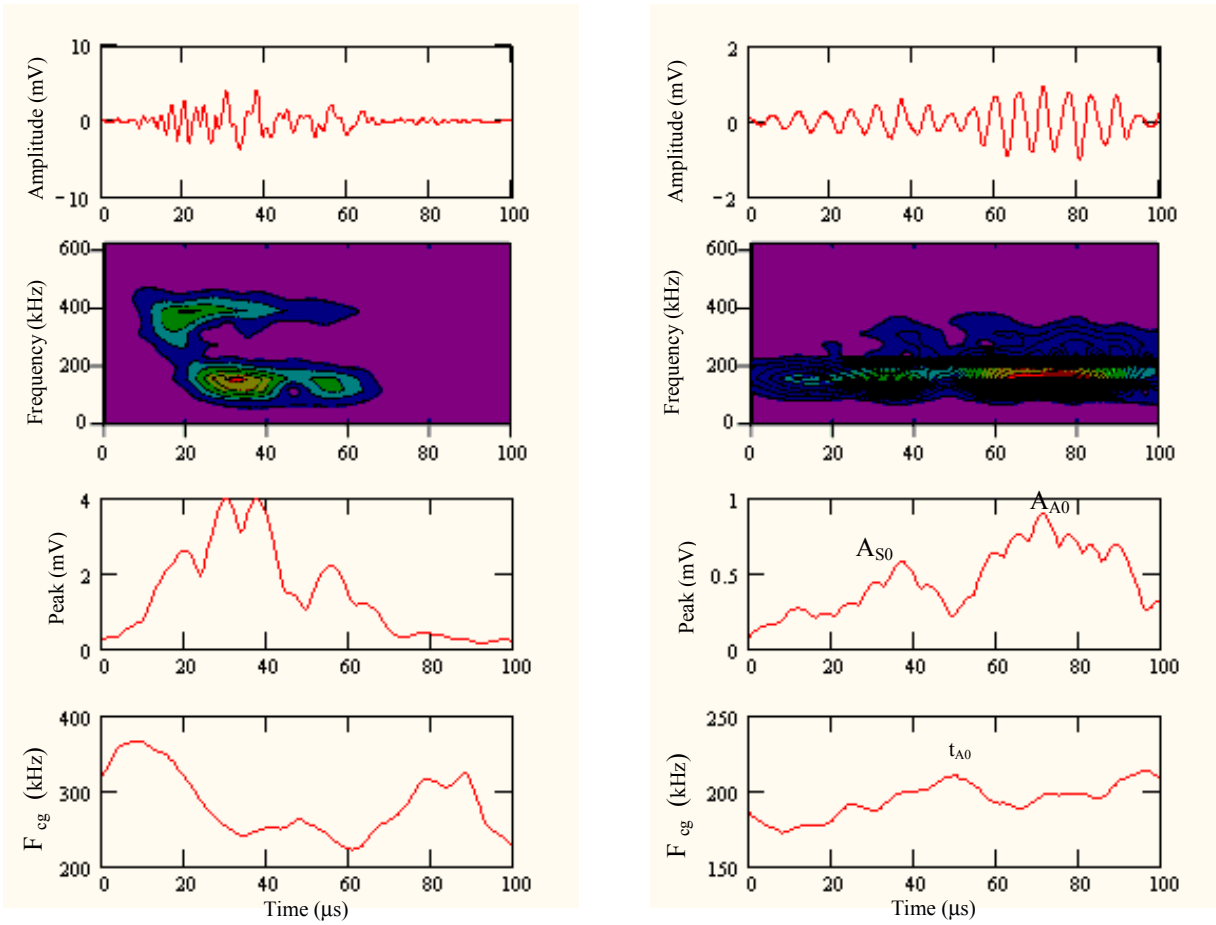

Fig. 12 Event 6, a) showing high frequency on sensor 1 and b) $A_{S0}/A_{A0} = 0.67$ on sensor 2.

Fracture surface investigation also showed crack blunting during the pressure tests. It is implied that the AE events were due to the crack blunting phenomenon.

Further work in developing the WFT as a tool in identifying the two modes is recommended. This could be in the direction of making automated analysis that could be utilised online.

NOTATION

x_1, x_3	Co-ordinate axes
σ_{13}, σ_{33}	Normal stress
h	Half plate vessel thickness
ω	Frequency
k	Wave number
V_T	Transverse wave velocity
V_L	Longitudinal wave velocity
V_φ	Phase velocity
V_g	Group velocity
E	Elastic modulus
ρ	Density
ν	Poisson's ratio
λ	Wave length
S_0	Extensional wave mode (0th order)
A_0	Flexural wave mode (0th order)
F_{cg}	Frequency centre of gravity
t_{A0}	Arrival time of A_0 after trigger by S_0
A_{S0}	Amplitude of S_0
A_{A0}	Amplitude of A_0

REFERENCES

Carin, L., Felsen, L.B., Kralj, D.R., Oh, H.S., Lee, W.C., and Pillai, S.U., (1997), "Wave-Oriented Signal Processing of Dispersive Time-Domain Scattering Data", IEEE Transactions on Antennas and Propagation, **45** (4), 592-600.

Dunegan, H.L., (1997), "Modal Analysis of Acoustic Emission Signals," Journal of Acoustic Emission, **15** (1/4), 53.

Gorman, M.R., (1991), "Plate Wave Acoustic Emission," Journal of Acoustical Society of America, **90**, (1), 358.

Huang, W., (1998), "Application of Mindlin Plate Theory to Analysis of Acoustic Emission Waveforms in Finite Plates," Review of Progress in Quantitative Non-destructive Evaluation, Vol. 17, p. 493.

Rauscher, F., (1999), " Acoustic emission of vessels with partially penetrated longitudinal seams," Proceeding of the EWGAE conference AE'99, Brno, Czech Republic.

Royer, D., and Dieulesaint, E., translated by Morgan, D.P., (2000), "Elastic Waves in Solids I, Free and Guided Propagation," Springer, Berlin, pp. 311-321.

Suzuki, H., Kinjo, T., Hayashi, Y., Takemoto, M., and Ono, K., (1996), "Wavelet Transform of Acoustic Emission Signals", Journal of Acoustic Emission, **14**(2), 69-84.

EFFECTS OF LATERAL PLATE DIMENSIONS ON ACOUSTIC EMISSION SIGNALS FROM DIPOLE SOURCES

M. A. HAMSTAD*, A. O'GALLAGHER and J. GARY

National Institute of Standards and Technology, Boulder, CO 80305
* Department of Engineering, University of Denver, Denver, CO 80108

ABSTRACT

With a validated three-dimensional finite element code, the out-of-plane displacements corresponding to model sources of acoustic emission (AE) were calculated in aluminum plate samples of two different lateral dimensions. Both samples were 4.7 mm thick. The lateral dimensions were 480 mm by 25.4 mm, which represented a laboratory-size coupon, versus 1000 mm by 1000 mm, which represented a larger field-size sample. The displacement signals were calculated for positions of the receiver on the top plate surface at several different distances (in the far-field) from the source's epicenter. The signals were predicted for the same propagation distances of source-to-receiver in both the large and small samples. Models of both point-like sensors as well as sensors with a large aperture were used. The signals were filtered with either a 40-kHz high-pass filter or a 100-to-300-kHz bandpass filter. The AE sources were modeled as either a point single dipole (both in-plane and out-of-plane) or a point multi-dipole located at different depths within the plate thickness. Analysis of the simulated AE signals shows that the superposition of edge reflections on the arrivals of the direct signal significantly distorts and amplifies AE signals in the laboratory-size coupon relative to a larger field-sized sample. This results in significantly larger AE signal features such as amplitude, duration, and energy in the laboratory-sized sample. Edge reflections also distort the frequency spectrum of signals in the small sample.

1. INTRODUCTION

Since acoustic emission (AE) technology is widely used in both laboratory settings and field testing of large structures, a broad range of dimensions of test samples is encountered. Thus, some sample dimensions are conveniently described in millimeters and others in meters. A natural question arises; what effects do the sample dimensions have on the measured AE signals? In particular, how do these changes in signal affect the identification of the source of the detected AE? Further, what are the effects of specimen size on the detectability of AE and the determination of the significance of detected AE? The research described herein used a recently developed and validated dynamic-finite-element modeling method for wave propagation (Hamstad et al., 1999; Prosser et al., 1999) to examine the effects on predicted AE signals of varying the lateral dimensions of plate specimens. For the two different specimen dimensions considered, the same sensor positions relative to the source (i.e., propagation distances) were modeled. Due to the ability to include reflections from all sample boundaries (including the edges of the plate), the finite-element method can fully model cases that analytical AE modeling approaches have been unable to address.

An earlier study (Gorman, 1998) used experimental techniques to study the effects of lateral plate dimensions. However, the experimental source was an out-of-plane surface-applied pencil-lead break, which does not accurately represent an internal AE crack source. The current study modeled *buried dipole* point sources, which more closely represent real AE sources than lead-break *surface monopole* sources. Further, the previous study did not compare the AE signals at exactly the same distances from the source to the sensor in the small and large plates. Thus, quantitative comparisons with parameters such as peak signal amplitude were not possible. The current study does allow such comparisons. The current study also examines specimen dimension effects on frequency spectra. Both wideband point-type sensors as well as sensors of larger aperture with narrowband sensitivity are modeled.

2. FINITE ELEMENT AND SOURCE CONDITIONS

An extensive database was created by calculating AE signals for three different types of buried sources and several different source depths in the plate samples. In particular, the buried sources were (i) an in-plane single dipole aligned along the direction of propagation to the sensors; (ii) an out-of-plane single dipole; and (iii) a multi-dipole with three dipoles that represent initiation of a microcrack source (Scruby, 1985). For the latter source, the strongest dipole was again in-plane and aligned along the direction of propagation to the sensors. The dipole forces (body forces) were all 1 N except for the two smaller dipoles in the microcrack case, which were 0.52 N (based on the elastic constants of aluminum). Each dipole was made up of a "central" cell having no body force along with single cells on each side of the "central" cell having the body forces. This approach follows that used in a buried-source finite-element validation study (Hamstad et al., 1999). The source body forces had a "cosine bell" temporal dependence with a rise time of 1.5 μs. All the calculations were based on a uniform three-dimensional cell size of 0.313 mm (except as noted below). The material constants for the 4.7-mm-thick aluminum plate samples were: a bulk longitudinal velocity of 6320 m/s, a shear velocity of 3100 m/s, and a density of 2700 kg/m^3. The modeled sensor outputs were the out-of-plane top-surface displacement from a single nodal point for point-type sensors, and from the average of all the nodal points in a circle of 13-mm diameter in the case of a finite aperture sensor. The parameters for the finite-element code were selected in accordance with the conditions previously (Hamstad et al., 1999) determined to be necessary to model point sources with a particular rise time. In one case, convergence was checked by proving the modeled AE signals did not change for a calculation with a cell size decreased by 20 %. The conditions necessary for convergence (Hamstad et al., 1999) resulted in a time step of 44.62 ns for the computations, which were carried out for a total of 200 μs after the start of the operation of the dipole sources. For all the waveform figures in this paper, the zero time is the start of operation of the dipole source.

3. LATERAL PLATE GEOMETRY AND SOURCE/SENSOR LOCATIONS

The choice of geometry for the small coupon specimen was taken from a previous experimental study (McBride and Hong, 1992), in which a sample 480 mm by 25.4 mm was used to study the AE generated from fatigue crack growth in specimens of 7000-series aluminum alloys 4.7 mm thick. Lateral dimensions of 1000 mm by 1000 mm (4.7 mm thick) were selected

to represent a field-test configuration that does not have nearby sample edges. These lateral dimensions were sufficiently large such that reflections from the sample edges did not superimpose on directly arriving signals. A total of seven point-type sensor positions were selected. Two coincided with the sensor positions used in the referenced original experimental study. For the finite-element simulation, these two positions were modeled to obtain displacements representing both point-type and finite-aperture sensors. Figure 1 is a drawing of the small specimen superimposed on the large sample, identifying the various sensor positions along with the source position. The locations for the finite-aperture sensors used in the referenced crack-propagation study are at locations 2 and 5 (see Fig. 1) at 120 mm and 60 mm from the plane that contained the source. The source position (below sensor 4) is located in the same cross-sectional plane, in which the crack was propagated in the referenced experimental study. For most of the finite element (FEM) cases, the source was located halfway across the width of the small sample (see Fig. 1). A few computations were made with the source in the same plane, but not symmetrically located with respect to the long sides of the small sample.

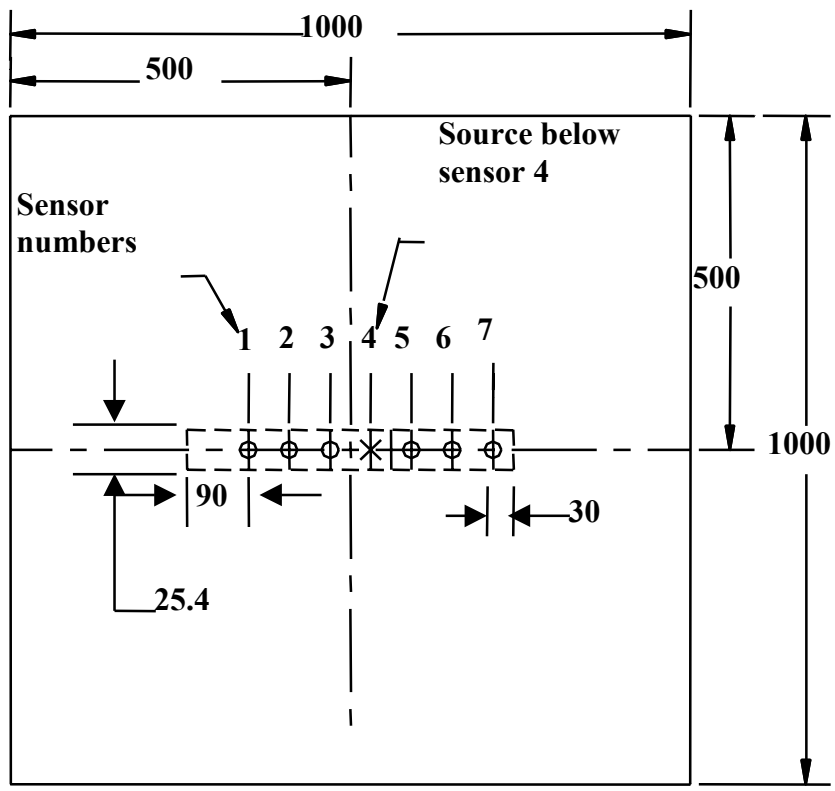

Fig. 1 Finite-element specimens. Dashed lines show the small sample superimposed on the large sample. Sensor numbers show location of sensors, and the source is below sensor 4. All dimensions in millimeters with sensors 60 mm apart.

4. FEM RESULTS AND DISCUSSION

The FEM signals include frequency content from zero hertz up to the highest frequencies generated by the source (based on calculated spectra, a little above the reciprocal of the rise time, hence about 700 kHz to 1 MHz in the current FEM modeling). To more closely approximate signals acquired with real AE sensors, the FEM signals were filtered with a recursive four-pole Butterworth filter. The selected filter ranges were: a bandpass of 100 to 300 kHz for the large

aperture sensor to represent conventional resonant-sensor AE technology, and 40-kHz high-pass for the point-type sensors to represent wideband nearly flat with frequency waveform-based AE technology. In some cases, the point-type sensor signals were also filtered with the 100-to-300-kHz filter.

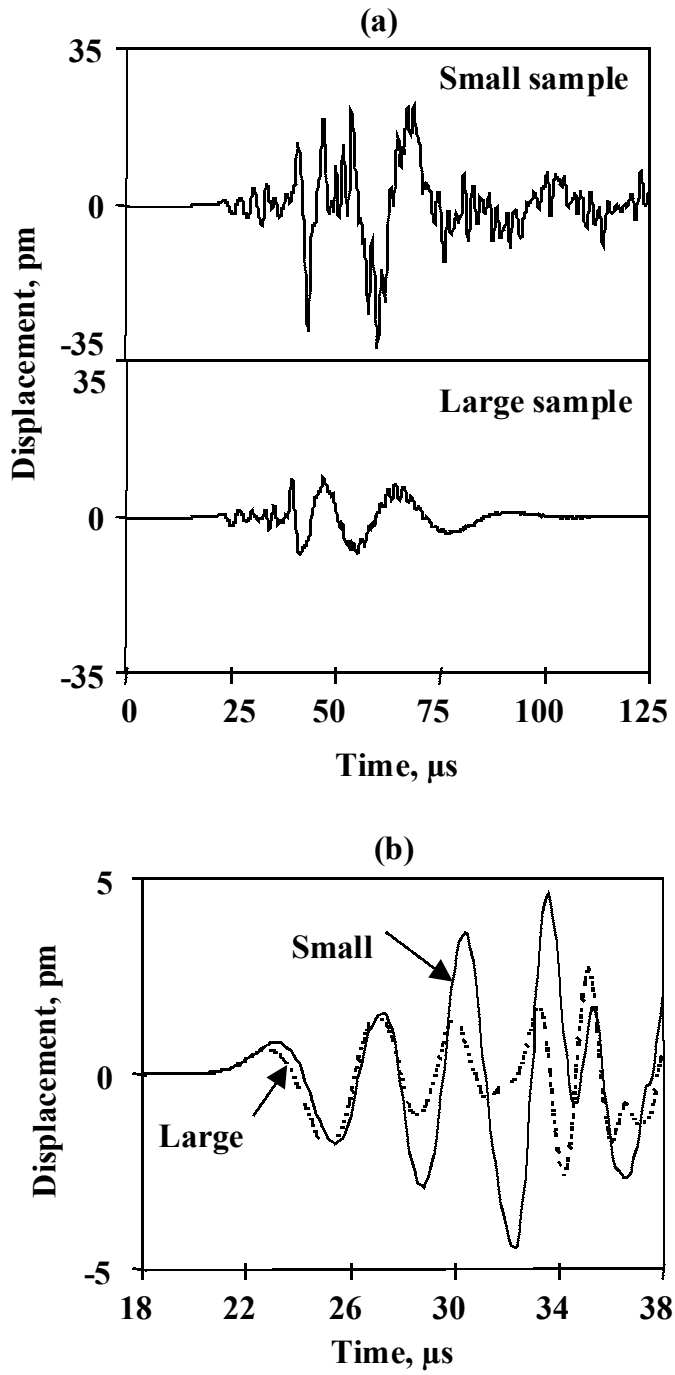

Fig. 2. Comparison of out-of-plane displacement signals at sensor 2 located at 120 mm from the in-plane dipole source centered at a depth of 0.783 mm below the top surface of the plate.
(a) a view of longer duration. (b) a view of expanded scale of the early part of the signals from the point-type sensors.

A. Signal Amplitude

Figure 2 compares the FEM-generated signals at sensor 2 for the large and small plate samples. These signals at 120 mm from the source were modeled for the point-type sensor with a single in-plane dipole source (dipole aligned along the axis of propagation to the sensor) with its center located at 0.783 mm below the plate top surface. Figure 2(a) shows the signals with the same vertical displacement scale, and Fig. 2(b) shows the initial portion of both signals with an expanded displacement scale. To provide results with a more complex source, Fig. 3 displays similar views for a microcrack initiation source (three dipoles, major dipole directed along the line of sensors) located at 1.723 mm below the top surface of the plate. These two figures demonstrate the fact that the signals in the laboratory sample have amplitude significantly larger than those in the large sample without nearby edges. The actual peak amplitude increases are about 11.1 dB for the single dipole and about 12.1 dB for the microcrack stimulation. Further, as Figs. 2(b) and 3(b) demonstrate, edge-reflection-based interference and distortion of the signal in the small sample begins only a few microseconds after the direct arrival of the signal. A more extensive examination of the signal database as a function of varying sources, depths and propagation distances indicates that the increase in amplitude of the peak signal relative to the peak amplitude without edge reflections is typically greater at sensors further from the source. As summarized in Table 1, this is consistent for both point-contact sensor signals and finite-aperture sensor signals, and also for both the bandpass of 100 to 300 kHz and the 40-kHz high-pass frequency range. Table 1 also indicates that peak amplitude increases with the point-type sensor were not as large when a bandpass filter of 100 to 300 kHz was used.

Table 1 Observed decibel ranges of increase in peak signal amplitude in the small specimen for the range of source types and depths

	At 60 mm (dB)	At 120mm (dB)
(i) Point-type sensor		
40 kHz H. P. filter	7.4 to 8	9.5 to 10.9
100-300 kHz filter	4.3 to 5.0	6.5 to 7.8
(ii) 13-mm aperture sensor,		
100-300 kHz filter	3.8 to 7.7	6.0 to 9.9

Edge reflections that can superimpose on the direct signals can come not only from the side edges of the small coupon, but also from the ends of the sample. Figure 4 demonstrates this aspect. In this figure, the signals are shown for the point-type sensors with a bandpass of 100 to 300 kHz, located at 60, 120, and 180 mm from the source. The source was an in-plane dipole located at a depth of 0.47 mm below the top surface. The end-edge reflections at the 60-mm and 120-mm sensors are clearly distinguishable from the earlier-arriving part of the signal that is composed of the direct signal and the side-edge reflections. The presence of end-edge reflections modifies the signal propagating from the other direction in a different fashion, as the sensor is positioned more closely to the specimen's edge. In such cases, the part of the end reflection of largest amplitude and the major amplitude portion of the signal coming from the other direction interfere with each other. In such cases, the amplification of amplitude may be further enhanced. We note that these sensor positions were not used in the original referenced experimental study. Also the fact that at the sensor positions of 60 and 120 mm the major-amplitude part of the end-edge reflections are more distinct from the major-amplitude part of the

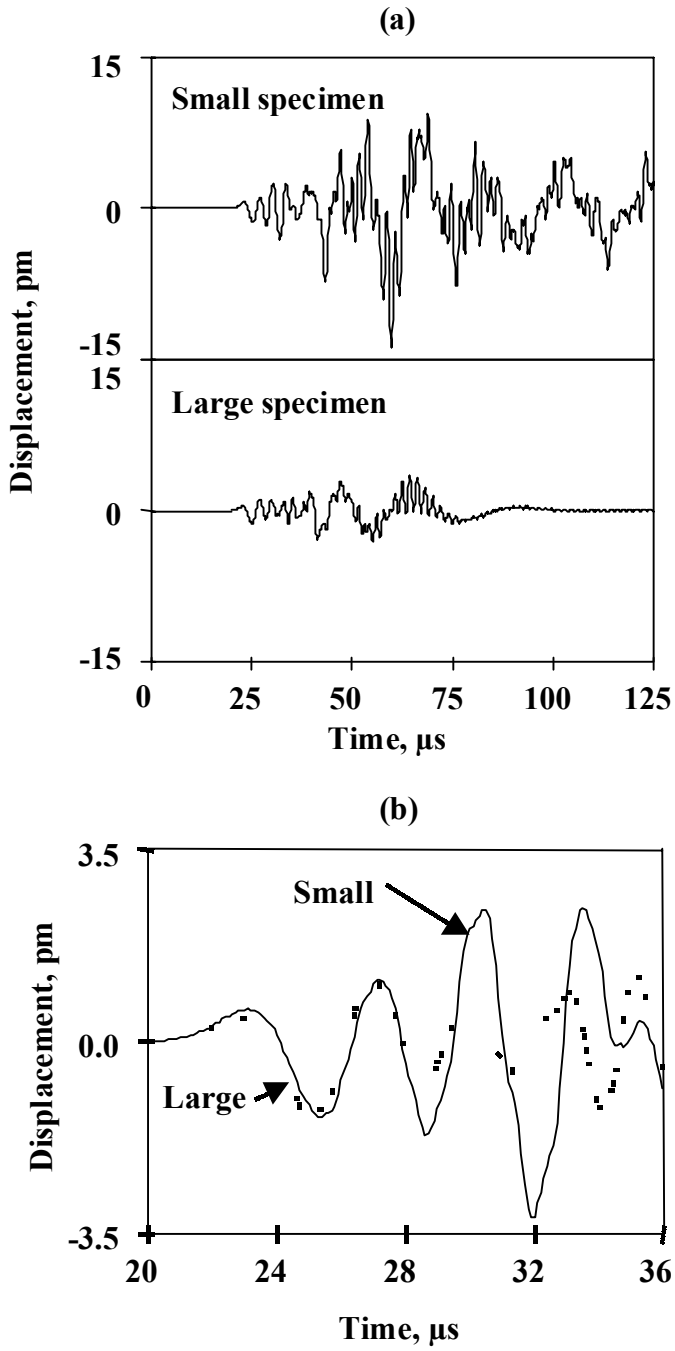

Fig. 3. Same views as in Fig. 2, but for a microcrack initiation source centered 1.723 mm below the top surface of the plate.

signal from the other direction means that these reflections could easily be mistaken as coming from a different AE source event.

Although attenuation due to material-based absorption of the wave is not included in these model calculations, significant decreases in signal amplitudes are observed with increasing propagation distance where no edge reflections are present. The origins of these attenuation effects are both geometric spreading and signal dispersion. This decrease in peak amplitude for the modeled signals versus propagation distance in the large plate is shown in Fig. 5. This figure

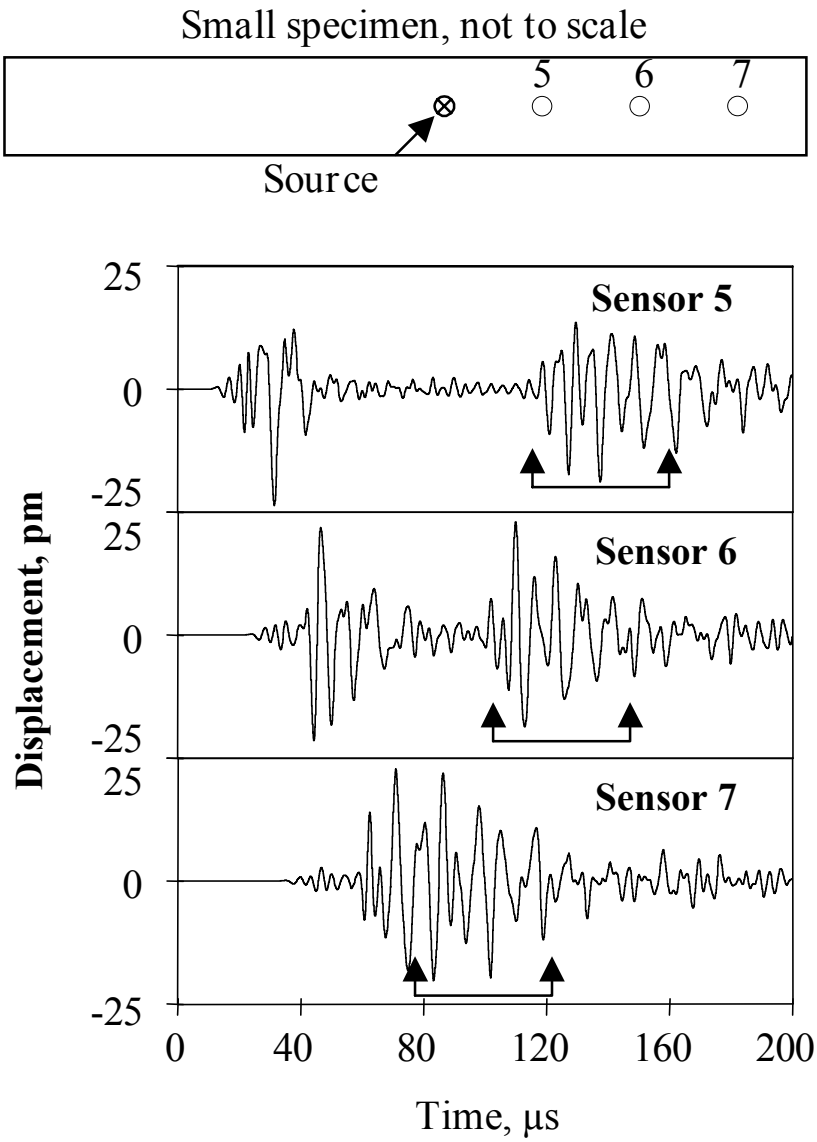

Fig. 4. Out-of-plane displacements at point-type sensors with 100 to 300 kHz bandpass located at 60, 120, and 180 mm from the in-plane dipole source located 0.47 mm below the top surface of the small sample. End-edge reflections from specimen right end shown by connected arrows.

also shows the theoretical prediction for geometric spreading ($1/\sqrt{r}$, where r is the propagation distance from the source). The source for the modeled signals in Fig. 5 was an in-plane dipole located at the mid-plane in the aluminum plate 4.7-mm thick. Additional sensor positions were added for the computation of the data for Fig. 5. The data shown are for the out-of-plane displacement after a 40 kHz high-pass filter for the point-type sensors. It seems clear that the $1/\sqrt{r}$ curve is valid out to 20 mm, but at farther distances dispersion begins to dominate.

In the case of the small coupon sample, the signal attenuation from the two effects of geometric spreading and dispersion is typically partially overcome by the signal amplification from edge reflections. Due to these reflections, a much larger share of the 360-degree radiation of source energy reaches the sensors. We have not calculated any coupon cases where destructive interference between the direct signal and the reflected signals resulted in a decrease

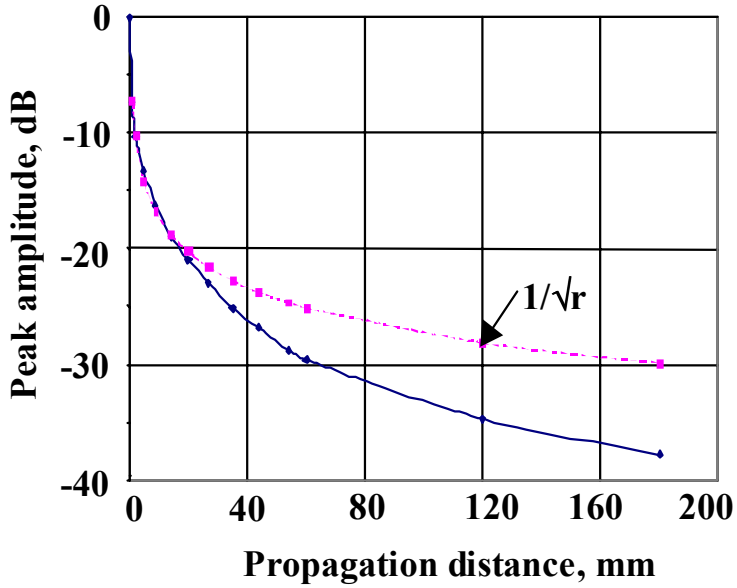

Fig. 5. Calculated loss of AE signal peak amplitude of out-of-plane displacement for a point-type sensor for a mid-plane dipole source with an in-plane orientation. The signal from the large specimen was filtered with a 40 kHz high-pass filter.

in peak signal amplitude. This fact is consistent with the many different reflections that transfer a larger fraction of the original source energy to the sensor in the small coupon. The largest increases in signal (see Table 1) were observed in the case of the 40-kHz high-pass signals with the point-type sensor. One possible explanation for this observation is that a larger fraction of the reflected signals contribute with the point sensor since a wider frequency window allows more of the modes in the reflected signals to contribute to the displacement at the sensor. Also, from Table 1 it is clear that the increases in signal varied considerably as the type and depth of source changed. Further, this table indicates a wider range of signal increases for the large-aperture sensor. This result is likely due to the wider range of reflection paths that can create displacements under the sensor of 13-mm diameter.

The question arises as to whether the observed amount of signal increase is particularly large due to (a) the symmetry of the source, and (b) the sensors being exactly one-half way across the small sample. To examine this question, some finite-element calculations were made with the in-plane dipole source at two non-symmetrical positions. These positions, at 6.13 mm and 3.3 mm from the sample side, are shown in Fig. 6 along with the symmetric position at 12.7 mm from the sample side. Figure 6 also compares the signals for both the symmetric source position and the two different non-symmetric positions. These results were for the point sensor at two distances (60 mm and 180 mm) from the source. Additionally, Fig. 6 includes values of the increase in peak amplitude relative to the same large-sample case. The in-plane dipole source for these calculations was 2.035 mm below the top surface, and the signal was filtered with a 40-kHz high-pass filter. The results shown in this figure indicate that the increases in signal amplitude, while still significant, typically are not as large for the non-symmetric source positions. Table 2 summarizes these results along with similar results for the large-aperture sensors. The range of increases for the large-aperture sensors is typically smaller compared to the point-type sensors.

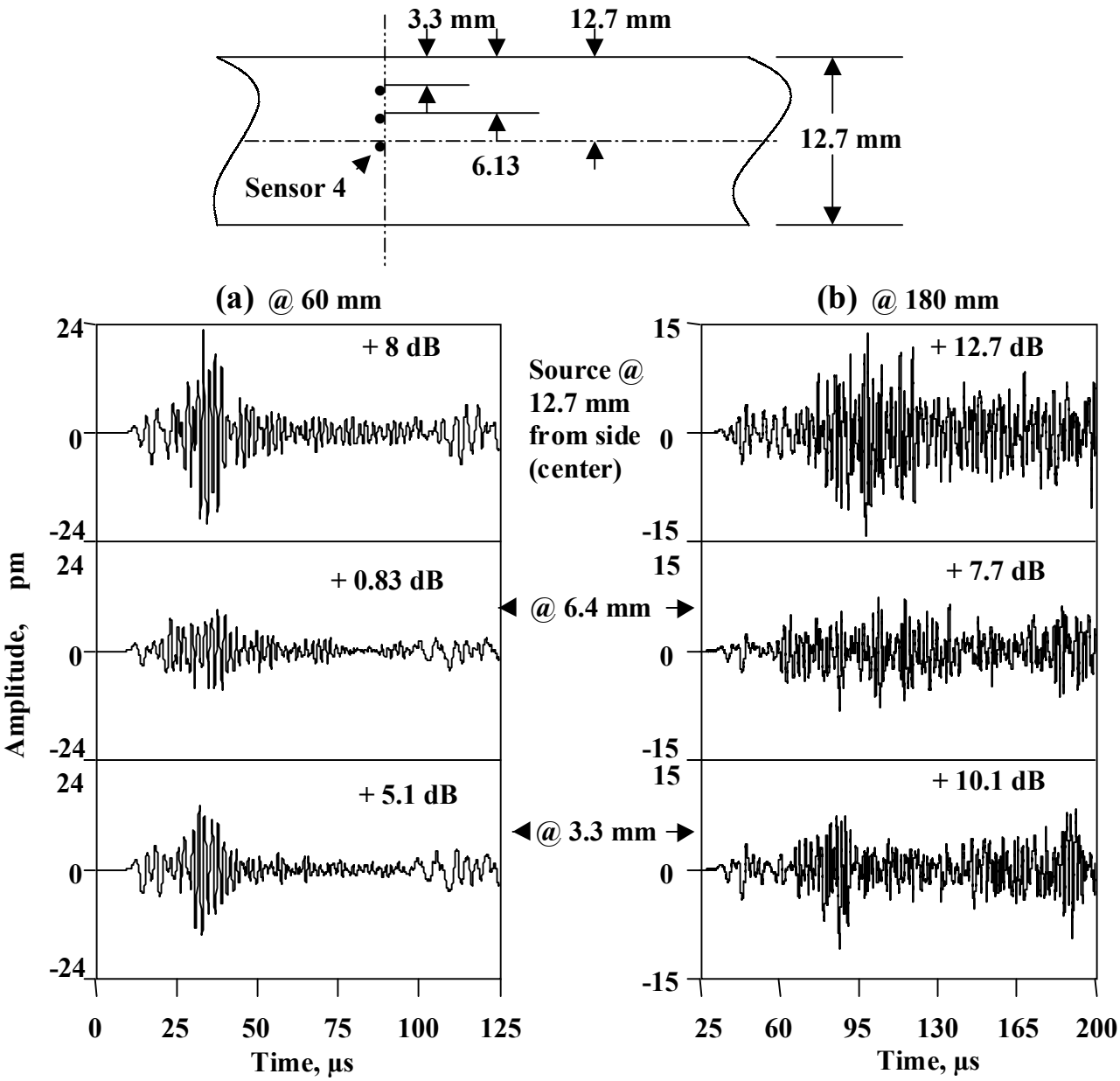

Fig. 6. Examples of point sensor out-of-plane displacement (40-kHz high-pass filter) when the source is located at three different transverse positions (12.7, 6.13, and 3.3 mm from small sample edge as shown, not to scale) in the source plane. Results shown for sensors nominally at 60 mm (sensor 3) and 180 mm (sensor 1) from the source plane with the source centered 2.035 mm below the plate's top surface (at the mid-plane).

The wide range of values as a function of source position and sensor position again results from the many differences in the reflections as these two variables change.

The effects of reflections have some practical implications for both AE field tests and AE laboratory tests. Probably most important is the fact that some AE sources detected in small laboratory coupons will *not* be detected in large specimens. Without the signal amplification from edge reflections, some sources will be hidden by the background noise (electronic noise from the preamplifier) in large samples. Thus, even with the sensors at the same distances

Table 2 Increase (dB) in peak signal amplitude as a function of position of source relative to the small specimen edge

(i) Point-type sensor (40-kHz H.P. filter)	Symmetric at 12.7 mm	at 6.13 mm	at 3.31 mm
(a) At 60 mm	8	0.83	5.1
(b) At 120 mm	12.7	7.7	10.1
(ii) Large-aperture sensor (100-300 kHz)			
(a) At 60 mm	9	0.1	3.8
(b) At 120 mm	10.3	1.5	4

relative to the source as in a small laboratory coupon, the database of detected signals will be smaller for large samples (same material and thickness) than for a coupon. A second important aspect relates to the use of peak amplitudes for source identification in a laboratory-size sample. As Fig. 6 shows, moving the sensor from 60 to 180 mm from the source typically results in a loss of signal amplitude (note vertical scale goes from ±24 pm to ±15 pm). An even larger effect is the potential change in peak amplitude as the source is moved laterally across a single cross-sectional source plane (from Fig. 6, 0.83 to 8 dB at 60 mm and 7.7 to 12.7 dB at 180 mm). In addition to the dependence of peak amplitude on lateral source positions, the peak amplitude also changes with the depth of the source. Figure 7 demonstrates these changes in the small specimen at 120 mm from the source. The point-type sensor results (40 kHz high pass at sensor 2) shown in this figure are for an in-plane dipole at depths of 0.47 mm and 2.35 mm (mid-plane). The peak amplitude difference for the same source at these two different depths is about 9.3 dB. The equivalent large-aperture sensor data (100 to 300 kHz bandpass) produces a difference of about a 8.1 dB in the small specimen. For the large sample, the peak amplitude changed by about 8.9 dB with the point sensor, and by about 8.4 dB for the large-aperture sensor under the same conditions.

B. Spectra of Signals

Numerous users of AE have attempted to use the frequency spectrum of an AE signal for the purpose of source identification. The premise for such studies is that different source types will have different frequency spectra. We note that some researchers have recognized the need to use wideband sensors of small aperture and relatively flat with frequency response, in such experiments. Typically, experiments analyzing frequency spectra have been performed in the laboratory with relatively small samples, which inherently have nearby edges. In some cases, the AE researchers have recognized that edge reflections could cause a problem. This recognition leads to the technique of calculating the spectrum of only some arbitrarily selected early portion of the measured signal. The database developed by the FEM modeling provides for a systematic investigation of the effects on spectra of reflections from nearby specimen edges in coupon specimens.

To develop key insight into the effects of edge reflections on spectra, we will first examine some results obtained from FEM calculations with the large sample. Figure 8 shows the out-of-plane displacement (40 kHz high-pass) for point sensors located at 180 and 60 mm from an in-plane dipole located at the mid-plane. The reflection from the left edge of the sample is shown by an arrow for both propagation distances. These reflections follow the expected pattern of

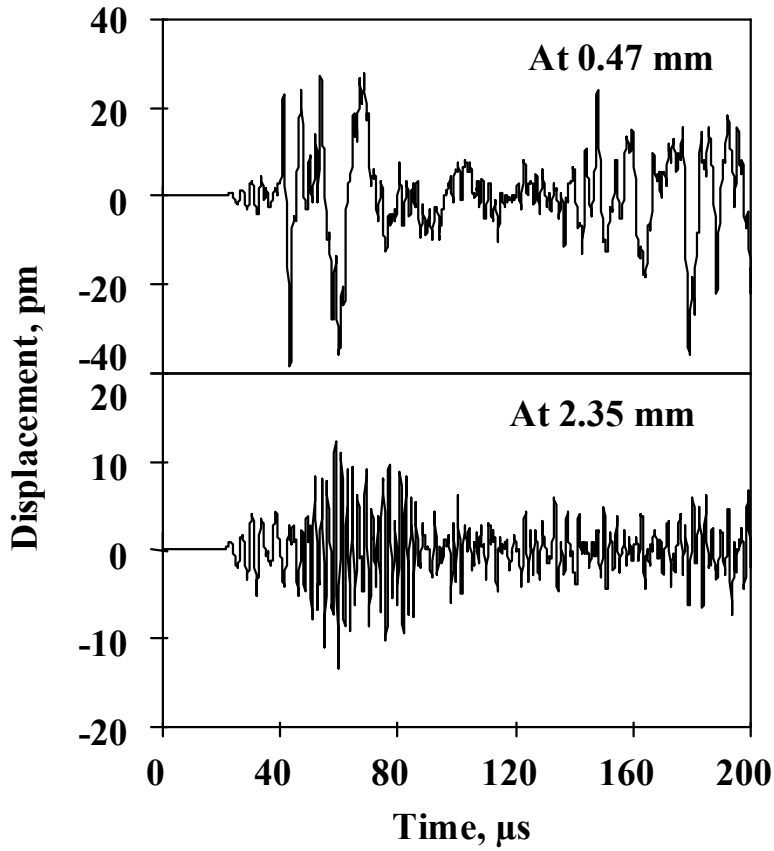

Fig. 7. Out-of-plane displacement in small sample at 120 mm for the same in-plane dipole source located at two different depths (0.47 mm and 2.35 mm below the top surface).

arriving first at the sensor farthest from the source, since it is nearer the left edge of the large sample. If the whole signal shown in Fig. 8(a) is used to calculate the Fast Fourier Transform (FFT), the result is shown in Fig. 9(a). If the signal in Fig. 8(a) is truncated at 145 µs (i.e. before the reflection arrival) and the FFT is calculated the result is shown in Fig. 9(b). As a part of the FFT calculation, both signals were extended with zeros so as to have the same number of points. By comparing Figs. 9(a) and 9(b) it is clear that the spectrum shown in Fig. 9(a) has been distorted due to the presence of the small reflected signal. Further, the distorted region of the frequency spectrum is the frequency range contained in the reflection signal. This fact was verified by calculating the FFT of the reflection signal and showing that it was nearly identical to the FFT of the first part of the direct signal. If we examine the spectrum for the same source case (0 to 145 µs signal) but in the small specimen, the presence of substantial distortion is shown in Fig. 10(a). Notice also that the peak amplitude of the spectrum in the small specimen is more than 16 dB higher than that in the large sample (Fig. 9(b)).

It is interesting to note that, if the result in Fig. 10(a) is substantially smoothed, then as shown in Fig. 10(b) a spectrum more similar to that of the large specimen (Fig. 9(b)) can be obtained. The amount of smoothing necessary was determined by trial and error. If Fig. 9(b) had not been available then the appropriate smoothing (in this case, over 150 kHz portions or over 30 digital points) could not have been easily determined.

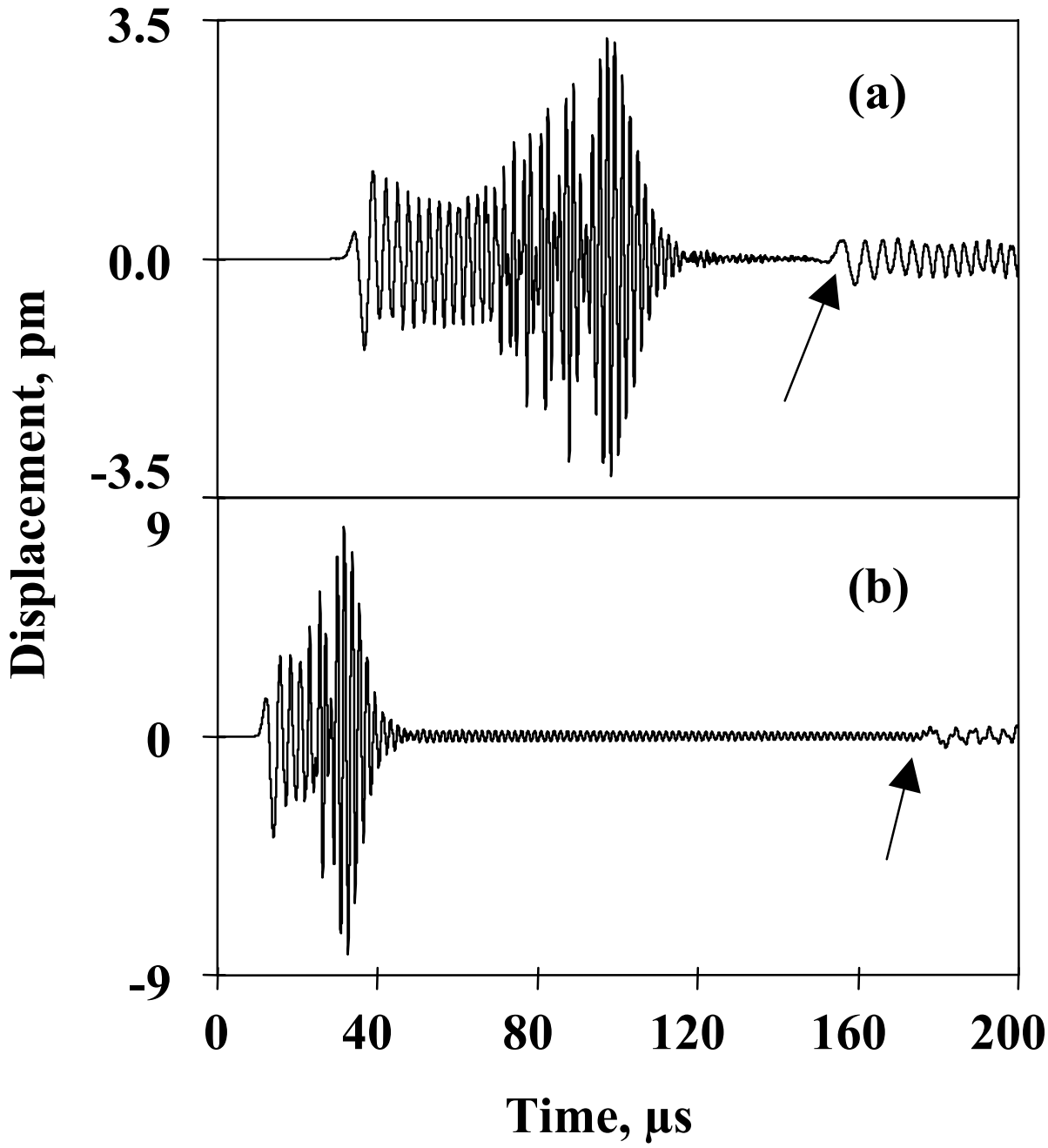

Fig. 8. Out-of-plane displacement (with point sensors and 40-kHz high-pass filter) at (a) 180 mm and (b) 60 mm from the source in the large sample. Edge reflection indicated by arrows. Source is an in-plane dipole located at the mid-plane.

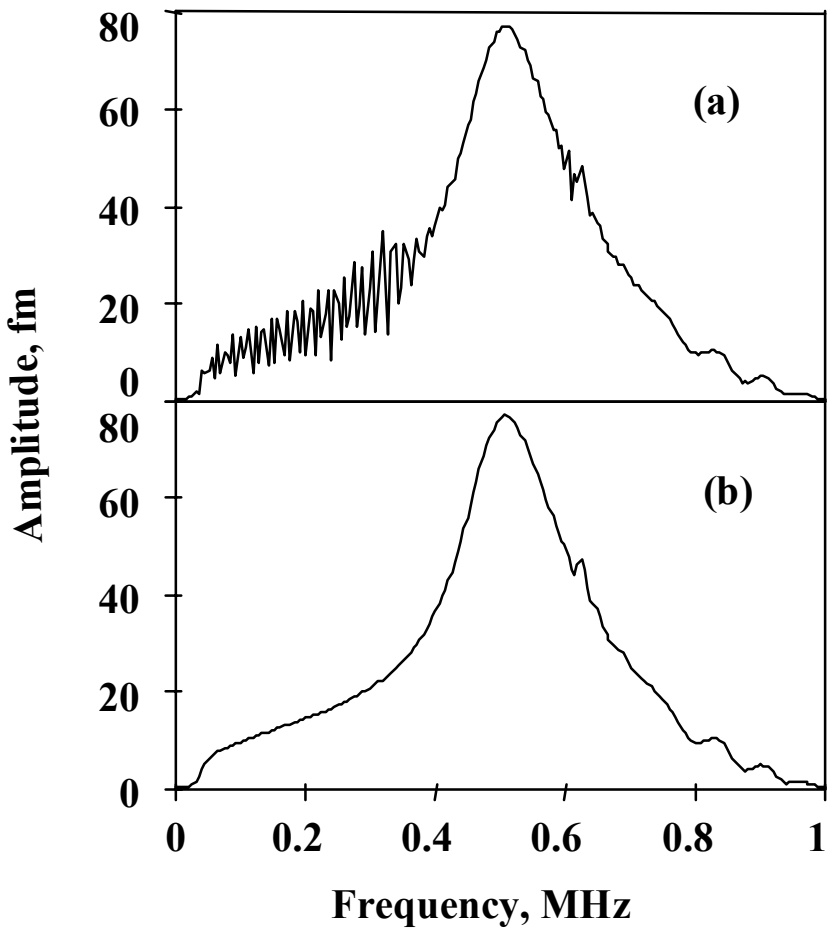

Fig. 9. FFT spectra of the signal shown in Fig. 8(a). Fig. 9(a) is for the whole time domain out to 200 μs (including the edge reflection of the highest-velocity part of the fundamental symmetric mode), and Fig. 9(b) is for the same time-domain signal truncated at 145 μs (prior to the reflection).

Distortion of the AE signals and their FFT due to edge reflections has several implications for the materials researcher who is attempting to use AE techniques to identify different damage mechanisms. Most obvious is that the use of a large sample that does not result in early edge reflections would significantly enhance the determination of the basic source characteristics of AE signals as determined in the far-field. This size sample has been used to monitor growth of fatigue cracks (Hamstad and McColskey, 1999). Further, the approach of using only a small portion of the beginning of the AE signal to calculate the FFT in small specimens does not provide useful information for identification of AE sources. The reason for this is two-fold. First, truncating the time-domain signal may eliminate source information present in the slower-velocity (direct-path) components of the signal. Second, even the early-arriving parts of the signal have experienced distortions from early edge reflections. These effects are illustrated in Fig. 11. Starting from the top of Fig. 11(a), a series of five truncated signals is shown for a small specimen with an in-plane dipole source located at 1.723 mm below the top surface. The point-type sensor data (40 kHz high-pass) are for a sensor located at 60 mm from the source epicenter. The durations of the *non-zero* portion of the signals are 10, 20, 30, 110, and 165 μs. The bottom signal in this figure is the large-specimen equivalent case truncated at 175 μs total duration.

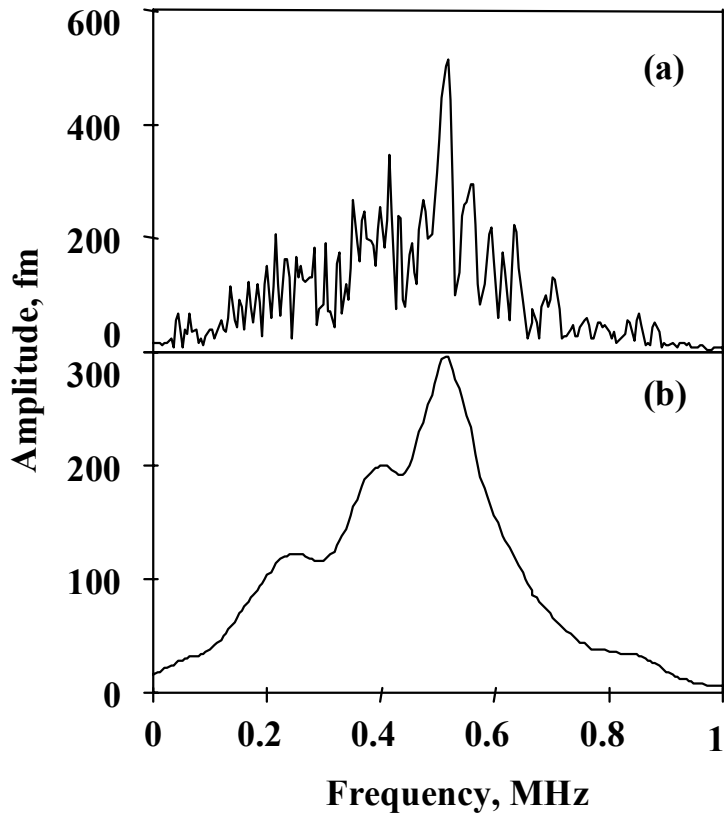

Fig. 10. FFT spectra of a 145-μs portion of the out-of-plane displacement at 180 mm for an in-plane dipole source located at the mid-plane of a small sample. (a): the spectrum without smoothing; (b): a smoothed version of (a). Note that the source type and location (relative to the sensor) is the same as shown in Fig. 9 for the large sample.

Figure 11(b) shows in the same order the calculated FFTs of the signals. We note that prior to calculating the FFTs all the signals were extended with zeros to the same number of points. Clearly the FFTs of the early part of the signal in the small sample fail to include the essence of the real spectrum as shown at the bottom of Fig. 11(b). And in fact a *longer* truncated signal (e.g. 110 μs of non-zero signal) provides a more correct (but still distorted) result. The reason for this fact, as indicated above, is that the slower-velocity parts of the signal define significant aspects of the true signal FFT. We conclude that it is not surprising that AE source identification by the use of spectra has not been a broadly successful approach since most researchers attempting to do this have used small samples.

C. Concluding Remarks

The user of AE technology who does not understand the effects of nearby specimen edges can make incorrect conclusions. On one hand, a field practitioner testing a large sample without nearby edges may not detect damage-indicating AE events. These same events may have been easily detected in small laboratory coupons due to edge reflections that amplify the direct signal. Further, if events are detected in the field case, the field practitioner may underestimate their significance. The reason is that the events will not have the amplitude, energy and duration levels associated with the same original source amplitude in the results for laboratory coupons. On the other hand, the materials scientist attempting to use AE techniques to identify certain

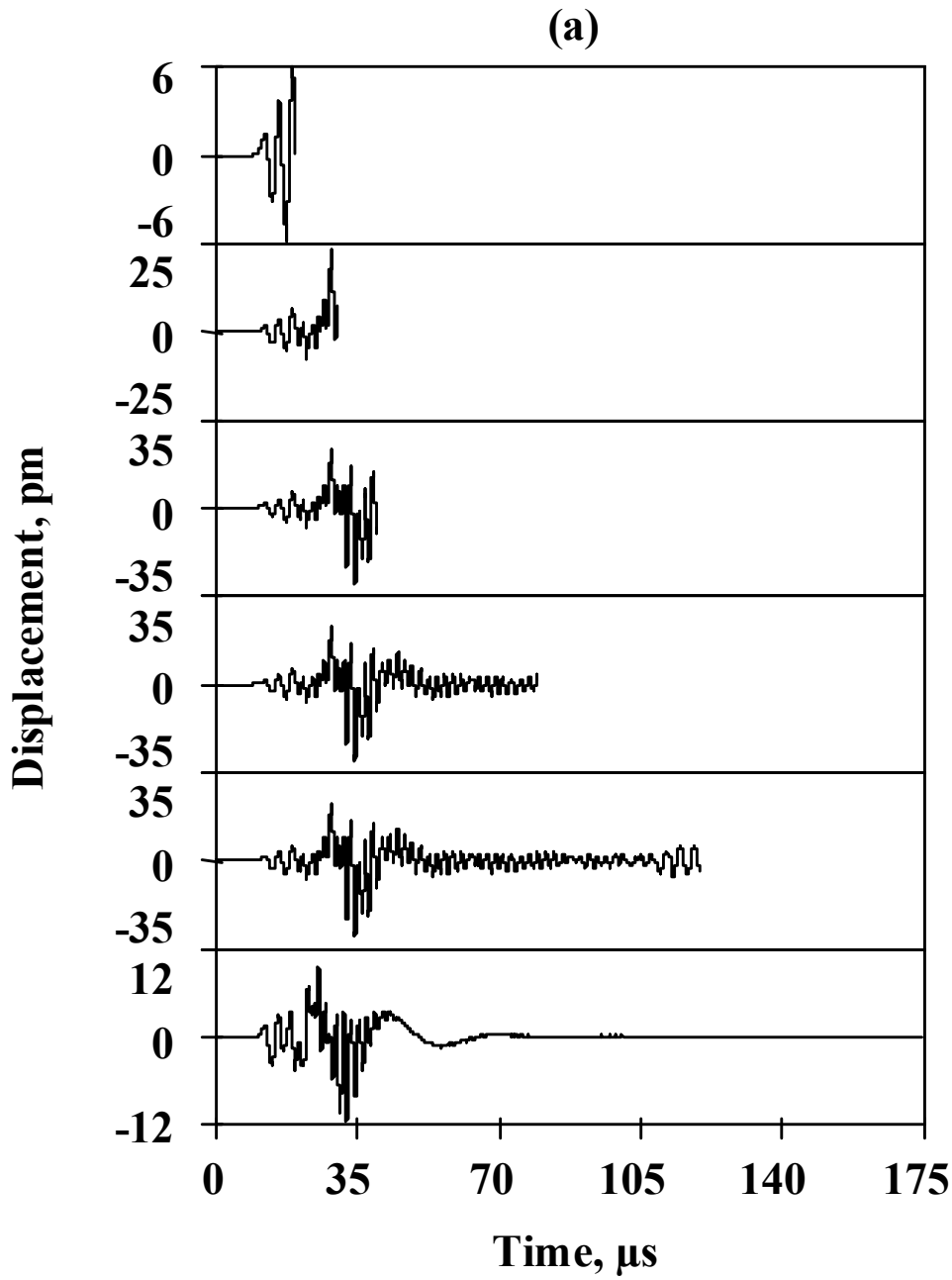

Fig. 11. (a) Out-of-plane displacement signals (truncated at different lengths) at 60 mm from the source.

types of damage in a small laboratory coupon may become frustrated with the lack of consistency in source identification using features such as the hit peak amplitude, energy, duration, and frequency content. In addition, the materials scientist may find that the distorted frequency spectra make it difficult or impossible to distinguish one type of source from another. Finally, we believe the development of AE technology could experience a much larger payoff in the practical application of the technology to large samples if associated laboratory research were regularly carried out on larger samples.

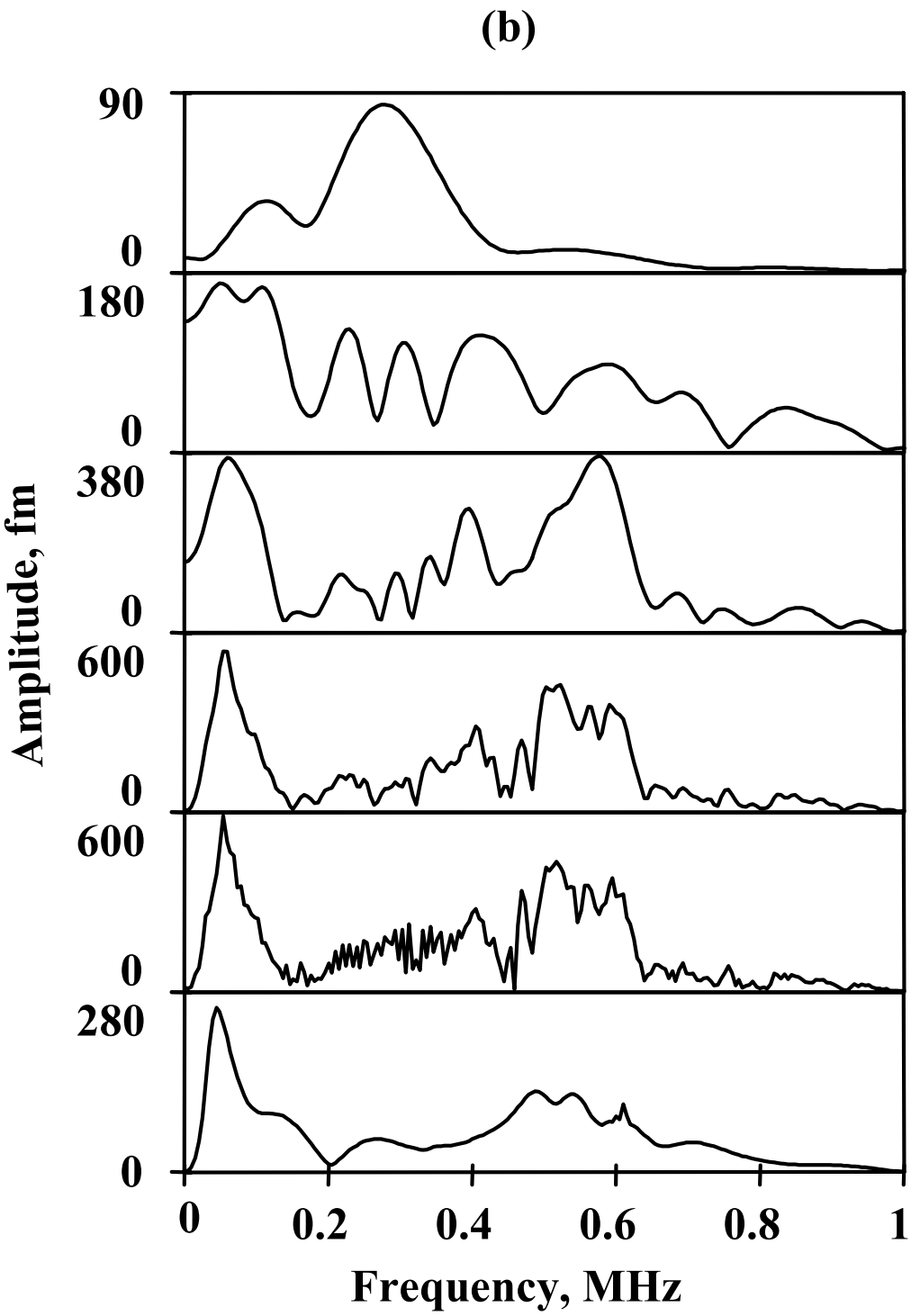

Fig. 11(b): FFTs for the signals in Fig. 11(a). In each figure, the first five plots (starting from the top) are for a small specimen, and the bottom plot is for the equivalent large specimen. The source was an in-plane dipole located at 1.723 mm below the plate's top surface in the small and large specimens, and the signals were for a point-type sensor (40-kHz high-pass).

REFERENCES

M. R. Gorman (1998), "Some connections between AE testing of large structures and small samples," Nondestr. Test. Eval., **14**, 89-104.

M. A. Hamstad, A. O'Gallagher, and J. Gary (1999), "Modeling of buried monopole and dipole sources of acoustic emission with a finite element technique," J. Acoust. Emission, **17**(3/4), 97-110.

M. A. Hamstad and J. D. McColskey (1999), "Detectability of slow crack growth in bridge steels by acoustic emission," Materials Evaluation, **57**(11), 1165-1174.

S. L. McBride and Y. Hong (1992), "Acoustic emission from crack growth in 7050 aluminum and 7075 aluminum as a function of temperature and heat treatement," *Progress in Acoustic Emission VI*, edited by T. Kishi, K. Takahashi, and M. Ohtsu, The Japanese Society for NDI, Tokyo, pp. 521-528.

W. H. Prosser, M. A. Hamstad, J. Gary, and A. O'Gallagher (1999), "Reflections of AE waves in finite plates: finite element modeling and experimental measurements," J. Acoust. Emission, **17**(1/2), 37-47.

C.B. Scruby (1985), "Quantitative acoustic emission techniques," Chapter 4 in *Non-destructive Testing, Vol. 8*, Academic Press Inc., London, pp. 141-210.

A WAVELET-BASED AMPLITUDE THRESHOLDING TECHNIQUE FOR AE DATA COMPRESSION

GANG QI and ENG T. NG

Department of Mechanical Engineering, The University of Memphis
Memphis, TN 38152-6576

ABSTRACT

Data compression is one of the major functions of the wavelet analysis. This paper addresses an application of the discrete wavelet analysis of digital compression of the acoustic emission (AE) signals. An amplitude thresholding algorithm was developed especially for the AE signals. To demonstrate the proposed algorithm, a simulated transient periodical signal and actual AE signal were used to compare the proposed and three existing signal compression algorithms. In the case of the simulated signal, the existing maximum absolute threshold (MAT) algorithm provided the highest compression ratio and maintained a low error. However, in the case of AE signal, all three existing algorithms failed to provide reasonable results. The proposed algorithm provided the highest compression ratio of 6.5 with a relatively low error. The results of this study indicated that the wavelet technique is an efficient tool to use in compressing the AE signals.

1. INTRODUCTION

Engineering data compression draws more and more attention to developing sophisticated instruments. Traditional data compression techniques (the Fourier transformation based techniques) are being challenged by the recently developed wavelet-based technique. Since the late-80s, numerous studies of wavelet analysis have been reported in the area of imaging process. Recently, researchers studied the wavelet-based signal processing method to compress various engineering testing data. Santoso [1] presented an algorithm to compress power quality disturbance data. Staszewski [2] and Tanaka [3] utilized the wavelet transformation to compress vibration data. In their studies, vibration data were decomposed into various wavelet levels for denoising. The denoised data were then compressed. The results showed that the compression ratio was between 5 and 10. They concluded that the wavelet-based signal processing method is a potential tool to compress digital test data. However, the above-mentioned methods failed to compress AE data. The reason for the failure may be due to the specific nature and the size of testing data volume of the AE signal. It is the intention of this paper to develop a new algorithm by using the discrete wavelet transformation method to compress AE data. The algorithm was then tested numerically using both the simulated transient data and actual AE signals.

2. DIGITAL DATA COMPRESSION ALGORITHMS

Recently, the wavelet-based signal processing techniques have shown superior advantages over the traditional data compression methods that were based on the Fourier transformation techniques [4]. In this section, a brief review of the wavelet-based signal processing technique and existing data compression methods are provided, and a new data compression algorithm based on the discrete wavelet techniques is proposed.

Algorithms for Digital Data Compression

Wavelet is a mathematical transformation method. One-dimensional wavelet analysis transforms a time-series signal into a two-dimensional representation of the signal in both time and scale (frequency) domains. Since the wavelet scale varies with the frequency components in the signal, wavelet decomposition is also called multi-resolution analysis technique. A pyramidal decomposition algorithm was developed by Mallat in the mid-90s [5]. In Mallat's pyramidal algorithm, the signal decomposition is completed by two operators h and g on l^2 space:

$$cA_i(n) = (HcA_i)_n = \sum_k h(k-2n)cA_{i-1}(k)$$

$$cD_i(n) = (GcA_i)_n = \sum_k g(k-2n)cA_{i-1}(k)$$

where H and G are called low- and high-pass filters, respectively, and h(n) and g(n) are the coefficients of the corresponding filter. These two equations defined iterative procedures for the wavelet decomposition. At each decomposition level, the components with low frequency are decomposed into low and high components. For instance, cA_i(n) is a smoothed approximation coefficient set processed by filter h(n), whereas the filter g(n) processes the detail coefficients, cD_i(n). After the completion of each decomposition, the length of level components is half of the previous one, and this procedure is known as downsampling. The inverse procedure is called signal reconstruction. The reconstruction is completed by a pair of reconstruction filters $(\bar{H}, \bar{G})$ and the corresponding coefficients of the filters $(\tilde{h}, \tilde{g})$ are given as follows:

$$\begin{aligned} A_i(n) &= (\bar{H}cA_i)_n + (\bar{G}cA_i)_n \\ &= \sum_k \tilde{h}(k-2n)cA_{i-1}(k) + \sum_k \tilde{g}(k-2n)cA_{i-1}(k) \end{aligned}$$

$$\begin{aligned} D_i(n) &= (\bar{H}cD_i)_n + (\bar{G}cD_i)_n \\ &= \sum_k \tilde{h}(k-2n)cD_{i-1}(k) + \sum_k \tilde{g}(k-2n)cD_{i-1}(k) \end{aligned}$$

In the actual calculations, the high-pass filter $\overline{G}$ only supplies a certain number of zeros to complete the upsampling process. The non-lossy signal reconstruction is given by:

$$S(t) = A_k(t) + D_k(t) + D_{k-1}(t) + D_{k-2}(t) + ... + D_1(t)$$

where k is the level of wavelet decomposition, and $S(t)$ is theoretically the original signal. On the other hand, this signal can also be reconstructed when certain high frequency components are discarded:

$$\hat{S}(t) = A_k + \hat{D}_k(t) + \hat{D}_{k-1}(t) + \hat{D}_{k-2}(t) + ... + \hat{D}_1(t)$$

Practically, the above equation establishes the ground for signal compression. There exists a number of wavelet-based data compression methods applicable to engineering testing data. These methods are reviewed in the following:

a) Maximum Absolute Threshold (MAT) [6]

This method used a simple absolute value as a threshold to limit the amount of unnecessary information in transient periodical signals. An absolute value, δ_{ab}, is a predetermined empirical threshold to discard those data that are below this value. This threshold, in general, can be set according to the following relationship:

$$\delta_{ab} = (1 - \theta) \times max|cD_k|$$

where cD_k are the wavelet decomposition detail coefficients at the associated scale of k, and θ is an adjustable parameter.

b) Unbiased Risk Estimate (URE) [1,2,6]

This method adapts thresholding selection using the principle of Stein's unbiased risk estimate. The threshold algorithm for this method is given by:

$$\delta_{re} = \sqrt{\frac{\log n}{3}} \sqrt{\frac{\alpha \log n}{2^{(m-j-1)/4}}}$$

where n is the length of the given signal, and α, m, and j are constants [6].

c) Square-Root of Log Length (SRLL) [1, 6]

This method establishes a threshold value using the square root of logarithm length of the given signal. The threshold value is given by:

$$\delta_{ll} = \sqrt{2 \log n}$$

d) Tail-Maximum Cut (TMC)

The algorithms listed above are frequently used for common signals such as vibration signals. However, because of the uniqueness of the AE signal, these algorithms are not necessarily suitable for the compression of AE signals. AE is known as a sonic wave due to the formation of new free surfaces under loading. The sound source information is often associated with various noises such as electrical, servo-valves hydraulic, mechanical fretting, and various other unknown noises. These acoustic sources form a systematic sound pattern. To be able to compress AE signals, it is required to distinguish and identify each of those individual sources. In general, the magnitude of the wavelet transformation coefficients of the AE signal associated with fracture and crack information are considerably larger than the noise in AE signals [7, 8], especially when the signals were decomposed into different wavelet levels [8]. This fact promotes the idea of using the wavelet transformation to compress the AE data. The compression procedure is employed in the wavelet transformation domain by retaining those wavelet transformation coefficients associated with failure information and disregarding all other transformation coefficients. The reverse of the above procedure was utilized to reconstruct the compressed AE data. In the actual practice, the compressed data was first decoded by the entropy decoder, and was returned to real values through a reverse quantizer. Then, the restored data was achieved through the inverse wavelet transformation. Because the AE data compression process discards over 90% of the total wavelet coefficients, a biased reconstruction is inevitable. However, because most of those discarded wavelet coefficients are associated with various noises, the reconstructed signal can still very well represent the original one with only a minimum loss. As a result, the restoration quality of the AE data is relatively high.

Considering the physical features of AE signals, the authors proposed the following algorithm:

$$\delta_{AE} = max(cD_k(integer(1.2 \times index) : length(cD_k)))$$

where *index* is the maximum amplitude of the detail coefficients at the associated scale *k*. In other words, it corresponds to the AE rise time (more details are provided in the following section). The $length(cD_k)$ is the total length for the detail coefficients at the same scale *k*.

To evaluate the quality of the reconstructed signal $\hat{S}(t)$, the normalized mean-square error (MSE) between the original *S(t)* and restored signal $\hat{S}(t)$ is:

$$MSE = \frac{\|S(t) - \hat{S}(t)\|^2}{\|S(t)\|^2}$$

The compression is measured by the ratio of the original file size to the compressed file size and given as below:

$$CR = \frac{original\ file\ volume}{compressed\ file\ volume}$$

3. NUMERICAL EXPERIMENTS AND RESULTS

To test and compare the existing compression algorithms, simulated transient signals and real acoustic emission signals were explored. In this paper, the one- and three-level wavelet decompositions were performed on the simulated data and actual AE signals. The fourth order Daubechies discrete wavelet [5] was used.

Experiment with the Simulated Transient Periodical Signal

To demonstrate a new data compression method, the existing SRLL, MAT, and URE thresholding methods were applied to a simulated transient periodical signal. This signal was applied to a first order wavelet decomposition. In Fig.1, the top curve is the original signal with a length of 500. The middle and bottom curves show the first level of approximation and detail coefficients, respectively. When the MAT, URE, and SRLL methods were applied, the corresponding numbers of nonzero coefficients were reduced to 2, 1, and 148 as shown in Fig.2. The total corresponding sample points of the first level compression were 256, 258, and 550. The file sizes of the original signal were reduced from 4400 bytes to 2064, 2048, and 4400 bytes apiece. Because the compression ratio of the SRLL method was less than one, it means that the SRLL thresholding method was not suitable for this type of signal and was not discussed. The normalized MSE between the original and reconstructed signals were computed for the MAT and URE methods.

When the third level wavelet decomposition was applied, the total numbers of nonzero elements were reduced dramatically to 82 and 72 for the MAT and URE methods, respectively, shown in Fig. 3. The relationships between the compression ratio and wavelet levels and corresponding errors were shown in Fig. 4. The results were summarized in Table 1 as well. In this table, it can be seen that the URE algorithm provides a slightly higher compression ratio than that of the MAT algorithm. But, the MAT algorithm introduces significantly less error relative

to the URE algorithm. It may be concluded that the MAT thresholding method is a better candidate to compress this type of transient periodical signals. However, when the MAT, URE, and SRLL methods were applied to the AE signals, all of them failed to provide a reasonable result compared with the new method proposed by the authors as demonstrated in the following section.

Table 1. The CR and Normalized MSE of Simulated Signals for Various Thresholding Methods.

Thresholding Method	First level wavelet decomposition		Third level wavelet decomposition	
	CR	Normalized MSE	CR	Normalized MSE
SRLL	0.91	-----	----	----
MAT	1.96	0.0003	6.11	0.0008
URE	1.94	0.0005	6.96	0.0017

----: yielded a CR that was less than 1.

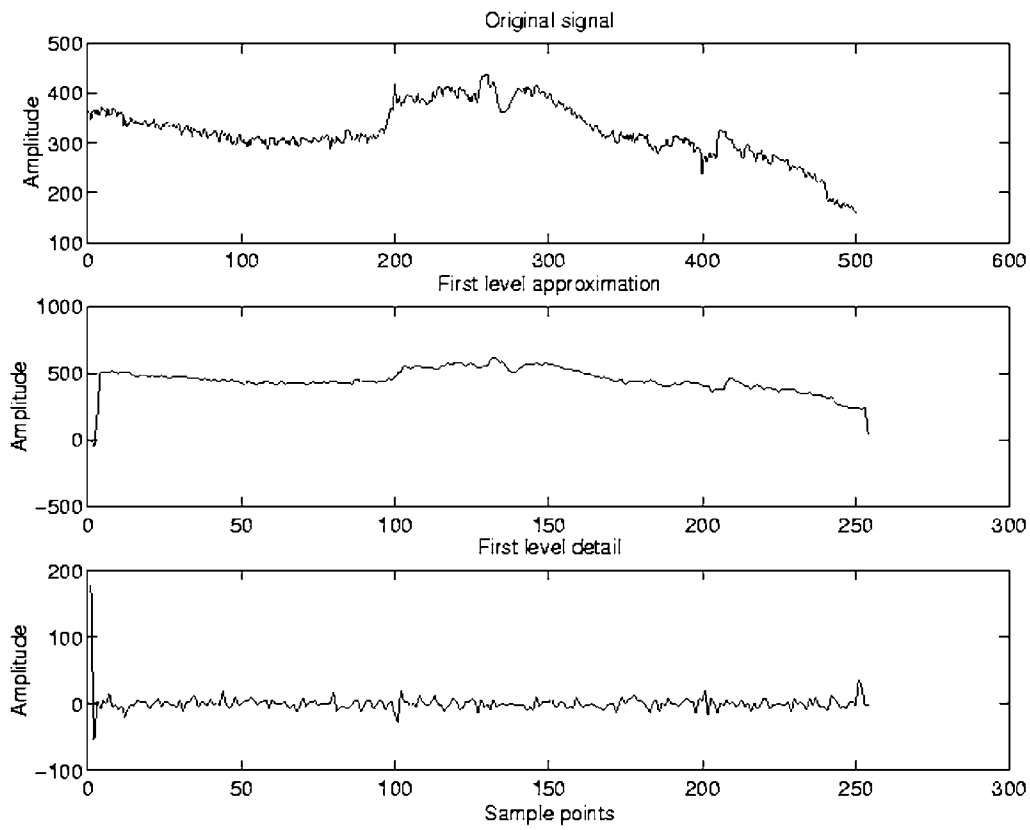

Fig. 1. First level wavelet decomposition of simulated signal.

Experiment with real AE Signal

Standard AE calibration signals (using pencil lead break) were generated to demonstrate the proposed method. A pencil lead break signal was recorded as shown in the top view of Fig. 5. Similarly, the one-level wavelet decomposition for the AE signal was performed. The original signal had 1024 sample points. The approximation and detail coefficients on the first scale had 512 sample data each as shown in the middle and bottom views. The SRLL algorithm again failed to provide a positive compression ratio and was not considered. When the MAT, URE,

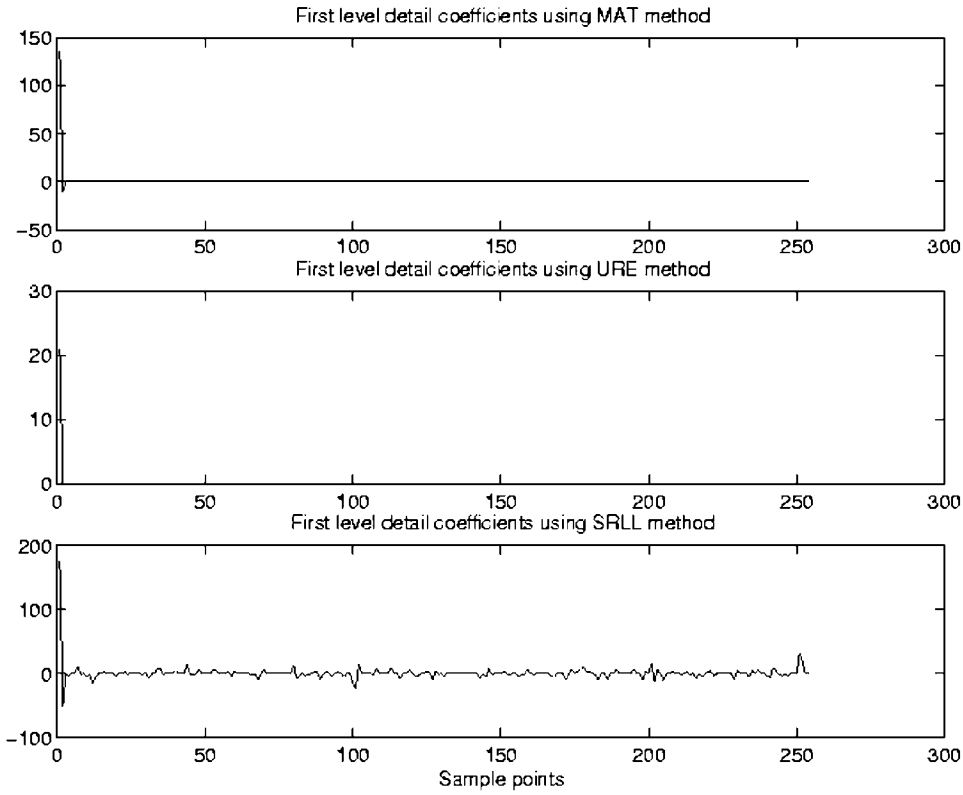

Fig. 2. The detail wavelet coefficients after thresholding of one level decomposition of simulated signal.

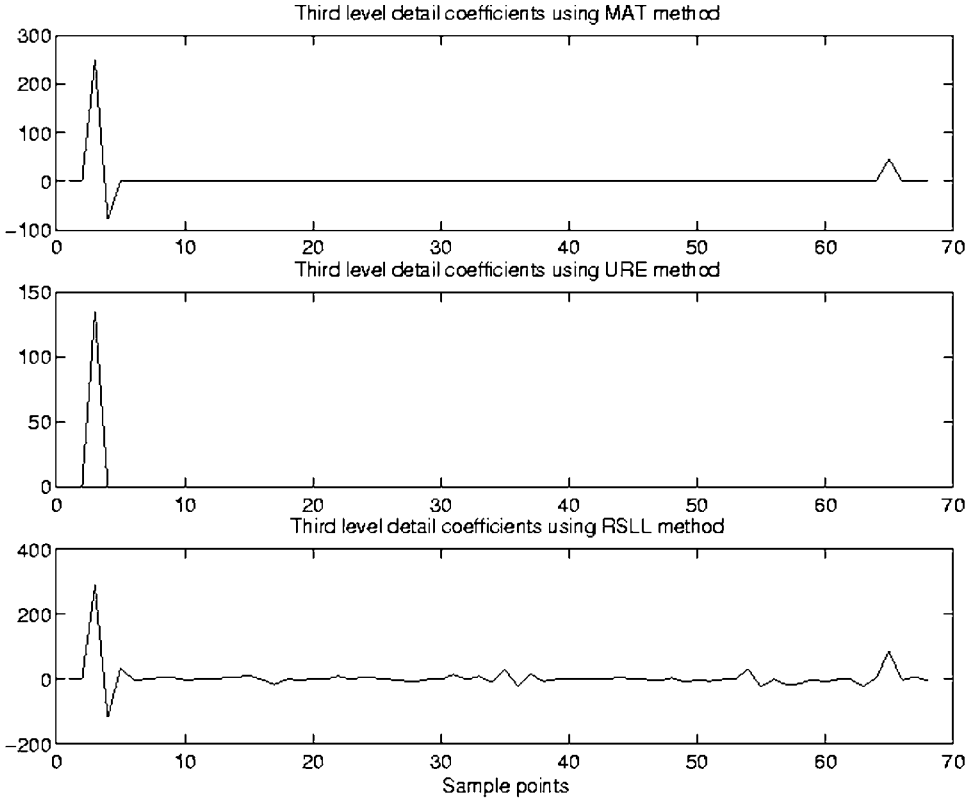

Fig. 3. The third level detail wavelet coefficients after thresholding of simulated signal.

and TMC algorithms were applied to the corresponding detail coefficients, cD_1, the numbers of nonzero elements in $c\hat{D}_1$ became 51, 305, and 0, respectively as shown in Fig. 6. The filtering procedures were completed by the simple thresholding determined in the MAT and URE algorithms. The TMC algorithm is to set a threshold related to the rise time and account for additional 20% (or more) for the second lobe. After the second lobe, any additional coefficients will discarded. For example, the maximum value of the first level detail coefficient is achieved at around the index of 60 in Fig. 5. In this particular case, all the detail coefficients were discarded according to the TMC algorithm. The total corresponding compressed data samples were 617, 1125, and 515, which means that the actual storage spaces were 4936, 9000, and 4120 bytes comparing to the original one that required 8192 bytes.

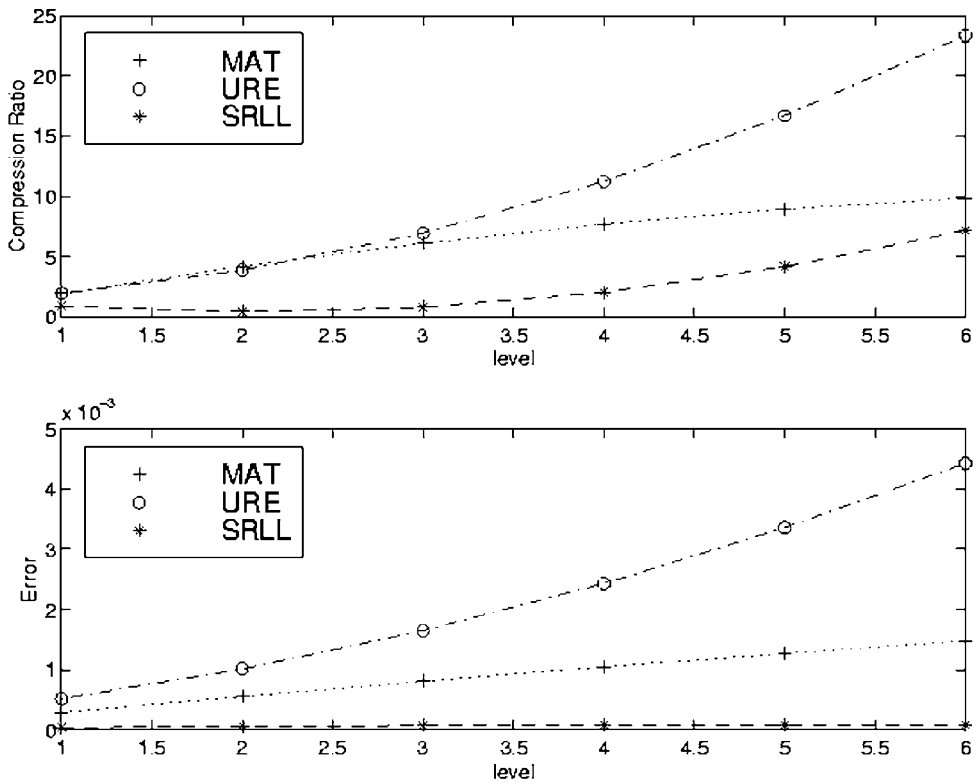

Fig. 4. The compression ratio and the normalized mean squared error of simulated signal using traditional method (MAT, URE, and SRLL).

When the third level wavelet decomposition was performed, the nonzero detail coefficients, $c\hat{D}_3$, from MAT and TMC algorithms were 141 and 11, respectively. URE failed to provide a positive compression ratio at this level and was discarded. The compressed data for the MAT and TMC algorithms were 416 and 156 sample points. The relationships between the compression ratio and wavelet levels and corresponding errors were shown in Fig.7. The results were summarized in Table 2 as well. In this table, it can be seen that the TMC algorithm provides the highest compression ratio and maintains a relative low error. Figure 8 shows the comparison of original and reconstructed AE signals from MAT and TMC algorithms. It can seen that there is almost no visible difference between the original and the reconstructed signal from TMC algorithm.

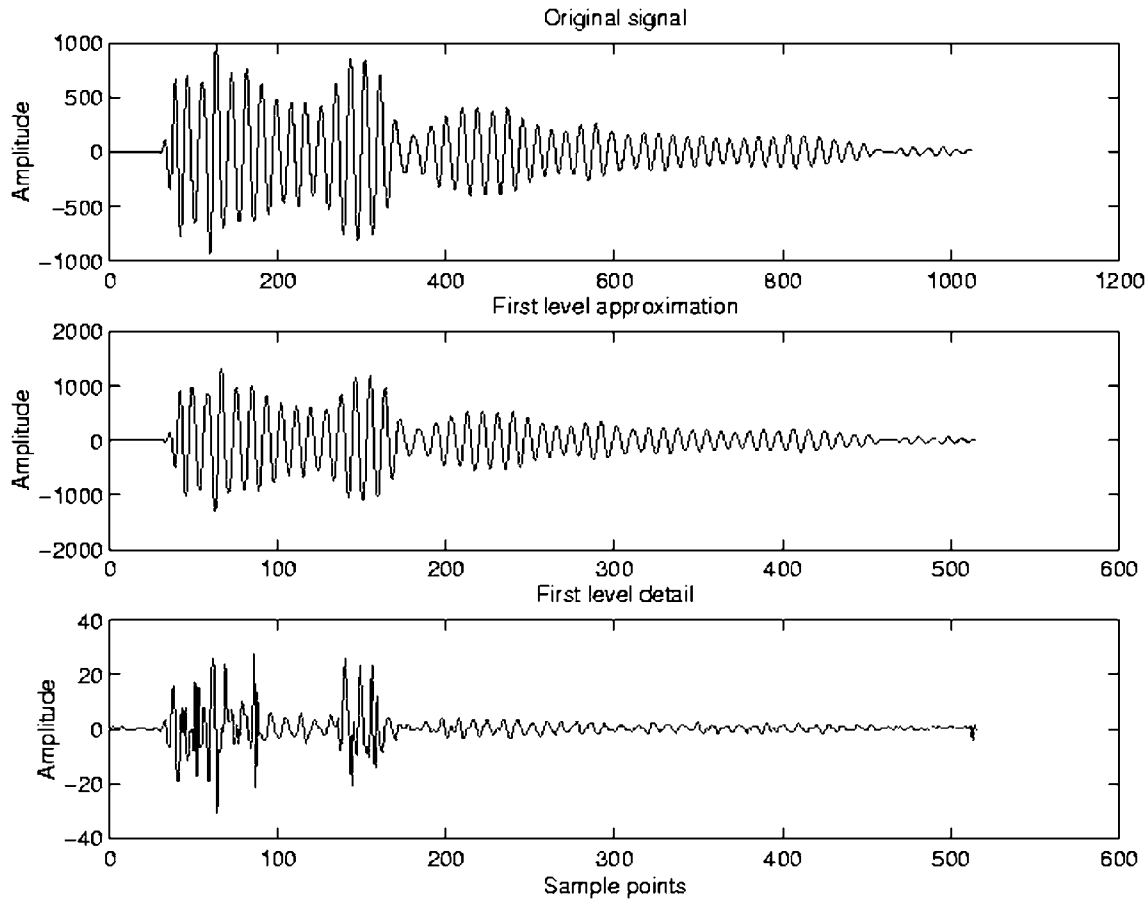

Fig. 5. First level wavelet decomposition of AE signal of one level decomposition.

Table 2. The CR and Normalized MSE of AE Signals for Various Thresholding Methods.

Thresholding Method	First level wavelet decomposition		Third level wavelet decomposition	
	CR	Normalized MSE	CR	Normalized MSE
MAT	1.6592	~10^{-4} to 10^{-3}	2.4615	0.3959
URE	0.9102	~10^{-4} to 10^{-3}	----	----
TMC	1.9883	~10^{-4} to 10^{-3}	6.5641	0.2994

----: yielded an CR that was less than 1.

4. CONCLUSIONS

The wavelet-based AE signal compression using the MAT, URE, SRLL, and TMC thresholding methods were described in this paper. In the case of the simulated transient periodical signal, the MAT algorithm provided a compression ratio as high as 7 with the normalized MSE in the order of 10^{-4} to 10^{-3}. While, the SRLL failed to compress the simulated signal. In the case of the real AE signal, only the TMC algorithm proposed by the authors provided a compression ratio as high as 6.5 and maintained the lowest error of 0.6 for three-level compression. It was also demonstrated that the wavelet-based AE data compression technique is a highly efficient method to significantly reduce storage space.

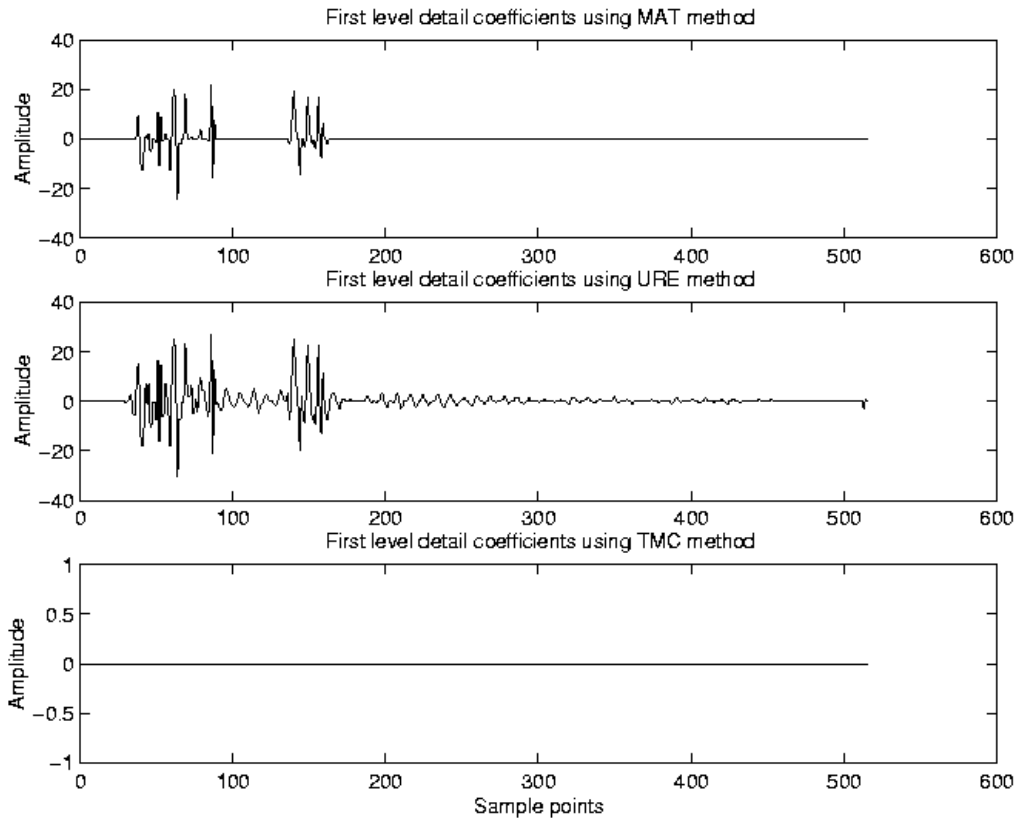

Fig. 6. The detail wavelet coefficients after thresholding of AE signal.

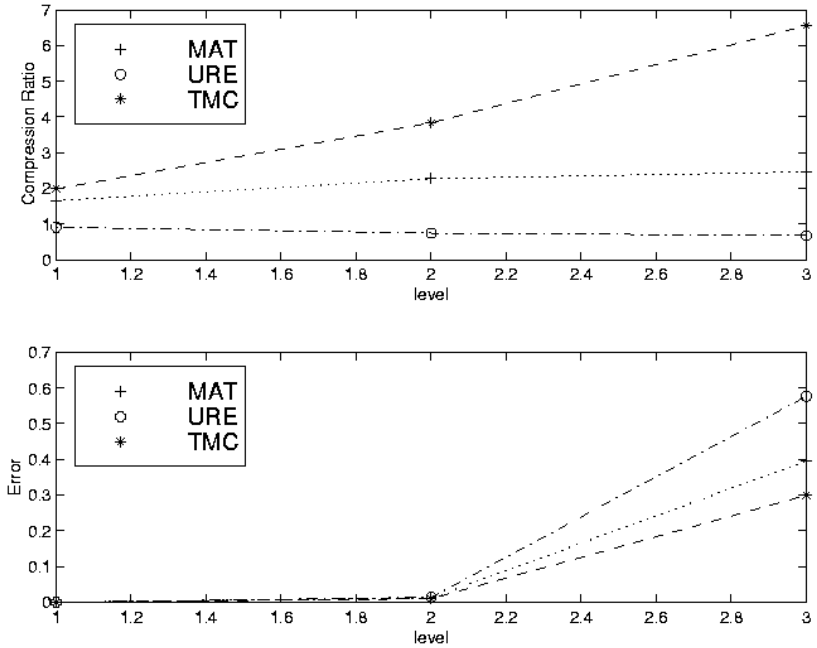

Fig. 7. The compression ratio and the normalized mean squared error of AE signal using traditional and wavelet-based methods. SRLL

REFERENCES

[1] Santoso, S., Powers, E. J., and Grady , W. M., (1997), "Power Quality Disturbance Data Compression Using Wavelet Transform Methods," IEEE Transactions on Power Delivery, **3**, 1250-1256.

[2] Stasewski, W. J., (1998), "Wavelets Based Compression and Feature Selection for Vibration Analysis," Journal of Sound and Vibration, **5**, 735-760.

[3] Tanaka, M. and Sakawa, M., (1998), "Application of Wavelet Transform to Compression of Mechanical Vibration Data,", Electronics and Communications in Japan, **1**: 1379-1387.

[4] Wickerhauser, M. V. (1994), "Adapted Wavelet Analysis from Theory to Software Algorithms," A.K. Peters, Wellesley, MA.

[5] Mallat, S.G. (1994), "A Theory for Multi-Resolution Signal Decomposition: The Wavelet Representation", IEEE Pattern Anal. and Machine Intell. **11**(7): 674-693,.

[6] Misiti, M., Misiti, Y., Openheim, G., and Poggi, J.-M., (1996), *Wavelet Toolbox*, The Mathworks, Inc., Matick, MA.

[7] Fang, D. and Berkovits, A. 1995 "Fatigue Design Model Based on Damage Mechanism Revealed by Acoustic Emission Measurements." Journal of Engineering Materials and Technology, **117**: 200.

[8] Qi, G., (2000) "Wavelet-based AE Characterization of Composite Materials," NDT & E International, **33**(3): 133-144.

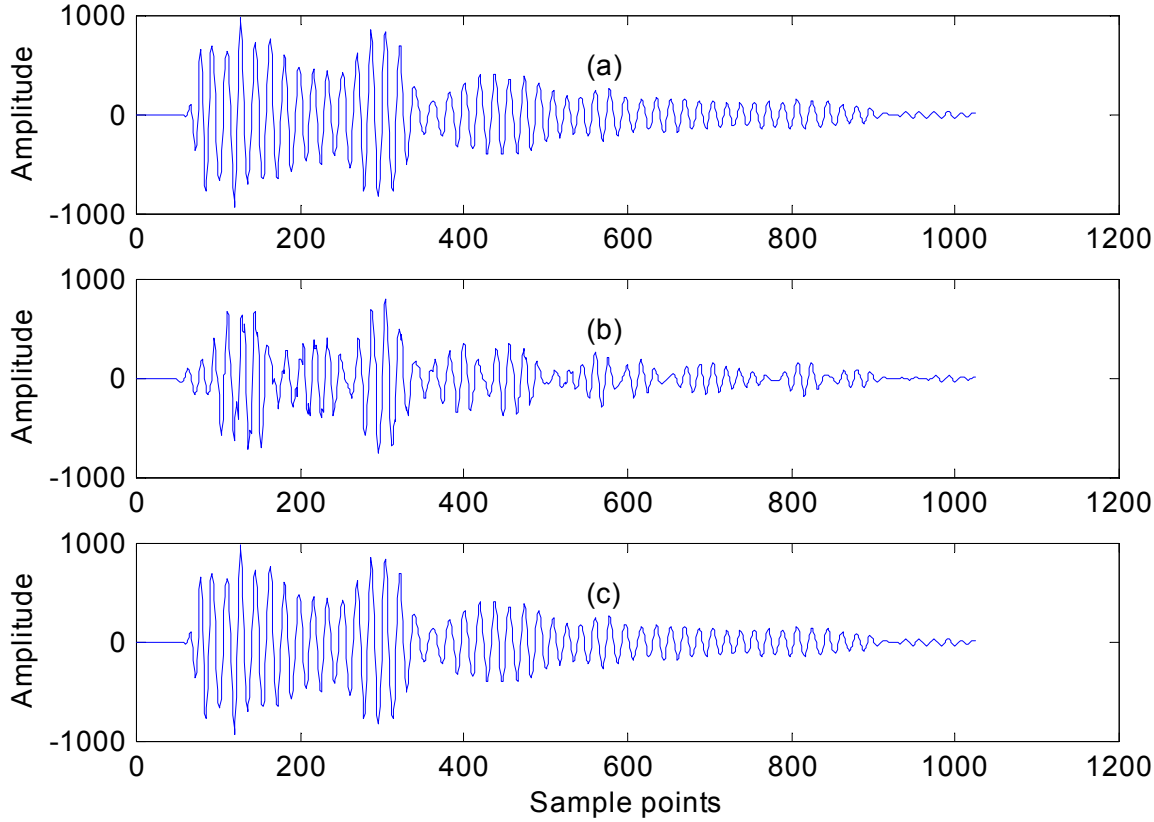

Fig. 8. Original and reconstructed AE signals: (a) original signal; (b) reconstructed signal from MAT algorithm and (c) reconstructed signal from TMC algorithm.

ACOUSTIC EMISSION MONITORING OF FATIGUE OF GLASS-FIBER WOUND PIPES UNDER BIAXIAL LOADING

PAWEL GEBSKI, LESZEK GOLASKI and KANJI ONO*,

Department of Civil Engineering, Kielce University of Technology, Kielce, Poland
*Department of Materials Science and Engineering, University of California,
Los Angeles, California, USA

ABSTRACT

Damage accumulation during combined fatigue loading has been monitored by acoustic emission (AE) technique in filament wound pipes. The tests were made on epoxy resin-E-glass-fiber filament wound pipes with winding angle $\phi = \pm 55^{\circ}$. In order to simulate the service conditions more fully, the pipes were subjected to two loading modes: M II and M III. Depending on the loading modes fatigue processes were controlled either by transverse or shear stress component in reference to fiber direction. During fatigue the acoustic emission was recorded. The damage evolution with fatigue cycles for each loading mode was estimated on the basis on acoustic emission parameter analysis. Emphasis has been placed on changes in AE activity for different fatigue loading ranges during fatigue progression. AE signals after filtration and multi-parameter analysis show that not only the beginning of failure but also the pre-failure changes in angle-ply pipes can be estimated. A procedure of AE signal analysis that warns about incipient failure before any serious damage takes place in the composite/laminate structures, has been suggested. This procedure is valid for both applied loading modes in spite of the differences in failure modes. The approaching fatigue failure is detected by changes in selected AE parameters, when samples exceeded 70-90% of fatigue life. Using this procedure, when multi-channel AE equipment and zonal localization are applied, the time and location of fatigue failure in large laminated structures can be predicted experimentally.

1. INTRODUCTION

Acoustic emission (AE) technique has been applied with success for testing of composites and composite laminates. Advantages of this technique are volume inspection, real time monitoring, damage accumulation assessment and possibility of damage localization. AE is used for first damage detection, strength prediction, damage history estimation and quality control of composite materials and structures [1-6]. Most studies concern statically loaded coupons and composite structures. Fatigue testing of composites by AE methods started in early seventies [7-9]. These and further results [10-14] indicated that there exists qualitative relationship between AE activity and damage evolution. AE procedures usually are used for fatigue damage initiation detection, damage progression and accumulation. However, the inadequacy of AE method in warning against fatigue failure of composite and composite laminate structures -is evident as reviewed by Hamstad [15]. This problem is important for composite users because the scatter in real service time for the same loading conditions may differ as much as ten or more. Moreover warning against failure together with failure localization makes it possible to repair the composite under consideration.

In this paper the AE behavior during fatigue of laminate tubular specimens was analyzed. In particular an attempt was made to exploit AE results for the monitoring of imminent fatigue

collapse. To relate the tests with the service conditions more fully fatigue loading was performed in two different loading modes leading to different failure mechanisms.

2. EXPERIMENTAL

The tests were made on E-glass-fiber filament wound pipes with the winding angle $\Phi = \pm 55^0$. Electrotechnical Institute – Wroclaw, Poland, fabricated the pipes from epoxy resin EPIDIAN 53 mixed with Z -1 catalyst and PPG JFG E C15 120-glass fiber. The nominal fiber volume fraction was $V_v = 0.5$. All tests were made on tubular specimens with dimensions: length 300 mm, internal diameter 42 mm and wall thickness 1.5 mm. The pipes were subjected to variable internal pressure giving rise to biaxial fatigue loading with frequency 1 or 2 Hz, stress ratio R = 0.1 and different pressure amplitude. The loading of samples were performed using a modified Schenck computer-controlled pressurization system.

In laminates the fatigue processes depend only indirectly on external loads, which usually are applied along symmetry axis of a laminate. In reality, fatigue damage is controlled by stress components in laminae of the laminate oriented with regard to fiber direction. They are normal stress along fiber $\sigma_{||}$, transverse to fiber stress $\sigma_{\perp}$ and shear stress $\tau_{\#}$ along fiber. Because the strength of the laminae in fiber direction is relatively high, it can be expected that incipient fatigue cracking depends mainly on shear and transverse stress components.

To analyze fatigue processes under conditions where either transverse stress or shear stress is dominant in fatigue damage development, two loading modes were applied. They were Mode 2 (M II) giving rise to high transverse to shear stress ratio and Mode 3 (M III), where the shear to transverse stress ratio was high. In M II, both ends of a pipe sample were closed and the ratio of hoop stress σ_H to axial stress σ_A was equal to two while in M III both ends of pipe can slide on seals so that the axial stress was equal to zero. No reinforcing mandrels at pipe ends were applied in M III loading.

Damage evolutions during fatigue loading was investigated using acoustic emission (AE) technique. For AE signals acquisition, a two-channel PAC MISTRAS 2001 instrumentation together with wideband sensors (PAC WD) was used. Channel No. 1 was furnished with 20 kHz high-pass filter while in channel No. 2 the high-pass filter cut-off was 100 kHz. The gain of pre-amplifiers was 40 dB while 40-dB threshold level was applied for all the tests. During loading classical AE parameters were recorded. They are:

1. event rate / cumulative events
2. count rate / cumulative counts
3. duration / cumulative duration
4. rise time / cumulative rise time
5. energy / cumulative energy
6. AE signal amplitude.

To select appropriate load amplitude the fatigue tests were preceded by failure analysis of pipes under smooth pressurization. These tests were performed on two sets of pipes with different matrix resin. They were epoxy matrix and polyester matrix while lamina sequences and fibers arrangements were the same in both sets. The pipes were loaded in axial tension and internally pressurized in M II and M III. To estimate failure evolution AE parameters listed above were analyzed. In addition, waveforms of AE signals were recorded and analyzed with fast Fourier transform. Comparison of results for the two sets of pipes demonstrated that,

although the failure strength was close to each other, the differences in AE behavior were pronounced. The classical AE parameters depended on loading modes, filtration and sensor position. Especially AE behavior was influenced by matrix resin confirming earlier result [16]. Among the considered AE parameters, those less dependent on testing conditions appeared to be event summation. Variability of AE parameters makes it difficult to develop a general AE failure criterion for both sets of pipes. However, changes in AE parameter qualitatively indicated the incipience of damage processes and damage accumulation or damage evolution. Details concerning pipes behavior during smooth pressurization are given elsewhere [17].

The waveform analysis, which was performed during quasi-static loading, revealed the same waveforms for all of tested pipes independently of matrix resin and loading mode. Three types of waveforms denoted as A, B and C prevailed. The matrix resin and loading mode changed only the proportion between them. When pipes were loaded in tension additional waveforms appeared, which were not observed during internal pressurization [17]. The observed changes in waveforms, which took place during smooth pressurization and tension testing of pipes, suggested that waveforms of AE signals cannot be used to characterize damage accumulation or to warn against failure. Therefore during fatigue tests emphasis was put on the classical AE parameters analysis.

In this study, two types of variable loading were performed during fatigue tests. Firstly, continuous fatigue loading with constant load amplitude, and secondly, fatigue loading in blocks containing 1000 cycles each separated by constant load-hold periods at maximum stress for 300 seconds each. Pipes were loaded up to failure.

3. RESULTS

3.1 Fatigue in Mode III (Hoop loading; No axial loading)

To estimate the strength of pipes under static loading, which is necessary for fatigue load selection, the pipes were smoothly internally pressurized in mode M III up to failure. During loading AE signals were recorded for damage evolution evaluation. A typical AE event rate and AE duration vs. pressure (the latter in point graph) are shown in Figs. 1a and 1b, respectively. Increase in AE activity took place at internal pressure in the vicinity of 100 bars, indicating intensification of failure processes. This pipe burst at pressure of 201 bars. For fatigue tests in M III internal pressure of 100 bars was taken as the maximum load. Pressurization with this pressure is leading to hoop stress equal to 140 MPa while the axial stress is 0. Such hoop stress, in accordance to Puck theory [18,19], produced shear stress along fibers of 50 MPa in laminae. This stress was below the shear strength of a single lamina, which was approximately equal to 62 MPa. However, it was high enough to exceed the stress of 37 MPa, at which departure from the linearity on shear stress - strain curve took place. The transverse to fiber component was only about 4 MPa; i.e., well below the transverse strength of lamina. For this reason, when specimens are loaded in M III, incipient fatigue damage by shear is expected.

Most of fatigue tests in M III were performed at pressure range p_{max} = 100 bars and p_{min} = 10 bars. Some pipes were loaded at lower pressure ranges. The applied load and number of cycles up to failure are given in Table I.

All pipes, which were fatigued in M III, showed failure by burst. Failure was not preceded by swelling or buckling. The origin of fatigue crack is situated at a fiber interlacing point. Next,

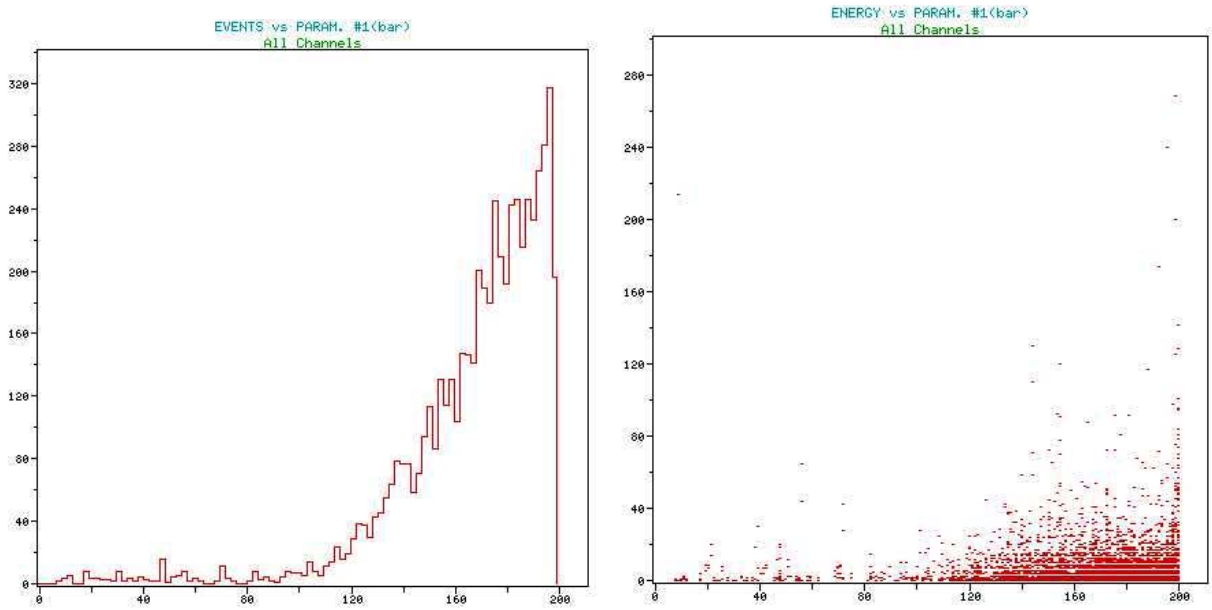

Fig. 1. AE events rate and energy point plots vs. pressure during smooth pressurization of GRP pipe in M III.

cracks spread in two directions. These directions are parallel to fiber directions in internal layer of pipe. The pipe after fatigue failure is shown in Fig. 2a (on the left side). When pipes were smoothly pressurized in M III, failure took place by delamination and fiber matrix decoupling. This failure was not accompanied by intensive fiber breakage, which was observed in pipes after fatigue tests. For comparison a typical damaged pipe surface after smooth pressurization is shown in Fig. 2b on the right side.

Table I Fatigue strength data of pipes loaded in M III

Sample No	Pressure in bars		Number of cycles	Failure by
	max	min		
MIII/001	Failure at 201 bars after smooth pressurization			Burst
MIII/002	100	10	4 981	Burst
MIII/003	100	10	8 452	Burst
MIII/004	100	10	6 990	Burst
MIII/005	100	10	6 134	Burst
MIII/006	100	10	5 301	Burst
MIII/007	80	8	53 000	No damage
MIII/008	90	9	15 075	Burst
MIII/009	90	9	105 623	Burst

The micrograph of fatigue fracture surfaces, which is demonstrated in Fig. 3, revealed that in the first lamina (internal) and third one the cracking took place along fibers by shear while in the second and fourth (external) laminae failure was accompanying by intensive fiber breakage and fiber pull out. In the vicinity of the crack, in external lamina, the resin was crumbled. During

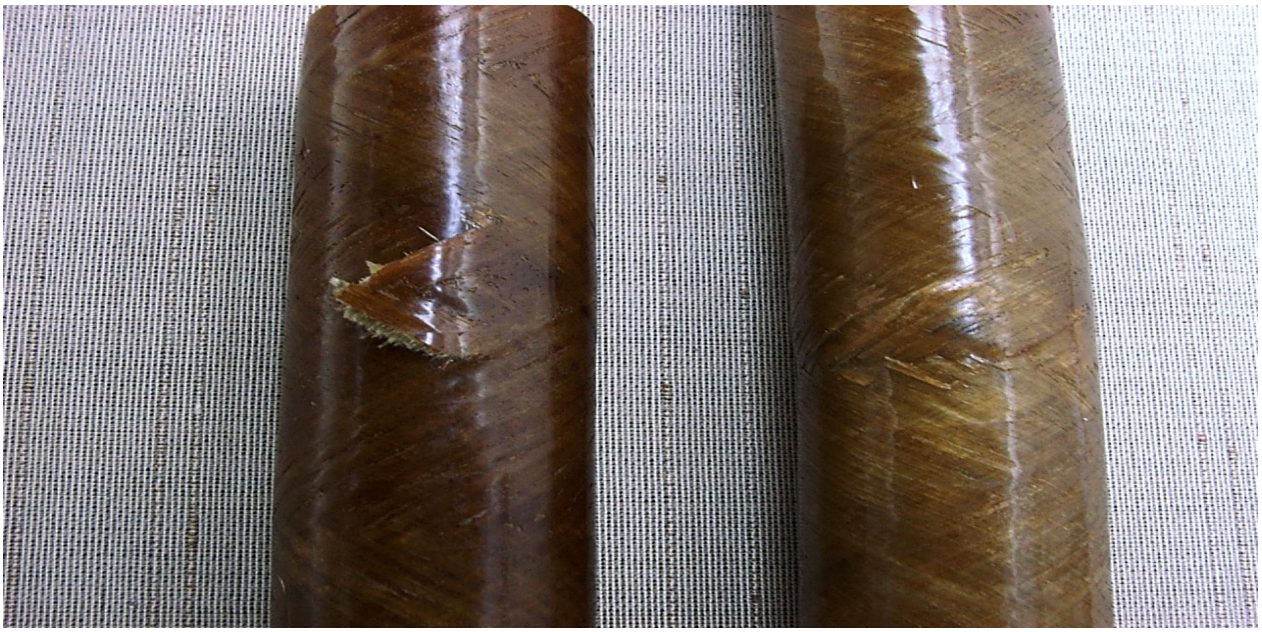

Fig. 2. Failure pipes as a result of (left) fatigue in M III, (right) smooth pressurization in M III.

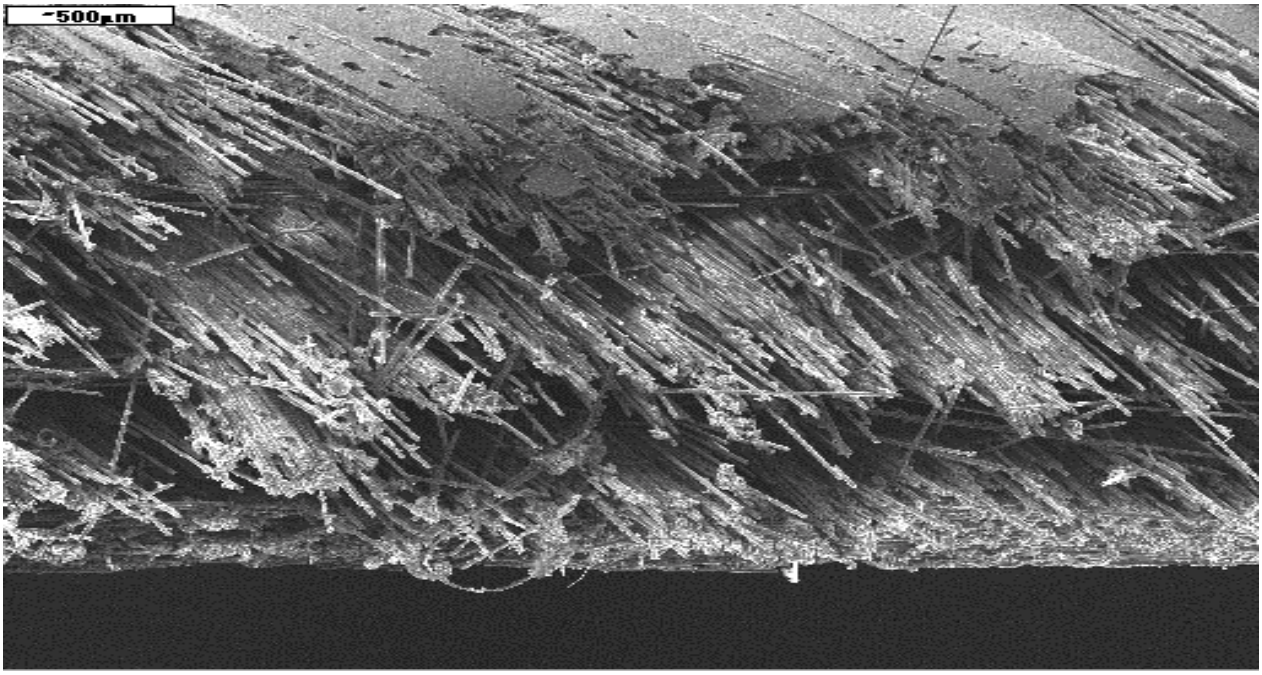

Fig. 3. Fatigue fracture surface of pipe loaded in M III.

samples washing and preparation for microscopic examination, crumbs of resin were removed and naked fibers can be seen as it is demonstrated in Fig. 4.

The test procedure evaluation criteria, which were used in this paper, are based on acoustic emission technique. However, most of AE evaluation criteria, assessing the integrity of composite structures, do not consider the components loaded by variable loading and fatigue damages. The most frequently used criteria for smoothly loaded composite structures are the total number of acoustic emission counts and number of large amplitude hits. Applicability of

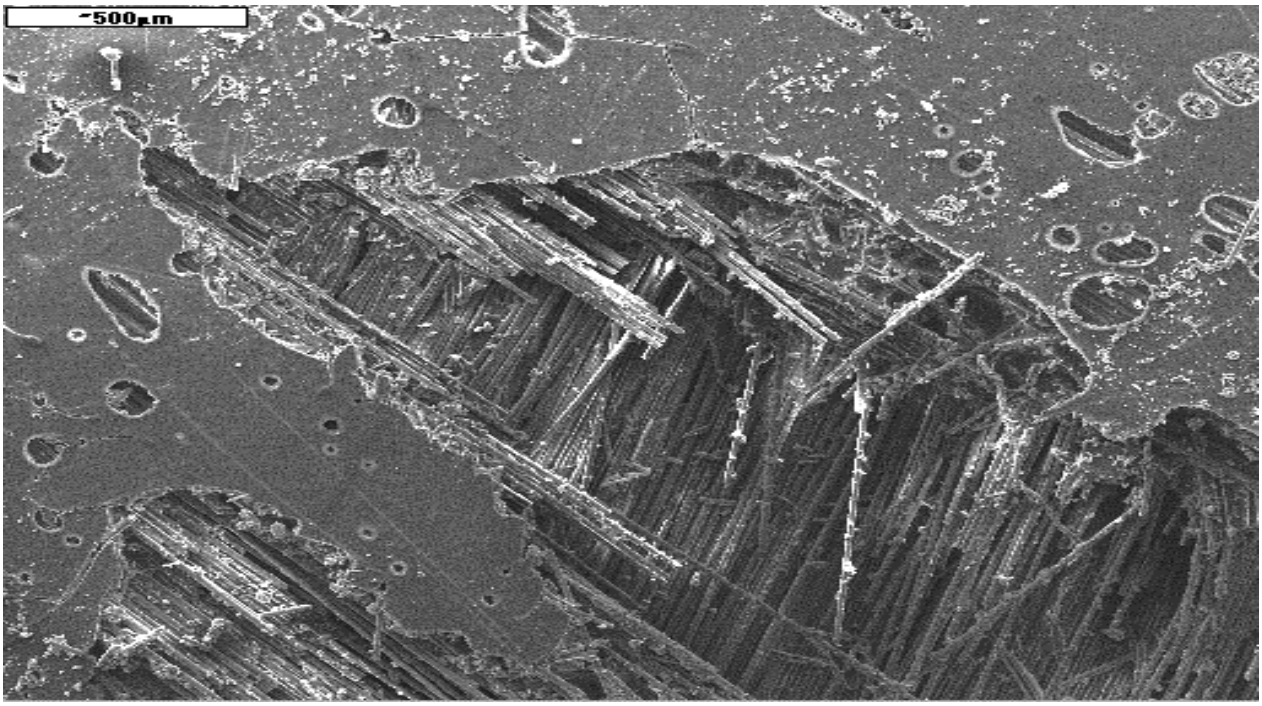

Fig. 4. Micrograph of fatigue area on pipe surface loaded in M III.

these criteria for composite damage evaluation under fatigue loading conditions has been analyzed in this study.

The summation of classical AE parameters, which were recorded during fatigue loading of pipes in Mode III, is given in Table II. The only AE parameter, which does not depend on filtration, is AE event summation. As it was indicated elsewhere [17], AE events do not depend on sensor position on these pipes as well. For this reason AE summation in all analysis is taken as the basic AE parameter, while the other parameters were taken as complementary ones. It should be noticed that in some samples (for example sample No 004 and 005) number of cycles up to failure is higher than number of AE events. This means that there is a number fatigue cycles, during which no AE signals above 40 dB threshold were produced.

Table II AE parameters recorded during fatigue of pipes loaded in M III

Sample No	Cycles to failure	20 kHz high-pass filter					100 kHz high-pass filter				
		AE Events	AE Counts	AE Duration	AE rise time	AE Energy	AE Events	AE Counts	AE Duration	AE rise time	AE Energy
002	4 981	7800	$3,8*10^3$	82000	$1,6*10^4$	$2,7*10^3$	7800	$4,0*10^3$	43000	$0,9*10^4$	$0,5*10^3$
003	8 452	15 600	$440*10^3$	6 500	$118*10^4$	$114*10^3$	15 600	$310*10^3$	3 600	$92*10^4$	$42*10^3$
004	6 990	3 200	$100*10^3$	3 000	$64*10^4$	$34*10^3$	3 200	$72*10^3$	1 500	$34*10^4$	$12*10^3$
005	6 134	5 200	$130*10^3$	2 200	$48*10^4$	$35*10^3$	5 200	$70*10^3$	1 050	$25*10^4$	$12*10^3$
006	5 301	5 400	$120*10^3$	4 800	$50*10^4$	$40*10^3$	5.400	$75*10^3$	3 800	$50*10^4$	$21*10^3$
007	53 000	48 000	$980*10^3$	38.000	$220*10^4$	$82*10^3$	48 000	$420*10^3$	35 000	$200*10^4$	$74*10^3$
008	15 075	12 200	$200*10^3$	13 400	$24*10^4$	$61*10^3$	12 200	$98*10^3$	13 000	$20*10^4$	$20*10^3$
009	105 623	94 000	$1120*10^3$	88 000	$80*10^4$	$220*10^3$	94 000	$560*10^3$	84 000	$75*10^4$	$36*10^3$

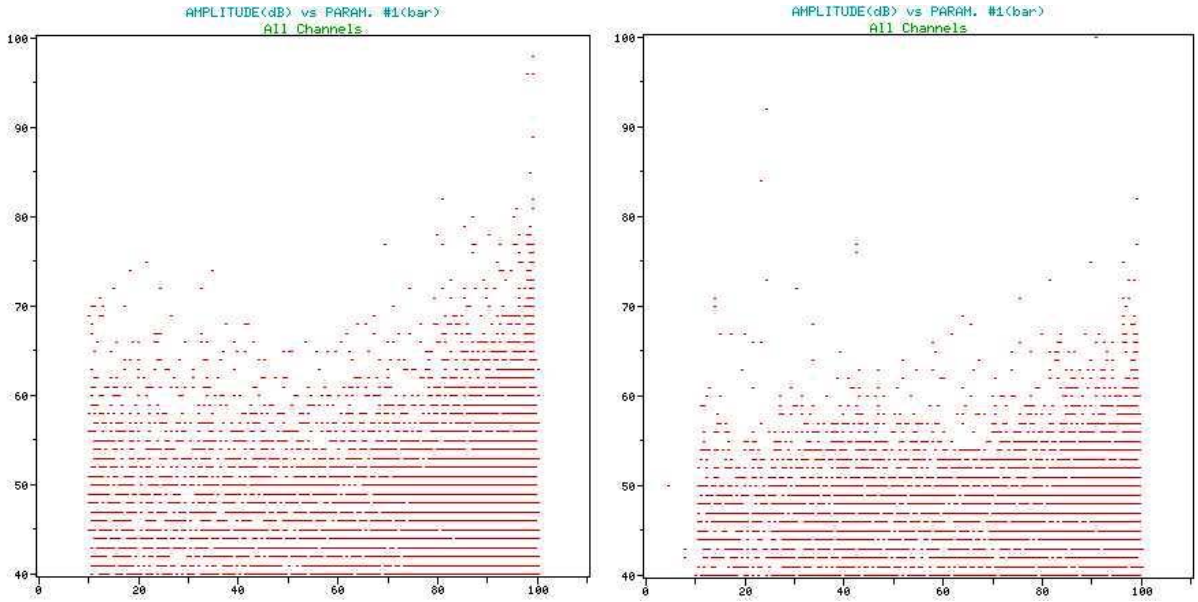

Fig. 5. Point diagrams of AE signal amplitude (in dB) vs. pressure (in bars) for GRP pipes fatigue-loaded in M III: (a: left) sample 005, (b: right) sample 006.

The results demonstrated that there is no relationship between the number of cycles to failure and number of AE events. This behavior can be expected because during fatigue loading of laminated composites two categories of AE sources are active. The first one is randomly distributed in structure and started from the beginning of variable loading. This category of sources is attributed to cracking processes and friction of cracked surface in all volume of sample. Another type of fatigue-related AE sources starts to become active after a number of fatigue cycles and is localized in comparatively small volume of sample. AE sensors record signals generated by both groups of AE sources. Thus, the AE signals, which are collected during variable loading, depend both on general damages, which took place in all volume of the sample and on localized processes leading to fatigue failure. The proportion between the two types of signals may vary from sample to sample. For this reason total summation of classical AE parameters could not be used as a measure of residual fatigue life.

For the evaluation of using large amplitude signals as an indicator of fatigue damage verification, AE amplitudes were recorded as a function of pressure within fatigue cycle up to failure. Typical AE signal amplitude point diagrams plotted against pressure range of fatigue cycles for two GRP pipes loaded in M III are given in Fig. 5. The distribution of large amplitude hits depends on load value; in Fig. 5a, signals over 75 dB and in Fig. 5b, signals over 70 dB are found above 75 bar. The maximum amplitude value can change from sample to sample. The differences may be as much as 20 dB. In all samples the signals with the highest amplitudes took place at or near the maximum loads. However, high amplitude (>60 dB) signals were observed at the lowest load of the fatigue cycles as well. As shown in Fig. 5, these are abundant over the lower half of the loading cycles. In most of the samples, the AE activity remains constant until 70-85% of the maximum load, followed by an increase. General shape of these diagrams did not depend on the number of fatigue cycles and is nearly identical when AE data from only a limited number of total fatigue cycles are taken into account. Nevertheless it should be noticed that AE parameters varied from sample to sample, both in the intensity and maximum values, even for samples, which exhibited similar numbers of cycles to fatigue failure. In some samples, there was a slight reduction in AE amplitude at mid-range of applied pressure.

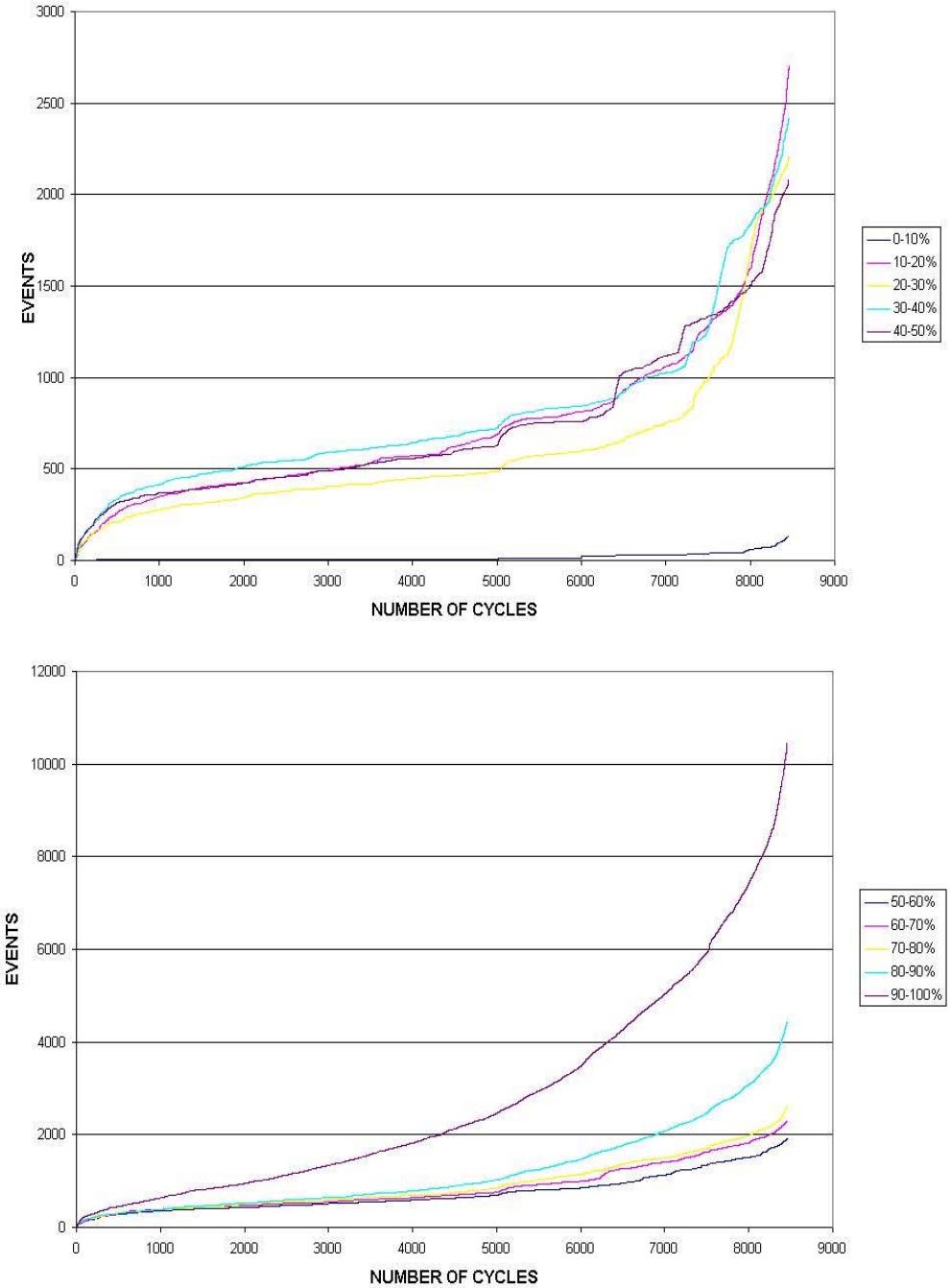

Fig. 6. AE events summation as a function of number of fatigue cycles for GRP pipe loaded in M III (sample 003). a) loading ranges 0 – 50% of fatigue load cycle (top), b) loading ranges 50 – 100% of fatigue load cycle (bottom).

Because it is unlikely that cracking occurs at low load levels, a large number of high amplitude signals were produced by friction. This assumption is in accordance with data presented by Awerbuch et al. [10]. Undoubtedly, when laminate composites are loaded by variable loading in M III, which produces shear cracking along fibers, significant part of AE is produced by friction. These data demonstrate that criteria based on high values of AE amplitude parameter should be used with great caution for warning against fatigue failure of composite structures.

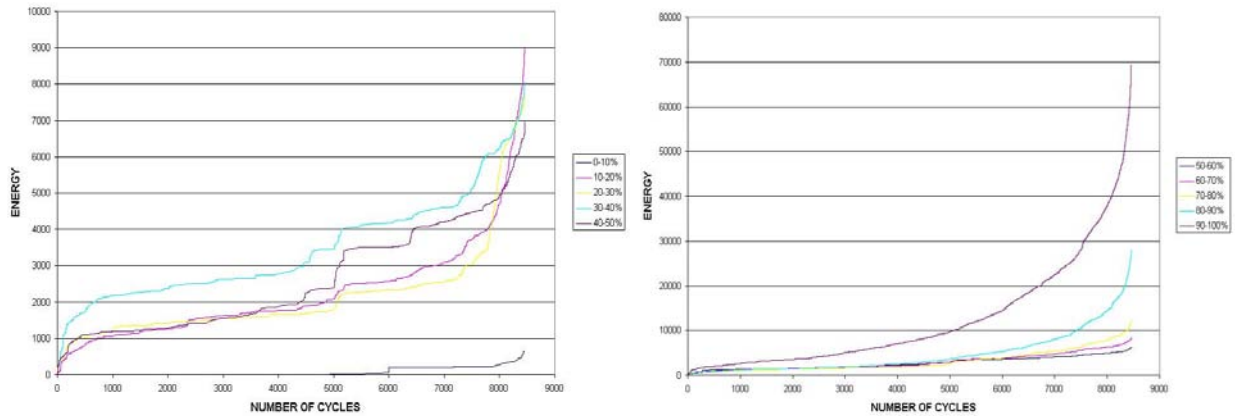

Fig. 7. AE energy summation as a function of number of fatigue cycles for GRP pipe loaded in M III (sample 003). a) loading ranges 0 – 50% of fatigue load cycle (left), b) loading ranges 50 – 100% of fatigue load cycle (right).

More promising are the criteria based on changes in AE parameter with number of fatigue cycles. The load cycle was divided into ten load range (LR). The AE parameters, which were analyzed, are summations of events, counts, duration, rise time and energy. The data for analyses were taken from both channels; that is channel with 20 kHz high-pass filter and 100 kHz high-pass filter. However, for fatigue loading in M III, filtration has little influence on the shape of AE parameter diagrams. It was expected that the sensitivity of AE parameter variation with fatigue processes improves, when the recorded parameters are subjected to different types of filtration; namely, low frequency signals from friction and high frequency signals from cracking. In the present case, it appears that both types of signals may originate primarily from friction. While cracking may contribute, the dominant AE is from friction. As discussed earlier in conjunction with Table II, the summations of events had little effect of filtration, implying that separate cracking signals were not detected. This is most likely the result of the laminate stacking sequence; that is, when a shear crack develops, the fibers in the next lamina are subjected to shear loading. The bending load may not be high enough for immediate fiber failure, but fatigue loading produces resin crumbling as observed in Figs. 3 and 4. Fibers are subsequently fractured under low loads, giving rise to only low level AE signals. Thus, the fiber failure in shear does not produce high level AE signals as normally found under tensile loading of fibers.

Typical AE event summation vs. No of cycles graphs, for different LR of fatigue load cycle, are shown in Fig. 6a and 6b while the same diagrams concerning AE energy summation are given in Fig. 7a and 7b. As expected, these plots depend on LR and number of cycles. AE event summations decrease with lower LR value. The only exception is for the lowest LR, where event summation is greater than that for the next higher LR. The shape of the other AE parameters (number of counts, duration, rise time) vs. number of fatigue cycle plots, for the same sample, are generally similar; however, they can differ in details. The differences concern sudden increases (jumps) in AE parameters. Mostly the jumps are observed in some of LR, while in the other no or little changes in AE parameters could be seen. It is interesting to notice that frequently a jump in one AE parameter was not accompanied by a jump in another AE parameter. The origin of these sudden increases of AE parameters in random places of fatigue processes is unknown; however, they underline the intermittent nature of fatigue processes in composite laminates.

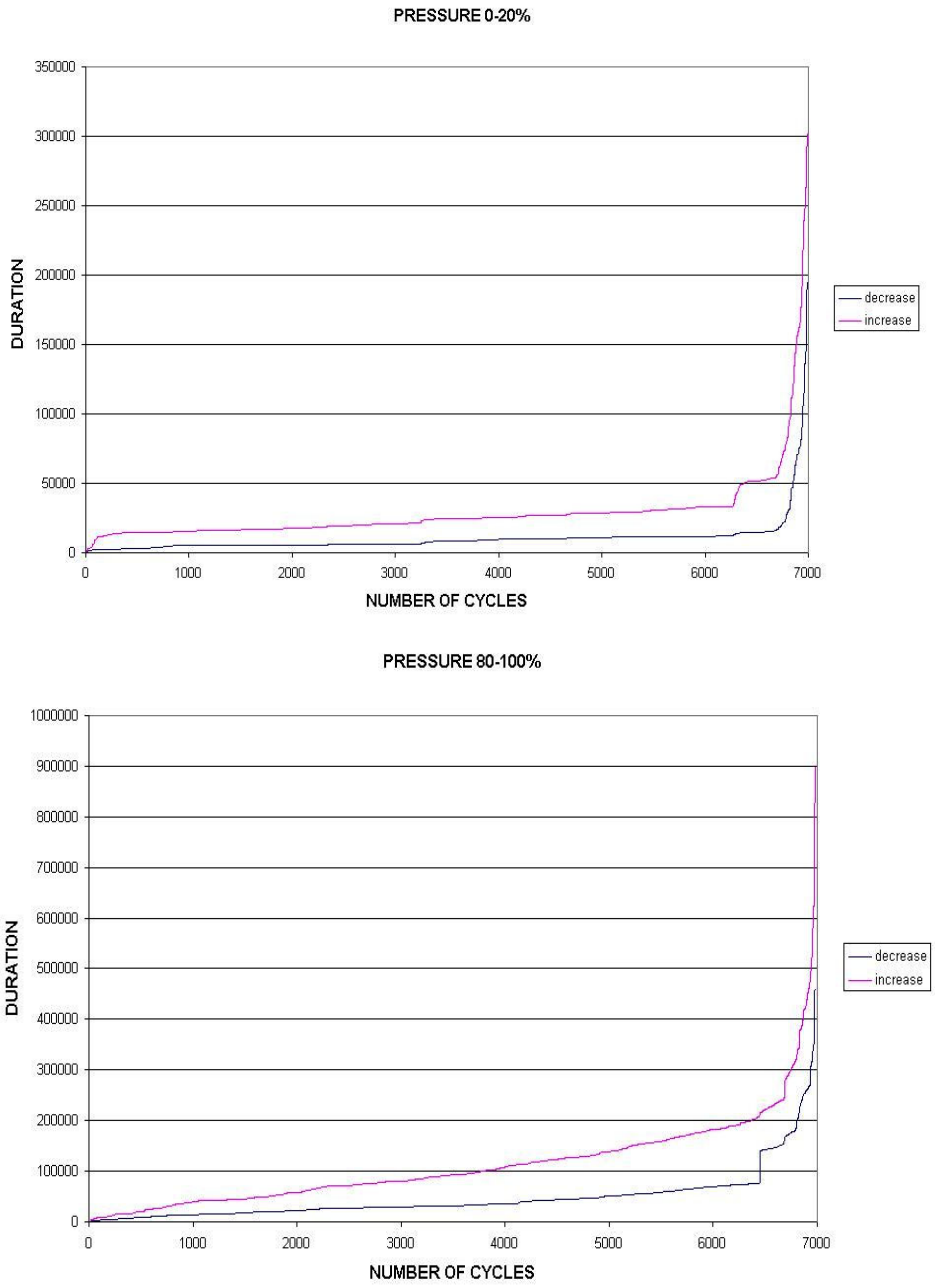

Fig. 8. AE duration summation for increasing and decreasing part of fatigue cycle as a function of number of fatigue cycles for pipe loaded in M III (sample No 004). a) loading range 0 –20% of fatigue load cycle (top): b) loading range 80 – 100% of fatigue load cycle (bottom).

In addition the AE parameter changes with number of fatigue cycles were separately recorded for increasing and decreasing parts of LR. It was noticed that while the parameter values recorded during both parts of loading cycles are the same when the data concern the whole fatigue test of sample, differences took place when AE activity is recorded during selected LR. When higher LRs are considered, parameter summation during load decreasing part is higher in comparison with that which is recorded during load increasing part, while for lower LRs data recorded during load increasing part are higher. Examples are given in Figs. 8a and 8b, where event summation curves during increasing and decreasing parts of loading for 0-20 % and 80-100% of load are presented.

In all the pipes fatigue tested in M III, the oncoming fatigue failure is anticipated by an increase in AE parameter values with the number of fatigue cycles. This increase is observed during the last 7 to 15 percent of fatigue life. In close observation, changes can be noted starting at 50-60% of fatigue life. The general shape of these curves is identical to the classical AE behavior under fatigue of metallic materials or structures.

These changes did not occur in all AE parameters at the same degree. The most pronounced changes are in energy and duration while the weakest was in event summation. On the other hand, the changes in event summation with fatigue cycle are the most regular. When one parameter would be taken into consideration only (for example energy), jumps in diagrams can complicate the diagram interpretation and the fatigue failure prediction could be misleading. Usually the most distinct changes are observed when AE parameters are recorded during low part of LR; however; this cannot be taken as a rule. Therefore, for warning against fatigue failure, more than one AE parameter and more than one LR of fatigue load cycle should be analyzed. Results from this study suggest that increases in AE events, energy and/or duration diagrams vs. time or number of cycles jointly, for upper and lower 20 % of LR are the most useful in warning against fatigue failure. When these two loading ranges of fatigue load cycle are considered both effects of cracking processes (at high loads, giving rise to increased friction AE) and of existing fatigue cracks (at low loads, from friction AE as well) are used for fatigue collapse prediction.

The AE signals, which are produced by processes leading to fatigue collapse, are “hidden” by general AE activity, which took place in all volume of the test piece through the friction following local shearing failure. Many factors, for example components of laminate, laminae configuration and quality and loading conditions, affected this activity. Therefore AE parameter changes with number of fatigue cycles may differ from sample to sample even when they are made from the same material and were underwent to the same loading conditions. These differences can be seen when compare the demonstrated data for sample No 003 (Figs. 6 and 7) with data for sample No 004 (Fig. 9). The number of fatigue cycles to their failure is close to each other while the differences between AE parameters are pronounced. However, for both of them, increases in AE parameters provided the warning against incipient fatigue failure.

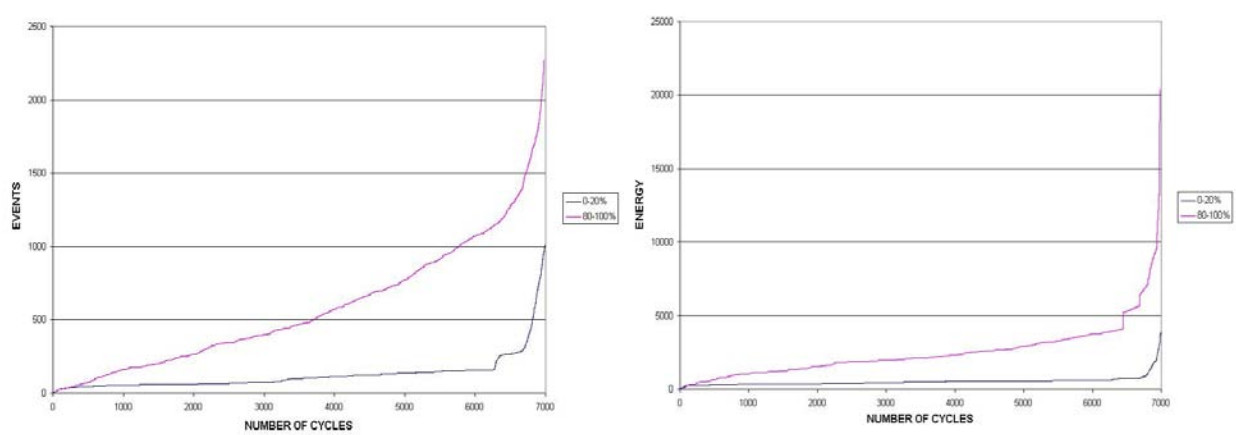

Fig. 9. AE parameters summations as a function of fatigue cycles for different load ranges for GRP pipe loaded in M III (sample 004). a) event summation (left), b) energy summation (right).

Fatigue failure prediction may also be possible by AE signal amplitude vs. the number of fatigue cycles plots. In this type of diagrams, both the increase in AE activity (events rate) and increase in AE parameter values can be seen. The incipient fatigue failure is well indicated when the selected AE parameter is recorded during high or low LRs. An example is shown in Figs. 10a and 10b, where the AE amplitude vs. number of cycles for the upper and lower 20 % of fatigue

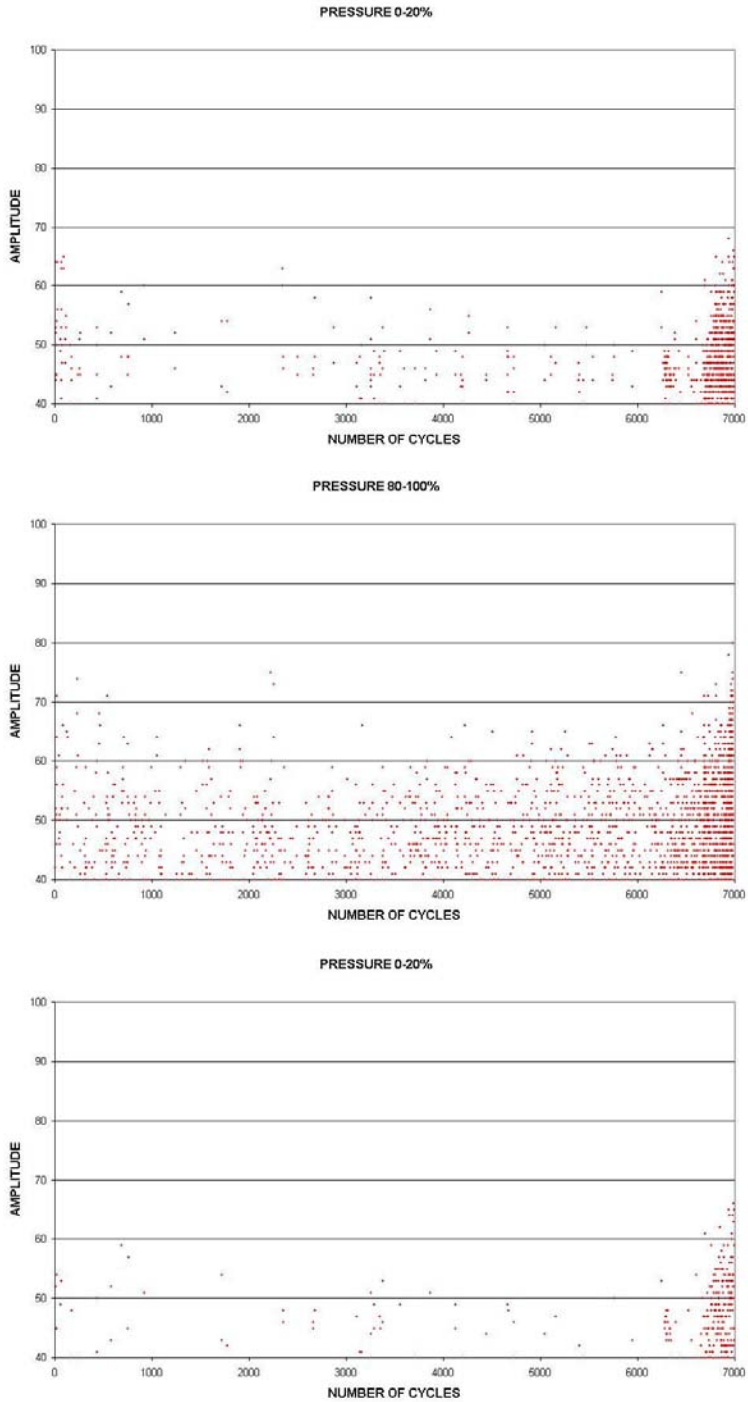

Fig. 10. AE signal amplitudes point graph event and energy summation as a function of fatigue cycles for pipe loaded in M III (sample 004) for loading ranges equal: a) 0 – 20% of fatigue load range, b) 80 – 100 % load range, c) 0 – 20 % load range, decreasing part of cycle only.

loading cycle for sample No. 004, are presented. Results are more distinct when the parameters are recorded during decreasing part of lower 20% of fatigue load cycle as it is shown in Fig. 10c. These again illustrate the role of friction AE in revealing impending failure due to the presence of fatigue damage.

The above procedures need continuous structure monitoring over a long period of time. However, in engineering practice it is important to predict the fatigue collapse when loading history is unknown and, in addition, except fatigue, damages introduced by stress corrosion, impact or wear may lower fatigue and service resistance. When monitoring includes the final fatigue cycles only, the recorded changes in AE parameters may be insufficient for fatigue collapse prediction. In this situation, an alternate procedure is needed. In this study, fatigue loading of selected samples was periodically interrupted and during each pause the loading was held constant for 300 seconds. AE event summation and energy summation recorded for the first and the last load holds are presented in Fig. 11. These diagrams show AE activities during few cycles before pause, during pause and few cycles after pause. The spots in these diagrams indicate the beginning and the end of pauses. During the first pause some stability in AE parameters can be observed and an increase in AE parameters was insignificant, but, in the last one, AE activity is as strong as during fatigue loading before and after. These results indicated that, in fatigue-damaged areas, further damage progression as a result of creep was observed. This phenomenon suggests that in the final part of fatigue life, fatigue damage is serious enough to produce creep damage and fatigue-creep interaction, influencing the durability of laminate

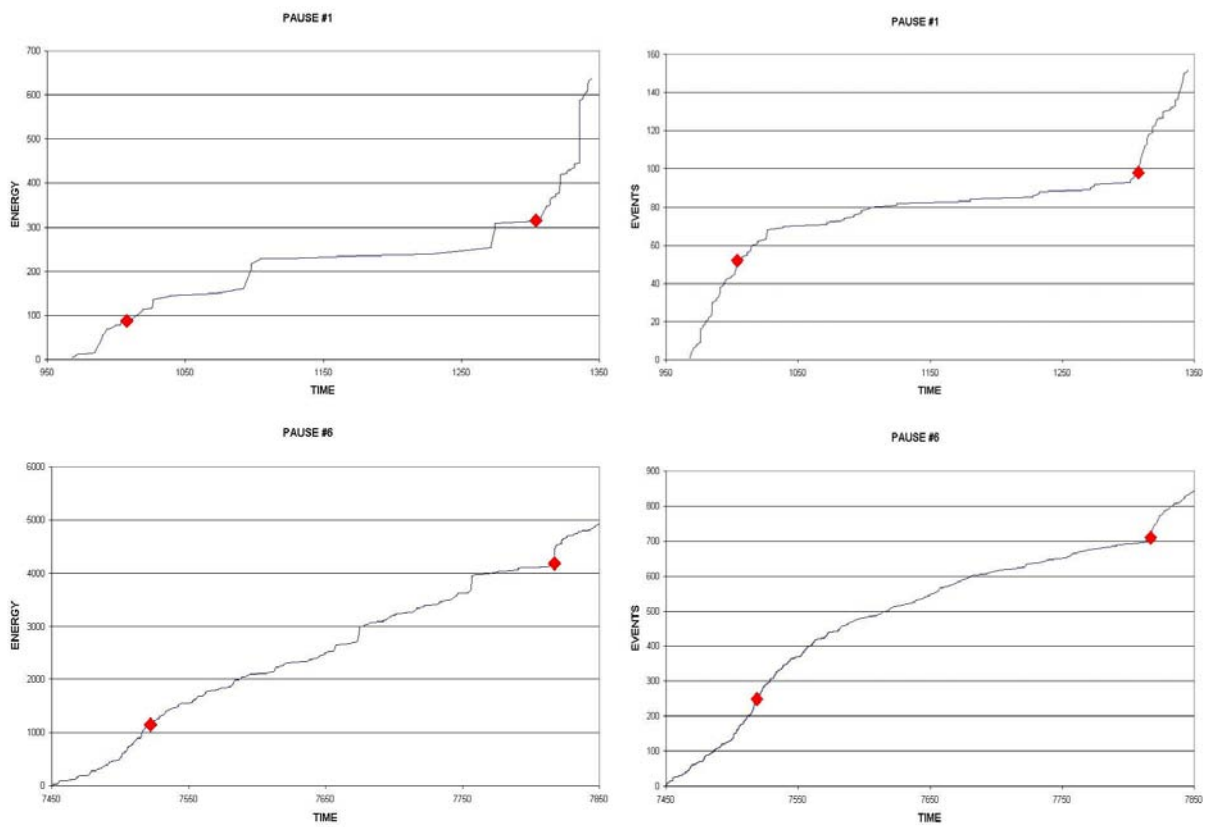

Fig. 11. AE event and energy summation during constant loading holds for pipe loaded in M III (sample No 005 failure after 6990 cycles). a) first pause after 1000 fatigue cycles, b) last pause after 6000 fatigue cycles.

under variable loading conditions. The comparison of AE activity during fatigue loading before pause and AE activity during pause provide the data, which may serve for warning against failure.

3.2 Fatigue in Mode II (Internal pressure loading; $\sigma_H/\sigma_A = 2$*)*

Mode II (M II) loaded pipes initiate laminae cracking as a result of stress component transverse to fiber. This is in contrast to pipes loaded in M III, where the cracking initiation is controlled by shear along fibers. The transverse strength of lamina in tested pipes is comparatively low (14 MPa) and the beginning of cracking, estimated on the basis of laminate theory, is expected at internal pressure in the vicinity of 30 bars. For winding angle $\pm 55^0$ and M II loading, after a relatively small amount of transverse cracking, the load is transferred entirely to the fibers.

To select the internal pressure range for further fatigue tests, the pipes were smoothly pressurized in M II. No protection against weepage was applied. During the pressurization, AE activity was recorded. The AE activity evolution is demonstrated in Fig. 12, where AE event rate and duration point graphs are presented. The loading was stopped at 232 bars. At this pressure transverse cracking together with cracks, which intersect boundaries between laminae, produced complete weepage path and intensive leakage made impossible further pressure increase. AE activity started at pressures in the vicinity of 40 bars, indicating the beginning of failure processes. At pressure exceeding 100 bars, AE intensity decreased leading to local minimum at the pressure of 140 bars. When rubber sleeve protected against leakage, these pipes failed by burst at pressure in the vicinity of 420 bars.

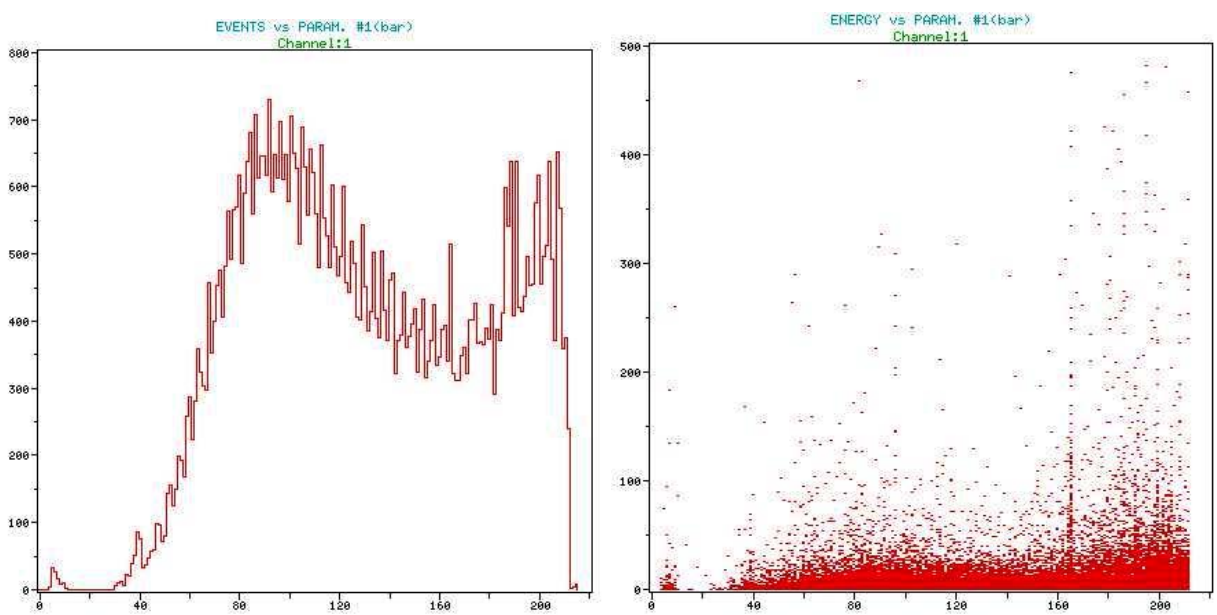

Fig. 12. AE events rate and energy plots vs. pressure (in bars) during smooth pressurization of GRP pipe loaded in M II.

The fatigue tests in M II were performed for maximum pressures in the range from 100 to 140 bars and stress ratio R = 0.1. For these pressure ranges, shear stress component, along fiber in laminae was low and has no influence on crack formation. The maximum of variable pressure,

applied during fatigue in M II, corresponds to 30 % of the burst pressure. It was 40 % higher in comparison with the maximum fatigue pressure in M III. The numbers of cycle up to failure for pipes loaded in M II are given in Table III. As can be seen, fatigue life for both loading modes and maximum applied pressure were close to each other. Nevertheless, the failure mechanisms changed with the loading modes.

Table III Fatigue strength data of tested pipes loaded in M II

Sample No	Pressure in bars		Number of cycles	Failure by
	max	min		
MII/010	212	Smoothly pressurized		Leakage
MII/011	232	Smoothly pressurized		Leakage
MII/012	140	14	854	Leakage
MII/013	140	14	1 000	Leakage
MII/014	140	14	9 853	Leakage
MII/015	120	12	47 028	Leakage
MII/016	120	12	89 231	Leakage
MII/017	100	10	121 789	Leakage
MII/018	100	10	150 000	No leakage

The failure of all pipes loaded in M II occurred by intensive leakage, which exceeded the capacity of applied hydraulic system, making impossible further fatigue loading. Samples loaded in M II exhibited higher scatter in number of cycles to failure than the pipes loaded in M III. For example, the number of cycles to failure varied by a factor of ten between samples 012, 013 and 014. This is because in our M II fatigue tests, failure is not a typical one, where fiber breaking and perforation of pipes wall take place. Instead, the present “fatigue failure” in M II occurred by “opening transverse cracking” of the matrix and through thickness slots that have enough width for liquid to flow out. The cross-sections of pipe wall after fatigue in M II are shown in Fig. 13. During fatigue cycles in M II the width of transverse cracks are changed periodically allowing the penetration of oil into the laminate (see Fig. 13b). This process facilitated the development of weepage paths. However, after the tests and unloading no visible damage on pipe surfaces could be seen.

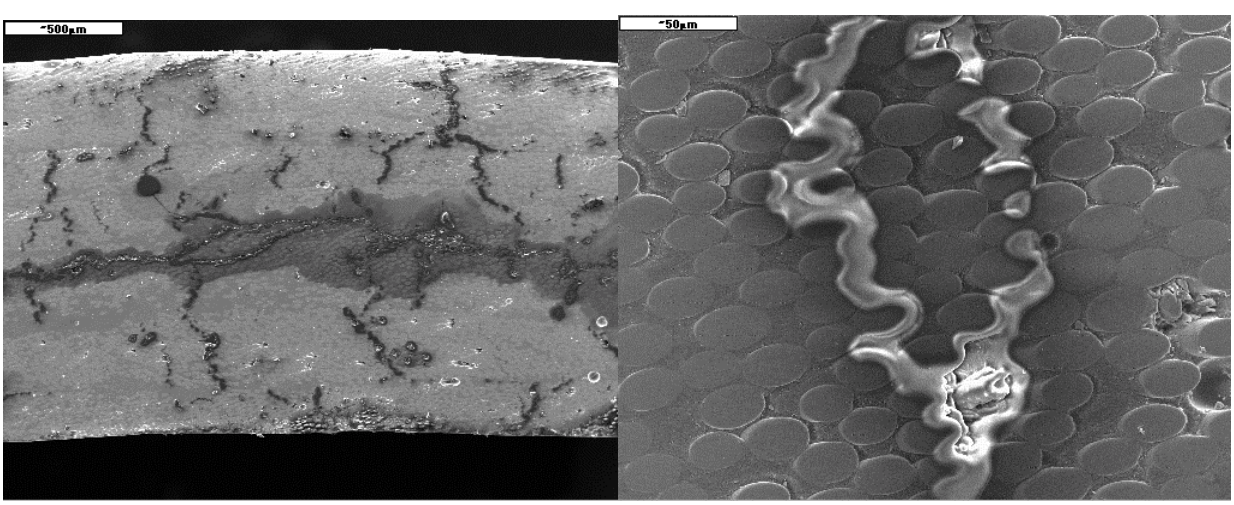

a. Magnification x50; b. Magnification x500.

Fig. 13. Cross-section of pipe wall after fatigue failure in M II loading.

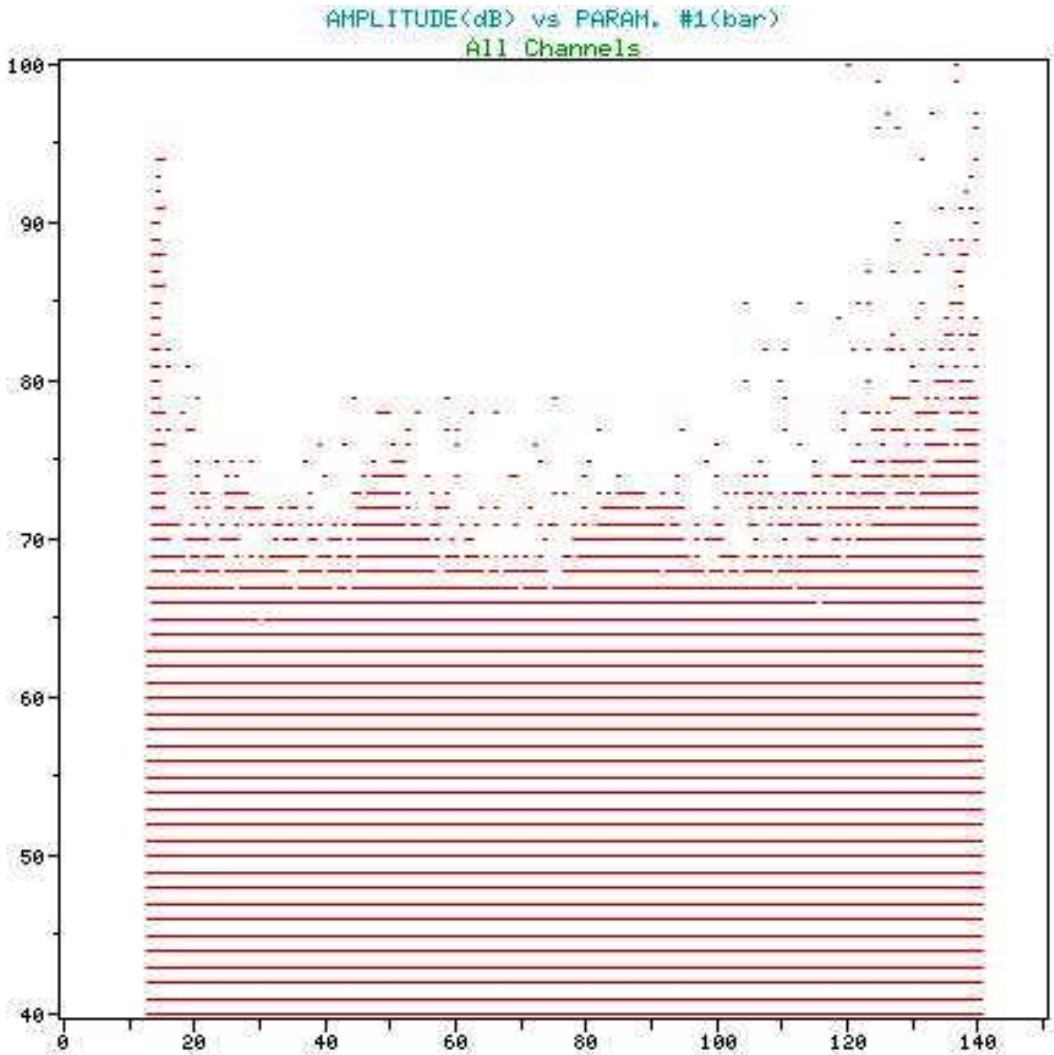

Fig. 14. AE signal amplitude point diagram as a function of pressure for after fatigue in M II.

Complexity of fatigue processes during M II is reflected by AE activity evolution with load changes within the fatigue load cycles and number of cycles. The AE event amplitudes in M II fatigue generally were higher in comparison with the event amplitudes recorded during fatigue in M III. Compare Fig. 5 and Fig. 14. Under M II loading, numerous hits with 80+ dB amplitude were observed. High amplitude events were generated at the maximum or minimum pressure of fatigue cycles (high and low LR). At high pressure ranges, very high amplitude signals occurred at 120-140 bars, but 80+ dB signals started at about 100 bars or higher, as shown in Fig. 14. The high amplitude hits were generated at different parts of fatigue cycles, as demonstrated in Figs. 15 and 16. Here, event summation, energy summation and energy point graphs are plotted against the number of cycles for the increasing and decreasing parts of fatigue loading. The events with amplitudes in the range from 80 to 100 dB appeared during the first 20% of loading cycles only. That is, most strong events occurred at the beginning and between 800 and 2100 cycles. However, there are differences in number, energy and duration depending on whether the signals were recorded during the increasing or decreasing part of a load cycle. High amplitude AE signals first appeared during the initial loading cycles in their increasing part. Although some high amplitude signals also occurred during the decreasing part of cycles, their energy was significantly lower. It is likely that during increasing parts of a load cycle the AE events were

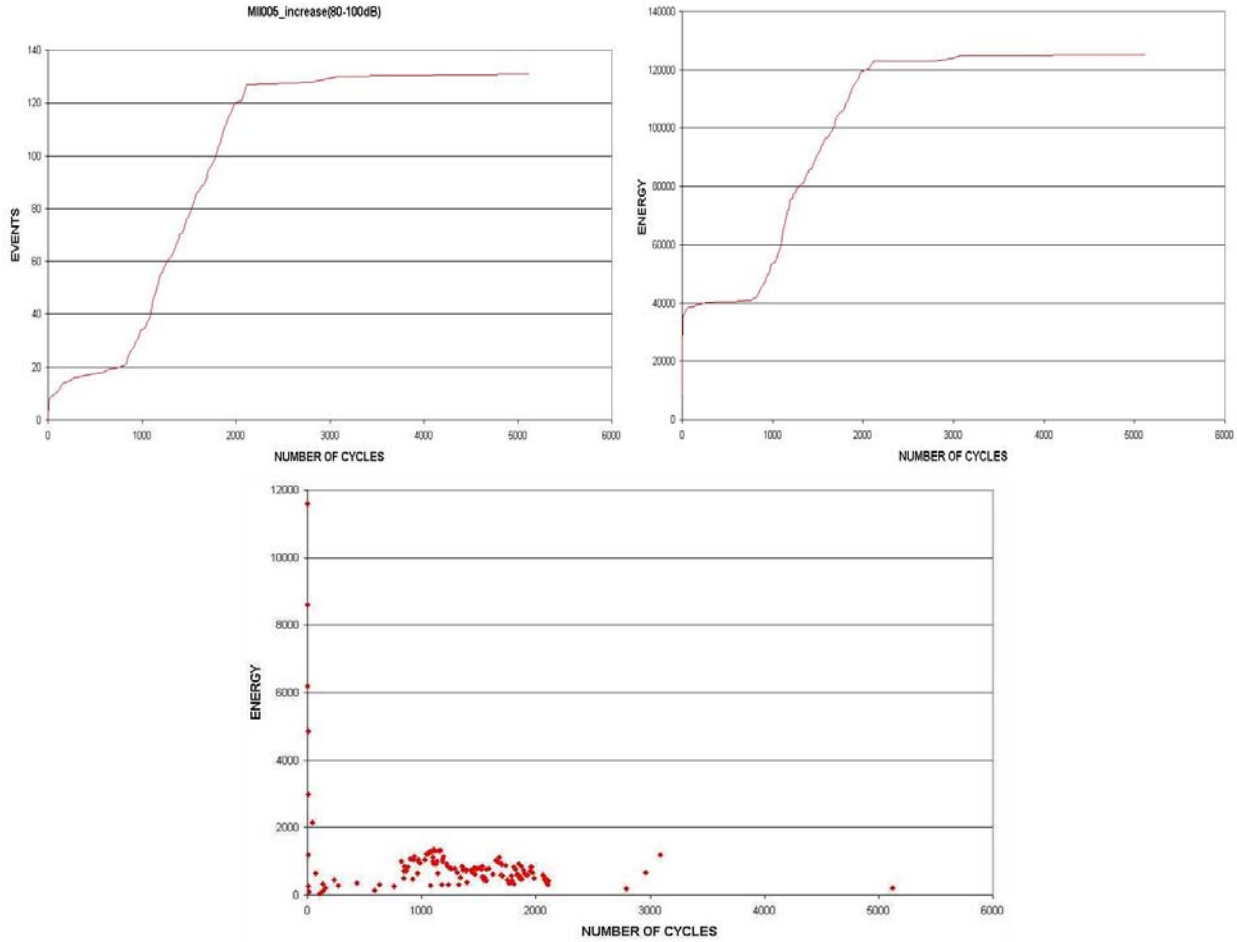

Fig. 15. AE high amplitude events (in the range 80 to 100 dB), energy summation and energy graphs vs. number of cycles for pipes loaded in M II fatigue. Increasing part of loading cycle.

generated by transverse cracking processes while those produced during decreasing parts of a load cycle were attributed to the friction of crack surfaces. Subsequently, low activities of strong signals were observed until 800 fatigue cycles have passed. From 800 to 2100 cycles, high amplitude hits appeared again in abundance (up to the second loading pause). Beyond this, almost no hits with amplitude exceeding 80 dB were recorded. This is shown in the energy plots as well. The data demonstrates that serious damage took place during the first cycles of fatigue and during a limited cycle interval, as indicated by very high amplitude signals.

For the pipes fatigue-loaded in M II, the filtration of AE signals significantly affected the duration and energy of AE events. When pipes were fatigued in M III, in contrast, the filtration did not influence recorded AE parameters. The influence of filtration on AE parameters is demonstrated in the duration vs. number of cycles plots (see Fig. 17 and Fig. 18). Beyond about 10 % of fatigue life, AE signals, which are recorded by the channel with 20 kHz high-pass cut-off, started to divide themselves into two groups with different duration. One group had duration below 40,000 μs and the other above 100,000 μs. Duration of the second group increased with number of cycles and, as shown in Fig. 17, after 40% of fatigue life, it increased to the range from 200,000 to 250,000 μs. At the same time, the duration of AE signals recorded by the channel with 100 kHz high-pass filter was mostly below 10,000 μs and did not exceed 50,000 μs (see Fig. 18). Filtration removed the low frequency components with extended signal length. It is

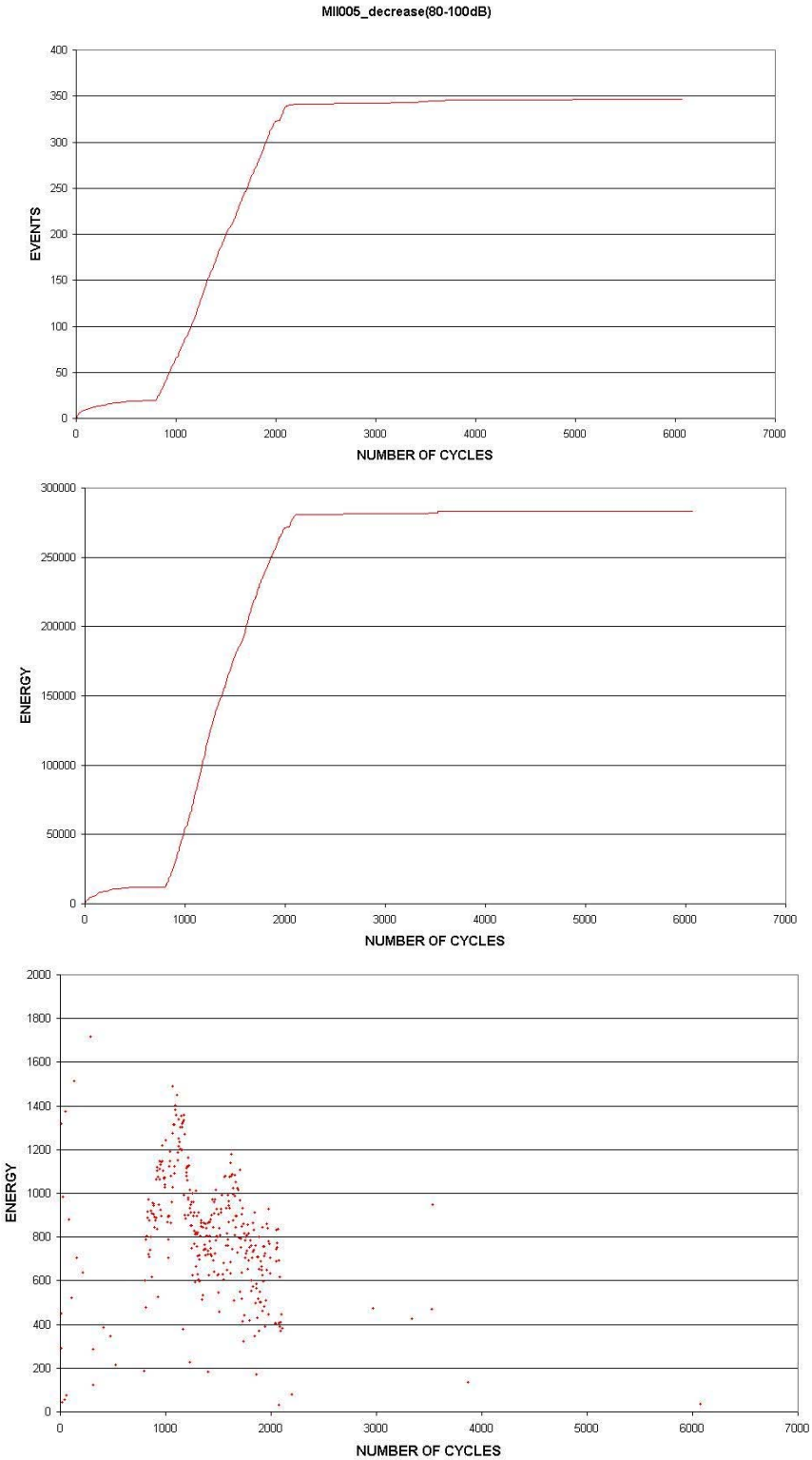

Fig.16. AE high amplitude events (in the range 80 to 100 dB), energy summation and energy graphs vs. number of fatigue cycles for pipes loaded in M II and decreasing part of loading cycle.

noticed that the long-duration AE signals appear in a narrow LR from 20 to 50 % (Fig. 19), exhibiting the energy values of more than 500. In comparison, AE signals during LR up to 20% had energy values less than 30, while those near the maximum load (LR: 80-100%) were more consistent and of intermediate strength. Amplitudes of these signals were mainly contained

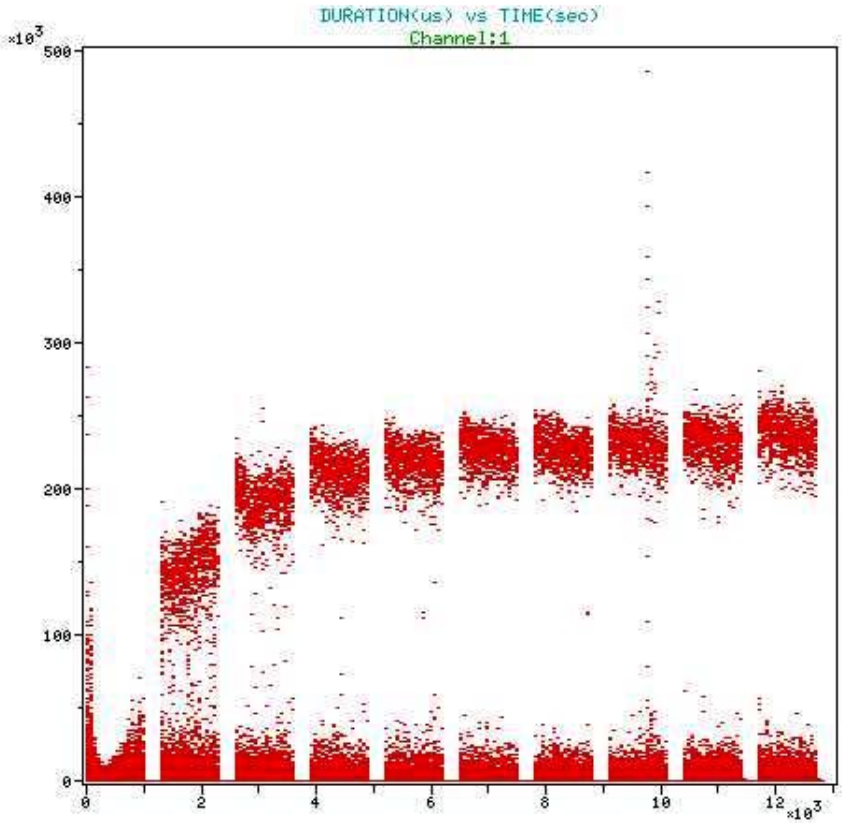

Fig. 17. AE duration vs. number of fatigue cycles (time) recorded by 20 kHz HP channel for pipe loaded in M II

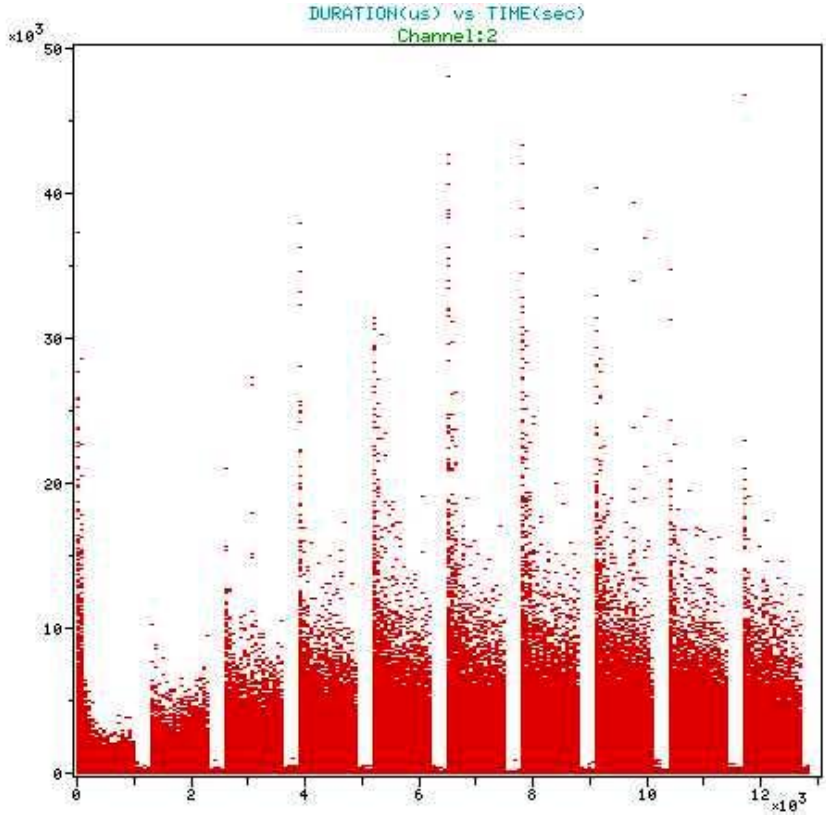

Fig. 18. AE duration vs. number of fatigue cycles (time) recorded by 100 kHz channel for pipe loaded in M II.

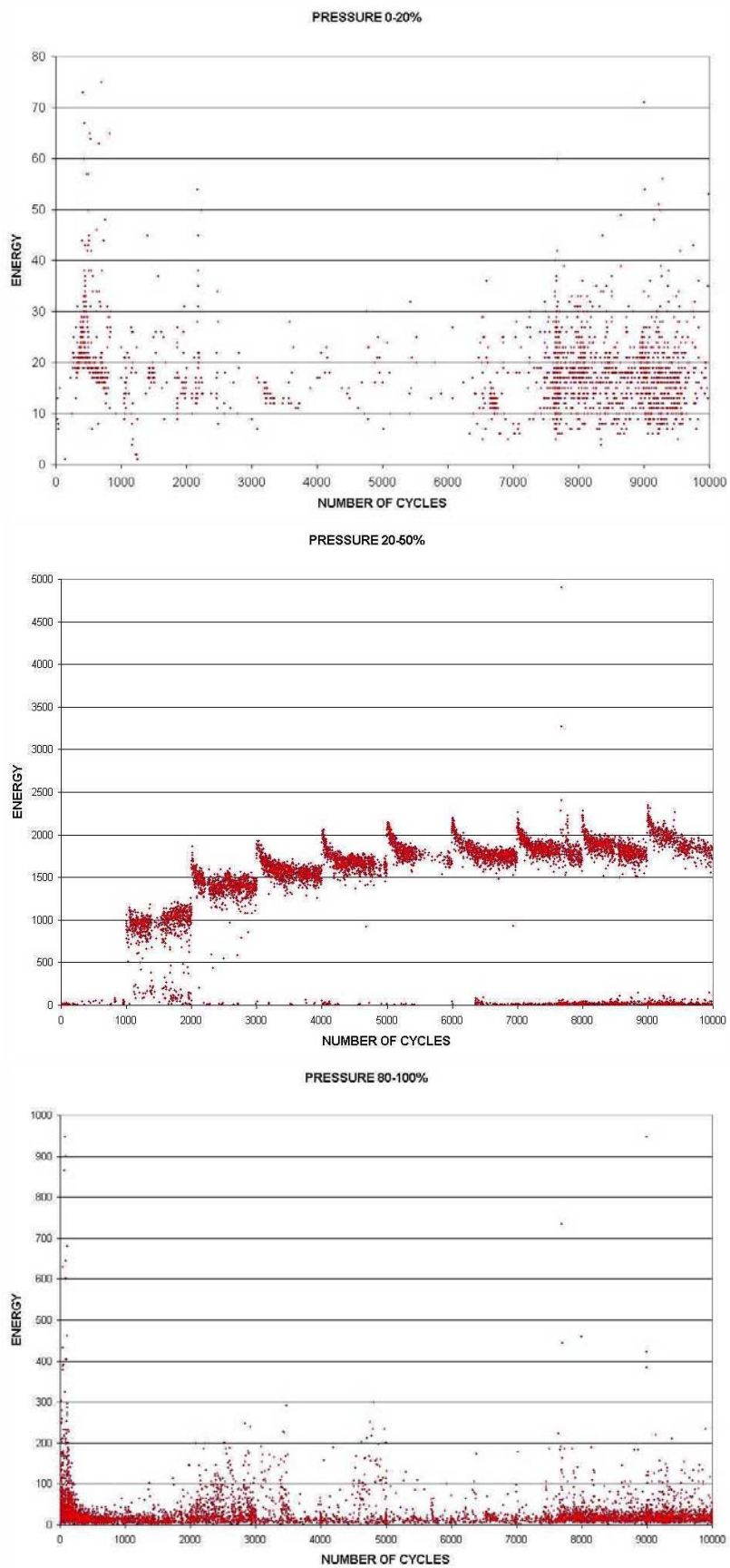

Fig. 19. AE energy vs. number of cycles for different load ranges of fatigue load cycle recorded by 20 kHz HP channel for pipe loaded in M II.

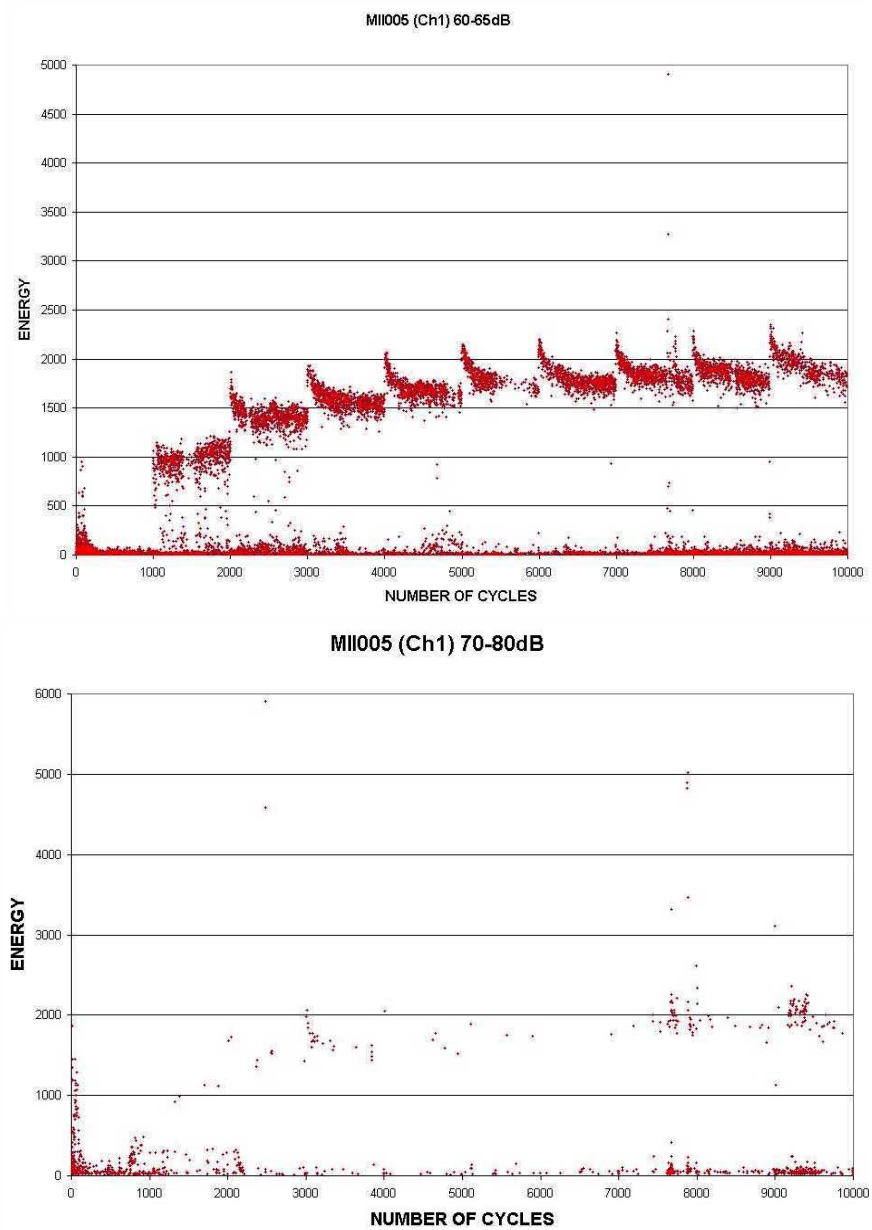

Fig. 20. AE energy point graphs vs. number of cycles for two amplitude ranges. Unfiltered channel for pipe loaded in M II. a) amplitude range 60-65dB (top), b) 70-80dB (bottom).

within the range from 60 to 65 dB (Fig. 20a), although some had higher amplitudes to 80 dB (Fig. 20b).

It should be noticed that when fatigue cycles were interrupted with pauses, during which a constant load was maintained, AE signal duration increased during first cycles after each pause. This was especially evident in 100-kHz-filtered channels (see Figs.17 and 18).

When leakage was not protected in M II fatigue, no fiber breakage was observed and therefore no AE signals from fiber cracking or friction of fractured fibers can be expected. Possible sources of AE activity in tested pipes loaded in M II fatigue loading are transverse resin cracking and fluid migration inside composite during loading. This is because M II loading

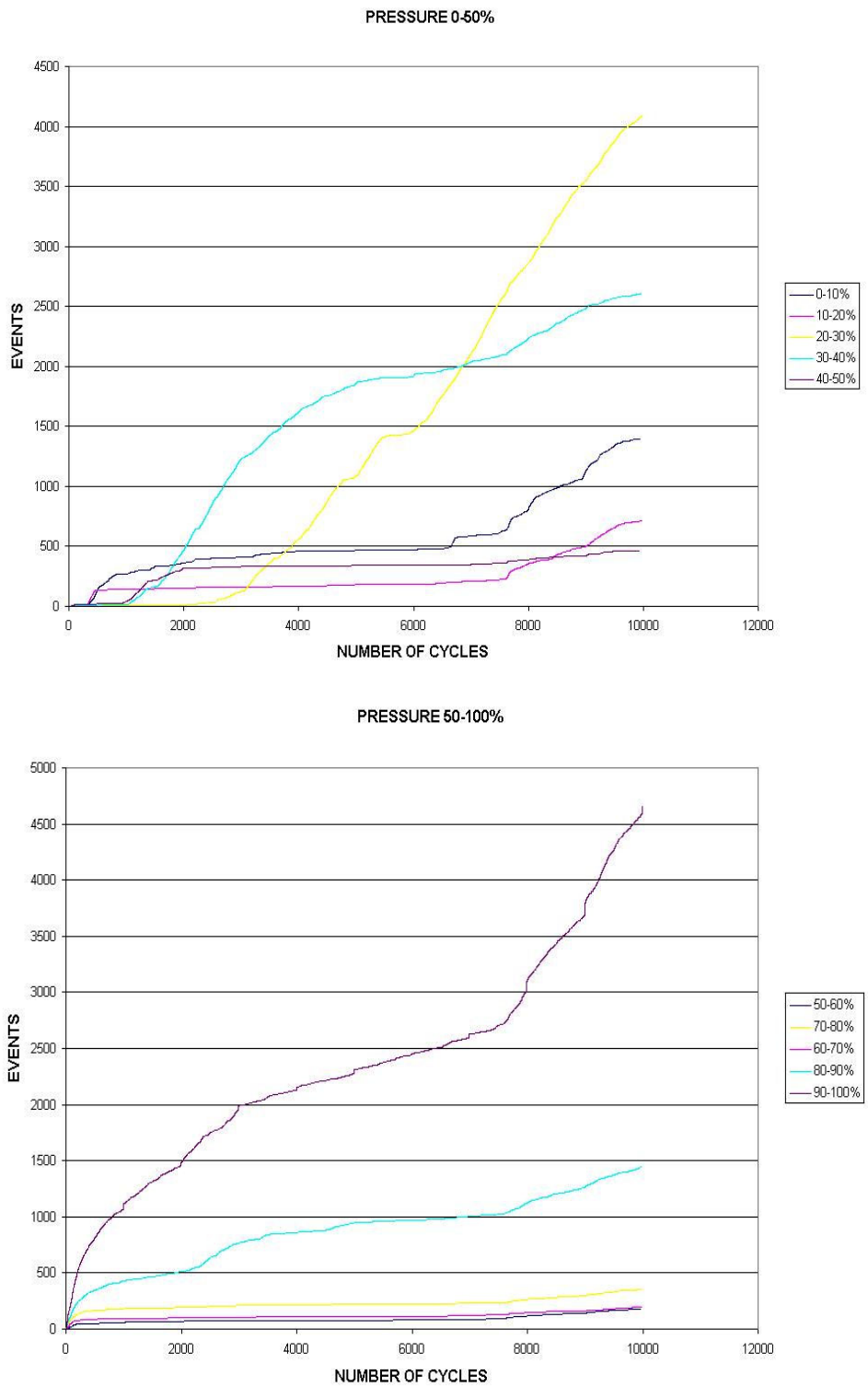

Fig. 21. AE event summation as a function of number of fatigue cycles recorded by unfiltered channel for pipe loaded in M II. a) load ranges 0 – 50% of fatigue load cycle (top), b) load ranges 50 – 100% of fatigue load cycle (bottom).

produces no fiber rotation and only "opening type" of transverse cracking in laminae takes place. AE signals by friction are also expected when cracking between laminae occurs.

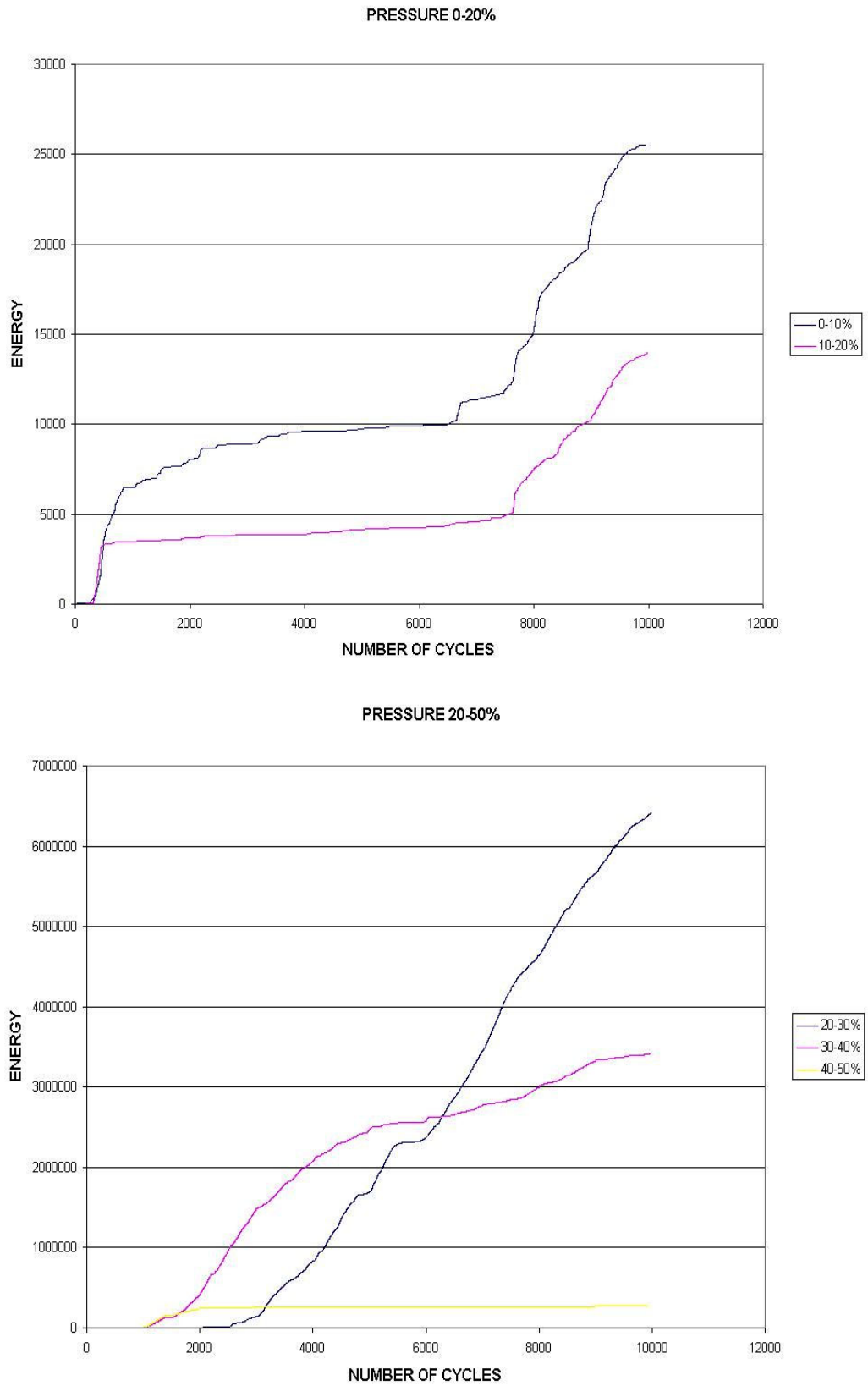

Fig. 22. AE energy summation as a function of number of fatigue cycles recorded by 20 kHz HP channel for pipe loaded in M II. a) load ranges 0 – 20% of fatigue load cycle, b) load ranges 20 – 50% of fatigue load cycle.

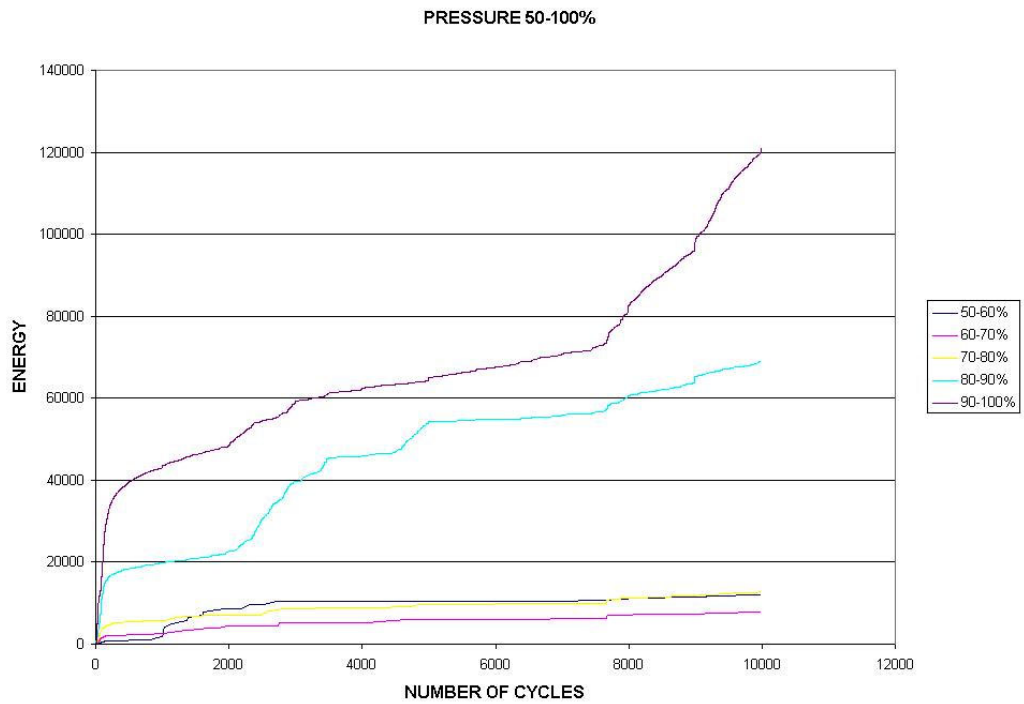

Fig. 22. AE energy summation as a function of number of fatigue cycles recorded by 20 kHz HP channel for pipe loaded in M II. c) load ranges 50 – 100% of fatigue load cycle.

The observed AE signals are dominated by very long duration (50-250 ms) signals, especially from 20 kHz-filtered channels. These appear to be produced by one type of AE source, which are related to oil penetration into transverse resin cracks and interlaminar cracks upon loading. This is consistent with microstructural findings of Fig. 13. Resin cracking certainly generates AE, but is unlikely to have signal duration more than several ms. Here, we observe 50-250 ms duration signals that cannot be attributed to cracking. It is possible that such cracking AE contributed to those signals observed in the first few hundred cycles (see Fig. 19, 80-100% LR).

We are interested in predicting incipient fatigue failure, although in M II loading only produces massive weepage. Toward this objective, AE parameter summations as a function of fatigue cycles have been analyzed. The data were recorded for different LR of fatigue load cycle separately. Changes in event summation with number of cycles are presented in Fig. 21. This figure reveals that AE events summation for several LRs of fatigue load cycle increased at the end of fatigue life. Specifically, the summation curves started to rise (or showed a knee) at 65 to 77% of the fatigue life for 10, 20, 40, 90 and 100% LRs. This trend was most clearly exhibited for 100%LR curve, but the two lowest LRs also indicated distinct knee behavior. More pronounced changes are observed in energy summation for the same three LRs, as shown in Fig. 22. Increase in AE activity took place after 75% of fatigue life. This data is from the 20-kHz-high-pass channel. Most of AE energy is attributed to very-long-duration AE activity, which occurs in narrow LR of 20-40 % of fatigue load cycle. However, in this LR, no change in energy plots is observed. This feature implies that these AE events are related to oil penetration toward interlaminar cracks, rather than weepage through transverse resin cracks. The latter contributes to oil leakage that defines fatigue failure in this loading mode and is closely related to AE emitted during the low and high LRs. The incipient fatigue failure is better indicated by changes in AE event summation and energy summation vs. number of fatigue cycles plots when AE activity was recorded by 100-kHz-high-pass filtered channel. These plots are presented in Fig. 23 and

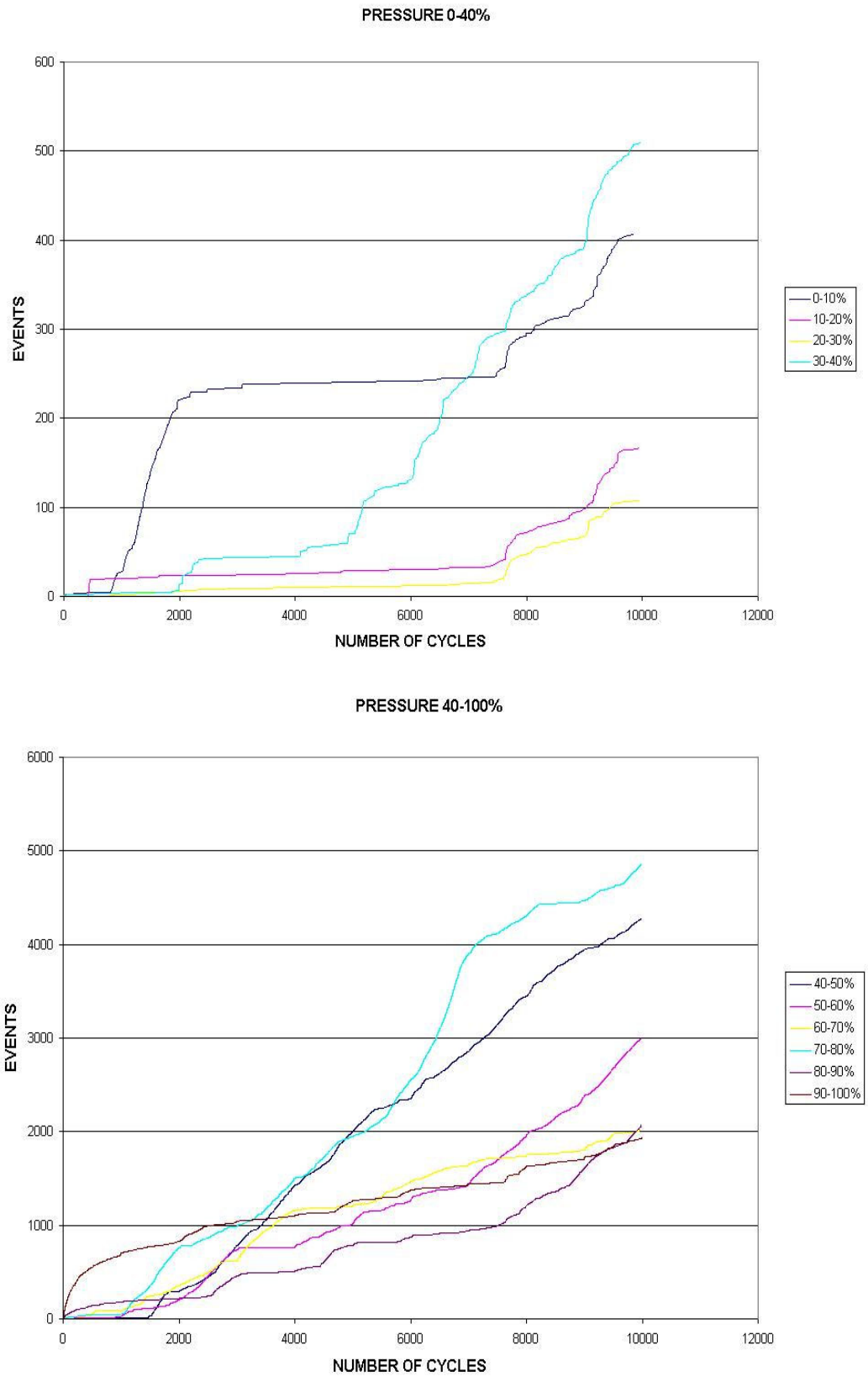

Fig. 23. AE event summation as a function of number of fatigue cycles recorded by 100 kHz HP filtered channel for pipe loaded in M II. a) load ranges 0 – 40% of fatigue load cycle, b) loads ranges 40 – 100% of fatigue load cycle.

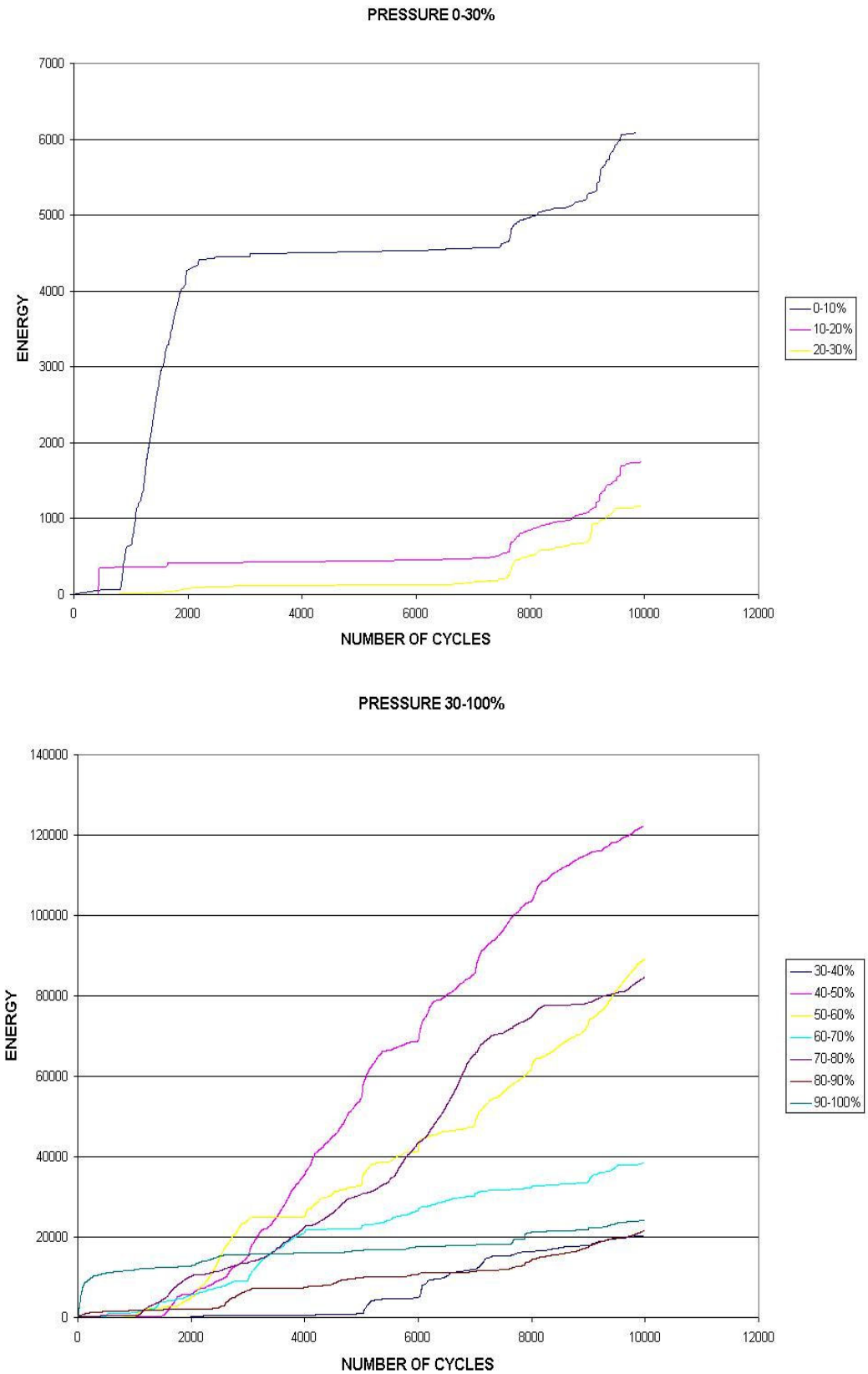

Fig. 24. AE energy summation as a function of number of fatigue cycles recorded by 100 kHz HP filtered channels for pipe loaded in M II. a) load ranges 0 – 30% of fatigue load cycle, b) load ranges 30 – 100% of fatigue load cycle.

Fig. 24, respectively. The changes in AE activity, which can serve as warning against fatigue failure, are found in low LRs of fatigue load cycle (Fig. 24a). Detectable changes are absent when data are recorded during higher LRs (Fig. 24b) or for all of the fatigue cycle. This finding again emphasizes the importance of proper filtration in fatigue damage monitoring by AE.

The changes in AE activity in selected LR of fatigue load cycle are useful in assessing the incipient failure. In M II loaded fatigue, the loss of pipe strength is not so serious because no fiber breakage occurs. This is confirmed by low AE activity, when constant load was maintained during a pause in fatigue loading.

The above methodology for incipient fatigue failure of laminated composites was developed on the basis of experiments performed on tubular specimens and laboratory generated data. The sample dimensions were significantly smaller than typical dimensions of engineering structures. In large heterogeneous structures, laboratory data application to full-size structure testing should be applied with caution [15,21]. Large dimensions, complicated geometry and signal attenuation can significantly change the waveforms. However, this testing procedure should be valid for local failure of larger structures.

4. DISCUSSION

AE activity has been monitored during fatigue of filament wound pipes. The analysis of AE signals aims at field-testing development for warning against fatigue failure. We studied two loading modes. In the first fatigue mode, (M III), shear along fibers in lamina was dominant. The fatigue failure occurred by shear fracture at the fiber-matrix boundaries. This leads to secondary failure of fiber breakage (in bending on the next lamina), resin crumbling and, finally, wall perforation. In the second fatigue mode, (M II), fatigue process was controlled by the transverse-to-fiber stress component. Because no protection against fluid leakage was applied in M II, fatigue induced matrix cracking led to intensive leakage on all the surface of pipe, defining the failure point. In M II, no massive fiber breakage and wall perforation was observed.

A large scatter in AE parameters allowed no quantitative relationship between AE parameters and fatigue durability. The scatter for fatigue cycles to failure was also substantial, even when the loading conditions were the same and tested pieces were cut off from the same tube.

High amplitude hits appeared weakly dependent on number of fatigue cycles both in M III and M II fatigue modes. Observed high amplitude hits both at low and high stresses of fatigue load cycle indicate that not only fracture processes produce high amplitude hits. These results demonstrate that high amplitude hit criterion cannot be applied or should be applied with caution in fatigue testing of composites.

In this study, we anticipated that waveforms recorded by broadband sensors depend on AE sources. Careful examination showed waveforms or their fast Fourier transforms are insensitive to loading modes and signal origin [17]. Beside the usual reasons, it is likely that AE signals are dominated by a single source for each loading mode; that is, friction for M III and oil penetration in M II. Therefore, waveform analysis cannot identify the damage modes of composite laminate structures.

Fatigue damage, however, is revealed by an increase in AE parameters that were recorded for selected LR of fatigue load cycle. The analysis indicated that for pipes loaded in M III, AE parameter increasing with number of fatigue cycles took place both at the high and low LRs. For

pipes loaded in M II, AE parameters increased with fatigue cycles only at low LRs. In both modes, AE parameters are indicative of secondary AE sources, rather than the primary sources (shear cracking or fiber bend fracture in M III and transverse resin cracking in M II). It is also important to define the "failure" in warning against incipient failure since this varies depending on the loading mode applied.

The results of these studies demonstrated that many factors strongly affect acoustic emission activity from GRP laminates. Serious scatter in AE parameters between samples with the same loading conditions is observed even when test pieces were cut off from the same tube. The complementary tests performed on similar pipes and similar failure envelope with different matrix resin indicated different AE behavior. In addition the waveform of AE signals when they travel through laminate is altered, making it difficult for AE source identification. All these variability in AE parameters complicate the development of general fatigue failure criteria on the basis of critical value of AE parameters. Damage accumulation as a result of fatigue in laminates and laminated structures can be characterized by changes in AE activity with the number of cycles (or time). However, the useful information about incipient fatigue failure is "hidden" in a narrow cyclic loading range. Also different filtration of AE signals should be explored. The performed experiments demonstrated that the most sensitive to fatigue damage is AE activity, in a narrow LR at bottom and at top of fatigue load cycles. In combination with zonal localization of AE sources, the present analysis scheme allows the prediction of incipient fatigue failure in samples and in laminated structures. Further studies are necessary with other types of composite laminates and more complicated loading modes.

5. CONCLUSIONS

Damage accumulation during combined fatigue loading has been monitored by acoustic emission (AE) technique in filament wound pipes. The tests made on epoxy resin-E-glass-fiber filament wound pipes subjected to two loading modes: M II and M III. Fatigue processes were controlled either by transverse (M II) or shear (M III) stress component in reference to fiber direction. The damage evolution with fatigue cycles for each loading mode was estimated on the basis on acoustic emission parameter analysis. Based on changes in AE activity for different fatigue loading ranges during fatigue progression, incipient failure can be predicted. This procedure is valid for both applied loading modes in spite of the differences in failure modes. The approaching fatigue failure is detected by changes in selected AE parameters, when samples exceeded 70-90% of fatigue life. It was also found that high amplitude hit criterion and waveform analysis were ineffective, as secondary AE sources were predominantly detected.

ACKNOWLEGMENT

This research was supported by the U.S.-Poland Maria Sklodowska-Curie Joint Fund II, administered by the US Department of Energy. Foundry Research Institute, Krakow, Poland, provided technical support. The authors are grateful for all the financial and technical assistance.

REFERENCES

1. Williams J.H., Lee S.S., Promising Quantitative Nondestructive Evaluation Techniques for Composite Materials, Materials Evaluation **43**, 1985, pp. 561-565.

2. Jeng J.S., Ono K., Yang J.M., Fracture Mechanism Studies of Carbon/PMR-15 Composites by Acoustic Emission, Journal of Acoustic Emission **8**, 1989, pp.151-165.
3. McNally D.J., Inspection of Composites rocket Motor Cases Using Acoustic Emission, Materials Evaluation **43**, 1985, pp. 728-732.
4. Golaski L., Kumosa M., Hull D., Acoustic Emission Testing of Filament-Wound Pipes under Repeated Loading, Journal of Acoustic Emission **1**, 1982, pp. 95-113.
5. Recommended Practice for Acoustic Emission Testing of Fiberglass Reinforced Plastic Resin (RP) Tanks/Vessels. Reinforced Plastics/Composites Institute, the Society of the Plastic Industry, Inc New York, 1982. Revised and Republished, 1987.
6. Fowler T.J., Blessing J.A., Strauser F.E., Intensity Analysis, AECM-4 Fourth International Symposium on Acoustic Emission From Composite Material, Seattle, ASNT, 1992, pp. 237-242.
7. Williams R.S., Reifsnider K.L., Investigation of acoustic emission during fatigue loading of composite specimens, Journal of Composite Materials, **8**, 1974, 340-355
8. Hamstad M.A., Chiao T.T., Acoustic emission from stress rupture and fatigue of an organic fiber composite, Composite Reliability, ASTM STP 480 American Society for Testing and Materials, 1975, pp.191-201
9. Williams R.S., Reifsnider K.L., Real-time Nondestructive evaluation of composite materials during fatigue loading, Materials Evaluation, **35**, 1977, pp.50-54
10. Awerbuch J., Gorman M.R., Madhukar M., Monitoring damage accumulation in filament wound graphite/epoxy laminate coupons during fatigue loading through acoustic emission, First Int. Symp. On Acoustic Emission from Reinforced Composites, SPI, New York, 1983, Session 2, pp. 1-30.
11. Eckles W.E., Awerbuch J., Monitoring acoustic emission in cross-ply graphite/epoxy laminates during fatigue loading, Journal of Reinforced Plastics and Composites, **7**, 1988, pp.265-283
12. Roy C., Ghorba M., Monitoring progression of mode II delamination during fatigue loading through acoustic emission in laminated glass fiber composite, Polymer Composites **9**, 1988, pp. 345-351
13. Awerbuch J., Ghaffari S., Analysis and characterization of the acoustic emission associated with matrix splitting during fatigue loading through acoustic emission in notched unidirectional graphite/epoxy composite, Journal of Reinforced Plastics and Composites, **7**, 1988, pp.245-264
14. Henriksson A., Thesken J.C., Acoustic emission and residual strength in fatigue loaded notched carbon/epoxy composites, Fifth Int. Symp. On Acoustic Emission from Composite Materials, Sundsvall, Sweden, ASNT 1995, pp. 81-90
15. Hamstad M.A., An examination of acoustic emission evaluation criteria for aerospace type fiber/polymer composites, AECM-4 Fourth International Symposium on Acoustic Emission From Composite Material, Seattle, USA, ASNT, 1992, pp. 436-449.
16. Schmidt J., Baran I., Golaski L., Failure behavior of gass fabric laminates in dependence on resin matrix and temperature, First Int. Conf. "Integrity Reliability, Failure, University of Porto, Portugal, 19-22 July, 1999, pp.56 –57.
17. Golaski L., Gebski P., Baran I., Ono Kanji, Waveform analysis of acoustic emission during pressurization of glass-fiber composite pipes, Journal of Acoustic Emission, **17**, 1999, pp. S37-S44
18. Puck A., Zur Beanspruchungund Verformung von GFK - Mehrschichtenverbund - Bauelementen, Kunstoffe, **57**, 1967, pp. 284-293, 573 - 582 and 965 - 973.
19. Puck A., Schneider W., On failure mechanisms and failure criteria of filament-wound glass-fibre/resin composites, Plastics and Polymers, **59**, 1969, pp.33 – 37.
20. Perreux D., Joseph E., Effect of frequency on the fatigue performance of filament-wound pipes under biaxial loading, Composites Science and Technology, **57**, 1997, pp. 353-364.

21. Fowler T.J., Revisions to the CARP recommended practice for tanks and vessels. AECM-5 Fifth International Symposium on Acoustic Emission From Composite Material, Sundsvall, Sveden, ASNT, 1995, pp. 263-271.
22. Leszek Golaski, Pawel Gebski, "Diagnostyka mostu kablobetonowego metod_ emisji akustycznej", accepted for presentation during conference Diagnostyka i badania mostów, Opole czerwiec 2001 (in Polish).

EWGAE 2002

25-th European Conference on Acoustic Emission Testing

First Announcement

September 11 - 13, 2002, Prague, Czech Republic

CONFERENCE WILL BE ORGANISED BY.

- European Working Group on Acoustic Emission
- Czech Society for Non-destructive Testing (Acoustic Emission Working Group)
- Czech Technical University in Prague
  Bmo University of Technology

Prague, a city with over a thousand-year history, was established and developed at the intersection of strategic routes connecting key centres on the European continent. Its leading position and favourable climate led to the successful development of trade, arts and crafts, scientific research and knowledge. The past centuries have left their mark here primarily in art and architecture. Through the course of time, Prague has gained a reputation as a major European centre of culture, education and humanism. In recent years, Prague has become a top tourist destination and has been recognised by UNESCO as a gem of the world's cultural heritage. The unique magic of our city is down to the outstanding quality of its architectural sights and to a harmonious relationship between the various historical styles. It is this harmony that helps to create an environment of mutual understanding, tolerance, respect and partnership.

EWGAE 2002: European Working Group on Acoustic Emission

The European Working Group on Acoustic Emission (EWGAE) was founded in 1971 to exchange information with particular emphasis on scientific and engineering developments of Acoustic Emission

Organizing Committee invites all companies to active participation through corporate sponsorships. Corporate sponsors are sought to host evening reception

Language: English will be the only official language of the conference .

Call for papers:

Authors are invited to contribute papers on the areas of conference topics (in both oral and poster session)

Deadlines:

October 31, 2001	• pre-registration, submitting paper abstract (200-300 words)
November 2001	• notification of acceptance, second call for papers
May 31, 2002	• full papers, preliminary payment
August 2002	• announcement of the final programme
September 11-13, 2002	• Conference

Further information on web site:

http://www.cndt.cz
E-mail: cndt@cndt.cz

Conference Topics:

AE utilisation in material engineering
AE signal detection
AE signal processing
Localisation of defects
Practical applications of AE technique
AE in civil engineering and geology
AE in transport engineering
Standardisation and certification in the area of AE
Developments in AE instruments and sensors
Software
Others

Accompanying Actions:

Get-together party
Sight-seeing tour
Lady's programme

Scientific Committee:

Mohammed Cherfaoui	France
Philip Cole	UK
David Dornfeld	USA
Tomasz Boczar	Poland
Len Rogers	UK
Joachim Sell	Germany
Josef Sikula	Czech Republic
Peter Tscheliesnig	Austria
Martine Wevers	Belgium
Jan Zizka	Czech Republic

National Organising Committee:

Vaclav Svoboda	Chairman
Petr Benes	
Jifi Blaha	
Pavel Mazal	
Jaroslava Polednova	Secretary

FIRST CALL FOR PAPERS

The 16th International Acoustic Emission Symposium (IAES-16)

November 12 – 15, 2002

The University of Tokushima, Tokushima, JAPAN

Topics to be discussed at the symposium (IAES-16) will cover all the areas of acoustic emission testing, including: **Materials Research, Structures, Manufacturing, Diagnostics, Instrumentation, Code and Standards, Applications to Medical Field, Geo-structures, Civil Engineering and so on.**

Call for Papers

Prospective authors are requested to submit title, author's names, affiliation and address by fax or e-mail with an abstract of 100-200 words with key words. The deadline for submission of abstract is **April 30, 2002**. The official language of the symposium and the proceedings will be English.

Time Table

April 30, 2002 Deadline for arrival of abstract.
June 30, 2002 Notification of acceptance and instruction for authors.
August 31, 2002 Deadline for full papers. Registration and remittance of registration fee.
September 30, 2002 Second announcement and program.

Note

Papers will be included in the symposium proceedings only if the authors have definitely registered and made a remittance before August 31, 2002.

Venue

The symposium will be held at the University of Tokushima to which it takes 2 hours and a half by limousine bus from the Kansai International Airport near Osaka. Tokushima is a small city and famous for the " Awa dance", ethnic dance, the Naruto tidal vortex, the indigo dying and so on. We have some sightseeing programs and make all participant and companion welcome. Information on accommodation in Tokushima will be available from Symposium-Secretariat.

Symposium Organization

(1) Organizing Committee
Co-chairperson : T. Kishi (National Institute for Materials Science)
Y. Higo (Tokyo Institute of Technology)
(2) Secretary Committee
Chairperson : K. Yoshida (The University of Tokushima)

Symposium-secretariat and Mailing Address :

Prof. Kenichi YOSHIDA
Department of Mechanical Engineering, The University of Tokushima
2-1 Minamijosanjimacho, Tokushima 770-8506, JAPAN
Phone: +81-88-656-7358 Fax: +81-88-656-9082
E-mail: yoshida@me.tokushima-u.ac.jp

CUMULATIVE INDEX

J. of Acoustic Emission, Volumes 1 - 10, 1982 - 92

Authors Index

Authors with four or more contributions

Contents

Volume 1 (1982)

Volume 2 (1983)

Volume 3 (1984)

Volume 4 (1985)

Numbers 2 and 3
Pages S1-S332

Proceedings of the Second International Conference on Acoustic Emission, Oct. 28 - Nov. 1, 1985

Volume 5 (1986)

Volume 6 (1987)

Volume 7 (1988)

Volume 8 (1989)

Volume 9 (1990)

Volume 10 (1991/92)

INDEX to Journal of Acoustic Emission, 1993-2000

Volume 11, 1993

Contents

Number 1

Number 2

Number 3

Number 4

Volume 12, 1994

Contents

Number 1/2 **Acousto-Ultrasonics**

Volume 13, 1995

Contents

Numbers 1/2

Numbers 3/4

Volume 14, 1996

Contents

Number 1

Number 2

Conferences and Symposia

Number 3/4

Proceedings of International Workshop at Schloss Ringberg

Volume 15, 1997

Contents

Conferences and Symposia

Fourth Far East Conference On NDT (FENDT '97)

October 8-11, 1997, Cheju-Do, Korea, sponsored by Korean Society of Nondestructive Testing.

Congreso Regional de Ensayos No Destructivos y Estructurales

Oct. 27-30, 1997, Mendoza, Argentina, sponsored by Comisión Nacional de Energía Atómica and Universidad Tecnologica Nacional.

Volume 16, 1998

Contents

Number 1-4

Volume 17, 1999

Contents

Numbers 1/2

Numbers 3/4

Volume 18, 2000

Contents

Selected papers from "EWGAE 2000, 24th European Conference on Acoustic Emission Testing", published by CETIM, Senlis, France

AEWG43 Presentation

EWGAE 2000 (EWGAE.pdf)

Authors Index

RECOMMENDED PRACTICE FOR ACOUSTIC EMISSION EVALUATION OF FIBER REINFORCED PLASTIC (FRP) TANKS AND PRESSURE VESSELS

Draft I
October 1999

The Committee on Acoustic Emission from Reinforced Plastics (CARP),
a Division of the Technical Council of
The American Society for Nondestructive Testing, Inc.

1. SCOPE

1.1 **General** - This recommended practice provides guidelines for acoustic emission (AE) examination of fiber reinforced plastic (FRP) vessels under liquid load, pressure, and/or vacuum to determine structural integrity.

1.2 **Defect Detection** - Acoustic emission will only detect defects that are stressed during the course of the test

1.3 **Pressure** - This recommended practice is limited to vessels designed to operate at an internal pressure no greater than 5000 psig (33.8 MPa) above the pressure due to the internal contents. It is also applicable to vessels designed for external differential pressure between 0 and 15 psi (0 MPa and 0.1 MPa).

1.4 **Temperature** - This recommended practice is limited to vessels operating in the temperature range of -65°F (-54°C) to 250°F (121°C).

1.5 **Type of Vessels** - This recommended practice applies to tests of new, repaired and in-service equipment.

1.6 **Materials** - FRP materials covered under this recommended practice are fabricated using thermoset resins. Fibers covered under this recommended practice are glass, aramid, carbon or graphite, and asbestos. More than one type of fiber may be used in a vessel. The fibers must comprise at least 10% by weight of the structural laminate.

1.7 **Linings** - This recommended practice does not provide an evaluation of the condition of non-FRP linings or lamina such as rubber or thermoplastics.

1.8 **Table of Contents** - This recommended practice includes the following sections and appendixes.

2. APPLICABLE DOCUMENTS

2.1 American Society for Testing and Materials (ASTM) - Standards:

E 569	Standard Practice for Acoustic Emission Monitoring of Structures During Controlled Stimulation.
E 650	Standard Guide for Mounting Piezoelectric Acoustic Emission Sensors.
E 750	Standard Practice for Characterizing Acoustic Emission Instrumentation.
E 976	Standard Guide for Determining the Reproducibility of Acoustic Emission Sensor Response.
E 1067	Standard Practice for Acoustic Emission Examination of Fiberglass Reinforced Plastic Resin (FRP) Tanks/Vessels
E 1316	Standard Terminology for Nondestructive Examinations.

2.2 The American Society of Mechanical Engineers (ASME) - Boiler and Pressure vessel Code:

Section V, Article 11, Acoustic Emission Examination of Fiber-Reinforced Plastic Vessels.

Section X, Fiber-Reinforced Plastic Pressure Vessels, including Article RT-6, Acceptance Test Procedure for Class II Vessels.

2.3 American Society for Nondestructive Testing (ASNT)

Recommended Practice No. SNT-TC-1A, "Personnel Qualification and Certification in Nondestructive Testing".

3. DEFINITIONS AND INTERPRETATIONS

3.1 **Definitions** - Table 3.1 provides a cross reference for a number of commonly used AE terms.

Common Term	Refer to:
Count	Acoustic emission count
Duration	Hit duration
Event	Acoustic emission event
Hit	Sensor hit

Table 3.1 - Cross Reference for Commonly Used AE Terms

The following definitions shall apply to this recommended practice:

3.1.1 **Acoustic Emission Channel** - An assembly of sensor(s), preamplifier, filters, secondary amplifier, connecting cables, detector, processor and/or other instrumentation as needed (ASTM E 1316). A channel for examining fiber reinforced plastic vessels may utilize up to two sensors with associated electronics. Each channel shall be analyzed independently.

3.1.2 **Acoustic Emission Count (count, emission count)** - The number of times the acoustic emission signal exceeds a preset threshold during any selected portion of the test (ASTM E 1316).

3.1.3 **Acoustic Emission Event (event, emission event)** - A local material change giving rise to acoustic emission (ASTM E 1316).

3.1.4 **Acoustic Emission Signal Amplitude** - The peak voltage (measured in decibels) of the largest excursion attained by the signal waveform from an emission event (ASTM E 1316).

3.1.5 **Acoustic Emission Source** - The position of one or more AE events.

3.1.6 **Count Criterion (N_C)** - An acceptance criterion based on the total number of counts defined in Section B5.1.

3.1.7 **Duration Criterion (N_D)** - An acceptance criterion based on the cumulative duration defined in Section B5.1.

3.1.8 **Design Pressure** - The pressure used in the design of a vessel component together with the coincident design temperature, for the purpose of determining the minimum permissible thickness or physical characteristics of

the different zones of the vessel. When applicable, static head shall be added to the design pressure to determine the thickness of any specific zone of the vessel (ASME Code, Section VIII, Division 1, Appendix 3).

3.1.9 **Electronic Calibrator** - A device which can repeatably induce a transient signal into an acoustic emission processor for the purpose of checking, verifying, and calibrating the test instrument.

3.1.10 **Felicity Effect** - The presence of detectable acoustic emission at a fixed predetermined sensitivity level at stress levels below those previously applied (ASTM E 1316). The fixed sensitivity level will be the same as was used for the previous loading or test.

3.1.11 **Felicity Ratio** - The ratio of the stress at which the Felicity effect occurs to the previously applied maximum stress (ASTM E 1316). As used in this procedure, the Felicity ratio is determined from the ratio of the load (Section 3.2.1) at the onset of significant emission to the previously applied maximum load.

3.1.12 **Fiber Reinforced Plastic (FRP)** - A plastic with high strength fiber imbedded in the composition, resulting in some mechanical properties superior to those of the base resin (modified from ASTM D 883).

3.1.13 **High Amplitude Hits** - Hits having an amplitude greater than or equal to the Reference Amplitude Threshold.

3.1.14 **Historic Index** - A measure of the change in signal strength throughout a test.

3.1.15 **Hit Arrival Time** - The time of the first threshold crossing of a sensor hit, measured against a time reference that is common to all sensors (global clock). For time-of-arrival source location, a hit arrival time corresponding to the global clock time of the peak amplitude, or other predefined point on the signal waveform, may be used.

3.1.16 **Hit Definition Time** - A specified time interval defining the end of a hit during which no additional threshold crossings occur. The hit definition time is measured from the last threshold crossing of the hit. The first threshold crossing following the hit definition time is part of the next hit.

3.1.17 **Hit Duration (duration)** - The time from the first threshold crossing to the last threshold crossing of the signal or envelope of the linear voltage time signal. Hit duration does not include the hit definition time at the end of a hit..

3.1.18 **Intensity** - A measure of the structural significance of an acoustic emission source. An intensity analysis compares the change in signal strength throughout the test (historic index) with hits having large signal strength values (severity). For purposes of this procedure, intensity is measured on a per channel basis and is referred to as channel intensity.

3.1.19 **MARSE** - Measured area of the rectified signal envelope. A measurement of the area under the envelope of the rectified linear voltage time signal from the sensor (ASME Code Section V, Article 12).

3.1.20 **Operating Pressure** - The pressure at the top of a vessel at which it normally operates. It shall not exceed the design pressure and it is usually kept at a suitable level below the setting of the pressure relieving devices to prevent their frequent opening.

3.1.21 **Pressure Vessel** - A vessel generally used for containing liquids or gases under pressure. Pressure vessels normally have a design internal or external pressure at or above 15 psig and are designed within the scope of the ASME or similar pressure vessel codes. In this procedure, vessels which have internal or external design pressures less than 15 psig but are designed in accordance with the ASME or similar codes are considered as pressure vessels.

3.1.22 **Processor** - A circuit that analyzes the AE waveform as required in Section 7.3.

3.1.23 **Rearm Time** - An interval following acquisition of a hit during which the instrument is unable to accept additional data.

3.1.24 **Reference Amplitude Threshold** - A threshold for large amplitude hits, defined in Appendix B, section 1.3.

3.1.25 **Sensor Hit (Hit)** - Any signal that exceeds the threshold and causes a system channel to accumulate data (ASTM E 1316).

3.1.26 **Sensor Spacing Distance** - The recommended maximum spacing between sensors as defined in Appendix B6.1.

3.1.27 **Severity** - A measure of hits having large signal strength values. Severity is the average signal strength for a predefined number of hits having the largest numerical value of signal strength.

3.1.28 **Signal Strength** - The area under the envelope of the linear voltage time signal from the sensor. The signal strength will normally include the absolute area of both the positive and negative envelopes. For purposes of this procedure, MARSE (see 3.1.19) can be used as an approximation of the signal strength.

3.1.29 **Simulated Acoustic Emission Source** - A device which can repeatedly induce a transient elastic stress wave into the structure (ASME Section V, Article 12).

3.1.30 **Source Location** - Determination of the position of the local material change giving rise to the acoustic emission.

3.1.30.1 **First Hit Location** - A zone location method defined by which channel among a group of channels first detects the signal (ASTM E 1316).

3.1.30.2 **Zone Location** - A source location method which uses sensor activity as an indication of the general region of the source of an event.

3.1.31 **Tank** - A vessel generally used for liquid service at or near atmospheric pressure. Tanks will typically have flat bottoms and are usually designed within the scope of the API or similar standards. Design pressures normally range from atmospheric to the lower limit for pressure vessels.

3.1.32 **Voltage Threshold (Threshold)** - A voltage level on an electronic comparator such that signals with absolute amplitude larger than this level will be recognized.

3.1.32.1 **Test Threshold** - The threshold setting for a particular test. Normally, this will be below the data analysis threshold.

3.1.32.2 **Threshold of Detectability (Data Analysis Threshold)** - A threshold number used in the analysis of the test data. The test data shall be recorded with a test threshold at or below the data analysis threshold. For analysis purposes the data may need to be filtered.

3.1.32.3 **Reference Amplitude Threshold** - A threshold used to define the high amplitude hits used as an evaluation criteria in Table 12.6.1.

3.1.33 **Zone** - The area surrounding a sensor from which AE can be detected and from which AE will strike the sensor before striking any other sensor.

3.1.33.1 **Zone Radius** - The maximum distance from the sensor at which the amplitude of a specified simulated source can be detected by the sensor at or above a specified decibel level.

3.2 **Interpretations** - The following interpretations shall apply to this Procedure:

3.2.1 **Load** - The pressure at the bottom of a vessel. The load is the sum of the liquid head and the superimposed pressure.

3.2.1 **Inspector(s)** - The individual(s) conducting the acoustic emission examination in accordance with this recommended practice.

3.3.2 **Vessel** - A pressure vessel or a tank.

4. SUMMARY OF METHOD

4.1 **General** - The method consists of subjecting vessels to programmed increasing stress levels to a predetermined maximum and monitoring with sensors capable of detecting acoustic emission (transient stress waves) caused by stressed defects. Instrumentation, test methods, evaluation criteria, and report preparation are described in this procedure.

4.2 **Structural Integrity Evaluation** - This recommended practice provides guidelines to determine the location and significance of structural flaws with evaluation criteria and intensity criteria as a basis to assess the structural integrity of the equipment.

4.3 **Loading** - The procedure requires loading of the vessel by filling and pressurization. Mechanical loading may be used to test attachments, nozzles, or to simulate specific loading conditions. Chapter 11 gives details of the loading sequence. The loading test assesses the structural significance of defects and damage in FRP vessels.

4.4 **Data Evaluation** - Data evaluation is on a per channel basis. The evaluation is based on number of hits during load holds, Felicity ratio, cumulative duration, high amplitude hits, and intensity analysis. Data are recorded during loading and load hold periods. Specific evaluation criteria and intensity analysis methods are given in Chapter 12.

4.5 **Test Report** - Following data evaluation a test report is issued for each vessel tested. The report presents the results of the test, as specified in Section 13.

5. PERSONNEL QUALIFICATION

5.1 **Personnel** - Personnel performing acoustic emission testing of FRP equipment (inspectors) are required to attend a dedicated training course on the subject, pass a written examination, and have the recommended experience level. The training course shall be appropriate for specific NDT Level II qualification according to Recommended Practice No. SNT-TC-1A of the American Society for Nondestructive Testing, and should include as a minimum the following general topics:

1. basic technology and terminology of acoustic emission;
2. FRP vessel construction;
3. failure mechanisms of reinforced plastics;
4. acoustic emission instrumentation;
5. instrument checkout;
6. vessel filling requirements;
7. the provisions of this recommended practice;
8. characteristics of spurious emission;
9. data collection and interpretation;
10. test report.

The experience level shall be that recommended by SNT-TC-1A for Level II certification in acoustic emission.

5.2 **Level I Examinee** - Personnel who have attended the training course prescribed above, and passed a Level I examination, may perform the test but only to the instructions of, and with adequate supervision from, a person who meets the requirements of 5.1.

5.3 **Trainees** - Personnel who have not attended training as prescribed above and passed an examination are considered trainees. Such persons may participate in FRP vessel testing for the purposes of familiarization prior to attending the training course and sitting the examination. Trainees may participate only under the direct instruction of a person who has passed the examination. They may not take any direct responsibility for performance of the recommended practice.

6. SIGNIFICANCE AND USE

6.1 **General** - The AE test method detects damage in FRP equipment. The damage mechanisms that are detected in FRP are as follows: resin cracking, fiber debonding, fiber pullout, fiber breakage, delamination, and bond failure in assembled joints (for example, nozzles, manways, etc.).

6.2 **Application of Procedure** - This recommended practice is used for determining the structural integrity of FRP tanks and pressure vessels. The test will detect significant structural flaws and defects, and can be used to evaluate new, repaired, and in-service equipment.

6.3 **Unstressed Areas** - Flaws in unstressed areas and flaws that are structurally insignificant will not generate AE.

6.4 **On-Line Use** - This recommended practice is convenient for on-line use under operating stress to determine the structural integrity of in-service equipment. Usually, application of the test will result in minimal process disruption.

6.5 **Follow-Up Actions** - Flaws located with AE should be examined on the basis of the significance of emission by other techniques such as, visual, ultrasound, dye penetrant, and may be repaired and retested as recommended in Chapter 12. Specific examination and repair procedures are outside the scope of this recommended practice.

7. INSTRUMENTATION

7.1 **General** - The AE instrumentation consists of sensors and electronic signal processing and recording equipment, and digital hardware and software for analyzing and displaying data in accordance with the provision of this procedure. Additional information on AE instrumentation can be found in ASTM E 750.

7.2 **Sensors**- Except as noted in 7.2.1 and 7.2.2 sensors shall have a resonant response centered on 150 kHz. Each sensor shall utilize preamplifier circuitry which includes a band pass filter centered on the resonant peak and shielded against electromagnetic (EMI) and radio frequency interference (RFI). Integral sensors incorporate the sensor and preamplifier in the same shielded casing. As a result, they are very effective at rejecting EMI and RFI and are recommended for use in situations where this type of interference is a potential problem. No more than two sensors may be commoned (teed) into a single channel. Channels with teed sensors may exhibit a loss in sensitivity and shall only be permitted when this loss is within the limits specified in 10.2. As defined in Section A5, band pass filers, matched to the resonant frequency of the sensor shall be incorporated into the preamplifier and processor

7.2.1 **High Frequency Channels**. When excessive background noise is present, it may not be possible to conduct a test with the test threshold at or below the Threshold of Detectability (See Section B1.2) and still meet the background noise requirements of Section 11.3. In these circumstances, and if a spectrum analysis of the background noise indicates that a satisfactory test can be conducted with sensors having a resonant response greater than 150 kHz, the provisions of Section 7.2 can be waived and higher frequency sensors used. When the provisions of Section 7.2 are waived, the numerical values of the evaluation criteria and intensity analysis chart boundaries given in Chapter 12 will no longer apply. Use of Chapter 12 criteria for sensors with a resonant frequency of greater than 150 kHz will severely underestimate the severity and intensity of indications.

7.2.2 **Low frequency** - Low frequency components of elastic stress waves are less attenuated during travel through the structure than are the higher frequency components. Accordingly, low frequency sensors are sometimes used to monitor a large area of the vessel. Typically, low frequency sensors have a nominal resonant frequency of 60 kHz. If significant activity is detected on one of the low frequency channels, and not on the 150 kHz frequency channels, consideration should be given to relocating or adding more 150 kHz sensors. Unfortunately, low frequency sensors are susceptible to background noise and data obtained with these sensors is often spurious. Data from low frequency sensors is to be used for guidance only, and shall not be used with

the evaluation criteria (Section 12.6) or for the intensity analysis (Section 12.9).

7.3 **Data Measurement and Recording** - AE instrumentation shall be capable of measuring and recording by channel number and within the specified frequency range the following parameters for each AE hit: hit arrival time, hit duration, peak amplitude, and signal strength. Hit arrival time shall be measured to an accuracy of at least one millisecond. Counts may be recorded instead of duration when monitoring is within the 100 kHz to 200 kHz frequency range. The instrumentation shall be capable of measuring and recording data at a minimum sustained rate of 100 hits per second. This rate shall apply to the entire instrument, regardless of the number of channels and the distribution of hits between channels. The data acquisition system shall have sufficient channels to provide sensor coverage as defined in Section 9.5. The instrument shall store the year, month, day, hour and minute of the start of each data file as part of the test record. Instrumentation can be digital or analog based.

7.3.1 **Rearm Time** - Individual channel rearm times are permitted under this procedure. If used, the rearm time shall commence immediately following the end of the hit definition time. The rearm time shall apply only to the channel which detected the hit, and shall not effect other channels. The rearm time shall not exceed the limit specified in A8.7.

7.4 **Front End Filters** - Band pass filters of the type defined in Appendix A shall be incorporated into the instrumentation. No other front end filters shall be used. Data from all hits having an amplitude greater than the test threshold shall be recorded as defined in Section 7.3.

7.5 **Lockouts and Guard Sensors** - These techniques shall not be used.

7.6 **Instrument Displays** - The instrumentation shall be capable of providing the following real time displays.

1. Bar chart by channel of cumulative signal strength - Enables the inspector to identify which channel is recording the most data.

2. Amplitude Per Hit Versus Time - Provides the inspector with early warning of an impending failure.

3. Duration Per Hit Versus Time - Useful for identifying rubbing or sliding.

4 Log duration (or counts) per hit versus amplitude per hit - Helps the inspector determine the presence of false emission signals

5. Cumulative Signal Strength Per Channel Versus Time - Useful for identifying certain types of instrument malfunctions.

6. Cumulative Amplitude Distribution or a tabular listing by channel number of total hits equal to and greater than defined amplitude values. Tabular amplitude values shall be in increments of not greater than 5 dB and shall be for at least a 35 dB range beginning at the threshold of detectability - These displays are used to provide warning of significant fiber breakage of the type that can lead to sudden structural failure. The displays also provide information about the micro-mechanisms giving rise to the emission and warn of potential instrument malfunctions.

7.7 **Data Analysis** - Provision shall be included for playback, post-test filtering, and hard copy listing of the test data.

7.8 **Performance Requirements and Calibration** - The AE instrumentation shall meet the performance requirements of Mandatory Appendix A and shall be calibrated at intervals not exceeding one year. Calibration shall be in accordance with Appendix A requirements and the calibration values defined in Mandatory Appendix B. Certification of the date of the most recent calibration shall be carried with the instrumentation.

7.9 **Other Instrumentation** - The time from the beginning of the test shall be monitored continuously to an accuracy of one second. The liquid level, pressure and/or vacuum in the vessel shall be monitored continuously to an accuracy of ±2% of the maximum test value. If a fluid with a specific gravity different from that of the normal process fluid is used for the test, recalibration of the level instrument may be required. The test time, liquid level, applied mechanical load, and pressure/vacuum shall be recorded in the test log at the beginning and end of each change in load.

8. TEST PREPARATION

8.1 **Safety** - All safety requirements unique to the test location shall be met.

8.1.1 Protective clothing and equipment that is normally required in the area in which the test is being conducted should be worn.

8.1.2 A fire permit may be needed to use the electronic instrumentation.

8.1.3 The vessel pressure rating must be known before pressurization begins. Where appropriate, the relief valve set pressure, and safety vent burst pressure should also be known. It is important to assure that the vessel is not overpressurized and to establish a safe maximum test pressure. Precautions shall be taken to protect against the consequences of catastrophic failure when pressure testing, for example, flying debris and impact of escaping liquid. Care should be taken to avoid overstressing the lower section of the vessel when liquid test loads are used to simulate operating gas pressures. Care shall be exercised to avoid the consequence of sudden and unexpected premature release of relief valves and safety vents. This is particularly important when testing vessels containing potentially hazardous fluids.

8.1.4 **Gas or Pneumatic Testing** - Pressurizing under pneumatic conditions is not recommended except when normal service loads include either a superposed gas pressure or gas pressure only. Special safety precautions shall be taken when pneumatic testing is required and the inspector shall satisfy himself that it is safe to conduct the test. Such precautions may include the use of safety valves, explosion barriers, and a rapid release valve. Pressurization shall be terminated and the vessel unloaded if the acoustic emission characteristics described in Section 12.7.3 and Note (e) to Table 12.6.1 are observed. Pressurized attachments such as manways, nozzles, and instrument openings are a particular concern. These shall be inspected before testing to ensure that the secondary bond does not show signs of severe deterioration. Bolted and screwed connections should also be inspected to ensure that bolts and other attachment components are in place, adequate for the test pressure, properly torqued, not seriously corroded, or otherwise deteriorated.

8.2 **Vessel Conditioning** - The operating conditions for vessels that have been stressed previously shall be reduced prior to testing according to the schedule shown in Table 8.2.

Percent of Operating Load	Time at Reduced Load
10 or less	12 hours
20	18 hours
30	30 hours
40	2 days
50	4 days
60	7 days

Table 8.2 - Requirements for Reduced Operating Level Immediately Prior to Testing

8.3 **Vessel Stressing** - Arrangements should be made to stress the vessel to the maximum operating load. The stress rate shall be consistent with Section 11.1 and sufficient to expedite the test with minimum extraneous noise. Holding load at a constant level is a key aspect of an acoustic emission test. Accordingly, provision must be made for holding the load at designated check points.

8.3.1 **Atmospheric Tanks** - Process liquid is the preferred fill medium for atmospheric tanks. If water must replace the process liquid, the designer and user must be in agreement on the procedure to achieve acceptable load levels.

8.3.2 **Vacuum Tank Stressing** - A controllable vacuum pump system is required for vacuum tanks.

8.3.3 **Pressure Vessel Stressing** - Safe means for increasing the pressure under controlled conditions shall be provided.

8.4 **Vessel Support** - The vessel should normally be tested in its operating position and supported in a manner consistent with good installation practice. Occasionally, it is necessary to test tall vessels in the horizontal rather than vertical position. In this situation, care must be taken to ensure that adequate load is applied to the bottom of the vessel (defined by the final installed position), and that the top is not overstressed. Flat bottomed tanks tested in other than the intended location, shall be mounted on a pad (for example, rubber on a concrete base or equivalent) to reduce structure-borne noise between the tank and base.

8.5 **Minimum Temperature** - The normal minimum acceptable vessel wall temperature is -65°F (-54°C). Ice cracking can be a significant source of emission which can be confused with genuine emission. Tests should not be conducted on vessels with ice

on the surface of the vessel or in the insulation. In cold weather, particular care must be taken to melt any ice that might have formed in the insulation. Acceptance criteria are based on test experience at temperatures above -20°F (-29°C).

8.6 **Maximum Temperature** - The normal maximum acceptable vessel wall temperature is the lower of:

1. 250°F (121°C);
2. 35°F (19°C) below the maximum use temperature of the resin.

When testing at elevated temperature, care should be taken that the maximum use temperature of the sensor is not be exceeded. Where this is a concern, high temperature sensors or waveguides may be required. Waveguides shall be integral with the surface of the vessel being tested. Signal losses between the waveguide and the vessel shall be no greater than 10 dB.

8.7 **Background Noise** - It is important to capture real emissions during monitoring periods. To accomplish this, background noise must be at a minimum. Noise sources in the frequency and amplitude range of the test, such as rain, spargers, and foreign objects contacting the vessel, must be minimized since they mask the AE signals emanating from the structure. The inlet should be at the lowest nozzle or as near to the bottom of the vessel as possible, that is, below the liquid level. Liquid falling, swirling, or splashing can invalidate data obtained during the filling phase. Guidelines for an unacceptable level of background noise are given in paragraph 11.3.

8.7.1 The inspector shall review the process and loading techniques to identify all potential sources of extraneous acoustic noises.

8.7.2 Field experience has shown that care should be exercised in dealing with electrical background noise sources; for example, electromagnetic interference (EMI) is usually due to motors, switch gear, solenoids, and the like. It can also be caused by a bad power supply, particularly an inadequate ground. Radio frequency interference (RFI) can be distinguished from EMI with an oscilloscope and correlation plot. Both RFI and EMI shall be controlled by using suitably shielded or designed sensors and narrow band filters. Power source EMI can be controlled with a constant voltage supply unit.

8.8 **Power Supply** - A stable grounded power supply, meeting the specification of the instrumentation, is required at the test site.

9. SENSORS

9.1 **Sensor Mounting** - Refer to ASTM E650 for additional information on sensor mounting. Location and spacing of the sensors are discussed in Section 9.5. Sensors shall be placed in the designated locations with a couplant between sensor and test article. Sensors shall be held in place utilizing methods of attachment which do not create extraneous signals. Methods of attachment include hot melt glue, other adhesive systems, or duct tape. All signal cables must be constrained to prevent stressing the sensor or loss of coupling and to avoid extraneous noise from wind induced movement of the cables.

9.1.1 **Attachment** - Sensors shall be attached against the vessel with a suitable couplant applied between the sensor face and FRP surface. In order to test an insulated vessel from the outside, it is necessary to cut a hole through the insulation so that the sensor face can be mounted against the vessel surface. The preferred methods of securing sensors in place are hot melt glue or duct tape. When using hot melt glue, the glue serves as an acoustic couplant, making it important that the glue layer be as thin as possible to minimize signal losses. Silicone stopcock grease is recommended as a couplant for sensors attached with duct tape. Couplant losses shall be checked per the procedures described in Section 9.2.2.3. After completion of a test of an insulated vessel, all insulation and jacket holes shall be refilled with insulation and completely sealed to prevent water or other foreign materials from leaking underneath the insulation.

9.1.2 **Surface Contact** - The sensor shall be mounted with the center of the sensor face directly coupled to the surface of the vessel. Reliable coupling between the sensor and FRP surface must be assured and the surface in contact with the sensor face must be clean and free of particulate matter. Signal loss can be caused by certain types of paint or coatings and encapsulants, geometric discontinuities, and surface roughness. The magnitude of this type of signal loss can be determined using the procedures defined in Section 9.2. In certain cases, it may be necessary to reduce signal loss by locally removing degraded resin, loose glass, paint, etc. from the surface of the vessel.

9.2 **Sensor Locations** - Locations on the vessel shell are determined by the need to detect structural flaws at critical sections; for example, high stress areas geometric discontinuities, nozzles, manways, repaired regions, support rings and visible flaws. Spacings are governed by the attenuation of the FRP material. Care should be taken to avoid shielding by large openings such as manways. This section gives minimum sensor location requirements. It is important to provide complete coverage of the vessel and not exceed the maximum sensor spacing described in Section 9.2.1. Whenever possible, the sensor location procedures given in this section should be

based on attenuation characterization of an empty vessel. An attenuation characterization with the vessel full of the test fluid may result in closer sensor spacings than the minimum required. Additional sensors can be used at the option of the inspector to provide supplemental data from regions of interest or to provide reduced zone sizes for source location.. Sensor placement guidelines and illustrations showing typical sensor arrangements are given in Appendix C.

9.2.1 **Sensor Spacing** - Sensors will normally be located so that the distance between sensors does not exceed the sensor spacing distance (See Appendix B3). This requires determination of the zone radius according to the procedure defined in 9.2.2. In the case of large vessels or vessels with high attenuation characteristics, it may not be possible to stay within this guideline with the number of instrument channels available. Under no circumstance shall the maximum spacing exceed 1½ times the sensor spacing distance. Another way of stating this is that the sensor spacing shall be not greater than 3 times the distance at which detected signals from the attenuation characterization equal the threshold of detectability. Within the limitation of 7.2, additional sensors may be commoned into a single channel to ensure complete coverage of a vessel.

9.2.2 **Attenuation Characterization** - Typical signal propagation losses and the zone radius should be determined accordance with the following procedure. The procedure provides a relative measure of the attenuation. Near field attenuation of a genuine event is likely to be less. It should be noted that the peak amplitude from a pencil break may vary with surface hardness, resin condition, and cure. The attenuation characterization should be made above the liquid line.

9.2.2.1 Select a representative region of the vessel away from manways, nozzles, etc. Mount a sensor and strike out a line from the center of the sensor parallel to one of the principal directions of the surface fibers (if applicable). Break 0.3 mm (2H) pencil leads next to the sensor and then at 3 inches (7.6 cm), 6 inches (15.2 cm) and at 12 inches (30.5 cm) from the sensor. Continue with pencil breaks at 1 foot (30.5 cm) intervals along this line until the pulse can no longer be reliably detected. The breaks shall be done with the lead at an angle of approximately 30 degrees to the test surface and with a 0.1 inch (2.5 mm) lead extension. The amplitude shall be recorded as the average of three lead breaks at each point. Repeat the procedure along a line that bisects the principal directions of the surface fibers or, if the surface fibers have a random orientation, inclined at 45° to the direction of the original points. Plot amplitude vs distance from the sensor for

each set of lead breaks and draw attenuation curves through each set of points. The zone radius is determined as the minimum distance at which an amplitude equal to the threshold of detectability is measured. Figure 9.2.2.1 illustrates the procedure for determining the zone radius. The attenuation data shall be retained as part of the original experimental record.

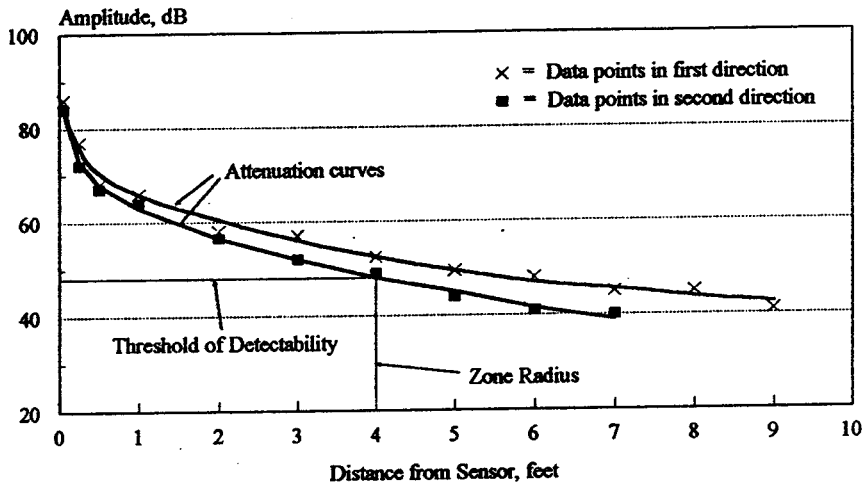

Figure 9.2.2.1 - Attenuation Curves and Determination of Zone Radius

9.2.2.2 Except as noted in section 9.2.1 for large vessels or vessels with high attenuation, sensors should be arranged so that the distance from any point on the vessel to a sensor is no greater than the zone radius. Figure 9.2.2.2 illustrates the concept of zone radius and sensor spacing distance for a triangular arrangement of sensors. The sensor spacing distance depends on the sensor layout, and will be different in different directions. Generally, the sensor spacing distance will be greater than the zone radius but less than twice the zone radius. Figure 9.2.2.2 shows sensors at the maximum allowable spacing. In most cases, the geometry of the vessel will result in sensors being spaced at less than the sensor spacing distance.

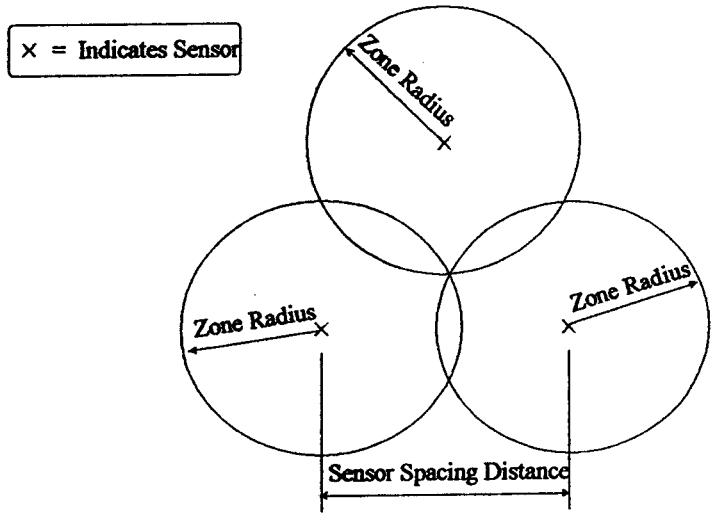

Figure 9.2.2.2 - Zone Radius and Sensor Spacing Distance

9.2.3 **Typical Sensor Arrangements** - Sensor location guidelines are given in Appendix C.

9.3 **Source Location** - Real time source location shall be based on the first hit method of zone location.

9.3.1 **Location Refinement** - An improved approximation of the location of a source can be obtained by a number of different methods including the following:

9.3.1.1 **Hit sequence Source Location (also known as the Jolly-Stuart Method)** - A refinement of the zone location method which uses the order that sensors in an array are struck by the stress waves from an AE event to subdivide the zone determined by first hit location.

9.3.1.2 **Comparative Signal Strength** - This method is based on a comparison of the relative signal strength at adjacent sensors responding to the same source. Large emission bursts on multiple channels are recognized as being from a common source when

responding channels show a sharp increase in signal strength at the same time. Such occurrences can be seen on the cumulative signal strength per channel vs time plots. When this is observed, the relative distance of the source from each sensor can be estimated from the relative magnitude of the signal strengths at the time of the emission burst.

9.3.1.3 **Reduced Zone Sizes** - If an AE test indicates a source in a particular zone, the zone can be subdivided into smaller zones by adding additional channels to the original zone. The emission source is then stimulated to emit by a small additional increase in load. For this follow-up test, channels which had originally covered zones away from the region of interest can be used to provide the additional zone coverage within the region of interest.

9.3.1.3 **Time-of-Arrival (Time Difference) Source Location** - If an acoustic emission event causes sensor hits on two or more sensors, the difference in hit arrival time between the hits can be used to calculate the location of the source. When source location is based on data from two sensors, the method is referred to as linear location. The difference in the distance of the source from each of the two sensors is calculated from the hit arrival times. The location of the source will lie on a locus defined by this result. Time-of-arrival source location can also be used with more than two sensors. However, field experience has shown that locations based on more than two sensors often give very poor results because of the anisotropy of the FRP, the sensitivity of the calculations to errors in defining the exact position of the sensors, inaccuracies in the hit arrival time, and variations in wave speed. It is recommended that linear location be used as the primary method of time difference source location. The accuracy of the hit arrival time measurement has a major influence on the accuracy of the source location calculation. Data recorded with instruments able to measure hit arrival time to a greater accuracy than that required in Section A8.5 will provide a better estimate of the position of the source.

10. INSTRUMENTATION SYSTEM PERFORMANCE CHECK

10.1 **Threshold**- The test threshold shall be set at or below the threshold of detectability. Normally, the test threshold will be set as low as possible. However, care must be taken to set the threshold above the level of background noise.

10.2 **Sensor Coupling and Circuit Continuity Verification** - Verification shall be performed before testing begins and immediately upon completion of testing using the following methods:

10.2.1 **Before Testing** - Three 0.3 mm (2H) pencil leads shall be broken at a specific distance from each sensor. The average peak amplitude of the breaks at each sensor shall not vary more than 4 dB from the average of all sensors. Any channel failing this check shall be investigated and replaced or repaired as necessary. These data shall be recorded and retained with the examination record.

10.2.2 **Before and After Testing** - The vessel shall be pulsed before and after testing. If necessary, the pulse shall be repeated at different locations on the vessel in order to check all instrument channels. It is recommend that the pulse have sufficient magnitude to be detectable on a number of channels. A center punch on a 1/16" minimum thickness backup plate is often used for this purpose. Channels which do not respond to the pulse before the test shall be repaired or replaced. Channels which do not respond to the pulse or have low sensitivity after the test shall be noted in the test report.

11. TEST PROCEDURE

11.1 **General Guidelines** - The vessel is subjected to programmed increasing stress levels to a predetermined maximum while being monitored by sensors that detect acoustic emission (stress waves) caused by growing structural flaws.

11.1.1 **Loading Rate** - Fill and pressurization rates shall be controlled so as not to exceed a strain rate of 0.005% per minute based on calculated values or actual strain gauge measurements of principal strains.

11.1.2 **Test Temperature** - The test temperature shall be as required by the governing codes or standards. In the absence of such codes and standards the following are offered as guidelines.

- For vessels with a design operating temperature at or below 120°F (49°C), the temperature of the test fluid will normally be at ambient temperature, but shall be not greater than 120°F (49°C).
- For vessels with a design operating temperature greater than 120°F (49°C) the temperature of the test fluid shall be within ±5°F (2.8°C) of the design operating temperature.

11.2 **Data** - The data specified in Section 7.3 shall be measured and recorded during the acoustic test.

11.2.1 **Data Quality** - Acquisition of genuine, valid, acoustic emission is essential to the success of the test. To achieve this, the following actions shall be carried out:

- Thoroughly check the instrumentation performance immediately prior to the start of testing and after testing is completed.
- Identify and characterize extraneous noise during the initial load hold period and judge its impact on data quality. Refer to Section 11.3 for additional information on background noise sources or to Section 12.2 for techniques which can be used to evaluate data quality during the course of the test.
- Monitor the performance of the instrumentation during the test.
- Monitor the data during the test to note possible extraneous noise and to ensure that spurious emission, such as that generated by a leak, does not contaminate the data.

11.2.2 **Test Log** - The inspector shall maintain a test log recording data file names, the information specified in Section 7.9 and Chapter 13, and other significant test occurrences.

11.3 **Background Noise** - Extraneous noise must be identified and minimized. If the inspector judges background noise to be unacceptable, either before or during the test, the test may be terminated. "Unacceptable" background noise either before or during the test is a matter of judgement based on experience. The following is offered as guidelines for unacceptable background noise during a 10 minute initial hold period immediately prior to loading.

- Not more than 5 hits above the threshold of detectability.
- An average data rate greater than 5 hits per minute.
- Any hit having an amplitude more than 5 dB above the threshold of detectability.
- Any hit duration greater than 3.5 milliseconds

Section 8.7 lists sources of extraneous emission that should be checked during pre-test preparation. Section 12.3 provides information on the use of correlation plots to help in the identification of real time extraneous noise. The following paragraphs identify possible sources of background noise.

11.3.1 **Fill Noise** - Liquid falling, swirling or splashing into the vessel, or a fill rate that is too high may require that the loading procedure be modified.

11.3.2 **Process Related Noise** - As discussed in Section 8.7, noise from pumps, motors, spargers, agitators, other mechanical devices, and electromagnetic interference and radio frequency interference can also be a problem.

11.3.3 **Leaks** - Background noise due to a leak will show as a continuous steady emission. Leaks can occur in the shell of a vessel, but more commonly occur across improperly sealed valves, or at gaskets. The noise generated by a leak may be of sufficient quantity and magnitude to require the test to be stopped until the leak can be sealed.

11.3.4 **Movement** - False emissions can be caused by movement between components such as the vessel and insulation, or the vessel and its supports. Such emissions are generally sporadic and can be identified and filtered out in post-test analysis.

11.3.5 **Wind and Vibration** - Visually examine the sensors and other hardware to verify the vessel is securely mounted and will not be subject to wind or vibration induced movement. Isolate the vessel and AE hardware from uncontrollable sources of noise.

11.3.6 **External Noise** - Uncontrolled noise caused by conditions such as rain, sleet, hail, snow, wind blown particles, (for unprotected vessels), air hoses, leaks,

blasting, etc., shall be evaluated as they occur. The effects of such sources shall be minimized by acoustic isolation where practical. In extreme cases it may be necessary to delay testing until the uncontrolled sources can be eliminated.

11.4 **Fluid Loading** - This Section specifies liquid and gas loading procedures for tanks, vacuum vessels and pressure vessels. Vessels shall be continuously monitored during the entire load sequence.

11.4.1 **Maximum Test Load** - The evaluation and intensity categories detailed in Chapter 12 provide an assessment of the structural integrity of vessels for loads up to the maximum test load. Accordingly, vessels tested under the provisions of this recommended practice should be loaded to the maximum operating load. For tanks, this will normally be the maximum design load. For vacuum vessels the test pressure will normally be the maximum operating vacuum. Pressure vessels are designed to experience an internal operating pressure of 1.1 times the design pressure when the relief valve vents or the safety vent bursts. Accordingly, pressure vessels are normally tested to a maximum test load of 1.1 times the design load.

11.4.2 **Load Holds** - All of the loading procedures require programmed load holds:

11.4.2.1 **Initial Hold** - An initial hold period is monitored to check background noise. Loading should not be commenced until acceptably low levels of background noise have been confirmed. The initial hold period should also be used to determine a baseline of the background noise. This data provides an estimate of the total background noise contribution during the test. Background noise shall be discounted in the final data analysis. The data recorded during the background noise check shall be stored in a separate file and retained as part of the test record. Recording of the test data file shall begin upon completion of the background noise period.

11.4.2.2 **Intermediate Load Holds** - For all vessels, intermediate load holds shall be for four minutes.

11.4.2.3 **Final Load Hold** - For all vessels, the final load hold shall be for 30 minutes.

11.4.3 **Tanks** - Tanks that operate with liquid head and additional superposed pressures of up to 15 psig (0.1 MPa), shall be loaded in a series of steps. The load schedule is shown in Figure 11.4.3. Intermediate load holds occur at 50,

75, 87½, and 100% of the maximum test load. For tanks that have been stressed previously, the test can begin with the liquid level as high as 60% of the operating or maximum test level (see Section 8.2). In this situation, Figure 1 should be modified to show the initial hold period at the partially full level. If the initial liquid level is above 50%, the 50% load hold is dispensed with. Initial filling of an empty tank is often noisy. The noise is due to a number of causes such as oil canning of the bottom, air entrainment, and an undrowned fill nozzle. For this reason, it is often appropriate to delay AE monitoring until the fill level reaches 10% of the maximum fill level. The background noise baseline determination is important for tank tests.

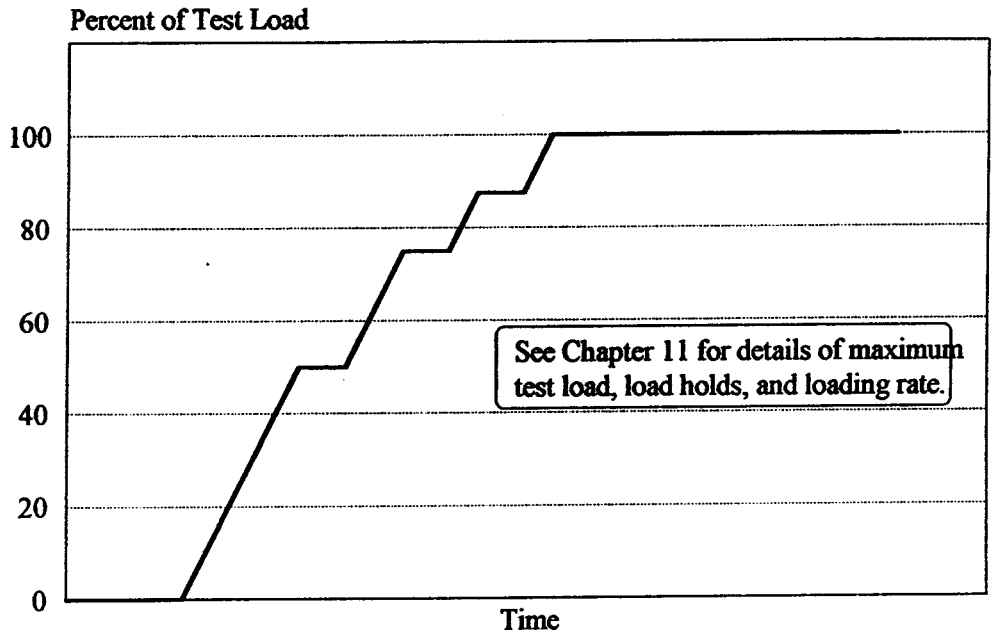

Figure 11.4.3 - Load Schedule for Tanks

11.4.4 **Vacuum Vessels** - The load schedule for vacuum vessels is shown in Figure 11.4.4. Intermediate load holds occur at 50, 75, 87½, and 100% of the maximum test load. For vacuum tests, a quick release valve shall be provided to handle any imminent catastrophic failure condition. For vacuum vessels subjected to pressure and/or liquid (positive) loads, it will normally be necessary to run two tests to obtain a complete assessment of the vessel. The first test is run under positive load and the second under vacuum load. Many vessels operate with liquid contents and partial vacuum. However, for the vacuum portion of the test, this type of vessel is normally tested empty.

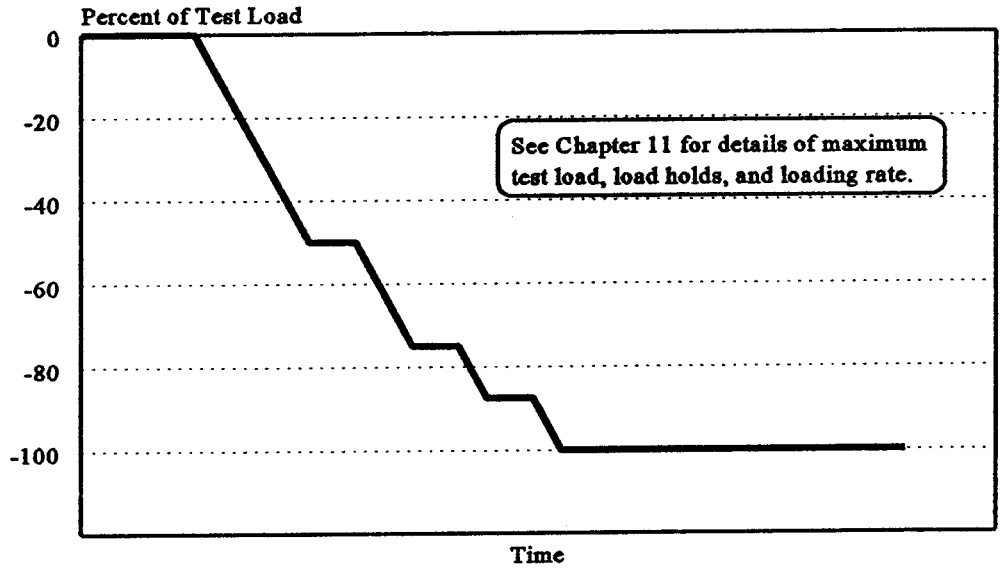

Figure 11.4.4 - Load Schedule for Vacuum Vessels

11.4.5 **Pressure Vessels** - Vessels that operate with superimposed pressures of 15 psig or greater (0.1 MPa) shall be loaded as shown in Figure 11.4.5. The load procedure requires that the load be applied in steps up to 30% of the maximum test load. The load is then decreased by 10% of the maximum test load before proceeding to the next load level. Following the decrease in pressure, the load is held for four minutes. 20% load increases followed by 10% load decreases are then continued until the maximum test load is reached. If no significant emission is detected during loading up to the 30% load level, the unload/reload step can be omitted and the load can be increased to the 40% level. Unload/reload steps can be dispensed with until significant emission is detected. "Significant emission" is a matter of judgement based on experience. However, if emission levels exceed the guidelines given in Section 11.3 for unacceptable background noise the emission shall be judged as significant emission.

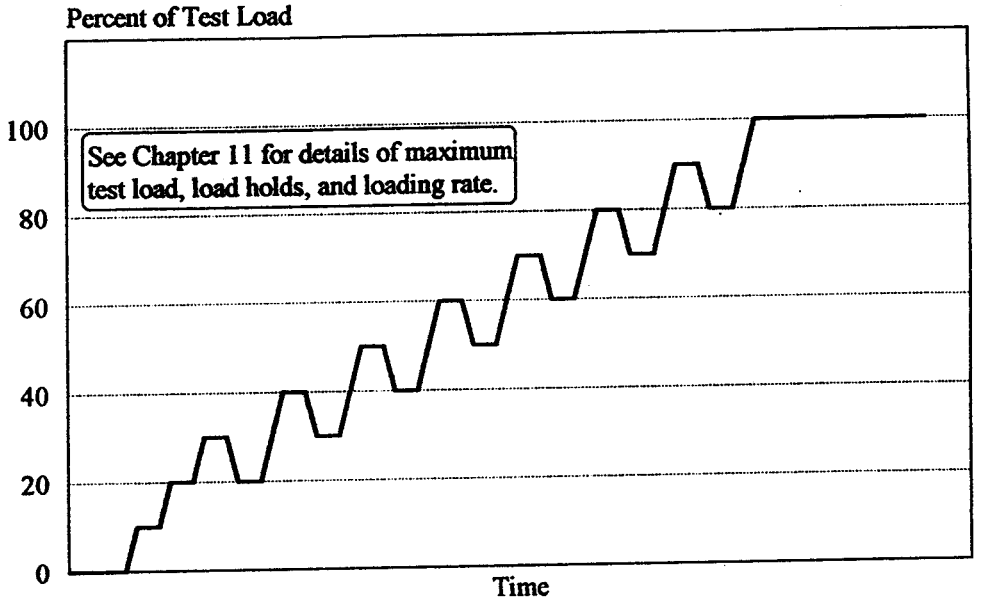

Figure 11.4.5 - Load Schedule for Pressure Vessels

11.5 **Mechanical loading** - Mechanical loading may be used to test attachments, nozzles, or to simulate specific loading conditions. Depending on the stress conditions, mechanical loads may be applied separately or in conjunction with the fluid loadings. Vessels shall be continuously monitored during the entire load sequence.

11.5.1 **Maximum Test Load** - Loads shall be applied up to the maximum design load.

11.5.2 **Load Holds** - The following load holds shall be used when testing under mechanical loading conditions.

11.5.2.1 **Initial Hold** - An initial hold period of the type described Section 11.4.2.1 shall be monitored to check background noise. Loading should not be commenced until acceptably low levels of background noise have been confirmed. Recording of the test data file shall begin upon completion of the background noise period.

11.4.2.3 **Final Load Hold** - The final load hold for all mechanical loading tests shall be for 10 minutes.

11.5.3 **Load Procedure** - Mechanical loads shall be applied in a single step followed by a ten minute final load hold. The rate of loading is not important, provided

that the rate of loading is consistent with the background noise requirements of Sections 8.7 and 11.3. Data from mechanical loading tests shall be evaluated against the criteria given in Section 12.6. As is the case with data from fluid loading, the test data shall be evaluated on the basis of whether the vessel is a tank or pressure vessel, and whether the loading is a first or subsequent loading. Intensity analysis cannot be applied to data obtained from a mechanical loading test.

12. INTERPRETATION OF RESULTS

12.1 **General** - Real-time data analysis is required in order to provide a warning of imminent vessel failure, excessive background noise, or malfunction of the instrumentation. Preliminary data analysis shall be completed at the test site. The analysis can be performed as the test proceeds or at the completion of the test.

12.2 **Test Termination** - The real-time instrument displays required by Section 7.6 shall be continuously monitored during the test. If any of these displays indicate approaching failure, the vessel shall be unloaded and the test terminated. If the inspector judges background noise to be excessive during the test, the test shall be terminated. "Excessive" background noise is a matter of judgement based on experience. However, loading shall be terminated and the vessel unloaded if the acoustic emission characteristics described in Note (e) to Table 12.6.1 are observed.

12.3 **Data Quality Analysis** - ASTM E1316 states that an indication is subject to interpretation as false, nonrelevant, or relevant. This is also shown in Figure 12.3. In order to make this interpretation, the emission characteristics shall be examined to determine if data from nonstructural sources are included in the data set and that genuine AE hits have been recorded. This examination should include a review of data correlation plots, graphs, and data listing. The test log should be reviewed to determine if any unusual occurrences or background noise were observed during the test. In the analysis of the test data, background noise shall be properly discounted. Post-test filtering can be used to eliminate spurious data.

12.3.1 **Graphical Displays** - The following paragraphs describe plots which are useful in performing the data quality analysis.

12.3.1.1 **Correlation of Log Duration (or counts) per Hit vs Amplitude per Hit** - Genuine AE is characterized by hits concentrated in the 30 μs to 2 ms range of hit duration. As amplitudes increase, duration also increases, giving the data a banded appearance on the correlation plot. An exception to this occurs when delamination is present. AE data from a delamination may include long duration hits with amplitudes 5 to 15 dB above the threshold. Low amplitude, long duration hits may indicate sliding or rubbing. Leaks are characterized by a narrow band of long duration hits in the 40-50 dB range. Hits above 55 dB with a duration less than 60 μs are often caused by electromagnetic interference (EMI). Radio frequency interference (RFI) appears as long duration hits(>3.5 milliseconds) in a low amplitude range (40-50 dB).

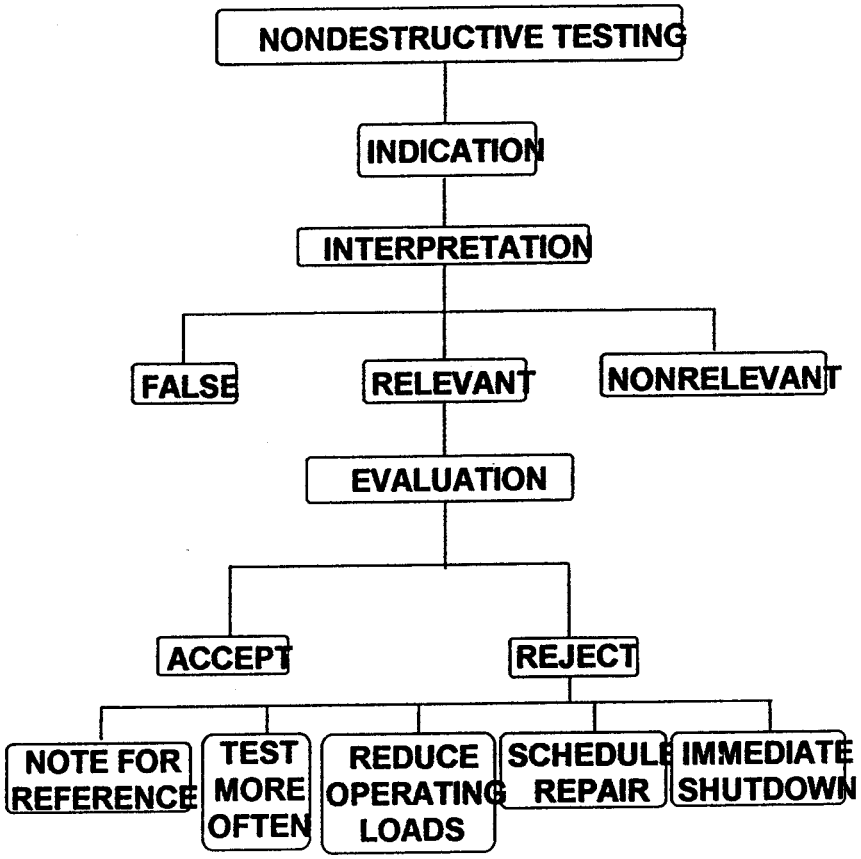

Figure 12.3 - ASTM E1316 Nondestructive Examination Chart Modified to include Intensity Analysis

12.3.1.2 **Correlation of Log Signal Strength per Hit vs Amplitude per Hit** - This plot is a valuable aid in determining the quality of the AE data and is used to identify false emission from sources other than structural damage. Low amplitude, high signal strength hits may indicate an instrument problem. Genuine AE has a banded distribution similar to that described in Section 12.3.1.1. Intensity analysis is based on signal strength. Accordingly, it is important to identify any hits with unusually high signal strength and to examine the validity of these hits and the associated data.

12.3.1.3 **Correlation of Amplitude per Hit vs Time and Duration per Hit vs Time** - These two correlation plots are helpful in identifying hits due to sliding or rubbing which will typically occur over a short time window of approximately 0.1 seconds. Genuine

data, such as that due to a delamination, will occur over a longer time window.

12.3.1.4 **Cumulative Amplitude Distribution** - A plot of genuine AE will consist of two or more straight lines. If the plot has a continuously changing slope, it may indicate an instrument problem.

12.4 **Post-test Filters** - Post-test filters are used to remove non-genuine data.

12.4.1 **Time Filters** - Time filters are used to eliminate bursts of extraneous noise such as wind noise, mechanical sliding, impact, and noise from opening and closing valves. Time filtering is often done on the basis of test log entries. Accordingly, it is important to maintain an accurate test log and to check the entries during data analysis.

12.4.2 **Channel Filter** - Many noise sources, such as a leak or faulty instrumentation, will effect only a limited number of channels. All hits on the channel(s) showing a response to a noise source must be removed from the data set for the period of the noise. If a large percentage of data for a particular channel is removed, an AE evaluation of the nearby areas of the vessel is not possible. An inclusive channel filter is often used to allow a closer examination of data on a particular channel.

12.4.3 **Amplitude Filter and Signal Strength Filter** - Amplitude and signal strength filters are used to allow the inspector to closely examine data characteristics within a given range of amplitudes or signal strengths. For example, the inspector may wish to examine high signal strength or large amplitude hits to determine the source and seriousness of fiber breakage.

12.4.4 **Swansong Filters** - Swansong filters shall not be used with data acquired from FRP vessels because Swansong filters can misinterpret data from FRP delamination as mechanical sliding.

12.5 **Duration (or Count) Adjustment for Different Thresholds** - This Procedure defines a threshold of detectability for data evaluation. However, for a meaningful intensity result, an analysis requires at least 20 hits on a channel, and at least 100 hits to obtain a historic index value which is not unity. This is often not the case when the threshold of detectability defined in this recommended practice is used. Accordingly, tests are typically run with a data acquisition threshold 8 to 10 dB below the threshold of detectability. The evaluation criteria defined in Table 12.6.1 are applied to the subset of data above the threshold of detectability, and the intensity analysis is applied

to the full data set. In order to apply the evaluation criteria to data acquired at a threshold lower than the threshold of detectability, an adjustment of the duration (or count) value is required. The duration of an individual hit depends on the threshold used to acquire that hit. A higher threshold will result in a shorter duration. The following procedure uses an adjustment technique based on regression studies of representative data sets from FRP vessels. Duration values shall be adjusted as follows:

If, H_m is the test threshold.
H_e is the threshold of detectability, and
$H_e - H_m \geq 0$

$$D_e = F \cdot D_m$$

Where:
D_e is the hit duration adjusted to the threshold of detectability.
D_m is the hit duration as measured.
F is the duration ratio function defined in Table 12.5.

If, A is the hit amplitude.

Hit Amplitude minus Threshold of Detectability	F
$(A - H_e) < 0$	0
$0 \leq (A - H_e) \leq 10$	$(A - H_e)C + 0.01$
$(A - H_e) > 10$	$Q(A - H_e) / Q(A - H_m)$

Table 12.5 - Duration Ratio Function

Where Q(x) is a polynomial defined by:

$$Q(x) = 0.5x^2 - 2.9x - 4.6$$

and C is defined by:

$$C = 1.64 / Q(10 + H_e - H_m) - 0.001$$

The above algorithm only applies when the evaluation threshold is greater than the measurement threshold. Adjusting duration to an evaluation threshold less than the measurement threshold is not permitted. Values of the coefficients of Q(x) are for

150 kHz resonant sensors. For other sensors the coefficients shall be adjusted to take account of the different frequency and sensor response.

12.6 **Evaluation Criteria** - The acoustic emission evaluation criteria given in Table 12.6.1 shall form the basis for accepting or rejecting FRP vessels. Evaluation shall be on a per channel basis. An acceptable vessel must meet all of the criteria listed in the Table. The first loading criteria shall apply if the vessel has not been loaded to greater than 90% of the test pressure prior to the test. Otherwise, the vessel shall be evaluated against the subsequent loading criteria, and prior to testing shall be conditioned by holding at reduced load as required by Section 8.2.

	Tanks		Pressure Vessels	
Criterion (a)	First Loading	Subsequent Loading	First Loading	Subsequent Loading
Emission during load hold (b)	*No hits having an amplitude greater than A_m beyond 2 mins.*	*No hits beyond 2 mins.*	Less than 5 hits per min. having an amplitude greater than A_m beyond 2 mins.	*No hits beyond 2 mins.*
Felicity ratio	Not applicable	*Greater than 0.95*	*Greater than 0.95*	*Greater than 0.95*
Cumulative duration, N_D (c), (d)	*Less than N_D*	Less than $N_D/2$	Not excessive (e)	Less than $N_D/2$
High amplitude hits (f)	*Less than 5*	None	*Less than 5*	*None*

Table 12.6.1 - Individual Channel Evaluation Criteria

Notes to Table 12.6.1:

(a) Italicized criteria carry the greatest weight.

(b) Decibel value A_m defined in Section B2.1.

© Total counts may be used instead of cumulative duration. N_c for counts shall be determined using the same procedure as N_D for duration, with count values used in place of duration numbers (Section B2.1).

(d) Varies with instrument manufacturer. See Section B2.1.

(e) Excessive duration is defined as a significant increase in the rate of emission as a function of load. On a plot of cumulative duration versus load, excessive duration will show as a departure from linearity.

(f) See Section 3.1.13

12.7 Significance of Criteria

12.7.1 **Emission During Load Hold** - The criterion based on emissions during load hold is particularly significant. Continuing emission indicates continuing damage. Fill and other background noise will generally be at a minimum during a load hold. Accordingly, this criterion is relatively easy to apply and interpret.

12.7.2 **Felicity Ratio** - The criterion based on Felicity ratio is important for in-service vessels. The criterion provides a measure of the severity of previously induced damage. The Felicity ratio is not measured during the first loading of atmospheric tanks. The Felicity ratio is measured from the unload/reload cycles during the first loading of pressure vessels. For subsequent loadings of both tanks and pressure vessels, the Felicity ratio is obtained directly from the ratio of the load at onset of significant emission to the previously applied maximum load. For pressure vessels, a secondary Felicity ratio is determined from the unload/reload cycles. The onset of "significant" emission for determining the Felicity ratio is a matter of operator experience. The following are offered as guidelines for determining onset of significant emission on an individual channel:

- More than 5 bursts of emission during a 10% increase in load. One or more hits constitute a burst, and all hits for the five seconds following the initial hit are considered part of the same burst.
- More than $N_D/20$ duration (counts) during a 10% increase in load, where N_D is the duration criterion defined in Section B2.1.
- Emission continues at a load hold. Continuing emission is defined as a rate of more than 3 hits per minute for each minute of a load hold. For purposes of this guideline, a short (one minute or less) load hold can be inserted in the procedure.

12.7.3 **Cumulative Duration** - Excessive duration (counts) is important for all vessels and is a warning of impending failure. Experience has shown that numerical criteria based on total duration (counts) are valuable for atmospheric and vacuum tanks. Pressure vessels, particularly on first loading, tend to be noisy and it is not possible to define a specific number of duration (counts). Because the emission on first loading of pressure vessels may be of

minor structural significance, trends in count data rather than fixed numbers are generally used for evaluation.

12.7.4 **High Amplitude Hits** - The criterion based on high amplitude hits is important for new vessels. The criterion is often associated with fiber breakage and is indicative of major structural damage. This criterion is less likely to govern for in-service and previously loaded vessels where emission during a load hold and Felicity ratio are more important.

12.8 **Retest of a New Vessel** - First loading of a new vessel is often noisy due to emission caused by nonstructural activity such as cracking of excess resin and brittle putty, and the bond between internal form materials for stiffeners. This activity is a one time occurrence and will not be present for subsequent loadings. Accordingly, if a new vessel is unacceptable by the first loading criteria, the item may be retested and judged against the criteria for subsequent loadings. Prior to retesting, the vessel shall be conditioned as required in Section 8.2. At the option of the owner, acoustic emission monitoring of the first loading can be waived and the vessel monitored and evaluated during the subsequent loading. In order to minimize nonstructural emission during the first loading, some fabricators use a flexible, vinyl ester based putty.

12.9 **Repaired Vessels** - The following procedure shall be used to retest a vessel that has been tested under the provisions of this Procedure and has subsequently been repaired:

(a) Load the vessel as specified in this Procedure without monitoring for acoustic emission.
(b) Hold the maximum load for at least 30 minutes.
© Condition the vessel by holding at reduced load as required by Section 8.2.
(d) Retest the vessel as required by this Procedure.
(e) The vessel shall be judged against the evaluation criteria for subsequent loadings.

12.10 **Intensity Analysis** - The evaluation criteria specified in Section 12.6 are accept/reject criteria and indicate the presence of defects. If a vessel fails one or more of the evaluation criteria for subsequent loading an intensity analysis can be performed. Figure 12.3 is a modification of the ASTM 1316 chart detailing nondestructive examination procedures. An intensity analysis provides the inspector with a range of options when an evaluation ends in rejection of the component. This is shown as the additional row of boxes at the bottom of the chart. Intensity analysis is particularly important for in-service vessels where it provides guidance about repair options to the owner and operator of the vessel. Intensity analysis is a method for measuring the structural significance of an indication and is carried out on a per channel basis. The method uses two factors based on signal strength. The first factor is known as historic index, and compares the signal strength of the most recent hits to the signal

strength of all hits. The second factor, referred to as severity, is the average of the largest signal strength hits striking a sensor. The use of signal strength to define severity reduces the effect of distance from the sensor, and allows the intensity analysis to be used on the full range of field geometries. Intensity analysis has been used extensively for analysis of defects in both metal and FRP equipment and is based on destructive vessel tests, controlled tests with detailed follow-up nondestructive evaluation, and a substantial number of field tests. The empirical factors and intensity grades have been developed by comparing the acoustic emission data with observation, experience, and theoretical studies of the laboratory and field detected defects. Intensity analysis cannot be applied to data from a first loading (Section 12.6)

12.10.1 **Historic Index** - Historic index is defined by:

$$H(t) = \frac{N}{N-K} \frac{\sum_{i=K+1}^{i=N} S_{Oi}}{\sum_{i=1}^{i=N} S_{Oi}}$$

where:

H(t) is the historic index at time *t*.
N is the number of hits (ordered by time) up to and including time *t*.
S_{Oi} is the signal strength of the *ith* hit.
K is an empirically derived factor that varies with the number of hits. Values for K are given in Table 12.10.1

Number of Hits, N	K
<20	Not applicable
20 to 100	0
101 to 500	0.8N
>500	N - 100

Table 12.9.1 - K Factor for Historic Index

Historic index has been found to be a sensitive method of detecting a change in slope in the cumulative signal strength versus time curve. This change in

slope is often referred to as the "knee in the curve". At the knee, the historic index will increase sharply. This will be followed by a decline in value until another knee is encountered. Historic index is particularly valuable for determining onset of new damage mechanisms. Historic index is essentially independent of specimen size. Historic index is a form of trend analysis, and is performed continuously for each hit. The greater the number of hits on a channel the more accurate will be the results. An analysis requires a minimum number of data points, and is not valid when only a small number of hits are recorded. The historic index is set to unity if a channel has 100 or fewer hits.

12.10.2 **Severity** - Severity S_r is defined as the average signal strength for the J hits having the largest numerical value of signal strength:

$$S_r = \frac{1}{J} \sum_{m=1}^{m=J} S_{Om}$$

where:

S_{Om} is the signal strength of the *m*th hit. *m* is ordered on the magnitude of the signal strength with m=1 being the hit having the largest signal strength.

J is an empirically derived constant that depends on the material of construction. Values for J are given in Table 12.9.2

Total Number of Hits	J
<20	Not applicable
>20	20

Table 12.9.2 - J Factor for Severity

Severity is a measure of structural damage. An increase in severity will often correspond to new structural damage of the type detected by a Felicity ratio measurement. Severity is based on the hits with the largest signal strength magnitude. Accordingly, severity cannot decrease during a test.

12.10.3 **Intensity Category** - The results of the intensity analysis for each channel are plotted on a chart of log historic index versus log severity. As defined in Figure 12.10.3 each channel is assigned an intensity category based on its historic index and severity values. The results are plotted on an intensity

chart divided into zones labeled "Insignificant", "Minor", "Intermediate", "Follow-up", and "Major". If less than 20 hits are recorded on a channel, the intensity cannot be calculated because the channel only detected a small number of hits. If this occurs, it should not be interpreted as an indication that defects are minor or insignificant. Decisions for these channels should be on the basis of the acceptance criteria in Table 12.6.1. The boundaries between the intensity zones are defined in Table 12.10.3.

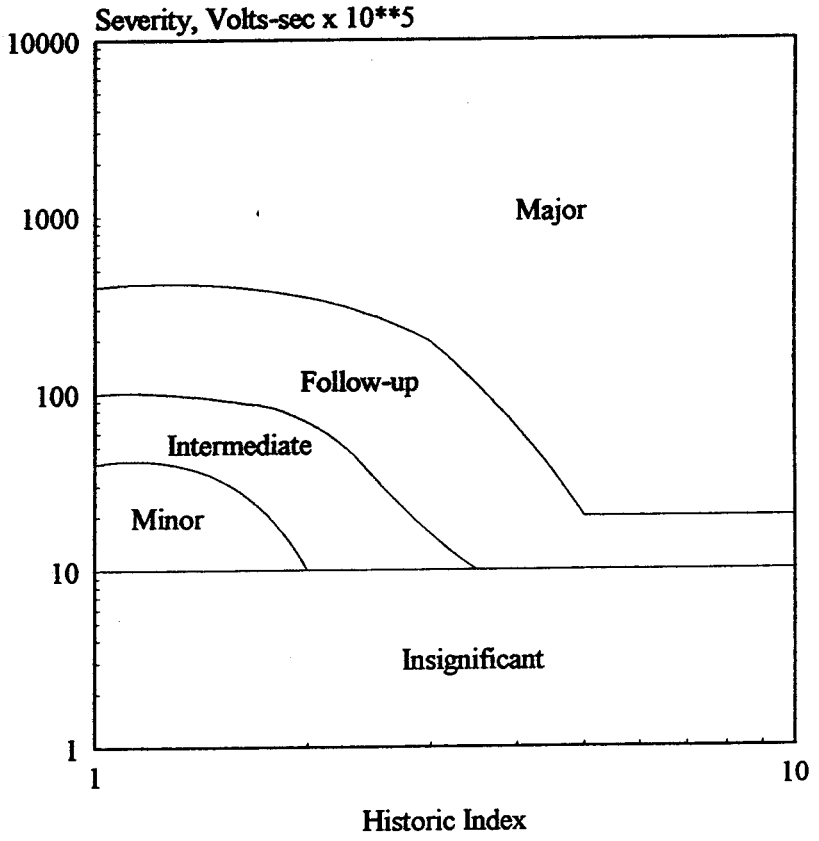

Figure 12.10.3 - Intensity Chart for FRP Vessels Monitored with 150 kHz Sensors

Zone	Upper Boundary
Insignificant	$S_r = 10$ Where: S_r = Severity
Minor	$S_r = -30(H)^2 + 60H + 10$ for $1 \leq H \leq 2$ Where: H = Historic Index
Intermediate	$S_r = -31.1(H)^2 + 62.2H + 69$ for $1 \leq H \leq 2.4$ $S_r = 24(H)^2 - 168H + 304$ for $2.4 \leq H \leq 3.5$
Follow-up	$S_r = -51(H)^2 + 102H + 349$ for $1 \leq H \leq 3$ $S_r = 43.8(H)^2 - 438.2H + 1116$ for $3 \leq H \leq 5$

Table 12.10.3 - Upper Boundaries Between the Intensity Zones Shown in Figure 5

12.10.4 **Follow-up Action** - Recommended follow-up actions for the different intensity categories are set out in Table 12.10.4. These recommended actions are considered minimum requirements. In some cases more extensive inspection may be justified. The vessel owner and the inspector should make decisions regarding follow-up inspections on the basis of the zone intensities and the consequences of a leak or equipment failure. In some instances where leakage or failure cannot be tolerated, it may be necessary to shutdown and perform detailed inspection for Minor intensity indications.

Intensity Category	Recommended Action
Insignificant	Emission source is structurally insignificant.
Minor	Minor emission. Note for future reference. Visually inspect accessible areas.
Intermediate	Defect requiring follow-up evaluation. Evaluation may be based on further data analysis, retest, or complementary nondestructive examination. Visually inspect accessible areas.
Follow-up	Significant structural defect. Requires immediate inspection using complementary nondestructive examination methods.
Major	Major structural defect. Immediate shutdown and nondestructive examination.

Table 12.10.4 - Minimum Recommended Follow-up Action for Channel Intensities

13. TEST REPORT AND RECORDS RETENTION

13.1 **Test Report** - A test report shall be issued for each vessel tested. The following information shall be included with each test report:

1. Complete identification and description of the vessel tested, including material type, source, method of fabrication, and a manufacturer's name.
2. Vessel sketch or manufacturer's drawing with dimensions of vessel and sensor location.
3. Test fluid employed.
4. Test fluid temperature and density.
5. Test type, including loading rate, hold times and hold levels.
6. Comparison of test data with the acceptance criteria, and an assessment of the location and severity of structural flaws based on the data.
7. Show on sketch or manufacturer's drawing the location of any zones with acoustic emission activity exceeding the acceptance criteria.
8. Any unusual effects or observations during or prior to the test.
9. Test location.
10. Dates of test. Also include date of previous AE certification if a prior AE test has been performed.
11. Test organization and name(s) of test inspector(s).
12. A complete description of AE instrumentation including manufacturer's name, model number, sensor type, system gain, serial numbers or equivalent, software title and version number.
13. Date of most recent calibration of instrumentation.
14. Permanent record of AE data.
15. Attenuation Characterization.

13.2 **Records Retention** - Calibration and AE examination records shall be kept by the organization conducting the AE test for a period of at least five years.

APPENDIXES

MANDATORY APPENDIX A - INSTRUMENTATION PERFORMANCE REQUIREMENTS

A1 AE Sensors

A1.1 **General-** AE sensors shall be temperature-stable over the range of intended use, and shall not exhibit sensitivity changes greater than guaranteed by the manufacturer over this range. Sensors shall be shielded against radio frequency interference (RFI) and electromagnetic noise interference (EMI) through proper shielding practice and/or differential (anticoincident) element design. Band pass filters shall be used to reduce EMI and RFI. Sensors shall have omnidirectional response, with variations not exceeding 2 dB from the peak response.

A1.2 **Sensor Characteristics** - Sensors shall have a resonant response in the 100 kHz to 200 kHz range. Minimum sensitivity shall be -80 dB referred to 1 volt/microbar, determined by face-to-face ultrasonic calibration. This method measures relative sensitivity of the sensor. AE sensors used in the same test should not vary in peak sensitivity more than 3 dB from the average.

A2 **Couplant** - Commercially available couplants for ultrasonic flaw detection may be used. Silicone based stopcock grease and hot melt glue has been found to be particularly suitable. Frangible wax or quick-setting adhesives may be used, provided couplant sensitivity is no lower than with fluid couplants. Couplant selection should be made to minimize changes in coupling sensitivity during a test. Consideration should be given to testing time and to the surface temperature of the vessel.

A3 **Preamplifier** - The preamplifier shall be shielded against RFI and EMI through proper shielding practice. If the preamplifier is of differential design, a minimum of 40 dB of common-mode noise rejection shall be provided. The unfiltered frequency response shall not vary more than 3 dB over the operating frequency and temperature range of the sensors, filters and preamplifiers.

A4 **Signal Cable** - The signal cable from sensor to preamplifier shall not exceed 3 ft in length and shall be shielded against electromagnetic interference. This requirement is omitted for integral sensors, or line-driving (matched impedance) sensors.

A5 **Filters** - Filters shall be located in the preamplifier, or may be integrated into the component design of the sensor and preamplifier. Additional filters shall be incorporated into the processor to limit frequency range and thereby EMI and RFI. The combination of sensor/preamplifier and processor filters shall be of the band pass

type, and shall provide a minimum of 24 dB/octave signal attenuation. Except as permitted in Sections 7.2.1 and 7.2.2, filters and/or integral design characteristics shall ensure that the principal processing frequency of the signal is in the range 100 to 200 kHz.

A6 **Power-Signal Cable** - The cable providing power to the preamplifier and conducting the amplified signal to the main processor shall be shielded against electromagnetic noise. Signal loss shall be less than 1 dB per 100 ft (30 m) of cable length. Five hundred feet is recommended maximum cable length to avoid excessive signal attenuation. Digital or radio transmission of signals is allowed consistent with standard practice in transmitting these signal forms.

A7 **Main Amplifier** - The main amplifier, if used, shall have signal response with variations not exceeding 3 dB over the frequency range of 100 kHz to 200 kHz, and temperature range of 40° to 125°F (4° to 52°C).

A8 **Main Processor**

A8.1 **General**- The main processor(s) shall have processing circuits through which sensor data will be processed. It shall be capable of processing hits, hit arrival time, hit duration (or counts), peak amplitude, and signal strength on each channel. No more than two sensors may be commoned into a single channel.

A8.2 **Signal Strength** - Signal strength shall be measured on a per channel basis and shall have a resolution of 1% of the value obtained from a one millisecond duration, 150 kHz pulse having an amplitude 25 dB above the threshold of detectability. Useable dynamic range shall be a minimum of 35 dB. Relative values of signal strength given in Table B7 shall be accurate to ± 5%.

A8.3 **Peak Amplitude Detection** - Amplitude shall be measured in decibels referenced to 0 dB as 1 μV at the preamplifier input. Comparative calibration must be established per the requirements of Appendix B. Usable dynamic range shall be a minimum of 60 dB with 1 dB resolution over the frequency band of 100 kHz to 200 kHz, and the temperature range of 40° to 125° F (4° to 52° C). Not more than 2 dB variation in peak detection accuracy shall be allowed over the stated temperature range. Amplitude values shall be stated in dB, and must be referenced to a fixed gain output of the system (sensor or preamplifier).

A8.4 **Hit Duration** - Hit duration shall be accurate to ± 5 microseconds.

A8.5 **Arrival Time** - Hit arrival time shall be recorded globally by channel accurate to within one millisecond.

A8.6 **Hit Definition Time** - The hit definition time shall be 400 microseconds.

A8.7 **Rearm Time** - It is recommended that the rearm time be as short as possible. Under no circumstances shall the rearm time be greater than 200 microseconds.

MANDATORY APPENDIX B - INSTRUMENT CALIBRATION

B1 **General** - The performance and threshold definitions vary for different types of acoustic emission instrumentation. Parameters such as signal strength and amplitude vary from manufacturer to manufacturer and from model to model by the same manufacturer. This appendix describes techniques for generating common baseline levels for the different types of instrumentation. The amplitude decibel values are for a typical piezoelectric crystal using the measurement method specified in Section B4. Signal strength values are typical MARSE values measured in volt-seconds multiplied by 10^5. This appendix also defines procedures for determining the Threshold of Detectability, Reference Amplitude Threshold and Duration Criterion N_D (or Count Criterion N_C), to meet the criteria contained in Table 12.6.1. The procedures defined in this appendix are intended for baseline instrument calibration at 60° to 80° F (15° to 27° C). It is recommended that instrument users develop approximate calibration techniques, along the lines outlined in this appendix. For field use, a portable acrylic rod can be carried with the equipment and used for periodic checking of sensor, preamplifier, and channel sensitivity.

B2 **Threshold of Detectability** - The threshold of acoustic emission detectability shall be determined using 1 ft x 10 ft x ½ in (30 cm x 300 cm x 1.3 cm), 99% pure lead sheet. The sheet shall be suspended clear of the floor with the long side parallel to the floor. The Threshold of Detectability is defined as the average measured amplitude of ten hits generated by a 0.3 mm mechanical pencil pencil (2H) lead break at a distance of 4 feet (122 cm) from the sensor. All lead breaks shall be done at an angle of approximately 30 degrees to the test surface with a 0.1 in (2.5 mm) lead extension. The sensor shall be mounted 12 inch (30 cm) from the end of the sheet and mid-distance between the 10 foot (310 cm) sides. The sensor may be mounted using duct tape tightly wrapped around the back side of the sheet to firmly hold the sensor against the lead sheet. Silicone stopcock grease shall be applied as couplant between the face of the sensor and the lead sheet.

B3 **Reference Amplitude Threshold** - For large amplitude hits, the Reference Amplitude Threshold shall be determined using a 10 ft x 2 in. x 3/4 in. (300 cm x 5 cm x 2 cm) clean, mild steel bar. The bar shall be supported at each end on elastomeric, or similar, isolating pads. The reference amplitude threshold is defined as the average measured amplitude of ten hits generated by a 0.3 mm mechanical pencil pencil (2H) lead break at a distance of 7 feet (210 cm) from the sensor. All lead breaks shall be done at an angle of approximately 30 to the surface with a 0.1 inch (2.5 mm) lead extension. The sensor shall be mounted 12 inches (30 cm) from the end of the bar on the 2 inch (5 cm) wide surface.

B4 **Decibel Calibration** - Instruments shall be calibrated using the 1 ft x 10 ft x ½ in (30 cm x 300 cm x 1.3 cm), 99% pure lead sheet. Decibel values shall be determined as

the average measured amplitude of ten hits generated by a 0.3 mm (2H) mechanical pencil pencil lead break at the distances shown in the table below. Each lead break shall be done at an angle of approximately 30 degrees to the lead sheet surface with a 0.1 in (2.5 mm) lead extension from the pencil. Typical decibel values are given in Table B4.

Distance of Mechanical Pencil Break from sensor	Typical Decibel value
6 ft - 0 in (183 cm)	40
5 ft - 0 in (152 cm)	44
4 ft - 0 in (122 cm)	48
3 ft - 0 in (91 cm)	52
2 ft - 0 in (61 cm)	56
1 ft - 0 in (30 cm)	61
6 in (15 cm)	66
4 in (10 cm)	70

Table B4 - Decibel Calibration Values

B5 **Duration Criterion N_D** - The Duration Criterion N_D shall be determined either before or after the test using a 0.3 mm mechanical pencil pencil (2H) lead broken on the surface of the vessel. All lead breaks shall be done at an angle of approximately 30 to the test surface with a 2.5 mm (0.1 in.) lead extension. Calibration points shall be chosen so as to be representative of different constructions and thicknesses and should be performed above and below the liquid (if applicable) and away from manways, nozzles, etc. A sensor shall be mounted at each calibration point and two calibrations shall be carried out at each location. One calibration shall be in the principal direction of the surface fibers (if applicable), and the second calibration shall be carried out along a line 45 to the direction of the first calibration. Lead breaks shall be at a distance from the calibration point so as to provide an amplitude decibel value A_m midway between the Threshold of Detectability (see Section B2) and Reference Amplitude Threshold (see Section B3). The Duration Criterion at each calibration point is defined as one hundred times the average duration (counts) per lead break from ten 0.3 mm mechanical pencil pencil (2H) lead breaks at each of the two lead break locations. When applying the Duration Criterion, the value which is representative of the region where activity is observed should be used.

B5.1 **Count Criterion N_C** - Total counts may be used instead of cumulative duration. N_C for counts shall be determined using the same procedure as N_D for duration, with count values used in place of duration numbers

B6 **Sensor Spacing Distance** - The sensor spacing distance is the spacing between sensors such that a lead break at any location is detected by at least one sensor at an amplitude equal to or above the threshold of detectability. This distance shall be calculated on the basis that no point on the vessel will be further from a sensor than the zone radius (Section B6.1). It should be noted that in certain circumstances Section 9.2.1 permits actual sensor spacings to exceed this calculated sensor spacing distance.

B6.1 **Zone Radius** - The zone radius is determined on the basis of the distance at which the average of three 0.3 mm pencil (2H) lead breaks gives an amplitude equal to the threshold of detectability (see B2). The zone radius shall be determined by interpolation from the amplitude vs distance plots required for attenuation characterization (see 9.2.2).

B7 **Signal Strength Calibration** - The signal strength calibration values given in Table B7 shall be confirmed electronically with a constant amplitude 150 kHz pulse of 1 millisecond duration input to each channel. The intensity analysis (Section 12.10) is based on these values. Signal strength calibration values may vary between instruments, but should maintain the same relative values as listed in Table B7.

Amplitude (dB) of Input Signal (a) (b)	Typical Signal Strength Calibration Value	Relative Value ©
45	25	1.0
55	79	3.2
65	251	10.0
75	791	31.6

Table B7 - Signal Strength Calibration Values

Notes:
(a) See Appendix B4 for explanation of decibel values.
(b) Input signal is a constant amplitude 150 kHz pulse of 1 millisecond duration.
(c) Relative Value is the ratio of the signal strength calibration value of a constant amplitude 150 kHz pulse of 1 millisecond duration with a given amplitude (dB) to the signal strength calibration value of a constant amplitude 150 kHz pulse of 1 millisecond duration with an amplitude of 45 dB.

B8 **Hit Duration** - The accuracy of the hit duration measurement shall be confirmed electronically with a constant amplitude 150 kHz pulse, varied from 50 to 500 microsecond duration, input to each channel. A calibrated transient waveform recorder shall be used to confirm the time duration of the input pulse.

NONMANDATORY APPENDIX C - SENSOR PLACEMENT GUIDELINES

C1 **Typical Sensor Arrangements** - The cases and figures included in this Appendix show suggested sensor arrangements for representative vessels. In all figures, sensor positions are represented by an "X". The following sensor placement guidelines are recommended.

- Sensors should be arranged to provide complete coverage of the vessel. Determination of the distance between sensors is described in Section 9.2 and requires measurement of the sensor spacing distance and the zone radius using the procedures detailed in Sections 9.2.2, B6, and B6.1.
- For cylindrical vessels sensors are equally spaced in rings around the circumference. Adjacent rings have sensors placed out of phase (i.e. a sensor in one ring is placed on the bisector of two sensors in the adjacent ring).
- Sensor positions are adjusted and additional sensors used, based on the need to detect structural flaws at high stress areas such as, geometric discontinuities, nozzles, manways, repaired regions, support points, stiffener rings, and known flaws.
- Openings in the shell of more than 15 inch (380 mm) diameter can cause shielding of the stress waves and two sensors are normally placed on opposite sides of manways and large diameter nozzles.
- Particular attention should be paid to joints in the laminate. Joints are often located in areas of high local stress. Fabrication deficiencies are frequently associated with joints. In addition, high attenuation is likely to occur across a butt joint. It is recommended that a local attenuation check be carried out at butt joints and other joint areas which might attenuate the stress wave.

The cases that follow are typical for vessels with diameters in the range of 6 to 10 feet (1,800 mm to 3,050 mm). The vertical vessel depictions are typical for vessel heights in the range of 12 to 25 feet (3,650 mm to 7,620 mm). The horizontal vessels are typical for vessels 20 to 40 feet long. The cases illustrate the types of factors that must be considered when locating sensors.

C1.1 **Case CI - Vertical Atmospheric Storage Tank** - The tank shown in Figure C1 has a flat bottom and a dished top head. The vessel operates with liquid load but no superimposed pressure. Three rings of sensors are used to monitor the cylindrical wall of the vessel. The number of sensors in each ring, the number of rings, and the spacing between rings, will vary from vessel to vessel depending on the size of the vessel and the attenuation measurements. The lowest ring of sensors is generally placed within 18 inches (460 mm) of the bottom of the tank wall in order to detect emission originating in the knuckle region of the wall and in the outer portion of the floor. The uppermost ring of sensors is placed approximately 3 feet(920 mm) of the top of the tank in order to detect emission from the top knuckle. However, as the top head is not stressed, emission will not originate in this area and it is not necessary to place the sensors high enough to detect emission beyond the knuckle. For the same reason, sensors are not placed on the top head. Intermediate rings of sensors should be placed so as to provide complete coverage of the cylindrical tank wall. The lower ring of sensors is arranged so that one of the sensors provides good coverage of the small nozzle at the bottom of the tank.

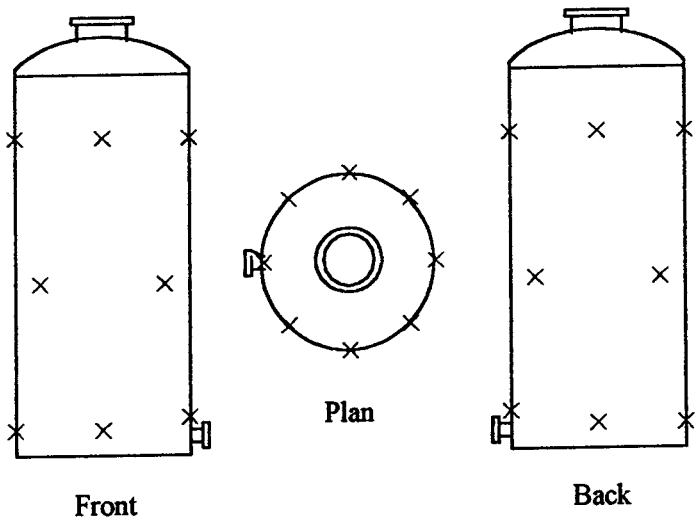

Figure C1 - Vertical Atmospheric Storage Tank

C1.2 **Case C2 - Vertical Atmospheric Storage Tank** - Figure C2 shows a flat bottom tank with a dished top head. The tank operates full of liquid but with no superimposed pressure. The cylindrical shell is fabricated in two sections and joined with a butt joint. Other details are as shown. Sensor layout follows the basic pattern used for Case C1. Attenuation measurements showed high signal losses across the butt joint. Accordingly, a ring of sensors is located on each side of the joint to monitor this critical region. As described in Section C1, the two rings of sensors are placed out of phase from each other. Two sensors are used to monitor the manway, one is part of the bottom ring and the other is placed on the opposite side of the nozzle. An additional sensor is used to monitor the smaller nozzle. Sensors are orientated to monitor the attachment points for the dip pipe. This is particularly important for in-service tests because vibration during operation can cause fatigue cracks in these attachments. The small nozzle near the top of the cylindrical wall is an overflow and very little stress is present, even with the tank full. Accordingly, the area around this nozzle is monitored by the ring of sensors covering this area and no special provision is made to monitor the nozzle.

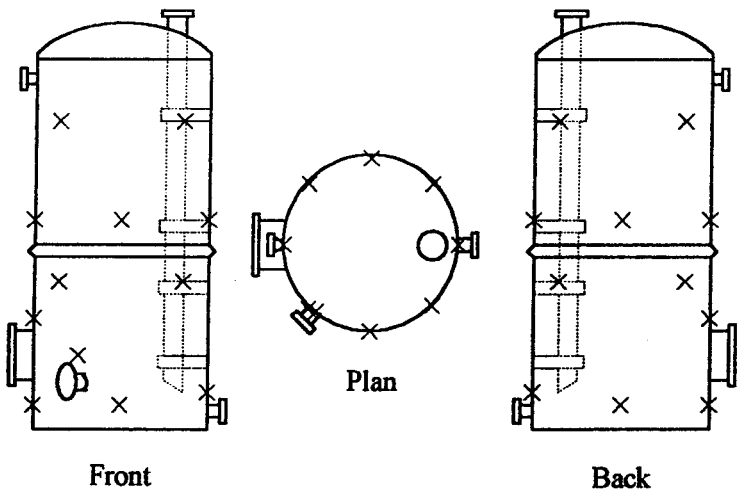

Figure C2 - Vertical Atmospheric Storage Tank with Full Body Joint

C1.3 **Case C3 - Vertical Tank with Superimposed Pressure** - The tank shown in Figure C3 has a flat bottom and a dished top head. The vessel operates with liquid load and superimposed pressure. The holdown lugs around the bottom of the tank anchor the vessel and resist the upward forces caused by pressure acting on the inside of the top head. The sensor layout is similar to that shown in the previous cases, with staggered rings of sensors on the cylindrical wall. The lowest ring of sensors is placed with a sensor at each lug. Depending on the construction of the holdown lugs, the sensors may be placed at the side of the lugs. If the lugs are attached by a filament wound band laid over the lugs, the sensor are normally placed above. This is because high attenuation between the overwrap and tank may make it difficult to monitor the knuckle and bottom of the tank. The pressure in the tank stresses the top head. Accordingly, the top ring of sensors is placed closer to the top of the tank wall than is the case with a tank without pressure. Generally, the upper ring of sensors is placed within 18 inches (460 mm) of the top knuckle. Two sensors are used to monitor the manway and the top head of the vessel. An additional sensor is used to monitor the small nozzle in the lower portion of the tank.

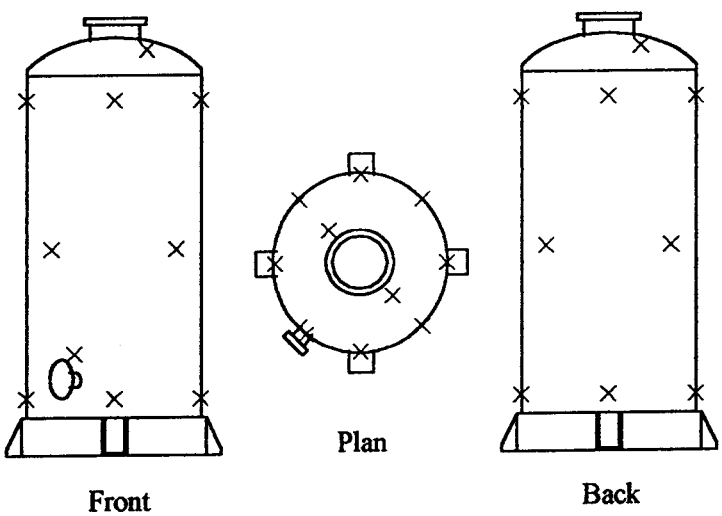

Figure C3 - Vertical Storage Tank with Superimposed Pressure

C1.4 **Case C4 - Vertical Pressure Vessel** - Figure C4 shows a pressure vessel supported on lugs. In addition to internal pressure, the vessel is designed to be full of liquid. As in the previous cases, the cylindrical portion of the vessel is covered by rings of sensors. High tensile stresses occur under the lugs due to the combination of the weight of the vessel and contents, the pressure, and the bending stresses from the eccentricity of the support. For this reason, a sensor is placed under each lug. A ring of sensors is placed above the support ring to monitor the high stresses that occur in this region. The pressure stresses the entire vessel, including the top head which is monitored in the same way as case C3. The rings of sensors at the top and bottom of the vessel monitor most of the top and bottom head. Two sensors are used to monitor the center of the top head which has a large diameter manway opening. A single sensor is used to monitor the center of the bottom head and the small nozzle.

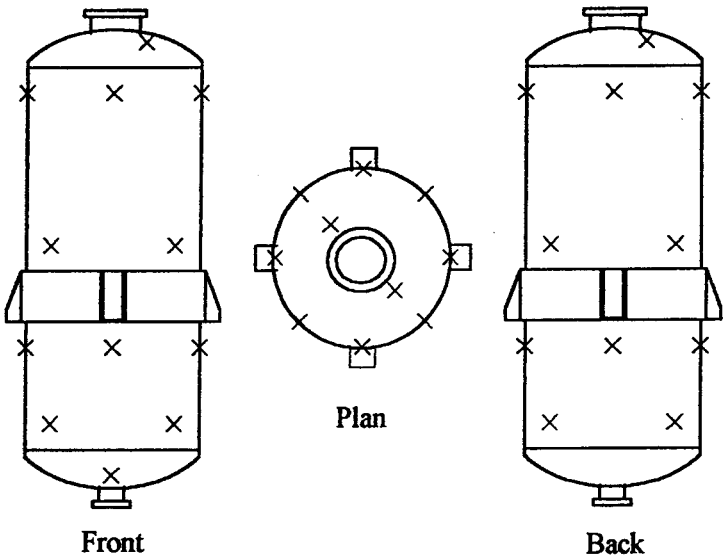

Figure C4 - Vertical Pressure Vessel

C1.5 **Case C5 - Vertical Pressure Vessel** - The vessel shown in Figure C5 is supported on legs. The sensor arrangement for the bottom portion of the vessel is shown in the figure and follows the guidelines given in the previous cases. Particular attention is paid to the leg attachments. A sensor is normally placed at the side of each leg, as close to the bottom of the straight sidewall as possible. In this manner, each sensor monitors a single leg. To provide adequate coverage of the leg attachment areas, at least two sensors are placed on the bottom head, 180° apart.

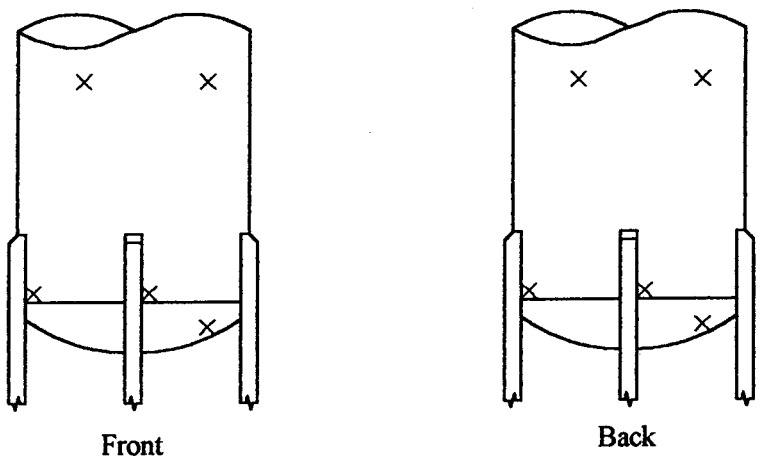

Figure C5 - Vertical Pressure Vessel

C1.6 **Case C6 - Horizontal Pressure Vessel** - The horizontal pressure vessel shown in Figure C6 is supported on four saddles. The cylindrical portion of the vessel is covered by rings of sensors, with adjacent rings placed out of phase. The heads are monitored by a sensor in the middle of each head and by the rings of sensors at the end of the cylinder. The manway is monitored by two sensors in a nearby ring of sensors and an additional sensor on the opposite side. In this example, additional sensors are not required to monitor the smaller nozzles in the vessel because of the proximity of other sensors. In some situations it may be necessary to add additional sensors, or relocate other sensors in order to monitor nozzles. Sensors are added to cover the high stress areas at each end of each of the saddle supports. These sensors are placed on the opposite side of the saddle from the closest ring of sensors.

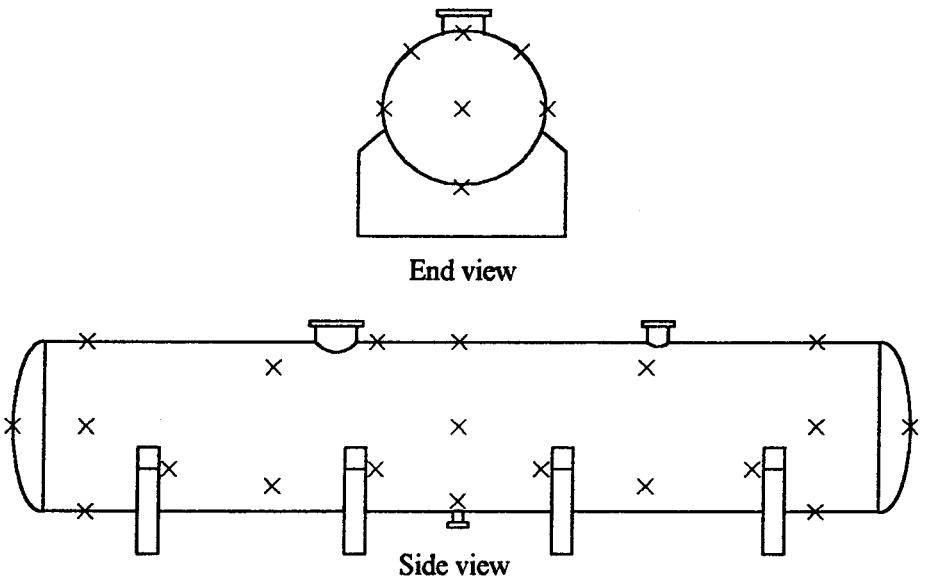

Figure C6 - Horizontal Pressure Vessel

C1.7 **Case C7 - Horizontal Pressure Vessel** - The vessel shown in Figure C7 is a horizontal pressure vessel with external stiffeners. The sensor arrangement is similar to that used in Case C6. A ring of sensors is placed between each of the stiffener rings. If one of the stiffener rings is a source of emission, this arrangement allows the inspector to determine which stiffener is the source. In this case, additional sensors are not added at the end of the saddle supports. Instead, sensors in nearby rings are used to monitor the saddles. Two sensors are placed on opposite sides of the manway. One sensor is part of a ring of sensors and would normally be placed at the top of the vessel. This sensor is moved down the vessel and slightly towards the end. Another sensor, which cannot be seen in the views shown in Figure C7, is placed on the opposite side of the manway.

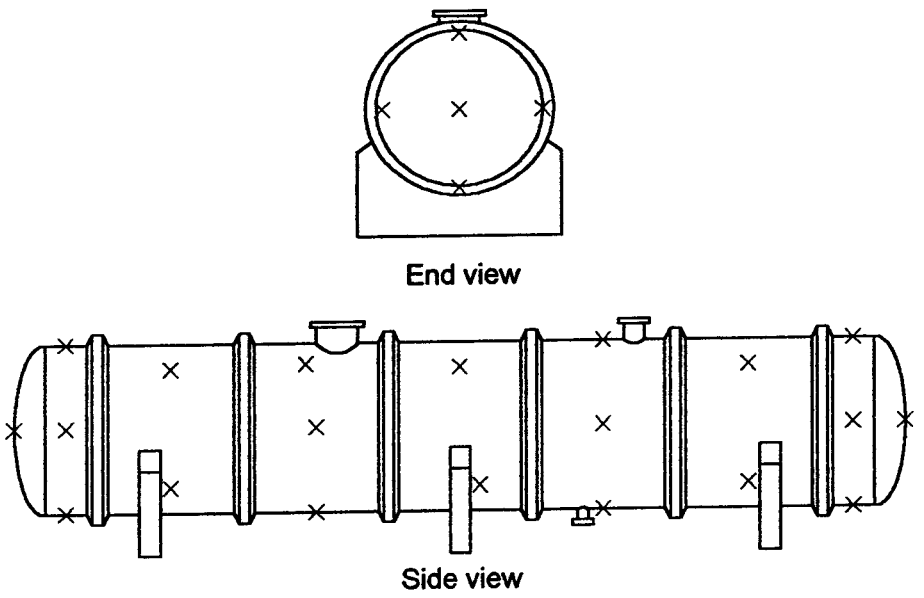

Figure C7 - Horizontal Pressure Vessel

TEXAS DEPARTMENT OF TRANSPORTATION

PROCEDURE FOR ACOUSTIC EMISSION MONITORING OF PRESTRESSED CONCRETE GIRDERS

DRAFT B
MAY 2001

THE FERGUSON STRUCTURAL ENGINEERING LABORATORY
THE UNIVERSITY OF TEXAS AT AUSTIN

CHAPTER 1 - SCOPE

1.1 General[1] - This procedure defines instrumentation requirements, test procedures, and evaluation criteria for acoustic emission (AE) monitoring of prestressed concrete girders for the purpose of evaluating structural integrity. This procedure applies to new and in-service girders. It is also applicable to girders that exhibit premature concrete deterioration due to alkali-silica reaction (ASR) or delayed ettringite formation (DEF). An authorized representative of the Texas Department of Transportation shall approve in writing any deviation from this procedure. The test method requires loading of the girder. Typically, such loads will be applied by traffic as part of normal operation.

1.2 Limitations - The test method described in this procedure is subject to the following specific limitations.

1.2.1 Loading - Acoustic emission will only detect defects and overloads in portions of the girder that are stressed during the course of the test.

1.2.2 Materials - This procedure is limited to prestressed concrete. Reinforced concrete beams without prestressing cannot be evaluated under this procedure.

1.2.3 Applicability - The AE test detailed in this procedure will detect structural deterioration or structural overloads in a prestressed concrete girder, and applies to flexure-dominated and shear-dominated regions of the girder. The test method will also detect strand slippage.

1.2.4 Portions not Covered - The monitoring procedure will normally be used to evaluate a local region of a girder. When used in this manner, the procedure will not provide a structural evaluation of other regions of the girder.

1.3 Table of Contents - This procedure includes the following chapters:

[1] Inquiries about this procedure should be addressed to Mr. Brian D. Merrill, P.E., Texas Department of Transportation, 125 E. 11th Street, Austin TX, 78701-2483

CHAPTER 2 – APPLICABLE DOCUMENTS

2.1 ASTM - American Society for Testing and Materials.

E 569 Standard Practice for Acoustic Emission Monitoring of Structures During Controlled Stimulation.

E 650 Standard Guide for Mounting Piezoelectric Acoustic Emission Sensors.

E 750 Standard Practice for Measuring Operating Characteristic of Acoustic Emission Instrumentation.

E 976 Standard Guide for Determining the Reproducibility of Acoustic Emission Sensor Response.

E 1316 Standard Terminology for Nondestructive Examinations.

E 2075 Standard Practice for Verifying the Consistency of AE-Sensor Response Using an Acrylic Rod.

2.2 ASNT – American Society for Nondestructive Testing.

Recommended Practice No. SNT-TC-1A, "Personnel Qualification and Certification in Nondestructive Testing".

CHAPTER 3 – DEFINITIONS

3.1 Definitions - The following definitions shall apply to this Procedure.

3.1.1 Amplitude – See signal amplitude, acoustic emission.

3.1.2 Channel, Acoustic Emission - An assembly of sensor(s), preamplifier or impedance matching transformer, filters, secondary amplifier or other instrumentation as needed, connecting cables, and detector or processor (ASTM E 1316). Each channel shall be analyzed independently.

3.1.3 Electronic Calibrator - A device that can repeatably induce a transient signal into an acoustic emission processor for the purpose of checking, verifying, and calibrating the test instrument.

3.1.4 Event, Acoustic Emission (Emission Event) - A local material change giving rise to acoustic emission (ASTM E 1316).

3.1.5 Felicity Effect - The presence of detectable acoustic emission at a fixed predetermined sensitivity level at stress levels below those previously applied (ASTM E 1316). The fixed sensitivity level will be the same as was used for the previous loading or test.

3.1.6 Felicity Ratio - The ratio of the stress at which the Felicity effect occurs to the previously applied maximum stress (ASTM E 1316). As used in this procedure, the Felicity ratio is determined from the ratio of the load (Section 3.2.1) at the onset of significant emission to the previously applied maximum load.

3.1.7 Filter – A hardware or software tool that is used to identify a data set based on specified characteristics. Filters are normally used to identify and eliminate unwanted data, such as emission caused by mechanical sliding or nonrelevant sources.

3.1.8 First Hit – If stress waves from an event cause signals to exceed the threshold on more than one sensor, the signal with the earliest time of arrival is termed the first hit.

3.1.9 Historic Index - A measure of the change in signal strength throughout a test.

3.1.10 Hit – Any signal that exceeds the threshold and causes a system channel to accumulate data (ASTM E 1316).

3.1.11 Hit Definition Time - A specified time interval defining the end of a hit during which no additional threshold crossings occur. The hit definition time is measured from the last threshold crossing of the hit. The first threshold crossing following the hit definition time is part of the next hit.

3.1.12 Hit Duration (Duration) - The time from the first threshold crossing to the last threshold crossing of the signal or envelope of the linear voltage time signal. Hit duration does not include the hit definition time at the end of a hit.

3.1.13 MARSE - Measured area of the rectified signal envelope (ASME Code, Section V, Article 12). A measurement of the area under the envelope of the rectified linear voltage time signal from the sensor.

3.1.14 Nonrelevant Indication – An NDT indication that is caused by a condition or type of discontinuity that is not rejectable. False indications are nonrelevant (ASTM 1316).

3.1.15 Processor - A circuit that analyzes the AE waveform as required in Section 7.4.

3.1.16 Rearm Time - An interval following acquisition of a hit during which a channel is unable to accept additional data.

3.1.17 Signal Amplitude, Acoustic Emission - The peak voltage of the largest excursion attained by the signal waveform from an emission event (ASTM E 1316). For purposes of this procedure signal amplitude shall be measured in decibels.

3.1.18 Signal Strength - Area under the envelope of the linear voltage time signal from the sensor. The signal strength will normally include the absolute area of both the positive and negative envelopes. For purposes of this procedure, MARSE is used as a relative measure of signal strength.

3.1.19 Simulated Acoustic Emission Source - A device that can repeatably induce a transient elastic stress wave into the structure.

3.1.20 Time of Arrival – The time of a specified point on an AE signal. The specified point may differ for different instruments and different source location analysis methods. Example specifications are the first threshold crossing and the time at peak amplitude.

3.1.21 Voltage Threshold (Threshold) - A voltage level on an electronic comparator such that signals with amplitudes larger than this level will be recognized (ASTM E 1316).

3.1.21.1 Test Threshold - The threshold setting for monitoring conducted according to this procedure.

3.1.22 Zone - The area surrounding a sensor from which AE can be detected and from which AE will strike the sensor before striking any other sensors.

CHAPTER 4 - SUMMARY OF METHOD

4.1 **General** - The method consists of subjecting prestressed concrete girders to normal traffic loads and monitoring with sensors capable of detecting acoustic emission (transient stress waves) caused by overstressed regions of the girder. Acoustic emission is generated by microcracking, crack initiation and or growth, closing of cracks, strand slippage, and yielding and breakage of strands.

4.2 **Structural Integrity Evaluation** - This procedure provides guidelines to determine the location and significance of structural flaws. Evaluation criteria provide a basis to assess the structural integrity of the equipment.

4.3 **Data Evaluation** - Data evaluation is on a per channel basis and is based on Felicity ratio and large amplitude hits. For Felicity ratio calculations, onset of significant emission is based on historic index. Data are recorded continuously. Specific evaluation criteria and analysis methods are given in Chapter 12.

CHAPTER 5 - PERSONNEL QUALIFICATION

5.1 **Personnel** - Personnel performing acoustic emission testing of prestressed concrete girders (inspector) are required to attend a dedicated training course, pass a written examination, and have the recommended experience level. The training course shall be appropriate for specific NDT Level II qualification according to Recommended Practice No. SNT-TC-1A of the American Society for Nondestructive Testing, and should include as a minimum the following general topics:

1. Basic technology and terminology of acoustic emission.
2. Acoustic emission instrumentation.
3. Instrument checkout.
4. Characteristics of background noise and nonrelevant emission.
5. Data collection and interpretation.
6. Data analysis including historic index calculations.

The inspector shall be familiar with the construction of prestressed concrete beams, failure mechanisms, and the provisions of this procedure. The experience level shall be that recommended by SNT-TC-1A for Level II certification in acoustic emission.

CHAPTER 6 - SIGNIFICANCE

6.1 **General** – This procedure detects overstressed regions in prestressed concrete girders. The overstress can occur because the structure is overloaded, or because the structure has degraded and can no longer carry the traffic and other loads with an adequate margin of safety. Common types of degradation are distributed cracking caused by alkali-silica reaction or delayed ettringite formation. Among the mechanisms that generate emissions are: cracking of the cement matrix and aggregates; crushing of the cement matrix and aggregates; breakage of the bond between the aggregate and cement matrix; failure of the bond between the prestressing strand and the concrete; yielding of the prestressing strand; and failure of the prestressing strand.

6.2 **Applicability** - Experimental and theoretical studies have been performed on prestressed concrete girders as part of a six year research project that led to development of this procedure[2,3,4]. AASHTO Type I girders with a 6.5 inch thick cast-in-place concrete slab were tested in shear and flexure. The compressive strength of the concrete slabs varied from 5,000 psi to 15,000 psi. Shear and flexure tests were performed on I-shaped Type C girders and on hollow box girders that showed distributed cracking due to alkali-silica reaction and delayed ettringite formation.

6.3 **Continuous Monitoring** – This procedure is suitable for continuous monitoring of in-service girders under normal traffic loads. Usually, application of the procedure will not result in traffic disruption.

6.4 **Follow-up** – Overstressed regions of the girder detected by AE should be examined on the basis of the significance of emission. Other nondestructive examination techniques, repair, and retest may be required. Recommendations for repair and examination by other nondestructive test methods are outside the scope of this procedure.

---

[2] Yepez Roca, Luis Octavio, "Acoustic Emission Examination of High Strength Prestressed Concrete Girders", Thesis, Master of Science in Engineering, The University of Texas at Austin, August 1997.

[3] Tinkey, Brian Victor, "Nondestructive Testing of Prestressed Bridge Girders with Distributed Damage", Thesis, Master of Science in Engineering, The University of Texas at Austin, May 2000.

[4] Piya, Chotickai, "Acoustic Emission Monitoring of Prestressed Bridge Girders with Premature Concrete Deterioration", Thesis, Master of Science in Engineering, The University of Texas at Austin, May 2001.

CHAPTER 7 - INSTRUMENTATION

7.1 **General** - The AE instrumentation consists of sensors, electronic signal processing and recording equipment, together with digital hardware and software for analyzing and displaying data in accordance with the provisions of this procedure.

7.2 **Sensors** – Sensors shall have a resonant response centered on 150 kHz. Each sensor shall utilize preamplifier circuitry that includes a band pass filter centered on the resonant peak and shielded against electromagnetic (EMI) and radio frequency interference (RFI). Integral sensors incorporate the sensor and preamplifier in the same shielded casing. As a result, they are very effective at rejecting EMI and RFI and are required for this application. Sensors shall be temperature-stable over the range of intended use, and shall not exhibit sensitivity changes greater than guaranteed by the manufacturer over this range. Sensors shall have omnidirectional response, with variations not exceeding 2 dB from the peak response. Minimum sensitivity shall be -80 dB referred to 1 volt per microbar, determined by face-to-face ultrasonic calibration. This method measures relative sensitivity of the sensor. AE sensors used in the same test shall not vary in peak sensitivity by more than 3 dB from the average. If the preamplifier is of differential design, a minimum of 40 dB of common-mode noise rejection shall be provided. The unfiltered frequency response shall not vary more than 3 dB over the operating frequency and temperature range of the sensors, filters, and preamplifiers.

7.2.1 **Teed Sensors** - Sensors shall not be teed (commoned) into a single channel.

7.2.2 **Filters** – Band pass filters shall be located in the preamplifier, or may be integrated into the component design of the sensor and preamplifier. Additional filters shall incorporated into the processor. Characteristics of these filters are specified in Paragraph 7.8.

7.3 **Power Signal Cable** - The cable providing power to the preamplifier and conducting the amplified signal to the main processor shall be shielded against electromagnetic noise. Signal loss shall be less than 1 dB per 100 ft of cable length. The cable length shall not exceed five hundred feet.

7.4 **Data Processor, Measurement, and Recording** - The main processor(s) shall have processing circuits through which sensor data will be processed. If used, the main amplifier shall have signal response with variations not exceeding 3 dB over the frequency range of 100 to 200 kHz, and temperature range of 0 to 140°F. The instrumentation shall measure and record data by channel number. The following parameters for each hit shall be measured and recorded within the specified frequency range:

- Hit arrival time.
- Hit duration.
- Peak amplitude.
- Signal strength or MARSE.
- Relative load.

Details and accuracy of data measurement shall be as specified in below. The instrument shall store the year, month, day, hour, and minute of the start of each data file as part of the test record. The maximum relative load for each of the past 30 days shall be recorded and stored.

7.4.1 **Data Analysis Threshold** – A fixed threshold shall be used and shall be set according to the procedure given in Paragraph A.2.1. For most instruments, the threshold will be 55 dB.

7.4.2 **Number of Channels** - The data acquisition system shall have the minimum number of channels necessary to provide coverage of the primary region(s) of interest, and sufficient guard channels to prevent background noise contaminating the relevant data. Separate instruments can be used to monitor different regions of interest on the same girder.

7.4.3 **Arrival Time** - Hit arrival time shall be recorded globally by channel to an accuracy of 500 nanoseconds and shall be based on the peak amplitude.

7.4.4 **Hit Duration** - Hit duration shall be accurate to +/-5 microseconds.

7.4.5 **Peak Amplitude Detection** - Amplitude shall be measured in decibels referenced to 0dB as 1 μV at the preamplifier input. Comparative calibration must be established per the requirements of Appendix A. Usable dynamic range shall be a minimum of 45 dB with 1 dB resolution over the frequency band of 100 to 200 kHz, and the temperature range of 0° to 140° F. Not more than 2 dB variation in peak detection accuracy shall be allowed over the stated temperature range. Amplitude values shall be stated in dB, and must be referenced to a fixed gain output of the system (sensor or preamplifier).

7.4.6 **Signal Strength or MARSE** - Signal strength or MARSE shall have a resolution of 1% of the value obtained from a one millisecond duration, 150 kHz pulse having an amplitude 15 dB above the data analysis threshold. Useable dynamic range shall be a minimum of 35 dB. Relative values of signal strength given in Table A.4 shall be accurate to ±5%.

7.4.7 **Data Acquisition Rate** - The instrumentation shall be capable of measuring and recording data at a minimum rate of 200 hits per second. This rate shall apply to the entire instrument, regardless of the number of channels and the distribution of hits between channels.

7.4.8 Rearm Time - Individual channel rearm times are permitted under this procedure. If used, the rearm time shall commence immediately following the end of the hit definition time. The rearm time shall apply only to the channel that detected the hit, and shall not affect other channels. The rearm time shall be as small as possible, but not greater than 200 microseconds.

7.4.9 Hit Definition Time - The hit definition time shall be 400 microseconds.

7.5 Relative Load – A relative measure of the load applied to the structure must be continuously monitored during the monitoring period and recorded as part of the data record for each hit. The load will generally be the normal traffic load. In certain circumstances, such as during a follow-up test when AE has indicated an overstress condition, it may be desirable to apply a known load at a controlled rate. The relative load can be based on a measurement of strain, displacement, or acceleration in the region of interest. The load measurement shall be supplied to the instrument in the form of a DC current. As specified in Paragraph 7.4, the daily maximum relative load shall be recorded and stored for Felicity ratio calculations.

7.6 Front End Filters - Band pass filters of the type defined in Paragraph 7.8 shall be used. Guard sensors are also required. No other front end filters shall be used. Data from all hits having amplitude greater than the test threshold shall be recorded as defined in paragraph 7.4.

7.7 Guard Sensors – Guard sensors shall be used to eliminate background traffic noise from the data. Guard sensors shall be controlled by the instrument hardware with real time rejection of nonrelevant emission. Arrangement and set-up of the guard sensors is detailed in Paragraph 9.3.

7.8 Filters - Additional filters shall be incorporated into the processor to limit frequency range and thereby EMI and RFI. The combination of sensor/preamplifier and processor filters shall be of the band pass type, and shall provide a minimum of 24dB/octave signal attenuation. Filters and/or integral design characteristics shall ensure that the principal processing frequency from the sensors is in the range of 100 to 200 kHz.

7.9 Power Supply – Provision must be made for a stable power supply. For remote monitoring, this may require internal batteries operating in combination with an external source. The instrument shall retain data records in the event of a power failure.

7.10 Real Time Data Analysis - The instrumentation shall be capable of providing the following real time or near real time analyses:

7.10.1 Previous Maximum Relative Load – The maximum relative load for each day of the past thirty days is required for Felicity ratio determination. This value shall be updated once per day.

7.10.2 Onset of Significant Acoustic Emission – The historic index shall be calculated for each hit according to the procedure given in Paragraph 12.4.1. As defined in Paragraph 12.4.1, the onset of significant emission occurs when the historic index exceeds 1.85. Once this value is exceeded, it shall be assumed that significant emission continues to occur until the historic index again falls to 1.85 or less.

7.10.3 Felicity Ratio – If significant emission is detected, the relative load corresponding to the onset of significant emission shall be divided by the maximum relative load during the previous thirty days to determine the Felicity ratio. The Felicity ratio shall be determined for each new onset of acoustic emission.

7.10.4 Analysis Records - The AE instrument shall record the value of Felicity ratio, global time, previous maximum relative load, and the relative load corresponding to each onset of significant emission. The global time shall be recorded to an accuracy of one second.

7.11 Post-test Data Analysis - Provision shall be included for downloading the data to an IBM format personal computer (PC) for playback, display, post-test filtering, analysis, and permanent storage. PC software to accomplishing these functions shall be available.

7.12 Performance Requirements, Calibration, and Verification - The AE instrumentation shall meet the performance requirements specified in Paragraph 7.4. Calibration shall be in accordance with these requirements and the calibration values defined in Mandatory Appendix A. Calibration and instrument verification shall be as follows:

- A complete calibration at intervals not exceeding one year.
- Instrument users shall develop and document an instrument and sensor verification technique that shall be performed at three month intervals. Pencil lead breaks are a commonly used technique. A portable acrylic rod has been found to provide a satisfactory method of checking the channel sensitivity and the performance of sensors that will be installed. Additional information is given in ASTM E 2075. ASTM E 976 is a standard guide for determining the reproducibility of sensor response.
- Permanent copies of the document certifying the date of the most recent calibration and instrument verification shall be provided to the Texas Department of Transportation.

CHAPTER 8 - TEST PREPARATION AND DATA ACQUISITION

8.1 Preliminary Information - Prior to setting up the test instruments, the inspector shall be furnished with the following information.

- Girder configuration. In most instances this information can be obtained by visually examining the girder or by reviewing the drawings.
- Date of manufacture, installation, and operation, together with any unique operating conditions.
- Test History. Previous visual inspection and acoustic emission examination results.

8.2 Safety - All safety requirements unique to the test location shall be met.

8.3 Environmental – It may be necessary to suspend monitoring if the ambient temperature falls below 32°F (0°C) and ice builds up on the structure. Ice will act as a source of emission.

8.4 Background Noise - It is important to capture real emissions during data monitoring periods. In order to accomplish this, background noise must be at a minimum. Prior to a test, the inspector shall review the test site to identify all potential sources of extraneous acoustic noise. The following paragraphs identify some frequently encountered sources of background noise.

8.4.1 EMI and RFI - Field experience has shown that care should be exercised in dealing with electrical background noise sources; for example, EMI is usually due to motors, switch gear, solenoids, and the like. It can also be caused by a bad power supply, particularly an inadequate ground. RFI can be distinguished from EMI with an oscilloscope and correlation plot. Design and shielding of sensors, and/or narrow band filters, can control both RFI and EMI. Power source EMI can be controlled with a constant voltage supply unit.

8.4.2 Wind and Vibration - Visually examine the sensors and other hardware to verify that the equipment is securely mounted and will not be subject to wind or vibration induced movement.

8.4.3 External Noise - Uncontrolled noise caused by rain, sleet, hail, snow, wind blown particles, air hoses, air horns, blasting, etc., shall be evaluated. Where practical, sensors shall be acoustically isolated from air borne noise sources. In some cases it may be necessary to suspend monitoring until weather conditions change. The United States Department of Transportation is sponsoring two Small Business Incentive Research projects on acoustic emission monitoring. The technology developed by these projects may be suitable for dealing with background noise from rain and other weather related sources.

8.5 Data Acquisition and Data Quality - Acquisition of genuine, valid, acoustic emission is essential to the success of the acoustic emission examination. In order to acquire consistent accurate data the following actions shall be carried out:

- Use the procedures given in Chapter 10 to thoroughly check the instrumentation performance immediately prior to the start of monitoring, after a long delay, and after completion of monitoring.
- Conduct a background noise monitoring check before each load application, as required by section 11.2, to ensure that a source of extraneous noise is not present during the test.
- Periodically monitor the performance of the instrumentation during the test.
- Periodically monitor the data during the test to note possible extraneous noise and to ensure that nonrelevant emission, such as that generated by an internal instrument malfunction, or EMI, does not contaminate the data. Refer to Section 12.2 for techniques that can be used to evaluate data quality during the course of the test.

8.6 Test Log - The inspector shall maintain a test log recording data file names, test times, and other significant test occurrences.

CHAPTER 9 – SENSOR MOUNTING AND LOCATION

9.1 **General** – In order to obtain consistent AE data sensors must be securely mounted and coupled to the girder. Sensor mounting is discussed in Section 9.2. The sensors shall be placed with a couplant between the sensor face and the concrete surface. All signal cables must be constrained to prevent stressing the sensor or loss of coupling and to avoid extraneous noise from wind induced movement of the sensors and cables.

9.2 **Mounting** - ASTM E 650 provides guidance for mounting sensors. Acceptable types of couplant are given in Paragraph 9.2.2. Care must be exercised to assure that adequate couplant is applied. The preferred method of securing sensors in place is shown in Figure 9.2. The surface of concrete tends to be rough with dust and loose particles. Accordingly, it is difficult to attach sensors and hold-downs. Duct tape is unsatisfactory, and attaching the sensors directly to the concrete surface with glue does not work well. The spring steel hold-down shown in Figure 9.2 maintains a continuous pressure on the sensor. The hold-down is one inch wide and each attachment tab should be approximately 2" long. The large glued area with a thick glue line seems to work best. Hot melt glue has been found to provide a satisfactory long lasting bond. Couplant loss shall be checked per the procedures described in paragraph 10.2.

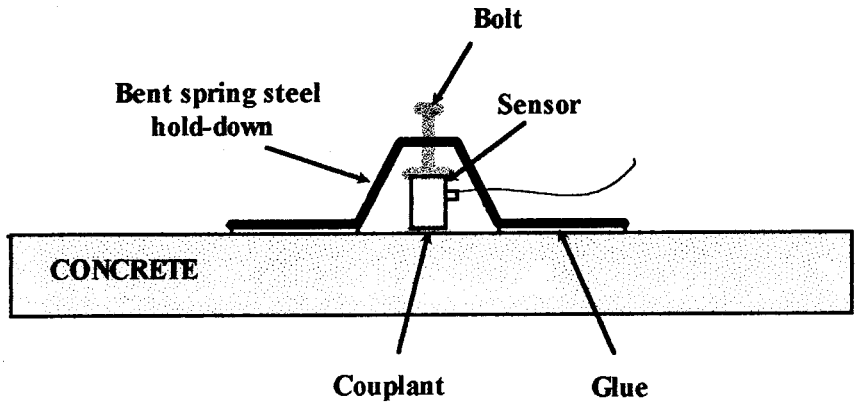

Figure 9.2 – Recommended Method for Attaching Sensors to Concrete.

9.2.1 **Surface Contact** - The sensor shall be mounted with the center of the sensor face directly coupled to the surface of the girder. Reliable coupling between the sensor and concrete surface must be assured and the surface in contact with the sensor face must be clean and free of particulate matter. Certain types of paint or coatings, geometric discontinuities, and surface roughness can cause signal loss.

The magnitude of this type of signal loss shall be checked using the procedure defined in Paragraph 10.2. In certain cases, it may be necessary to reduce signal loss by locally removing paint from the surface of the girder.

9.2.2 **Couplant** - Commercially available couplants for ultrasonic flaw detection may be used. Silicone based stopcock grease has been found to be particularly suitable. Couplant selection should minimize changes in coupling sensitivity during a test. Consideration should be given to the length of the monitoring period and to the expected ambient temperature at the site.

9.3 **Sensor Locations** – The primary consideration in choosing sensor locations is the need to detect structural defects in regions of the girder that exhibit premature concrete deterioration, or in regions of concern identified by an authorized representative of the Texas Department of Transportation. Figure 9.3 illustrates the basic scheme for monitoring the designated regions. The hatched area is the surface representation of the region to be monitored. This is termed the area of interest. The primary sensors acquire data from this region. The guard sensors are arranged around the area of interest to detect nonrelevant emission originating outside the monitoring zone. The perpendicular bisectors of the lines between the primary sensors and the adjacent guard sensors define the boundary of the area of interest. If a guard sensor detects a "first hit", the hardware shall suspend data acquisition of the primary sensors for sufficient time to allow the stress wave to pass the primary sensor. The guard sensors are used to reject data and do not participate in the measurement function. The lockout time for the guard sensors shall be the time for a pencil break induced stress wave to travel from the guard sensor to the primary sensor plus 50%. As discussed in Paragraph 10.4, the efficacy of the guard sensors shall be checked during the system performance check.

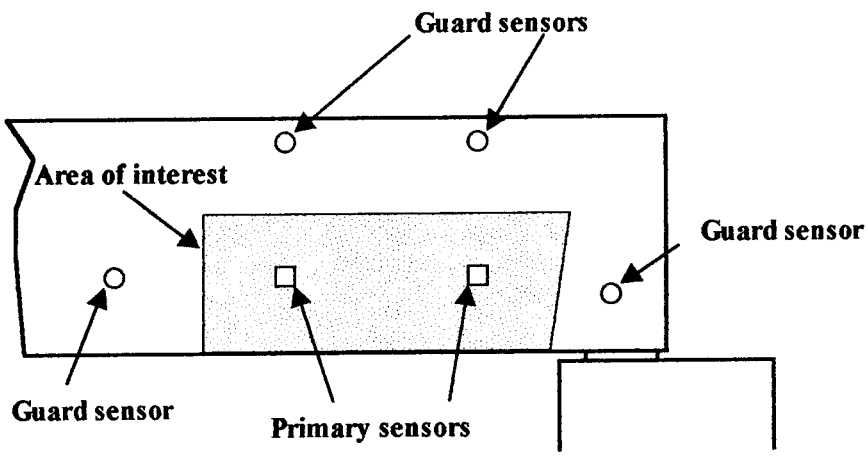

Figure 9.4 – Primary and Guard Sensors

9.4 **Sensor Spacing** - Sensors shall be spaced such that a 0.5 mm mechanical pencil (2H) leads broken on the surface of the concrete within the area of interest is detected by one of the primary sensors. All lead breaks shall be done at an angle of approximately 30 degrees to the concrete surface with a 2.5 mm lead extension. The maximum distance between primary sensors shall be 24 inches.

CHAPTER 10 – INSTRUMENTATION SETTINGS AND PERFORMANCE CHECK

10.1 Channel Sensitivity – Hsu pencil lead breaks are used as the primary technique for assuring channel sensitivity (ASTM E 976). With this technique, 0.5 mm (2H) pencil leads are broken at an angle of approximately 30° to the test surface with a 0.1 inch (2.5 mm) extension. Prior to testing three breaks shall be made at the same distance from each sensor. The average peak amplitude shall meet the provisions of paragraph 10.2 and shall not vary more than 4 dB from the average of all sensors. Any channel failing this check shall be investigated and replaced or repaired as necessary. The channel shall be rechecked with three more lead breaks and the new data used in place of the data from the defective channel. The average peak amplitude of the entire data set shall be recalculated to check that all channels meet the ±4 dB criterion. These data shall be recorded and retained with the examination record.

10.2 Coupling Loss - Signal loss between the sensor and concrete surface shall be determined by comparing data obtained from pencil breaks with the data shown in Table 10.2. Amplitude values shall be not less than those shown in the table.

Table 10.2 – Minimum Average Amplitude of Pencil Breaks

Distance of Break from Sensor	Minimum Amplitude, dB
Next to sensor	70
6 inches	58

10.3 Primary and Guard Sensors – The efficacy of the guard sensor arrangement and the ability of the primary sensors to detect emission from the area of interest shall be checked with random pencil breaks in the area bounded by the guard sensors. At least five breaks shall be within the area of interest, and at least five shall be outside.

10.4 Circuit Continuity Verification - All sensor/channel combinations shall be checked at intervals not exceeding one month and at the end of the monitoring period using the pencil lead break technique. The purpose of this verification is to check that all sensors are functioning and in contact with the concrete. Channels that do not respond to the pencil break or have low sensitivity during the monitoring period shall be repaired or replaced. Channels that do not respond to the lead break or have low sensitivity after the monitoring period shall be noted in the test report.

CHAPTER 11 – LOADING AND BACKGROUND NOISE

11.1 **General** – As defined in Paragraph 7.5, the loading shall be by traffic and the relative value recorded with each AE hit.

11.2 **Background Noise Monitoring** – A monitoring period for background noise is required before each acoustic emission inspection. This period shall be one hour. Sources of background or extraneous noise must be identified and minimized. Types of background noise are discussed in Section 8.4. If the inspector judges background noise to be excessive, either before or during the monitoring period, the AE test shall be terminated. "Excessive" background noise either before or during the test is a matter of judgement based on experience.

CHAPTER 12 - INTERPRETATION OF RESULTS

12.1 General - Analysis of the test data shall be performed real time, or near real time by the monitoring instrument. A data quality analysis according to the procedures given in Paragraph 12.2 shall be conducted if an emission category of "warning" or "serious" is reported. This shall be followed by post-test analysis of the data to confirm these indications. If required, post-test filtering shall be performed as detailed in section 12.3. Structural evaluation procedures are given in section 12.4. Felicity ratio per channel is used to determine emission categories defining the structural significance of an indication.

12.2 Data Quality Analysis - ASTM E 1316 states that an indication is subject to interpretation as false, nonrelevant, or relevant. In order to make this interpretation, the emission characteristics shall be examined to determine if data from nonrelevant sources are included in the data set and that genuine AE hits have been recorded. This examination should include a review of data correlation plots, graphs, and data listing. Other sources shall be reviewed (weather bureau records, accident records, etc.) to determine if any unusual occurrences or background noise were present at any time during the test. In the analysis of the test data, background noise shall be properly discounted. Post-test filtering shall be used to eliminate nonrelevant data.

12.3 Post-test Filters - Post-test filters are used to remove non-genuine data that may give a false or nonrelevant indication (ASTM E 1316), or extraneous noise.

12.3.1 Time Filters – A time filter is used to eliminate bursts of extraneous noise such as caused by wind gusts, rain and impacts.

12.3.2 Channel Filter - Many noise sources, such as faulty instrumentation, will affect only one or two channels. All hits on the channel(s) showing a response to an external noise source must be removed from the data set for the period of the noise.

12.4 Structural Evaluation – The acoustic emission categories given in Table 12.4a define evaluation criteria that shall be used to determine the significance of the indication. The criteria are based on Felicity ratio for each channel and shall be applied in turn to the data recorded by each channel. The emission must satisfy both criteria in order to be classified in a particular category. The evaluation shall be based on the minimum Felicity ratio recorded during the monitoring period. If no emission is recorded, no category is assigned.

Table 12.4a – Acoustic Emission Categories and Evaluation Criteria

Evaluation Criteria	Emission Category					
	All Regions of the Girder		Flexure-Dominated Region		Shear-Dominated Region	
	Not Significant	Minor	Warning	Serious	Warning	Serious
Felicity ratio	Not Measurable	Measur -able	≤0.95	≤0.60	≤0.90	≤0.60
Maximum amplitude during loading	≥Threshold	≥75	≥75	≥75	≥75	≥75

12.4.1 Onset of Significant Emission – The Felicity ratio is defined as the ratio of the load at onset of significant emission to the previously applied maximum load. Under this procedure, onset of significant emission is defined by a historic index greater than 1.85. Historic index calculations shall be limited to the last 2000 hits recorded on a channel. The historic index is defined by the following equation.

$$H(t) = \frac{N}{N-K} \frac{\sum_{i=K+1}^{i=N} S_{Oi}}{\sum_{i=1}^{i=N} S_{Oi}}$$

Where:

H(t) is the historic index at time *t*.
N is the number of hits (ordered by time) up to and including time *t*.
S_{Oi} is the signal strength of the *ith* hit.
K is an empirically derived factor that varies with the number of hits. Values for K are given in Table 12.4b.

Table 12.4b – K Values to be used for Historic Index Analysis

Number of Hits	K
<50	Not Applicable
50-200	N-30
201-500	0.85N
500-2000	N-35

12.4.2 Significance of Indication – The significance of the emission categories defined in Table 12.4a are given in Table 12.4c.

Table 12.4c – Structural Significance of AE Categories

Category	Structural Significance
None	None
Minor	Minor indication, note for future tests. No further action required.
Warning	Follow-up inspection and evaluation required. Repair may be necessary.
Serious	Indication of significant structural deterioration. Inspection and repair shall be performed. It may be necessary to remove the girder from service.

CHAPTER 13 – TEST REPORT

13.1 Requirement - A test report shall be issued for each concrete girder tested.

13.2 Content - A test report shall include but not be limited to the following:

1. Complete identification and description of the girder tested. This is to include the location of the test site, the designation of the girder, and the girder type.

2. Sketch showing sensor locations and numbers.

3. Structural evaluation based on the acoustic emission data and analysis method specified in Chapter 12. Defect areas can be marked on the sensor location sketch.

4. Recommendations for follow-up action.

5. Emission categories, Felicity ratio, and maximum amplitudes for each occurrence of significant emission from the monitored region(s).

6. Data recorded during the instrumentation settings and performance check specified in Chapter 10

7. Any unusual effects or observations during or prior to monitoring.

8. Period of monitoring.

9. A description of the AE instrumentation, including manufacturer's name, model number, and sensor type.

10. Dates of most the recent calibration and instrument verification.

11. Test organization and name(s) of inspector(s).

MANDATORY APPENDIX A - INSTRUMENT CALIBRATION

A.1 **General** - The performance and threshold definitions vary for different types of acoustic emission instrumentation. Parameters such as signal strength and amplitude vary from manufacturer to manufacturer and from model to model by the same manufacturer. This appendix describes techniques for generating common baseline levels for the different types of instrumentation. The amplitude decibel values are for a typical piezoelectric crystal using the measurement scale specified in Paragraph 7.7.4. Signal strength values are typical MARSE values measured in Volt-seconds multiplied by 10^5. The procedures defined in this appendix are intended for baseline instrument calibration at 60 to 80° F. Instrument manufactures are permitted to use other procedures consistent with ASTM Standards, industry practice, and written in-house practices. Procedures used by instrument manufacturers must be shown to provide threshold, amplitude, and signal strength values that can be directly related to the values obtained by use of this appendix. It is recommended that instrument users develop approximate calibration techniques, along the lines outlined in this appendix. For field use, a portable acrylic rod can be carried with the equipment and used for periodic checking of sensor, preamplifier, and channel sensitivity.

A.2 **Data Analysis Threshold** - The data analysis threshold shall be determined using a 1 foot x 10 foot x 1/2 inch, 99% pure lead sheet suspended clear of the floor with the long side parallel to the floor. The data analysis threshold is defined as the average measured amplitude of 10 hits generated by a 0.3 mm pencil lead (2H) break at a distance of 27 inches from the sensor. Each break shall be done at an angle of approximately 30 degrees to the test surface with a 0.1 in lead extension. The sensor shall be mounted 12 inches from the end of the sheet and mid-distance between the 10 foot sides of the sheet. The sensor may be mounted using duct tape tightly wrapped around the backside of the sheet to firmly hold the sensor against the lead sheet. Silicone based stopcock grease shall be applied between the face of the sensor and the lead sheet. Based on the calibration procedure given in this paragraph the data analysis threshold for most instruments is 55 dB.

A.3 **Decibel Calibration** - Instruments shall be calibrated using the 1 foot x 10 feet x 2 inches, 99% pure lead sheet. Decibel values shall be determined as the average measured amplitude of ten hits generated by a 0.3 mm (2H) pencil lead break at the distances shown in the table below. Each pencil lead break shall be done at an angle of approximately 30 degrees to the lead sheet surface with a 0.1 in lead extension from the pencil. Typical decibel values are given in Table A.3.

Table A.3 – Decibel Calibration Values

Distance of Pencil Break from Sensor	Typical Decibel Value
6' – 0"	40
5' – 0"	44
4' – 0"	48
3' – 0"	52
2' – 0"	56
1' – 0"	61
6"	66
4"	70

A.4 **Signal Strength Calibration (MARSE)** - The signal strength calibration values given in Table A.4 shall be confirmed electronically with a constant amplitude 150 kHz pulse of 1 millisecond duration input to each channel. The evaluation criteria given in Section 12.4 are based on these values. Signal strength calibration values may vary between instruments, but should maintain the same relative values as listed in the table.

Table A.4 - Signal Strength Calibration Values

Amplitude of Input Signal [1,2], dB	Typical Signal Strength[3] Calibration Value, V-sec x 10 [5]	Relative Value [4]
45	25	1.0
55	79	3.2
65	251	10
75	791	31.6

Notes:

1. See Appendix A.3 for explanation of decibel values.
2. Input signal is a constant amplitude 150 kHz pulse of 1 millisecond duration.
3. Signal strength values are typical MARSE values measured in Volt-seconds multiplied by 10^5.
4. The "Relative Value" is the ratio of the signal strength calibration value of a constant amplitude 150 kHz pulse of 1 millisecond duration with a given amplitude (dB) to the signal strength calibration value of a constant amplitude 150 kHz pulse of 1 millisecond duration with an amplitude 5dB above the data analysis threshold.

A.5 **Hit Duration** - The accuracy of the hit duration measurement shall be confirmed electronically with a constant amplitude 150 kHz pulse, varied from 50 to 500 microseconds duration, input to each channel. A calibrated transient waveform recorder shall be used to confirm the time duration of the input pulse.